Int J CARS (2018) 13 (Suppl 1):S1–S273
https://doi.org/10.1007/s11548-018-1766-y

CARS 2018—Computer Assisted Radiology and Surgery Proceedings of the 32nd International Congress and Exhibition Berlin, Germany, June 20–23, 2018

Preface

Publishing, Reviewing and Editing Process of Extended Abstracts and Original Articles

Two of the primary functions of the International Foundation for Computer Assisted Radiology and Surgery (IFCARS) is the organization and presentation of the International Journal of Computer Assisted Radiology and Surgery (IJCARS) and the annual CARS Congress and Exhibition. Authors from all over the world submit abstracts and articles to the Journal and the Congress, so that the results of their research and studies may be shared with a larger community. For the reasons enumerated in this communication, IFCARS will be inaugurating a new activity at the 2018 CARS Congress: a Journal Club that will be organized to explore important issues relating to the process of reviewing submitted research.

The publishing, reviewing and editing process (PREP) of extended abstracts and original articles implies that a highly professional job is being carried out by all parties involved. Authors, who submit original articles and/or extended abstracts, reviewers who voluntarily agree to review and give their very valuable time to this endeavor and editors, who have signed contracts with publishers to ascertain that the result of the PREP contributes towards a high quality archival documentation of human knowledge.

Even though the three parties involved in this very demanding professional activity share the common goal of enriching human knowledge, no licensing or board exam related to their respective qualifications for being able to do so, is required. Typically, members of each party strive for and impact their learning curve through trial and error only. Whatever comes out of the PREP, however, readers rightfully expect that publications in scientific/medical journals such as IJCARS, fulfill the highest professional standard possible. This implies, in these days more than ever before, that a rigorous search and screening for sustainable truths and verified facts has preceded any publication.

Perhaps the observation made above may not be applicable to all authors, reviewers and editors alike, nevertheless, in order to assist all three parties involved in the PREP, some organizations offer guidelines and rules which are recommended by publishers as a reference for writing, reviewing and editing. The most important organizations for biomedical journals providing this guidance are:

- Council of Science Editors (CSE)
- Committee on Publication Ethics (COPE)
- International Committee of Medical Journal Editors (ICMJE)
- Directory of Open Access Journals (DOAJ)
- Open Access Scholarly Publishers Association (OASPA)
- World Association of Medical Editors (WAME)

In addition or as a complement, some editors, reviewers and authors of medical journals, including those involved in IJCARS, built up their own list of points to be observed in the PREP (I have compiled some 30+ items of such a list over a lengthy period of time as an author, reviewer and editor, see below). For the benefit of all actors involved in the PREP, there is a need to expose and exchange views on questions and answers relating to the PREP. In order to provide a platform for such a forum, the program of CARS 2018 includes, for the first time, a "Journal Club" which is open to all interested parties in the PREP.

A possible checklist of frequent issues for authors, reviewers and editors to consider for extended abstracts and original articles in the PREP for a peer-reviewed journal such as IJCARS, could be (not in order of importance):

Positive attributes	Potential pitfalls
1. Appropriate scope for IJCARS	1. Out of scope of IJCARS
2. Unique or substantial/transformational innovation; Innovative Clinical Investigations (ICI)	2. No unique or substantial/transformational innovation
3. Topic of wide appeal or application	3. Only of clinical and/or radiological/surgical relevance
4. Research at appropriate stage of development	4. Relatively early stage of development; Submission has the status of a "PROPOSED" work
5. Application/evaluation of standard or open-source software/systems	5. Proprietary; commercial product oriented
6. Technology—general, widespread, available	6. Technical, too specific

7. Appropriate content and organization	7. Overall length of manuscript, figures, tables, references, keywords, citations, captions, etc. are inappropriate; Inappropriate structure and/or sections in manuscript
8. Abstract or article is well-written and easily understood	8. English language issues and style of writing

Review process	Major problems
1. arXiv issues	1. Authorship issues
2. Review article issues	2. Salami slicing/partitioning of publications
3. Corrections in production and in proof reading	3. Double publication
4. Title and/or abstract need revision	4. Re-submission of rejected manuscript
5. Authors do not respond to reviewers comments	5. Under consideration for publication elsewhere
6. Biases and de-biasing	6. Fabricated data and enquiries
7. Statistical methods and their application domains	7. Plagiarism in manuscript
–FOL, deduction, abduction and induction	
–Frequency and Bayesian statistics	
–V^2E and statistical significance	

This relatively specific list may easily be augmented by other more overarching considerations such as:

Overarching considerations
• Conflict of interest
• Conflicting reviews
• Confidentiality issues
• Bibliometrics (e.g. citation indices, impact factor)
• Populistic and/or political correctness comments
• Editorial process structure and timing issues,
• Predatory Journals
• Retraction watch

There are a number of international initiatives which have made it their objective to assist in the reporting and assessment activities of innovative health care technologies, similar to those which are being developed in the context of CARS. These initiatives also try to provide frameworks (e.g. protocol design and validation methods) for assisting investigators and authors in their publication endeavors. One of the main organization which falls into this category is the IDEAL Collaboration [1].

The IDEAL Collaboration is an UK initiative which developed a framework for the different stages in innovation in surgery or other interventional procedures defined as Idea, Development, Exploration, Assessment and Long-term study (IDEAL). The purpose of IDEAL is to improve the quality of research by emphasizing on appropriate methods, transparency of data and rigorous reporting of outcomes. Applying a formal method such as IDEAL to IJCARS publishing activities, the Idea, Development and Exploration stages in IDEAL (see Table 1) seem to provide the right framework for classifying manuscripts into the categories of work-in-progress, original technical innovations and innovative clinical investigations, respectively.

Table 1 IDEAL stages (courtesy Peter McCulloch, University of Oxford) and activities marked (within the circle) for IJCARS Extended Abstracts, Original Articles and Innovative Clinical Investigations

IDEA (Stage 1)	DEVELOPMENT (2A)	EXPLORATION (2B)	ASSESSMENT (3)	LONG TERM STUDY (4)
Initial report	"Tinkering" (rapid iterative modification)	Technique now more stable	Gaining wide acceptance	Monitoring late and rare problems, changes in use & quality of surgical performance
Innovation may be planned, accidental or forced	Small experience from one centre	Replication by others	Considered as possible replacement for current treatment	
Focus on explanation and description	Focus on technical details and feasibility	Focus on adverse effects and potential benefits	Comparison against current best practice (RCT if possible)	
		Learning curves important		
		Definition and quality parameters developed		

[1] IDEAL framework for surgical innovation 1: the idea and development stages BMJ 2013; 346 doi: https://doi.org/10.1136/bmj.f3012 (Published 18 June 2013) Cite this as: BMJ 2013; 346: f3012

For being publishable in IJCARS, the 11 different study activities suggested in the Idea, Development and Exploration stages would need to be carefully selected, defined and appropriately considered for each manuscript in the PREP. In general, there is a tendency to present publishable results from the activities in the Idea stage as abstracts in conferences. The CARS Congress may serve here as an example, by providing the possibility to publish extended abstracts in the IJCARS Supplement. Supplements in IJCARS are collections of extended abstracts or short communications that deal with related issues or topics, and are published as separate issues of the journal.

Publishable results from the Development stage typically find their way into regular or special issues of IJCARS. To be considered for being published in IJCARS as an innovative clinical investigation, manuscripts should have a focus which addresses the Exploration stage, in particular the activities "Focus on adverse effects and potential benefits", "Learning curves important" and "Definition and quality parameters development".

Manuscripts which pertain to the IDEAL stages Assessment and Longterm Study, typically belong to the domains of dedicated clinical journals and not to IJCARS.

Ordinarily, a Journal Club provides a forum for its members to review important articles on a particular subject of interest from a wide variety of sources. The CARS Journal Club will have a more focused purpose: analysis and process improvement for the PREP of material submitted to IJCARS and the CARS Congress. The Journal Club, by exploring the issues outlined above, will provide a forum for continuous quality improvement and standardization that may serve as an industry-wide roadmap for other meetings and journals. Primarily, this implies a thorough search for sustainable truths and verified facts, and an awareness of issues relating to the truth value, impact factor and publication media. Those who participate in the Journal Club will have the opportunity to help design the specific goals, activities, and functions of this unique and important endeavor.

Finally, I should like to thank all authors and reviewers for submitting and/or reviewing for IJCARS in 2018 and I hope and look forward to see some of you in the IJCARS Journal Club on 23rd June, 2018 in Berlin.

Heinz U. Lemke
Berlin, June 2018

Computer Assisted Radiology—32nd International Congress and Exhibition

Chairman: Ulrich Bick, MD (D)

Towards online surgical margin assessment using micro-CT

J. Nijkamp[1], L. Ploeger[2]
[1]NKI-AvL, Surgery, Amsterdam, Netherlands
[2]NKI-AvL, Radiation Oncology, Amsterdam, Netherlands

Keywords Breast surgery · Resection margin · MicroCT · Reconstruction

Purpose
Breast conserving surgery (BCS) is the cornerstone of breast cancer treatment. An essential quality indicator for BCS is the surgical resection margin, which unfortunately is positive in 10–30% of cases, and is not known until several days after surgery. If we could assess the margin in an online setting while the patient is still on the OR table, the resection could be extended when needed during the same procedure. Several technologies, e.g. frozen section and cytology were developed for intraoperative margin assessment (IMA). Unfortunately, all have failed to penetrate routine practice due to limitations, slow reporting times, low accuracy, and complex logistics [1]. An IMA technology gaining attention recently is micro-computed tomography (μCT) [2]. With μCT the entire lumpectomy specimen is scanned, allowing 3D analysis of the entire margin. State of the art systems take approximately 8 min to acquire the data and another 4 min for reconstruction. Image quality is highly influenced by metal implants in the tumour, which are often present as markers for biopsy locations, or as guides for the surgeon (wire-guides or radioactive seeds). In this study we aimed to reduce the reconstruction time by implementing inline-reconstruction, and to improve the image quality by removing the metal implants from the projection images before reconstruction.

Methods
Images were acquired with a Bruker Skyscan® 1275 (Bruker, Kontich, Belgium). All specimens were scanned at 50 kV, 200 mA, using 1 mm Aluminium filter and step-and-shoot acquisition of 901 projection images at 0.4° spacing (470 s scan time). The detector has 1944×1536 pixels, with 75 μm pixels, a focus detector distance of 283 mm, and images are stored in 16-bit tiff format. The focus to object distance is variable, and was between 100 and 125 mm. The μCT system comes with standard back-projection reconstruction software [3] which utilizes the GPU (nRecon), and can only be used for offline reconstruction. We implemented inline reconstruction software, which can start with back-projection calculations as soon as the first projection image is available. Calculations were done multithreaded on the CPU, implemented in C++. The main aim was to determine at which reconstruction resolution the software was fast enough to cover the acquisition speed. We started at an in-plane resolution of 512×512, increasing in steps of 64. Calculations were performed on a 64 bit Intel Xeon 3.4 GHz dual-core with six threads each with 128 GB RAM.

For metal artefact reduction the affected areas were removed from the projection images. The replacement method of the pixels was inspired on texture synthesis by non-parametric sampling [4]. The metal implant region was replaced pixel by pixel by comparing the neighbourhood of a pixel (a patch) to all possible patches in a sample region in the same image. The centre pixel of the patch in the sample region with the least squares difference with the target pixel was used to replace the pixel.

Segmentation of the implants was done using the following steps: absolute vertical and horizontal derivative filtering followed by a closing operation using a 12 voxel kernel (optimized for radioactive seeds) was added to the image to highlight the implants, followed by simple thresholding. The segmentation was expanded by 12 pixels, resulting in the target region which needed to be replaced. The sample region was determined by taking a 40 pixel expansion around the target region. The optimal patch size was empirically determined at 11×11 pixels. To assess image quality and segmentation accuracy, 3D μCT reconstructions were calculated with and without the artefact reduction, and were subsequently subtracted. The difference image was used to assess if only the metal artefacts were removed without changing the remainder of the scan. Calculations were done on a 64 bit 2.4 GHz 4-core i7 with 16 GB RAM, and calculation speed per image was evaluated.

Reconstruction and metal artefact reduction was evaluated on a dataset of 16 breast lumpectomy scans. Cases were selected on the presence of one or multiple metal objects, and the presence of naturally occurring calcifications, which needed to be preserved.

Results
Fourteen of the samples contained one radioactive iodine seed, of which five had an additional biopsy marker. One sample contained four surgical clips, and one sample contained a twist marker.

Up until a reconstruction cube of $832 \times 832 \times 704$ with 70 μm resolution and down-sampling of the projection images by a factor 2 the inline reconstruction was capable of processing the images at the acquisition speed, making the reconstruction available to the user within seconds after acquisition. At $896 \times 896 \times 768$ a 73 s delays started to appear. Besides the change in resolution, image quality of the inline reconstructions was comparable to the offline nRecon reconstructions.

In 13 of the 16 samples, the metal implants were adequately segmented. In the remaining samples (with multiple implants) there was some oversampling at regions outside of the implants. After digital removal of the metal implants it was impossible to recognize the original location of the metal implant (Fig. 1). With metal artefact reduction the implants were almost entirely removed from the reconstruction images (Fig. 2). Only the border of the implant was still visible, but streak artefacts were gone. The implementation was notably slow, ranging from 1.6 s per projection image for the smaller implants to 16 s for removal of the four surgical clips at the full 1944×1536 resolution.

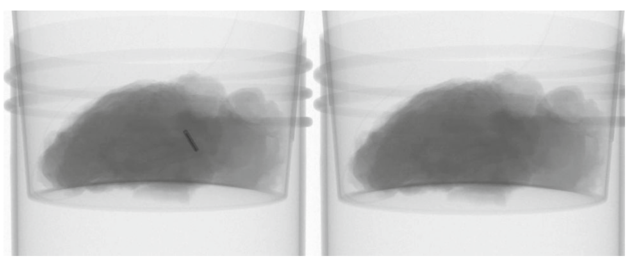

Fig. 1 Projection image of a sample (4 cm diameter) containing a radioactive iodine marker (left). The same projection image after digital removal of the iodine seed (right)

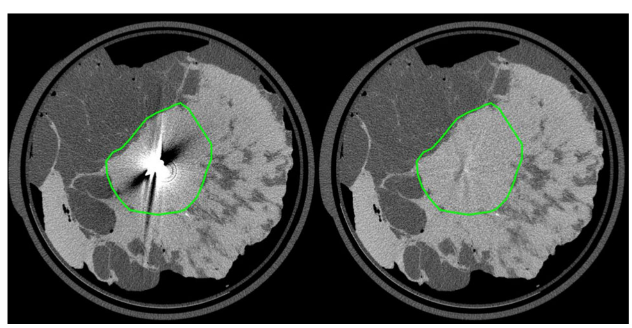

Fig. 2 Scan of a lumpectomy specimen containing a radioactive iodine seed (left). The tumour is manually outlined in green. On the right the same scan after metal artefact reduction

For one case with one implanted iodine seed the inline reconstruction and metal artefact reduction was combined. The artefact reduction was performed after downsizing the projection images. At a reconstruction cube of 512 × 512 × 448 isotropic voxels of 110 μm and a projection image downsize factor 4 it was possible to keep up with image acquisition.

Conclusion

With our inline reconstruction it is possible to provide the users with a scan with sufficient resolution several seconds after scan acquisition. The metal artefact reduction fully removes the streak artefacts from the scans, but needs further speed up to perform fast enough at a sufficient resolution. It is now possible to assess the surgical margins on a μCT within 10 min, which is clinically acceptable.

References

[1] St John ER, Al-Khudairi R, Ashrafian H, Athanasiou T, Takats Z, Hadjiminas DJ, Darzi A, Leff DR (2017) Diagnostic accuracy of intraoperative techniques for margin assessment in breast cancer surgery. Ann Surg 265(2): 300–310

[2] Tang R, Buckley JM, Fernandez L, Coopey S, Aftreth O, Michaelson J, Saksena M, Lei L, Specht M, Gadd M, Yagi Y, Rafferty E, Brachtel E, Smith BL (2013) Micro-computed tomography (micro-CT): a novel approach for intraoperative breast cancer specimen imaging. Breast Cancer Res Treat 139(2): 311–316

[3] Feldkamp LA, Davis LC, Kress JW (1984) Practical cone-beam algorithm. J Opt Soc Am A 1(6): 612

[4] Efros AA, Leung TK (1999) Texture synthesis by non-parametric sampling. IEEE Proceedings of the Seventh IEEE International Conference on Computer Vision 2

Non-iterative reconstruction based image enhancement of lung cancer screening low-dose CT using a neural network

Y. Nagaraj[1], G. van Praagh[1], D. Han[1], M. A. Heuvelmans[1], M. Rook[1], M. D. Dorrius[1], M. Oudkerk[1], P. M. A. van Ooijen[1]

[1]University of Groningen, University Medical Center Groningen, Center for Medical Imaging North East Netherlands, Groningen, Netherlands

Keywords Artificial neural network · Measurement variability · Nodule volume measurement · Low dose CT

Purpose

Every improvement made in medical imaging enables doctors to work more efficiently with their patients, ultimately leading to faster and more accurate diagnoses. Image quality improvement without sacrificing the diagnosis accuracy for low dose benefits both patients and hospitals, especially for lung cancer screening [1, 2]. Hence, a post processing software or technique which can provide a better image quality maintaining the diagnosis accuracy is needed. Recently, a non-iterative reconstruction (NIR) technique based on artificial neural network for image-enhancement was developed. The objective of this study is to perform a technical validation of the effects of NIR image-improvement technique on lung nodule volume and characterization in low dose CT including both phantom and human scans.

Methods

For the phantom study, we performed 16 phantom CT scans for a total of 45 nodules (ten nodules < 50 mm^3, 32 nodules 50–500 mm^3, three nodules > 500 mm^3). Scan protocol of low-dose CT (120 kV, 20 mAs, 0.75 mm slice thickness with pitch 1.55) was achieved using Somatom Force (Siemens Medical solutions, Erlangen, Germany). For the human study, we selected 23 nodules ($4 < 100$ mm^3, $13 < 500$–1000 mm^3, $6 > 1000$ mm^3) from 22 different scans from the Groningen cohort of a randomized lung cancer screening trial [3]. All nodules could be detected by the human eye without the help of computer-aided detection software. Scanning was performed on 16-multi-slice CT Siemens (Sensation-16, Siemens Medical solution, Forchheim, Germany) using a standard protocol [16 × 0.75 mm collimation and 15 mm table feed per rotation (pitch 1.3)]. Size of nodules in both phantom and human data was measured before and after application of NIR (Pixelshine-AlgoMedica, Palo alto, CA, USA) (Fig. 1), which is a post-processing image enhancement tool based on artificial neural network (ANN). All nodules were characterized (based on density shape and edge of nodule [4]) by three different radiologists for inter-observer variability. Each nodule volume was evaluated and measured using the same clinically available software (Aquarius INtuition, Terarecon).

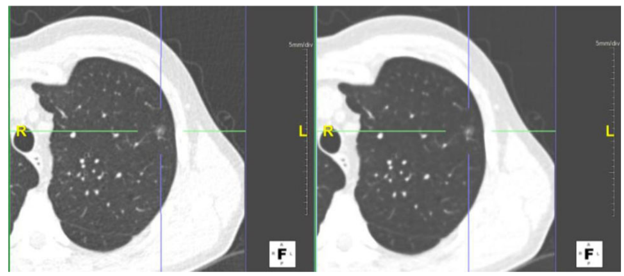

Fig. 1 A low dose CT scan of lung before and after NIR processing. The left image is from the original scan and the right one represents the NIR processed scan

Results

In the phantom scans, volumes were slightly overestimated on the low-dose original CT as compared to true physical volume ($p < 0.05$). Application of NIR significantly reduced this overestimation, as NIR processed scans showed values closer to physical volume than the measurements on the original scans. For example, in the phantom, a nodule with an actual physical volume of 72.60 mm^3 measured 77.7 mm^3 with NIR, whereas without any processing the volume measured 79.10 mm^3. There was no significant mean difference (d) in volume between physical volume and NIR processed volume ($p > 0.05$, d = 8.077 mm^3, SD = 13,419 mm^3). The regression line between hypothetical measurements of human lung nodule volume measured in original low-dose CT and NIR processed showed high correlation (r = 0.9998) with a slope of 1. The mean difference (d) between the original and NIR processed scans was − 5.921 mm^3 and standard deviation was 16.021 mm^3.

The classification of nodules based on density, shape and edge varied between observers. However, the application of NIR did not change the classification significantly ($p > 0.05$). For density, kappa value (κ) for inter-observer agreement was good (κ = 0.627). Whereas shape and edge showed less inter-observer agreement, this did not change by application of NIR. The difference between measured and physical volume can be partly explained by the fact that the Aquarius iNtuition Viewer software also has some variation in measurement with repeated measurement by the same observer for original scans (SD = 0.988 mm^3).

Conclusion

The artificial neural network based post-processing NIR technique shows perfect resemble agreement in volume or classification of lung nodules as assessed by low dose CT. Our results imply that the NIR technique does not change the scans in a way that would alter the diagnosis of the nodules both in phantom and human data. Further research is needed to analyze the effect of NIR on image quality and nodule detectability.

References

[1] Fornell D (2011) Reconstruction software improves quality of low-dose CT scans. Diagnostic interventional cardiol

[2] Aberle DR, Adams AM, Berg CD, Black WC, Clapp JD, Fagerstrom RM, Gareen IF, Gatsonis C, Marcus PM, Sicks JD (2011) Reduced lung-cancer mortality with low-dose computed tomographic screening. N Engl J Med 365: 395–409. https://doi.org/10.1056/nejmoa1102873

[3] Ru Y, Xie X, Koning HJ De, Vliegenthart R (2011) NELSON lung cancer screening study. 79–84. https://doi.org/10.1102/1470-7330.2011.9020

[4] Xu DM, Gietema H, de Koning H, Vernhout R, Nackaerts K, Prokop M, Weenink C, Lammers JW, Groen H, Oudkerk M, van Klaveren R (2006) Nodule management protocol of the NELSON randomised lung cancer screening trial. Lung Cancer 54: 177–184. https://doi.org/10.1016/j.lungcan.2006.08.006

Validation of a 4D CT method for quantitative analysis of carpal motion using clinical CT protocols

J. Dobbe[1], M. G. De Roo[2], S. Strackee[2], G. Streekstra[1]

[1]Academic Medical Center, University of Amsterdam, Biomedical Engineering and Physics, Amsterdam, Netherlands

[2]Department of Plastic, Reconstructive and Hand Surgery, Academic Medical Center, University of Amsterdam, Amsterdam, Netherlands

Keywords 4D-CT · Carpal motion · Motion analysis · Kinematics

Purpose

Three-dimensional CT imaging can be used to provide a static image of a pathologic wrist. If the pathology is related to motion, such as in the case of ligament injury, a static image may not reveal the pathology. A series of 3-D images (4D-CT) with the wrist in motion is more likely to reveal pathologic motion patterns [1, 2]. However, if the carpal bones move too fast, 3-D image reconstruction will contain blurring artifacts. Although this phenomenon is hardly investigated [2, 3] the blur in the time frames of a 4D image sequence will cause an error in kinematic analysis. In this paper we investigate the motion-induced error in finding the position of carpal bones in a 4D image sequence.

Methods

4D-CT images were acquired of a setup with a wrist phantom at stasis and while rotating inside the scanner at different angular velocities (Fig. 1). The wrist phantom was created by segmenting a wrist from a CT-scan and subsequent 3D printing by additive manufacturing. A cavity in the phantom contained the lunate, scaphoid and capitate of a cadaver specimen. We used dedicated 4D-CT scan protocols, based on a partial and a full gantry rotation, on regular CT scanners (Philips Brilliance 64 slice, Siemens SOMATOM Force). Joint kinematics was estimated by 4D image analysis methods involving segmentation of carpal bones from a static CT scan and subsequent image registration of the segmented bones to the time frames of a 4D scan [2]. The error of kinematic parameters is determined for the phantom at stasis, while rotating about an axis parallel to the gantry and while rotating perpendicular to it (i.e., as in clinical evaluation of flexion–extension motion). Custom software was used for semi-automatic segmentation and registration.

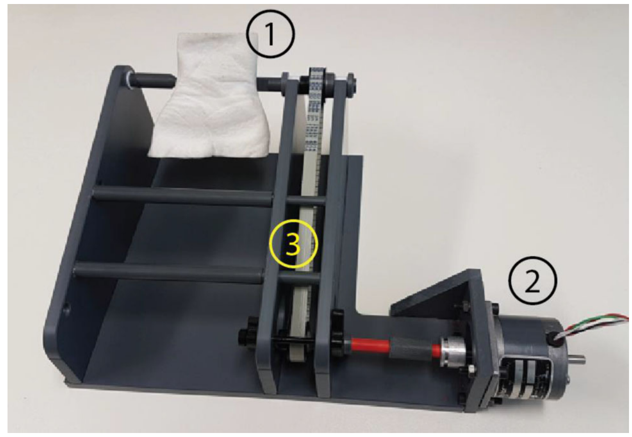

Fig. 1 Setup for evaluating the error in kinematic analysis showing (1) 3D-printed phantom containing actual bones, (2) stepper motor, (3) driving belt

Results

If the phantom is at stasis and partial gantry rotation is used, a periodic error is observed showing a displacement error of about 1 mm. This error is reduced to < 0.2 mm if full gantry rotation is used for reconstruction of images in a 4D image series. This error is probably related to mechanical instability of the scanner. Subsequent experiments were therefore performed using full gantry rotations. The motion-induced error (Fig. 2) was quantified by placing the setup inside the scanner to simulate flexion–extension motion, at angular carpal bone velocities equal or higher than 25 s per revolution, the error of joint kinematics estimation is < 2 degrees for rotational and < 1 mm for translational parameters. Systematic errors in kinematic parameters increase with angular velocity. If the phantom is rotating about an axis parallel to the rotation axis of the gantry, and in a direction opposite to the gantry, the error in kinematic parameters increases, probably because of the apparent increase in angular velocity.

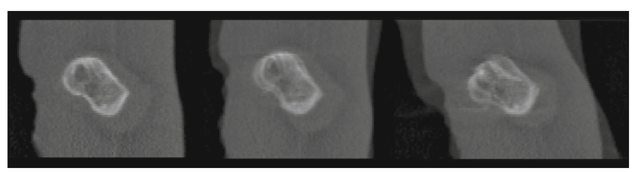

Fig. 2 From left to right: no blurring of the scaphoid image at stasis, moderate blur when the phantom rotates at 0.1 rps (10 s per phantom revolution), and strong blurring effect at 0.2 rps (4 s per phantom revolution)

Conclusion

Four-dimensional imaging of slow carpal motion is feasible with a regular CT-scanner. In this condition the error in kinematic analysis is low if full gantry rotations are used for reconstruction of the images in a 4D series. The error in kinematic analysis increases with the angular velocity of the wrist phantom. The error further increases if the phantom rotates in a direction opposite to the gantry.

References

[1] Carelsen B, Bakker NH, Strackee SD, Boon SN, Maas M, Sabczynski J, Grimbergen CA, Streekstra GJ, 4D rotational X-ray imaging of wrist joint dynamic motion, Med Phys, 32(9): 2771–2776, 2005.

[2] Carelsen B, Jonges R, Strackee SD, Maas M, van Kemenade P, Grimbergen CA, van Herk M, Streekstra GJ, Detection of in vivo dynamic 3-D motion patterns in the wrist joint, IEEE Trans Biomed Eng, 56(4): 1236–1244, 2009.

[3] Neo PY, Jais ISM, Panknin C, Lau CC, Chan LP, An KN, Tay SC, Dynamic imaging with dual-source gated computed tomography (CT): Implications of motion parameters on image quality for wrist imaging, Med Eng Phys, 35: 1837–1842, 2013.

Assessment of cerebral ischemic changes in rats using different diffusion-weighted signal models for intravoxel incoherent motion analysis at 11.7 T

S. Fujiwara[1,2], Y. Mori[3], D. M. de la Mora[2,4], K. Yoshida[1], K. Ogasawara[1], Y. Yoshioka[2,4]

[1]Iwate Medical University, Neurosurgery, Morioka, Japan

[2]Osaka University, Open and Transdisciplinary Research Initiative, Suita, Japan

[3]University of Copenhagen, Center for Translational Neuromedicine, København N, Japan

[4]NICT and Osaka University, Center for Information and Neural Networks (CiNet), Suita, Japan

Keywords MRI · diffusion · Brain · IVIMtpb 2tpb 2

Purpose

Rats with common carotid artery occlusions (CCAO) have an advantage in that, cerebral hemodynamic changes and post-ischemic neural degenerations can be observed without serious surgical injuries to the cerebral cortex, as the chronic cerebral hypoperfusion model [1–3]. However, such CCAO, especially bilateral CCAO (bCCAO), causes a high mortality rate of rats and it has remained unclear how cerebral ischemic changes and/or damage are associated with the mortality of rats at the early phase after CCAO. Intravoxel incoherent motion (IVIM) analysis can non-invasively and simultaneously assess cerebral hemodynamic states and ischemic damages using diffusion-weighted imaging (DWI) dataset obtained by the one scan with multiple b values [4, 5]. The aim of this study is to investigate whether cerebral hemodynamic states and ischemic damages are different between long and non-long survival groups, using intravoxel incoherent motion (IVIM) analysis at ultra-high-field 11.7 T pre-clinical magnetic resonance imaging (11.7 T MRI).

Methods

We performed a surgical treatment to nine female Wistar rats (8-week-old) under the general anesthesia with isoflurane as the following procedures: (1) a right common carotid artery was occluded by a ligation with a 4-0 surgical thread; (2) a left CCA was occluded 6 days after the previous unilateral occlusion. The 6 days between the first and second ligations were selected for the low mortality ratio as described in a previous work [3]. We defined the 3-week after bCCAO as a criteria to judge whether rats can be long-survivors because cerebral blood flow recovery in long-survival rats after bCCAO has been observed from 3 weeks in the previous work [4]. Thus, rats that survived during 3 weeks after bCCAO were assigned to a long survival (LS) group, while the other rats were grouped in a non-LS group. All experimental protocols were approved by the Research Ethics Committee of Osaka University. All experimental procedures involving animals and their care were carried out in accordance with the Guidelines of Osaka University for Animal Experimentation and the National Institutes of Health Guide for the Care and Use of Laboratory Animals. IVIM-DWI (multi-shot spin echo echo-planar imaging sequence; in-plane resolution: 0.2 × 0.2 [mm^2]; slice thickness: 0.8 [mm]; slice gap: 0.2 [mm]; 12 b values: 0–3000 [s/mm^2]; motion probing gradient: three different directions) was performed on a preclinical vertical 11.7 T MRI scanner (AVANCE II 500WB, Bruker) before (Pre) and 3 days after the first surgical treatment for a right CCAO (rCCAO), and within 1 h after the second one for the left side occlusion (bCCAO). For IVIM analysis, we used the following three typical diffusion-weighted signal models [4, 5]: mono-exponential model (Mono): $S = S_0\{f_{ivim}\exp(-bD^*) + (1 - f_{ivim})\exp(-bADC)\}$kurtosis model (Kur): $S = S_0\{f_{ivim}\exp(-bD^*) + (1 - f_{ivim})\exp(-bADC + K(bADC)^2/6)\}$bi-exponential model (Bi): $S(b) = S_0[f_{ivim}\exp(-bD^*) + (1 - f_{ivim})\{f_s\exp(-bD_s) + (1 - f_s)\exp(-bD_f)\}]$ (S(b), diffusion-weighted signal at the b value; S_0, baseline (T2-weighted) signal; f_{ivim}, volume fraction of perfusion compartment; b, b value; D*, pseudo-diffusion coefficient; ADC, apparent diffusion coefficient; K, kurtosis; f_s, volume fraction of slow diffusion compartment; D_s and D_f, slow and fast diffusion coefficient).

Each IVIM parameter was estimated using averaged DWI signals in regions of interest (ROI) on the cortex of each rat. Three ROIs were automatically placed on each right and left side of the cortex. Each ROI was automatically placed on the cortex by a house-made software developed on MATLAB (Mathworks, Natick, MA, USA). The significant difference of each f_{ivim}, $f_{ivim} \times D^*$ and $ADC^\dagger$ in three phases (Pre, rCCAO, bCCAO) was examined in each group (LS and non-LS) because f_{ivim}, $f_{ivim} \times D^*$ and ADC correspond to cerebral blood volume (CBV), cerebral blood flow (CBF) and cerebral ischemic damage (ADC reduction), respectively. Significant level ($p < 0.05$) was judged using Friedman test with post hoc test on MedCalc ver. 17.9.7 (MedCalc Software bvba, Ostend, Belgium). †, ADC for Bi = $f_sD_s + (1 - f_s)D_f$.

Results

All surgical procedures and MRI scans were successfully performed in all rats except one which showed strong deteriorations on images. Two and seven rats were assigned to LS and non-LS groups, respectively. In LS group, f_{ivim} at bCCAO is significantly higher than that at Pre with Kur and Bi, while the f_{ivim} at bCCAO in non-LS group is significantly lower than that at Pre with Kur (Figs. 1, 2). In addition, $f_{ivim} \times D^*$ and ADC in non-LS group were significantly lower at both rCCAO and bCCAO with any formulas than that at Pre. On the other hand, in LS group, no significant difference of $f_{ivim} \times D^*$ between any pairs in three phases was observed with any formulas. ADC at rCCAO in LS group significantly was lower than that at Pre with Kur and Bi.

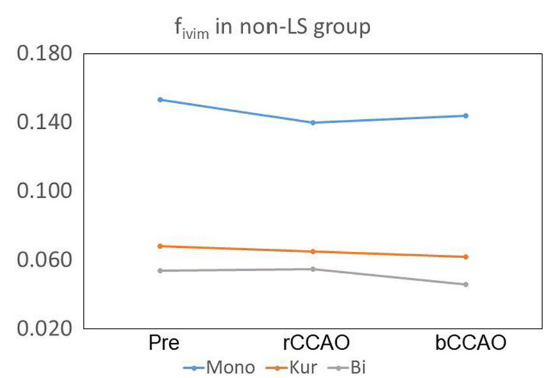

Fig. 1 f_{ivim} of non-long survival (non-LS) group obtained by each diffusion-weighted signal model in three phases

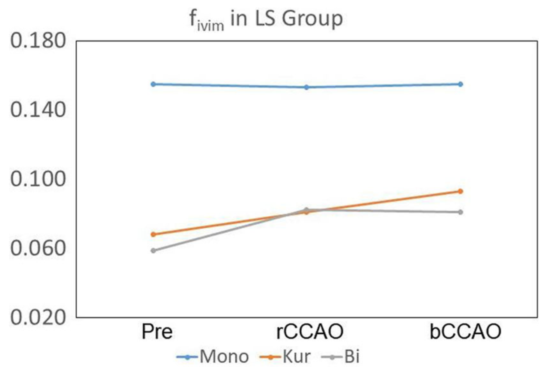

Fig. 2 f_{ivim} of long survival (LS) group obtained by each diffusion-weighted signal model in three phases

Conclusion

IVIM parameters can identify abnormal cerebral ischemic changes in rats after CCAO and the parameters may indicate CBV increase to maintain CBF in LS group and severe ischemic damage due to CBF reduction in non-LS group.

References

[1] Ouchi Y, Tsukada H, Kakiuchi T, Nishiyama S, Futatsubashi M (1998) Changes in cerebral blood flow and postsynaptic muscarinic cholinergic activity in rats with bilateral carotid artery ligation. J Nucl Med 39(1): 198–202.

[2] Fateev IV, Bykov VN, Chepur SV, Pokrovskaya LA, Shemeleva NI, Vladimirova OO, Alekseeva II (2012) A model of cerebral circulation disorders created by staged ligation of the common carotid arteries. Bull Exp Biol Med 152(3): 378–381.

[3] Jing Z, Shi C, Zhu L, Xiang Y, Chen P, Xiong Z, Li W, Ruan Y, Huang L. (2015) Chronic cerebral hypoperfusion induces vascular plasticity and hemodynamics but also neuronal degeneration and cognitive impairment. J Cereb Blood Flow Metab 35(8): 1249–1259.

[4] Le Bihan D, Turner R (1992) The capillary network: a link between IVIM and classical perfusion. Magn Reson Med 27(1): 171–178.

[5] Iima M, Reynaud O, Tsurugizawa T, Ciobanu L, Li JR, Geffroy F, Djemai B, Umehana M, Le Bihan D (2014) Characterization of glioma microcirculation and tissue features using intravoxel incoherent motion magnetic resonance imaging in a rat brain model. Invest Radiol 49(7): 485–490.

Pulmonary perfusion diagnosis based on time-series analysis of X-ray translucency with dynamic flat-panel detector imaging: an animal-based study

R. Tanaka[1], T. Tani[2], N. Nitta[3], T. Tabata[4], N. Matsutani[5], S. Muraoka[5], S. Noji[5], T. Yoneyama[5], S. Sanada[6]

[1]Kanazawa University, Radiological Technology, Kanazawa, Japan
[2]Shiga University of Medical Science, Biomedical Innovation Center, Otsu, Japan
[3]Shiga University of Medical Science Hospital, Radiology, Otsu, Japan
[4]Shiga University of Medical Science Hosp., Emergency and I.C.U., Otsu, Japan
[5]Konica Minolta, Inc., Corporate R&D Headquarters, Hachioji, Japan
[6]Komatsu College, Clinical Engineering, Komatsu, Japan

Keywords Chest radiography · Time-series analysis · Perfusion · Pulmonary embolism

Purpose

X-ray translucency in the lung fields changes during cardiac pumping on sequential chest radiographs, due to relative increases and decreases in the blood volume per unit lung volume [1, 2]. Pulmonary circulation can thus be evaluated based on time-series of pixel value in the lungs fields. Although many reports have described the feasibility of pulmonary densitometry and digital fluoroscopic approaches to evaluate pulmonary circulation, these techniques are not used clinically because of technical limitations such as the need for special instrumentation, poor image quality, and a small field of view. Functional X-ray imaging using a dynamic flat-panel detector (FPD) can overcome such limitations. Previous clinical studies indicated that blood flow impairments could be detected by dynamic FPD imaging as decreased changes in pixel value, even without the use of contrast media [3]. However, the diagnostic performance of the dynamic FPD imaging remains to be determined. The aim of the present study was to investigate the usefulness of time-series analysis of X-ray translucency in the lung fields for detecting pulmonary embolism (PE). We demonstrate preliminary results of experimentally modeled PE in an animal-based study.

Methods

Animal preparation: The experimental protocol for this prospective study was approved by the Institutional Animal Care and Use Committee at our institution. Six domestic pigs (body weight 20–30 kg) were assessed. Respiration depended exclusively on a ventilator to provide continued, volume-controlled, mechanical ventilation throughout the experiment. Pulmonary embolism (PE) models were constructed by a catheter procedure (Fogarty catheter, T-080-8F, Edwards Lifesciences). Imaging procedures: Sequential chest radiographs were obtained using an indirect-conversion FPD system (PaxScan, 4343CB, Varex Imaging Corporation, Salt Lake City, UT, USA). Imaging was performed in a supine position and anteroposterior monitoring electrocardiogram (100 kV; 0.22 mAs/pulse; 15 frames/s; SID = 1.2 m). We confirmed high linearity between the entrance dose to the detector and the pixel value output, and total dose in 10 s less than double the conventional dose. High pixel values were related to dark areas in the images, and these, in turn, were related to high X-ray translucency in the system. Matrix size was 1024 × 1024 pixels, pixel size was 417 × 417 μm^2, and the gray-scale image range was 16 bits.

Image analysis: To investigate relationship between cardiac phase and changes in pixel value of the lungs, average pixel values were measured in manually located regions of interest (ROIs) in each lung. To facilitate visual evaluation, differences in pixel value from an image at the end of diastole phase were calculated and superimposed on the original images in the form of a colour display (called functional colour images hereafter). Changes in pixel value measured in an obstructed area were compared with changes in unaffected area. In addition, we visually evaluated the diagnostic performance of PE in the functional colour images.

Results

Average pixel values in the lungs changed according to cardiac pumping; lower X-ray translucency (increased blood volume) during systole and higher X-ray translucency (decreased blood volume) during diastole (Fig. 1). Changes in pixel value relating to inspired volume were successfully visualized as changes in colour intensity on the functional coloured images. In addition, pulmonary embolism displayed significantly reduced changes in pixel values ($P < 0.05$), to 30–40% of that in unaffected areas. We confirmed that PE was detected as lower intensity in colour on functional colour images (Fig. 2).

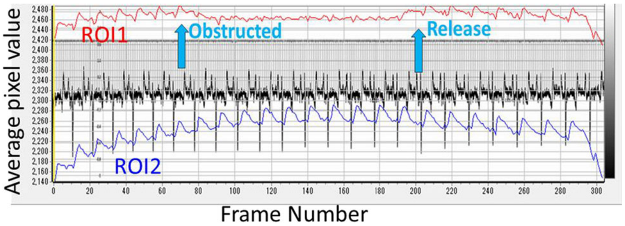

Fig. 1 Average pixel values measured in the lung regions

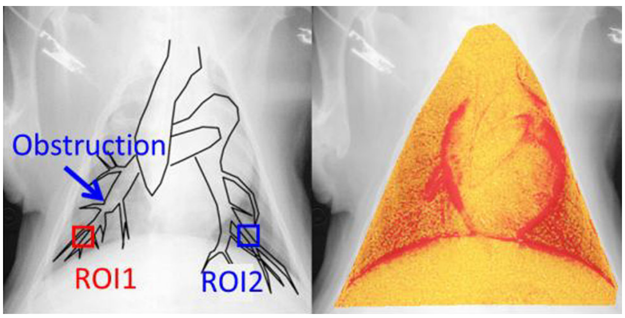

Fig. 2 (Left) Locations of obstruction and regions of interest (ROIs) for measuring average pixel values. (Right) resulting functional coloured image of a porcine model of pulmonary embolism (PE)

Conclusion

The usefulness of this approach was confirmed in the experimentally modeled pulmonary embolism. Perfusion defect was able to be detected as decreased changes in pixel value without the use of contrast media; dynamic FPD imaging allows for relative evaluation of pulmonary circulation as changes in pixel value. The method used in this study is expected to be a low-dose and cost-effective functional X-ray imaging for pulmonary perfusion assessment.

References

[1] Hansen JT, Koeppen BM (2002) Cardiovascular Physiology, In: Netters Atlas of Human Physiology (Netter Basic Science). Teterboro, New Jersey: Icon Learning Systems

[2] Silverman NR, Intaglietta M, Simon AL, Tompkins WR (1972) Determination of pulmonary pulsatile perfusion by fluoroscopic videodensitometry. J Appl Physiol 33: 147–149

[3] Tanaka R (2016) Dynamic chest radiography: flat-panel detector (FPD) based functional X-ray imaging. Radiol Phys Technol 9(2): 139–153

Ultrasound stone detection: discovery and analysis of two stone-related components in reflected signal and their role in etiology of twinkling artifact

D. Leonov[1,2], N. Kulberg[1,3], A. Gromov[1], V. Fin[1], M. Usanov[1,3], V. Kovbas[1], K. Sergunova[1], N. Strelkov[2], A. Vladzimirskiy[1], S. Morozov[1]

[1]Research and Practical Center of Medical Radiology, Department of Health Care of Moscow, Moscow, Russian Federation

[2]Moscow Power Engineering Institute, Moscow, Russian Federation

[3]Federal Research Center 'Computer Science and Control' of Russian Academy of Sciences, Moscow, Russian Federation

Keywords Doppler ultrasound · Twinkling artifact · Micro calcification · Cavitation

Purpose

Calculi within a human body can be detected via CT or X-ray exams, which are known for ionizing radiation exposure. Researchers, patients, and clinicians are concerned about possible health hazards and interested in a safer way of diagnostics. Ultrasound holds a prominent position as it is a relatively cheap and widespread medical visualization technique with no known harmful effects. Although some calculi are easily diagnosed with ultrasound by looking for bright areas and posterior acoustic shadows, other buildups are too small, cannot produce sufficient shadowing and look isoechoic on grayscale images.

Doppler ultrasound twinkling artifact can improve calculi detection. It appears as a rapid color alteration behind hyperechoic objects. Many physicians implement this phenomenon for stone localization [1]. Nonetheless, it can be misinterpreted as a blood flow or noise. Furthermore, its appearance is inconsistent among different ultrasound diagnostic machines making it unreliable for stone diagnostics.

To overcome this difficulty and turn ultrasound diagnostics into a more reliable and predictable instrument a rigorous signal model could be developed. This model should take into account stone-related components and differentiate them from blood reflections.

Methods

The main tool used in this study was commercially available ultrasound machine Sonomed-500 with linear probe 7.5 L38. The machine was modified by its producer to provide researchers access to the raw data just before the color frame mapping channel. The only digital processing stages before data acquisition were bandpass filtering and Hilbert transform.

As an additional tool, we used Medison Sonoace 8000 EX Prime with linear probe L5-9EC. It was used to test ambiguous results.

In the experiment, the probe was held in a clamp ensuring its stationarity. Research was carried out with a unique ultrasound phantom, which was developed and 3D-printed by our team (Fig. 1) [2]. We also used a breast phantom and in vivo data (Fig. 2).

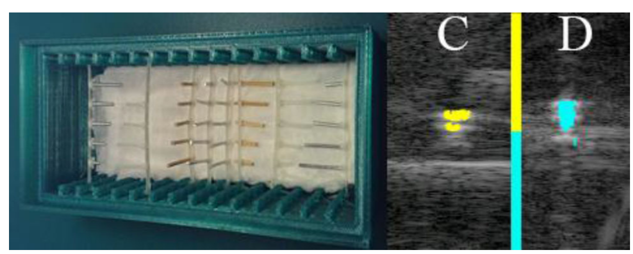

Fig. 1 Experiments with the specially developed and 3D-printed phantom. Left: photo of the phantom (with dimensions mm^3). Right: component C most apparent on a plastic rod in ethanol and component D observed upon aluminum rod in water

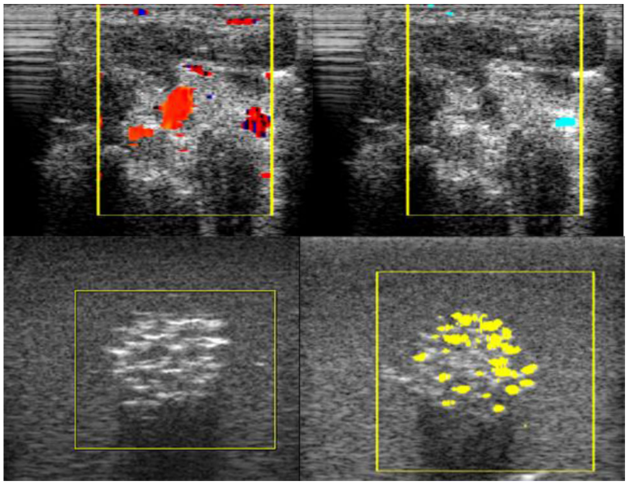

Fig. 2 Comparison between CFM images and the novel ultrasound mode for stone detection. Left: standard CFM image of the carotid artery and breast mass. Right: images in the novel mode for stone detection (component D is marked in blue; component C is marked in yellow)

For the experiment, a program was created, which contains a set of standard Doppler signal processing algorithms. Data at each processing stage can be studied; algorithms can be modified to take advantage of the special properties of calculi signals.

Results

The raw data received from ultrasound machine Sonomed-500 was analyzed with our program. Based on this analysis a new echo signal model was proposed [2]. This model contains five major components: (A) a component describing an echo from soft tissues; (B) an echo from a blood flow; (C) an echo from object's harmonic oscillation (e.g., calcium buildup motion caused by acoustic radiation force), which is believed to be the first cause of the twinkling artifact; (D) an echo from cavitation microbubbles, a second cause of the artifact [3, 4]; (E) noise of a receiver.

Components C and D characterize the signals from calculi. In order to map calculi, we need to distinguish the stone-related components from other signals. It can be done by masking specific signals. We used a mask based on the correlation between real and imaginary parts of a complex input signal. In case of component C, this correlation is high. Component D can be distinguished by its power, which is greater than the power of a receiver noise. Component D can also be distinguished by its pairwise correlation [2], which is lower than that of an echo from the red blood cells flowing through vessels. For components C and D, the area of their detection was mapped. The map was superimposed on a grayscale image of anatomical structures.

Based on these notions we created a set of algorithms comprising a specific diagnostic mode for stone detection. These algorithms were uploaded to Sonomed-500 and tested in real time.

In the phantom, component C was most reliably observed in ethanol, while component D most often appeared on metallic rods in agar and water (Fig. 1). Component D was also observed on a calculus in the neck area in the patient with a previously diagnosed cervical hematoma. In CFM mode the twinkling artifact appeared upon calculus. Component C was detected in the breast phantom (Fig. 2).

Conclusion

The diagnostics of small calculi can be enhanced by implementing the novel Doppler mode with improved signal processing. This mode takes into account properties of echoes received from calculi, thus allowing for more reliable diagnosis of stone-related diseases. The results of comparison between the novel mode for stone detection and Doppler twinkling artifact show that under the same condition the first is sufficiently more reliable. The novel mode not only detects stones better than Doppler Twinkling Artifact, but also distinguishes two types of reflection: C-signals, received from oscillating objects, and D-signals, received from cavitation microbubbles. This distinction may serve as an additional source of diagnostic information.

Acknowledgements

This research was supported by the Russian Foundation for Basic Research under Grants 17-01-00601 and 18-32-00237.

References

[1] Denstedt J, Rosette J (2014) International Consultation on Urological Diseases. Stone Diseases, Société Internationale d'Urologie. Glasgow, Scotland

[2] Leonov DV, NS Kulberg NS, Gromov AI, Morozov SP, Kim SY (2018) Causes of Ultrasound Doppler Twinkling Artifact. Acoustical Physics, 2018, 1(64): 105–111. https://doi.org/10.1134/s1063771018010128.

[3] Lu W (2012) Ultrasonic Detection and Expulsion of Kidney Stones [dissertation]. Seattle: Department of Bioengineering, University of Washington

[4] Simon JC, Sapozhnikov OA, Kreider W, Breshock M, Jr Williams JC, Bailey MR. The Role of Trapped Bubbles in Kidney Stone Detection with the Color Doppler Ultrasound Twinkling Artifact. Physics Med. Biol., 2017, 13 Nov. DOI: https://doi.org/10.1088/1361-6560/aa9a2f.

Improvement of robustness of SLAM-based bronchoscope tracking by posture guided feature matching

C. Wang[1], M. Oda[2], Y. Hayashi[2], H. Takabatake[3], M. Mori[4], H. Honma[4], H. Natori[5], K. Mori[2]

[1]Graduate School of Information Science, Department of Media Science, Nagoya, Japan

[2]Graduate School of Informatics, Nagoya, Japan

[3]Sapporo-Minami-Sanjo Hospital, Sapporo, Japan

[4]Sapporo-Kosei General Hospital, Sapporo, Japan

[5]Keiwakai Nishioka Hospital, Sapporo, Japan

Keywords Bronchoscope navigation · SLAM · Feature matching · Endoscope tracking

Purpose

This paper presents an improved feature matching method for video-based bronchoscope navigation. Bronchoscope navigation assists a bronchoscopist during bronchoscopic examination. Since the information obtained directly from the bronchoscope video is not enough for physicians to localize the current location inside the bronchus, the bronchoscope navigation system that provides the information on the current bronchoscope location is expected to be developed. So far many bronchoscope navigation systems have been proposed to assist physicians. These navigation systems used electromagnetic (EM) tracker-based methods or video-EM tracker based methods. However, additional devices are required in EM tracker-based method and this makes the tracking system complex [1]. Another way is to estimate the bronchoscopic location and posture and the bronchus structure simultaneously from the single bronchoscope video.

Wang et al. proposed a bronchoscope tracking method that is based on the ORB-SLAM [2] based bronchoscope tracking method [3]. The previous SLAM-based tracking method estimated camera's location and posture, and generated a map (bronchus structure) by using the matched points among bronchoscopic video frames. It introduced the RANSAC + EPnP algorithms to remove the outlier matches. However, if the remaining matches are too less after removing the outlier, tracking may fail. To solve this problem, this paper introduces an additional posture-guided feature matching method to find more matches in SLAM based tracking method.

Methods

We estimate the bronchoscope location and posture of one frame by using a pre-built map. The pre-built map mainly contains the 3D reconstructed map points and the corresponding feature points in previous frames [2]. The frame at time t is denoted as I^t, feature points extracted from I^t are denoted as F^t. Three steps are used to estimate the camera posture of I^t: (1) find matches between I^t and previous frame I^p for initial posture estimation; (2) posture guided feature matching; and (3) posture optimization.

(1) Match searching and posture estimation

We use the feature points in I^p that have corresponding map points as the input. The I^p is set to I^{t-1} for an initial matching. The corresponding points between F^{t-1} and F^t are matched by calculating the similarity of feature points in the predicted area of I^t. The predicted area is computed by using alpha–beta velocity model [4]. If the found matches are less than a given threshold, I^p is selected from several frames earlier than I^{t-1} and is searched with the help of vocabulary tree [2]. The camera location and posture of I^t (denote as P^0) are estimated using matched points under the RANSAC + EPnP algorithm.

(2) Posture guided feature matching

This procedure is used to find more corresponding points by using the initial posture P^0. The corresponding point's position in I^t can be computed by using P^0, its position in I^p and its 3D position in the map. Corresponding points between F^p and F^t are searched around the position of feature points using ORB feature. If the similarity of the ORB feature points between two points is greater than a threshold, then it is decided as the corresponding point.

(3) Posture optimization

This procedure computes the camera's location and posture in I^t with P^0 and matches obtained in step (2), by minimizing the Huber function based reprojection error of the map points in I^t [2]. The optimized posture is decided as the final posture of frame I^t.

Same as the previous method, we use a subset of the matched feature points to estimate the location and posture of I^t. However, we employ the posture-guided feature matching to find more corresponding points. More inlier matches can be found and used to ensure an accurate posture. Therefore, our method can track the bronchoscope more robust.

Results

We validated our method with two in vivo and two phantom videos, which were used in literature [5]. The in vivo videos recorded the bronchus examination with a resolution of 362 × 370 pixels at 30 fps. "Successfully tracked frame" is defined as the frame where the number of matched feature points in one frame is larger than a threshold t_1 (t_1 was set 15 in our experiments) and the reprojection error is less than threshold t_2 (t_2 was set to 2 for one point). One example of the matched feature points between two frames was shown in Fig. 1. Our method found more inlier matches in frames. The number of success tracked frames in four videos were shown in Table 1. Our method tracked more frames than the previous method.

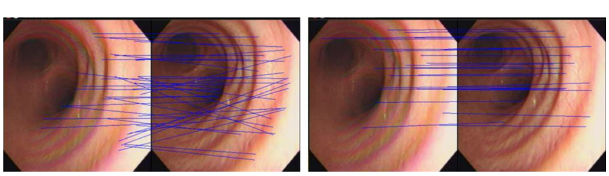

Fig. 1 the left pair is the previous method [3]; the right pair is proposed method. Our proposed method can find more inlier matches

Table 1 Number of successfully tracked frames comparison with previous method

Case	Sequence length	Previous method [3]	Proposed method
1	450	449	449
2	1000	707	749
3	379	175	185
4	900	797	829

"Successfully tracked frames" are defined as the frames where the number of matched feature points in one frame is larger than 15 points and reprojection error is less than 2 pixels

Our proposed method can find more corresponding feature points than the previous method. Therefore, the camera can be tracked more robustly. However, the tracked frames are not enough for a successful bronchoscope navigation. We need to track more frames in the future.

Conclusion

In this paper, we improved the feature matching by exploiting the posture guided feature matching to find more matches in bronchoscope tracking. By using the improved feature matching, spurious matches can be detected and removed even the spurious data is high in matched feature points. The posture guided feature matching can obtain more correct matches. Therefore, bronchoscope tracking is more robust. In the future, we need to track more frames and apply the tracking result to bronchoscope navigation.

Acknowledgements

Parts of this study were supported by JSPS KAKENHI (Grant Nos. 26108006, 17K20099 and 17H00867), and the JSPS Bilateral International Collaboration Grants.

References

[1] Merritt S, Khare R, Bascom R, Higgins W (2013). Interactive CT-Video Registration for the Continuous Guidance of Bronchoscopy. IEEE transactions on medical imaging 32(8): 1376–1396.

[2] Mur-Artal R, Jose M, Juan D (2015). ORB-SLAM: A Versatile and Accurate Monocular SLAM system. IEEE Transactions on Robotics 31(5): 1147–1163.

[3] Wang C, Oda M, Hayashi Y, Honma H, Takabatake H, Mori M, Natori H, Mori K (2017). Study on Robustness of ORB-SLAM Based Outlier Elimination in Bronchoscope Tracking. IEICE technical report 117(281): 47–52.

[4] Penoyer R (1993). The alpha–beta filter. C User's Journal 11(7): 73–86.

[5] Luo X, Mori K (2014). Robust Endoscope Motion Estimation Via an Animated Particle Filter for Electromagnetically Navigated Endoscopy. 6(1): 85–95.

Breast tissue segmentation and density quantification from MRI using convolutional neural networks

M. I. García Ocaña[1], K. López-Linares Román[1,2], G. Maclair[1], M. Azpíroz Puente[3], J. A. Romero Martin[3], V. Belloch Ugarte[3], J. M. Santabárbara[3], M. î González Ballester[2], I. Macía[1]

[1]Vicomtech, San Sebastián, Spain

[2]Universitat Pompeu Fabra, Barcelona, Spain

[3]ERESA Grupo Médico, Valencia, Spain

Keywords Breast · MRI · Segmentation · CNN

Purpose

Breast density (BD) is a risk factor associated with the development of breast cancer; higher density is associated with an increased risk of cancer [1]. BD is defined as the ratio between fibroglandular tissue

(FGT) and fat tissue. Radiologists usually assess BD by visual examination of the mammograms, and most CAD systems nowadays provide automatic mammographic density assessment. Since a mammogram is a projection image, differences in body position, level of compression or X-ray intensity can lead to an inaccurate measure of breast density. Thus, recent studies aim at quantifying BD using magnetic resonance images (MRI) [2, 3], which provide strong contrast between tissues and three-dimensional coverage of the entire breast.

Two steps are required to calculate BD from MRI: (1) segmentation of the whole breast from the rest of the body and (2) differentiation of fat and FGT within the breast. The first task is challenging due to poor contrast between pectoral muscle and breast tissue. FGT shows varying contrast due to intensity inhomogeneities and appears as very thin fibers, which make its segmentation difficult.

We propose a convolutional neural network (CNN) to simultaneously segment the breast from the body and to segment fat and FGT. This automatic segmentation is then used to compute breast density.

Methods

Datasets

We use 2D slices extracted from non-fat-suppressed T2-weighted MRI volumes from 34 different patients, provided by ERESA Grupo Médico. All images were annotated twice by a radiologist and a trained expert using an inhouse-developed annotation software.

Breast segmentation

We have designed a CNN for 3-class MRI tissue segmentation. Figure 1 shows a representation of the proposed network, which is composed of a single-stream deep network divided in three blocks of convolution and pooling layers producing several feature maps. The first two blocks include a local response normalization layer and dropout after the second convolution to avoid overfitting the data, mostly for FGT. The last block includes dropout after each convolution. Multiple side connections are inserted after the last convolution layer of each of the three blocks to extract output feature maps at different scale levels. This is important since FGT appears with a pattern of thin fibers while fat tissue is more homogenous and compact.

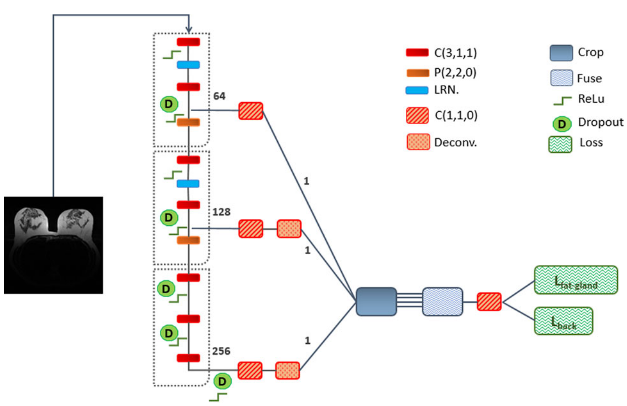

Fig. 1 Scheme of the proposed convolutional neural network for breast tissue segmentation

The loss function to be minimised is a weighted combination of two softmax loss functions: the first softmax is computed taking into account only the pixels corresponding to FGT and fat tissue, and a weight of 0.8 is assigned to it; the second one is computed considering only background pixels and it has a weight of 0.2. This allows the network to deal with the unbalance between the pixels corresponding to FGT, fat and background.

The network was trained and validated from scratch with 2564 and 284 images, respectively. All images are resized to 256 × 256 and rotations of 90°, 180° and 270° are applied to augment the data. For testing, images of nine different patients are employed.

Thresholding and morphological operations were applied to the output probability maps from the network to remove the skin, which was incorrectly classified as FGT in some cases.

Finally, BD is calculated as the ratio (BDr) between FGT pixels and fat pixels, and each case is assigned to the corresponding class: (1) mostly fat—BDr < 25%; (2) moderately dense—25% < BDr < 50% (3) heterogeneously dense—50% < BDr < 75%; and (4) dense—BDr > 75%.

Results

We evaluated the automatic segmentation quality by:

1. Comparison to the ground truth segmentation from the radiologist and the trained expert, in terms of total overlap, Jaccard index, Dice coefficient, false negative rate and false positive rate.
2. Extracting the BD class from the automatic segmentation and comparing it with the ground truth provided by the radiologist.

Figure 2 shows an example of the final segmentation. Table 1 summarizes the quantitative results of the segmentation against manual annotations provided by the radiologist and trained expert respectively, as the mean values for all the datasets. Even if the Dice coefficient for FGT is not high, it is not far from inter-observer variability for this tissue, as shown in Table 2. Regarding fat tissue segmentation, averaged total overlap is higher for automatic segmentation than for inter-reader (0.93 and 0.91 between automatic segmentation and manual segmentation for the radiologist and trained expert, respectively; 0.88 for inter-observer).

Fig. 2 Example of the segmentation of fat (yellow) and fibro glandular tissue (green)

Table 1 Segmentation accuracy: (a) between the automatic segmentation and ground truth from the radiologist and (b) between the automatic segmentation and ground truth from the trained expert

	Total overlap	Jaccard	Dice	False negative	False positive
(a) Radiolgist					
Fat tissue	0.934399	0.821444	0.879134	0.065601	0.129933
FG tissue	0.548389	0.426361	0.581118	0.451611	0.370274
(b) Trained expert					
Fat tissue	0.91742	0.788581	0.879134	0.08258	0.153491
FG tissue	0.524943	0.440866	0.590155	0.475057	0.315243

Table 2 Segmentation accuracy between the manual segmentations provided by the radiologist and the trained expert

	Total overlap	Jaccard	Dice	False negative	False positive
Fat tissue	0.91742	0.788581	0.879134	0.08258	0.153491
FG tissue	0.524943	0.440866	0.590155	0.475057	0.315243

Additionally, the breast density class assigned to the images was correct in all cases except one (which was incorrectly assigned to class 1 but had a BDr close to 50%), indicating that our method is useful for BD classification.

Conclusion

We have proposed a fully automatic method for BD assessment from MRI, based on DCNN automatic segmentation of breast tissues, and we have validated it against manual segmentations from two different observers and BD classification accuracy.

The method was able to correctly and objectively classify the images in four BD classes. The network found correctly the boundaries between breast and air and between breast and pectoral muscle in all cases. As for tissue segmentation, the segmentation accuracy was higher for the fat tissue than for FGT. This is consistent with the results for inter-reader variability and with results published in previous studies [4, 5], that show that FGT segmentation is a challenging task due to variability in breast size and morphology, distribution of FGT and signal inhomogeneities.

Currently, we are working on improving FGT segmentation, trying different network architectures and increasing the number of images used for training and testing.

Acknowledgement

This research was undertaken as part of the Decision Support and Information Management System for Breast Cancer (DESIREE) project. The project has received funding from the European Union's Horizon 2020 research and innovation programme under Grant Agreement No. 690238.

References

[1] Saslow D, Boetes C, Burke W, Harms S, Leach MO, Lehman CD, Smith RA (2007) American Cancer Society guidelines for breast screening with MRI as an adjunct to mammography. CA: A Cancer J. Clin, *57*(2), 75–89.

[2] Petridou E, Kibiro M, Gladwell C, Malcolm P, Toms A, Juette A, Denton E (2017) Breast fat volume measurement using wide-bore 3 T MRI: comparison of traditional mammographic density evaluation with MRI density measurements using automatic segmentation. Clinical Radiol, *72*(7), 565–572

[3] Doran SJ, Hipwell, JH, Denholm R, Eiben B, Busana M, Hawkes DJ, dos Santos Silva I (2017) Breast MRI segmentation for density estimation: Do different methods give the same results and how much do differences matter? Med Phys.

[4] Wu S, Weinstein SP, Conant EF, Kontos D (2013) Automated fibroglandular tissue segmentation and volumetric density estimation in breast MRI using an atlas aided fuzzy C means method. Med Phys, *40*(12).

[5] Pujara AC, Mikheev A, Rusinek H, Rallapalli H, Walczyk J, Gao Y, Melsaether AN (2017) Clinical applicability and relevance of fibroglandular tissue segmentation on routine T1 weighted breast MRI. Clinical imaging, *42*, 119–125.

Surgical tools segmentation in laparoscopic images using convolutional neural networks with uncertainty estimation and semi-supervised learning

Y. Hiasa[1], Y. Otake[1], S. Nakatani[1], H. Harada[2], S. Kanaji[2], Y. Kakeji[2], Y. Sato[1]

[1]Nara Institute of Science and Technology, Graduate School of Information Science, Ikoma, Japan

[2]Kobe University, Department of Surgery, Graduate School of Medicine, Kobe, Japan

Keywords Segmentation · Convolutional neural networks · Uncertainty · Semi-supervised learning

Purpose

Annotation of laparoscopic images is important for skill assessment, surgical navigation and other applications [1]. Deep learning is widely used to improve accuracy in semantic segmentation. While the design of model architecture has been gaining more attention to further improve accuracy in segmentation of surgical tools [2], the existing methods focus less on the uncertainty estimation.

The uncertainty estimate in semantic segmentation is useful in a number of aspects. Generally, the manual annotation by experts is costly, labor-intensive, and time-consuming task. Maier-Hein et al. [1] proposed an interactive segmentation method using random forest regressors for estimating uncertainty, which reduces the annotators' burden by suggesting uncertain pixels. In contrast, in this study we use the uncertainty estimate to leverage information in unlabeled images which are readily available using a framework known as self-training [3].

The purpose of this study is to develop and validate a surgical tools segmentation method for laparoscopic images that estimates uncertainty, which are used to incorporate unlabeled images for self-training of convolutional neural network (CNN). The unlabeled images automatically segmented with high confidence are added to the training dataset.

Methods

Automatic segmentation with confidence estimate

We employ the U-net architecture proposed by Ronneberger et al. [4], which is widely used in medical image analysis and demonstrated high performance with a limited number of annotated images. We extended the U-net model in a way that it allows to estimate uncertainty based on a technique in Bayesian SegNet proposed by Kendall et al. [5], which used the dropout at the test phase allowing to approximate the posterior distribution. We insert the dropout before each max pooling and after each up-convolution layer in U-Net. We call the proposed network "Bayesian U-Net". At the test phase, the probabilistic output is obtained from stochastic dropout sampling. We take the mean and the variance of these softmax outputs as the segmentation results and the uncertainty estimates, respectively.

Semi-supervised learning of CNN model

The semi-supervised learning (SSL) of the CNN model is carried out in the following two steps. First, we train the model with only labelled data, i.e. supervised learning (SL). Then, the model is applied to unlabeled images and the segmentation and uncertainty are automatically predicted. The confident pixels are used for the fine-tuning of CNN, the loss function for the optimization is calculated with only those pixels with high confidence.

Results

We conducted experiments to evaluate the performance of uncertainty estimation and self-training. In the experiments, two-class classifications (surgical tools and background) were performed on real surgery video of 35 different patients. A short video clip with 300 frames at 30 fps of the scene during dissection of no. 6 infrapyloric lymph nodes in gastrectomy was extracted from each surgical video by an expert surgeon. Five clips were manually segmented by the expert surgeon.

In SL, the Bayesian U-Net was trained with four labelled video clips, and tested with the remaining one, i.e. leave-one-patient-out cross-validation (LOPOCV). The experimental result is shown in Fig. 1. In order to assess reliability of the uncertainty estimate, we compared two cases: Evaluation on (1) all pixels and (2) pixels with a confidence above the chosen threshold (95% from the top in this experiment). As a result, the average Dice coefficient for the five video clips was 0.852 ± 0.087 and 0.907 ± 0.101, respectively, suggesting the higher certainty, the higher Dice.

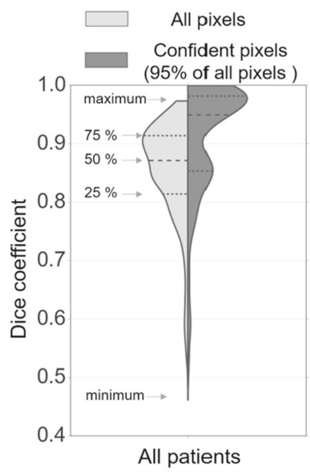

All pixels	0.852 ± 0.087
Confident pixels	0.907 ± 0.101

Fig. 1 Dice coefficient for evaluating reliability of our uncertainty metric. The higher Dice was shown in pixels with higher confidence

In SSL, the Bayesian U-Net was fine-tuned with four labelled and 30 unlabeled video clips, and LOPOCV was performed. The results are shown in Fig. 2. The self-training yielded improvement of the first quartile and the average of Dice in 4 patients except for patient #5, in which visible areas of the tools are small making the Dice error metric unreliable.

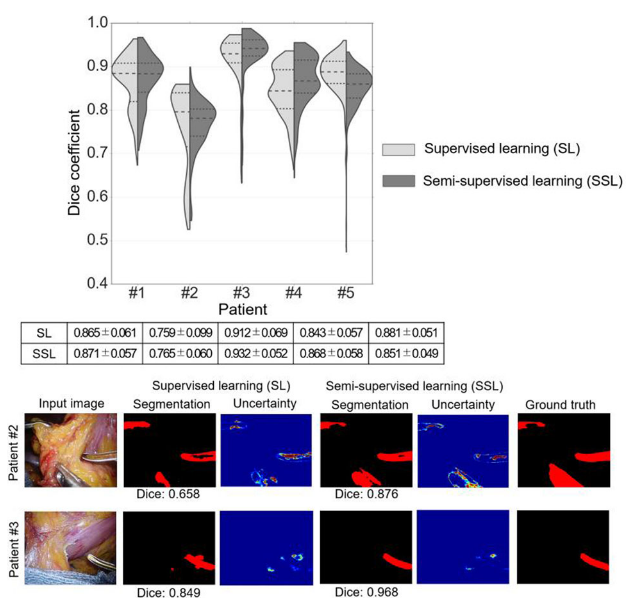

	#1	#2	#3	#4	#5
SL	0.865 ± 0.061	0.759 ± 0.099	0.912 ± 0.069	0.843 ± 0.057	0.881 ± 0.051
SSL	0.871 ± 0.057	0.765 ± 0.060	0.932 ± 0.052	0.868 ± 0.058	0.851 ± 0.049

Fig. 2 Effectiveness of semi-supervised learning. Improvement of the first quartile and the average of Dice was obtained in four patients except for patient #5. Visualization of representative results for patient #2 and #3

Conclusion

In this study, we proposed a surgical tools segmentation method for laparoscopic images with uncertainty estimation, and the self-training of CNN to incorporate unlabeled images. Evaluation experiment was conducted with real surgery videos. In the experiment of SL, we found that the uncertainty is correlated with miss-segmentation. The experiment with self-training demonstrated potential accuracy improvement by incorporating unlabeled images for training of CNN. To the best of our knowledge, no previous work developed and validated the uncertainty estimation in the segmentation of surgical tools using CNN. In addition, we showed an example use case of the estimated uncertainty in the self-training framework. One limitation of the proposed method is computation time for self-training of CNN because of the requirement of multiple forward and backward propagation to update the parameters of CNN. Thus, it would not suitable for application in an interactive annotation method such as [1]. In the future work, we will increase unlabeled images to investigate the relationship between the number of training images and segmentation accuracy. Also, we will the accuracy would be further improved by iterating the fine-tuning process.

References

[1] Maier-Hein L, Ross T, Gröhl J, Glocker B, Bodenstedt S, Heim E, Götz M, Wirkert S, Kenngott H, Speidel S, Maier-Hein K (2016) Crowd-algorithm collaboration for large-scale endoscopic image annotation with confidence. International Conference on Medical Image Computing and Computer-Assisted Intervention, 9901: 616–623

[2] Laina I, Rieke N, Rupprecht C, Vizcaíno JP, Eslami A, Tombari F, Navab N (2017) Concurrent Segmentation and Localization for Tracking of Surgical Instruments. International Conference on Medical Image Computing and Computer-Assisted Intervention, 10434: 664–672

[3] Zhu X (2005) Semi-supervised learning literature survey. Technical Report 1530, Computer Sciences, University of Wisconsin-Madison

[4] Ronneberger O, Fischer P, Brox T (2015) U-net: Convolutional networks for biomedical image segmentation. International Conference on Medical Image Computing and Computer-Assisted Intervention, 9351: 234–241

[5] Kendall A, Vijay B, Roberto C (2015) Bayesian segnet: Model uncertainty in deep convolutional encoder-decoder architectures for scene understanding. arXiv preprint arXiv:1511.02680

Unsupervised 3D micro-CT image segmentation based on a hybrid of VAE and GAN

T. Moriya[1], H. Roth[1], S. Nakamura[2], H. Oda[3], K. Nagara[3], M. Oda[1], K. Mori[1]

[1]Nagoya University, Graduate School of Informatics, Aichi, Japan
[2]Nagoya University, Graduate School of Medicine, Aichi, Japan
[3]Nagoya University, Graduate School of Information Science, Aichi, Japan

Keywords Segmentation · Unsupervised deep learning · Micro lung cancer structure · Micro-CT

Purpose

The purpose of our study is to develop a novel unsupervised segmentation method for 3D microstructure in micro-CT images. Micro-CT allows the nondestructive imaging of the interior of a specimen at micrometer resolutions in 3D. If observation of tumor invasion and measurement of tumor diameter in three dimensions become possible on micro-CT images, pathological diagnosis using micro-CT images could be used to support or substitute current pathological diagnosis using microscopic images. Therefore, automatic separation of cancer components and normal tissue on the micro-CT images would improve the accuracy of future pathological diagnosis [1]. However, due to difficulty of manually annotating cancer components on micro-CT images, it is difficult to acquire a sufficiently large dataset for training supervised segmentation methods using deep neural networks. In order to cope with unlabeled micro-CT images, we extend a state-of-the-art unsupervised image generation method to be able to generate labels for unsupervised segmentation.

Methods

The proposed segmentation method is the novel application of a principled hybrid of two major unsupervised learning approaches, variational auto-encoders (VAE) [2] and generative adversarial networks (GAN) [3]. The underlying idea of our method is that generative models allowing the inference of class labels are applicable to image segmentation. Our method consists of a training phase and a segmentation phase. In the training phase, our method iterates two steps: (1) inference of pairs of continuous and discrete latent variables of image patches randomly extracted from an unlabeled image and (2) generating image patches from the inferred pairs of latent variables. While iterating these steps, we update the parameters of the networks in order to obtain better pairs of latent variables and labels so that they optimize a specifically designed loss function. For this work, we adopt α-GAN [4] as the strategy of inference and learning, which is a principled combination of VAE and GAN. In the segmentation phase, our trained network assigns labels to patches from a target image.

Hybrid of VAE and GAN: We employ α-GAN as a hybrid of VAE and GAN. α-GAN uses four networks: (1) the encoder; (2) the generator; (3) the image discriminator; and (4) the code discriminator. The encoder estimates continuous latent variables z from observed input $\boldsymbol{x}$. The generator reconstructs images from the latent variables. The image discriminator distinguishes between real data and reconstructed data from the latent variables or generated data from a Gaussian prior. The code discriminator distinguishes between the estimated latent variables and a Gaussian distribution. This encourages the encoder to produce latent variables that follow a Gaussian distribution which is more tractable distribution than the true distribution.

Extension of α-GAN: In order to apply α-GAN to image segmentation, we conducted some extensions. First, we alter the architecture of the encoder in order to generate not only the continuous latent variables z but also the discrete variables $\boldsymbol{y}$. In the training phase, these discrete variables behave as conditional labels controlling which classes of images the generator creates, in the segmentation phase, they behave as segmentation labels. Our extended generator utilizes both continuous latent variables and discrete latent variables. Moreover, we add a new code discriminator which distinguishes between the encoded discrete variables and randomly generated one-hot vectors. To distinguish the added code discriminator from the original code discriminator, we call the new one 'the categorical discriminator' D, and call the original one 'the Gaussian code discriminator' C. The categorical code discriminator imposes a categorical distribution on discrete latent variables, similar to the adversarial network in adversarial auto-encoders [5]. When we generate a fake image from true distribution, we input a pair of a Gaussian prior and one-hot vector. The number of dimensions of the discrete variables is the same as the desired number of classes K. A loss function L of extended α-GAN is defined as

$$\begin{aligned} L(\boldsymbol{\theta},\boldsymbol{\eta}) = {} & \mathrm{E}_{Q(y,z|x,\eta)}[-\lambda\|\boldsymbol{x}-\boldsymbol{G}_{\theta}(\boldsymbol{y},z)\|_1 \\ & + \log(\boldsymbol{D}_{\Phi}(\boldsymbol{G}_{\theta}(\boldsymbol{y},z))/(1-\boldsymbol{G}_{\theta}(\boldsymbol{y},z))) \\ & + \log(\boldsymbol{C}_{\omega}(z)/(1-\boldsymbol{C}_{\omega}(z))) \\ & + \log(\boldsymbol{H}_{\psi}(\boldsymbol{y})/(1-\boldsymbol{H}_{\psi}(\boldsymbol{y})))], \end{aligned} \tag{1}$$

where $\boldsymbol{Q}$ is the encoder, $\boldsymbol{G}_{\theta}$ is the generator, $\boldsymbol{D}_{\Phi}$ is the image discriminator, $\boldsymbol{C}_{\omega}$ is the Gaussian discriminator, and $\boldsymbol{H}_{\psi}$ is the categorical code discriminator. λ is a weight for adjusting the reconstruction loss. Our method alternately updates the parameters of the encoder $\boldsymbol{\eta}$, generator $\boldsymbol{\theta}$, discriminator $\boldsymbol{\Phi}$, Gaussian code discriminator $\boldsymbol{\omega}$, and the categorical code discriminator $\boldsymbol{\psi}$. The process of extended α-GAN is illustrated in Fig. 1.

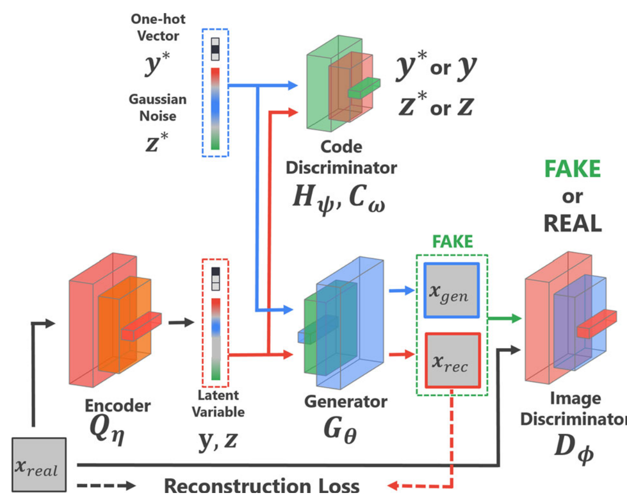

Fig. 1 Illustration of the extended α-GAN. For simplicity, the categorical and Gaussian code discriminators are represented as one network in the illustration, but practically each has a different network architecture

Segmentation: We extract a certain number of patches of $w \times w \times w$ voxels from the target image separated by s voxels each. The encoder trained by iterating the extended α-GAN generates a label l $(1 \le l \le K)$ given each patch. We project each label onto a subpatch of $s \times s \times s$ voxels centered at the corresponding patch.

Results

We used three specimens of resected lung cancer tissue scanned with a micro-CT scanner (inspeXio SMX-90CT Plus, Shimadzu Corporation, Kyoto, Japan) in order to evaluate our proposed method. The lung cancer specimens from the respective patients were scanned with similar isotropic resolutions of 27–29 µm. Each micro-CT volume consists of 544, 1083 and 1625 slices of 1024 × 1024 pixels. The original micro-CT volumes have a lot of background and thus we utilized cropped images around the cancer region. We aimed to divide the images into three histopathological regions: (a) invasive carcinoma; (b) noninvasive carcinoma; (c) normal tissue. In the training phase, we used 10,000 patches of 27 × 27 × 27 voxels randomly extracted from the target image. In the segmentation phase, we extracted all patches of 27 × 27 × 27 voxels with a stride of five voxels so that they cover the entire image and assigned labels to them using the trained encoder. Figure 2 shows qualitative examples. These results show the potential ability to learn features of pathological and healthy regions to distinguish between them.

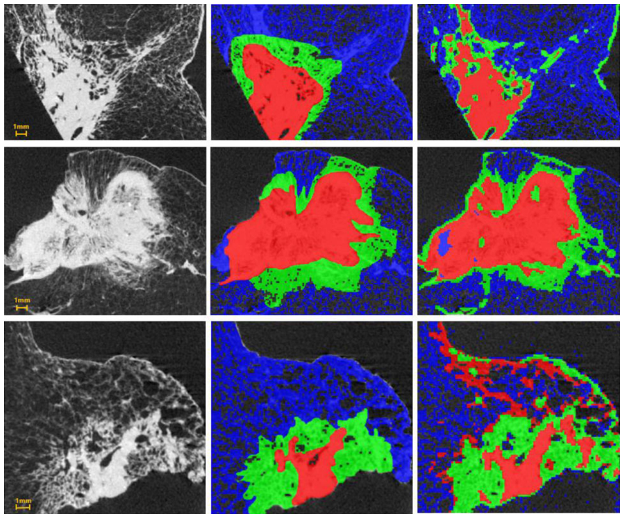

Fig. 2 Our segmentation results. Each row corresponds to each specimen. Left: The original images. Middle: Ground truth. Right: Segmentation results. In the ground truth, the red, green, and blue regions correspond to regions of invasive carcinoma, noninvasive carcinoma, and normal tissue, respectively. The colors indicate the same cluster

Conclusion

We showed that our segmentation method based on a hybrid of variational inference and adversarial learning can produce promising results for segmentation on micro-CT images. The proposed method could potentially be extended to supervised or semi-supervised segmentation methods by comparing generated labels and true labels.

Acknowledgements

Parts of this research were supported by the Kakenhi by MEXT and JSPS (26108006, 17H00867, 17K20099) and the JSPS Bilateral International Collaboration Grants.

References

[1] Nakamura S, Mori K, Okasaka T, Kawaguchi K, Fukui T, Fukumoto K, Yokoi K (2016) Micro-computed tomography of the lung: Imaging of alveolar duct and alveolus in human lung. D55. Lab methodology and bioengineering: just do it, A7411–A7411, Am Thoracic Soc.

[2] Kingma D. P, Welling M (2013) Auto-encoding variational bayes. arXiv preprint arXiv:1312.6114.

[3] Goodfellow I, Pouget-Abadie J, Mirza M, Xu B, Warde-Farley D, Ozair S, Courville A, Bengio Y (2014) Generative adversarial nets. Advances in neural information processing systems: 2672–2680.

[4] Rosca M, Lakshminarayanan B, Warde-Farley D, Mohamed S (2017) Variational approaches for auto-encoding generative adversarial networks. arXiv preprint arXiv:1706.04987.

[5] Makhzani A, Shlens J, Jaitly N, Goodfellow I, Frey B (2015) Adversarial autoencoders. arXiv preprint arXiv:1511.05644.

LSTM fully convolutional neural networks for umbilical cord segmentation in TTTS foetal surgery planning

J. Torrents-Barrena[1], G. Piella[1], N. Masoller[2], E. Gratacós[2], E. Eixarch[2], M. Ceresa[1], M. A. Gonzalez Ballester[1,3]

[1]BCN MedTech, Universitat Pompeu Fabra, DTIC, Barcelona, Spain

[2]Fetal i + D Fetal Medicine Research Center, BCNatal—Barcelona Center for Maternal–Fetal and Neonatal Medicine (Hospital Clínic and Hospital Sant Joan de Déu), Institut Clínic de Ginecologia, Obstetricia i Neonatologia, Institut d'Investigacions Biomèdiques August Pi i Sunyer, Universitat de Barcelona, and Centre for Biomedical Research on Rare Diseases (CIBER-ER), Barcelona, Spain

[3]ICREA, Barcelona, Spain

Keywords Twin-to-twin transfusion syndrome · Fetal surgery · 3D CNN · LSTM networks

Purpose

Twin-to-twin transfusion syndrome (TTTS) is a fatal condition that affects around 10–15% of monochorionic twin pregnancies between 16 and 26 gestational weeks (GW). It originates from the blood vessels (small anastomoses) located inside and on the surface of the shared placenta connecting both foetuses [1]. Fetoscopic laser coagulation of the placental vascular equator is currently the most effective TTTS treatment [2]. The TTTS surgical outcome depends considerably on the selection of a suitable uterus entry point to coagulate the vascular anastomoses. The location of this point, taking into account the umbilical cord insertions, directly affects the maneuverability of the fetoscope and the chance to close all connected vessels.

In this paper, we report for the first time an approach to automatically extract the entire umbilical cord and its insertions from MRI and 3D US to subsequently aid the choice of the best entry point. Our deep learning method is motivated by the inherent challenges associated to foetal imaging (e.g., poor acquisition quality and huge variations among pregnancies) and the use of a global and recurrent analysis of the extracted features.

Methods

61 MRI scanning (with axial, sagittal and coronal views) and 58 3D US scanning (with colour Doppler) of singletons and (normal/monochorionic) twin pregnancies between 15 and 38 GW were collected. The ground-truth segmentations were delineated by means of the *MITK*.

We propose a new framework combining two deep learning components: a fully convolutional network to exploit the intra-slice context [4] and a recurrent neural network [3]. Our implementation uses the *Caffe* library with GPU support. The proposed architecture firstly extends a contracting path, in which a sequence of pooling operators progressively reduces the size of the network by adding successive layers where these operators are replaced by upsampling operators. In this aspect, the design is similar to [4] where the expanding path is characterized by large number of feature channels allowing the network to propagate context information to higher resolution layers. The motivation behind the use of a recurrent model for this problem is to explore the spatial dependences that are observed across adjacent MRI/US slices and learn image features that capture the global (and intricate) anatomical structure of the umbilical cord from the full image stack. Hence, three main phases define our recurrent network (see Fig. 1): a downsampling step, a recurrent component and an upsampling step. The former is independently employed to each MRI/US slice. It also deploys successive convolutional layers followed by a rectified linear unit (ReLU) and max-pooling operations to learn higher level features and remove local redundancy. In an attempt to extract global features that capture the spatial changes observed from the first to the last slice, we introduce a recurrent mechanism called long short-term memory (LSTM) [3]. For each slice, the feature maps learned by the LSTM module are upsampled to compensate the max pooling reduction of the input size. These upsampled features are then concatenated with a high resolution parallel layer aligned to the feature extraction path. The expansion stage is based on a convolutional layer, a feature map concatenation module (that combines both the upsample layer output and the parallel feature extraction), more convolutional layers followed by ReLU and a softmax function.

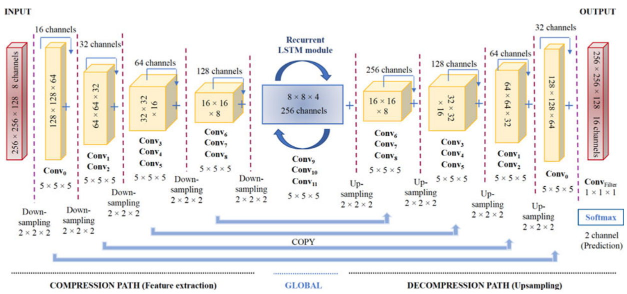

Fig. 1 Our proposed LSTM fully CNN architecture for umbilical cord segmentation

Results

Our approach was applied to 10 cases and visually validated by two experienced foetal surgeons (see Fig. 2). The 3D isosurfaces reveal that the interlaced structure of the umbilical cord precludes its precise segmentation in some patients. An additional problem is the occurrence of partially shown fetus hands and legs, which can be confused with the umbilical cord as they share a similar pixel intensity (darkest contrast). Nevertheless, we obtained a mean AUC, sensitivity, specificity, Dice and Jaccard coefficients of 0.82 ± 0.07, 0.71 ± 0.03, 0.86 ± 0.05, 0.79 ± 0.03 and 0.71 ± 0.02, respectively. Hence, our 3D representations could be used in a clinical environment to train the fetoscope movements before the surgery, to foresee the localization of the umbilical cord insertions and, consequently, to successfully improve the TTTS preoperative planning [5].

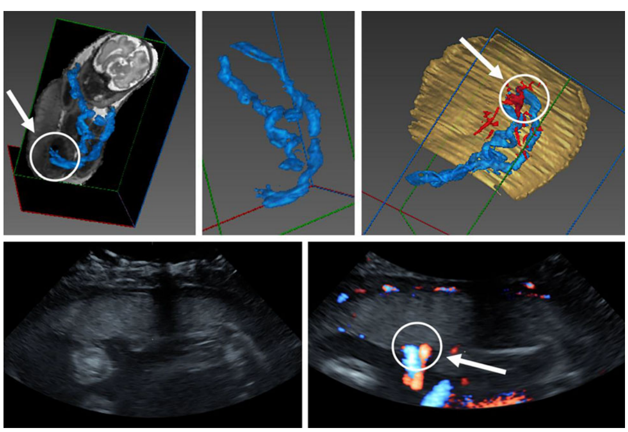

Fig. 2 Obtained results: *Row 1)* Singleton fetal MRI slice with our umbilical cord 3D segmentation (blue). The last image also shows the 3D model of the placenta (yellow) and blood vessels (red) provided by [5]. *Row 2)* Singleton fetal US slice with its colour Doppler image. The umbilical cord insertions are marked through the white arrow and circle

Conclusion

We present a 3D recurrent fully-convolutional network capable to segment the complex umbilical cord structure from a stack of MRI or US slices. It possesses the ability to leverage inter-slice spatial dependences and convolutional correlations through internal LSTM memory units. The network combines both the anatomical localization of the umbilical cord insertion and its complete extraction into a single architecture that is trained end-to-end.

Acknowledgements

This work was supported by CELLEX Foundation and the Google Women Techmakers scholarship awarded to Jordina Torrents-Barrena.

References

[1] Valsky DV, Eixarch E, Martinez-Crespo JM, Acosta ER, Lewi L, Deprest J, Gratacós E (2011) Fetoscopic laser surgery for twin-to-twin transfusion syndrome after 26 weeks of gestation. Fetal diagnosis and therapy 31(1): 30–34.
[2] Slaghekke F, Lopriore E, Lewi L, Middeldorp JM, van Zwet EW, Weingertner AS, Klumper FJ, DeKoninck P, Devlieger R, Kilby MD, Rustico MA, Deprest J, Favre R, Oepkes D (2014) Fetoscopic laser coagulation of the vascular equator versus selective coagulation for twin-to-twin transfusion syndrome: an open-label randomised controlled trial. The Lancet 383(9935): 2144–2151.
[3] Hochreiter S, Schmidhuber J (1997) Long Short-Term Memory. Neural Computation 9(8): 1735–1780.
[4] Milletari F, Navab N, Ahmadi S-A (2016) V-net: Fully convolutional neural networks for volumetric medical image segmentation. In: 4th International Conference on 3D Vision: 565–571.
[5] Ceresa M, Torrents-Barrena J, Alises A, Masoller N, Eixarch E, Gratacós E, Gonzalez Ballester MA (2017) Surgical planning system for twin-to-twin transfusion syndrome fetal surgery. International Journal of Computera Assisted Radiology and Surgery 12(Suppl 1): S100–S101.

Auto-context 3D fully convolutional networks for multi-scale semantic segmentation of abdominal CT volumes

H. Roth[1], C. Shen[1], H. Oda[1], T. Sugino[1], M. Oda[1], Y. Hayashi[1], K. Misawa[2], K. Mori[1]
[1]Nagoya University, Nagoya, Japan
[2]Aichi Cancer Center, Nagoya, Japan

Keywords Segmentation · Deep learning · Abdominal imaging · Convolutional neural networks

Purpose

Recent advances in deep learning, like 3D fully convolutional networks (FCNs) [1], have made it feasible to train models on large sets of annotated data for dense semantic segmentation of medical images. However, most network architectures require to severely downsample or crop the images in order to fulfill the memory limitations of GPU cards. In this work, we propose a multi-scale 3D FCN approach that utilizes auto-context in order to perform semantic image segmentation at higher resolutions.

Methods

While efficient implementations of 3D convolutions and growing GPU memory have made it possible to deploy FCN on 3D biomedical imaging data [2, 3], image volumes in practice are often cropped and downsampled in order to cover enough context to enable learning effective segmentation models, resulting in a loss of detail in the final segmentation.

In order to process an image at higher resolutions, we propose a method that is inspired by the auto-context algorithm [4]. Our method both captures the context information at lower resolution (downsampled) images and learns more accurate segmentations from higher resolution images in a two-stage approach. For this purpose, we employ a segmentation model inspired by 3D U-Net [2], a type of FCN [1] developed for bio-medical image segmentation and popular in the medical imaging community. This architecture utilizes transpose convolutions in order to remap the abstract and lower resolution feature maps within the network to the denser space of the input images. A constant input and output size of $64 \times 64 \times 64$ randomly cropped subvolumes is used for training in each stage. For inference, we employ network reshaping [1] in order to more efficiently process the testing image with a larger input size while building up the full image in a tiling approach [2].

In the first stage, a 3D FCN is trained at very low resolution of the input volumes, downsampled with a factor of ***ds1***. In the second stage, we use the predicted segmentation maps as a second input channel to the 3D FCN while learning from the images at a higher resolution, downsampled by a factor of ***ds2 = ds1/2***. For input as a second channel, the first stage prediction maps are upsampled by a factor of ***2*** in order to spatially align with the higher resolution images. This idea is shown schematically in Fig. 1. The resulting segmentation masks for both stages are shown in Fig. 2. It can be observed that the second stage auto-context network markedly outperforms the first stage predictions and is able to segment structures with improved detail.

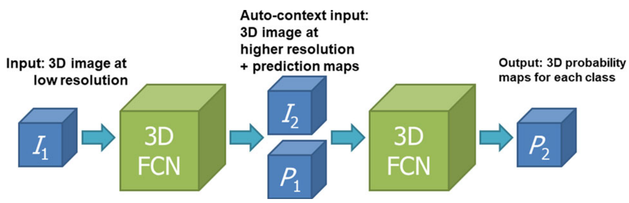

Fig. 1 Schematic of the proposed auto-context 3D FCN approach

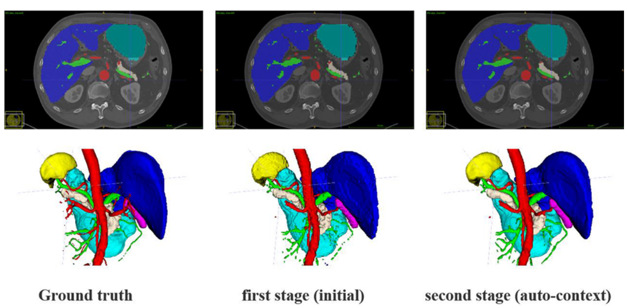

Fig. 2 Axial CT images and 3D surface rendering of the two proposed stages in comparison with ground truth. Especially the vessels are segmented more completely and in greater detail in the second auto-context stage result

We implement our approach in Keras using the TensorFlow backend. The Dice loss [3] is used for optimization with Adam and batch normalization layers are inserted throughout the network. We use a mini-batch size of three and sampled from different CT volumes and train on a NVIDIA Quadro P6000 s with 24 GB.

Results

Our data set includes 377 contrast-enhanced clinical CT images of the abdomen in portal venous phase used for pre-operative planning in gastric surgery. Each CT volume consists of 460–1177 slices of 512 × 512 pixels. Voxel dimensions are [0.59–0.98, 0.59–0.98, 0.5–1.0] mm. We use manual annotations of seven anatomical structures (artery, portal vein, liver, spleen, stomach, gallbladder, pancreas) for training.

We downsample each volume by a factor of ***ds1*** = 4 in the first stage and a factor of ***ds2*** = 2 in second stage. A random 90/10% split of 340/37 patients is used for training and testing the network. We achieve Dice similarity scores for each organ labelled in the testing cases as summarized in Table 1 for the first stage and the second auto-context stage, respectively. In comparison to previous work that employed 3D U-Net in a cascaded fashion on the same dataset [5], a marked improvement of 8.9 percentage points is achieved. We furthermore show the impact of using the auto-context channel at a higher resolution by comparing to not using that channel while training from same input resolution from scratch.

Table 1 Dice scores of both initial and auto-context 3D FCN stages

Dice	artery	vein	liver	spleen	stomach	gall-bladder	pancreas	Avg
First stage: initial 3D FCN								
Avg	0.754	0.640	0.954	0.940	0.937	0.802	0.798	0.832
Std	0.039	0.054	0.010	0.008	0.076	0.155	0.085	0.061
Min	0.674	0.413	0.915	0.926	0.484	0.273	0.497	0.597
Max	0.823	0.709	0.964	0.958	0.965	0.935	0.906	0.894
10th	0.699	0.569	0.945	0.931	0.932	0.592	0.722	0.770
Median	0.752	0.659	0.956	0.939	0.952	0.866	0.818	0.849
90th	0.805	0.686	0.962	0.950	0.962	0.899	0.877	0.877
Second stage: auto-context 3D FCN								
Avg	0.825	0.768	0.967	0.966	0.959	0.844	0.834	0.881
Std	0.041	0.064	0.010	0.007	0.080	0.140	0.084	0.061
Min	0.733	0.463	0.929	0.944	0.481	0.280	0.539	0.624
Max	0.900	0.835	0.979	0.980	0.987	0.960	0.934	0.939
10th	0.774	0.704	0.960	0.958	0.952	0.676	0.763	0.827
Median	0.825	0.784	0.970	0.966	0.977	0.890	0.852	0.895
90th	0.876	0.815	0.975	0.976	0.984	0.936	0.914	0.925

Conclusion

We showed that an auto-context approach can result in improved semantic segmentation results for 3D fully convolutional networks based on the 3D U-net architecture. While the low resolution network is able to benefit from a larger context in the input image, the higher resolution auto-context model can segment the image with greater detail resulting in better prediction maps.

Acknowledgment

Supported by MEXT KAKENHI (26108006, 17H00867, 17K20099) and JPSP International Bilateral Collaboration Grant.

References

[1] Long J, Shelhamer E, Darrell T (2015) Fully convolutional networks for semantic segmentation. IEEE Conference on Computer Vision and Pattern Recognition: 3431–3440

[2] Çiçek Ö, Abdulkadir A, Lienkamp SS, Brox T, Ronneberger O (2016) 3D U-Net: learning dense volumetric segmentation from sparse annotation. International Conference on Medical Image Computing and Computer-Assisted Intervention: 424–432

[3] Milletari F, Navab N, Ahmadi SA (2016) V-net: Fully convolutional neural networks for volumetric medical image segmentation. IEEE 3D Vision: 565–571

[4] Tu Z, Bai X (2010) Auto-context and its application to high-level vision tasks and 3D brain image segmentation. IEEE Transactions on Pattern Analysis and Machine Intelligence 32(10): 1744–1757

[5] Roth H, Oda H, Zhou X, Shimizu N, Yang Y, Hayashi Y, Oda M, Fujiwara M, Misawa K, Mori K (2018) An application of cascaded 3D fully convolutional networks for medical image segmentation. Computerized Medical Imaging and Graphics 66: 90–99

Abdominal artery segmentation from CT volumes using fully convolutional network for small artery segmentation

M. Oda[1], T. Kitasaka[2], K. Misawa[3], M. Fujiwara[4], K. Mori[1]
[1]Nagoya University, Graduate School of Informatics, Nagoya, Japan
[2]Aichi Institute of Technology, School of Information Science, Toyota, Japan
[3]Aichi Cancer Center, Nagoya, Japan
[4]Nagoya University Graduate School of Medicine, Nagoya, Japan

Keywords Segmentation · Abdominal artery · Fully convolutional network · CT volume

Purpose

This paper presents an abdominal artery segmentation method from contrasted CT volumes. Understanding abdominal artery positions and structures of a patient is important for diagnosis and treatment. Patient-specific abdominal artery information also helps surgeons. Contrasted CT volume is one of modalities suitable for extracting 3D abdominal artery information. Recently, deep learning techniques are getting popular in the medical image processing field. Among deep learning techniques, fully convolutional networks (FCNs) can be used to perform segmentations. FCNs are applicable to segment abdominal arteries from CT volumes.

There are many blood vessel segmentation methods using deep learning techniques [1–4]. FCN [1] and convolutional neural network (CNN) with the structured prediction technique [2] are used to segment retinal blood vessels from 2D images. 3D FCN or autoencoder is used to segment brain arteries from magnetic resonance angiography volumes [3]. CNN is also used to reduce false positives of abdominal artery regions in CT volumes [4]. In these methods, FCNs provided promising results but small blood vessels were difficult to segment.

We propose an abdominal artery segmentation method from contrasted CT volumes using an FCN designed for small artery segmentation. Similar to the previous methods, we employ a patch-based process which means a patch (small image clipped from CT volume) is given to an FCN. We use larger patches (64 × 64 pixels) compared to the previous methods (28 × 28 [1], 27 × 27 [2], 16 × 16 × 16 [3], and 36 × 36 [4] pixels) to capture relationships between arteries and its surrounding tissues. Also, we use maximum intensity projection (MIP) images as patches to capture artery shapes. We use a specially designed FCN that can output segmentation result of a small region such as artery regions from global information contained in a large patch.

Methods

Overview

Arterial phase contrasted abdominal CT volumes smoothed using a median filter are used in the proposed method. Thick arteries including the abdominal aorta are segmented using the region growing method. The remaining arteries are segmented using an FCN. In a training step, we clip pairs of patches from CT volume (CT patch) and patches from ground truth artery volume (artery patch) from training volumes. The ground truth artery volume not contains thick arteries. An FCN is trained using the CT patch as input image and the artery patch as target image. In a testing step, CT patches clipped from a testing volume are given to the trained FCN. Estimated artery patches are reconstructed in an estimated artery volume.

Patch generation

We generate 2D patches from CT volumes and corresponding ground truth artery volumes. Intensity values of the patches are sampled on axial slices in the volumes. If we use patches containing single axial slice information, artery regions appear as very small region in them. Strong unbalancing of artery and other regions in patches reduce segmentation performance of the FCN. Therefore, we use MIP images as patches. MIP images contain more artery information compared to single slice images.

We define sizes of CT and artery patches as 64 × 64 and 32 × 32, respectively. We use large CT patches to capture information of not only artery but also its surrounding tissues. We use small artery patches to reduce unbalancing of artery and other regions in patches. Both of the CT and artery patches are MIP images.

FCN for artery segmentation

We designed an FCN to estimate artery patches from CT patches (Fig. 1). The FCN has an encoding path to extract features from an input image and a decoding path to reconstruct an output (target) image. Similar to the U-net [5], the FCN has filter concatenations between the encoding and decoding paths. We use a short decoding path to make output image smaller compared to input image.

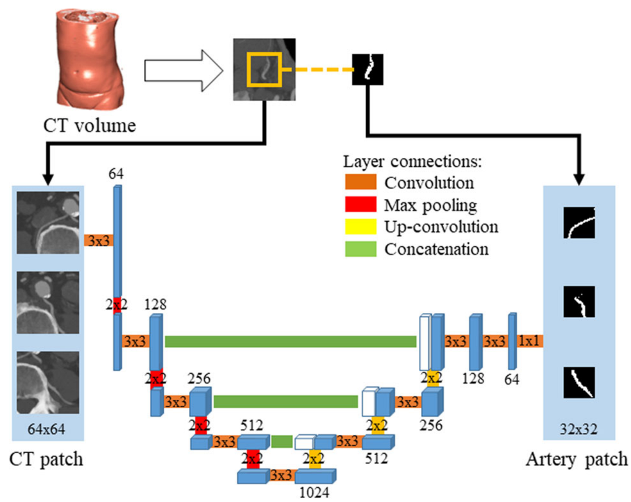

Fig. 1 Structure of FCN for artery segmentation. Numbers shown top or bottom of layers are kernel numbers

In the training step of the FCN, about 30,000 pairs of CT and artery patches generated from training volumes are used. The FCN is trained in 50 epochs.

Artery segmentation method

For a testing CT volume, thick arteries including the abdominal aorta are segmented using the region growing method. The remaining arteries are segmented using the proposed FCN. CT patches generated from the testing CT volume are given to the trained FCN. Output images of the FCN are mapped to a segmentation result volume. False positive reduction using thresholding is applied.

Results

We applied the proposed FCN on four cases of CT volumes and tested on an another CT volume. Figure 2 shows segmentation result. The recall rate of the proposed method was 81.4%, which was higher than the previous method [4] (78.3%). The proposed FCN segmented small arteries with good accuracy. However, bone regions were also segmented. We will reduce false positives including bone regions.

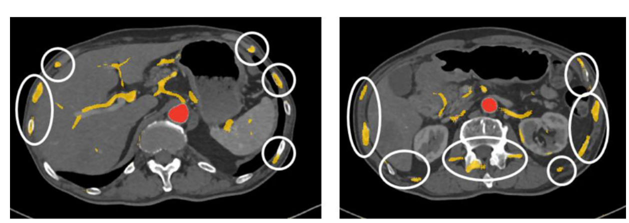

Fig. 2 Segmentation results of proposed method. Red regions were segmented by region growing method and orange regions were segmented by proposed FCN. False positives (bone) are indicated by circles

Conclusion

We proposed an abdominal artery segmentation method from CT volumes using the FCN. To obtain better segmentation performance, we used large patch of MIP image as FCN input. The special FCN having large patch input and small patch output is used to perform segmentation. Future work includes use of 3D information in segmentation and improvement of small artery segmentation performance.

Acknowledgments

Parts of this research were supported by the MEXT/JSPS KAKENHI Grant Nos. 25242047, 26108006, 17H00867, 17K20099, the JSPS Bilateral Collaboration Grant, and the JST ACT-I (JPMJPR16U9).

References

[1] Dasgupta A, Singh S (2016) A fully convolutional neural network based structured prediction approach towards the retinal vessel segmentation. arXiv:1611.02064v2

[2] Liskowski P, Krawiec K (2016) Segmenting retinal blood vessels with deep neural networks. IEEE TMI 35(11): 2369–2380

[3] Chen L, Xie Y, Sun J, Balu N, Mossa-Basha M, Pimentel K, Hatsukami TS, Hwang JN, Yuan C (2017) Y-net: 3D intracranial artery segmentation using a convolutional autoencoder. arXiv:1712.07194

[4] Oda M, Yamamoto T, Yoshino Y, Mori K (2017) False positive reduction of abdominal artery segmentation from CT volumes based on deep convolutional neural networks. Int J CARS 12(1): S27–S29

[5] Ronneberger O, Fischer P, Brox T (2015) U-Net convolutional networks for biomedical image segmentations. MICCAI 9351: 234–241

Evaluation of 3D fully convolutional networks for multi-class organ segmentation in contrast-enhanced CT

C. Shen[1], H. R. Roth[1], H. Oda[2], M. Oda[1], Y. Hayashi[1], K. Misawa[3], T. Miyamoto[4], K. Mori[1]

[1]Nagoya University, Graduate School of Informatics, Nagoya, Japan
[2]Nagoya University, Graduate School of Information Science, Nagoya, Japan
[3]Aichi Cancer Center, Nagoya, Japan
[4]Chiba Kensei Hosptial, Chiba, Japan

Keywords Abdominal CT · Multi-organ segmentation · Fully convolutional network · Computed tomography

Purpose

In this work, we investigate the influence of balancing weights in the loss function and data augmentation for multi-class abdominal organ segmentation. Automated multi-organ segmentation is challenging, because the large shape and appearance differences between patients. Deep learning has become the dominant approach for medical image analysis. For example, 3D fully convolutional networks (FCNs) have achieved impressive results for segmentation of 3D computed tomography (CT) scans [1]. However, to use 3D FCNs for multi-organ segmentation, low segmentation accuracies for smaller organs are still a problem because loss functions are typically influenced mostly dominating organ class. We evaluate the segmentation accuracies of a 3D FCN trained on 377 abdominal CT volumes with seven organ labels under different loss function and data augmentation settings. We furthermore show the segmentation results using the trained 3D FCN on a completely unseen abdominal CT dataset in order to confirm whether these trained FCNs work well across different datasets or not.

Methods

FCNs can be trained using a large number of annotated 3D volumes $S = \{(I_n, L_n), n = 1, \ldots, N\}$, where I_n represents a CT volume and L_n represents a ground truth label volume. Here, N is the total number of training volumes. We utilized a FCN architecture which is similar to 3D U-Net [2]. This network architecture is composed of symmetric analysis and synthesis paths. In order to remap the lower resolution feature maps, up-convolution was used to allow denser voxel-to-voxel predictions [3]. Batch normalization layers were applied throughout the network to converge faster. We use randomly cropped subvolumes of size 64 × 64 × 64 voxels for training.

The Dice similarity coefficient [4, 5] was used as a loss function. In order to increase the segmentation accuracy for smaller organs such as the pancreas or the gallbladder, we introduce some balancing weights. We applied three types of different class weights that adjust the loss for each organ: $w_u = 1$ (uniform), $w_s = N/(L|R_l|)$ (simple) and $w_q = N/(L|R_l|)^2$ (square). Here, we define L as the number of label classes and $|R_l|$ as number of labelled voxels in class i. Our dataset consists of eight classes including background and seven organs (the artery, the portal vein, the liver, the spleen, the stomach, the gallbladder and the pancreas).

We utilize on-the-fly data augmentation, as to artificially increase the training dataset in order to improve the robustness properties of the network and avoid overfitting. For augmentation, we apply random 3D translation and rotations together with elastic B-spline deformation. In training, 30,000 augmented subvolumes were generated through 10,000 iterations with mini-batch size three, randomly sampled from different training cases.

We implement all models in the Keras with the TensorFlow backend. For optimization, we trained the network with the initial learning rate 0.01 using the adaptive moment estimation (Adam) which based on stochastic gradient descent.

For robustness evaluation, we deploy the trained FCN on completely unseen data with a large number of types of different CT contrast enhancement phases from a different hospital.

Results

We utilized 377 abdominal clinical CT volumes in portal venous phase divided into training and testing datasets with 330 and 37 volumes respectively. Each CT volume contains 460–1177 slices of 512 × 512 pixels. The input size of the network is 64 × 64 × 64 voxels, which is chosen based on the memory consumption of the 3D FCNs. All volumes were down-sampled by the factor of four. The ground truth includes seven organs and background was established manually using a semi-automated segmentation tool. We used a NVIDIA GeForce GTX 1080 GPU with 8 GB memory for all experiments in this study.

For evaluation, we compute the Dice similarity score for each organ from models with different types of weighting with and without data augmentation. The results are shown in Table 1. The segmentation accuracy increased 3.3% for uniform (w_u) and 10.2% for square (w_q) type of weighting after performing data augmentation. The result has barely changed on the simple (w_s) type of weighting. The best performing segmentation in this experiment is using the uniform type of weighting with data augmentation. The average accuracy was achieved 87.8%.

Table 1 Dice similarity scores for three types of weightings: uniform, simple and square with data augmentation (AUG) and without data augmentation (NOAUG)

Case	Artery (%)	Vein (%)	Liver (%)	Spleen (%)	Stomach (%)	Gallbladder (%)	Pancreas (%)	AVG (%)
Uniform NOAUG	79.50	75.10	95.60	92.00	93.90	73.20	82.40	84.50
Uniform AUG	80.20	78.50	95.30	**94.90**	95.90	**83.30**	**86.20**	**87.80**
Simple NOAUG	80.20	**79.30**	**96.30**	93.90	**96.10**	80.80	84.70	87.30
Simple AUG	79.40	77.70	96.20	93.60	95.30	77.90	83.70	86.30
Square NOAUG	72.40	73.00	87.70	91.60	82.40	54.20	70.30	75.90
Square AUG	**80.50**	77.60	94.50	93.00	95.90	76.30	85.20	86.10

To confirm that these trained FCNs work well for different datasets, 138 non labelled clinical CT volumes in different scanning condition taken in another hospital were utilized.

Figure 1 shows 3D renderings for the three types of weightings (uniform, simple and square) with data augmentation and no data augmentation. Figure 2 shows the results of different contrast enhancement phases using the simple type weighting without augmentation on the unseen data from another hospital. We can observe these trained FCNs work well on segmenting abdominal organs in CT volumes. Not only big organs like the liver, but also small organ like the pancreas were successfully segmented in artery and portal vein phases CT volumes. Even in non-enhancement and artery phase CT volumes not seen during training, organs were reasonably well segmented.

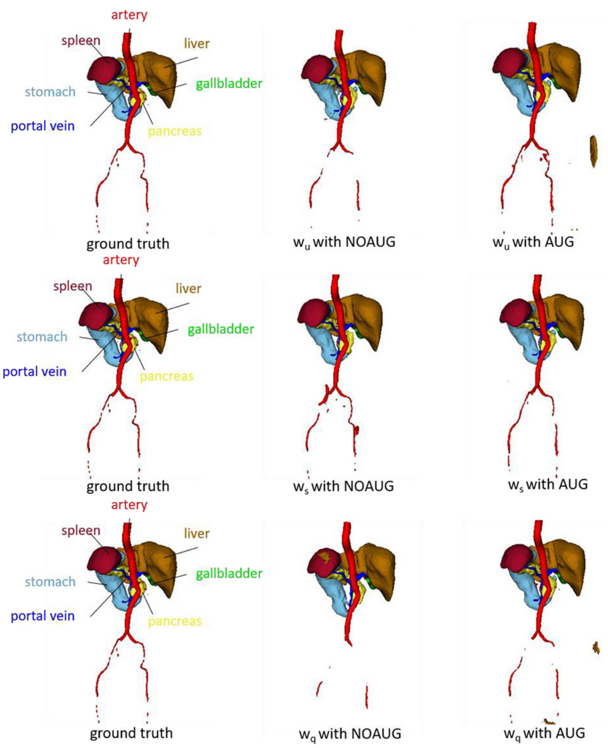

Fig. 1 3D renderings for three type of weightings: uniform (w_u), simple (w_s) and square (w_q) with data augmentation (AUG) and without data augmentation (NOAUG)

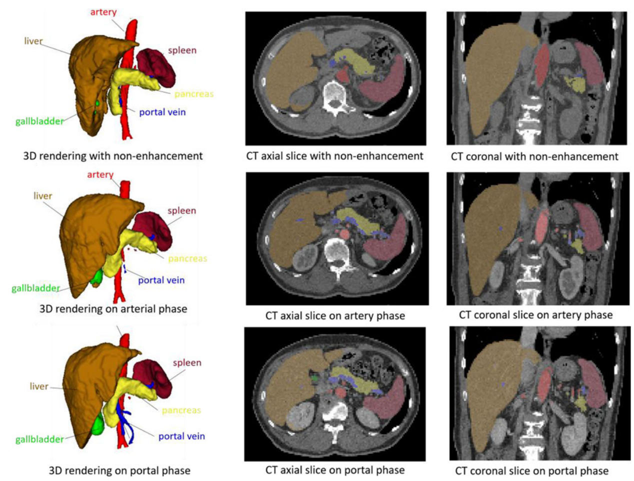

Fig. 2 Results of different CT contrast enhancement phases using simple type without augmentation for unseen data in abdominal CT

Conclusion

We evaluated the influence of different weighting types of Dice loss function and data augmentation on the segmentation accuracy. In the case where the initial learning rate remains the same, data augmentation contributes to increase the average segmentation accuracy on the uniform and the square type of the Dice loss weighting. The uniform type of weighting with data augmentation showed the best performance in this experiment. Furthermore, the experimental results showed the promising segmentation results of our trained FCNs on unseen datasets. Our model works well on these datasets taken in different scanning condition and varying contrast enhancement. The introduction of balancing weights of organs with data augmentation improved the trained model's performance especially for small organs. As future work, we will evaluate other factor on the segmentation accuracies that could further improve the performance of multi-class organ segmentation.

Acknowledgments

Parts of this reserach was supported by the JSPS Kakenhi (26108006, 17H00867, 17K20099) and the JSPS Bilateral Collaboration Grant.

References

[1] Roth H R, Oda M, Shimizu N, Oda H, Hayashi Y, Kitasaka T, Fujiwara M, Misawa K, and Mori K (2017) Towards dense volumetric pancreas segmentation in CT using 3D fully convolutional networks. arXiv:1711.06439

[2] Çiçek Ö, Abdulkadir A, Lienkamp S S, Brox T, and Ronneberger O (2016) 3D U-Net: learning dense volumetric segmentation from sparse annotation. MICCAI 2016: 424–432

[3] Long J, Shelhamer E, and Darrell T (2015) Fully convolutional networks for semantic segmentation. Proceedings of the IEEE Conference on Computer Vision and Pattern Recognition: 3431–3440

[4] Sudre C H, Li W, Vercauteren T, Ourselin S, and Cardoso M J (2017) Generalized Dice overlap as a deep learning loss function for highly unbalanced segmentations. Deep Learning in Medical Image Analysis and Multimodal Learning for Clinical Decision Support 2017: v.10553: 240–248

[5] Milletari F, Navab N, and Ahmadi S A (2016). V-Net: Fully Convolutional Neural Networks for Volumetric Medical Image Segmentation. 3D Vision: 2016 Fourth International Conference on IEEE

Constrained convexity shape prior segmentation of retinal cross-related structures

J. Escorcia-Gutierrez[1], J. Torrents-Barrena[1], P. Romero-Aroca[2], A. Valls[1], D. Puig[1]
[1]Universitat Rovira i Virgili, Department of Computer Science and Mathematics, Tarragona, Spain
[2]University Hospital Sant Joan de Reus, Ophthalmic Service, Reus, Spain

Keywords Diabetic retinopathy · Blood vessel and macula segment · Computer aided diagnosis · Convexity shape prior

Purpose

Diabetic retinopathy (DR) is a well-known ocular complication of diabetes and the leading cause of new blindness over the last years. DR is mainly caused when high blood glucose levels damage the retinal vessels. The simultaneous extraction of the whole anatomical eye structure (e.g., optic disk (OD), macula and blood vessels) is crucial to detect potential DR pathologies such as microaneurysms, hemorrhages and exudates. The automatic segmentation of these structures from colour fundus images is an arduous task in the development of a computer-assisted diagnosis (CAD) system [1]. The presence of noise and brightness inconsistencies, other related ophthalmologic pathologies, vessels of several dimensions, and the retinal vascular occlusion phenomenon make the implementation of an interactive pre-processing DR CAD (pre-DR-CAD) module a non-straightforward task.

This work in progress aims to design a pre-DR-CAD framework capable to simultaneously segment the blood vessels and macula from DR fundus images. Two objectives are mainly tackled: (1) the analysis of the eye structure to differentiate the healthy vascular tree from abnormal upgrowing blood vessels and its tortuous shape produced by advanced DR symptoms, and (2) the elimination of these structures to further increase the detection rate of microaneurysms, hemorrhages and exudates.

Methods

Our full pre-DR-CAD system is developed under Matlab R2015a. The implementation is being adapted to an open source platform using Python 2.7. All experiments were conducted on an Intel Core i7 3.5 GHz, 16.0 GB of RAM, GPU Nvidia GTX 960, and Windows 10. We use both our own private database composed by 800 colour fundus images and the public dataset collected from the *Messidor Hôpital Lariboisière Paris*.

We base our multi-platform plugin on exploiting the convex property [2]. To this end, an efficient optimization algorithm of the energy function is required, which demands some user-defined constraints (e.g., colour separation, geometric interactions, or linear intensity appearance). We also theorize that an examination of the color spaces and its intrinsic components can offer benefits to address the identification of these structures using a renowned length-based regularization of the higher-order functionals [2].

Results

Our proposed pre-DR-CAD module relies on the following stages: pre-processing, colour interpolation, and blood vessels/macula segmentation.

Pre-processing: We utilize the contrast limited adaptive histogram equalization (CLAHE) algorithm [3] twice to compensate the non-uniform lighting effect. The brightness preserving dynamic fuzzy histogram equalization [4] is also applied on the first CLAHE response. By this way, we improve the local contrast avoiding the amplified noise found in homogeneous colour regions of fundus images.

Colour interpolation: The green RGB-component is widely used to highlight the entire eye vasculature. Nevertheless, we discover that other components of the Gray Scale, Opponent and CieLab*, and the CMY, Ohta and YIQ colour spaces are more appropriate for blood vessels and macula segmentation, respectively (see Fig. 1). Due to the high-resolution of images and the strong similarity between foreground and background information, the convexity shape prior regularizer cannot be optimized via Graph Cuts. To deal with the colour separation constraint, we split the images in different 4-4 tiles. An ophthalmologist randomly selects a tile and traces a small vessel or non-vessel sample (see Fig. 1), in which the mean and standard deviation are extracted. A threshold is then determined based on the previous statistical parameters using a conditional model.

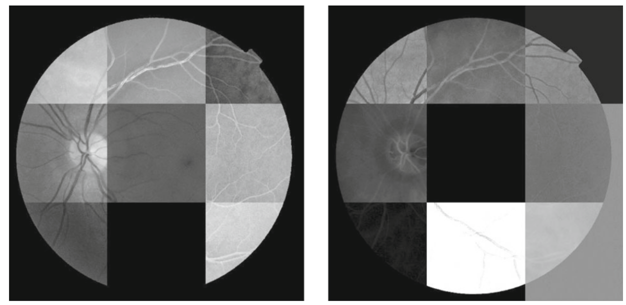

Fig. 1 Most appropriate color spaces for blood vessels and macula segmentation: (1) RGB, Opponent and CieLab* color spaces and its components, and (2) CMY, Ohta and YIQ

Simultaneous blood vessels and macula segmentation: The proposed methodology relies on the energy-based formulation for the convexity shape prior discrete optimization [2]. The optimal segmentation energy is minimized by. The former term corresponds to a length-based regularization and a convexity prior with some user-defined constraints (e.g., intensity appearance, boundary length, colour separation…). The latter is a non-submodular high-order term.
The convexity shape prior algorithm is especially suitable to deal with colour fundus images due to the existing overlap between the foreground and background information. The sub-modular colour separation term can be found based on the distance between their non-normalized colour histograms. Afterwards, a fully-automatic foreground and background selection is propagated, which starts from different colour components. Subject to these minimal user interactions, we choose 16 bins per component to combine the colour separation term with the convexity prior.

Promising results have been obtained using the designed approach (see Table 1). This methodology is combined with our previous OD extraction method [5] to implement the aforementioned pre-DR-CAD framework. Hence, our module can distinguish the main anatomical eye structures (see Fig. 2) to facilitate later the automatic grading of serious DR pathologies.

Table 1 Quantitative segmentation performance of our proposed methodology on both databases

MESSIDOR				SANT JOAN			
Precision TP/(TP + FP)	Sensitivity TP/(TP + FN)	Specificity TN/(TN + FP)	Accuracy	Precision TP/(TP + FP)	Sensitivity TP/(TP + FN)	Specificity TN/(TN + FP)	Accuracy
0.71053	0.61247	0.98141	0.95584	0.55125	0.70368	0.96354	0.94800
0.49372	0.76145	0.92716	0.91302	0.39626	0.67843	0.93522	0.92007
0.63391	0.47208	0.97975	0.94464	0.55042	0.76883	0.95506	0.94262
0.49443	0.41730	0.96970	0.93307	0.35357	0.76714	0.90371	0.89494
0.62394	0.44488	0.97742	0.93606	0.30991	0.59963	0.93088	0.91458
0.59897	0.43667	0.97965	0.94432	0.45714	0.71521	0.94312	0.92881
0.42050	0.57214	0.93696	0.90995	0.36292	0.66486	0.93064	0.91573

Table 1 continued

MESSIDOR				SANT JOAN			
Precision TP/ (TP + FP)	Sensitivity TP/ (TP + FN)	Specificity TN/ (TN + FP)	Accuracy	Precision TP/ (TP + FP)	Sensitivity TP/ (TP + FN)	Specificity TN/ (TN + FP)	Accuracy
0.42881	0.65863	0.92408	0.90294	0.42455	0.79852	0.93342	0.92560
0.58319	0.56892	0.96275	0.92969	0.43982	0.54450	0.95400	0.92853
0.72855	0.39999	0.98873	0.94735	0.47199	0.77210	0.93829	0.92721
0.57165	**0.53445**	**0.96276**	**0.93169**	**0.43178**	**0.70129**	**0.93879**	**0.92461**

The mean values are highlighted in bold

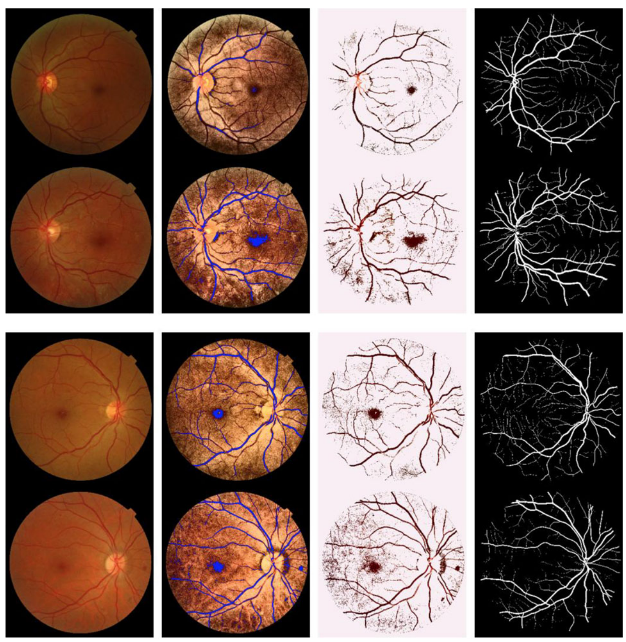

Fig. 2 Qualitative results of color fundus images selected from Messidor (rows 1–2) and our private dataset (rows 3–4). Each column represents: (1) RGB image, (2) Blood vessels color interpolation, (3) Blood vessel segmentation obtained from the Convexity shape prior algorithm, and (4) Ground truth

Conclusion

We present a complete pre-processing plugin (pre-DR-CAD) to be incorporated directly in a DR CAD system. The design of an ad-hoc colour interpolation is carried out to uncover the foreground pixels (blood vessels and macula) against the entire background. Samples of both classes are then collected as input seeds of the convexity shape prior method. To the best of our knowledge, this is the first approach that (in combination with [5]) extracts the entire anatomical eye structure using the same, fast and robust, segmentation-based algorithm.

Acknowledgement

The financial support was given by the Grant 2015PFR-URV-B2-60 and the projects PI15/01150 and PI12/01535. José Escorcia-Gutierrez is grateful to Fundación Carolina for his Ph.D. scholarship.

References

[1] Fraz MM1, Remagnino P, Hoppe A, Uyyanonvara B, Rudnicka AR, Owen CG, Barman SA (2012) Blood vessel segmentation methodologies in retinal images—a survey. Computer methods and programs in biomedicine 108(1): 407–433.

[2] Gorelick L, Veksler O, Boykov Y, Nieuwenhuis C (2017) Convexity shape prior for binary segmentation. IEEE transactions on pattern analysis and machine intelligence 39(2): 258–271.

[3] Pizer S, Amburn EP, Austin JD, Cromartie R, Geselowitz A, Greer T, ter Haar Romeny B, Zimmerman JB, Zuiderfeld K (1987) Adaptive histogram equalization and its variations. Computer vision, graphics, and image processing 39(3): 355–368.

[4] Sheet D, Garud H, Suveer A, Mahadevappa M, Chatterjee J (2010) Brightness preserving dynamic fuzzy histogram equalization. IEEE Transactions on Consumer Electronics 56(4).

[5] Escorcia-Gutierrez J, Torrents-Barrena J, Romero-Aroca P, Valls A, Puig D (2016) Interactive optic disk segmentation via discrete convexity shape knowledge using high-order functionals. In: Artificial Intelligence Research and Development, 288, 39–44.

Magic wand: a 3D-based interactive algorithm to accelerate CBCT segmentation

P. Yuan[1], F. Afonso[1], H. Deng[1], J. Li[1], C. F. Yao[1], J. Vu[1], W. Xi[1], M. Huang[1], F. Elias[2], D. Alfi[1], J. Gateno[1], J. Xia[1]
[1]Houston Methodist Research Institute, Oral and Maxillofacial Surgery, Houston, United States
[2]School of Dentistry of the University of Sao Paulo, Oral and Maxillofacial Surgery, Sao Paulo, Brazil

Keywords CBCT images · Auto segmentation · 3D prediction · Region growing

Purpose

Cone-beam computed tomography (CBCT) is commonly used in computer-aided surgical simulation (CASS) for craniomaxillofacial (CMF) surgery [1]. Three-dimensional (3D) skull models are generated based on segmented CBCT images. Cephalometric analysis is then completed on the 3D models to quantify the deformity. Virtual osteotomies are done to mimic the surgical procedures performed in the operating room. Once the bony segments are repositioned at the desired final position, intermediate and final digital splints are designed and printed. They are used at the time of the surgery to guide the repositioning of bony segments. One challenge of CASS is the time consumed in image segmentation. Due to the low signal-to-noise ratio, low contrast and excessive artifacts of CBCT images, it often takes at least 6 h to complete the segmentation by manually erasing the noise and filling in missing structures [2]. It is currently not practical for surgeons and orthodontists to use CASS due to this limitation. Thus the planning process is frequently outsourced to expensive commercial services. To significantly reduce the time spent on segmentation and allow doctors to efficiently plan surgery in their own offices, we developed a 3D based interactive algorithm, *Magic Wand*, to accelerate CBCT segmentation.

Methods

Magic Wand can efficiently and accurately segment CBCT sequences three dimensionally through a gradual learning process from fine-tuned segmented images. It consists of the following three steps. The first step is initialization. CBCT is first preprocessed by anisotropic diffusion [3], Laplacian filter and mean-shift algorithm [4]. The initial region-of-interest (ROI) and threshold values are customized. A representative previously-segmented adjacent image with complex anatomy is then selected. The second step is coarse prediction. A fast coarse contour prediction algorithm is developed to predict the initial contours of a new image from the adjacent previously-segmented image. This is done by computing the similarities of pixel values, and the coefficient of variance between the two images. Thus, the contours are propagated automatically from image to image throughout the sequence. The last step is final segmentation. A region growing (RG) algorithm is developed to segment the desired ROI based on results from the previous step. The initial user-determined threshold is scaled based on similarities between weighted mean of the initial ROI and the updated (newly grown) ROI boundary pixels, as well as their neighbors. Using the scaled threshold, the initial ROI continuously grows into the final desired ROI.

Seven sets of CBCT image sequences (approximately 460 images per sequence) from patients with CMF deformities were used to test the *Magic Wand* algorithm. The segmentation, including midface, mandible, spine and soft tissue, was completed twice on each set of data. The first segmentation was completed using the *Magic Wand*, with traditional thresholding and manual editing tools (Fig. 1A–D). This served as the experimental group. The second segmentation was completed only using traditional thresholding and manual editing tools (the current gold standard), without the use of *Magic Wand* (Fig. 1E). This served as the control group. Both segmentations were completed by an experienced oral and maxillofacial surgeon (F.A.) using *AnatomicAligner*, a software programmed using Microsoft Visual Studio 2008, VTK and ITK [5]. The results were compared in two regards. The first was to compare the time spent on segmentation. Wilcoxon signed ranks test was used to detect if there was a statistically significant reduction in time spent on segmentation. The second was to compare segmentation quality, which was done by an independent CMF surgeon (J.X.) who was not involved in the segmentation process and blinded from the method used for segmentation. The CMF surgeon visually not only compared the quality of the 3D reconstructed surface models, but also went through the contours of the mask (segmentation) slide by slide to ensure each contour was correctly extracted.

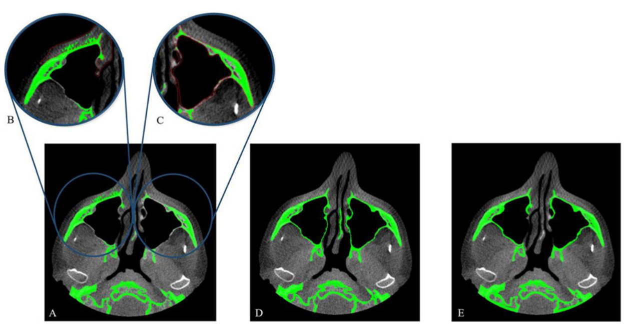

Fig. 1 Results comparison between 2 methods. (**A**) Immediately after traditional thresholding. (**B**) *Magic Wand* detects the noise area to be erased. (**C**) *Magic Wand* detects an area of bone to be filled. (**D**) Result of using *Magic Wand*. (**E**) Manual segmentation result

Results

The mean segmentation time spent in the experimental group was 3.9 h (range 1.8–4.5 h), while the mean segmentation time spent in the control group was 6.4 h (range 5.2–8.5 h). Wilcoxon Signed Ranks Test demonstrated that the *Magic Wand* algorithm significantly reduced segmentation time. The results of the quality evaluation showed that the segmentation achieved in the experimental group was at least as good as the one achieved in the control group (Table 1). Moreover, the quality of midface segmentation in the experimental group was consistently better (Fig. 2).

Table 1 The results of the quality evaluation showed that the segmentation achieved in the experimental group was at least as good as the one achieved in the control group

3D model	"*Magic Wand*" better	No difference noticed	"*Magic Wand*" worse
Midface	7	0	0
Mandible	0	7	0
Spine	3	4	0
Soft tissue	2	5	0

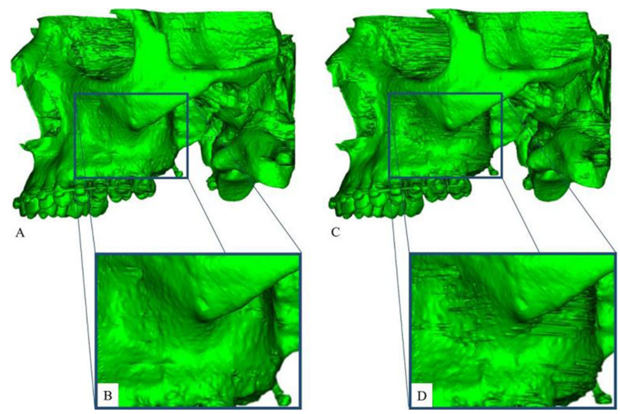

Fig. 2 A 3D midface model from a randomly-selected patient after the segmentation. (**A**) The midface segmented using *Magic Wand*. (**B**) Regional enlarged view of (**A**) The results are smooth and detailed. (**C**) The midface segmented using the manual segmentation tools. (**D**) Regional enlarged view of (**C**) The results are rough and less detailed

Conclusion

CBCT segmentation is important in generating 3D models, whose quality directly impacts the quality of surgical planning. *Magic Wand* not only reduces the time needed for segmentation, it also improves the segmentation quality. It is especially helpful in the segmentation of thin bones. In CMF surgical planning, the midface is an important anatomic region with many thin bones. As previously mentioned, it is extremely difficult to accurately and efficiently segment these bones from the background, either soft tissue or noise, on CBCT. *Magic Wand* helps to efficiently segment the bones and create smoother surfaces, especially in the regions of the anterior maxillary sinus wall, hard palate, pterygoid plates, and orbital floor. Thus it enables surgeons and orthodontists to perform segmentation and surgical planning on their own. With respect to the mandible, it is expected that the quality of mandibular segmentation is equally good between the two methods due to the relative thickness of the mandible and its high contrast. In the future, we will optimize and validate this algorithm using a larger sample size. Ultimately, the *Magic Wand* algorithm will be implemented in all CASS systems.

References

[1] Xia JJ, Gateno J, Teichgraeber JF, Yuan P, Chen KC, Li J, Zhang X, Tang Z, Alfi DM (2015) Algorithm for planning a double-jaw orthognathic surgery using a computer-aided surgical simulation (CASS) protocol. Part 1: planning sequence. Journal of Oral and Maxillofacial Surgery. 44(12): 1431–1440.

[2] Zhang J, Gao Y, Wang L, Tang Z, Xia JJ, Shen D (2015) Automatic craniomaxillofacial landmark digitization via

segmentation-guided partially-joint regression forest model. Medical Image Computing and Computer-Assisted Intervention—MICCAI 2015—18th International Conference. 9351: 661–668.
[3] Perona P, Malik J (1990) Scale space and edge detection using anisotropic diffusion. IEEE Transactions on Pattern Analysis and Machine Intelligence. 12(7): 629–639.
[4] Fukunaga K, Hostetler L (1975) The estimation of the gradient of a density function, with applications in pattern recognition. IEEE Transactions on Information Theory. 21(1): 32–40.
[5] Yuan P, Mai H, Li J, Ho DC, Lai Y, Liu S, Kim D, Xiong Z, Alfi DM, Teichgraeber JF, Gateno J, Xia JJ (2017) Design, Development and Clinical Validation of Computer-Aided Surgical Simulation System for Streamlined Orthognathic Surgical Planning. International Journal of Computer Assisted Radiology and Surgery. 12(12): 2129–2143.

Parotid salivary gland segmentation in Sialo-CBCT scans: method and preliminary results

O. Shauly[1], L. Joskowicz[1], E. Istoyler[2], C. Nadler[2]
[1]The Hebrew University of Jerusalem, Jerusalem, Israel
[2]Hadassah School of Dental Medicine, The Hebrew of University of Jerusalem, Israel, Oro-Maxillofacial Imaging, Oral Medicine Department, Jerusalem, Israel

Keywords Salivary ducts · Sialo-CBCT scans · Segmentation · Modeling

Purpose

The main pathologies of the major salivary glands include infectious, obstructive and inflammatory diseases. Diagnosis is based on clinical examination supplemented with sialography—radiographic imaging following the introduction of iodine contrast solution into the orifice of the salivary gland [1–3]. Cone-Beam Computerized Tomography (CBCT) imaging of the salivary glands has recently replaced planar X-ray imaging, thereby enabling the visualization of the gland architecture with high spatial resolution and lower radiation dose as compared to MDCT [4, 5]. In another work, we show that about a quarter of parotid sialo-CBCT is signed-out as normal, e.g. with normal arbitration without aberration of the ductal diameter or ductal tree [4]. However, there is currently no definition of what constitutes a normal salivary-gland architecture. We hypothesize that the quantitative analysis of salivary gland model obtained from normal parotid Sialo-CBCT scans will help to find and characterize the normal glandular structure and improve the diagnosis of abnormal conditions.

Methods

We have developed a method for segmentation and modeling of the parotid salivary ducts. The input is Sialo-CBCT scan including the patient's head with the contrast media in the parotid gland's ductal system; the output is a segmentation of each of the parotid salivary ducts and a model and analysis of the ducts. The algorithm is fully automatic and consists of two phases: segmentation and modeling. The segmentation phase includes: (1) preprocessing: Region of interest (ROI) extraction and adaptive thresholding to remove unwanted bright structures, e.g., the mandible and the teeth; (2) detection of tubular structures by applying Hessian filtering followed by connected components and geometric analysis; (3) level-set segmentation with the results of the previous step as initialization; (4) identification of the tree-like salivary ducts structure by connected component analysis. The modeling phase includes: (1) skeletonization of the segmentation to obtain a graph with nodes and edges; (2) identification of the root of the tree and extraction of its branches and levels (orders in clinical parlance) with Breadth First Search; (3) generation of maximum intensity projection (MIP) images of the resulting model over the Sialo-CBCT and extraction of the characteristics of the duct model.

Results

We defined a partial, semi-quantitative evaluation method for our algorithm based on maximum intensity projection (MIP) images from various directions with the segmentation results superimposed on them. This is because manual, ground-truth segmentation of teh ducts is impractical and unreliable due to their small size and appearance in the scans. The evaluation is performed by assigning the first and second level branches grades between 0 and 4 (0—branch not detected, 4—branch fully detected), and counting how many of the bifurcationswere found in those branches. Based on this scoring, we measure what percent of the ducts branches and bifurcation were detected by our algorithm.

We evaluate our method on 13 normal ducts in 20 sialo-CBCTs of different patients. The scans were labelled as normal by at least two blinded experts. Our algorithm successfully identified 92% of the gland's ducts; the rest were not identified mostly because of scan artefacts caused by teeth or because of their small diameters. For the successfully identified ducts, an average of 96% (range 50–100, SD = 14) of the primary ducts and 85% (range 17–100, SD = 22) of the second level branches, were correctly detected, based on visual inspection. The average detection rate for the second level branches was 66% (range 4–96, SD = 25) and 55% (range 0–100, SD = 32) for the bifurcations. Figure 1 shows three illustrative examples.

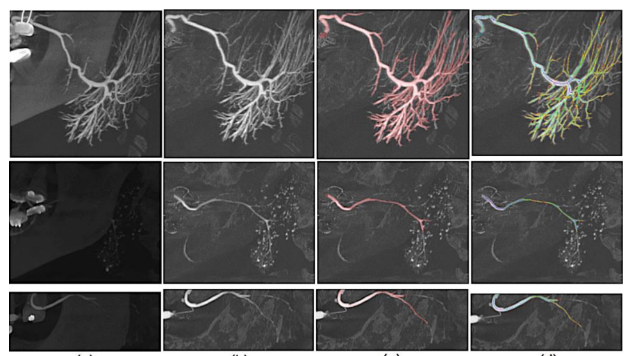

Fig. 1 Three examples of normal (top) and abnormal (middle and bottom) Parotid salivary ducts shown on maximum intensity projection (MIP) reconstruction images of Sialo-CBCT: **a** original image; **b** image after bright background structures removal; **c** segmentation (in red) superimposed on the image after bright structures removal; **d** centerlines colored by the duct's diameter

Conclusion

Our preliminary results indicate that automatic computer-based image analysis diagnosis of patient Sialo-CBCT scans may be a useful tool for the characterization of normal salivary gland architecture and for the diagnosis of pathologies. Ongoing and future work includes improving the segmentation success and the analysis of pathologies.

References

[1] Obinata K, Sato T, Ohmori K, Shindo M, Nakamura M (2010) Comparison of diagnostic tools for Sjogren syndrome, with emphasis on sialography, histopathology and ultrasonography. *Oral Surg Oral Med Oral Pathol, Oral Radiol Endo* (109): 129–134
[2] Aframian DJ, Keshet N, Koplewitz B, Nadler C (2016) Sialo-CBCT for salivary gland imaging in Sjogren's syndrome. *IMAJ* (18): 770
[3] Walach KA, Barenboim SF, Nadler C, Aframian DJ *(2014)* Recurrent parotitis in a young woman. *Oral Diseases* (20): 29

[4] Loubele M, Bogaerts R, Van Dijck E, Pauwels R, Vanheusden S, Suetens P, Marchal G, Sanderink G, Jacobs R (2009) Comparison between effective radiation dose of CBCT and MSCT scanners for dentomaxillofacial applications. *Eur J Radiol* (71): 461–468
[5] Pauwels R (2015) Cone beam CT for dental and maxillofacial imaging: dose matters. *Radiat Prot Dosimetry* (165): 156–161

Semi-supervised spherical K-means for segmenting idiopathic interstitial pneumonia from chest CT images

C. Wang[1], T. Moriya[2], Y. Hayashi[2], M. Oda[2], H. Ohkubo[3], K. Mori[2]
[1]Nagoya University, Graduate School of Information Science, Nagoya, Japan
[2]Nagoya University, Graduate School of Informatics, Nagoya, Japan
[3]Nagoya City University, Graduate School of Medical Sciences, Nagoya, Japan

Keywords Semi-supervised · Spherical K-means · Lung disease · IIP

Purpose

This paper presents a semi-supervised spherical K-means method to segment idiopathic interstitial pneumonias (IIP) regions from CT volume into normal and abnormal regions, automatically. Classification of lung disease patterns is still a challenge in clinical diagnosis, especially for IIP patterns [1]. IIP can be divided into seven histological patterns. Figure 1 shows two typical IIP cases. Normal and abnormal regions are outlined in green and red, respectively. An automatic classification method using computer aided diagnosis techniques is in pressing need. Machine learning or deep learning techniques are preferred for such task. However, it is difficult for radiologists to create pixel-wise gold-standard labels used for the learning. In this work, we use both normal cases and pathological cases to detect the abnormal regions in pathological cases using a semi-supervised approach. By using the proposed method, we can obtain the pixel-wise labels without any manual labelling work.

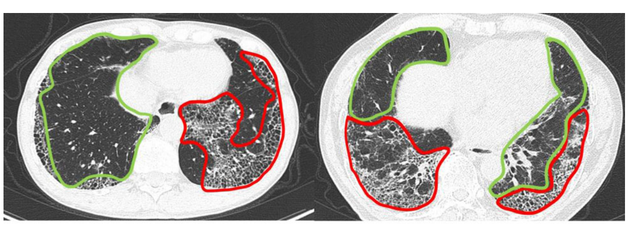

(a) IPF case (b) NSIP case

Fig. 1 Two typical IIP cases. **a** Is idiopathic pulmonary fibrosis (IPF) pattern and **b** is nonspecific interstitial pneumonia (NSIP) pattern. Normal regions are outlined in green and abnormal region are outlined in red

Methods

In this work, input data is 3D CT volume, output is labelling mask of normal and abnormal regions. Unsupervised spherical K-means clustering [2] is used to segment the CT volumes. However, the clustering results of spherical K-means are inconstant, i.e. normal and abnormal regions are labeled randomly. Such clustering results cannot be used in the further supervised classification. To solve this issue, we proposed a semi-supervised approach in this paper. A brief introduction of spherical K-means is described in part (1) and our proposed semi-supervised approach is described in part (2).

(1) Spherical K-means:

Different from conventional K-means, spherical K-means do the clustering in a high dimensional space using cosine dissimilarities. The aim of spherical K-means is to compute another N dimensional representation for N sub-volume patches cropped from original CT volumes. Spherical K-means clustering [2] used this work can be divided into four principal steps: (1) learning a feature extractor $f(\mathbf{x}; \mathbf{D})$, i.e. a function that maps input patches $\mathbf{x}$, sub-volumes cropped from original CT volumes, to k-dimensional feature space R^k. $\mathbf{D}$ is a bank of filters. Assume the size of $\mathbf{D}$ is s, $\mathbf{D}$ is computed by calculating s centroids of higher dimensional space. (2) Cropping CT volume into N sub-volume patches, and then use the trained feature extractor $f(\mathbf{x}; \mathbf{D})$ to compute the representations for these patches. Thus we can get a $N*k$ dimensional feature vector. (3) Applying traditional K-means using the Euclidian distance to cluster the representation into two clusters. (4) Merging all clustered patches into single label volume to get the final segmentation result.

(2) Semi-supervised scheme:

To fix the output labels in unsupervised clustering, a semi-supervised scheme is performed. We add one normal case for each spherical K-means training phase. Assume that C_η is normal case and C_i ($i \in n$) is one case with disease in all n cases. In our semi-supervised scheme, both C_η and C_i will be used for learning feature extractor $f(\mathbf{x}_\eta, \mathbf{D})$ and $f(\mathbf{x}_i, \mathbf{D})$, and their representation $\mathbf{\Phi}_\eta$ and $\mathbf{\Phi}_i$ will also be computed, respectively. At the last clustering step, a classic semi-supervised K-means [3] is applied using $\mathbf{\Phi}_\eta$ as a labeled representation and $\mathbf{\Phi}_i$ as an unlabeled representation data. We set the label of $\mathbf{\Phi}_\eta$ to be $0 \in \{0, 1\}$, thus the label of abnormal region will be clustered to label 1.

Results

Experiments were performed on seven CT volumes with lung diseases. Image size ranges from $512 \times 512 \times 258 \sim 705$ voxels, pixel spacing ranges from 0.55 to 0.75 mm and slice thickness ranges from 0.625 to 1.0 mm. Algorithm was implemented in Python language. All cases were processed using an 8-core 3.2 GHz Intel Xeon machine. Parallel computing programming technique was used to accelerate computing speed. It took about 5–7 min for each case. Recall ratio is used to measure the ability of detecting abnormal regions. The segmentation results of all seven cases were illustrated in Fig. 2. As a comparison, clustering results of the classical K-means using the Euclidean distance was also shown. The average recall ratio of our method is 63.8%. The result showed that our method is able to capture texture information comparing to the classic K-means which has 35.8% recall ratio. However, segmentation result of Case 1 and Case 4 shown in Fig. 2 indicated that the proposed method classified the lung vessels and abnormal regions into same cluster. They can be removed by a simple blood vessel segmentation as post-processing. In Case 3, undersegmentation occurred when pattern scale is larger than trained representation scale.

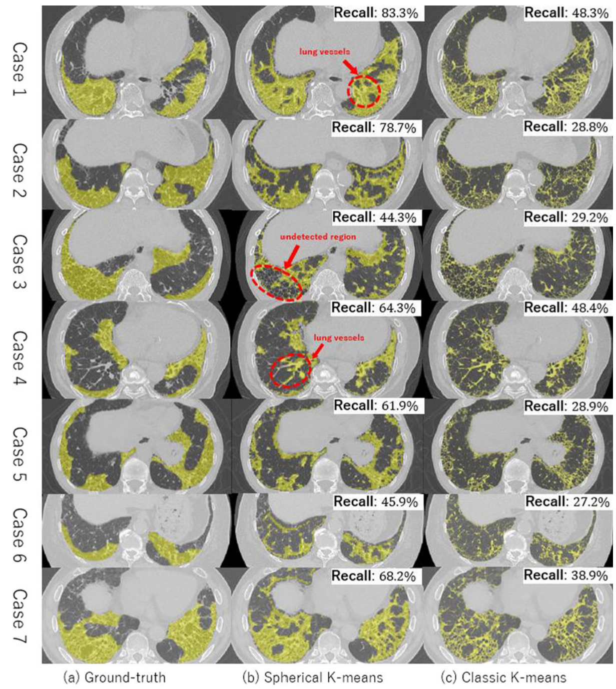

Fig. 2 Experimental results of spherical K-means and classic K-means. Abnormal region is highlighted in yellow. Case 1 and case 4 showed that oversegmentation was occurred mainly in lung blood vessel regions. Case 3 showed that large scale pattern was undetected

Conclusion

The main contribution of this work is to propose an effective segmentation method for IIP patterns. The experimental results showed that the proposed semi-supervised spherical K-means method is able to classify the IIP pattern in a reasonable accuracy. The segmented results can be used as ground-truth label for further supervised training. By using the proposed method, it will effectively reduce human labor to create pixel-wise ground-truth labels. Reducing the FPs, mainly the blood vessel regions, is one of our future works. Also, to solve the undersegmentation issue, a multi-scale scheme is considerable.

Acknowledgement

Parts of this research was supported by the JSPS Kakenhi (26108006, 17H00867, 17K20099) and the JSPS Bilateral Collaboration Grant.

References

[1] Nicholson AG (2002) Classification of idiopathic interstitial pneumonias: making sense of the alphabet soup. Histopathology 41(5): 381–391.
[2] Coates A, Ng AY (2012) Learning feature representations with k-means. Neural networks: Tricks of the trade: 561–580
[3] Basu S, Banerjee A, Mooney R (2002) Semi-supervised clustering by seeding. In proceeding of International Conference on Machine Learning-2002: 19–26.

Analysis of scaphoid fracture kinematics, a clinical application of 4-dimensional computed tomographic imaging

M. G. de Roo[1,2], J. G. Dobbe[1], G. J. Streekstra[1], S. D. Strackee[2]
[1]Academic Medical Center, Biomedical Engineering and Physics, Amsterdam, Netherlands
[2]Academic Medical Center, Department of Plastic, Reconstructive and Hand Surgery, Amsterdam, Netherlands

Keywords Dynamic imaging · 4D-CT · Scaphoid fracture · Quantitative imaging

Purpose

A scaphoid fracture is the most common carpal fracture and is notorious for problems with healing. When healing of the fracture fails (nonunion), a specific pattern of osteoarthrosis occurs, resulting in pain, restricted wrist motion and disability. An important factor associated with the development of nonunion is scaphoid fragment instability [1], i.e. the fragments move with respect to one another during active wrist motion (Fig. 1). To assess fragment instability, an imaging technique is required that can analyze wrist motion in three-dimensional space over time [2, 3]. To this end, a four-dimensional (4D) computed tomographic (CT) imaging technique is readily available in our hospital. This technique is used to quantify if scaphoid nonunion fragment instability depends on the position of the fracture line relative to the scaphoid apex. We hypothesize that fragment instability is increased if the fracture line runs distal to the scaphoid apex [4].

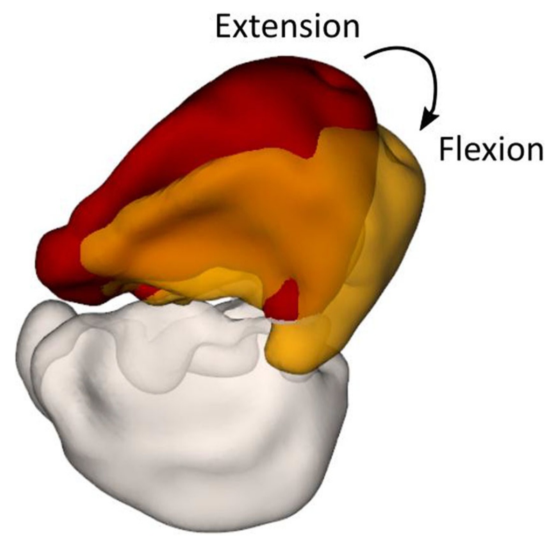

Fig. 1 Observed displacement of the distal scaphoid fragment with respect to the proximal scaphoid fragment (white), if the wrist is moved from extension (red) to flexion (yellow)

Methods

Eleven adult patients were included with a one-sided scaphoid nonunion and no history of trauma to the contralateral wrist, which serves as kinematic reference. In 10 patients the fracture line runs distal to the scaphoid apex and in 1 patient the fracture line runs proximal to the scaphoid apex. Both wrists were scanned with a Philips Brilliance 64 slice CT scanner to obtain static 3D and 4D images. Guided by a dedicated wrist motion device, 4D-CT images were acquired during 10 s of active flexion–extension and subsequent radio-ulnar deviation motion. Custom software is used for segmentation of the wrist bones from the static 3D scan and image registration of the segmented bones to the time frames of the 4D scan. The error of our 4D-CT imaging join kinematic estimation technique is < 2 degrees for rotational and < 1 mm for translational parameters.

Results

In the patient group with the fracture line distal to the scaphoid apex, some scaphoid nonunion fragments demonstrate minimal to no (< 2 degrees) interfragmentary motion, whilst others reach 12, 6, 8, 7 degrees of fragment motion for extension, flexion, ulnar-, and radial deviation, respectively. For the patient in which the fracture line runs proximal to the scaphoid apex, the amount of rotation ranges from 4, 6, 4, 3 degrees for extension, flexion, ulnar-, and radial deviation, respectively. The translations measured fell within the kinematic estimation error of our technique.

Conclusion

No clear trend can yet be found in the amount of fragment motion in relation to the scaphoid apex. However, these results suggest that with 4D-CT imaging we can quantitatively differentiate between stable and instable scaphoid fractures. This promising new imaging technique creates opportunities to quantitatively evaluate normal and pathological wrist kinematics and—in the future—can enable patient-specific fracture treatment (cast treatment versus surgical treatment) and detection of ligament damage.

References

[1] Ten Berg PW, Drijkoningen T, Strackee SD, Buijze GA (2016) Classifications of Acute Scaphoid Fractures: A Systematic Literature Review, *J Wrist Surg,* vol. 5, pp. 152–159

[2] Leventhal EL, Wolfe SW, Moore DC, Akelman E, Weiss AP, Crisco JJ (2008) Interfragmentary motion in patients with scaphoid nonunion, *J Hand Surg Am,* vol. 33, pp. 1108–1115

[3] Buijze GA, Jorgsholm P, Thomsen NO, Bjorkman A, Besjakov J, Ring D (2012) Factors associated with arthroscopically determined scaphoid fracture displacement and instability, *J Hand Surg Am,* vol. 37, pp. 1405–1410

[4] Moritomo H, Murase T, Oka K, Tanaka H, Yoshikawa H, Sugamoto K (2008) Relationship between the fracture location and the kinematic pattern in scaphoid nonunion, *J Hand Surg Am,* vol. 33, pp. 1459–1468

Vascular virtual handling in three-dimensional image for endovascular intervention assistance

T. Shinohara[1], Y. Nishida[1], N. Nakasako[1], M. Ogura[2]
[1]Kindai University, Kinokawa-shi, Japan
[2]Wakayama Medical University, Wakayama-shi, Japan

Keywords Virtual reality · Vascular virtual handling · Endovascular intervention · Three-dimensional image

Purpose

In recent years, the development of medical diagnostic imaging systems has enabled us to create three-dimensional (3D) images in various modalities, such as computed tomography (CT), magnetic resonance imaging (MRI), and so on for clinical use. The 3D expression helps us to intuitively understand the shape of objects. In interventional radiology (IVR), 3D images are also created. For instance, a hepatoma feeding arteriogram [1] is created via CT during aortography (CTAo) using an IVR-CT, a technique that combines an angiographic imager with CT for navigation of transcatheter arterial chemoembolization in hepatocellular carcinoma cases. IVR-CT enables simultaneous, rapid depiction of hepatic and extrahepatic feeding arteries without using an excessive volume of contrast medium. The hepatoma feeding arteriogram is a navigation image for interventional radiologists used to localize the feeding artery immediately before catheterization. The hepatoma feeding arteriogram consists of three volume-rendered (VR) images; a background bone, an aorta-to-hepatic-branch artery, and a tumor-feeding artery. The hepatoma feeding arteriogram can be applied to a variety of endovascular interventions, such as cerebrovascular intervention. However, as the vasculature is intricate, the blood vessel of interest, such as the feeding artery, is not easily observed because of blind areas caused by other blood vessels. One cause for the difficulty of observing a 3D image is the existence of blind areas. Thus, if physicians can virtually handle the blood vessels obstructing the view of the blood vessel of interest in the 3D image, they can more effectively perform catheter treatments. In this study, therefore, we propose a vascular virtual handling system where physicians can three-dimensionally observe the vasculature using a head-mounted display (HMD) as if the blood vessels existed in front of their eyes, and circumvent the difficulty of other blood vessels obscuring the blood vessel of interest using a pointing device to observe the latter.

Methods

The vascular virtual handling system consists of an HMD, a 3D pointing device to handle the blood vessel and a personal computer. Another cause of the difficulty to observe the 3D image displayed on a 2D monitor is the inability to recognize the depth of the 3D image. Thus, the HMD, which utilizes stereo vision, is used. Additionally, the HMD used in this system is assumed to have a sensor to track head movement so that the viewpoint of the user can change according to the head position and its attributes. The effect of the viewpoint change provides a sense of reality as if the blood vessels existed in front of their eyes, so that the blood vessel can be intuitively observed and handled. In this system, the vascular virtual handling is realized by moving a sequence of the center points of the blood vessels because it is difficult to directly move the voxels of the blood vessels in the 3D image. The sequences of the center points of the blood vessels are estimated by the proposed method [2]. This method estimates the diameter of the blood vessel at each center point as well as the sequence of the center points. The blood vessels are reconstructed using the sequence of the center points of the blood vessels as follows. The centerline of the blood vessel is parametrically reconstructed by interpolating each coordinate of the center points with a common parameter using a third-order spline interpolation. Subsequently, the circle with the estimated diameter perpendicular to the resulting centerline is created. The orientation of the centerline corresponds to the derivative of the centerline at each center point. Finally, the blood vessels are reconstructed using polygons made with four neighbor points on two adjacent circles. When the blood vessel is handled, the center points are handled. The handled blood vessel is reconstructed using the handled center points in the same manner. The center points are moved so it seems as though the blood vessel were a string, that is, only some center points near the pointer, indicated by the pointing device, are moved according to the movement of the pointing device. It should be noted that as the handled blood vessel is the one that obscures the blood vessel of interest the shape of the handled blood vessel is not important. Thus, the handled blood vessel does not need to behave like an actual blood vessel.

Results

A prototype of the proposed vascular virtual handling system actually developed is described below. In this system, Oculus Rift and Oculus Touch [3] are used which are an HMD and a 3D pointing device, respectively. The appearance of the system is shown in Fig. 1. These have infrared light-emitting diodes (LEDs), and the infrared light emitted from the LEDs is obtained by two sensors put on the desk near the monitor, so that the positions and attitudes of the HMD and 3D pointing device can be estimated. The 3D head CT Angiography (CTA) image used in this system consists of 430 cross-sectional CT images, which are obtained at approximately 0.35 mm intervals and have a resolution of approximately 0.35 mm/pixel. The sequences of the center points of the blood vessels and the diameter at each center point are estimated from the CTA image by the proposed method [2]. Figure 2 (upper) shows the original cerebral vasculature reconstructed by the sequence of the center points, while Fig. 2 (lower) was taken after the vertebral artery was handled. The internal carotid artery (inside blue dotted circle in Fig. 2 (lower)) obscured by the vertebral artery has become visible.

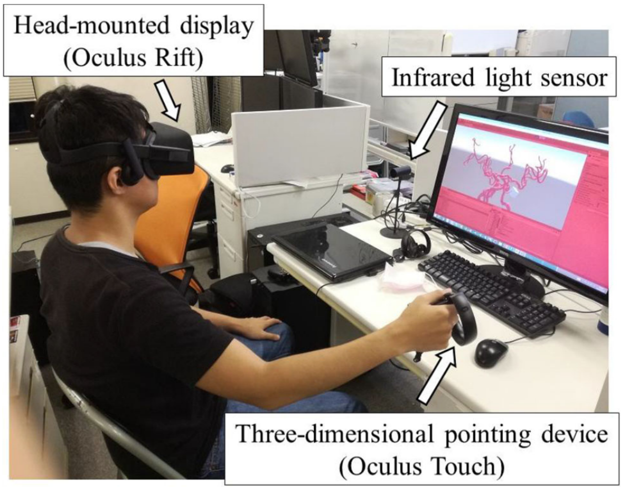

Fig. 1 Appearance of the developed vascular virtual handling system

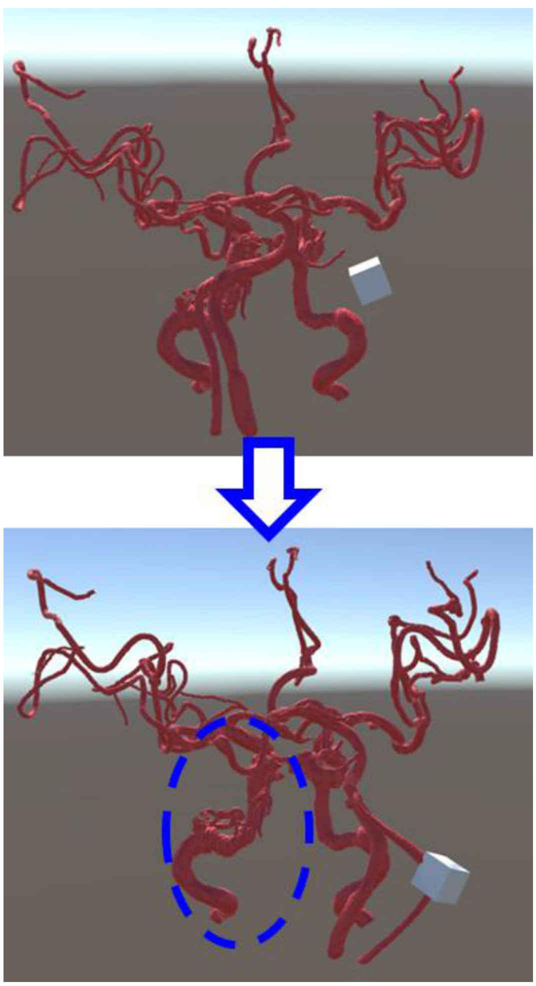

Fig. 2 Vascular virtual handling: before handling (upper) and after handling (lower) of vertebral artery

Conclusion

In this study, vascular virtual handling has been proposed for endovascular intervention assistance. In this system, a physician can observe a vasculature as if the blood vessels existed in front of their eyes through an HMD and subsequently handle the blood vessel, making blind areas. A vascular virtual handling system has been developed using a HMD and 3D pointing device. The blind areas made by the blood vessels in a 3D head CTA image have become visible using this system. In future research, the utility of this system in clinical practice will be further evaluated.

References

[1] Minamiguchi H, Kawai N, Sato M, Ikoma A, Sanda H, Nakata K, Tanaka F, Nakai M, Sonomura T, Murotani K, Hosokawa S, and Nishioku T (2013) Hepatoma feeding arteriogram created by CT during aortography using IVR 64-multidetector-row CT for catheterization in transcatheter arterial chemoembolization for hepatocellular carcinoma. Japanese Journal of Radiology 31(6): 428–436

[2] Shinohara T, Maekawa M, Nakayama M, and Nakasako N (2012) Estimation of centerline and diameter of brain vessel in 3d head cta image by using model matching method. Proceedings of International Forum on Medical Imaging in Asia

[3] Oculus Rift web page (2017) http://www.oculus.com

Background lung tissue deformation correction and ground glass nodule tracking using a feature-based affine registration

K. Ben Zikri[1,2], M. Helguera[1,2], N. Cahill[2,3], D. Shrier[2], C. Linte[1,3,4]
[1]Rochester Institute of Technology, Center for Imaging Science, Rochester, United States
[2]University of Rochester Medical Center, Radiology, Rochester, United States
[3]Rochester Institute of Technology, Rochester, United States
[4]Rochester Institute of Technology, Biomedical Engineering, Rochester, United States

Keywords Computer-aided diagnosis · Lung CT imaging · Image registration · Accuracy assessment/validation

Purpose

Current criteria for assessing lung ground glass nodule (GGN) growth rely on visual comparison and diameter measurements from axial slices of initial and follow-up CT images that show the largest extent of the lesion, without any co-registration [1]. Volumetric analysis is rarely used clinically, as it requires segmentation of the nodule, which is highly inaccurate and could mislead diagnosis, since GGN boundaries are often blurry and not easily distinctive for segmentation. Moreover, the nodule appearance between the initial and follow-up scans is also influenced by complex deformations of the surrounding background lung tissue caused by changes in patient position, the parenchyma surrounding the nodules, heart rate, and respiratory motion, all of which significantly change lung volume and shape [2]. To objectively and accurately assess changes in GGN size and shape due to disease, the initial and follow-up CT images must first be co-registered, while accounting for any background lung tissue deformation that may influence the nodule size and geometry, not caused by the disease. Since the lung is a soft tissue organ, a rigid registration of the initial and follow-up scans will not capture the lung tissue deformation adequately. Although deformable registration may be considered optimal, most deformable registration algorithms are highly dependent on the parameter initialization, are computationally inefficient, and pose a high risk of convergence to local rather than global minima, resulting in unrealistic deformations. As such, depending on the optimization trade-off between the similarity and regularization terms, if the registration is allowed to proceed extensively, the lesion depicted by the registered follow-up image will look similar to the lesion in the initial image, therefore compromising nodule progression assessment. As a result, the difficulty of assessing background lung tissue deformation and using it as a baseline when quantifying the disease-induced lesion changes still exists, and a sufficiently reliable solution is still pending.

Methods

To address this challenge, here we describe and validate a feature-based affine registration method to co-register the initial and follow-up lung CT images. This registration compensates for the background lung deformation, such that the remaining differences in lesion size and shape attributable to the disease could be identified using a digitally subtracted image post-registration as suggested in [3]. Following automatic segmentation and separation of the lungs from both the initial and follow-up CT scans, the registration was initialized by a centroid alignment of the lung- or lesion-centered region of interest (ROI), followed by a feature-based rigid registration. We used an approach that minimizes the Chi squared statistic between the histograms of the initial and follow-up images to identify the optimal initial rotational transform. The subsequent feature-based registration method (Fig. 1) followed a modified formulation and implementation of the iterative closest point (ICP) algorithm. The features used for registration were edges extracted from both the initial and follow-up CT scans using monogenic filtering [4]. Unlike the ICP algorithm in which the objective function minimizes the distance between estimated corresponding points using the closed-form solution of the Euclidean distance, we built a distance map (Maurer et al. 2003) of the initial image by assigning each voxel a value equal to its distance from the closest edge. We then multiplied the distance map of the initial edge image by the transformed follow-up edge image, then computed the sum of the distances from the transformed edges to the edges in the initial image, which served as the objective function to be minimized. Moreover, we separated the edges of the lung boundaries from the edges of the lung content and defined the Energy Dissimilarity (ED) function as the weighted sum of the distances between lung boundary edges and the lung content edges from the initial and follow-up scans. To identify the optimal weighting factor *alpha*, we evaluated the similarity metric (normalized cross-correlation (NCC)) for several values of *alpha* and selected the parameter value that yielded the highest NCC. The registration was implemented on both a lung-centered and a lesion-centered ROI.

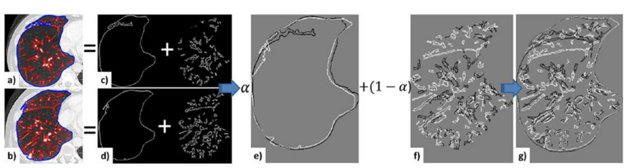

Fig. 1 Feature-based registration algorithm as a weighted sum between lung boundary and lung content edges

Results

We tested the developed registration algorithm on twelve image datasets consisting of initial and follow images of patients at various stage of disease. To assess registration accuracy, we computed the target registration error (TRE) across a set of 30–50 homologous fiducial markers selected by a collaborating radiologist in both the initial and follow-up scans. We compared the TRE achieved using the proposed registration to the TRE achieved using the ANTS Symmetric Normalization deformable registration method deemed optimal by the EMPIRE10 lung registration challenge [5]. In addition, we used the residual fiducial registration error (FRE) across the homologous fiducial landmark datasets selected from the initial and follow-up images as a registration accuracy baseline control, as it assesses the homology of the landmarks based on a rigid least squared fit registration. Lastly, we also conducted a qualitative visual assessment of the registration. Two radiologists were asked to assess the nodule changes across the twelve patient datasets first using the customary standard of care approach (with no registration), then by using a digital subtraction image following feature-based affine registration. Our accuracy study showed differences on the order of 0.5 mm between the TRE achieved using feature-based affine vs. deformable registration (Table 1, Fig. 2), however with significant computing performance improvements (Table 2) under affine registration. Similarly, the visual assessment using digital subtraction images clearly showed the correct changes in lung nodules between the initial and follow-up scans (Fig. 2).

Table 1 Target registration error (TRE in mm) across 12 patient datasets for affine, deformable and baseline registration

Registration method// TRE (mm)	Lung-centerd ROI		Lesion-centered ROI	
	Mean ± SD	Median	Mean ± SD	Median
Affine registration	1.8 ± 1.6	1.4	1.5 ± 1.2	1.1
Deformable registration	1.2 ± 1.2	0.8	1.2 ± 1.2	0.8
Rigid least squared fit FRE (control)	1.6 ± 1.1	1.3	1.5 ± 1.2	1.2

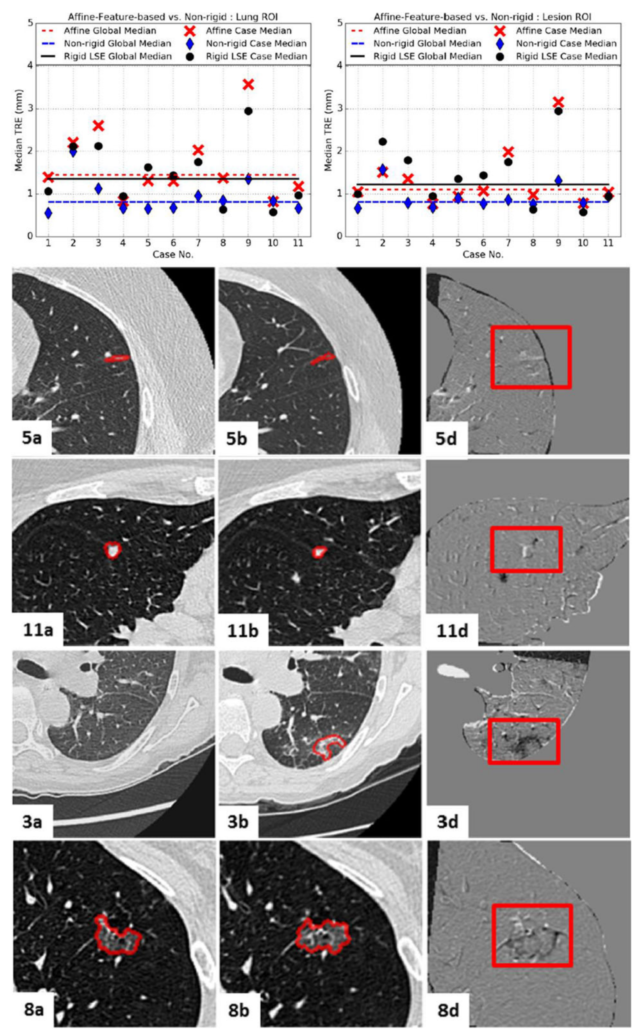

Fig. 2 TRE comparison across 12 patients between, deformable, and baseline control (rigid least squared fit) registration (*upper panel*); Visual assessment of post-registration subtraction image: no nodule change (5), slight nodule change (11), new nodule (3), and severe nodule change (8) (*lower panel*)

Conclusion

We described and validated a feature-based affine registration method designed to co-register initial and follow-up lung CT images to correct for the background lung tissue deformation to help objectively assess lung nodule changes induced by disease. Our study showed less than 1 mm difference between the registration accuracy achieved using the feature-based affine registration, deformable registration, and baseline control registration, with significant performance improvement when using the affine registration. Moreover, the qualitative visual assessment conducted by two radiologists confirmed similar conclusions about the nodule changes using the digital subtraction image post-registration as the current standard of care assessment method (Table 2).

Table 2 Performance (min) of rigid, affine, and deformable intensity- and feature-based registration on lung- and lesion-centered ROI

Registration method	Lung-centered ROI (357 × 248 × 455)		Lesion-centered ROI (144 × 152 × 93)	
	Intensity	Feature	Intensity	Feature
Affine registration	119.0 ± 10.3	8.0 ± 10.0	1.3 ± 2.3	0.7 ± 1.5
Deformable registration	245.0 ± 40.0	N/A	17.2 ± 10.2	N/A

References

[1] Ko JP, Berman EJ, Kaur M, Babb JS, Bomsztyk E, Greenberg AK, Naidich DP, Rusinek H (2012) Pulmonary Nodules: growth rate assessment in patients by using serial CT and three-dimensional volumetry. Radiology. 262: 662–671.

[2] Zheng Y. Proc. IEEE CVPR. 101–108. 2009.

[3] Staring M, Bakker ME, Stolk J, Shamonin DP, Reiber JH, Stoel BC (2014) Towards local progression estimation of pulmonary emphysema using CT Med Phys. 41: 021905-1–021905-13.

[4] Rajpoot K, Grau V, Noble JA (2009) Local-phase based 3d boundary detection using monogenic signal and its application to real-time 3-d echocardiography images. In: Proceedings—2009 IEEE international symposium on biomedical imaging: from nano to macro, ISBI 2009, pp. 783–786

[5] Song G, Tustison N, Avants B, Gee JC (2010) Lung CT image registration using diffeomorphic transformation models. Medical Image Analysis for the Clinic: A Grand Challenge, pp. 23–32

Research PACS for diabetic retinopathy screening

C. Costa[1], M. Pedrosa[1], J. M. Silva[1], S. Matos[1]

[1]Universidade de Aveiro, DETI/IEETA, Aveiro, Portugal

Keywords Medical imaging · PACS · Diabetic retinopathy · Screening

Purpose

This article presents a research PACS that supports the SCREEN-DR project, an image analysis and machine learning platform for innovation in diabetic retinopathy (DR) screening. This pathology is a leading cause of blindness worldwide [1] obligating many communities to promote regular screening programs [2]. The research goals are to develop a collaborative PACS platform that could address the specific requirements of the project, which cannot be satisfied by conventional ICT platforms available in radiology departments, and to promote collaboration between physicians and researchers in the scope of a regional DR screening program. The clinical partner is the Portuguese North Health Administration (ARSN) that is implementing a mass DR screening to reach around 75% of a population of 250,000 diabetic patients in the north of Portugal. The screening process consists in taking pictures of the patients' eye fundus through mobile retinographers, which are then sent to a centralized repository and posteriorly analyzed by experts.

The SCREEN-DR project contemplates three stages. First, the system will determine if fundus eye images have sufficient diagnosis quality. Then, the system will evaluate the images for normality, i.e. if they exhibit diseased or normal characteristics. Finally, the system will grade the severity of DR pathology. This article focuses on the development of a collaborative Web platform that integrates a multimodal Retinopathy-PACS (R-PACS) oriented to research purposes. Namely, it aims to investigate new solutions for extracting, merging and searching over multimodal data, including DICOM metadata and annotations. The platform collects the studies from ARSN repository in an anonymized way, indexes the images metadata, and allows the creation and management of distinct datasets according to researcher needs and their annotation process, including visual annotation of lesions. These processes will be supported by an agile collaborative platform that targets research purposes, namely construction of phenotype-specific databases to feed artificial intelligence algorithms, and even teaching. Functionally, the platform aims to create, annotate, search and retrieve retinopathy datasets.

Methods

R-PACS was developed as an extension to Dicoogle open-source [3] solution with a plug-in-based architecture (Fig. 1). It can receive and export retinopathy images and associated data using the DICOM standard interface or REST web services. An authentication module was developed with single-sign-on support. A new annotation database was created for supporting structured data (e.g. image quality assessment or diagnosis) and visual annotation of lesions. The multimodal search was developed to work over DICOM metadata, image features and retinopathy annotations. A new anonymization tool supports metadata but also visual information burned in the pixel data.

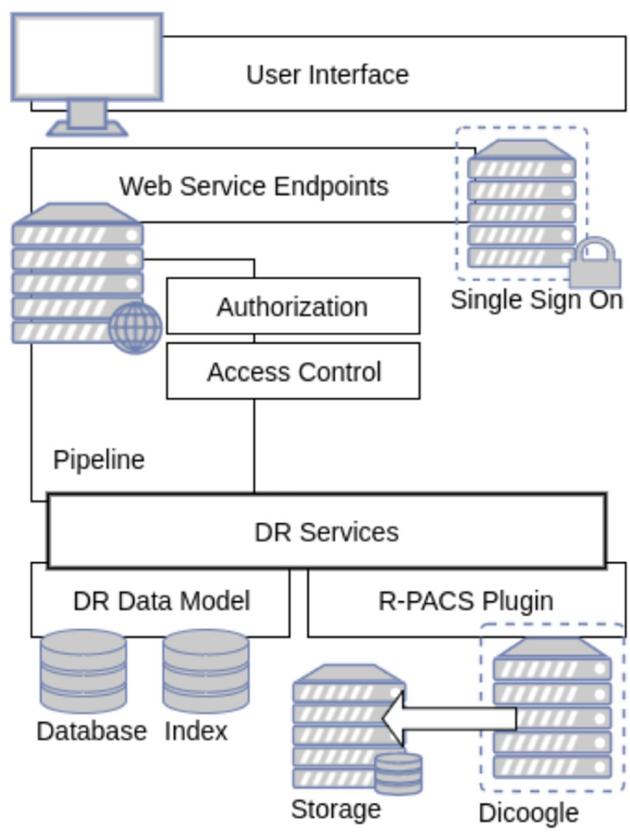

Fig. 1 SCREEN-DR collaborative platform architecture

The web portal is fully integrated with R-PACS and supports four use cases:—Web upload of cases by dragging into the portal studies that are indexed and stored in the R-PACS;—Annotation of datasets, including grading and lesion annotation;—Advanced search and retrieve over any attribute contained in R-PACS DICOM metadata and annotations database, allowing the query results to be downloaded or used to create annotation datasets;—Visualization of archived studies, supported by a zero-footprint Web DICOM viewer provided by BMD Software.

Results

SCREEN-DR Web platform can be accessed at http://demo.dicoogle.com/screen-dr. It supports the project use cases and it is fully integrated with R-PACS. All images available in the R-PACS can be used to create a dataset according to distinct criteria (e.g. patient gender, equipment, study date). R-PACS repository is in production and includes 1655 studies imported from ARSN. It supports the storage of distinct datasets, including textual and visual annotation according with research requirements (Fig. 2). The platform is fully integrated with the Web collaborative portal.

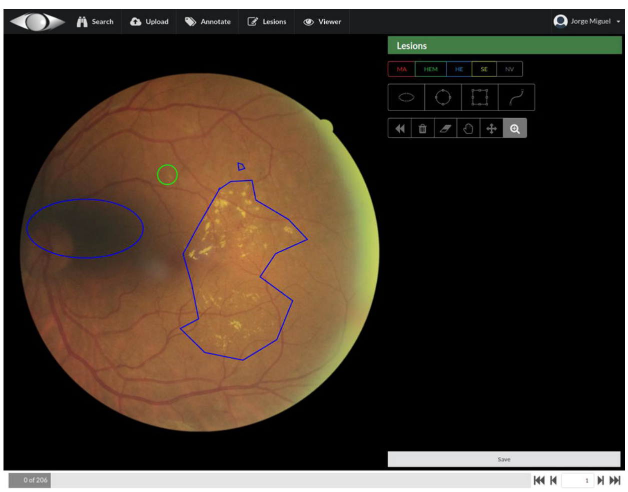

Fig. 2 Annotation module

Conclusion

This article presents a novel collaborative Web platform of the SCREEN-DR project that promotes collaboration between physicians and researchers in the scope of a regional DR screening program. The role of researchers is to create classification algorithms to evaluate image quality, discard non-pathological cases, locate possible lesions and grade DR severity. Physicians are responsible for annotation of datasets, including visual delineation of lesions. The collaborative platform collects the studies, indexes the images metadata, and manages the datasets creation and respective annotation process. An advanced searching mechanism supports multi-source queries over annotated datasets and exporting of results for feeding artificial intelligence algorithms.

Acknowledgements

This work is financed by the European Regional Development Fund through the Operational Programme for Competitiveness and Internationalization—COMPETE 2020 Programme, and by National Funds through the Fundação para a Ciência e a Tecnologia (FCT) within Project CMUP-ERI/TIC/0028/2014. SM is supported by a FCT Investigator Grant.

References

[1] World Health Organization, Global Data on Visual Impairments 2010, Technical Report, 2010

[2] Yau JW, Rogers SL, Kawasaki R, Lamoureux EL, Kowalski JW, Bek T, Chen SJ, Dekker JM, Fletcher A, Grauslund J, Haffner S, Hamman RF, Ikram MK, Kayama T, Klein BE, Klein R, Krishnaiah S, Mayurasakorn K, O'Hare JP, Orchard TJ, Porta M, Rema M, Roy MS, Sharma T, Shaw J, Taylor H, Tielsch JM, Varma R, Wang JJ, Wang N, West S, Xu L, Yasuda M, Zhang X, Mitchell P, Wong TY, (2012) Meta-Analysis for Eye Disease (META-EYE) Study Group, Global Prevalence and Major Risk Factors of Diabetic Retinopathy, Diabetes Care 35 556–564

[3] Valente F, Silva LAB, Godinho TM, Costa C (2016) Anatomy of an Extensible Open Source PACS. Journal of Digital Imaging 29 284–296

Target definition with 3D surface scanning for orthovoltage radiation therapy planning

A. Ilina[1], C. Pinter[1], A. Lasso[1], I. Lai[2], C. Joshi[2], K. Alexander[2], L. J. Schreiner[2], T. Hanna[2], G. Fichtinger[1]
[1]Queen's University, School of Computing, Kingston, Canada
[2]Queen's University, Department of Physics, Engineering Physics, and Astrophysics, Kingston, Canada

Keywords 3D surface scanning · Orthovoltage · Radiotherapy · Skin cancer

Purpose

Orthovoltage radiation therapy (ORT) is a non-invasive cancer treatment technique commonly used to treat superficial tumours, such as non-melanoma skin cancer. This treatment can be preferred to surgical excision in cases where surgery could cause poor cosmetic outcomes [1]. Currently, there is no commercially available treatment planning system for ORT. Non-melanoma skin cancers treated with ORT present on the surface of the skin, typically in the head and neck region. As part of treatment planning process, the extent of the skin cancer must be localized in a CT scan [2]. As the skin cancer does not show in CT, prior to scanning the radiation oncologist marks the tumor contour on the skin with a cutout fiducial, which then is visible in the CT image. This process is suboptimal for a several reasons: it is prone to human error, and it is expensive for requiring the radiation oncologist to be present during an otherwise routine CT scanning. We propose to use non-contact optical three-dimensional surface scanning to acquire colored and textured image of the patient at the time of CT scanning, segment the tumour and overlay its contour on the CT images for subsequent dosimetry planning.

Methods

A red sticker representing a skin lesion was placed on a male plastic mannequin phantom. The head and neck phantom was segmented from a CT image using thresholding based on image intensity. The resulting segment was cropped to remove the shoulders and traces of the bed table and pillow, keeping only the head of the phantom. The surface of the phantom's face was scanned using the Artec Eva 3D Surface Scanner (Artec 3D, Luxembourg), to obtain a full-coloured textured 3D mesh. The Artec Eva is a handheld 3D scanner that can be used to make fast high-quality scans of medium sized objects, such as the head and neck phantom. The segmented head model and surface scan model were pre-registered using five fiducials manually placed on the nose tip, inner corners of eyes, and front of ears. After pre-registration, the iterative closest points (ICP) algorithm was used to align the two models more precisely (Fig. 1). The pre-registration step is needed to ensure the two models are sufficiently close to each other before running the ICP algorithm; if the pre-registration step is skipped, an incorrect registration may be found by the ICP algorithm. The tumour was manually segmented by following the outline of the lesion from the surface scan model. The tumour was segmented to a depth of approximately 1 cm, to mimic depth of superficial NMSCs.

The defined tumour was saved with the CT scan to DICOM-RT, for use in treatment planning (Fig. 2). The software platform 3D Slicer, an open-source application for medical image visualization and analysis, was used for segmentation and registration [3].

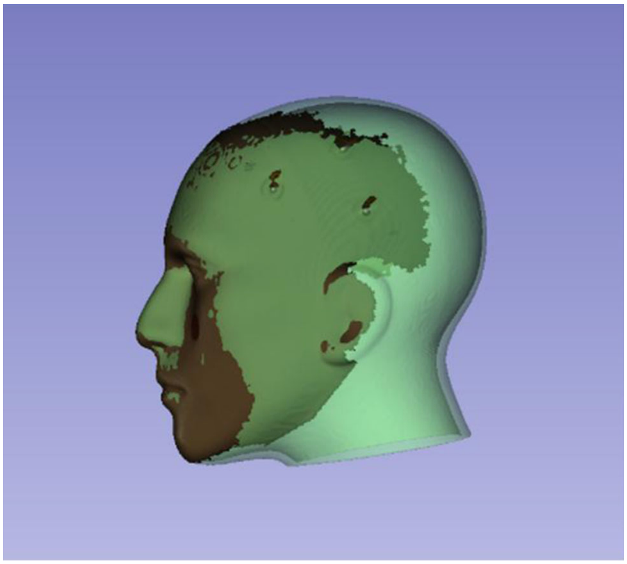

Fig. 1 Following pre-registration using fiducials, the ICP algorithm is used to register the surface scan model of the head to the model of the head segmented from CT

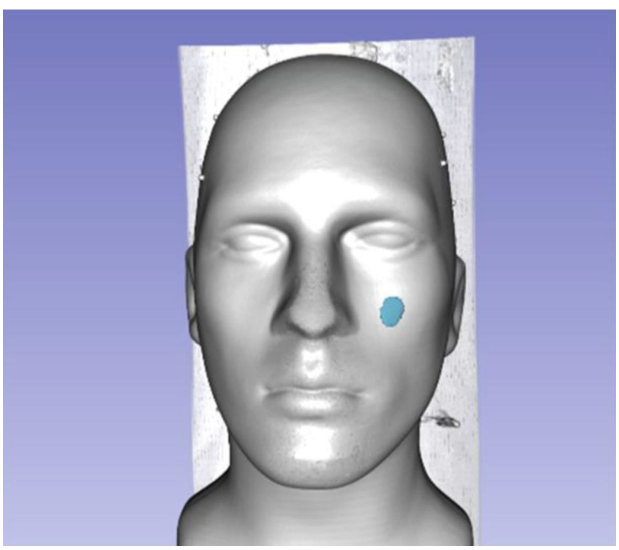

Fig. 2 The tumour (blue) was segmented from a 3D surface scan. The segmented tumour is shown with the CT image of the mannequin head; both of these are needed for treatment planning

Results

The Artec Eva was chosen for 3D surface scanning because is can provide 3D resolution of up to 0.5 mm and has colour capture capability. The red sticker placed on the mannequin to mimic a skin legion was clearly visible on the textured mesh created using the scanner's software, and could be easily segmented by following the outline of the lesion. After pre-registration using five fiducials placed on the segmented head model and the surface scan model, the two models were roughly aligned. Performing registration using the ICP algorithm on the two pre-registered models yielded the final registration, with a mean distance after registration of 0.25 mm. The mean distance was computed between the points which constitute the surface scan model and the nearest corresponding points on the triangulated cells of the model segmented from CT. The workflow of 3D surface scanning, segmenting the head from CT, registering the 3D surface scan model to the segmented phantom model, and segmenting the tumour was completed in about 7 min.

Conclusion

Tumour location for lesions visible at the surface of the skin can be defined with the help of 3D surface scanning, leading to a quick workflow and eliminating the need for more complex methods of localizing the tumour. This project presents the first step toward developing a free open-source treatment planning system for orthovoltage radiation therapy. Finally, this method of using 3D surface scanning to define target location can be extended beyond non-melanoma skin cancer, to define the location of any superficial or shallow tumours and lesions which are visible at the skin's surface.

References

[1] Kharofa J, Currey A, Wilson J (2013) Patient-Reported Outcomes in Patients with Nonmelanomous Skin Cancers of the Face Treated with Orthovoltage Radiation Therapy: A Cross-Sectional Survey. International Journal of Radiation Oncology

[2] Burnet N, Thomas S, Burton K, Jefferies S (2004) Defining the tumour and target volumes for radiotherapy. Cancer Imaging 4(2): 153–161

[3] Fedorov A, Beichel R, Kalpathy-Cramer J, Finet J, Fillion-Robin JC, Pujol S, Bauer C, Jennings D, Fennessy F, Sonka M, Buatti J, Aylward S, Miller JV, Pieper S, Kikinis R (2012) 3D slicer as an image computing platform for the quantitative imaging network. Magnetic Resonance Imaging 30(9): 1323–1341

A stochastic optimization approach accounting for uncertainty in HDR brachytherapy needle placement

T. Yu[1], F. A. Siebert[2], A. Schlaefer[1]
[1]Hamburg University of Technology, Institute of Medical Technology, Hamburg, Germany
[2]Universitätsklinikum Schleswig–Holstein Campus Kiel, Medical Physics, Kiel, Germany

Keywords Brachytherapy · Inverse planning · Stochastic optimization · Uncertainty

Purpose

HDR brachytherapy requires the optimization of dwell times to shape the dose distribution according to the planning target volume (PTV) and organs at risk (OAR). Often, this is done after needle placement, i.e., when the needle geometry is already fixed. However, the flexibility in arranging the needles can impact the plan quality. We include the selection of the needle geometry in the inverse planning problem and study whether uncertainties due to tissue deformation and needle deflection can be handled by a novel stochastic optimization scheme. To evaluate and illustrate the approach we consider a prostate brachytherapy scenario. Particularly, we consider uncertainty in the needles tip position, e.g., due to overly conservative insertion to avoid risking bladder damage, due to errors defining the needle tip in the images, or due to the limited seed positioning repeatability of the afterloading unit.

Methods

Following standard inverse planning approaches, we first discretize the PTV and the OAR into virtual point clouds. Needles are modeled as line segments starting from the perineum and ending at the basal part of the prostate gland before the bladder base. They are allowed to be skew to reflect possible robotic needle insertion. Dose calculation is conducted for a HDR source of 47,000 U using the TG-43 formalism. Dwell positions are defined with 2 mm distance in our study. Inverse planning is implemented using stochastic linear optimization, which extends standard linear programming to account for uncertainty. We set fixed upper bounds on the OAR and minimize an objective penalizing underdosage of the PTV. To maintain a conformal dose distribution, we define a SHELL structure consisting of points on an extruded surface of the PTV. The distance between SHELL and PTV is 5 mm, and we set upper bounds of 450 and 400–700 cGy on the OARs (bladder, rectum) and the SHELL, respectively. The upper bound on the SHELL is tuned to allow for maximum coverage of the PTV at its lower bound of 850 cGy.

To model uncertainty with respect to the needle placement, we consider the position of the tip of each needle to undergo independent random displacements, i.e., we add random displacement vectors to the planned tip positions inside the prostate. Subsequently, we use B-Splines to interpolate a deformed PTV shape from these random displacements using the shifted and static needle tips as control points. Essentially, each set of random displacements results in a new geometry of the PTV with respect to the needles. We then extend the above linear program to a stochastic linear program using sample average approximation. For each sample of needle tip displacements we add a new set of variables corresponding to the deformed PTV as well as new terms to the objective analogous to those of the original problem scaled by the reciprocal of the number of samples used. We keep the fixed upper bounds on the OAR and SHELL. In the end, we obtain a large scale stochastic linear program (SLP) with substructures which mirror the structure of the original linear program (LP).

Given a configuration of needles and a patient geometry, applying the stochastic optimization results in a set of stochastic dwell times (SDT) for the configuration which is robust to needle placement errors and tissue deformation. In contrast, assuming a single fix geometry, i.e., without uncertainty in the needle position with respect to the PTV, we would solve a conventional LP to compute deterministic dwell times (DDT).

We compare the difference in coverage between DDT and SDT solutions. For a concrete example, we consider axial uncertainties where the random displacements are constrained to lie on the needle axes. We sample from a truncated Gaussian distribution with means ranging from 2 to 10 mm and standard deviations of 1–5 mm to obtain the magnitude of the random displacements. To account for the randomized needle selection, we use the best out of 10 randomly generated configurations. For each mean magnitude, we apply the stochastic optimization to 10 × 10 random needle configurations of 7 needles. In addition, to see the effect of varying the number of needles, we apply the stochastic optimization with mean magnitude 6 mm to 10 × 10 random needle configurations for each number of needles ranging from 4 to 14. In each case, we draw a set of 200 random displacements as the sample to setup and solve the SLP. A second, independent set of 300 random displacements serves as a test set to evaluate the DDT and SDT solutions under uncertainty.

Results

For the 300 samples of the test set we summarize results for different mean displacements in Fig. 1. The figure illustrates that the median improvement due to the SLP solution is positive starting from displacements as small as 2 mm. For larger displacements, the improvement can be as much as 12 percentage points. For example, if we expect a displacement of 6 mm the median improvement of SDT versus DDT would be 7 percentage points, increasing coverage from app. 84% to app. 91%. At worst, the solutions do not differ much, which is reasonable as our modelled uncertainty allows for zero displacements. In fact, the robust solution may perform worse when there was no deviation from the static geometry, as can be seen from the small negative values for 2 and 4 mm displacements. Note, that this will be rather unlikely as illustrated by the quantiles shown by the boxes.

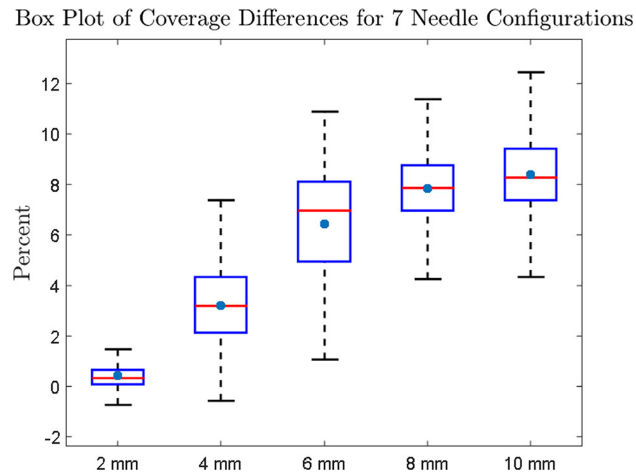

Fig. 1 Difference in the PTV coverage for mean displacements ranging from 2 to 10 mm. A positive value shows the improvement in PTV coverage for the SLP solution in percentage points. The boxes represent the quantiles, the circle represents the mean

Figure 2 shows that the effect of using the SLP to compute SDT is maintained with growing number of needles considered during optimization. Note that more needles result in more freedom to combine dose delivery from different directions to cover the complete PTV and coverage approaches 100% for the SDT case. Hence, the maximum improvement decreases. Still the SDT solutions outperform DDT solutions with a mean improvement in coverage of app. 6 percentage points.

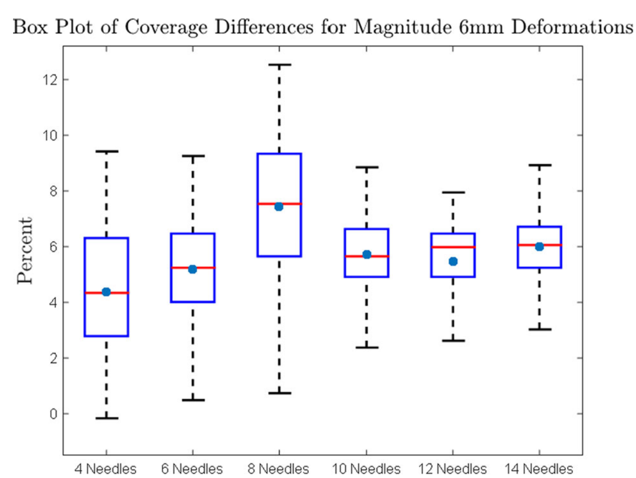

Fig. 2 Difference in the PTV coverage for 4–14 needles and an expected displacement of 6 mm. A positive value shows the improvement in PTV coverage for the SLP solution in percentage points. The boxes represent the quantiles, the circle represents the mean

Conclusion

For the vast majority of needle configurations, stochastic optimization accounting for uncertainties in the needle placement can substantially improve coverage over deformed geometries while maintaining the coverage of traditional inverse planning on static geometries.

Mathematical modeling of acute rectal toxicity to compare two patient positioning methods for prostate cancer radiotherapy

M. Fatyga[1], X. Liu[2], J. Li[2], S. Schild[1], W. Wong[1], S. Vora[1], M. Herman[3], M. Schild[1]
[1]Mayo Clinic Arizona, Radiation Oncology, Phoenix, United States
[2]Arizona State University, School of Computing, Informatics, Decision Systems Engineering, Tempe, AZ, United States
[3]Mayo Clinic Rochester, Radiation Oncology, Rochester, United States

Keywords Prostate cancer · Toxicity modeling · Rectal toxicity · Setup error

Purpose
Intensity modulated radiation therapy (IMRT) for prostate cancer benefits patients by creating steep dose gradients at the boundaries of the treated volume which enables dose escalation to the tumor, while sparing adjacent organs. However, this treatment technique is more sensitive to the patient positioning error than older, less precise techniques. If clinicians escalate the dose to the target but fail to control the setup error, an IMRT technique can increase, rather than decrease, the treatment toxicity. The goal of this study was to investigate whether mathematical modeling of acute rectal toxicity in radiation therapy for prostate cancer could be useful as a tool to monitor the clinical quality of an IMRT program. The validity of mathematical modelling of clinical outcomes in radiation therapy critically depends on an assumption that dose distributions in treatment plans are correlated with dose distributions that are delivered during treatments. If setup errors were well controlled one expects to observe a clear correlation between rectal dosimetry in the treatment plans and rectal toxicities which were recorded during treatments. In contrast, if setup errors were poorly controlled the correlation between treatment plans and the toxicity outcomes could be degraded. To achieve the goal of the study we modeled grade $\geq$ 2 acute rectal toxicity in two groups of patients who were treated with dosimetrically similar IMRT protocols but very different patient setup techniques: Image Guided technique with implanted fiducial markers (FMIGRT) and transabdominal ultrasound guided patient positioning technique (USGRT). We quantified the degree of correlation between planning dosimetry and toxicity outcomes in both groups to determine if the correlation could be affected by patient positioning technique. We used modelling to compare the incidence of acute rectal toxicity in both groups to determine if differences in the incidence of toxicity could be accounted for by the planning dosimetry alone.

Methods
79 patients treated with IMRT and Image Guidance with implanted fiducial markers (FMIGRT), and 302 patients treated with trans-abdominal ultrasound guided IMRT (USGRT) were selected for this study. Kilovoltage imaging was used in the FMIGRT group and the trans-abdominal ultrasound BAT system was used in the USGRT group. Treatment plans were available for the FMIGRT group and hand recorded dosimetric indices were available for both groups. We fit Lyman–Kutcher–Burman (LKB) model and univariate logistic regression (ULR) model to planning dosimetry in FMIGRT group and ULR model to recorded indices in both groups. We extrapolated the ULR model which was developed for the FMIGRT group to predict the incidence of acute rectal toxicity in the USGRT group. We compared predicted and observed incidences of toxicity in the USGRT group. We performed receiver operating characteristics (ROC) analysis on all models and compared area under the ROC curve (AUC) for both groups. We used FMIGRT patients to simulate an effect of a systematic posterior shift of the isocenter by 5 mm on the incidence of acute rectal toxicity. For each patient a new treatment plan was created with an isocenter shifted by 5 mm posteriorly and the ULR model was used to estimate an increase in the expected incidence (normal tissue complication probability) of acute rectal toxicity.

Results
Incidence of grade $\geq$ 2 rectal toxicity was 20.3% (N = 16) in FMIGRT patients and 54% (N = 162) in USGRT patients. LKB model parameters in FMIGRT group were, TD50 = 56.8 Gy, slope m = 0.093, and exponent n = 0.131. The most predictive indices in the ULR model for FMIGRT group were D25% and V50 Gy (Fig. 1, Table 1). The AUC for both models in FMIGRT group was similar (AUC = 0.67) and in good agreement with previously published models of rectal toxicity [1]. A fit of the ULR model to USGRT data did not yield a predictive model (AUC = 0.5) for any of the four dosimetric indices available in the database. The predicted incidence of grade $\geq$ 2 acute rectal toxicity in the USGRT group was 27%, while the incidence of 54% was actually observed. The simulation of an effect of a posterior shift of the isocenter by 5 mm in the FMIGRT group predicted approximate doubling of the incidence of acute rectal toxicity (Table 2).

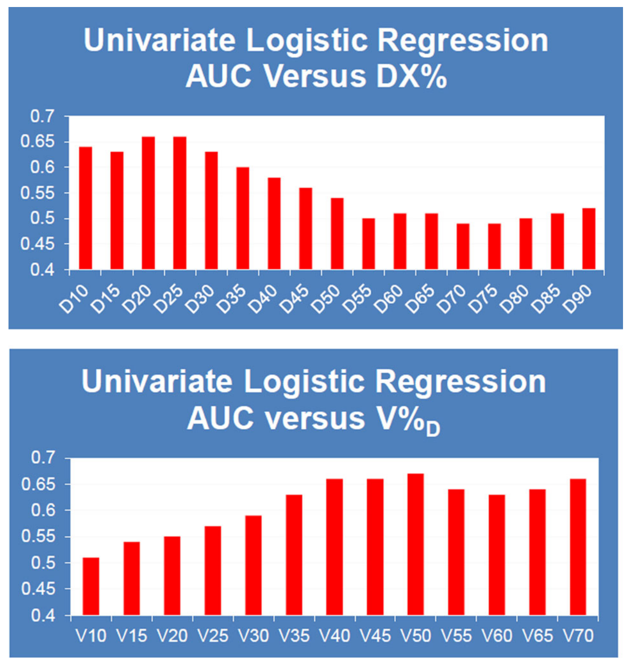

Fig. 1 AUC of ULR models for a range of dosimetric indices. The "optimum index" maximizes the AUC

Table 1 Parameters and 95% confidence intervals of the LKB and univariate logistic regression models obtained with DVHs for FMIGRT patients, describing grade $\geq$ 2 acute rectal toxicity

LKB				
	TD_{50}	m	n	AUC
Acute toxicity	56.8 [53.7, 59.9]	0.093 [0.077, 0.108]	0.131 [0.099, 0.163]	0.67 [0.54, 0.80]
QUANTEC	76.9 [73.7, 80.1]	0.13 [0.10, 0.17]	0.09 [0.04, 0.14]	0.67 [0.54, 0.81]
Univariate				
$D_{25\%}$			$\log\left(\frac{NTCP}{1-NTCP}\right)$	
a_0			-5.23 [-9.93, -1.40]	
			$P = 0.015$	

Table 1 continued

Univariate	
γ	0.098 [0.002, 0.212]
	$P = 0.064$
AUC	0.66 [0.49, 0.76]

QUANTEC late rectal toxicity model is shown for comparison. The AUC for the QUANTEC model was obtained by applying to acute rectal toxicity data in this work

Table 2 A comparison of FMIGRT and USGRT databases

	Mean index value FMIGRT	Mean index value USGRT	Estimated incidence of acute rectal toxicity in USGRT (%)	Observed incidence of acute rectal toxicity in USGRT (%)	AUC (based on recorded indices) FMIGRT	AUC (based on recorded indices) USGRT
$D_{1.8\%}$	77.5 ± 1.7 Gy	75.4 ± 4.4 Gy	12	54	0.63 [0.48, 0.78]	0.54 [0.47, 0.6]
$D_{10\%}$	64.9 ± 5.8 Gy	68.4 ± 5.2 Gy	29		0.58 [0.43, 0.72]	0.52 [0.45, 0.58]
$D_{30\%}$	42.5 ± 6.8 Gy	52.5 ± 6.6 Gy	37		0.62 [0.47, 0.77]	0.52 [0.46, 0.59]
$D_{40\%}$	34.6 ± 7.6 Gy	47.4 ± 6.3 Gy	30		0.58 [0.43, 0.74]	0.49 [0.44, 0.57]

ULR models derived from the FMIGRT database were applied to USGRT to estimate expected incidence of acute rectal toxicity in USGRT database under an assumption that planning dosimetry was the only factor that influenced toxicity in both databases. ULR models were fit to hand extracted indices in both databases and AUCs for both are shown in the last two columns

Conclusion

We observed a correlation between planning dosimetry and acute rectal toxicity for the FMIGRT patients and the strength of this correlation was similar to published work on modeling of rectal toxicity [1]. In contrast, no such correlation was observed in USGRT patients in spite of a much larger number of patients in this group. In addition, the observed incidence of acute rectal toxicity in USGRT patients was approximately twice as large as predicted by the planning dosimetry alone. A literature search revealed a 2010 study [2] which compared patient positioning with the trans-abdominal ultrasound BAT system to patient positioning with implanted electromagnetic transponders. The study concluded that patient positioning with the BAT system may have been associated with a systematic shift of the isocenter posteriorly, by as much as 5 mm, on average. Our simulation of a posterior shift of the isocenter in FMIGRT patients estimated that a shift of this magnitude would approximately double the expected incidence of acute rectal toxicity. This estimate is broadly consistent with our acute rectal toxicity data, as the incidence of 27% was predicted in the USGRT group on the basis of planning dosimetry alone, while the incidence of 54% was actually observed. In summary, a correlation between acute rectal toxicity and planning dosimetry could be measured in a relatively small sample of patients. Lack of such correlation in clinical data should be always concerning as it may indicate a potentially significant systematic setup error in the delivery of IMRT treatments.

References

[1] Michalski J, Gay H, Jackson A, *Tucker S, Deasy J (2010)* Radiation Dose-Volume Effects in Radiation-Induced Rectal Injury. *International Journal of Radiation Oncology Biology Physics* 76(3): S123–S129.

[2] Foster R, Solberg T, Li H, Kerkhof A, *Enke C, Willoughby T, Kupelian P (2010)* Comparison of transabdominal and electromagnetic transponders for prostate localization. *Journal of Applied Clinical Medical Physics* 11(1): 57–67.

Efficient Multi-Organ Segmentation of the Head and Neck area using Hierarchical Neural Networks

E. Tappeiner[1], S. Pröll[1], M. Hönig[1], P. F. Raudaschl[1], P. Zaffino[2], M. F. Spadea[2], G. C. Sharp [3,4], R. Schubert[1], K. Fritscher[1]

[1]University for Health Sciences, Medical Informatics and Technology, Hall in Tirol, Austria

[2]Magna Graecia University of Catanzaro, Catanzaro, Italy

[3]Harvard Medical School, Boston, United States

[4]Massachusetts General Hospital, Boston, United States

Keywords Multi-organ segmentation · Neural network · Head and neck · Radiotherapy

Purpose

In radiation therapy, a key step for a successful cancer treatment is image-based treatment planning. One objective of the planning phase is the fast and accurate segmentation of organs at risk and target structures from medical images. However, the manual delineation of organs, which is still the gold standard in many clinical environments, is time consuming and prone to inter-observer variations. Consequently, many automated segmentation methods have been developed. With Head and Neck (HaN) cancer being among the most common cancer types, we present a highly efficient approach that is entirely based on the usage of convolutional neural networks, to segment organs in the HaN area. Using the presented pipeline, multiple organs at risk (OAR) can be segmented simultaneously without the need of pre-registration or other time consuming pre-processing steps.

Methods

In our work, we hierarchically train two fully convolutional 3D Neural Networks based on the HighRes3DNet architecture [1]. The HighRes3DNet is a end-to-end trainable segmentation network, using dilated convolutions. Contrary to typical segmentation architectures the HighRes3DNet upscales the convolutional kernels with a dilation factor to increase the receptive field but keep the resolution of the volume constant through the training process. The training of one path, reduces the number of parameters and is shown to achieve better results than other architectures for the brain parcellation task.

Roth et al. [2] proposed to train two hierarchical networks to segment multiple organs in the abdominal area. Accordingly, we train a coarse network on size- reduced medical computed tomography (CT) images to first locate the organs of interest. For each image, the patient's body is detected and following used as binary mask. To fit the images into the GPU memory we uniformly draw sampling windows (patches) with their central pixel positioned on the binary mask. The patches are then used to train the first network. The consecutive fine stage network is trained on the full-resolution CT images for a more detailed segmentation. At this stage the patches are drawn from a dilated binary mask created from the results of the first, coarse stage network. Again, the patches are used for training the fine stage network and the final results are generated after a simple post-processing step. For the post-processing the binary mask of each organ generated by the coarse network is used to remove segmented voxels

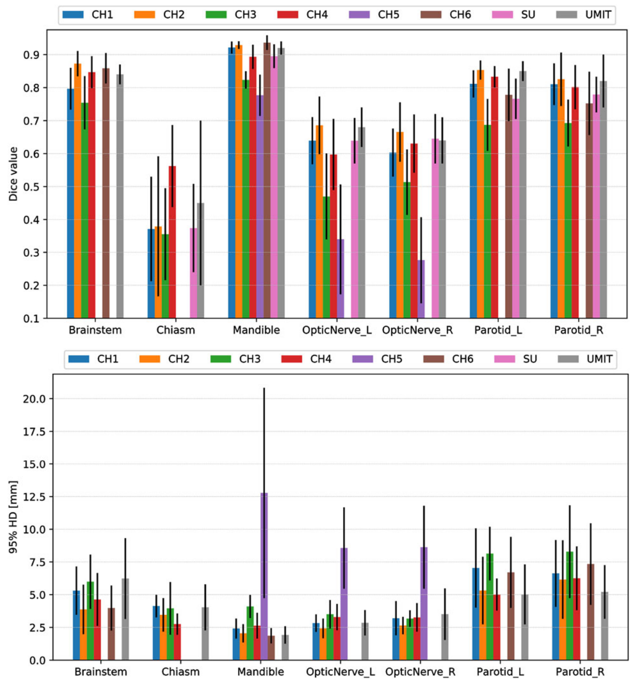

Fig. 1 Results of the participants of the MICCAI 2015 Head and Neck Auto-Segmentation Challenge (Ch1-Ch6) [3] and the patch-based CNN of the Stanford University USA (SU) [5] in comparison to the best configuration of our presented hierarchical HighRes3DNet (UMIT). (Top) Organ wise average Dice value over the test image dataset. (Bottom) 95% HD average over the test images

outside this mask. To segment an image, at inference time, the patches are sampled form a overlapping grid on the binary masks from each stage.

Results

The approach is applied on a publicly available CT dataset, created for the MICCAI 2015 Auto-Segmentation challenge [3]. In an extensive evaluation process, the best configurations for the trained networks is determined. For the evaluation we train the coarse and fine stage networks, with quarter, half and full resolution images, learning rates from 10^{-5} to 10^{-3} and large, medium and small sized patches. All configurations are trained using a dice based loss function and the generalized dice loss [4], which normalizes the dice score using the patch-wise volume of the organs to segment. Finally, the best configurations for the coarse and the fine stage are selected to generate the segmentation results. The best coarse stage results could be achieved using half sized CT images, medium sized patches and a learning rate of 10^{-3}. For the fine stage the configuration using full resolution CT images, small sized patches and again, a learning rate of 10^{-3} works best. Compared to existing state-of-the-art methods, our presented approach show similar performance for the segmented structures in the head and neck area. A single test image can be segmented in less then a minute, on a Nvidia GeForce GTX 1080 GPU. Figure 1 illustrates the achieved results on the MICCAI Auto-Segmentation [3] test set in comparison to the participants of the challenge and the Deep Learning approach of Ibragimov et al. [5]. The code used to generate the results and the configuration files with corresponding trained models can be found on Github (https://www.github.com/elitap/NiftyNet).

Conclusion

We conclude that 3D Neural Networks outperform most existing model- and atlas-based methods for the segmentation of organs at risk in the head and neck area. The high accuracy, easy usage and test time efficiency of the method makes it highly valuable for image-based radiotherapy treatment planning in clinical practice.

References

[1] Li W, Wang G, Fidon L, Ourselin S, Cardoso M J, Vercauteren T (2017) On the compactness, efficiency, and representation of 3D convolutional networks: Brain parcellation as a pretext task. Information Processing in Medical Imaging 348–360. https://doi.org/10.1007/978-3-319-59050-9_28

[2] Roth HR, Oda H, Hayashi Y, Oda M, Shimizu N, Fujiwara M, Misawa K, Mori K (2017) Hierarchical 3D fully convolutional networks for multi-organ segmentation. arXiv preprint arXiv:1704.06382

[3] Raudaschl PF, Zaffino P, Sharp G, Spadea MF, Dawant BM, Albrecht T, Gass T, Langguth C, Lüthi M, Jung F, Knapp O, Wesarg S, Mannion-Haworth R, Bowes M, Ashman A, Guillard G, Brett A, Vincent G, Orbes-Arteaga M, Cárdenas-Peña D, Castellanos-Dominguez G, Aghdasi N, Li Y, Berens A, Moe K, Hannaford B, Schubert R, Fritscher KD (2017) Evaluation of segmentation methods on head and neck CT: Auto-segmentation challenge 2015. Medical Physics 44(5):2020–2036. https://doi.org/10.1002/mp.12197

[4] Sudre CH, Li W, Vercauteren T, Ourselin S, Cardoso MJ (2017). Generalised Dice overlap as a deep learning loss function for highly unbalanced segmentations. Deep Learning in Medical Image Analysis and Multimodal Learning for Clinical Decision Support 240–248. https://doi.org/10.1007/978-3-319-67558-9_28

[5] Ibragimov B, Xing L (2017) Segmentation of organs-at-risks in head and neck CT images using convolutional neural networks. Medical Physics 44(2):547–557. https://doi.org/10.1002/mp.12045

22nd Annual Conference of the International Society for Computer Aided Surgery

President: Pierre Jannin, PhD (F)

A novel medical robot architecture with ORiN for efficient development of telesurgical robots

N. Iwamoto[1], A. Nishikawa[1], T. Kawai[2], Y. Horise[3], K. Masamune[3]
[1]Shinshu University, Faculty of Textile Science and Technology, Ueda, Japan
[2]Osaka Institute of Technology, Department of Robotics, Osaka, Japan
[3]Tokyo Women's Medical University, Institute of Advanced Biomedical Engineering and Science, Tokyo, Japan

Keywords Telesurgical robots · Master–slave robotic devices · Middleware · Medical robot architecture

Purpose

Various telesurgical robots, such as da Vinci, AESOP, and ZEUS, have been developed. In general, in telesurgical robots, a master operated by a surgeon or a surgical assistant and its slave are connected in a one-on-one fashion. The master and the slave cannot be separated and exchanged with a master or a slave of another system. The evaluation of the robots has been limited to specific master/slave combinations of telesurgical robots. The development of a robot architecture that allows researchers to freely select and connect masters and slaves between different telesurgical robots enables rapid evaluation of different master/slave combinations. Then, the robot architecture will provide a system wherein an operator selects a master suitable for him/her to assign it to a certain slave. And more, the master/slave robot should have the inter-connectivity to exchange various time-synchronized information, such as bio-signals, navigation information, robot's log data, via an integrated system of medical devices in OR. In the proposed robot architecture, the information can be easily obtained via smart cyber operating theater (SCOT) system [1] which has been developed in our group. The use of the proposed robot architecture will lead to a more efficient research and development of telesurgical robots.

Methods

We propose a new open resource interface for the network (ORiN [2])-based medical robot architecture, MRLink, to freely select and connect masters and slaves between different telesurgical robots. Figure 1 illustrates the concept of MRLink with ORiN. By separating the master from the slave and passing through the middleware, this architecture provides a quick evaluation of the master/slave combination and enables a more efficient development of telesurgical robots. In addition, we aim to develop two systems: a system integrating a general interface device and a commercial slave robot and a system wherein an operator selects a master suitable for him/her to assign it to a certain slave.

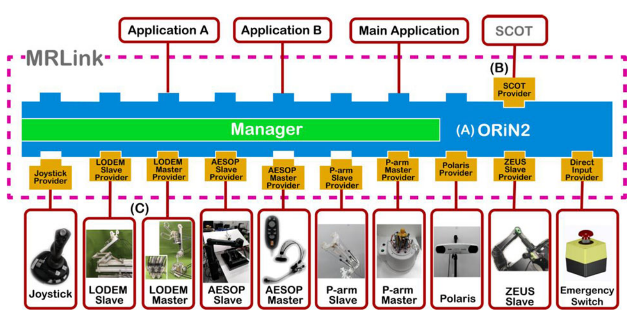

Fig. 1 Schematic of conceptual MRLink, an open resource interface for the network (ORiN)-based medical robot architecture

ORiN (Fig. 1A) is a commercial middleware advocated by the Japan Robot Association, and has already been used in industry and has been shown to be highly reliable (ISO20242). The ORiN middleware runs on both Windows and Linux platform, and supports RS232C, TCP/IP, UDP and so on as a standard communication protocol to connect devices. In order to make the connection of the equipment easy, we have to prepare for each device a wrapper class which hides equipment specific access procedure called "provider". The wrapper class has four functions: Init(), Execute(), get_Value(), and put_Value(), and these four functions are implemented using the C++ programming language. Conversely, higher level applications can be coded in various languages, such as C++, C#, visual basic for applications (VBA), and Java.

The development of a medical system called smart cyber operating theater (SCOT) is currently being advanced in our group. SCOT is a fully functional integrated operation system that can be used for practical treatments. Because SCOT uses the ORiN middleware, there is a natural similarity between SCOT and MRLink that enables an easy connection between MRLink and SCOT (Fig. 1B).

Results

Currently, MRLink supports some commercial master/slave devices and interfaces as follows: the AESOP slave, the ZEUS slave, the P-arm master/slave [3], the LODEM master/slave [4], keyboards, joystick controllers, Polaris Vicra, Polaris Accedo, and web cameras. We conducted simple connection tests with each device, and developed a system that exchanges masters and slaves between the AESOP and the P-arm. Furthermore, we succeeded in controlling a manipulator of the ZEUS slave from an application on ORiN. We analyzed the signal output from the original master of ZEUS and developed a custom controller board capable of outputting the signal. The custom controller board is controlled from a GUI application (self-made master in Fig. 2) on a PC in real time via ORiN.

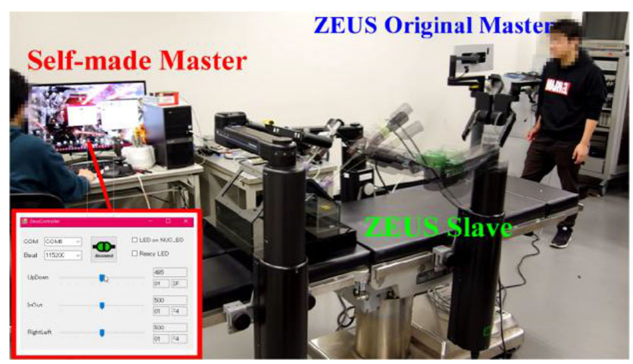

Fig. 2 This figure shows the result of manipulating the ZEUS slave via ORiN from a GUI application developed as a self-made master

Apart from connecting the commercial robots, the newly developed robotic forceps LODEM are also connected to MRLink (Fig. 1C). LODEM is a locally operated unilateral master/slave control system with a mechanically separable handy device for a surgery support forceps manipulator when the surgeon is in the sterilized area. It is assumed that multiple LODEMs are placed around the surgical table and that one master operates by switching the slave to be controlled. Since MRLink can provide a system independent of the number of masters, it is suitable for systems such as LODEM.

Conclusion

Herein, we proposed a new medical robot architecture, MRLink, for connecting freely selected master/slave robotic devices. The ORiN middleware is adopted as the core technology of MRLink. So far, several devices have been connected to MRLink and a simple connection test has been performed.

This research is partly supported by KAKENHI (JP16H01859).

References

[1] Okamoto J, Horise Y, Masamune K, Iseki H, Muragaki Y (2016) Development of a Prototype Model of "Hyper SCOT (Smart Cyber Operating Theater)". Proceedings of the CARS2016 11: S163.

[2] ORiN. http://www.orin.jp/e/ visited 01.10.2018.

[3] Sekimoto M, Nishikawa A, Taniguchi K, Takiguchi S, Miyazaki F, Doki Y, Mori M (2009) Development of a Compact Laparoscope Manipulator (P-arm). Surgical Endoscopy 23(11): 2596–2604.

[4] Kobayashi H, Kawai T, Nishikawa A, Horise Y, Masamune K (2017) Locally Operated Master–Slave Control System with Mechanically Separable Master Device for Laparoscopic Forceps Manipulator. Annu. Int. Conf. Eng. Med. Biol. Soc.

Pilot study toward autonomous surgical system with the markerless navigation and compact robot for oral and maxillofacial surgery

Q. Ma[1], E. Kobayashi[1], J. Wang[2], K. Hara[1], K. Masamune[3], H. Suenaga [4], I. Sakuma[1]

[1]The University of Tokyo, Department of Precision Engineering, Tokyo, Japan

[2]Beihang University, School of Mechanical Engineering and Automation, Beijing, China

[3]Tokyo Women's Medical University, Institute of Advanced BioMedical Engineering and Science, Tokyo, Japan

[4]Department of Oral-Maxillofacial Surgery, Dentistry and Orthodontics Tokyo, Tokyo, Japan

Keywords Surgical robot · Oral and maxillofacial surgery · Navigation · Autonomous system

Purpose

Human-related factors affect the accuracy and safety of the oral and maxillofacial surgery (OMS). Some surgical navigation method and clinical robot have been proposed in OMS to guide the operation and relieve the physical burden of the surgeon. However, previously proposed navigation method mainly use the fiducial markers and tracking devices, which encountered the problems of line-of-sight constraints and the marker shift. Moreover, most of the existing OMS robots adopted a conventional mechanical design, their bulky figuration make them fail to satisfy the requirement of OMS which has a relatively small working space. In our previous work, a markerless navigation system [1] and a compact OMS robot [2] were individually developed for the AR guide and precise positioning, respectively. In this study, we further integrate these two different systems into an autonomous surgical system, aiming to develop an intelligent surgical system to decrease the influence of human-related factors on the OMS. This autonomous surgical system may work as an artificial surgeon while the current surgeon may become an assistant or surveillance. Such fundamental role change between human and machine could finally benefit the outcomes of OMS.

Methods

This autonomous surgical system mainly consists of three modules: markerless navigation module, compact robot module, and position correlation module. The markerless navigation module conducts the image matching between the subject's teeth model with intraoperative video to obtain its pose, which consists of offline and online phase. In the offline phase, the hierarchical aspect graphs of teeth models were built based on the patient's CT image. Then in the online phase, the aspect graphs were compared with the real images of exposed teeth captured by a homograph camera (2048 × 2048 pixels). The tracking-learning-detection (TLD) method and the iterative closest point (ICP) method were used for the coarse and refined detection of the 6-DOF pose of the teeth model with respect to the camera in real time, which is further used for the robot control and AR display.

The compact robot module consists of three parts: 3DOF orientation mechanism, 3DOF position mechanism, and workspace limitation mechanism. The orientation mechanism adopted the remote center of motion (RCM) design to change end-effector's orientation by three individual motors. The position mechanism had a novel parallel mechanism to change the end effector's axial coordinate in working space with other three motors. The workspace limitation mechanism used a limitation block made by 3D printing based on the subject's CT image and the preoperative plan, which can mechanically protect the subject from any unintended injury.

The position correlation module used a marker tracking system to obtain the position of navigation module and robot module and connected them to work as an integrated system. The infrared markers were attached to the camera and robot to identify their relationship in working space and initialize the origin of the robot.

The operational accuracy of the whole system was evaluated by analyzing the individual accuracy of each module. For navigation module, a phantom experiment was conducted to evaluate the registration accuracy by using target registration errors (TRE) on the target points. For robot module, the robot's drilling and cutting performance were tested on the 3D printed mandible models, which was further analyzed by statistically evaluating the error of operation by 3D scanning on the models.

Results

The system overall view was shown in the attached figure. All the application software for navigation, robot control, marker tracking were exclusively developed for this system. The work flow of this system includes three procedures. First, the CT data of the subject was obtained for making the preoperative plan, building the offline aspect graph of teeth model, and 3D printing workspace limitation block. Second, the limitation block was installed onto the robot and the robot's origin was automatically initialized based on the coordinate information. Third, the system application will integrate the information of planned trajectory, post-initialized position of the endpoint, and intraoperative movement of subject's head. Then the endpoint will finally move based on calculated trajectory (Fig. 1).

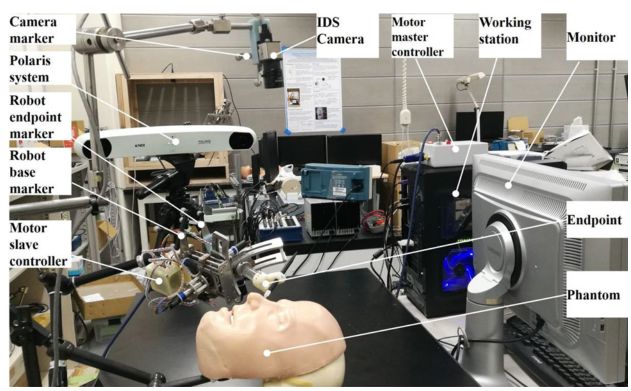

Fig. 1 The overview of the whole system. The phantom, camera, and robot were supported by the mechanical arm, respectively. The motor slave controller and motor master controller of robot was connected with a customized cable first, then the motor master controller connected to working station with USB cable

The overall accuracy of the system is affected by the individual accuracy of each module. The registration accuracy of navigation module yielded the satisfactory results, which varied from 0.67 to 1.05 mm in different parts of the model. The drilling and cutting accuracy of robot module were 1 and 0.5 mm, respectively. The accuracy of position correlation directly depends on the tracking system's own properties and the Polaris Spectram's tracking accuracy is 0.35 mm. Above analyzing numbers indicate that current accuracy in navigation and robot module are acceptable, and the possible way to further improve the accuracy of the whole system will be the topic of our future study.

In the proposed system, the camera worked as surgeon's eye, the robot work as surgeon's hand, with marker tracking system connecting the "eyes" and "hands", we could create an artificial surgeon. Although the proposed system may not be a completed unmanned surgical system at its current status due to the hardware limitation and safety consideration, nevertheless it provides a possible way to let robot be the operator, while the surgeon may act as the assistant and surveillant. That means this autonomous surgical system can work as a surgery-assistance or surgeon-surveillance system, which may fundamentally change the role of surgeon and reshape the scene of the future operation room.

Conclusion

Human-related factors affect the accuracy and safety of the oral and maxillofacial surgery (OMS). This study proposed the workflow toward autonomous surgical system aiming to conduct the OMS under the assistance and surveillance of surgeon. The results show that individual accuracy of each module is acceptable and there are potentials to further improve the whole system's accuracy. The proposed system has promising potential for future clinic use since it may shift the surgeon's working priority from the intraoperative implement to the preoperative planning. In the future study, we plan to conduct experiments to test this system's performance in a more practical environment.

References

[1] Wang J, Suenaga H, Hoshi K, Yang L, Kobayashi E, Sakuma I, Liao H (2014) Augmented reality navigation with automatic marker-free image registration using 3-D image overlay for dental surgery, IEEE transactions on biomedical engineering 61: 1295–1304

[2] Hara K., Suenaga H, Masamune K (2015) Error analysis of the surgical robot with novel positioning mechanism for oral and maxillofacial surgery, in Proceedings of JSME-IIP/ASME-ISPS Joint Conference on Micromechatronics for Information and Precision Equipment: IIP/ISPS joint MIPE 2015, 2015, pp. _TuD-2-5-1–_TuD-2-5-3.

Evaluation of robotically-assisted ureteroscopy for kidney exploration in a phantom study

R. Zee[1], H. Fooladi Talari[1], C. Peters[2], R. Monfaredi[1], C. Bayne[1], K. Cleary[1]

[1]Children's National Health System, Washington, United States

[2]UT Southwestern, Urology, Dallas, United States

Keywords Urology · Robotics · Kidney · Phantom

Purpose

We present the development and evaluation of a system for robotically-assisted ureteroscopy of the kidney. Ureteroscopy is a minimally invasive procedure for the treatment and diagnostic evaluation of a wide range of upper urinary tract pathology. In a typical ureteroscopy procedure, a flexible ureteroscope (endoscope) is guided into the urethra followed by the ureteral orifice, up the ureter and into the renal pelvis under fluoroscopic guidance. The ureteroscope is then manipulated manually to inspect the kidney. However, maneuvering the ureteroscope throughout the entire kidney and ensuring complete coverage can be challenging, particularly in the lower pole of the kidney where the instrument must be simultaneously flexed, rotated, and pulled back to guide the scope into the lower calyces. In addition, the physician is forced to constantly hold the ureteroscope during the entire procedure. This can lead to arm fatigue, subsequent arm tremors, and loss of long-term productivity for the urologist due to chronic motion injury. Therefore we developed a robotic device to hold and manipulate the ureteroscope under joystick control.

Methods

The robotic device is shown in Fig. 1. The device allows independent control of the three degrees of freedom of the ureteroscope via brushless motors. In the proposed clinical workflow, the device would be positioned between the legs of the patient and the ureteroscope would be snapped-in after the tip of the ureteroscope is at the level of the renal pelvis. This snap-in capability makes the device independent of the brand of ureteroscope used and could be adapted for other endoscopes in the future. The device can then be controlled via a joystick interface.

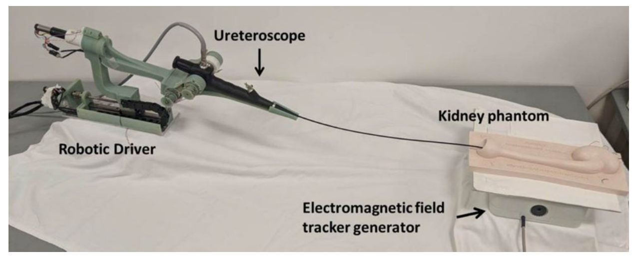

Fig. 1 Experimental setup showing the ureteroscope and robotic driver on left and kidney phantom on right. Underneath the phantom is the electromagnetic tracking field generator

For the evaluation studies, a kidney phantom was used and three target wires were inserted: a black wire in the upper calyx, a red wire in the middle, and an orange wire in the lower calyx. An electromagnetic tracking system was used to track the position of the ureteroscope tip through a small sensor embedded in the working channel and a field generator positioned under the phantom. An MRI scan of the phantom was done and the phantom images were registered with the tracking coordinate system using paired-point registration. This allowed for image overlay of the tip position within the phantom anatomy.

The evaluation study was approved by the local ethics board. Nine urologists (1 attending, 3 fellows, 5 residents) and one urology researcher were recruited to participate from our pediatric hospital. After training briefly with the joystick interface, the participants used the system to navigate from the ureteropelvic junction (UPJ) to the black wire, then the red wire, and finally, to the orange wire. Time between each target was recorded to evaluate efficiency.

Results

The results are shown in Fig. 2. Of the 30 targeting attempts, the wires were found in 29 of them. In one case the orange wire was not found after 3 min and the experiment was stopped. The average time from renal entry to the black wire was 36.5 s, from the black wire to the red wire was 44.8 s, and from the red wire to the orange wire was 82.4 s.

	Black wire	Red wire	Orange wire	Total
Subject	Time (s)			
1	55	15	44	114
2	20	34	21	75
3	34	48	not found	incomplete
4	73	20	45	138
5	27	131	58	216
6	12	7	248	267
7	44	143	57	244
8	40	6	62	108
9	42	14	132	188
10	18	30	75	123
count	10	10	9	9
sum (s)	365	448	742	1473
average (s)	36.5	44.8	82.4	163.7
st dev	18.5	50.3	69.1	67.3

Fig. 2 Results of the phantom study with 10 subjects

At the conclusion of the trial, the participants were asked to answer the following questions: (1) Are there are any urologic procedures where the device could be useful?; (2) Did you find the system easy or difficult to use?; and (3) Do you have any suggestions for improving the system? Eight of 10 participants responded to question 1. Of those, six respondents stated that the ureterbot may be useful for procedures such as diagnostic ureteroscopy, upper tract tumor ablation, and nephrolithiasis.

For question 2, six of the 10 participants found the user interface intuitive and easy to use, while 2 did not, and 2 did not provide an answer. Three respondents, including one who deemed the system easy to use (participant #10) indicated that it would be easier to perform ureteroscopy manually. One user (participant #6) commented that the inspection could be performed faster manually but the device would be much more ergonomic.

For the final question of improvements to pursue, most respondents cited a delay between manipulation of the joystick and movement of the ureteroscope. This may have been attributable to a slight lag in the responsiveness of the system which needs to be improved in future versions. Additionally, two respondents suggested that tactile feedback may improve the success of the ureterobot.

Conclusion

This abstract presented a phantom study evaluation of robotically-assisted ureteroscopy. A majority of participants found the device easy to use. While the concept is promising and the implementation has some ergonomic benefits, more work needs to be done before the system can be applied clinically. The integration of the device with pre-operative imaging and navigation might also allow better visualization of the tip position without the need for fluoroscopic imaging.

Robotic and electromagnetic navigation system for automatic guidance of biopsy catheters to peripheral pulmonary airway targets

L. Gruionu[1], C. Constantinescu[2], C. Ciobirca[2], A. Soimu (Iacob)[2], A. L. Udristoiu[2], A. Saftoiu[3], G. Gruionu[4]
[1]University of Craiova, Faculty of Mechanics, Craiova, Romania
[2]University of Craiova, Faculty of Automation, Computers and Electronics, Craiova, Romania
[3]University of Medicine and Pharmacy Craiova, Research Center of Gastroenterology and Hepatology, Craiova, Romania
[4]Harvard Medical School, Department of Surgery, Boston, United States

Keywords Robot · Navigation · Lung · Electromagnetic tracking

Purpose

The purpose of this research was to develop and bench test a novel robotic and electromagnetic tracking navigation system for guiding medical catheter placement inside the peripheral pulmonary airways. This system will increase the precision of placement and significantly decrease X-ray exposure to both patient and doctor.

Methods

The robotic system consists of a planning and navigation software, iMTECH, an electromagnetic tracking system (ETS) AURORA (Northern Digital Inc.,), a trackable catheter and a 2-degree-of-freedom robotic system that can insert and guide the catheter to reach a specific target in bronchial system. The robot generates insertion and rotational motions and can use any clinically available catheters, in manual or autonomous driving mode (Fig. 1, left side panel). In the linear motion, the robot insert and extract the catheter at a specific speed. The rotational motion is used to twist the catheter while it is advanced or retracted. The robot is controlled by two electric motors with encoders and planetary gearheads, connected to a motion controller trough drivers developed in our lab.

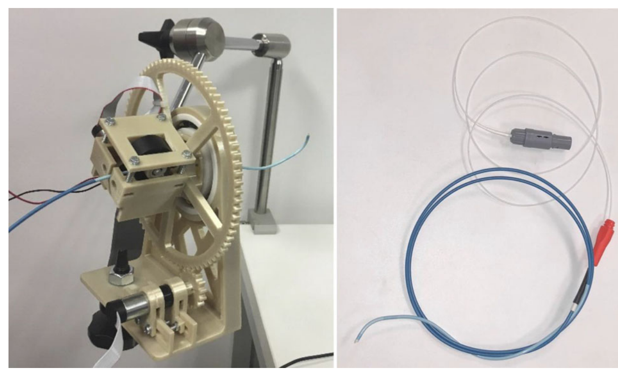

Fig. 1 Robot prototype, with most parts developed from polyetherimide (ULTEM) material by 3D printing using STRATASYS Fortus 400 mc (left side), and the custom made catheter with a pre-bended tip and a 6 DOF electromagnetic tracking sensor (right side)

A guidewire with an electromagnetic tracking sensor and a pre-bended tip is inserted in the working channel of a single-use catheter to track its tip during the procedure (Fig. 1, right side panel). After the target is reached and confirmed, the wire can be retracted from the catheter channel and another instrument such as a biopsy needle can be inserted.

The iMTECH software is using CustusX libraries (https://www.custusx.org) and consists of a planning module used by the surgeon to identify the target on the patient's CT scan before the procedure, and a navigation module used by the robot to navigate. The system's feasibility testing was performed on a lung phantom constructed from a lung airway model (AK092 Bronchoscopy Training Model, Koken Co. Ltd) placed in a plastic box equipped with two electrical motors to simulate the breathing motion (Fig. 2).

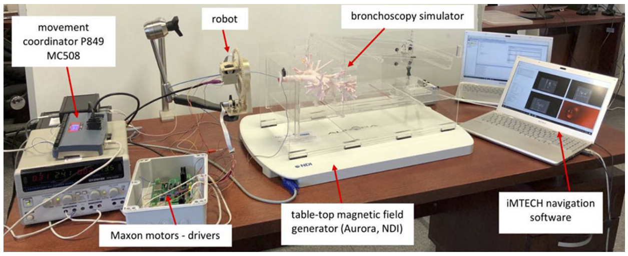

Fig. 2 Testing set-up using the robot and the bronchoscopy phantom

A CT scan of the phantom was performed prior to the robotic procedure and a virtual 3D model of the phantom was created by the iMTECH software to visualize the navigation path in the context of the entire anatomical structure. The surgeon plans the procedure using iMTECH by identifying on the phantom's CT an entry point on the trachea and a target (nodule) in the airways and the software generates the navigation path as a continuous line through airways.

In the intervention room, the magnetic field generator was placed underneath the phantom (Fig. 2) and the navigation catheter was placed in the robot's device and was connected to the ETS. The iMTECH navigation module is started and the phantom CT data is loaded. The registration between the model and CT data is initially performed by the surgeon using a proprietary algorithm for manual registration and correction. The robot is placed close to the starting point on the trachea and at doctor's command, starts to insert and guide the catheter in the phantom airways by translation and rotation movements. To control catheter movement, the robot is continuously checking the tip position relative to the path and target, choosing a specific branch in an intersection or performing trajectory corrections. During catheter insertion its tip's live position is visualized on the virtual model by the surgeon. As a safety feature, the catheter insertion can be corrected manually using a joystick and or stopped anytime. When the target is reached, a final fluoroscopy scan was performed for position confirmation, and the ETS sensor was removed from the catheter to allow insertion of a biopsy needle in its working channel.

Results

The phantom was used to test the navigation utility and accuracy, by steering the catheter towards 6 target points located at the end of the small airways with a speed of 3 mm/s. The feasibility tests were performed by two development engineers and two doctors. The catheter insertion was performed in 3 modes for comparison: (1) manual mode, when the operator is using a joystick to control the robot movements, (2) automatic mode when the robot moves the catheter by itself, and (3) manual insertion of the catheter by the operator without the robot but using the iMTECH for navigation. The targets were successfully reached during all tests. The procedure time in automatic robotic mode was slightly slower, but the procedure was executed at controlled and constant speed than the manual control or no robot procedures.

Conclusion

The preliminary tests using a complex phantom proved that our catheter driving robotic system is working and allows navigation, through a complex 3D channels structure like the bronchial tree, in both manipulator and robotic modes without fluoroscopy scanning. Because it could be controlled from a different room, using this system can drastically reduce radiation exposure of the patient and totally avoid the exposure of the doctor. Future developments will include placement of a force sensor at the tip of the catheter to "feel" the wall and adapt speed of insertion in order to avoid wall damage.

Acknowledgement

The research leading to these results has received funding from Competitiveness Operational Program 2014–2020 under the project P_37_357 "Improving the research and development capacity for imaging and advanced technology for minimal invasive medical procedures (iMTECH)", Contract No. 65/08.09.2016, SMIS: 103633.

Synthetic elastic mechanism for miniaturized neurosurgical robotic forceps

J. Arata[1,2], Y. Fujisawa[1], R. Nakadate[1], K. Harada[2], M. Mitsuishi[2], K. Kiguchi[1], M. Hashizume[1]
[1]Kyushu University, Fukuoka, Japan
[2]The University of Tokyo, Tokyo, Japan

Keywords Surgical robot · Manipulator · Neurosurgery · Mechanism

Purpose

Clinical demand for minimal invasiveness in surgery is increasing, as it is beneficial for both patients (e.g. improved postoperative pain relief with a minimal scar) and medical economy (e.g. by shorting the duration of hospitalization). Surgical robots have been widely studied for their ability to perform minimally invasive surgery, as the miniaturized robotic tools play a key role in reducing the size of the wound while providing multiple degrees-of-freedom (DOF) inside the body cavity for performing dexterous motions required for the surgery. Many studies have been conducted on miniaturized surgical robotic tools, and most of the mechanisms have been developed based on wire, link, and pneumatic mechanisms [1]. We have developed a laparoscopic surgical robotic tool using an elastic beam structure that is largely deformed during motion to transmit and transform the motion at the tip of the miniaturized surgical tool [2]. The elastic mechanism enables further compaction and simplicity, as an elastic structure requires a lesser number of mechanical parts than that required in the wire, link, and pneumatic mechanism. In this paper, we present novel robotic forceps for transnasal endoscopic pituitary tumor resection, which have been further miniaturized due to the elastic mechanism. One of the most difficult tasks in the current endoscopic pituitary tumor resection is the dura mater suturing procedure that is performed at the end of the surgery to prevent cerebrospinal fluid leakage; hence, we performed this procedure using our novel forceps. The surgery is performed through a transnasal endoscope, thus it must be performed using surgical tools that are smaller than laparoscopic surgical tools.

Methods

Figure 1 shows the overview of the newly developed prototype. The mechanism has 4 DOF—two bending, one grasping DOF at the tip and one rotation along the long axis, to perform dexterous motion for suturing within a diameter of 3.5 mm. The actuator unit is implemented as a palm-sized box, with a detachable tool unit to enable sterilization. There are five motors in the unit: four linear motors (Maxon Spindle Drive RE8 MR TypeS GP8S, Switzerland) and a rotation motor (Maxon Motor DCX10L ENX10 GPX10, Switzerland). The four linear motors actuate the mechanism to move the four bars back and forth that are connected to the tip mechanism, and the rotational motor is used for tip rotation along the long axis. Figure 2 shows the detail of the mechanical structure of the tip mechanism. The tip mechanism consists of five parts: a spring (A), two sets of springs (B), a pin joint, and an outer sheath. The spring (A) has a monocoque structure that provides a bending motion by moving the elastic beams differentially along the long axis. The spring (A) also plays a key role in providing mechanical constraint of two sets of springs (B) that are fixed by a pin joint. The springs (B) have the unique shape of an elastic beam that can be deformed along the pin joint like a spiral spring. This particular deformation allows the mechanism to transform the linear input of the linear actuator to the rotational motion within a single piece of mechanical element. Another part of the springs (B) is structured as a leaf spring, allowing deformation along with the deformation of the spring (A); thus, the force can be properly transmitted to the distal part of the springs (B). The springs (A) and (B) were fabricated by wire electro-discharge machining from a Ni–Ti rod 3 mm in diameter. The pin joint and the sheath were made from stainless steel. The springs were carefully designed by performing a series of finite element analyses, so as to not exceed the yield stress of the Ni–Ti within the deformation. The achievable working range of the prototype is ± 60° in two bending DOF, ± 60° in grasping, and ± 180° in rotation along the long axis. A notable feature of this novel mechanism is the small number of mechanical parts, which enables the system be miniaturized down to a diameter of 3.5 mm. Furthermore, the monocoque structure of spring (A) makes the mechanism further compact and simple compared with the authors' previously presented mechanism [2]. Note that the prototype can be attached to an external robotic arm to perform the complete motion required for suturing [3].

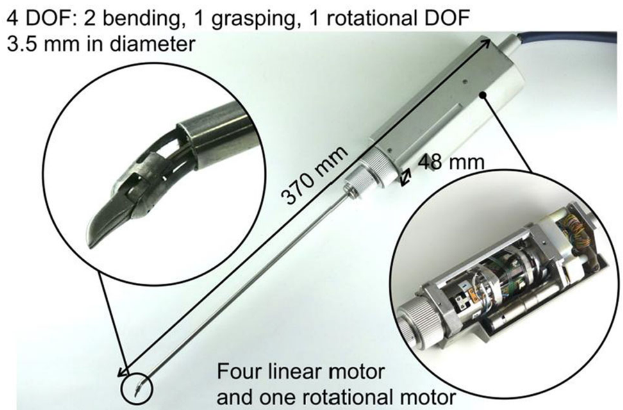

Fig. 1 Overview of the prototype

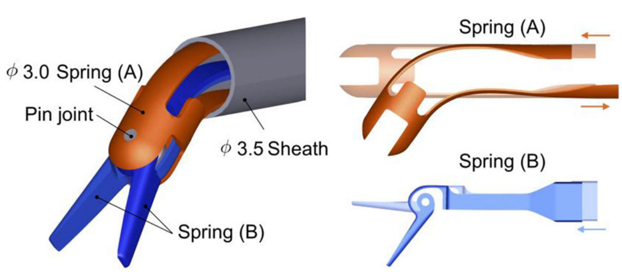

Fig. 2 Mechanical structure of the tip mechanism

Results

As preliminary evaluations, we performed a position accuracy test and a grasping force test. The prototype was implemented with a control system by Matlab (The MathWorks, Inc., USA) with simple PID control of five motors in a 1 kHz control loop. Observations of a periodic motion of the prototype using a vision motion tracking device (VW-6000, Keyence, Japan) revealed that the repeat accuracy of the prototype was 0.03° in a bending motion, and 0.17° in a grasping motion. The results revealed that the prototype has high accuracy, as mechanical play does not occur due to the elastic structure. We performed a preliminary suturing test by manually holding a prototype to provide a supplementary DOF that will be provided in future by an external robotic arm. The test was performed using a 10-0 needle on a phantom rubber sheet with a thickness of 0.2 mm. The suturing test revealed that the prototype provides sufficient force to steadily hold the needle to pierce the phantom membrane.

Conclusion

We proposed a synthetic elastic structure that can miniaturize the surgical robotic tools down to 3.5 mm in diameter to provide a greater degree of minimal invasiveness. The prototype showed promising results in accuracy and output force. We are currently working on a precise kinematic model that includes the spring deformation to further improve the position accuracy. We are also working on a system integration with an extra robotic arm to provide the full DOF to perform the suturing task, manipulated through a master interface.

References

[1] Le HM, Do TN, Phee SJ (2016) A survey on actuators-driven surgical robots, Sensors and Actuators A 247: 323–354

[2] Arata J, Kamura Y, Oguri S, Nakadate R, Kiguchi K, Hashizume M (2017) Multi-degree-of-freedom laparoscopic surgical manipulator using large deformation of elastic components, Int J CARS 12(Suppl 1): S90–S91

[3] Marinho MM, Nakazawa A, Nakanishi J, Ueyama T, Hasegawa Y, Arata J, Mitsuishi M, Harada K (2016) Conceptual design of a versatile robot for minimally invasive transnasal microsurgery, 27th 2016 International Symposium on Micro-NanoMechatronics and Human Science, https://doi.org/10.1109/mhs.2016.7824180

Intraoperative ultrasonography-based augmented reality for application in image guided robotic surgery

J. Shen[1,2], N. Zemiti[1], A. Viquesnel[1,3], O. Caravaca-Mora[1], A. Courtin[1], R. Garrel[3], J.-L. Dillenseger[2], P. Poignet[1]
[1]LIRMM, University of Montpellier, CNRS, Montpellier, France
[2]INSERM UMR 1099, Rennes, France; University of Rennes 1, LTSI, Rennes, France
[3]ENT Department, Centres Hospitaliers Universitaires Gui de Chauliac, Montpellier, France

Keywords Intraoperative ultrasonography · 3D ultrasound calibration · Augmented reality · Image guidance · Transoral robotic surgery

Purpose

Accurate Tumor delineation during the surgery is a big challenge for surgeons. For instance, in transoral robotic surgery (TORS) for tongue base tumor resection, the preoperative images cannot accurately reflect the tumor area in the tongue, because of the soft tissue deformation during the surgery. Furthermore, due to the camera's small field of view and the loss of cross-modality landmarks in the tongue base, it is difficult to register the preoperative image to the intraoperative stereo camera with deformable registration. We propose an intraoperative ultrasonography (IOUS)-based augmented reality (AR) framework which is able to accurately delimit the tumor boundaries and provide them to the surgeon's view. Instead of some works requiring manual registration [1], additional fiducial markers [2], or intraoperative imaging modalities using ionizing radiation [2, 3], our solution uses safe and cheap US imaging and does not need additional fiducial markers disturbing the TORS workflow.

Methods

Figure 1 shows the registration pipeline used to achieve AR on stereo camera. A tracking system was defined as the world coordinate system (WCS) w. The transformation between the coordinate system (CS) of the camera c and the WCS was found by camera calibration based on the mathematical framework given by ${}^{w}\mathbf{T}_c = {}^{w}\mathbf{T}_s\,{}^{s}\mathbf{T}_c$, where s represents the CS of the tracked marker. The tracking system computed the transformation ${}^{w}\mathbf{T}_s$ from the CS of the marker s to the

WCS, meanwhile, the marker was localized in the 3D camera and its position was used to compute the transformation ${}^{s}\mathbf{T}_{c}$.

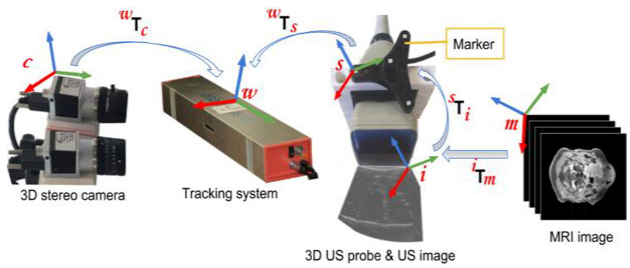

Fig. 1 Registration procedure for augmentation of stereo camera with MRI image

After calibrating the stereo camera in the WCS, the preoperative MRI image had to be registered to the WCS, in order to augment the camera view with the information extracted from the MRI. The corresponding mathematical registration framework can be presented as ${}^{w}\mathbf{T}_{m}= {}^{w}\mathbf{T}_{s}\,{}^{s}\mathbf{T}_{i}\,{}^{i}\mathbf{T}_{m}$, where m, i represent the CS of MRI image and US image. The transformation ${}^{i}\mathbf{T}_{m}$ was achieved in our experiment using Elastix toolbox performing a deformable registration between MRI image and US image. B-spline transformation model and Mutual Information similarity measure were used for the registration. The transformation ${}^{s}\mathbf{T}_{i}$ was obtained by US probe calibration. We developed a fast and automatic calibration method based on a custom-made 3D printed phantom and an untracked marker for 3D US probe calibration. Finally, the tracking system tracked and measured the position of the marker mounted on the probe and computed the transformation ${}^{w}\mathbf{T}_{s}$.

The performance of the setup was evaluated with 3 soft tissue phantoms made of soft polyvinyl chloride plastic. There was a triangle-shaped object embedded inside of each phantom. The invisible triangle-shaped objects could be distinguished under palpation and US imaging. Figure 2 shows the experimental setup. The participants used a calibrated Pointer to localize the boundaries of the invisible targets according to the augmented view projected in a head-mounted display system. The Pointer was tracked during the localization procedure.

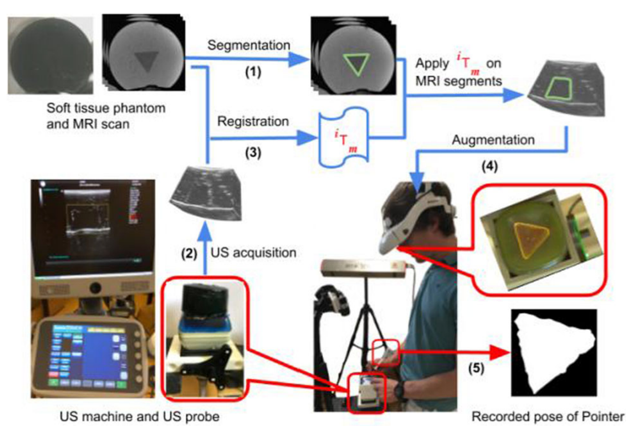

Fig. 2 Implementation of IOUS-based AR framework for soft tissue phantom experiment

Results

The errors of our setup are mainly from MRI/US registration and US probe calibration. The registration between MRI and US images of the phantoms was evaluated by target registration error (TRE) computing the distance, after registration, between corresponding landmarks. The 6 vertexes of the triangle-shaped objects in MRI and US images were used as the landmarks. The root mean square (RMS) of TRE for the 3 phantoms were 0.313, 0.19 and 0.41 mm, respectively. The US probe calibration was evaluated by point reconstruction tests and obtained the RMS of point reconstruction errors of 1.39 mm.

The presented approach was developed for our clinical application in TORS for tongue base tumor resection. Therefore, in the experiment, we compared our AR framework (*AR*) with conventional procedure (*palp*) where preoperative MRI and manual palpation were used to localize the tumor. With these two approaches, 6 participants using the tracked Pointer estimated the boundaries of the invisible targets inside of the 3 phantoms. The localization performance was quantified by Dice scores measuring the overlap between the boundaries estimated by the participants and the ground truth. We found the Dice scores obtained from the experiment *AR* remained clearly higher than those obtained from experiment *palp*. We achieved Dice ≥ 0.86 and Hausdorff distance ≤ 3.49 mm in the experiment with AR guidance.

Conclusion

We present a US-based AR framework for accurate tumor delineation in soft tissues. The performance was evaluated in an experiment delineating the boundaries of invisible targets in soft tissue phantoms. With our setup, the participants achieved higher accuracy of boundary delineation than with the conventional procedure. This framework was developed for the clinical application in TORS for tongue base tumor.

Acknowledgement

This work was supported in part by the French ANR within the Investissements d'Avenir Program (Labex CAMI, ANR-11-LABX0004, Labex NUMEV, ANR-10-LABX-20, and the Equipex ROBOTEX, ANR-10-EQPX-44-01), the ARC Foundation and the Région Bretagne.

References

[1] Su LM, Vagvolgyi BP, Agarwal R, Reiley CE, Taylor RH, Hager GD (2009). Augmented reality during robot-assisted laparoscopic partial nephrectomy: toward real-time 3D-CT to stereoscopic video registration. Urology, 73(4), 896–900.

[2] Liu WP, Reaugamornrat S, Deguet A, Sorger JM, Siewerdsen JH, Richmon J, Taylor RH (2013). Toward intraoperative image-guided transoral robotic surgery. Journal of Robotic Surgery, 7(3), 217–225.

[3] Mountney P, Fallert J, Nicolau S, Soler L, Mewes PW (2014). An augmented reality framework for soft tissue surgery. In International Conference on Medical Image Computing and Computer-Assisted Intervention (pp. 423–431). Springer, Cham.

A hyperspectral method to analyze optical tissue characteristics in vivo

E. L. Wisotzky[1,2], P. Arens[3], F. C. Uecker[3], A. Hilsmann[1], P. Eisert[1,2]
[1]Fraunhofer Heinrich-Hertz-Institute, Vision and Imaging Technologies, Berlin, Germany
[2]Humboldt-Universität zu Berlin, Institut für Informatik, Berlin, Germany
[3]Charité—Universitätsmedizin Berlin, Department of Otorhinolaryngology, Berlin, Germany

Keywords Image-guided surgery · Hyperspectral imaging · Multispectral image processing · Narrow band imaging

Purpose

During surgery, a surgeon differentiates between healthy tissue areas, which have to be maintained and abnormal or damaged tissue, which has to be removed, replaced or reconnected. This continuous differentiation is based on his experience and knowledge only and entails great risk because injuring important structures, as nerves, can cause permanent damage to the patient's health.

In order to support the surgeon's decision by detecting optical tissue characteristics not visible for human eyes, we developed in this preliminary study a hyperspectral in vivo tissue setup and analyzed several human tissue types relating to its optical behaviors.

Methods

We built an imaging setup including a digital camera featuring a monochromatic sensor as recording device and an illumination unit. In front of the illumination unit, a filter wheel selects the specific wavelength band that arrives at the tissue. This allows a spectral scanning of the surgical area and therefore the investigated tissue. The filter wheel includes 16 filters with wavelengths starting at 400 nm up to 700 nm in steps of 20 nm. The bandwidth of every filter is about 20 nm.

Using the 16 wavelength measurements of every tissue type, we are able to analyze the relating tissue properties in a 16-dimensional wavelength domain. Interesting tissue structures are annotated in the images by the surgeon. To transform the measured data into the wavelength domain, we register corresponding tissue regions in all wavelength images to achieve a three-dimensional (two spatial and one spectral) hyperspectral cube.

The measured multispectral data are normalized to handle different illumination strength in the different spectral bands caused by the light source with the corresponding spectral filters or scattered light.

In this study, we analyze several different healthy tissue types of six patients in two different surgery types, parotidectomy and neck dissection.

Results

We investigated artery, vein, bone, muscle, fat, skin, connective tissue, parotid gland, and different nerves as nervus facialis, nervus vagus and nervus hypoglossus. To evaluate the accuracy of our hyperspectral analyzer we compared the spectral behavior of the detected artery and vein data with well-known published oxygenated and deoxygenated blood results. Equal spectral behavior is observed in the investigated visible spectrum.

For the other tissue types, we are able to provide specific spectral behaviors analog to the artery and vein data. As a result, for each tissue type, we can present a spectrum that could allow a characterization of the tissue in the wavelength domain. Figure 1 depicts the spectra of bone, muscle, fat, connective tissue, parotid gland and nerve. Each curve represents the average tissue response of the corresponding tissue, annotated by the surgeon. As it can be seen there, each curve has a different trend, which allows an explicit classification using interesting wavelength ranges, e.g. 420–460 and 530–590 nm as well as 640–680 nm.

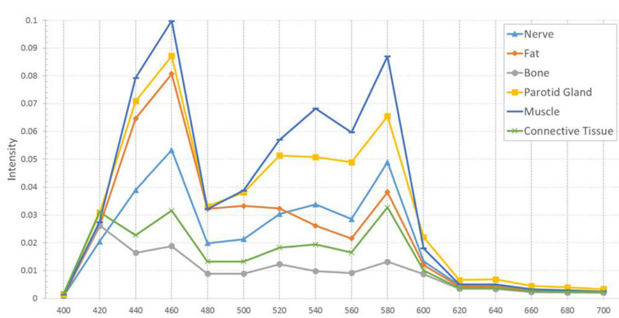

Fig. 1 The measured averaged intensities of six annotated tissue types at the analyzed 16 wavelengths

Using this 16 dimensional spectral space allows a robust differentiation of the annotated tissue data because spectral tissue data can be separated better than in three-dimensional RGB color space. As example the RGB vectors of parotid gland and muscle

$$p_{RGB} = (0.0311\ 0.0492\ 0.0548)^T \text{ and}$$
$$m_{RGB} = (0.0353\ 0.0587\ 0.0599)^T$$

are very similar and span a small angle of 2.29 deg. In the 16-dimensional hyperspectral case, both vectors are clearly different with crossovers and individual trends as shown in Fig. 1, as well as they span a larger angle in the hyperspectral space. Therefore, a differentiation between parotid gland and muscle becomes possible using hyperspectral imaging, while both tissue types appear equal in RGB color space and a differentiation is difficult.

Conclusion

These fundamental investigations give very promising results to develop a real-time system that allows hyperspectral tissue analysis for surgery.

To do so, several questions have to be solved. The image acquisition technique has to balance between acceptable image resolution and acquisition time, because a filter-wheel setup, as used in this study, gives a high spatial resolution but the acquisition of the complete three-dimensional hyperspectral data cube is with several seconds too time-consuming and therefore, not practical. Further, it has to be discussed how the hyperspectral data will be presented to the surgeon without concealing other important information in the surgical area but supporting treatment decisions.

In future, we will adapt the light source to extend the spectral range to near ultraviolet and near infrared. It is probable that in these regions further interesting tissue behaviors are detectable. This would make a tissue differentiation more robust.

Additionally we will investigate other interesting tissue structures.

Intraoperative electromagnetic navigation towards liver tumors: a feasibility study

O. Ivashchenko[1], B. Pouw[1], R. van Veen[1], K. F. Kuhlmann[1], N. F. Kok[1], E. G. Klompenhouwer[2], H. C. Groen[1], J. Nijkamp[1], T. J. Ruers[1,3]

[1]The Netherlands Cancer Institute—Antoni van Leeuwenhoek Hospital, Surgical Oncology, Amsterdam, Netherlands

[2]The Netherlands Cancer Institute—Antoni van Leeuwenhoek Hospital, Radiology, Amsterdam, Netherlands

[3]University of Twente, MIRA Institute of Biomedical Technology and Technical Medicine, Enschede, Netherlands

Keywords Liver surgery · Surgical navigation · Electromagnetic tracking · 3D model

Purpose

Annually, liver malignancies affect more than 1.4 million people worldwide, either as a result of primary liver cancer (> 780,000 cases worldwide) or as metastases from other cancer types [1]. For these patients, surgical resection is the best curative treatment option nowadays. Using various diagnostic imaging modalities, surgeons can carefully prepare a detailed surgical resection plan, keeping the tumor and important anatomical liver structures in mind. However, due to the lack of real-time information on the location of the lesion and patient-specific vascular anatomy during the procedure, 2–23% of liver resections result in irradical resections [1]. Intraoperative navigation could provide real-time feedback on liver anatomy and improve radical resections rates.

A few groups have tried to develop navigation systems for liver interventions. However, these systems mainly focused on intraoperative guidance for radiofrequency (RFA) and microwave (MWA) ablation needles [2], or on indication of intended resection lines prior to the start of surgical resections [3, 4] (e.g., prior to significant displacement and deformation of the organ). Thus, none of these approaches can provide sufficient feedback to the surgeon during the procedure itself. In this work, we incorporate intraoperative imaging and electromagnetic tracking of the organ to provide real-time information about the location of the lesion and surrounding vascular anatomy throughout the procedure. Initial results of the clinical feasibility study are presented.

Methods

Here, we introduce and evaluate an in-house-developed electromagnetic navigation (EM) system for visualization and EM-tool guidance during open liver surgery. First, a patient-specific 3D model of the liver, main vessels, biliary tree and target tumors was created from diagnostic CT or MRI scans using a custom extension of 3D Slicer [5]. Next, to enable real-time tracking of the model intraoperatively, a single 6 degrees of freedom (DOF) EM-sensor (Northern Digital Inc., Canada) and 4 surgical clips were attached to the surface of the liver in close proximity to the target tumor. After this, an intraoperative cone-beam computed tomography (CBCT) scan (Allura FD20, Philips, The Netherlands) with intravenous iodine contrast (Omnipaque 300, GE Healthcare, USA), visualizing the sensor and the clips, was performed and rigidly registered to the diagnostic scan containing the 3D model. Subsequently, EM-pointer tracking within the model was achieved by means of point-registration on the clips while reading out the sensor's position. Here, locally rigid anatomy within the area of the resection was assumed.

With the approval of the local ethics committee, a total of 25 patients were included in the study up to now. Selected patients were scheduled for an open liver surgery, had superficial liver lesion(s) with a diameter of at least 2 cm, had recent CT or MR scans, and their glomerular filtration level (GFR) was above 60. Complete list of patient inclusion criteria is provided in Table 1.

Table 1 Complete list of patient inclusion criteria

Step	Method
Patient inclusion criteria	• Scheduled for open liver surgery • Presents of superficial (< 3 cm from the surface) liver lesions with > 2 cm diameter • Recent MRI or CT scan (< 2 months old) • GFR level above 60 (required for administration of CT contrast agent) • Informed consent
Preoperative 3D model	• Automatically created from diagnostic MRI or CT scan • Contains liver, portal and hepatic veins, biliary ducts and tumor contours
Required electromagnetic (EM) tracking components	• EM field generator • 6 degrees of freedom (DOF) EM sensor (e.g. liver tracker) • 6 DOF EM probe (e.g. sterile EM pointer of the surgeon) • EM tracking and X-ray imaging compatible operation table
Attachment of the liver sensor	• Advanced topical skin adhesive (Ethicon, Dermabond) combined with surgical stitches
Intraoperative contrast-enchased CBCT imaging protocol	• Intravenous injection of Omnipaque 300 mg I/mL • Portal venous phase without bolus triggering, but generic 73 s delay between the injection and the start of CBCT imaging Iodine contrast injection protocol: • 45–65 kg use of 90 ml at 3.2 ml/s flow • 65–80 kg use of 115 ml at 4.0 ml/s flow • 80–100 kg use of 140 ml at 4.8 ml/s flow • > 100 kg use of 170 ml at 5.4 ml/s flow
CBCT to diagnostic scan registration	Rigid (6 DOF), gray-value based registration with region of interest restriction on the area of the liver containing the target lesion
CBCT to electromagnetic field registration	• Rigid point-based registration on 4–5 locations
Accuracy measurements	• Comparison between navigation-based to pathology results for the shortest distance between measurement points in the resection plane and the tumor (Fig. 1)

The study was divided into two stages. The first one is the initial "learning" curve that includes 10 patients. It reflects the early stage of the study with still developing intraoperative workflow of the technique. This includes selection of the optimal scanning protocol for intraoperative contrast-enhanced CBCT scan without bolus triggering, method of EM sensor fixation to the surface of the liver, and development of X-ray imaging and EM tracking compatible operating room (OR) table. The second stage is the "navigation" stage, where a standardized technique was used and evaluated. Here, accuracy of the technique was quantitatively assessed by comparing navigation-based to pathology measurements of the shortest distance between points in the resection plane and the tumor (Fig. 1). Additionally, various qualitative intraoperative correctness checks on visible anatomical landmarks (e.g., vessel bifurcations or liver surface) were performed for each patient. In total, 15 patients were included in the "navigation" stage; however, only 14 of them resulted in complete procedures.

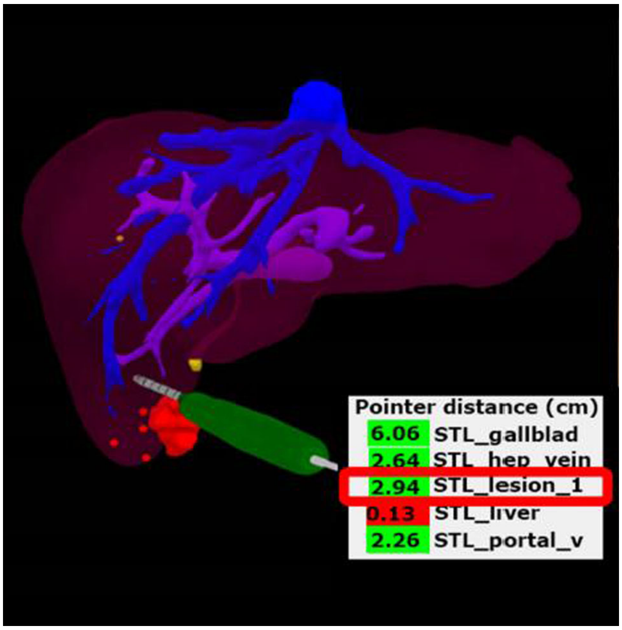

Fig. 1 Sample screen shot from the navigation software during open liver surgery

Results

A detailed description of the clinical workflow developed in the first stage of the study is provided in Table 1, while Fig. 2 illustrates the final design of the OR table. After development of the clinical workflow, a total of 14 navigated procedures with pathology–verified accuracy measurements were performed. The median surgical overhead time of the procedures was 32 min. This includes placement of the EM-sensor and surgical clips on the surface of the liver (8.5 min), sterile intraoperative contrast-enhanced CBCT scan (14 min), registration of the 3D model with a real-time situation and all navigation-related measurements (9 min). The navigation technology resulted in an accurate and intuitive real-time visualization of liver anatomy and tumor's location (Fig. 1), confirmed by intraoperative checks on visible anatomical landmarks. Additionally, surgeons indicated that the system aided in better anatomical insight, and helped to localize the lesion throughout the procedure. Based on 43 accuracy measurement verified by pathology (e.g., three to four locations per patient), the average accuracy of the system was 13 mm. Although pathology is the "gold" standard for resection margins assessment, this method is ultimately affected by inter-observer variation of pathologists and tissue deformation of *ex vivo* liver samples. Therefore, the accuracy of the navigation system may improve, if the current "gold" standard (i.e., pathology) for accuracy measurements will be replaced with an intraoperative imaging modality (e.g., ultrasound or CBCT).

Fig. 2 Adjusted operating table (OR) that combines X-ray "transparency" of carbon OR tables and electromagnetic (EM) tracking with NDI Tabletop Feld generator (left image). This is a combination of the Magnus carbon system (MAQUET, Germany) and a custom-made Perspex sleeve for positioning of the EM field generator

Conclusion

We successfully developed and implemented EM navigation for open liver surgery. This was done by combining a preoperative 3D liver model, intraoperative CBCT imaging and EM tracking of the liver and a sterile EM-pointer. Achieved accuracy shows that the assumption of locally rigid organ registration allows for accurate detection of critical anatomical structures within the resection area.

References

[1] Virani *S*, Michaelson JS, Hutter MM, Lancaster RT, Warshaw AL, Henderson WG, Khuri SF, Tanabe KK (2007) Morbidity and Mortality after Liver Resection: Results of the Patient Safety in Surgery Study. *J. Am. Coll. Surg.* 204(6): 1284–1292.
[2] Banz VM, Baechtold M, Weber S, Peterhans M, Inderbitzin D, Candinas D. Computer planned, image-guided combined resection and ablation for bilobar colorectal liver metastases (2014) *World J. Gastroenterol.* 20(40): 14992–14996.
[3] Kleemann M, Hildebrand P, Keller R, Bruch HP, Birth M (2004) Laparoscopic ultrasound navigation in liver surgery—technical aspects and feasibility. *Int. Congr. Ser.* 1268: 793–796.
[4] Chan Y, Siewerdsen JH, Rafferty MA, Moseley DJ, Jaffray DA, Irish JC (2008) Cone-beam computed tomography on a mobile C-arm: Novel intraoperative imaging technology for guidance of head and neck surgery. *J. Otolaryngol. Head Neck Surg.* 37(1): 81–90.
[5] Ivashchenko O, Rijkhorst EJ, ter Beek L, Pouw B, Hoetjes N, Nijkamp J, Kuhlmann KF, Ruers TJM (2017) Automated segmentation of complete 3D liver model including arterial, hepatic vasculature and biliary tree anatomy, from a single multiphase MR scan. *Int J CARS*, pp. S25–S26.

An intraoperative ultrasound based navigation method for laparoscopic ablation of liver tumors

I. Paolucci[1], M. Schwalbe[1], G. A. Prevost[2], A. Lachenmayer[2], D. Candinas[2], S. Weber[1], P. Tinguely[2]
[1]University of Bern, ARTORG Center for Biomedical Engineering Research, Bern, Switzerland
[2]University Hospital of Bern, Department of Visceral Surgery and Medicine, Bern, Switzerland

Keywords Image-guided liver surgery · Ablation · Laparoscopy · 3d ultrasound

Purpose

Local thermal ablation is a tissue sparing treatment option for selected malignant liver lesions. The laparoscopic access represents a minimally invasive approach suitable for patients with liver lesions not amenable to percutaneous ablation or if a combined treatment of ablation and resection is performed. For successful laparoscopic ablation, an ablation probe has to be accurately placed in the tumor while avoiding the injury of important intrahepatic structures at the same time. The ablation probe placement is conventionally performed under laparoscopic ultrasound (LUS) guidance, which requires significant experience and is challenging due to limited access and long probe trajectories [1]. Additionally, conventional LUS provides only limited feedback of technical success regarding the placement of the ablation probe prior to applying the ablative treatment. We therefore propose a navigation approach based on electromagnetically (EM) tracked laparoscopic ultrasound for intraoperative guidance of the ablation probe using 2D US, and validation of the probe placement using 3D US. While other navigation techniques rely on complex and time consuming registration processes relying on preoperative imaging [2], the proposed approach does not involve a registration process, potentially reducing intraoperative complexity.

In this study we aimed to evaluate positional accuracy and procedural efficiency of this technique in a laparoscopic model and compare it to the conventional approach for laparoscopic targeting of liver lesions.

Methods

A commercially available navigation system (CAS-One, CAScination AG, Switzerland) for liver surgery based on optical tracking was adapted for EM tracking. For tracking of the LUS probe (FlexFocus 800, BK Medical, Denmark) an EM sensor was attached to the flexible head of the LUS probe using a uniquely fitting adapter and was calibrated using a Z-wire phantom. For guidance of the ablation probe, an EM sensor (Pointershell, Fiagon GmbH, Germany) which can be reproducibly attached to a trocar, was used. The axis and entry point of this trocar were calibrated which allows to accurately measure the direction of the trajectory and the distance to the target. Both instruments were calibrated preoperatively to reduce the intraoperative setup time. Additionally, a workflow for placement of an ablation probe and validation of this placement by measuring the target positioning error (TPE) was implemented. This workflow consisted of the following steps (Fig. 1):

(A) Localization and selection of the tumor
(B) Placement of the ablation probe using a cross-hair viewer (Fig. 1)
(C) Acquisition of a 3D US scan of the tumor and the ablation probe
(D) Measurement of the resulting TPE on the 3D US scan

To evaluate the proposed technique, three surgeons with experience in laparoscopic ablation of liver tumors were asked to perform 10 targetings using the navigation and 10 using the conventional non-navigated approach. For targeting, a laparoscopic model consisting of a plastic torso and an agar liver phantom with intrahepatic tumors was used. The surgeons were allowed to reposition the ablation probe if they could not hit the tumor on the first targeting attempt. For each placement, the number of probe repositionings, the TPE, and the time for probe placement (step B) were measured.

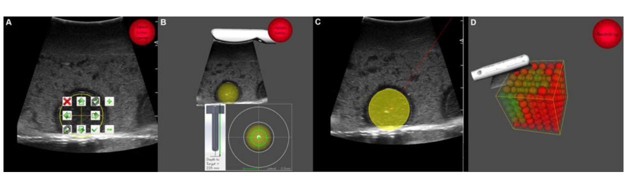

Fig. 1 Workflow for navigated laparoscopic placement of an ablation probe and acquisition of a 3D US scan for validation of the probe placement [3]

Results

Using the proposed navigated approach for targeting, the tumor was hit without requiring to repositioning the ablation probe in 30 out of 30 targetings. Contrarily, when using the non-navigated approach in 17 out of 30 (59%) targetings up to five repositionings were required (Fig. 2). Median TPE for targeting using the navigated and non-navigated approach were 4.2 mm (IQR 2.9–5.3 mm) and 6 mm (IQR 4.7–7.5 mm), respectively ($p < 0.01$). Median time for navigated and non-navigated targeting was 39 s (IQR 24–47 s) and 76 s (IQR 47–121 s) ($p < 0.01$). However, no difference in targeting accuracy and targeting time was found between the surgeons ($p = 0.32$ and $p = 0.27$). During navigation, the median time for localization and selection of the tumor (step A) was 49 s.

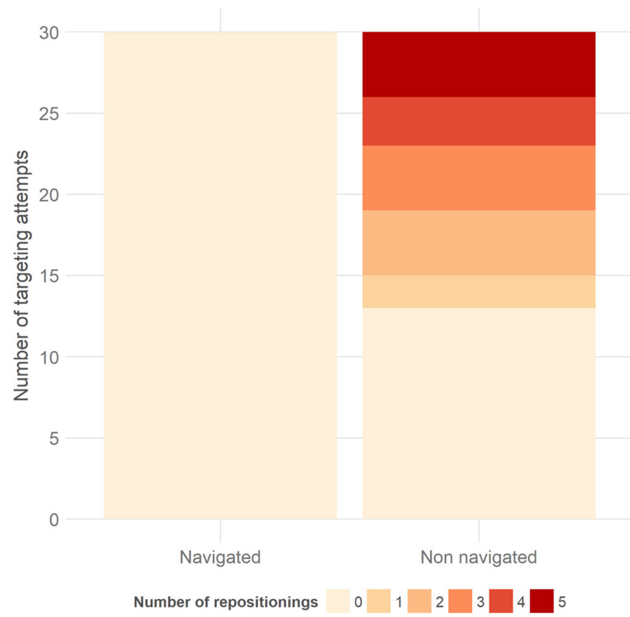

Fig. 2 Ablation probes repositionings required to hit the tumor [3]

Conclusion

Overall, the navigation approach allowed to accurately place the ablation probe into the tumor on the first attempt, compared to required repositionings of the ablation probe in 59% when using non-navigated targeting. This potentially reduces the risk of bleeding and seeding of tumor cells when using multiple repositionings. The evaluated accuracy of 4.2 mm is sufficient when considering an intended 5–10 mm ablation margin, as used in clinical practice. Also, the surgeons could perform the placement of the ablation probe significantly faster using the navigation compared to the conventional approach.

The evaluated navigation approach avoids potential inaccuracies caused by intraoperative registration due to the pneumoperitoneum and intraoperative tissue manipulation. These factors might be significantly reduced, as the trajectory is planned based on intraoperative imaging acquired after pneumoperitoneum and liver mobilization. As this navigation approach assumes a static environment for only a short time (mean 39 s) and could thus be applied during an extended end-expiration phase or using high frequency jet ventilation, organ motion compensation was not included in this study. In case of significant organ deformation, the method allows to quickly adapt the planned trajectory (mean 49 s). Additionally, the 3D US based validation method allows to assess the accuracy of the ablation probe placement intraoperatively, with the possibility of repositioning if needed.

To conclude, the proposed navigation method allows accurate and efficient placement of ablation probes using EM tracked US in a laparoscopic model. As this method relies only on real-time intraoperative imaging, it avoids potential inaccuracies caused by organ deformation during the procedure.

References

[1] Siperstein A, Garland A, Engle K, Rogers S, Berber E, String A, Foroutani A, Ryan T (2000) Laparoscopic radiofrequency ablation of primary and metastatic liver tumors: Technical considerations. Surg Endosc 14: 400–405. https://doi.org/10.1007/s004640000067

[2] Kenngott HG, Wagner M, Nickel F, Wekerle AL, Preukschas A, Apitz M, Schulte T, Rempel R, Mietkowski P, Wagner F, Termer A, Müller-Stich BP (2015) Computer-assisted abdominal surgery: new technologies. Langenbecks Arch Surg 400: 273–281. https://doi.org/10.1007/s00423-015-1289-8

[3] Paolucci I, Schwalbe M, Prevost GA, Lachenmayer A, Candinas D, Weber S, Tinguely P (2017) Design and implementation of a dynamic navigation technique for laparoscopic ablation of liver tumors based on electromagnetic tracked ultrasound (submitted). 1–22

Peripheral nerve block support system guided by ultrasonic image

N. Takahashi[1], A. Hanafusa[1], H. Hayashi[2]

[1]Shibaura Institute of Technology, Bio-science and Engineering, Saitama, Japan

[2]Osaka Minami Medical Ccenter, Osaka, Japan

Keywords Peripheral nerve block · Ultrasonic image · Stereo camera · Needle guidance

Purpose

A peripheral nerve block (PNB) is a type of anesthesia that involves the injection of anesthetic around the peripheral nerve to block pain transmission. Ultrasound-guided PNB is a PNB method that can visualize needle position and spread of anesthetic on the sonogram by inserting the needle under the ultrasound imaging probe. Therefore, ultrasound-guided PNB is becoming a common procedure in regional anesthesia [1]. However, high expertise is required by an anesthesiologist for procedures such as maintaining the needle tip in the sonogram as the needle is advanced towards the target, guiding the needle to the target nerve, and avoiding vascular puncture. Extant studies proposed different types of ultrasound-guided PNB support systems in conjunction with magnetic sensors or mechanical guidance. However, magnetic sensors are affected by metallic objects in the surroundings, and mechanical guides limit the freedom of movement [2].

In this research, two images captured by two small USB cameras are converted into top- and side-views, on which the navigation line for the guiding needle path is superimposed. Moreover, images of the needle at intervals of 10 and 20 mm are captured by stereo cameras fixed on the ultrasound imaging probe, and three-dimensional positions of marks on the needle, insertion position, angle, and depth are measured. The purpose of this research is to develop a system that can support navigation along the needle progression path, predict tip position, and superimpose the navigation line on the images to perform PNB in a precise and safe manner.

Methods

The proposed system consists of an ultrasonic diagnostic imaging system, a PC, and two small USB stereo cameras, as shown in Fig. 1. Intrinsic and extrinsic camera parameters from several views of the calibration board are obtained in advance, and distortion correction of the image is performed using these parameters. The image of the needle advanced towards the target is captured by the stereo camera, and the image is finalized. Then, the mark on the needle can be recognized automatically by label processing, and the three-dimensional coordinates of the marks are calculated using the stereo camera method. Subsequently, insertion position, angle, and depth are measured using the three-dimensional coordinates of the marks. From the results of insertion position, angle, and depth, the needle progression path and tip position are predicted and displayed on the sonogram. In addition, the navigation line that guides the needle under the ultrasound imaging beam to maintain the needle in the sonogram is displayed on the image taken from the overhead camera. Moreover, images taken from the camera diagonally overhead are converted to images representative of those taken from the side camera, to match the needle and guide line easily. Then, the guidance line, which guides the needle towards the target nerve, is displayed on the image (Fig. 1). These images are displayed on the PC monitor and support the ultrasound-guided PNB operation.

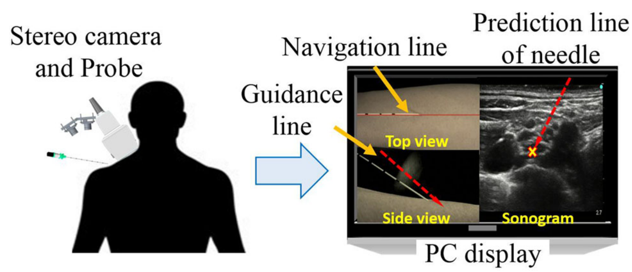

Fig. 1 System configuration of peripheral nerve block system

To verify the accuracy of the measured three-dimensional coordinates of the mark on the needle and calculated angle of the needle, experiments were performed using the needle employed in the operation.

Results

Stereo cameras were fixed as shown in Fig. 2 to measure the mark and calculate the inserted angle. The distance between the two cameras was set as 60 mm, and the heights of the left and right camera were set to 120 and 105 mm, respectively. The right camera was inclined at approximately 30° against the vertical line.

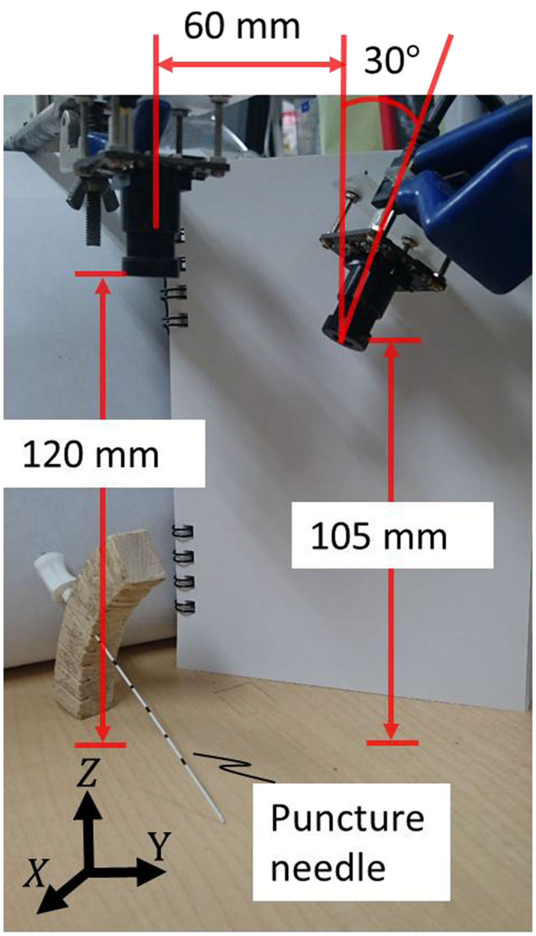

Fig. 2 Fixture of two cameras

The insertion angles were calculated by linearly approximating the measured three-dimensional coordinates of each mark on the needle. Theoretical insertion angle values were changed from 5° to 45° in 5° intervals. The procedures were repeated 10 times and the average angle error was calculated. The total average insertion angle error was 0.68° ± 0.39°. The maximum and minimum average angle errors were 1.63° and 0.46°, respectively, corresponding to insertion angles of 10° and 20°.

Conclusion

To support the PNB operation, a system that can measure three-dimensional coordinates of the marks on the needle, and calculate the insertion angle using the stereo camera method was developed. The main feature of the system is that it recognizes the needle automatically by image processing, and the image observed from a diagonally overhead camera is converted to an image representative of those taken from top- and side-cameras, for easy needle guidance.

To verify the accuracy of this system, experiments were performed to measure the mark, and to calculate the insertion angle. The average insertion angle error was 0.68°, which was accurate to support needle puncture for the 5 mm peripheral nerve and for 13 mm brachial plexus. In future studies, a model that resembles the human body will be used for measuring the insertion position, angle, and depth. In addition, a function will be developed for displaying a predicted needle position on the sonogram, and for superimposing the guidance line onto the image.

References

[1] Marhofer P, Greher M, Kapral S (2005) Ultrasound guidance in regional anaesthesia. British Journal of Anaesthesia 94(1): 7–17

[2] Najafi M, Rohling R (2015) Single-Camera Closed-Form Real-Time Needle Tracking for Ultrasound-Guided Needle Insertion. Ultrasound in Medicine and Biology 41(10): 2663–2676

3D gaze tracking for skill assessment in ultrasound-guided needle insertions

D. García-Mato[1,2,3], M. S. Holden[1], A. Lasso[1], A. Szulewski[4], J. Pascau[2,3], G. Fichtinger[1]

[1]Queen's University, School of Computing, Kingston, Canada

[2]Universidad Carlos III de Madrid, Departamento de Bioingeniería e Ingeniería Aeroespacial, Madrid, Spain

[3]Instituto de Investigación Sanitaria Gregorio Marañón, Madrid, Spain

[4]Kingston General Hospital, Department of Emergency Medicine, Kingston, Canada

Keywords Gaze tracking · Skill assessment · Needle insertion · Ultrasound

Purpose

Ultrasound (US) imaging is frequently used in image guided procedures due to its low-cost, availability and portability in the clinical environment. US-guided needle placement is a difficult procedure which demands precise hand–eye coordination by the practitioner and presents a long learning curve. Perk Tutor software has been developed for training and skill analysis of these procedures by position tracking and motion analysis of surgical tools [1]. However, eye tracking metrics have not been included for skill assessment.

Gaze patterns of individuals performing a task have been measured to evaluate expertise in many different areas. 2D eye tracking has been used in medicine for the quantitative assessment of surgical skills during minimally invasive surgeries. Significant differences have been found in the eye movements of novices and experts during the performance of surgical tasks [2], and it has been demonstrated that skill assessment is improved when eye-gaze data is added to surgical tool motion data [3].

Most studies use 2D eye tracking data since most applications are based on 2D images or videos. However, the increased importance of 3D imaging and image-guided surgical procedures in the operating room demands the analysis of gaze data in 3D space. The purpose of this work is to assess the feasibility of combining both eye tracking and head positioning to estimate gaze in 3D space and its utility in skill assessment for ultrasound-guided needle insertion.

Methods

The proposed framework (Fig. 1) combines the use of a wearable eye tracker device (Tobii Pro Glasses 2, Tobii Technology, Sweden), an optical tracking system (Polaris®, NDI, Canada) for the real-time positioning of the user's head and an electromagnetic tracking system (TrakStar, Ascension, VT) for the positioning of the needle, ultrasound probe and phantom. An application was developed in 3D Slicer, a free open-source platform for the analysis and visualization of medical images, which receives the gaze data from the eye tracking glasses through a wireless Ethernet connection and the positioning data from the optical and electromagnetic tracking systems using PLUS open-source toolkit.

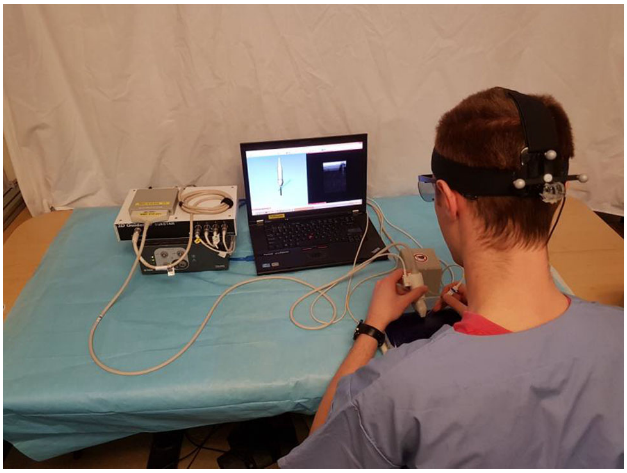

Fig. 1 Trainee performing ultrasound-guided needle insertion with 3D gaze tracking

3D gaze tracking data was obtained by combining the mobile eye tracking glasses (ETG) with head positioning data provided by the optical tracking system (OTS). First, the wearable ETG and a set of three OTS markers were attached to the user's head using elastic and adjustable straps. A 6-point calibration procedure, where the user gazes at six markers, is performed to compute the relationship between the ETG and the OTS coordinate systems. Once calibrated, the system is able to display the 3D gaze line in real-time and it is possible to visualize which region of the 3D workspace the user is looking at. The accuracy of this system was evaluated in a previous work [4]. The results of that study show a gaze line to marker position error of 6.0 ± 3.3 mm and a real to estimated gaze line error of 0.4° ± 0.2°.

To evaluate how useful the 3D gaze tracking data is for skill assessment, we tracked 10 insertions from two novices and 10 insertions from two experts (MDs who have completed formal ultrasound training) performing US-guided needle insertions on a vascular access phantom. During these procedures, we recorded 3D gaze tracking data in addition to the positions of the needle and the US probe with respect to the phantom. We computed the amount of time spent looking at and the number of times looking at the insertion site, the ultrasound image, and the 3D view, as well as the total amount of gaze rotation. The values of these metrics in both groups (novices and experts) were compared and the validity of the gaze tracking data for skill assessment was evaluated.

Results

Overall, novices spent more total time than experts performing the insertions (50.3 vs. 30.1 s). From gaze information, we determined that novices spent significantly more time than experts looking at the ultrasound image (29.9 vs. 11.3 s) and phantom (8.6 vs. 5.6 s) with large effect size. Novices looked at the ultrasound screen more times (13.0 vs. 7.5) (Fig. 2) and had greater total accumulated gaze rotation (1377° vs. 564°) than experts with large effect size, but these differences were not significant.

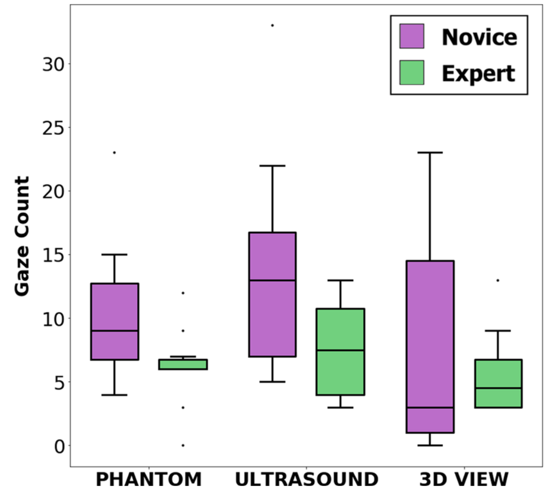

Fig. 2 Gaze count for phantom, ultrasound image, and 3D view for novices and experts performing ultrasound-guided needle insertion

Conclusion

Gaze tracking accuracy is affected by the devices' intrinsic errors, the calibration procedure and the attachment of the optical markers to the user's head. The system requires a 6-point calibration procedure which takes less than 30 s. The error of this system is below 10 mm and 1°. This is acceptable for the described experiment, and could be reduced even further by fixing the optical markers directly to the wearable eye tracking glasses.

This study demonstrates the feasibility of the proposed system for skill assessment using gaze information in ultrasound-guided needle insertion. The proposed metrics based on gaze show promise for distinguishing novices from experts, indicating their potential for use in skill assessment. This will enable the system to be used for the analysis and visualization of gaze data in 3D space for training applications, including the identification of which objects the operator is focusing on.

References

[1] Ungi T, Sargent D, Moult E, Lasso A, Pinter C, McGraw RC, Fichtinger G (2012) Perk Tutor: An Open-Source Training Platform for Ultrasound-Guided Needle Insertions. IEEE Transactions on Biomedical Engineering 59(12): 3475–3481

[2] Law B, Atkins MS, Lomax AJ, Mackenzie CL (2004) Eye Gaze Patterns Differentiate Novice and Experts in a Virtual Laparoscopic Surgery Training Environment. ETRA '04 Proceedings of the 2004 symposium on Eye Tracking Research and Applications 1(212): 41–48

[3] Ahmidi N, Hager GD, Ishii L, Fichtinger G, Gallia GL, Ishii M (2010) Surgical Task and Skill Classification from Eye Tracking and Tool Motion in Minimally Invasive Surgery. Lecture Notes in Computer Science 63(63): 295–302

[4] García-Mato D, Lasso A, Szulewski A, Pascau J, Fichtinger G (2017) 3D Gaze Tracking based on Eye and Head Pose Tracking. 10th Hamlyn Symposium on Medical Robotics

A laser modular system attached to a C-arm fluoroscopy for guidance of insertion position and posture with a mimicking fluoroscopy

S. Joung[1], C. W. Park[1], H. W. Lee[1], Y. Park[1], I. Park[1,2]
[1]Kyoungpook National University, Medical Device and Robot Institute of Park, Deagu, South Korea

[2]Kyungpook National University Hospital, Department of Orthopedic Surgery, Daegu, South Korea

Keywords Laser guidance · Modular system · Insertion accuracy · Fluoroscopic image

Purpose

Surgeons using a C-arm fluoroscopy have to guess appearance inside of body from two-dimensional fluoroscopic images. They guess the shape of lesion or the position/posture of an implant to be inserted. Some research groups tried to development a guidance system using line laser modules in order to guide the five degrees of freedom of the implant [1–3]. Previously reported most systems are a stand-alone type and need to use a position tracking system for calculating relative position of implants, a patient, a fluoroscopy, and laser modules. Some systems require pre-operative image scans like CT or MR [1–2]. These kinds of systems cause high installation cost and additional surgical procedures, medical staffs hesitate to install the systems in spite of its clinical usefulness. We are tried to eliminate the unnecessary device and procedure for this end and developed a minimal system, which guides the five degrees of freedoms in implant insertion. This paper reports the system configuration, spatial calibration methods, and control methods of a laser modular system attached to a C-arm fluoroscopy and shows laboratory experiment result with a mimicking fluoroscopy.

Methods

We designed a laser modular device comprising a green laser, a rotational line generator, and a rotational mirror. A MCU controls the rotational angle of line generator and mirror with a motor and an encoder, respectively. A plane vector of a line laser from the rotational mirror can be controlled from a mirror inclination and two angles of actuators. The size of the device is 88 mm × 106 mm × 30 mm (W × H × T). Two laser modular devices are attached to a C-arm fluoroscopy, and the spatial relation of coordinates of the C-arm, and two laser modular devices are calculated from fluoroscopic images. A custom calibration tool is designed to find the coordinate of two laser devices. Figure 1 shows the relationship of each coordinate and how to decide the plane vector of two line lasers. A mimicking C-arm was manufactured to evaluate the suggested system with a CCD camera and a transparent table. User can indicate the insertion position by clicking the mouse on a fluoroscopic image and set the insertion angle by input two digit numbers.

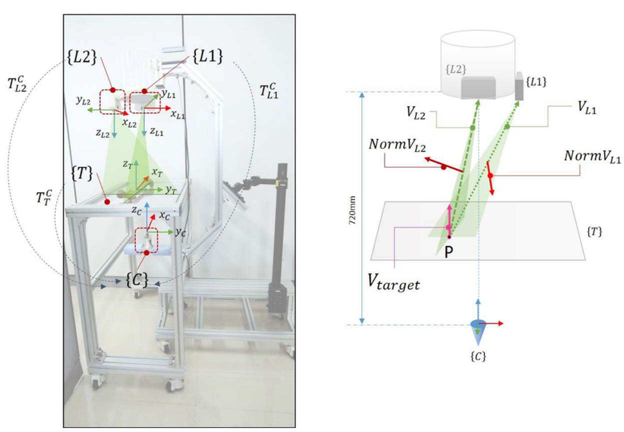

Fig. 1 A laser modular system attached to a C-arm fluoroscopy for guidance of insertion position and its coordinates relationship; left shows a mimicking C-arm with two laser module, right shows how to calculate the two plane vector of two line laser

We evaluated the accuracy of insertion position and posture with the proposed system. 20 random points are selected from the fluoroscopic image. And 20 random angles from zero degree to 32 degrees are inputted. Position error are calculated from distance difference between indication and cross potion of two line laser. Angle error are calculated from arctangentvalue of two cross points on a two layered phantom.

Results

Figure 2 shows the one case of the experiments. A green dot is indication position and the cross point of two line laser is guided position form the system in left of Fig.2. Angle error can be calculated from the two-layered phantom. Average position error of 20 points is 2.4 mm with standard deviation of 0.6. Maximum position error is 3.7 mm. Average insertion posture error is 2.1° with standard deviation of 1.5. Maximum angular error is 4.9°.

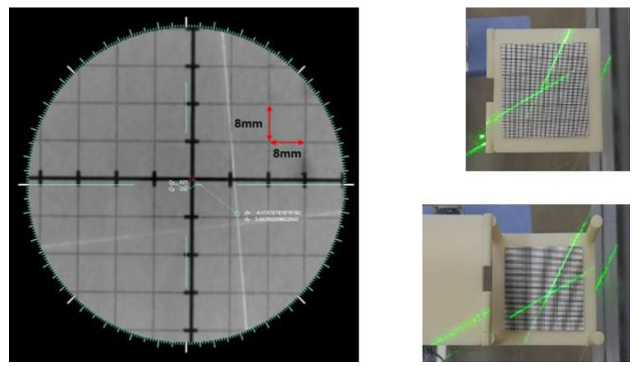

Fig. 2 Experimental results; left shows position error, right shows method to calculate angle error using a two-layered phantom

Conclusion

We developed the laser modular system that can be attached to a C-arm fluoroscopy for guidance of insertion position and posture, and evaluated the system with the mimicking fluoroscopy in laboratory. Position and posture accuracy show the possibility to apply clinical cases. Furthermore, the suggested system is very small and easy-to-use. We have to test the laser modular system with a real C-arm fluoroscopy and improve the accuracy in the next step.

References

[1] Liao H, Ishihara H, Tran HH, Masamune K, Sakuma I, and Dohi T., “Precision-guided surgical navigation system using laser guidance and 3D autostereoscopic image overlay.”, Comput Med Imaging Graph. 2010 Jan; 34(1): 46–54.

[2] Nakajima Y, Dohi T, Sasama T, Momoi Y, Sugano N, Tamura Y, Lim SH, Sakuma I, Mitsuishi M, Koyama T, Yonenobu K, Ohashi S, Bessho M, and Ohnishi I., “Surgical tool alignment guidance by drawing two cross-sectional laser-beam planes.”, IEEE Trans Biomed Eng. 2013 Jun; 60(6): 1467–1476.

[3] Doke T, Liang JT, Onogi S, Nakajima Y, “Fluoroscopy-based laser guidance system for linear surgical tool insertion depth control.”, Int J Comput Assist Radiol Surg. 2015 Mar; 10(3): 275–283.

Features from non-linear scale space using fast guided filter for navigation system in Water-Filled Laparoendoscopic Surgery (WaFLES)

M. Kontto[1], R. Nakamura[1]

[1]Chiba University, Engineering, Chiba, Japan

Keywords Laparoscopy · Organ tracking · Non-linear filtering · Surgical navigation

Purpose

We are working on surgical navigation technologies for a minimally invasive surgical (MIS) method called Water-Filled Laparoendoscopic Surgery (WaFLES). It differs from conventional laparoscopy in the way which medium is used to create the pressurized abdominal cavity. In conventional laparoscopic MIS procedures gas is used, whereas WaFLES utilizes liquid saline. Minimally invasiveness of WaFLES calls for development of assistive intraoperative surgical navigation systems. Previously, a navigation system for WaFLES using intraoperative ultrasound and preoperative CT-images has been introduced, but the use of endoscopic images this purpose has been overlooked. In system level, we aim to utilize recent advancements in semidense monocular simultaneous localization and mapping (SLAM) techniques which use feature matching techniques. The water irrigated abdominal cavity poses challenges in regard of organ tracking which are disregarded in current semidense SLAM platforms over speed and efficiency of computation. Liquid saline extends a hydrostatic lift to the organs, which in turn makes them more easily movable and lighter to manipulate by the surgeon. This also makes the organs move and deform more strongly when manipulated, causing large displacements and motion blur, hence making the organ surface tracking more difficult. Currently used tracking algorithms for semidense SLAM such as oriented binary robust invariant features (ORB), can be remarkably fast, but are susceptible to noise and large changes in images. Therefore, we are aiming to developing robust, computationally inexpensive features capable of tracking deforming surfaces in a semidense SLAM based navigation system for WaFLES.

Methods

For our features, we make use of the anisotropic diffusion. Methods using this such as AKAZE have been shown to be robust for matching features on deforming surfaces, but they are computationally costly on conventional computers. A major computational load of these methods is the creation of non-linear scale space. To address this issue, we use the fast guided filter (FGF) to create edge preserving image filtering. In our previous work, we have already shown that our method for computing a non-linear edge preserving scale space can be achieved at much faster speeds on a conventional computer single processor in comparison to the fast AKAZE [1]. To obtain invariance to scale change and blurring, we create a scale space pyramid size of O octaves and N sublevels, with exponential division as in SIFT. This allows usage of small 3 times 3 Gaussian kernels which are efficient and help avoid guided filter halos. Our first level is filtered with $\sigma = 1.0$ Gaussian. We use the Hessian affine detector to extract features from octave layers and only keep the characteristic responses across the scale space. As a follow-up improvement to our previous method using a basic fast guided filter with a constant error term, we are using dynamical error term based on the image gradient. This way image abstraction in the scale space can be made stronger whilst protecting valuable edge information. For comparison purposes, we use the modified local difference binary descriptor (MLDB) configured with orientation information for robustness against image rotations.

We set the detectors to extract similar number ($\approx$ 5500) of features from WaFLES liver images size of 720 times 640 pixels, using our method and AKAZE and described them using the MLDB descriptor. We created a scale space size of 3 octaves and 4 sublevels. All results are obtained using a single core of a quad core Intel i7-6400 3.4 GHz processor with 16 Gb of RAM. In this follow-up, we ran tests against only AKAZE method using OpenCV 3.0 library. More detailed method comparison results are available in our earlier work in [1].

Results

Our preliminary results show that in comparison to AKAZE method, our method can still produce features approximately 53–58% (75–100 ms) faster despite the added computation stage [1]. Our method showed performance of approximately 55 features per millisecond, whereas AKAZE equivalent number is 20 features per millisecond of computation time. Furthermore, it can be seen in Fig. 1 that AKAZE features are distributed mainly to the first octave, whereas our method distributes features more evenly across the whole scale space. On the other hand, our method strongly emphasizes the first layer in octave 0, while AKAZE features are mostly spread to first two layers.

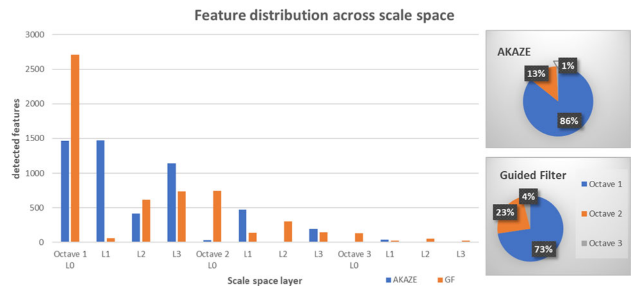

Fig. 1 Feature distribution across the scale space

We visually evaluated our method for tracking capability in vivo video sequence of WaFLES. We report that similar tracking can be obtained using our method in comparison to AKAZE method. It can be seen from Fig. 2 that small textures of liver surface were detected densely and tracked under tool manipulation of the organ and endoscope movements. Furthermore, tracking is capable to recover after occlusions by tissue particles and tool movements.

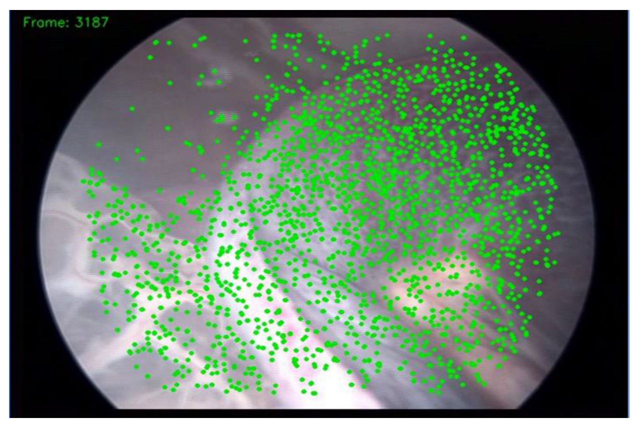

Fig. 2 liver surface tracking using our method

Conclusion

We have presented a method for creating non-linear scale space features, which has indicated to perform more efficiently and with better robustness to scale chance in WaFLES images and video than its closest competition. Despite it is not yet real-time capable on a single core, many its routines are feasible for parallel processing. Moreover, our method is simple to implement on an integrated or separate graphics processing unit (GPU) to accelerate it even further. Indeed, we are working on GPU implementation as well as more thorough testing. Interestingly, due to our selection of averaging filters in FGF our method is compatible with the affine Gaussian scale space. We consider investigating this feature in the future. We believe that our method can improve the deforming organ surface feature tracking in WaFLES navigation applications.

References

[1] Kontto M, Nakamura R (2017) Tissue Tracking using Features from Non-linear Scale Spaces for Water Filled Laparoendoscopic Surgery (WaFLES), JSCAS 19(4)

Enhancing depth perception for ORB-SLAM2 based endoscopic 3D mapping

D. Zhai[1], X. Deng[2], W. Si[3], X. Liao[3], Y. Dai[1], P. A. Heng[4]
[1]Wuhan University of Technology, Department of Information Engineering, Wuhan, China
[2]The Second People's Hospital of Shenzhen, Department of Hepatobiliary Surgery, Shenzhen, China
[3]Shenzhen Institutes of Advanced Technology, Chinese Academy of Sciences, Shenzhen Key Laboratory of Virtual Reality and Human Interaction Technology, Shenzhen, China
[4]The Chinese University of Hong Kong, Department of Computer Science and Engineering, Hong Kong, China

Keywords ORB-SLAM2 · Depth perception · Endoscopic surgery Dense reconstruction

Purpose

Endoscopic surgery poses visual challenges to the surgeons, since depth is not observable from monocular camera and the scale of the map is also unknown. The insufficient depth cues from the endoscopic environment could cause surgeons to misjudge spatial depth (especially in surgical resection), which could lead to performance errors thus jeopardizing patient safety [1]. By using binocular cameras all above issues are solved and allows for the most reliable ORB-SLAM2 solutions [2]. However, its remarkable tracking performance is at the expense of low map density [3], which is not beneficial for depth perception and augmented visualization of preoperative patient-specific three-dimensional model on intra-operative data.

Methods

Considering that endoscopic images are usually affected by specular reflections and low contrast, we employ the stereo images preprocessing method proposed in [4] to overcome these limitations, which can effectively improve the accuracy of camera localization and enhance details that are over- or under-exposed. Besides, to tackle the low map density limitation of ORB-SLAM2 induced by lack of repeatability of the ORB features in some body structures, we adopt the robust semi-global stereo matching (SGBM) algorithm to densely reconstruct the surface via disparity map.

Results

We download the rectified stereo images collected in da Vinci partial nephrectomy from Hamlyn Centre Laparoscopic/Endoscopic Video Dataset [5]. We have found that the endoscope tracking qualitatively quite robust and accurate. Figure 1a shows the original endoscopic image, and Fig. 1b, c are the comparison of reconstructed map obtained via our method and ORB-SLAM2, which clearly indicates that the reconstructed surface of our method are denser than that of ORB-SLAM2. When it comes to the performance, our method takes 62 s to process the 1000 endoscopic images, while ORB-SLAM2 takes 57 s. Experiment results demonstrate that our method can greatly improve the 3D map effects than that of the ORB-SLAM2 with only marginal computational cost. Figure 2a shows the endoscopic view with smoke, and Fig. 2b, c are the comparison of reconstructed map obtained via our method and ORB-SLAM2, which demonstrates that our method are robust to deal with the smoke presence.

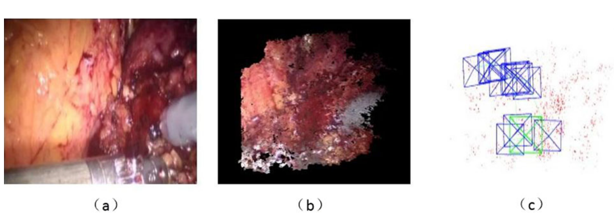

Fig. 1 **a** Original endoscopic image, and **b, c** are the comparison of reconstructed map obtained via our method and ORB-SLAM2

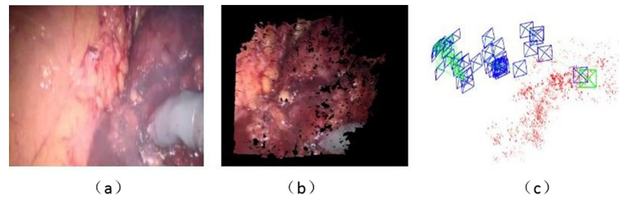

Fig. 2 **a** Endoscopic view with smoke, and **b, c** are the comparison of reconstructed map obtained via our method and ORB-SLAM2

Conclusion

We presented an effective but simple-to-implement method to extract the extract the depth information from stereo-endoscopic videos. However, its efficiency can not fulfill the requirements of surgical guidance, so that our immediately plan is to integrate the denoising stage and reduce the computation time for dense reconstruction. In addition, we are also interested in aligning these real-time data with preoperative patient-specific three-dimensional model of the vessel and tumor in liver, which is an automatic system for intra-operative guidance requires fast and reliable registration of the pre- and intra-operative data, reducing the risk of operating abdominal organs undergoing important deformations due to the pneumoperitoneum, respiratory and cardiac motion and the interaction with the surgical tools.

Acknowledgement

The work is supported by grants from Hong Kong Research Grants Council under General Research Fund (Project Nos. 14203115 and 14225616), a grant from the National Natural Science Foundation of China (Project No. 81601576), a Grant from Shenzhen Science and Technology Program (Project No. JCYJ20160429190300857), a grant from Guangdong province science and technology plan project (No. 2016A020220013) and a grant from China Postdoctoral Science Foundation (Project No. 2017M622831). Dandan Zhai and Xuesong Deng contribute equally to this work. Weixin Si and Xiangyun Liao are the corresponding authors of this work.

References

[1] Bogdanova R, Boulanger P, Zheng B. Depth Perception of Surgeons in Minimally Invasive Surgery. Surgical Innovation, 2016, 23(5): 515
[2] Mur-Artal R, Tardós JD (2016) ORB-SLAM2: An Open-Source SLAM System for Monocular, Stereo, and RGB-D Cameras. IEEE Transactions on Robotics, 33(5): 1255–1262.
[3] Mahmoud N, Hostettler A, Collins T, Soler L, Doignon C, Montiel JMM (2017) SLAM based Quasi Dense Reconstruction For Minimally Invasive Surgery Scenes. oai:arXiv.org: 1705.09107
[4] Penza V, Ortiz J, Mattos LS, Forgione A, De Momi E (2015) Dense soft tissue 3D reconstruction refined with super-pixel segmentation for robotic abdominal surgery. International Journal of Computer Assisted Radiology & Surgery, 11(2): 1–10.
[5] Ye M, Johns E, Handa A, Zhang L, Pratt P, Yang G-Z (2017) Self-Supervised Siamese Learning on Stereo Image Pairs for Depth Estimation in Robotic Surgery. Hamlyn Symposium on Medical Robotics.

3D printing customized titanium plates associated with surgical navigation guided precise correction of complex midfacial post-traumatic deformities

S. Zhang[1], C. Yang[1], J. Wu[1], Y. Zhang[1], B. Xu[1], S. G. Shen[1]
[1]Shanghai Ninth People's Hospital, Shanghai Jiao Tong University School of Medicine, Shanghai Key Laboratory of Stomatology, Department of Oral and Cranio-maxillofacial Surgery, Shanghai, China

Keywords 3D printing · Customized titanium plates · Surgical navigation · Midfacial deformities

Purpose
To evaluate the effectiveness of 3D printing customized titanium plates associated with surgical navigation guided precise correction of complex midfacial post-traumatic deformities.

Methods
Ten patients with midfacial post-traumatic deformities from 2017.01 to 2017.12 were involved in the present study. The preoperative planning and simulation data sets, including the generation of virtual models with the mirror tool, were used for a virtual template to design the surgical guides in case osteotomy is needed and customized fixation plates for all cases with Geomagic Studio 6.0 software (Raindrop Geomagic, Research Triangle Park, NC, USA) [1]. The customized fixation plates were made using a 3D printing technique for guiding repositioning the fracture fragments during operation. Furthermore, the AccuNavi-A navigation system (UEG Medical Devices Co. Ltd., Shanghai, China) was used to confirm the reduction of the fracture fragments, ensuring that the ideal positioning was achieved as virtually planned preoperatively (Fig. 1). The outcome was checked by both deviation chromatography analysis and clinical examination.

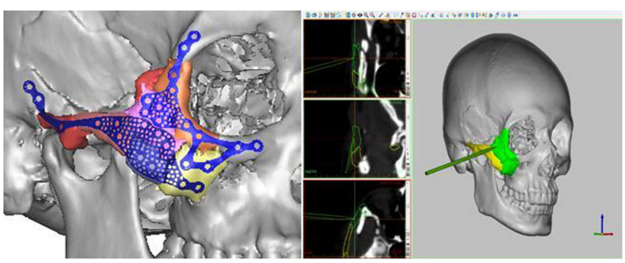

Fig. 1A Fig. 1B

Fig. 1 **A** The fabrication of 3D printing customized titanium plates, **B** intra-operative navigation for double-checking the reduction of the fracture fragments

Results
All the operations were successfully performed. There were no complications in positioning the osteotomy guides, the reduction and fixation. With the guidance of 3D printing customized titanium plates, which is confirmed by surgical navigation, the average differences between the virtual plans and the postoperative results were less than 1 mm. The deviation chromatography analysis was completed by superimposing the postoperative 3D computed tomography model onto the preoperative planning model (Fig. 2) [2]. The 3- to 6-month follow-up evaluation showed that the clinical complaint symptoms were alleviated, and the postoperative function and esthetics improved remarkably.

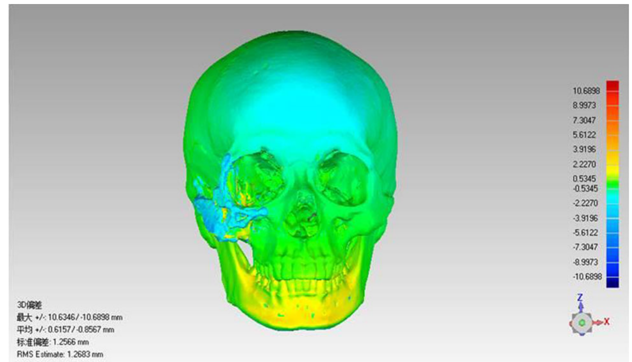

Fig. 2 The outcome was checked by deviation chromatography analysis

Conclusion
3D printing customized titanium plates was able to improve the surgical accuracy and the surgical navigation played a role of double-checking during this procedure. This technique could be regarded as an ideal and valuable option for this potentially complicated procedure.

Acknowledgements
This work was supported by the National Natural Science Foundation of China (81671035 and 81701034); Shanghai Science and Technology Committee (15441906000); the Project from Cooperative Innovation Center of Translational Medicine (TM201717); and the Interdisciplinary Program of Shanghai Jiao Tong University (Project No. YG2015QN05).

References
[1] Zhang S, Gui H, Lin Y, Shen G, Xu B. (2012) Navigation-guided correction of midfacial post-traumatic deformities (Shanghai experience with 40 cases). J Oral Maxillofac Surg 70(6): 1426–1433.
[2] Yu H, Shen SG, Wang X, Zhang L, Zhang S. The indication and application of computer-assisted navigation in oral and maxillofacial surgery-Shanghai's experience based on 104 cases. J Craniomaxillofac Surg. 2013; 41(8): 770–774.

Preclinical assessment of a novel intraoperative ultrasound probe for transsphenoidal surgery

S. Mihcin[1], H. Marcus[1,2], R. Delaunay[1], E. Maneas[1], W. Xia[1], S. Ourselin[1], A. Desjardins[1], N. Dorward[1,2], T. Vercauteren[1]
[1]UCL, Department of Medical Physics and Biomedical Engineering, London, United Kingdom
[2]UCLH, National Hospital for Neurology and Neurosurgery, London, United Kingdom

Keywords Evaluation verification · Work flow · US imaging · Transsphenoidal surgery

Purpose
Transsphenoidal surgery is the gold standard for pituitary adenoma resection, although some pituitary adenomas still remain challenging to cure [1]. Approximately a third of patients undergoing transsphenoidal surgery for pituitary adenoma are found to have an incomplete resection, and many of these patients will require further treatment [2]. Intraoperative CT and MRI are the imaging modalities that have been used as adjuncts in transsphenoidal surgeries to assess the extent of resection. Although they offer high-contrast and high-resolution imaging, because of the prolonged operating time and high costs

involved in both, they are not considered as ideal solutions [1]. Intraoperative ultrasound could be an alternative low cost imaging modality with real-time feedback, but existing ultrasound probes are too bulky for use in transsphenoidal surgery. To this end, we have developed a novel ultrasound probe specifically designed for transsphenoidal surgery, which can both pass through the nares and nasal cavity during surgical approach, and provide sufficient image resolution to allow for assessment of remaining tumour tissues (Fig. 1). In this preclinical study, we evaluate the device image quality by quantitatively assessing the image resolution on an ultrasound-phantom, and evaluate the device ergonomics on an anatomical-phantom within the workflow. Our purpose is to provide sufficient evidence for feasibility and safety to allow for subsequent clinical trials.

Fig. 1 A novel pituitary probe for transphenoidal surgeries for intraoperative ultrasound imaging and Kezlex anatomical model (Ono & Co., Tokyo, Japan) in a Mayfield clamp (Integra, Saint Priest, France)

Fig. 2 Scan of human finger by using the novel US probe, and by commercially available bulky probe (L40-8/12 Linear, BK Ultrasound, UK)

Methods

The ultrasound probe is a novel version of a previous prototype that was used successfully for patients undergoing transsphenoidal surgery for pituitary adenoma [3, 4]. The probe is forward-viewing, has a slender design (7 mm in diameter, to fit into the nares), and can be optically tracked by neuronavigation platforms (Fig. 1). The images were displayed using a standard CE-marked ultrasound image display system (SonixTouch, BK Ultrasound, UK).

Spatial resolution was used to evaluate the ability of the ultrasound system to detect and display structures that are close together. Since ultrasound image displays depth and width across a section of anatomy, resolutions are named as Axial & Lateral along each direction respectively. The axial resolution is the ability to display small targets along the path of the beam as separate entities. The lateral resolution is the ability to distinguish between two separate targets perpendicular to the beam path (same distance from the transducer). To assess the resolution, a 25-µm carbon fibre (Quorum Technologies Ltd., East Sussex, United Kingdom) was fixed in a water tank to be scanned by the new probe at frequencies of 20, 15, and 8 MHz at an imaging depth of 2.5 cm with 0.5 cm of intervals. To measure the spatial resolution at different locations relative to the US probe, an XY table was utilised to move the water tank with the carbon fibre in a fixed position. The full width at half maximum values (FWHM) of the axial and lateral profiles across the centre of the reconstructed objects were used as measures of the spatial resolution. We considered a spatial resolution of approximately 1.5 mm satisfactory to detect residual disease and identify neighbouring neurovascular structures.

Contrast resolution was defined as an ability to demonstrate differentiation between tissues having different characteristics with corresponding differences in grey scale image values. To assess the contrast a human finger was scanned and cross compared to a commercially available ultrasound probe (L40-8/12 Linear, BK Ultrasound, UK), which is too bulky for use in transsphenoidal surgery. We considered visualisation of vessels within the finger as satisfactory criteria to evaluate efficiency of the contrast.

The device ergonomics and surgical workflow were evaluated by two experienced surgeons (> 50 cases performed) using an existing Kezlex anatomical model (Ono & Co., Tokyo, Japan), alongside an endoscope and neuronavigation platform (Stealth Station S7, Medtronic) (Fig. 1). Workflow integration was assessed by using a chronometer to measure the total time using the US probe to provide the imaging of the pituitary gland. A 5-point Likert scale was provided to obtain user feedback on the safety, image quality, and willingness to use the system again. There was also an open-ended section for comments to provide an opportunity for more detailed feedback.

Results

The results for axial and lateral resolution were calculated for each depth and frequencies (Fig. 3). Average value of axial resolution was 0.25 (SD 0.02), 0.25 (SD 0.02), 0.27 (SD 0.02) at 8, 15 and 20 MHz respectively within the depth of 2.5 cm that was covered. Average value of lateral resolution was 1.3 (SD 0.3), 1.3 (SD 0.3), 1.3 mm (SD 0.3) at 8, 15 and 20 MHz respectively. But both were considered satisfactory when compared to the a priori working specifications. The standard deviation was high in lateral resolution this could be explained by difficulty in aligning the centre of the beam with the scanning plane in the experimental set up. Overall, axial resolution was better than lateral resolution. The axial resolution was found to be insensitive to the change of frequency, even at frequencies of up to 20 MHz.

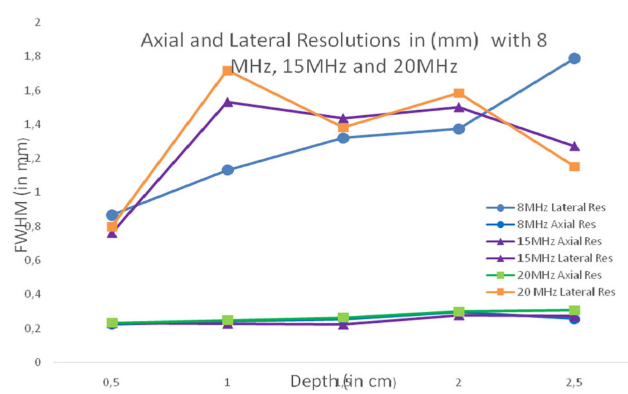

Fig. 3 Axial and lateral resolution values in mm for 8, 15 and 20 MHz over 2.5 cm scanning depth

The results for contrast resolution when scanning a human finger were favourable, with clear visualisation of the vessels that was comparable to the larger commercially available probe (Fig. 2).

The results of the ergonomics study were also encouraging with the probe size and configuration easily allowing for its use through the nares and nasal cavity during surgical approach, and could be optically tracked during the procedure. The overall time required to use the probe was in the order of several minutes. The survey demonstrated that surgeons felt the probe had an image quality comparable to larger existing probes, that they agreed it was safe, and they would be willing to use the device again.

Conclusion

In this preclinical study, a novel intraoperative ergonomic ultrasound probe was evaluated for its suitability for transsphenoidal surgery, and found to be feasible and safe. The maximum average axial resolution was calculated as 0.26 (SD 0.02) and 1.3 mm (SD 0.3) The calculated resolutions were considered satisfactory when compared to the a priori working specifications. The anatomical-phantom study shows that the probe has a size and configuration that is compatible with the transsphenoidal approach, and can be used alongside neuronavigation platforms. Moreover, use of the probe does not interfere excessively with the surgical workflow. We recommend a clinical study to further evaluate feasibility and safety of the ultrasound probe for transsphenoidal surgery.

References

[1] Marcus H, Vercauteren T, Ourselin S, Dorward NL (2017) Intraoperative Ultrasound in Patients Undergoing Transsphenoidal Surgery for Pituitary Adenoma: Systematic Review, In World Neurosurgery, 106: 680–685.

[2] Dallapiazza RF, Grober Y, Starke RM, Laws ER, Jr., Jane JA, Jr (2015) Long-term results of endonasal endoscopic transsphenoidal resection of non-functioning pituitary macro adenomas. Neurosurgery. 76(1): 42–52

[3] Solheim O, Johansen TF, Cappelen J, Unsgård G, Selbekk T (2016) Transsellar ultrasound in pituitary surgery with a designated probe: early experiences. *Operative Neurosurgery* 12(2): 128–134.

[4] Solheim O, Selbekk T, Lovstakken L, Tangen GA, Solberg OV, Johansen TF, Cappelen J, Unsgård G (2010) Intrasellar ultrasound in transsphenoidal surgery: a novel technique. Neurosurgery. 66(1): 173–185

Microscopic image-based determination of stapes prosthesis length

J. C. Rosenthal[1], N. Gard[1], A. Schneider[2], P. Eisert[1,3]
[1]Fraunhofer Heinrich Hertz Institute HHI, Vision & Imaging Technologies, Berlin, Germany
[2]Arnold and Richter Cine Technik GmbH, ARRI Medical, München, Germany
[3]Humboldt-Universität zu Berlin, Institut für Informatik, Berlin, Germany

Keywords Image-based measurement · ENT surgery · Microscopy · Augmented reality

Purpose

A common treatment for patients suffering from hearing loss caused by otosclerosis is stapedectomy, a surgical replacement of a part of the stapes with a micro prosthesis. During the intervention, the surgeon needs to choose an appropriate-sized prosthesis. An accurate measurement of the incus-footplate distance can improve the hearing outcome [1]. Furthermore, the selection of the correct fitting prosthesis with fewer tries reduces the overall costs of the operation. Since the size differences of the prostheses are small (e.g. 0.25 mm), it is difficult to judge the needed size by eye, especially in the magnified microscope image. Therefore, we provide an entirely image-based measurement approach to avoid usage of physical instruments in terms of handling and sterilization. In our case, the surgeon uses a joystick to select image points directly within the microscopic image, enabling metric point-to-point distance measurements. This leads to an integrated and improved workflow, reducing cost and surgery risk.

Methods

Precondition to perform image-based measurements is a calibrated stereoscopic system. Calibrating a surgical microscope is challenging. In contrast to stereo endoscopes, its optical system has optical properties, which are difficult to model, e.g. a variable focal length. Our calibration method differs from well-known checkerboard methods in that we apply a model-based approach using image registration technique to correlate captured patterns with the reference plane as described in [2]. The motor controlled zoom lens allows re-calling the correct calibration data, as they are stored together with exact motor positions in a database.

We use the surgical microscope ARRISCOPE (Arnold und Richter Cine Technik, Munich, Germany) that has a complete digital processing chain, meaning that it captures a digital image pair and displays it on OLED screens inside the binocular. Our method consists of three steps: First, we apply a scene dependent rectification of image pairs via detection of robust feature points [3, 4]. Second, we perform a dense disparity estimation [5] using such rectified image pairs as input. Disparity estimation fully works in parallel on a graphic card with CUDA support. The procedure makes use of a statistical approach on sub-pixel level to estimate new correspondences. These correspondences are distributed into the local neighborhood where new correspondences are determined within the next iteration. This independent propagation of new estimated correspondences guarantees that the whole image is constantly updated. The obtained disparity maps have sub-pixel accurate disparity values. Last, corresponding points are 3D reconstructed from the sub-pixel positions using triangulation. Reconstructed 3D points allow the measurement of point-to-point distances to choose the correct size of a stapes prosthesis. The measurement is performed on a still image to compensate micro movements of the microscope. Instant visual feedback is provided by an augmented overlay when the surgeon selects the points of interest via the joystick.

Results

In first tests, we examined the quality of the calibration by measuring distances in depth direction with a depth-of-field-test body using manually established correspondences. For 250 measurements of target distances between 1 and 5 mm in maximum zoom (9.6×, maximum field of view for working distance of 210 mm: 14 mm × 8 mm), the average error per distance varies between 0.04 and 0.09 mm. For 400 measurements of target distances between 5 and 40 mm in minimum zoom (1.6×, maximum field of view for working distance of 210 mm: 78 mm × 43 mm), the average error per distance varies between 0.2 and 1.3 mm. Second, we measured the edge length of test specimens with a known ground truth and the extensions of a real stapes prosthesis within a temporal bone model. We claim to achieve accuracies of ± 0.1 mm in both tests in the maximum zoom level. This is accurate enough to differ between two prostheses with a size difference of 0.25 mm. Just now, an intensive test series is still ongoing. First results already fulfill our target. Figure 1 shows the results of the disparity maps for our described test scenarios. Currently, we process 10 stereo pairs (1920 × 1080 px) per second. In addition, we integrated our measurement method into a live demonstrator shown at several ENT congresses and trade fairs. This incorporates the smart joystick user interaction and the augmented visualization of underlying depth information and measurement results inside the digital binocular.

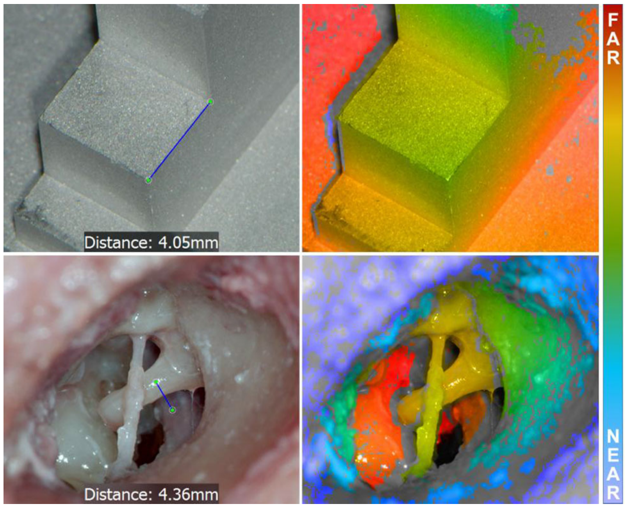

Fig. 1 AR overlay of image-based measurement results (left) and color-coded disparity information (right) showing a test specimen with known dimension (4 mm) and an in vivo image example

Conclusion

We developed an image-based measurement system for microscopic ENT surgery. Clinical studies show the need for a measurement support during the selection of a stapes prosthesis. The measurement function is integrated into the research module of the digital surgical 3D microscope (ARRISCOPE) and test measurements have been carried out on stapes prostheses within temporal bone models and on test specimens. Achieved measurement results show that the desired accuracy is within the needed range of ± 0.1 mm. Recorded in vivo data has been analyzed by visual interpretation of estimated disparity maps, which show promising results for intraoperative use. As a next step, our image-based solution will be evaluated in clinical studies comparing image-based measurements to measurements using a physical gauge and visually estimated distances. Moreover, the calibration model needs to be extended for continuous zoom. In future, our method can easily be transferred to other types of measurement like accumulated multiline or area measurements to survey tissue-of-interest (TOI), e.g. to observe tumor dimensions.

References

[1] Marchica CL, Saliba I (2015) The Relationship between Stapes Prosthesis Length and Rate of Stapedectomy Success. Int J Clinical Medicine Insights: Ear, Nose and Throat 8: 23–31
[2] Rosenthal J-C, Gard N, Eisert P (2017) Kalibrierung stereoskopischer Systeme für medizinische Messaufgaben. In Proceedings 16th Annual Conference—German Society for Computer- and Robot-Assisted Surgery (CURAC): 159–161
[3] Zilly F, Riechert C, Eisert P, Kauff P (2011) Semantic kernels binarized-a feature descriptor for fast and robust matching. In: Visual Media Production (CVMP), 2011 Conference for. IEEE, pp 39–48
[4] Zilly F, Müller M, Eisert P, Kauff P (2010) The Stereoscopic Analyzer—An image-based assistance tool for stereo shooting and 3D production. In: 2010 IEEE International Conference on Image Processing (ICIP): 4029–4032
[5] Waizenegger W, Feldmann I, Schreer O, Kauff P, Eisert P (2016) Real-time 3D body reconstruction for immersive TV. In: 2016 IEEE International Conference on Image Processing (ICIP): 360–364

3D real-time assisted surgery system development from using image-guided and electric-field sensing techniques

C. H. Cheng[1], D. G. Liu[1]
[1]Feng Chia University, Taichung, Taiwan

Keywords Image-guided surgery · Image tracking · Electrical-field sensing · Minimally invasive surgery

Purpose

Conventional single-lens endoscopes are widely used for various diagnoses and treatments in MIS. However, the limited scope range without depth information from the two-dimensional (2D) image of the endoscope often makes the endoscope as the most problematic issue faced by surgeons in MIS. The proposed technique of this study was aimed to reduce the difficulties in MIS with the single-lens endoscope of unknowing the depth. This research proposed an assisted system which provides information of distances and angles between the surgical scalpels and the target position. In addition to the 2D endoscope, an off-body electric-field sensing technique was developed to provide the three-dimensional (3D) locations of scalpels during surgical operations.

Methods

The proposed real-time surgery assisted system consisted of a 2D image-guided and a 3D object-tracking techniques, which provides global tracking information of the surgical scalpels and their positions during surgery. The image region-of-interest (ROI) and picture-in-picture (PIP) functionalities are included in the proposed image-guided techniques. The ROI would help the surgeon to focus on the correct surgical position, and the PIP provided an enlarged view of the operational region in the surgical area. The object-tracking system can provide the supplemental 3D depth information by electrical-field sensing out of the patient's body.

The Color Filtering controls the image HSV (hue-saturation-value) values, and this function is used to find the surgical scalpel location. Morphological Operations utilize the Erode and Dilate function to filter out the target image noise while enhancing the clarity of the target image.

This distance is defined by an image pixel quantity within the surgical position and the locking-point of the surgical scalpel.

1. The image HSV and morphological operations

HSV (Hue-Saturation-Value) is the most common cylindrical coordinate representation of a color image in an BGR model. The object's gray image produced by the HSV process can be dynamically tracked.

The morphological operations utilize the erode and dilate operations and can easily find the tracked scalpel. The images are processed by erode and dilate operations. The target distance and angle can then be dynamically calculated.

2. 3D object sensing with electric-field

An electric field is a vector with its intensity and orientation at a spatial point. Connecting these field vectors would form a series of flow lines to indicate the electric force around an object. We can call these lines as power lines to indicate the intensity of the electric fields. The electric-field intensity will induce some electric charges on the surface. Higher field intensities create more charges on the surface, and vice versa.

Results

1. The 2D image-guided experimental analysis

There are two screens to help the surgeon to monitor surgery procedures. The mother screen provides image-guided information and enlarged surgery target vision. The separated daughter screen shows the global and local views of the surgical operation.

There are two lenses that are required; the high-magnification large-focus lens is provided for the surgical region. The low-magnification small-focus lens provides the global view and shows the other organs during surgery. The results are validated by using the following experiments.

The global positioning information is shown on two monitors. The PIP technique overlaps with the original endoscope vision. The local-view and global-view monitors help doctors to know the whole surgical area information. The daughter screen is the surgical position from the far-focus lens.

The proposed image-guided system without the object-tracking system had provided accurate distance and direction up to 95% accuracy of surgical scalpels by the 2D information, as shown in Fig. 1. The enlarged local view with the information of distance and angle (direction) can help doctors be aware of the correct surgical target. The added object-tracking design is under reevaluation in animal experiments for further assistance with the image-guided system.

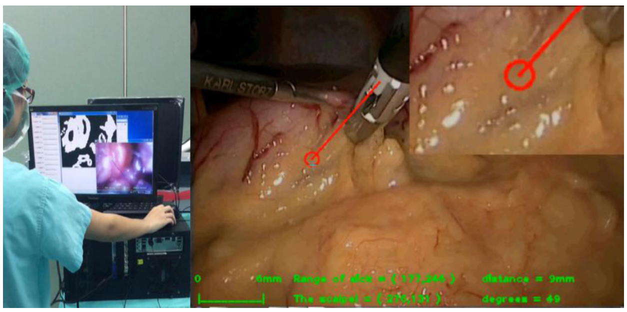

Fig. 1 The animal 3D real-time assisted surgery system

2. The 3D Electric-field sensing result and discussion
Figure 2 shows the setups of the proposed electric-field sensing system. The sensing technique can track and follow the scalpel position. The detection would be affected by objects around the subject. Further improvement to reduce the interference from the environment would be an issue for this technique to be applied in animal experiments.

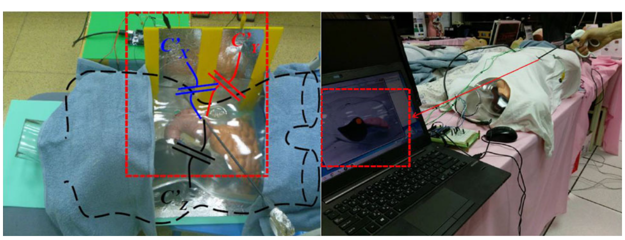

Fig. 2 The surgery tracking experiments and system demonstrations

3. The integration and demonstration of the two proposed technique
The image-tracking and object-tracking techniques are integrated as an assisted surgery system and demonstrated as shown in Fig. 2. The image-guided has been successfully validated with in vivo animal experiments as shown in Fig. 2. The hardware requirement is simple and can be implemented in a personal computer or embedded system, which means the less volume, and can be feasible practical in a single chip. Our future research needs to join the 2D and 3D calculations.

Conclusion
To reduce the difficulties of MIS, the proposed techniques provide the 3D location information from the surgical scalpel to the surgical position. The real time guiding system provides global positioning information by tracking the scalpel and surgical position during surgery. The 3D information will greatly assist doctors in accomplishing successful MIS surgical operations. With the principle employed in touch panels, the scalpel can be tracked by external sensor boards. This capacitive positioning technique would provide a new possibility to track the scalpel in addition to the use of endoscopes. Multiple sensors may also be employed to improve the accuracy. Future automatic surgical operations need to include and joint with machine control mechanism.

References

[1] Bradski G, Kaehler A (2008). Learning OpenCV: Computer Vision with the OpenCV Library. 1st ed. ed.; O'Reilly Media: Sebastopol, CA, USA

[2] Mastering Opencv with Practical Computer Vision Projects, http://www.inc.eng.kmutt.ac.th/inc161/project/opencv/Mastering_opencv.pdf

Development of a method of integration of electrical stimulation positions into standard brain coordinate system

K. Ohshima[1], I. Sato[1], T. Nagai[1], Y. Fujino[1], H. Yamada[2,3], M. Tamura[2], Y. Muragaki[2], K. Masamune[2]

[1]Future University Hakodate, Hakodate, Japan
[2]Tokyo Women's Medical University, Tokyo, Japan
[3]Murakumo Corporation, Tokyo, Japan

Keywords Normalized brain · Brain function · Non-rigid registration · Awake surgery for glioma

Purpose
For glioma resection surgery, "future-predicting glioma surgery" is suggested [1]. Future-predicting glioma surgery can facilitate decision-making by clinicians by predicting the survival rate and post-operative neurological complications with respect to the scheduled resection area. Due to its importance, past surgical data of numerous patients (glioma resection area, post-operative complications, and brain function response points) need to store and do statistical analyzed. This will enable the realization of evidenced-based resection surgery in glioma.

For pre-processing of data in future-predicting glioma surgery, we need to create datasets for statistical analysis by integrating past surgical data in one coordinate system. In a previous study, digitized brain functional position by brain and methods for creation of datasets for statistical analysis were suggested [1]. Using results of this study, we integrated the brain function points acquired by electrical stimulation into a brain template. However, the datasets for statistical analysis were not adequate.

In this study, we describe the methods of creating datasets of electrical stimulation positions for statistical analysis in future-predicting glioma surgery. These methods enable the integration of brain function points of numerous patients into the brain template. Subsequently, we evaluated the integration accuracy of these methods.

Methods
In the proposed method, pre-operative and intra-operative MR images and intra-operative information such as electrical stimulation points are non-rigidly integrated into the coordinate system of the brain template. Thus, intra-operative information of multiple patients can be analyzed in one coordinate system (Fig. 1).

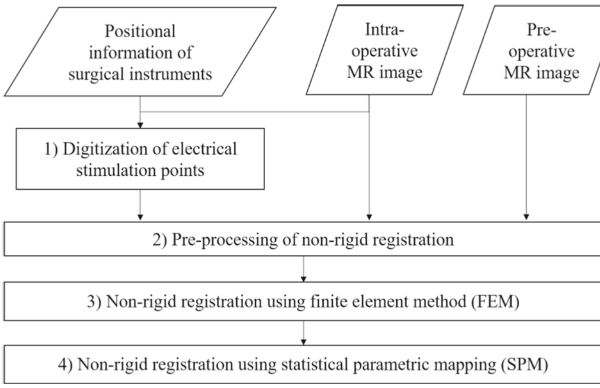

Fig. 1 Workflow into standard brain processed by steps 1–4 of method

The method consisted of the following four processes:

1. Digitization of electrical stimulation points
2. Pre-processing of non-rigid registration
3. Non-rigid registration using finite element method (FEM)
4. Non-rigid registration using statistical parametric mapping (SPM)

Process 1, involved the creation of images of the electrical stimulation positions diagnosed with the brain functional area. First, the brain functional area was determined using cortical mapping during glioma surgery. Next, brain functional area was identified on the MR image using intra-operative video, medical certificate, and log data of electrical stimulator position. The electrical stimulation position was mapped as a circle with a diameter of 8 [mm] points; an electrical stimulation position image was thus created.

Process 2 involved pre-processing for processes 3 and 4. We performed rigid-registration manually for the pre-operative and intra-operative MR images and the electric stimulus position image. Next, bias correction was performed on the pre-operative and intra-operative MR images. Then, the noise was eliminated using an unbiased non-local means filter for intra-operative MR images.

In process 3, the non-rigid registrations of the intra-operative and pre-operative MR images were performed. The intra-operative MR image and the electrical stimulation position image were deformed non-rigidly and fitted to the pre-operative MR image using non-rigid registration with finite element analysis [2].

In process 4, non-rigid registration of pre-operative images and MNI template was performed. In this process, the displacement of gray matter between of pre-operative MR images and brain template (ICBM 152 nonlinear asymmetric template; ICBM 152 template) were calculated using SPM [3]. Next, pre-operative MR images and results of process 3 were integrated non-rigidly to ICBM 152 template.

With the above processes, 1–4, pre-operative and intra-operative images and brain function points were integrated non-rigidly into the brain template.

Results

We evaluated the registration accuracy divided into 3 and 4 non-rigid registration. The compared images were pre-operative MR images and intra-operative MR images of process 3 non-rigid registration, and ICBM 152 template and pre-operative MR images of process 4 non-rigid registration of 4 patients. Then, we calculated the registration error using 3–4 sulci landmarks and the brain surface in the proximity of the glioma.

In process 3 registration, the overall registration errors were 4.3 ± 1.3 and 4.5 ± 1.0 [mm] for sulci landmarks and 4.1 ± 1.7 [mm] for the brain surface. In process 4 registration, the overall registration error was 7.2 ± 2.3 and 5.8 ± 1.4 [mm] for sulci landmarks and 8.6 ± 3.3 [mm] for the brain surface. We have provided the results with one case (Fig. 2).

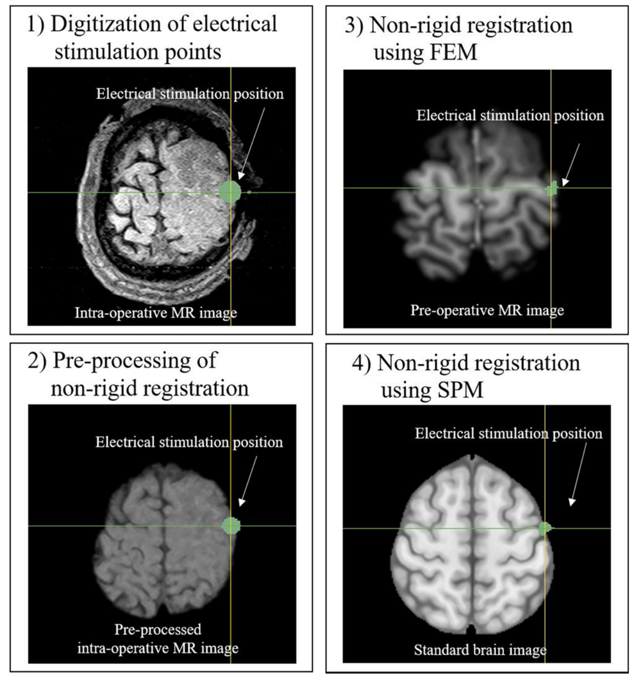

Fig. 2 Transformation of electrical stimulation position into standard brain processed by steps 1–4 of method

Conclusion

In this study, we described methods for creating datasets of electrical stimulation points for statistical analyses in future-predicting glioma surgery. This will enable the realization of evidenced-based resection surgery in glioma.Then, we evaluated the registration accuracy of these methods. The overall registration error of process 3 was 4.3 ± 1.3 [mm] and of process 4 was 7.2 ± 2.3 [mm]. From the above results, we conclude that process 4 is less effective than is process 3. Because, some cases in process 4 were not accurately deformed. A higher number of cases for integration renders a more detailed identification of brain functional location.

Acknowledgement

This research and development work was supported by the MIC/SCOPE #162101001.

References

[1] M. Tamura, et al., Digitized Brain-mapping and Functional Database for the Future-predicting Glioma Surgery, The 3rd International Symposium on Multidisciplinary Computational Anatomy, pp. 209–216, 2017.
[2] Liu Y, Kot A, Drakopoulos F, Yao C, Fedorov A, Enquobahrie A, Clatz O, Chrisochoides NP (2014) "An ITK implementation

of a physics-based non-rigid registration method for brain deformation in image-guided neurosurgery", Frontiers in neuroinformatics 8(33): 1–10
[3] SPM: Statistical Parametric Mapping, http://www.fil.ion.ucl.ac.uk/spm/. Last accessed at 2018/01/08

Preclinical quantitative validation of a laparoscopic augmented reality visualization system: preliminary results

X. Liu[1], L. Lau[1], W. Plishker[2], K. Sharma[1], T. Kane[1], R. Shekhar[1,2]
[1]Children's National Health System, Washington DC, United States
[2]IGI Technologies, Inc., College Park, MD, United States

Keywords Augmented reality · Laparoscopic surgery · Laparoscopic ultrasound · Image fusion

Purpose

Standard laparoscopy cannot visualize anatomy beyond what is present in front of the laparoscope. Conventional laparoscopic ultrasound (LUS) imaging provides information on subsurface anatomy, but can only be integrated with the laparoscopic images in the surgeons mind. Additionally, focus is distracted from the laparoscopy screen to look at ultrasound images on a separate screen. The desire to reduce this distraction and, ultimately, improve intraoperative efficiency in using and interpreting ultrasound images has motivated the development of LUS-based augmented reality (AR) systems that fuse real-time ultrasound images with live video. Many AR prototypes have been developed in the past. A few of these have been validated in animal studies, a necessary step toward clinical adoption. However, most of these preclinical studies focused on qualitative evaluation of the systems feasibility. This study introduces a validation method to quantitatively assess the performance of the AR system, developed by our team, in comparison with standard laparoscopy.

Methods

One major application of the LUS-based AR system is tumor resection. Our hypothesis is that the use of the AR technology leads to achieving optimal tumor margins and maximum sparing of the healthy tissues of the host organ. We have designed a series of animal studies involving up to 9 swine (40 kg). Each study will begin by creating up to 6 ultrasound visible artificial tumors—4 in the liver and 1 in each kidney (Procedure #1). An interventional radiologist will use the radiofrequency ablation equipment to create approximately 2-cm thermal burns simulating tumors, with percutaneous ultrasound guidance. After the ablation, the swine will be housed for a few days to allow for all liquids and gases resulting from ablation to be resorbed, and for ablations to become visible by ultrasound.

During the actual tumor removal surgery (Procedure #2), our AR system is used. The system includes: (1) a standard laparoscopy set (Karl Storz Inc.), (2) a laparoscopic ultrasound scanner (BK Medical Inc.), (3) an electromagnetic tracking system to track the 3D location and orientation of the ultrasound probe and laparoscopy camera (Northern Digital Inc.), and (4) a laptop computer running image fusion software. Whereas ultrasound image calibration is performed in advance, fast laparoscope calibration is performed immediately before the surgery starts. While preserving as much healthy tissue as possible, the operating surgeons will remove half of the artificial tumors using the conventional approach (LUS but no AR visualization) and the remaining half with enhanced visualization provided by the AR system. The resected samples will be sectioned for tumor margin measurements. Statistical analysis will be performed with these measurements.

Results

After IACUC approval, we have performed two animal studies so far. These experiments have begun yielding quantitative comparison data. Artificial tumors were successfully created in the liver and the kidney and could be visualized using ultrasound. Ablation time and days between the two procedures were varied to better control the size and ultrasound-visibility of the artificial tumor. When using the AR system, anatomic detail from ultrasound was able to be fused with the laparoscopic images in real time and presented on a single screen (Fig. 1). This provided continuous imaging guidance of the resection, allowing the surgeon to correct for depth and direction of resection in real time without distracting focus from the primary laparoscopy screen. The AR system was reported to be no more difficult to use than standard laparoscopy. The times for resection with and without AR were comparable. Gross resection margins of the resected samples could be clearly identified after sectioning (Fig. 2).

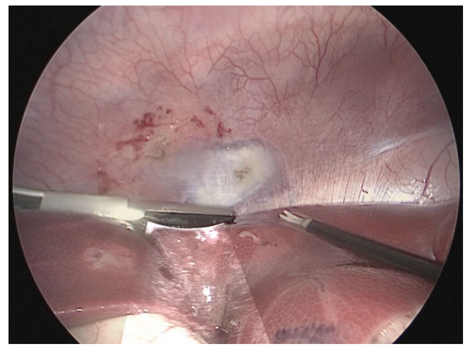

Fig. 1 Augmented reality fusion of ultrasound image with laparoscopic video during laparoscopic hepatic wedge resection

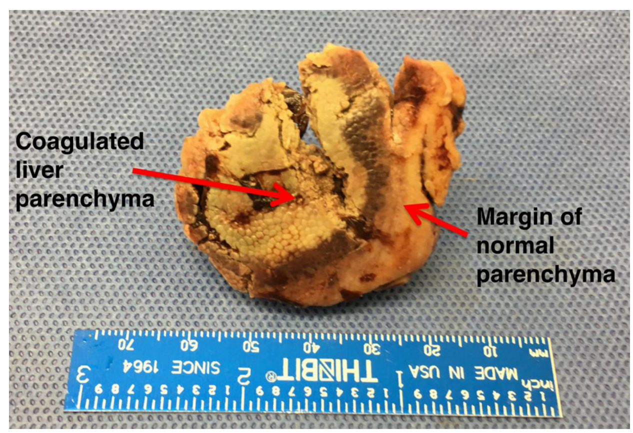

Fig. 2 Wedge resection of liver tumor model removed with augmented reality

Conclusion

With the experience gained and preliminary data obtained from the first two animal studies, we believe the ongoing preclinical study is feasible to generate meaningful quantitative metrics to evaluate the benefits of using a laparoscopic AR system. We will optimize the AR system as well as the design of the experiment based on the feedback from the primary users (operating surgeons) and our experience from the first two studies in general. Positive results from this study will support clinical demonstration and evaluation of the AR technology in a subsequent stage.

Virtual planning of mandibular reconstructions with Iliac crest transplants—a semi-automatic algorithm

S. Raith[1], M. Pritsch[1], N. Ayoub[1], F. Peters[1], F. Hölzle[1], A. Modabber[1]
[1]RWTH Aachen University Hospital, CMF-Surgery, Aachen, Germany

Keywords Surgery planning · Reconstructive surgery · Mandible · Iiiac crest transplant

Purpose

The rehabilitation of the lower jaw in large continuity defects is an extremely demanding task in cranio-maxillofacial surgery. Because of its versatility as avascular graft or bicortical microsurgical deep circumflex iliac artery flap (DCIA) and its generally large available bone supply, the autologous transplant from the iliac crest has established itself as one of the standard regions of choice for bone grafting in recent years. Due to the complex curvature of both, the mandible that requires reconstruction and the harvesting site at the iliac crest, the planning of these operations is a great challenge. Even when computer aided approaches are chosen, a large proportion of the planning procedure is manual, requires special training and still is a tedious and time-consuming endeavor. In contrast to reconstruction planning with fibular graft, there are yet no computational tools available for the iliac crest that propose reconstructions based on automated algorithms. The aim of the present study was to develop and test a method that is capable of automated surgery planning for mandibular reconstruction surgery with iliac crest transplants, while considering the individual geometrical curvatures of both the defect at the mandible and the donor site.

Methods

Volumetric image data from a CT scans of a physiological mandible and the respective CT data of the pelvic area of the same patient were collected and used as the basis of the present study. All sets of data were segmented using appropriate software tools (ProPlanCMF version 2.0, Materialise, Leuven, Belgium) to acquire the surface geometry of all relevant bony compartments. Based on the entire mandible model, several virtual defects were generated (defect classifications according to Jewer et al. [1]: C, L, H, HC, LC, LCL, HCL and HH). A tailor-made algorithm was developed in python programming language and transferred to the software tool Blender (version 2.78, Blender Foundation, Amsterdam, Netherlands), where a graphical user interface was implemented. The developed tool can deal with the individual demands of pelvic reconstruction and may be executed semi-automatically creating proposals for reconstruction surgery planning requiring minimal user interaction. The algorithm relies on individually defined curves on the contours of the relevant bones that follow certain characteristic anatomical shapes. For reconstructions that require only one segment to bridge the whole continuity defect, the algorithm is capable of proposing immediately reconstructions in a fully automated cascade of calculations. For more complex microvascular cases, where more segments are needed, the software allows manual user interactions for relative positioning and rotation of the segments, while obeying clinical and anatomical restrictions: the posterior medial cortical wall cannot be disconnected during surgery, as this would compromise the blood vessel supply, according planning interfaces are provided within the software. Thus, it is possible to perform hinge-like folding between the different segments respecting the curvature of the medial cortical wall of the iliac crest graft. All virtual reconstruction results were evaluated both by experienced clinicians that judged the applicability of the planning in the operation room and by calculation of geometric accordance between planned position of the transplant and the geometry of the missing mandibular parts that require reconstruction. With the automated procedure it was possible to design multitudes of different possibilities for reconstructions in a standardized and reproducible way, such as variations in harvesting positions to find optimal geometrical matches. Parametric studies on different harvesting positions were executed for reconstruction of missing parts that could be bridged with one single segment.

Results

For positioning of the transplant in the recipient site, the developed algorithm showed to deliver clinically valid proposals for reconstruction planning. This automated part of the procedure includes the cutting of the transplant with appropriate osteotomies and virtual back-transformation to the donor site for planning of the harvesting operation (Fig. 1). Single segmental reconstructions showed to be applicable for small and medium sized defects (i.e. defects C, L, LC, H). With this automated procedure different variations in harvesting positions were generated to find the positions with optimal geometrical matches. In the L defect, for example, the optimal geometrical match between the transplant curve and the recipient site was found to be 1.96 mm in average (integrated three-dimensional distance) corresponding to a relative position at the iliac crest of 105 mm (Fig. 2).

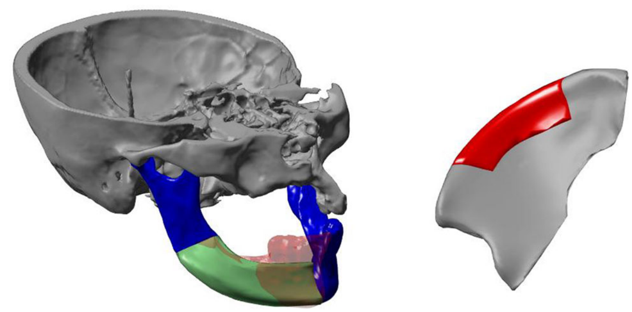

Fig. 1 Left: Automatically generated reconstruction proposal with residual mandible parts (blue), the missing part that needs to be reconstructed (semi-transparent red) and the planned transplant (green). Right: Harvesting at the donor site may be planned by back-transformation of the planned transplant part (red)

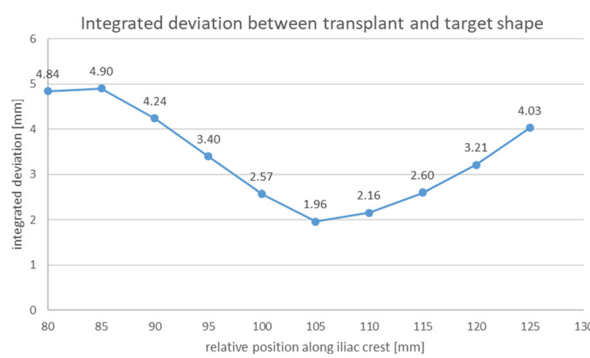

Fig. 2 Integrated deviation between transplant curve and target curve that needs to be reconstructed for the L defect. When different harvesting positions are investigated, an optimal geometrical accordance could be found, here with an average deviation of 1.96 mm at a relative position of 105 mm

For more extended defects (i.e. HC and LCL) multi-segment reconstructions are required to reestablish the initial curvature of the mandible. For these cases, the possibility of the designed software to apply hinge-like relative rotation has proven to be an applicable concept that relates theoretical planning to anatomical restrictions from operative experience.

For the largest defects (i.e. HCL and HH) it was found that the bone supply available for grafting is not sufficient to reconstruct the missing parts of the mandible; i.e. a finding that stays in accordance with clinical experience. However, for these defects reconstructions may be planned with DCIA flap from both iliac crest with the descried software tool.

Conclusion

The novel algorithm for computer assisted planning of mandibular reconstruction with DCIA flap showed to be applicable for the desired purpose. With this novel approach the complex task of three-dimensional reconstruction of the mandible was broken down to simpler parts that allow semi-automated usage and thus implementation in clinical routine may be envisioned. Parameter studies with different harvesting positions showed that the approach is capable of automatically producing reconstruction proposals with optimal geometrical accordance that are judged as critically applicable by experienced surgeons and that may be used as templates for subsequent planning of mandibular reconstructions, e.g. with 3D printed templates as surgical guides or as input data for real-time navigated surgery. The practical applicability of the developed methods for actual clinical use in the operating room needs to be investigated in future studies.

References

[1] Jewer DD, Boyd JB, Manktelow RT, Zuker RM, Rosen IB, Gullane PJ, Rotstein LE, Freeman, JE (1989) Orofacial and mandibular reconstruction with the iliac crest free flap: a review of 60 cases and a new method of classification. Plastic and reconstructive surgery 84(3): 391–403

Virtual surgical planning in the treatment of bony facial asymmetry

H. Yu[1], S. Shen[1]

[1]Ninth People's Hospital, Shanghai Joao Tong University School of Medicine, Oral and Craniomaxillofacial Surgery, Shanghai, China

Keywords Virtual surgical planning · Facial asymmetry · 3D printing · Virtual surgical guide

Purpose

Bony facial asymmetry is a clinical common deformation. Patients with facial asymmetry usually suffered from functional, esthetic and psychological problems. The anatomy of maxillofacial region is complex and the surgical incision and exposure are restricted. Therefore, how to reconstruct ideal morphology and rehabilitate facial symmetry is a great challenge, even for experienced surgeons.

Virtual reality technology provides us an ideal alternative in this complicated procedure. The purpose of this study was to explore virtual surgical planning and virtual guide in the treatment of facial asymmetry.

Methods

Patients

Data were collected from 11 asymmetrical patients with prognathism, 5 patients with hemifacial macrosomia, 3 patients with condylar osteochondroma, 5 patients with mandibular angle hypertrophia, and 6 cases with fibrous dysplasia from January 2014 to October 2015. These patients (13 males and 17 females) had a mean age of 20.5 years and a median age of 21 years (range 8–36).

Preoperative virtual surgical planning

1. CT scan and 3D reconstruction

Every patient underwent a preoperative thin-cut (0.625 mm), spiral computed tomography (CT) (Light speed 16, GE, Gloucestershire, UN) scan. The digital data were transferred directly to a computer workstation with Proplan software (Edition 1.0, Materialise, Leuven, Belgium) and stored in DICOM format. A 3D model, including the patient's craniofacial skeleton, teeth, and soft tissue was converted. A high-quality 3D CT model was reconstructed after the segmentation of maxilla and mandible using region growing and a Boolean operation.

2. Reconstruction of craniomaxillofacial dentition model

The maxillary, mandibular plaster models, combined with the final occlusion model were scanned separately by a high-accuracy laser scanner (Activity 880, Germany), which was used to visualize the 3D dentition model. Then the data was stored in stereo lithography (STL) files.

To get craniomaxillofacial dentition model, image fusion technology was used. The laser-scanned dentition model was aligned to the 3D CT model using the point registration based on 5–10 notable anatomic points in the teeth. Then the teeth of 3D CT model were replaced by the laser-scanned dentition model. Therefore, a precise digital model that represents the anatomy of jaw and the dental occlusion was established.

3. Virtual surgical planning and simulation

Osteotomies, which may include maxillary Le Fort I osteotomy, bilateral sagittal splint ramus osteotomy (BSSRO), genioplasty, facial contouring, mandibular distraction osteogenesis (DO), and TMJ arthroplasty were performed based on the digital craniomaxillofacial dentition model. Through try and errors methods, the optimal individual surgical plan was achieved.

Normal anatomical structures and contours of those patients presenting unilateral diseases or deformities were mirrored to the affected side. The median sagittal plane was used as reference plane. Thus the normal contour of the affected side, the osteotomy line, the anatomic position for fractured bone reduction and the location of the distraction device were defined and displayed on 3D reconstruction model. Then the real and virtual anatomic structure was defined and displayed on the 3-D model by different colors

Surgical splint or guide manufacture

The STL files of intermediate occlusions, final occlusions, and contouring bony structures were imported into Geomagic studio and Genmagic spark (North Carolina, USA) for the virtual design of surgical splints and guides, which would be manufactured by a 3D printer.

Surgical methods

The osteotomy was performed according to pre-surgical planning. Under the guidance of surgical splints and guides, the position of the jaw, the osteotomy line of contouring structure and the location of distraction device were defined.

Postoperative Evaluation

Postoperative evaluation including clinical examination and imageological examination was used to assess the accuracy of treatment plan's transfer. Clinical examination included facial morphology and occlusion evaluation. For this purpose, postoperative CT scans data were collected 3 days postoperatively by the same CT machine that had been used for the preoperative scans and the 3D images of the postoperative model were superimposed on the preoperative virtual planning. Thus, the maximal difference between postoperative model and preoperative plan was measured.

Results

Combined 3D CT and laser-scanned dentition model, the digital craniomaxillofacial dentition model was established. Precise dentition model was achieved through image fusion, which avoided the artifacts caused by the presence of steel orthodontic brackets and wires. Using this digital model, virtual surgical planning and simulation could be performed.

To rehabilitate facial symmetry, medial sagittal plane was used as reference plane. The desired anatomical structure and contour was mirrored from the contralateral side, thus the bony scope and amount to be resected was ensured. With the implementation of a surgical plan for orthognathic correction based on a pre-surgical model, the prediction of the post-operative jaw morphology was simplified and readily visualized, which was especially helpful for patients with facial asymmetry. By means of try and error, the optimal individual surgical plan was conformed. Then virtual surgical splint and guide was 3D printed.

Using surgical splints and guides, corrective surgeries were performed successfully in all selected cases with facial asymmetry. The facial contour was checked using postoperative CT, and it matched well with preoperative planning. Good coincidence with preoperative planning was achieved for osteotomy lines, the location of distraction device and resection amount. The maximal deviation between our surgical plan and the final surgical result was less than 2 mm.

Conclusion

Advancements in computer-aided design and manufacturing (CAD/CAM) technique have revolutionized the treatment of facial asymmetry. Fusion of relatively new technologies and techniques such as virtual surgical planning and 3D printed surgical guide can make surgery more efficient and effective for both patients and surgeons. Patients with facial asymmetry will benefit from the combination of these techniques. Virtual technology has a numerous clinical applications and shows extensive application potential.

Design of a PVA liver phantom with respiratory motion for simulation of needle interventions

T. L. de Jong[1], D. R. Adrichem[1], J. Dankelman[1], J. J. van den Dobbelsteen[1]

[1]Delft University of Technology, BioMechanical Engineering, Delft, Netherlands

Keywords Phantom · Liver · Breathing motion · Polyvinyl alcohol (PVA)

Purpose

Realistic physical liver phantoms are needed in interventional radiology for validation of novel instruments and for training of medical residents, because the use of biological tissues is not always a feasible option. Most research on liver phantoms focuses on the imaging mimicking qualities (e.g. [1, 2]). However, an ideal liver phantom should also mimic liver motion related to respiration and mechanical properties, such as instrument-tissue force interactions. A recent study indicated the suitability of polyvinyl alcohol (PVA) as a realistic liver mimicking material in terms of needle-tissue interaction [3]. The purpose of the current study is to design a PVA liver phantom with respiratory motion, to be used as a physical training model and/or a validation set-up for novel instruments in interventional radiology.

Methods

Phantom design: The developed phantom is a real size PVA liver phantom and consists of a support PVA abdominal cavity, a rib cage phantom, and a skin phantom (Fig. 1). To obtain the design requirements, we used MeVisLab 2.7 to segment the liver from a CT scan of a patient, with a resolution of 1 mm between subsequent slices. Data were saved as a point cloud and imported in SolidWorks to create a solid. A negative liver mold was created from this solid and 3D printed in Polylactid Acid (PLA) with 0.25 mm printing resolution. This mold was filled with 6 m% PVA-to-water (Selvol PVOH165, Sekisui Chemical Group NJ, USA), undergoing two freeze–thaw cycles for 40 and 20 h, to create the liver phantom. The abdominal cavity phantom was also made of PVA (4.0 m% PVA-to-water, 3 freeze–thaw cycles, 40 h/20 h), and used to support the liver phantom. The rib cage phantom was cut to size from an off-the-shelf skeleton. The skin phantom was made of a 2.5 mm layer of silicone (Ecoflex 00-30, Smooth-on Inc., Macungie, Texas, USA).

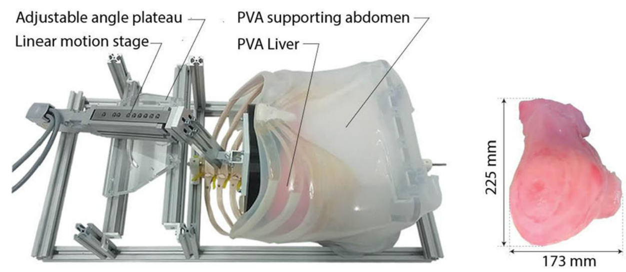

Fig. 1 The developed PVA liver phantom—A sinusoidal motion pattern is imposed upon the liver phantom by the use of the linear motion stage

Liver motion: First, we determined liver motion due to respiration in real patients. Livers from CT scans obtained during inspiration and expiration of five patients were segmented. The centers of mass of the reconstructed livers were used to calculate displacement vectors. The displacement vector of one patient was chosen as an input for the sinusoidal motion pattern imposed upon the liver phantom. The motion pattern was generated using an EMMS-ST-28-L-SE linear motion stage (Festo BV, Delft, the Netherlands), representing the sinusoidal movement of the diaphragm upon the liver.

Results

Phantom design: The PVA liver phantom is shown on the right side of Fig. 1. The maximal dimensions of the liver are $225 \times 173 \times 119$ mm, with a total volume of 1.19 dm^3. Different motion patterns can be applied to the phantom by use of the linear motion stage. In addition, the direction of the applied motion can be changed by altering the angle of the motion stage, with respect to the liver, indicated by the adjustable angle plateau.

Liver motion: From the state of expiration to inspiration, the centers of mass of the livers of the five patients moved towards the right (range − 0.8–15.4 mm), anterior (range 2.7–21 mm) and caudal (range 9.3–31 mm) direction. The movement of the liver of one patient during inspiration and expiration is shown in Fig. 2. Liver motion is more apparent than liver deformation. The displacement vector of this liver was used as an input for phantom motion, being 5.3 mm towards the right, 17 mm towards the anterior and 22 mm towards the caudal direction. The resulting total stroke of 28 mm was applied to the phantom using a sinusoidal motion pattern with 12 and 18 strokes per minute, to simulate breathing motion.

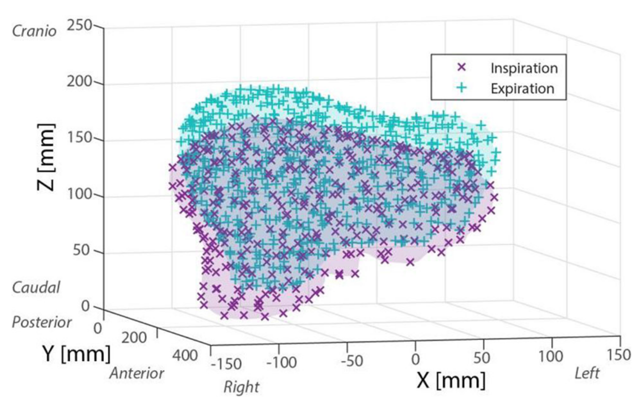

Fig. 2 Example of a segmented liver during inspiration and expiration. Calculated motion of the center of mass from expiration to inspiration was 5.3, 17 and 22 mm in the right, anterior and caudal direction, respectively

Conclusion

In the current study, the design of a PVA liver phantom with respiratory motion based on CT imaging data was presented. The developed liver phantom is capable of mimicking liver motion induced by breathing as seen in a real patient, and, due to the intrinsic properties of PVA, is ultrasound compatible and matches human liver in needle-tissue interaction.

Future work for this ongoing research project includes three developments. First, several liver motion patterns and liver phantom shapes will be added, as found on the CT scans, by altering the magnitude of the stroke of the linear stage and its angle. Secondly, a thorough validation of these phantom liver motions will be performed. We used the motion of the center of mass of the liver as an input for the movement of the linear stage. However, the livers not only show displacement due to respiration, but also deformation, dependent on the location inside the liver. Thirdly, the movement of the ribs with respect to the liver will be included. This relative motion is especially important for needle puncturing using an intercostal approach. As a start, the relative motion of the liver with respect to the ribs can be calculated from CT scans. Subsequently, a compliant rib cage will be used to mimic this motion.

We conclude that linear motion of the developed PVA liver phantom mimics appropriate respiratory motion as observed in a real patient. The developed phantom allows for applying several motion patterns and liver shapes/sizes, and is therefore suitable to mimic different motion patterns found among patients.

References

[1] Zell K, Sperl JI, Vogel MW, Niessner R, Haisch C (2007) *Acoustical properties of selected tissue phantom materials for ultrasound imaging*. Physics in medicine and biology **52**(20): p. N475

[2] Surry KJ, Austin HJ, Fenster A, Peters TM *(2004) Polyvinyl alcohol cryogel phantoms for use in ultrasound and MR imaging*. Physics in medicine and biology **49**(24): p. 5529

[3] de Jong TL, Pluymen LH, van Gerwen DJ, Kleinrensink GJ, Dankelman J, van den Dobbelsteen JJ (2017) *PVA matches human liver in needle-tissue interaction*. Journal of the Mechanical Behavior of Biomedical Materials, **69**(Supplement C): pp 223–228

Deformation matching of laparoscopic gastrectomy navigation based on finite element analysis

T. Chen[1,2], G. Wei[3], W. Shi[3], Y. Hu[1,2], J. Yu[1,2], Z. Jiang[3], K. Mori[4], G. Li[1,2]

[1]Nanfang Hospital, Southern Medical University, Department of General Surgery, Guangzhou, China

[2]Guangdong Provincial Engineering Technology Research Center of Minimally Invasive Surgery, Guangzhou, China

[3]School of Computer Science and Technology, Changchun University of Science and Technology, Changchun, China, Changchun, China

[4]Nagoya University, Graduate School of Informatics, Nagoya, Japan

Keywords Surgical navigation · Laparoscopic gastrectomy · Deformation matching · Finite element method

Purpose

Laparoscopy surgery as a minimally invasive procedure now is widely used in gastrointestinal surgery [1]. In spite of its benefits, the limited tubular vision of laparoscopy is not beneficial to observe the whole surgical field.

Image-guided surgery as a navigation can supplement the insufficient anatomical identification of laparoscopy [2].

However, vessels can be deformed due to pneumoperitoneum, surgical manipulation, heartbeat, respiration and other patient-specific changes [3]. But these deformations caused by heartbeat and respiration can be negligible because it is very mini. Additionally, some previous studies have reported how to correct the deformation due to the pneumoperitoneum in navigated laparoscopy [3]. The study about the deformation matching due to surgical manipulation has rarely been reported.

In our study, we aim to build Finite Element Method (FEM) model of gastric artery in the light of the deformation due to surgical manipulation. In addition, validate this model in animal experiment and surgical scene.

Methods

Animal experiment

Animal model and anesthesia

Our animal experiment was performed on a healthy male pig weighing 25 kg, which had received full approval by the Ethical Committee on animal experimentation. The pig was fasted for 24 h with free access to water before the study. 3% of thioethamyl (1 ml/kg) was injected percutaneously in the marginal vein of the ear. The pig was orotracheally intubated and maintained in a supine position (Fig. 1). The oxygen saturation and heart rate were monitored during the study.

Fig. 1 Simulation of laparoscopy surgery in an animal experiment

CT scans and images collection

The pig's CT images were obtained from CT scans with slice thickness of 1.25 mm, 120 kV, 167 mA and 512 $\times$ 512 matrix. There are two kinds of CT images for the experimental subject. The first one was taken with the pig in supine position before the operation. The second image was taken after pneumoperitoneum and the left gastric artery (LGA) was pulled up and fixed.

The ground-truth creating

CT images after LGA pulled up in the animal experiment were import to MIMICS 17.0 software (http://www.materialise.com) for visualization, including the threshold segmentation, semi-automatic segmentation and region-growing. Finally, the three-dimensional geometric model of LGA pulled up was established as a ground-truth.

Finite element model of animal

An ANSYS 17.0 software (http://www.ansys.com) was used to simulate the FEM model of the LGA after pulled up according to the need for the laparoscopic gastrectomy. The basic process of finite element analysis as follow:

1. Import geometric model and create a FEM model
2. Parameterize and mesh the geometric model
3. Set up static structural analysis
4. Apply loads and add boundary conditions

Using the ANSYS, we load progressive force to FEM model of the LGA, making it close to the position of LGA pulled up according to the requirement for the laparoscopic gastrectomy, which makes it possible to simulate the real deformation. The central lines of the ground-truth and FEM model were drawn. The average distance and the closest points between the two central lines were measured to evaluate the accuracy of the simulation.

Validation in surgical scene of laparoscopic gastrectomy

Finite element model of patient

Preoperative contrast-enhanced CT images of this patient were import to MIMICS 17.0 software to generate the geometric model, and then establish the finite element model, using the tuned parameters in animal experiment.

The evaluation in surgical scene

The FEM model was compared with the intraoperative laparoscopic image to estimate the coincidence of the deformation simulation.

Results

Animal experiment

FEM material and parameters

The Neo-Hookean and Ogden foams are both hyperelastic materials selected as candidates for vascular FEM model creation [4]. The FEM model was created with a density of 1150 kg/m^3 both in Neo-Hookean and Ogden foams material. In the Neo-Hookean material model, we added the force of 4.2015×10^{-5} N, while this force was 6.2944×10^{-5} N in the Ogden foam material model.

The comparison of the FEM model and ground-truth

In the Neo-Hookean model, the average distance of the corresponding points between the two center lines is 8.1 mm, and the average distance of their closest points is 6.9 mm. In the Ogden model, the average distance between the two central lines is 6.5 mm, and the average distance between their closest points is 3.8 mm (Fig. 2). Therefore, we selected the Ogden foams and its parameters to create the human FEM model.

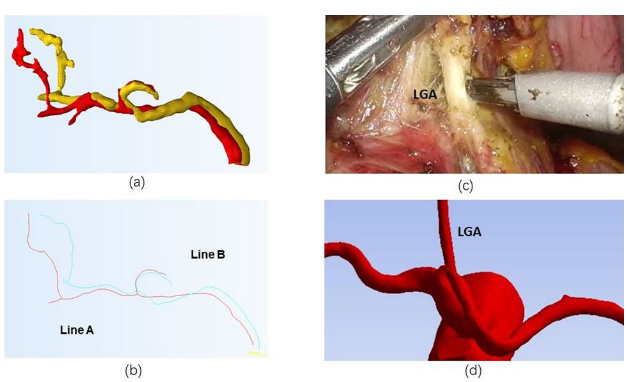

Fig. 2 Validation of animal and human FEM model. **a** The red one is the ground-truth; the yellow one is the FEM model. **b** The red line (Line A) is the central line of ground-truth; the blue one (Line B) is the central line of FEM model. **c** Patient's left gastric artery in surgical scene. **d** The FEM model of patient's left gastric artery

Validation in surgical scene of laparoscopic gastrectomy

The image of LGA pulled up in the laparoscopic gastrectomy video was applied for validation. The patient FEM model of LGA was generated from preoperative CT images using the parameters determined in the animal experiment. The fixed supports of LGA is the celiac trunk. The comparison between the FEM model and the true LGA pulled up during the laparoscopy demonstrated good coincidence (Fig. 2).

Conclusion

Our study explored a suitable hyperelastic material and parameters for gastric artery FEM model building and presented a new way to validate this model in an animal experiment. Additionally, the clinical feasibility of the proposed method was also validated in surgical scene of patient. Further work is necessary to reinforce our findings, nevertheless, our study supply a referable way for future research of the deformation matching in the laparoscopic gastrectomy navigation.

Acknowledgement

Supported by the State Key Project of Research and Development Plan (2017YFC0108300 and 2017YFC0108303).

References

[1] Parisi A, Reim D, Borghi F, Nguyen NT, Qi F, Coratti A, Cianchi F, Cesari M, Bazzocchi F, Alimoglu O, Gagnière J, Pernazza G, D'Imporzano S, Zhou YB, Azagra JS, Facy O, Brower ST, Jiang ZW, Zang L, Isik A, Gemini A, Trastulli S, Novotny A, Marano A, Liu T, Annecchiarico M, Badii B, Arcuri G, Avanzolini A, Leblebici M, Pezet D, Cao SG, Goergen M, Zhang S, Palazzini G, D'Andrea V, Desiderio J (2017) Minimally invasive surgery for gastric cancer: A comparison between robotic, laparoscopic and open surgery. World J Gastroenterol.; 23: 2376–2384

[2] Hayashi Y, Misawa K, Hawkes DJ, Mori K (2016) Progressive internal landmark registration for surgical navigation in laparoscopic gastrectomy for gastric cancer. Int J Comput Assist Radiol Surg; 11: 837–845

[3] Zijlmans M, Lango T, Hofstad EF, Van Swol CF, Rethy A (2012) Navigated laparoscopy–liver shift and deformation due to pneumoperitoneum in an animal model. Minim Invasive Ther Allied Technol.; 21: 241–248

[4] Hassan MA, Hamdi M, Noma A (2012) The nonlinear elastic and viscoelastic passive properties of left ventricular papillary muscle of a guinea pig heart. J Mech Behav Biomed Mater Jan; 5(1): 99–109

The use of augmented reality technology in the treatment of distal tibia fractures

A. Sitnik[1], R. Gromov[1], A. Pavel[1], S. Bradko[1]
[1]BRSPCTO, Adult Trauma Department, Minsk, Belarus

Keywords Distal tibia · Augmented reality · HoloLens · Surgical treatment

Purpose

The level of wound complications and quality of reductions in distal tibia fractures remain an issue despite advances in soft-tissue management (staged treatment) and reduction techniques [1]. Correct placement of surgical incision(-s) centered directly over the fracture line is important to minimize additional insult to vulnerable soft tissues in the region [2] Augmented reality (AR) technology allows the placement of holographic image of the fractured bone "within" the leg of the patient, and in this way may promote correct planning of surgical approach(-es) and fixation.

The purpose of study was to prove the efficacy of AR-technology in the pre-operative planning and surgical treatment of patients with complex distal tibia fractures.

Methods

In this randomized prospective study we included 24 patients with distal tibia fractures (43A–43C according to AO/OTA classification [3]), treated in our institution from January to September 2017.

Standard treatment (10 patients) consisted in initial application of external fixator (delta-frame) with subsequent definitive fracture reduction and fixation after resolution of soft-tissue swelling (av. 10.6 days after the injury). Planning of definitive fixation was performed according to CT-data, obtained after ExFix application [4].

The CT-data of 14 patients (AR-group) that underwent the same initial treatment in external fixator were additionally analyzed with the help of Microsoft HololensTM (VOKA® application, Innowise-group, Belarus). VOKA application builds the 3D model of the fractured bone on the base of voxel rendering of CT-data and also provides tools for final tuning and manipulation of the bone model. 3D models are saved in.fbx format and become available for the use in Microsoft HololensTM.

The holographic models of given fractures were initially analyzed more thoroughly with the use of the device and then placed "within" the limb of the patients for definitive planning and marking the surgical approach(-es) immediately in operating room. Mean time to definitive surgery was 11.2 days after the injury.

The correct placement of the model within the leg (Fig. 1) was controlled visually with the use of standard palpable anatomical landmarks (tibia tuberosity, tibia crest, tip of external malleolus, internal malleolus, calcaneal tuberosity and toes). Parts of external fixator served as additional reference points for correct placement of holographic bone model within the leg in cases that were operated directly in external fixator frame. For the purposes of this study we additionally checked the correct position of the holographic fracture model within the leg with image intensifier by placing the non-radiolucent instrument on the same projected anatomical landmarks of the model (tips of external and internal malleoli) and verifying its position in relation to radiologic picture.

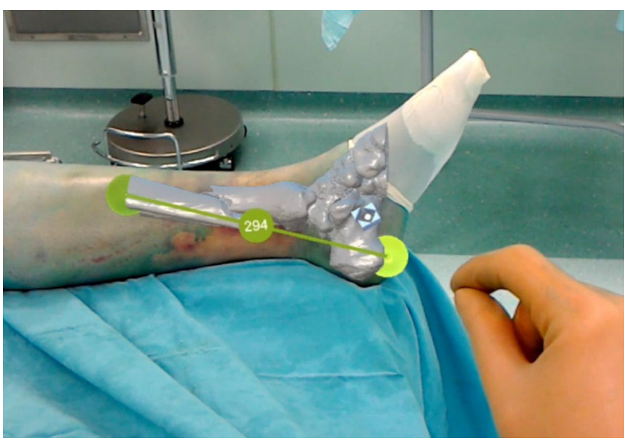

Fig. 1 Intraoperative view of the fracture 'within' the leg

The planned incision was marked on the skin with pencil after surgical draping (Fig. 2) with the purpose to go to the main fracture line as directly as possible (with respect to important anatomical structures). The accuracy of planned incision in relation to fracture line was graded as:

- excellent: incision was placed directly over the fracture line;
- good: incision was placed within 5 mm range near the desired fracture line;
- satisfactory: to access the desired fracture line the soft-tissue mobilization within 10 mm was required;
- non-satisfactory—the additional soft-tissue mobilization exceeded 10 mm from the marked skin incision.

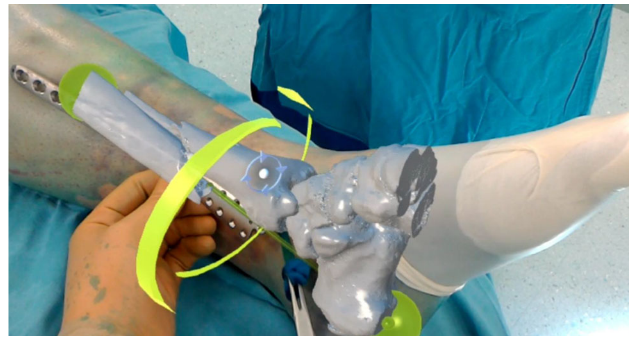

Fig. 2 Surgical mapping of planned incisions

Results

The general length of definitive surgery comprised 118 min in the main group and 124 min in the AR-group due to the time, required to place the holographic model in the leg and definitive marking the surgical approach(-es) (it took initially around 10–15 min).

The accuracy of surgical incisions was better in the AR-group of patients (8/14 of good or excellent placement vs. 3/10 in the standard group).

There were any intraoperative complications in both groups. One superficial wound infection occurred in AR-group and two in standard group (non-significant). The quality of reduction was accessed according to Ovadia and Beals criteria [5] and was slightly better in AR-group (78.6 vs. 70% of good reductions, non-significant).

Conclusion

The technology of placing the 3D-picture of given fracture within the limb is very promising. Potential advantages include more precise and accurate placement of surgical incisions. Technology allows also to place images of important anatomical structures (like vessels and nerves) in connection to boney structures. All this will potentially lead to safer surgery, faster post-operative recovery and restoration of limb function.

First reports on the use of AR-technology in the field of vascular reconstructive surgery have already appeared. The main issues include preparation of anatomical 3D-model and correct placement of this holographic model within the limb.

This is a preliminary report and the efficacy of the AR-technology use was not confirmed statistically. At the same time we did not noticed any adverse effects. AR-technology allowed us for better assessment of fracture morphology (that lead to slightly better reduction quality) and improved planning of surgical approaches with respect to soft-tissue condition. Potentially this technology will lead to the measurable decrease of additional surgical damage to soft-tissues in the fracture site.

References

[1] Krettek C, Bachmann S. Pilon-fractures. Part 1: Diagnostics, treatment strategies and approaches. Chirurg 2015; 86: 87–101.
[2] Sitnik A, Beletsky A, Schelkun S Intra-articular fractures of the distal tibia: Current concepts of management. EFORT Open Rev. 2017; 2(8): 352–361. https://doi.org/10.1302/2058-5241.2.150047.
[3] Müller ME, Nazarian S, Koch P, Schatzker J. The comprehensive classification of fractures of long bones. New York: Springer-Verlag, 1990.
[4] Sirkin M, Sanders R, DiPasquale T, Herscovici D Jr. A staged protocol for soft tissue management in the treatment of complex pilon fractures. J Orthop Trauma 1999; 13: 78–84.
[5] Ovadia DN, Beals RK. Fractures of the tibial Plafond, J Bone Joint Surg Am. 1986; 68: 543–551.

An authoring interface for surgeon-authored VR training

M. Sarov[1], R. Gao[1], J. Youngquist[1], G. Sarosi[1], S. Kurenov[2], J. Peters[1]
[1]University of Florida, Gainesville, United States
[2]Roswell Park Cancer Institute, Buffalo, United States

Keywords VR training · Surgeon-authored · Laparoscopy · Interface

Purpose

Virtual reality (VR) simulators allow trainees to practice decision-making and execution prior to entering the OR. VR-based training can thereby increase patient safety, reduce the need for in vivo animal practice, shorten time in the OR, and provide the repetition and learner control [1]. VR-training can also uncouple instruction place and time to address limitations placed by work-hour rules and real-life scheduling of surgeons, residents or medical and veterinary students.

Laparoscopic techniques, in particular, lend themselves to VR simulation due to their interface: tissue is manipulated only via tools and the surgical environment is visible only via a camera image on a monitor. Haptic devices resisting probing, tearing and cutting, provide the necessary force feedback for hands-on, interactive simulation of the critical steps of the laparoscopic procedure.

However, creating VR-training units is neither cheap nor fast due to the complexity of creating the training units and the back-and-forth between engineers, computer scientists and medical experts. Inspired by the success of many computer-tools, such as desktop publishing, a toolkit for illustrations of procedures in surgery (TIPS [2]) has recently been developed to more efficiently generate touch-enabled VR-training simulations. Specifically, the goal is to enable surgeon-educators to define the structure of training units.

Enabling surgeon-educators to create VR-training units promises greater variety, specialization and relevance of the units. It allows implementing variation in technique, an important component of traditional surgical education, and to create uncommon and specialized scenarios.

We report on a web-based authoring interface that allows surgeon-educators to assemble simulation-ready pieces of VR anatomy and tools to quickly specify new surgical scenarios. This interface has successfully been used by surgeoneducators to create laparoscopic training units for appendectomy, cholecystectomy and adrenalectomy.

Methods

The authoring interface is part of TIPS, a low-cost computer-based environment to create touch-enabled VR laparoscopic simulation scenarios. TIPS is based on C++ and OpenGL, runs on a high-end PC or laptop. Two touch styluses, attached to surgical tools, provide the interactive force-feedback required to practice critical steps of the surgical procedure. Over the past 2 years, 23 junior surgeons (residents and fellows) and five experienced surgeons trained and graded an adrenalectomy unit created with TIPS and judged it both effective and superior to physical props, one-on-one teaching, medical atlases, or video recordings.

TIPS leverages and integrates two open-source packages: Blender [3] for modeling anatomy and the Simulation Open Framework Architecture (SOFA [4]) for soft-tissue simulation. Blender is a professional open-source geometric modeling, rendering and animation software. Several animated movie shorts have been created using Blender as the main modeling and rendering environment. SOFA is an open-source collection of numerical, geometric and visual routines for developing simulation codes with focus on soft-tissue manipulation. TIPS' Blender2Sofa software [5] links the two packages and augments the Blender graphical user interface with control of physical behavior, attachment and collision properties. A single click starts the full force-feedback enabled anatomical scenario assembled in the augmented Blender environment.

When a scenario is judged to be complete and correct by peer review, a command in Blender2Sofa breaks the scenario apart into simlets. Simlets package compatible geometry, collision and physics models with their default parameters into anatomical clusters. Simlets fit together like Lego blocks and so form the basis for the interface that allows surgeon-educators to themselves create touchenabled VR training units. Simlets are uploaded to a cloud-based database.

Results

The author-level interface represents a layer of abstraction that insulates the surgeon-educator's high-level specification of the surgical steps from the technical details of the physical simulation and visual presentation. Our approach splits the scene creation work into a developer level where numerical simulation routines are selected or adjusted; the artist level where compatible geometry, collision and physics models with their default parameters are packaged into anatomical clusters, called simlets; and the author level where scenarios are created by selecting simlets.

The author-interface then follows the standard task-based approach in surgical education: a surgical procedure is specified as a series of steps, each of which consists of sub-tasks with their safety concerns. This task list is input in a fixed format: action, anatomy, tool, safety, comment. For example, the quintuple can be: Tear, fatty tissue, Maryland dissector, not close to vena cava, youtube-url. Auto-suggestion while typing guides the author towards stored simlets. For missing simlets (anatomy) the author enters pointers to videos or images in the comment slot.

The task list serves four functions. (1) Peer review and collaborative determination of scope among specialists: to give early feedback and to reach consensus on the basic steps of the VR unit. (2) Generation of instructional page templates: to serve as a scaffold for authors and to ensure that instruction is consistent with the peer-reviewed task list. (3) Initialization of the simulation scenario from simlets. (4) Enable sharing of training modules among specialists as lightweight pointers to simlets: this simplifies dissemination and enables educators to efficiently create variants of anatomy, pathology or surgical approach.

While safety criteria based on proximity such as "not cauterize near vena cava" are embedded into the simlet, more subjective criteria "not use excessive force" have their ranges determined by comparison with two or more virtual surgeries performed by the author.

Conclusion

To date, junior surgeons are exposed to only fraction of the full spectrum of laparoscopic procedures and scenarios in the OR. Engaging surgeons as authors promises greater variety, specialization and relevance of laparoscopic VR training.

The TIPS-author interface is a first step in this direction. It offers, for the first time, a high-level software infrastructure for authoring soft-tissue touchenabled VR training units. The task list assembled by the author auto-initializes the VR training progression (see Fig. 1) including pre-quiz and questionaires, instruction pages, the interactive haptic virtual simulation scenario, the proficiency report, and the post-quiz and questionaire.

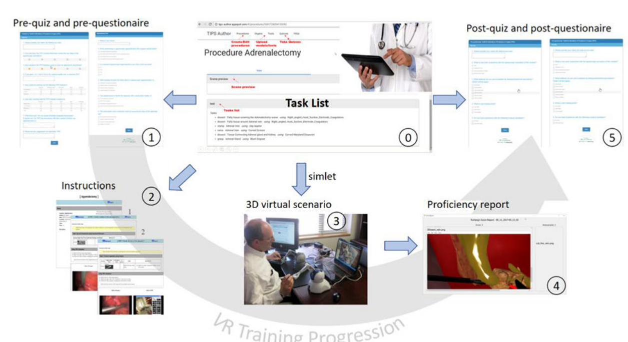

Fig. 1 The task list assembled by the author auto-initializes the VR training progression including: pre-quiz and questionnaires, instruction pages, the interactive haptic virtual simulation scenario, the proficiency report, and the post-quiz and questionnaire

The interface has successfully been used by surgeon-educators to create a number of variants of laparoscopic training units for appendectomy, cholecystectomy and adrenalectomy. Residents were able to train with the resulting units with minimal introduction, provided by TIPS. Residents found the visual feedback easy to interpret and the resulting simulations useful for understanding critical steps of the laparoscopic procedure. By publishing the touch-enabled VR training units under the author's name we have observed good buy-in and quality control.

References

[1] Gallagher AG, Ritter EM, Champion H, Higgins G, Fried MP, Moses G, Smith CD, Satava RM. Virtual reality simulation for the operating room: proficiency-based training as a paradigm shift in surgical skills training. Annals of surgery, 241(2): 364–372, 2005

[2] In Yeo Y, Dindar S, Sarosi G, Peters J (2011) Enabling Surgeons to Create Simulation-Based Teaching Modules, Proceedings of Medicine Meets Virtual Reality (MMVR) 18, 163, 723–729, Newport Beach, CA, Feb. 8–12

[3] Blender Foundation. Blender. http://blender.org

[4] Allard J, Cotin S, Faure F, Bensoussan PJ, Poyer F, Duriez C, Delingette H, Grisoni L. (2007) SOFA–an open source framework for medical simulation Stud Health Technol Inform, 125: 13–18.

[5] Dindar S, Nguyen T, Peters J (2016) Towards surgeon-authored VR training: the scene-development cycle. Proceedings of Medicine Meets Virtual Reality (MMVR) 22, 1–6, L.A., CA, Apr. 9–12

Surgical planner for cochlear implantation outcome predictions

N. Mangado[1], M. Ceresa[1], R. López-Velasco[1], P. Mistrik[2], M. A. González Ballester[1,3]
[1]BCN Medtech, Universitat Pompeu Fabra, Barcelona, Spain
[2]MED-EL, Innsbruck, Austria
[3]ICREA, Barcelona, Spain

Keywords Cochlear implantation · Surgical planner · In-silico models · Computational predictions

Purpose

Sensorineural hearing loss is a common cause of disability. According to the World Health Organization, 20% of the population suffering from hearing loss are eligible for a cochlear implantation (CI) surgery [1]. CI is a surgical procedure, performed on more than 300.00 people worldwide, that replaces the sense of hearing by implanting an electrode device, which bypasses the damages hair cells and stimulates directly the auditory nerves. The level of hearing restoration, however, still presents a vast variability across patients. The high dependence on patient-specific factors and the lack of predictive tools makes surgery outcomes difficult to estimate. We believe that the development of computer-based planning software tools can lead to more predictable and controlled CI surgery. Furthermore, we contend that advanced computational modeling can be useful to simulate different implantation scenarios of a given patient, and, moreover, can improve the selection of the surgical procedure parameters. In this context, we present a new methodology to perform patient-specific CI surgical planning, coupled with computational tools for image analysis, shape modelling and electrical finite element simulation and resulting neural response.

Methods

The planner includes the following modules: image processing, shape analysis, virtual implantation, functional assessment and final report. The image processing step loads, visualizes and analyzes routine radiological computed tomography (CT) images of the patients, where the cochlea and surrounding structure are automatically detected. The shape analysis element includes a high resolution statistical shape model of the cochlea and related structures. This model allows estimating the inner ear morphology from the low resolution clinical imaging data of the patient, effectively leading to patient-specific high-resolution models, in a level of detail that was unfeasible by simply analyzing the CT and MR images [2]. The virtual implantation simulates the surgical insertion of the cochlear implant considering surgical parameters defined by the surgeon prior to the intervention. It is a virtual reality module that incorporates advanced computational simulation algorithms, such as the biomechanical simulation of the insertion of the implants electrode array (flexible element inserted inside the cochlea) [3]. Next, the functional evaluation element simulates the spike electrical signals caused by the cochlear implant and how these are converted to nerve activations that travel to the brain via the auditory nerve fibers (ANF). For this, electrical finite element simulations are performed to compute the potential field generated by the implant. Then, the activation of the neural fibers is evaluated via a human ANF model. The final neural pattern is analyzed and quantified by a set of computational performance measures [4]. These elements allow us to predict the hearing restoration level gained by the patient, depending on the choice of implant design and surgical parameters, such as insertion depth and positioning. Finally, the planner generates a well-documented report to the surgeon, allowing for appropriate decision to be taken prior to the CI intervention.

Results

Figures 1 and 2 show different elements of the cochlear implantation planning system. From the low-resolution CT images of the patient a high-resolution shape of the inner ear is obtained (Fig. 1), and then used to compute the virtual insertion. The virtual implantation module allows defining surgical parameters and visualizing the final intra-cochlear location of the implant as well as the trajectory followed during the insertion. These two elements—the cochlear surface and the inserted implant—are then coupled with a full head model. The potential field created by the implant and the spike electrical signals can be visually evaluated, and the evoked ANF is provided in a 2D activation map (horizontal axis: active electrode; vertical axis: excited pitch) (Fig. 2). The user-friendly environment of the planner allows the clinician to follow easily each module, obtaining a in a reasonable amount of time a detailed report of the neural response of the patient.

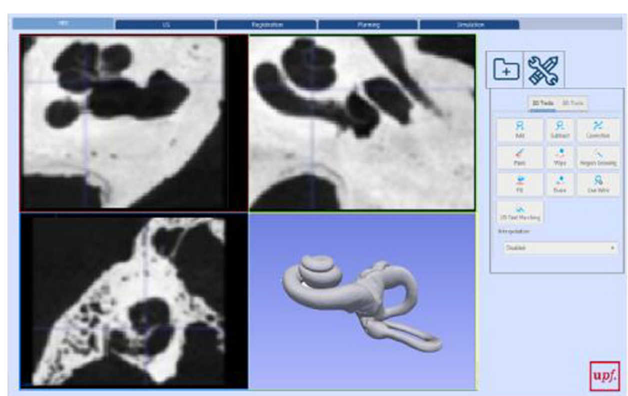

Fig. 1 Cochlear implantation planning system. Illustration of the image processing module

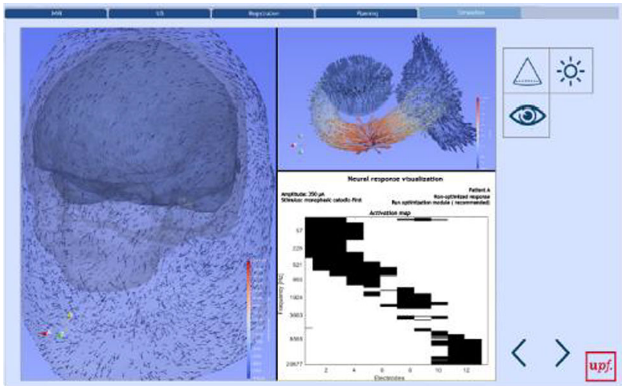

Fig. 2 Results provided by the functional evaluation module

Conclusion

We presented a new computed-based methodology for CI surgical planning software. The planner included a comprehensive CI computational modelling that allows predicting the neural response of an implanted recipient according to a set of implant and surgical parameters. To the best of our knowledge, there is no planning software for CI outcomes prediction. We believe that this tool has a great potential to support pre-operative decision thanks to its easy applicability to a range of surgical scenarios and patient-specific parameters, and its use prior to the innervation could lead to a more predictable and controlled CI surgeries. Moreover, the presented planner can also help hearing professionals to guide post-intervention procedures by providing the most favorable setting for the patient.

Acknowledgement

This work is partly supported by the Spanish Ministry of Economy and Competitiveness under the Maria de Maeztu Units of Excellence Programme (MDM-2015-0502), by the AGAUR Grant 2016-PROD-00047 and the QUAES Foundation Chair for Computational Technologies for Healthcare.

References

[1] World Health Organization. Deafness and hearing impairment, 2014.

[2] Kjer HM, Fagertun J, Vera S, Gil D, González Ballester MA, Paulsen RR (2016) Free-form image registration of human cochlear µCT data using skeleton similarity as anatomical prior. Pattern Recognit Lett, 76: 76 (82).

[3] Mangado N, Ceresa M, Duchateau N, Kjer HM, Vera S, Dejea H, Mistrik P, Paulsen RR, Fagertun J, Noailly J, Piella G, González Ballester MA (2016) Automatic Model Generation Framework for Computational Simulation of Cochlear Implantation. Ann Biomed Eng, vol 44, pp. 2453–2463.

[4] Mangado N, Ceresa M, Benav H, Mistrik P, Piella G, González Ballester MA (2018) Towards a complete in silico assessment of the outcome of cochlear implantation surgery. Mol. Neurobiol. 55(1): 173–186.

Feasibility of nerve proximity detection using tissue-impedance spectroscopy during robotic cochlear implantation

Y. Jegge[1], H. Kalvoy[2], A. Sauter[3], T. Wyss-Balmer[4], C. Rathgeb[1], D. Schneider[1], K. Gavaghan[1], M. Caversaccio[5], S. Weber[1], J. Anso[1]

[1]ARTORG Center for Biomedical Engineering, University of Bern, Image Guided Therapy, Bern, Switzerland

[2]Rikshospitalet University Hospital, Oslo, Department of Clinical and Biomedical Engineering, Oslo, Norway

[3]Rikshospitalet University Hospital, Oslo, Division of Anesthesiology and Intensive Care Medicine, Oslo, Norway

[4]ARTORG Center for Biomedical Engineering, Bern, Switzerland

[5]Inselspital Bern, Department of ENT Head and Neck Surgery, Bern, Switzerland

Keywords Facial nerve · Tissue impedance · Robotic cochlear implantation · Image guided therapy

Purpose

A number of studies have demonstrated the effective use of tissue conductivity to discriminate nerve structures using available intra-operative electrical impedance (EI) measured by nerve stimulators. Tsui et al. reported the successful use of EI measurements [1] for warning of intraneural needle placement in the sciatic nerve in vivo. Kalvoy and Sauter [2] proposed impedance spectroscopy to increase accuracy of nerve detection during needle guidance based on EI. Bolger et al. also demonstrated the use of EI for tool guidance during spine surgery using a pedicle screw driver with integrated electrodes in the tool tip [3]. We postulate that EI measurements of the mastoid bone (encompassing the facial nerve) could be used to enhance the safety of robotic cochlear implantation (RCI) by detecting an unsafe (unexpected) drilling transition towards the facial nerve. Bio-impedance spectroscopy could then be used as an additionally safety mechanism for preserving the FN during RCI. Furthermore, it may improve sensitivity and specificity of an existing neuromonitoring approach [4]. The aim of this study was to assess if impedance spectroscopy (100 Hz to 1 MHz) could be used to distinguish FN proximity during robotically drilled trajectories in the mastoid. It is hypothesized that discrimination of a transition from bone into the facial nerve can be discriminated using high frequency electrical impedance (> 100 kHz). Here in we present preliminary results from a pilot in vivo study.

Methods

An in vivo study (approved by Bernese cantonal animal commission, Nr. 113/15) was performed with a total of n = 3 subjects. Sheep was chosen as animal model due to its similarity of the human ear anatomy. The experimental surgery started with general anesthesia, before excising the temporalis muscle and implanting four titanium screws (2.2 mm Ø, 5 mm length, Medartis, Switzerland) near the external auditory canal that were used as registration fiducials.

Per animal, a computer tomography (CT) scan was acquired and a total of N = 8 trajectories were planned (Fig. 1) using a modified version of an otologic surgical planning software ([5]). The eight trajectories were divided in three groups based on lateral distance (LD) to the facial nerve boundary: (i) LD = 0.3 mm, LD = 0 mm (lateral), LD = 0 mm (frontal). Per trajectory, five measurement points were defined close to the FN, three of them before the level of the facial nerve and two of them further pass the FN level (or boundary) projected in the plan trajectory axis ([5]).

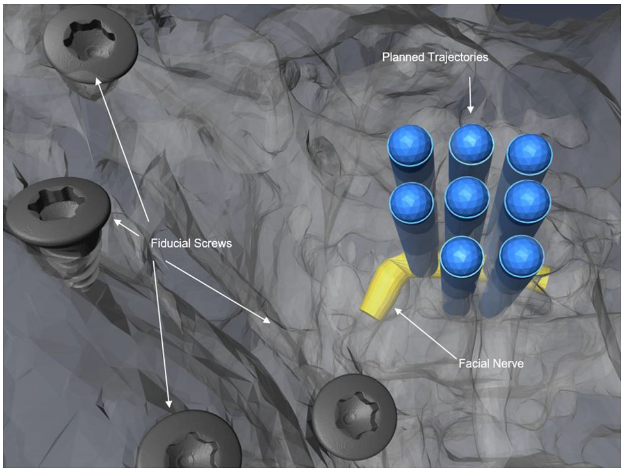

Fig. 1 3D models of the surgical plan with the mastoid bone (grey), the fiducial screws (dark grey), the facial nerve (yellow) and the planned trajectories

Robotic drilling
Each of the planned trajectories was drilled using a surgical robot system for Cochlear implantation (HEAROTM, CAScination AG, Switzerland). At each measurement point near the FN, the robot stops retracts automatically. The drilled cavity is irrigated with sodium chloride solution (NaCl 0.9%) to ensure similar electrical conductivity conditions at the boundary surface. A multiple electrode probe used during neuromonitoring of the facial nerve in RCI ([4]) was inserted into the tunnel and impedance spectroscopy was conducted (range: 100 Hz…1 MHz, 100 logarithmically distributed frequencies, V_{max} = 50 mVrms, Sciospec, ISX-3v2, Sciospec, Germany). To reduce electrode polarization impedance, implicit in a traditional two electrode setup, a three electrode measurement setup was defined.

The subject was euthanized postoperatively, the mastoid removed, and a micro-computed tomography (µCT) image was acquired (resolution: 18 μm^3, Scanco µCT40, Scanco Medical, Switzerland). The drilled tunnels and the FN were manually segmented (Amira, FEI, US). The centerline of each drilled hole was calculated using principle component analysis (Matlab, MathWorks, USA). The recorded impedance measurements (magnitude and phase) were mapped to each postoperative measuring position along the trajectory. Sensitivity/specificity of impedance magnitude and phase thresholds was performed following characterization of the measured point as "bone" versus "nerve" (FN-distance $>$ 0.2 mm).

Results
A total of 24 trajectories were drilled in three subjects. In three of the 24 cases the impedance measurements were excluded due to difficulties with the measurement equipment (n = 1), incorrect probe placement in the tunnel (n = 1) and difficulties to localize the FN (n = 1). Finally, 21/24 trajectories were used for further analysis. In Fig. 2, a representative example with a decrease in impedance magnitude relative to the FN is presented for four of the measured frequencies (10, 100, 300 and 500 kHz). Generally, patterns were observed in the frontal trajectories (drilled axis intersecting the FN) with an increase in impedance magnitude and a decrease in impedance phase when reaching the facial nerve canal. When drilling lateral to the facial nerve no reproducible pattern was found.

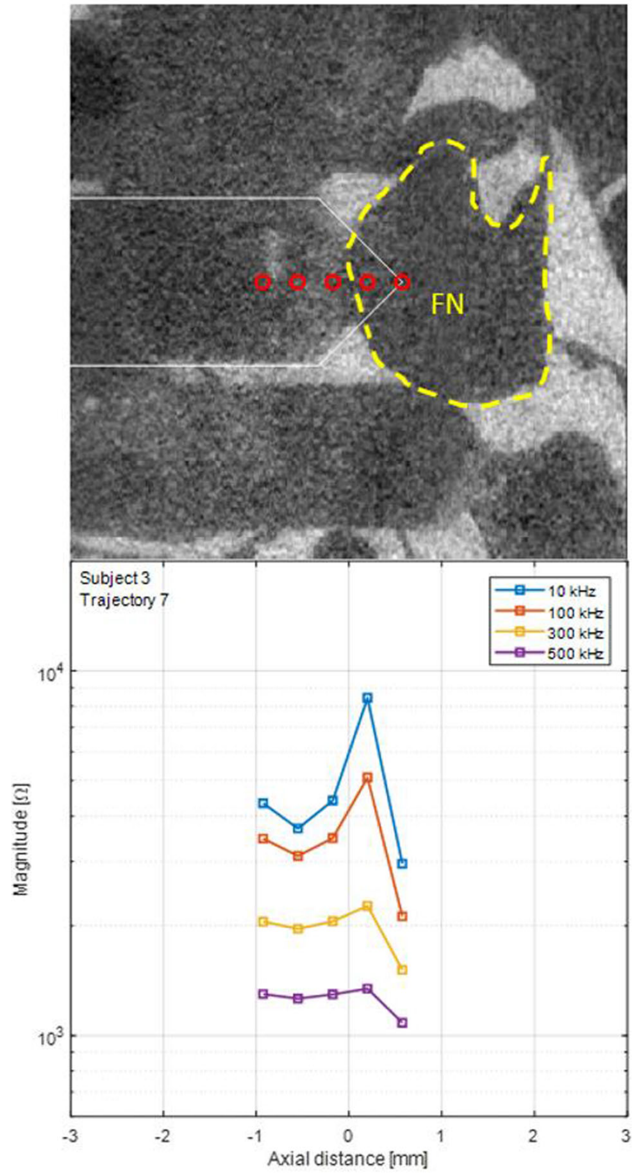

Fig. 2 Impedance magnitude relative to the FN along drill trajectory (e.g. with four frequencies)

In Table 1, the sensitivity and specificity of discrimination of "bone" and "nerve" tissue based on impedance magnitude thresholds (frequencies = 10 kHz, 100 kHz, 300 kHz, 500 kHz) is presented. Generally, impedance magnitude thresholds presented higher sensitivity and specificity than impedance phase (data not reported in abstract) for the four analyzed frequencies. The highest sensitivity and specificity results (67 and 65% respectively) were found at the frequency of 300 kHz.

Table 1 Maximum sensitivity and specificity results to discriminate facial nerve from bone

	Frequency (KHz)			
	10	100	300	500
Sensitivity (%)	60.61	61.02	66.67	63.64
Specificity (%)	59.32	61.02	64.41	66.1
Z Mag. threshold (Ω)	3900	3100	1700	1000

Conclusion

Sensitive and specific discrimination of "bone" tissue (FN-distance > 0.2 mm) versus "nerve" tissue (FN-distance < 0.2 mm) solely by means of tissue impedance spectroscopy might be difficult to achieve. The presented system and approach achieved lower sensitivity and specificity levels (67 and 65%) to discriminate a transition into the facial nerve canal than the existing neuromonitoring approach ($> 95\%$ at FN-distances 0.4 mm ("bone")) [4]. Future work will evaluate if a relative measurement of magnitude or phase between two neighboring frequencies can increase the accuracy to discriminate a transition of the drill trajectory into the facial nerve. Finally, machine learning approaches are being investigated (e.g. support vector machine, or decision tree) to assess the performance of a classification algorithm to discriminate "bone" and "nerve" tissue. Our vison is to combine neuromonitoring approaches [4] with impedance spectroscopy to enhance the safety of surgical robotic procedures that require opening of an access trajectory close to delicate nerves.

References

[1] Tsui BC, Pillay JJ, Chu KT, Dillane D (2008) Electrical impedance to distinguish intraneural from extraneural needle placement in porcine nerves during direct exposure and ultrasound guidance. *Anesthesiology* 109(3): 479–483

[2] Kalvøy H, Sauter AR (2016) Detection of intraneural needle-placement with multiple frequency bioimpedance monitoring: a novel method. *J. Clin. Monit. Comput.* 30(2): 185–192

[3] Bolger C, Carozzo C, Roger T, McEvoy L, Nagaria J, Vanacker G, Bourlion M (2006) A preliminary study of reliability of impedance measurement to detect iatrogenic initial pedicle perforation (in the porcine model). *Eur. Spine J.* 15(3): 316–320

[4] Ansó J, Dür C, Gavaghan K, Rohrbach H, Gerber N, Williamson T, Calvo EM, Balmer TW, Precht C, Ferrario D, Dettmer MS, Rösler KM, Caversaccio MD, Bell B, Weber S (2016) A Neuromonitoring Approach to Facial Nerve Preservation During Image-guided Robotic Cochlear Implantation. *Otol. Neurotol.* 37(1): 89–98

[5] Weber S, Gavaghan K, Wimmer W, Williamson T, Gerber N, Anso J, Bell B, Feldmann A, Rathgeb C, Matulic M, Stebinger M, Schneider D, Mantokoudis G, Scheidegger O, Wagner F, Kompis M, Caversaccio M (2017) Instrument flight to the inner ear. *Sci. Robot.* 2(4) eaal4916

Surface matching based on external and internal anatomy of the temporal bone applicable in lateral skull base surgery

D. Schneider[1], J. Hermann[1], K. Gerber[1], J. Anso[1], M. Caversaccio[2], S. Weber[1], L. Anschütz[2]

[1]University of Bern, ARTORG Center for Biomedical Engineering Research, Bern, Switzerland

[2]Bern University Hospital, University Department of Ear, Nose, Throat, Head and Neck Surgery, Bern, Switzerland

Keywords Registration · Surface matching · Endoscope · Lateral skull base

Purpose

Surgical navigation on the lateral skull base (LSB) demands submillimetre accuracies that are unachievable with commercially available image-guidance systems. Advanced image-guidance technology however, allows for navigation with sufficient accuracy as reported in several works during the last decades. The key element to fully exploit the capability of advanced image-guidance technology is the patient-to-image registration. The routine use of navigation in LSB procedures requires sufficient navigation accuracy provided at a low effort and a wide range of application. Utilising bone anchored fiducials, registration errors of approximately 0.1 mm are achieved [1]. However, the additional required computed tomographic (CT) imaging renders the approach unsuitable for most LSB procedures. For LSB procedures requiring a retroauricular incision, surface matching (SM) based registration of the mastoid (MAS) surface was proposed [2]. The effort inherent to SM based registration is low compared to registration based on PPM of artificial fiducials. However, the range of application of the proposed method is limited. Endoscopic transcanal LSB procedures, a set of surgical approaches with increasing popularity, additionally allow for the exploitation of the bony anatomy of the external auditory canal (EAC) and the middle ear cavity (MEC) for SM.

We hypothesize that SM applied on external and internal anatomy of the temporal bone provides target registration errors (TREs) errors below 1 mm. The aim of this study was to determine associated TREs on human cadaveric specimens.

Methods

Overview

In an experiment on two human cadaveric temporal specimens we measured TREs registrations based on SM of external and internal anatomical regions of the temporal bone. PPM with fiducial screws yielded ground truth (GT) registrations.

Sample Preparation and Surgical Planning

Subsequent to performing a retroauricular incision, the two specimens were implanted with four fiducial screws and underwent computed tomography imaging (0.16 mm $\times$ 0.16 mm $\times$ 0.2 mm). Finally, each specimen was prepared with an endoscopically performed tympanomeatal flap.

The screws were automatically localized in the images using a surgical planning software [3]. The surface of the mastoid (MAS), the EAC and the MEC were manually segmented in Amira (FEI, France). Furthermore, four points on the MAS were defined (mastoid process, temporal line posterior to EAC, two in between) to provide an initial coarse alignment for the SM based registrations.

Data Collection

The planned data was loaded onto our navigation system designed for LSB surgery. The registration tool (length: 6 cm, diameter: 1 mm) was calibrated for each specimen, prior to the experiments. The tracking camera (CamBar B1, Axios3D, Germany) was installed opposite to the surgeon. A dynamic reference base (DRB) was fixed on the specimens with a single surgical screw a few millimetres inferior the temporal line and posterior to the EAC.

For the initialisation of the SM based registrations, the four predefined anatomical landmarks on the MAS were digitized on each specimen. Subsequently, 50 points were scanned on the MAS, the EAC and the MEC successively six times by three surgeons on both specimens (Fig. 1). Surgeons were instructed to collect points with a wide spread whilst minimizing tool bending and ensuring the contact with the surface. A foot pedal was used for digitisation control.

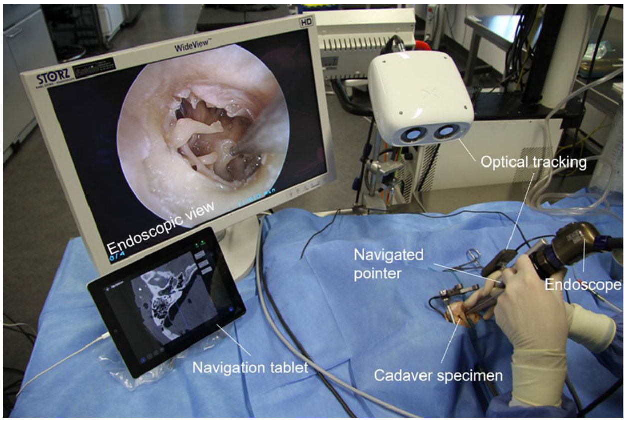

Fig. 1 Experimental setup

Prior to every second attempt of surface scanning, the implanted screws were digitized for the GT registrations. Care was taken to not move the specimen locator between the surface scanning and the screw digitisation.

Registration Analysis

SM based registrations were calculated using an iterative closest point algorithm [4] initialised by a coarse initial registrations based on PPM [5] of mastoid surface landmarks, resulting in 36 registrations per surface. Registrations based on combinations of the surface of the MAS, the EAC or the MEC were simulated 100 times for each attempt by randomly sampling equal portions of scanned points from the involved surfaces. Consequently, the resulting combinative surface also consisted of 50 points. This yielded 3600 registrations per combinative surface.

The GT registrations were calculated using PPM [5] of the fiducial screw positions in the image and reference frame.

The TRE of each registration was calculated at 10 anatomical landmarks: round window, facial nerve at the pyramidal eminence and at the geniculate ganglion, facial recess, oval window, jugular vein, internal carotid artery, fundus and porus of internal auditory canal, petrous apex. The TREs were calculated as the distance between the landmark (selected in the image frame) transformed to the specimen's reference frame by the registration to be evaluated, and the same landmark transformed to the specimen's reference frame via the corresponding GT registration.

Results

The median TRE of the most accurate SM based registration, SM based on all three surfaces combined, was 0.37 mm with 100% of all measured TREs below 1 mm (Fig. 2). Among the SM based registration procedures, at least 95% of all measured TREs of all procedures except SM based on the EAC were below 1 mm.

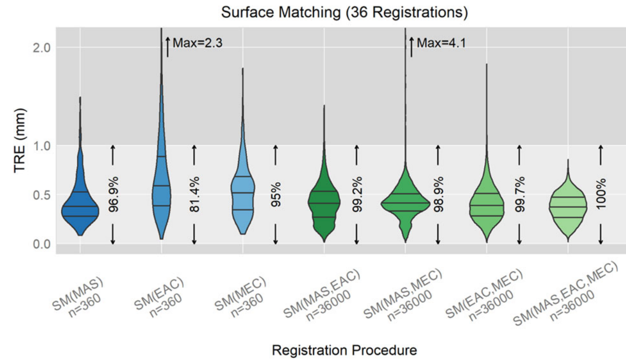

Fig. 2 TREs of measured (blue) and simulated (green) experiments. The violin-plots contain the TREs of all registrations at all 10 targets. The region of interest is highlighted (TRE < 1 mm). SM(i) refers to surface matching with surface(s) i

The time required for SM including the initial coarse alignment was 4.3 ± 1.5 min.

Conclusion

In this work SM based registration of internal and external anatomical structures of the temporal bone was evaluated and submillimetre TREs suitable for LSB navigation were observed.

While transcanal access to internal anatomy limits the diameter hence rigidity of the employed pointer thus increasing the error of surface digitisation, proximity of the structures to target anatomy results in accuracies and precisions similar to those observed in mastoid surface registration. TREs of registrations based on the mastoid surface alone were similar to those reported in earlier work [2]. However, the addition of surface points from internal anatomy improved the registration precision. Furthermore, this study suggests that surfaces exposed in transcanal procedures (EAC, MEC) provide sufficient accuracy for navigation in the LSB extending the area of application from microscopic transmastoidal to endoscopic transcanal procedures. While landmarks on the mastoid surface were used for SM initialisation in all registrations during this study, points from internal anatomy could alternatively be used to remove the need to expose the mastoid surface in transcanal procedures.

References

[1] Weber S, Gavaghan K, Wimmer W, Williamson T, Gerber N, Anso J, Bell B, Feldmann A, Rathgeb C, Matulic M, Stebinger M, Schneider D, Mantokoudis G, Scheidegger O, Wagner F, Kompis M, Caversaccio M (2017) Instrument flight to the inner ear. Sci. Robot., vol. 2, no. 4, p. eaal4916

[2] Zhou C, Anschuetz L, Weder S, Xie L, Caversaccio M, Weber S, Williamson T (2016) Surface matching for high-accuracy registration of the lateral skull base. Int. J. Comput. Assist. Radiol. Surg., pp. 1–7.

[3] Gerber N, Bell B, Gavaghan K, Weisstanner C, Caversaccio M, Weber S (2014) Surgical planning tool for robotically assisted hearing aid implantation. Int. J. Comput. Assist. Radiol. Surg., vol. 9, no. 1, pp. 11–20

[4] Besl P, McKay N (1992) A Method for Registration of 3-D Shapes. IEEE Transactions on Pattern Analysis and Machine Intelligence, vol. 14, no. 2. pp. 239–256

[5] Haralick RM, Joo H, Lee C, Zhuang X, Vaidya VG, Kim MB (1989) Pose estimation from corresponding point data. IEEE Transactions on Systems, Man and Cybernetics (Volume: 19, Issue: 6)

Quantitative evaluation of endoscopic sinus surgery using time series process analysis

S. Aoki[1], T. Sugino[2], A. Kuboki[3], N. Ohtori[3], R. Nakamura[2,4,5]
[1]Chiba University, Graduate School of Science and Engineering, Chiba, Japan
[2]Chiba University, Graduate School of Engineering, Chiba, Japan
[3]Jikei University School of Medicine, Department of Otorhinolaryngology, Tokyo, Japan
[4]Chiba University, Center for Frontier Medical Engineering, Chiba, Japan
[5]Japan Science and Technology Agency, Saitama, Japan

Keywords Skill assessment · Surgical education · Surgical navigation system · Motion analysis

Purpose

Surgical navigation systems are widely used for endoscopic surgeries with an increasing frequency in Endoscopic Sinus Surgery (ESS). In order to enhance the safety of ESS, which has a high risk of damaging important tissues and nerves including the eye and brain, it is important to quantitatively evaluate surgical procedures and improve surgical skills using navigation systems. In recent years, research for surgical processes and skill analyses aiming at optimizing surgery and improving surgical skills has attracted attention. We developed a method for the quantitative measurement and analysis of surgical procedures using surgical navigation systems [1]. This method identified differences in endoscopic manipulation performed by expert and resident surgeons during ESS. Since the skill parameters of this system use the average value or cumulative value of data related to the surgical instrument including average speed and density distribution of the instrument, it is difficult to detect problematic areas. Therefore, in this study, we aimed to identify improvement areas by analyzing and evaluating data on surgical instruments acquired using a navigation system in time series.

Methods

In order to describe what type of surgical operation was performed during a surgical process, a surgical process transition was modeled. Surgical process model (SPM) was used based on log data on surgical instruments acquired using a navigation system. In related research, the surgical process was modeled using data including surgical actions, anatomical structures, and instruments used as components called activities [2]. In this study, skill parameters calculated from surgical instruments (endoscopic, forceps, and microdebrider) including movement data and model were developed to use them as activities. We defined a total of six parameters including tip velocities (left/right hand), rotations of the surgical instrument (left/right hand), relative velocity, and distance between the tips of surgical instruments (Fig. 1).

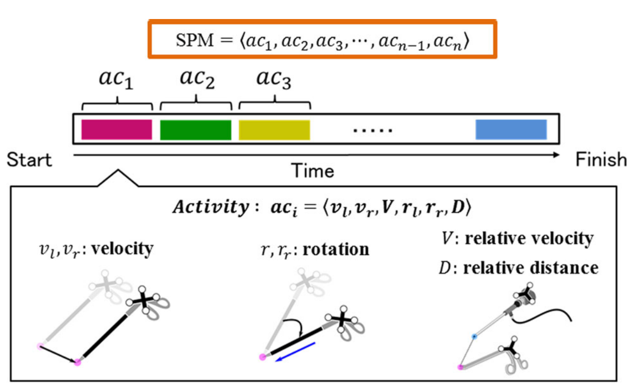

Fig. 1 Method of defining SPM

Since the duration of a surgery varies depending on the case, the length of the SPM can differ. In addition, for an accurate evaluation of skills, it is necessary to compare them on the same procedure. Thus, we utilized a method called dynamic time warping (DTW), which can find and capture similarities between SPMs. Using DTW, it is possible to align two SPMs to compare the level of skill in performing the same procedure. Furthermore, since the differences between the activities can be detected, we defined the difference as a similarity value and visualized it using a color bar. In addition, we automatically detected the areas where the expert and resident are not very similar (Fig. 2).

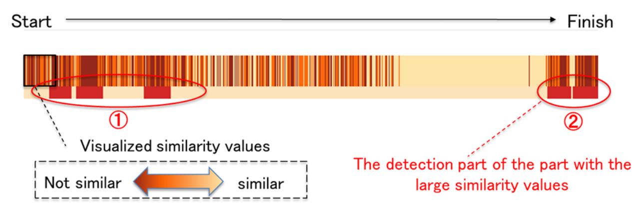

Fig. 2 Detection result

Using DTW, one-to-one comparisons between an expert and another are possible. However, it is expected to identify some differences in the characteristics of the procedure among experts. In order to compare SPMs more accurately, it is necessary to use the average SPM calculated from data from the expert group. Therefore, in this study, we used an algorithm called DTW barycenter averaging (DBA) extended to compare between three or more models and calculate an average SPM based on the DTW algorithm [3]. An expert SPM was developed using data from six cases of ESS performed by three experts. Comparing the average expert SPM with that of residents, we detected activities that were not similar to the average expert SPM.

Results

The results of the comparison of the expert SPM with that of residents are shown in Fig. 2. We reviewed endoscopic videos of the residents for the activities detected. In numbers 1 and 2 of Fig. 2, residents struggled to turn the teeth of the microdebrider. On other areas, the residents did not move the surgical instrument for a short period of time or moved it with the endoscope keeping a large distance between them. Those actions were not observed with experts. Accordingly, it was suggested that improvement areas for residents can be identified by calculating the similarity value and comparing it to the expert SPM.

In addition, activities that did not rely on skill level were detected. Those included insertion and evulsion of the endoscope and surgical instruments and nasal irrigation. Although those activities were performed by experts, it is believed that they were detected as differences due to the differences in the time taken to perform them by both groups. Therefore, it is necessary to break down the surgical process and compare the activities within it. As a result, data on surgical instruments and anatomical structures are required.

Conclusion

In this study, we presented a method for analyzing ESS in time series by developing SPMs from data on surgical instruments obtained using navigation systems and compared them between expert and resident surgeons. Results showed the possibility of identifying improvement areas in surgical procedures by comparing the average expert SPM to that of residents.

References

[1] Sugino T, Kuboki A, Nakayama T, Ohmura K, Asaka D, Yamaguchi T, Kojima H, Ohtori N, Nakamura R (2017) Quantitative Analysis of a Camera Operation for Endoscopic Sinus Surgery Using a Navigation Information:Clinical Study. Journal of Japan Society of Computer Aided Surgery, 19(1): 17–26

[2] Forestier G, Lalys F, Riffaud L, Trelhu B, Jannin P (2012) Classification of surgical processes using dynamic time warping. Journal of Biomedical Informatics, 45(22): 255–264
[3] Petitjean F, Ketterlin A, Gancarski P (2011) A global averaging method for dynamic time warping, with applications to clustering. Pattern Recognition, 44(3): 678–693

Determination of error sources and values for an individually mouldable surgical targeting system

T. S. Rau[1], L. Uhlenbusch[1], S. Witte[1], J. Lexow[1], L. A. Kahrs[2], T. Lenarz[1], T. Ortmaier[2], O. Majdani[1]
[1]Hannover Medical School, Department of Otolaryngology, Hannover, Germany
[2]Leibniz Universität Hannover, Institute of Mechatronic Systems, Hannover, Germany

Keywords Surgical template · Micro-stereotactic frame · Image-guided surgery · Cochlear implantation

Purpose

Highly accurate drilling of bore holes in bone, as well as positioning surgical tools or stimulation probes with submillimetre accuracy requires assistance devices to support the surgeon in performing these exacting tasks. Recently, we introduced a new concept for a surgical targeting system [1], which includes a surgical template ('jig') mouldable in a patient specific manner using bone cement (Fig. 1). Individualization of that template should be performed by the surgeon and its team inside the operation room using a manually operated alignment device (called 'Jig Maker'). Aim of this work is to provide insight into the major factors contributing to inaccuracies with special focus on the manual operation of the Jig Maker.

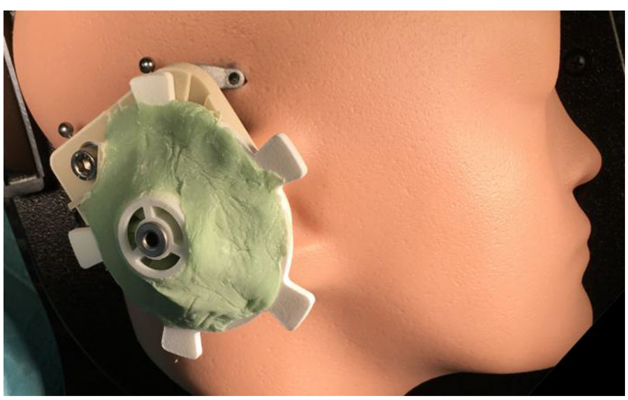

Fig. 1 Surgical targeting system fixed to a half-skull phantom with artificial skin. The drill bushing guides surgical tools, in this study a twist drill bit, strictly along the planned trajectory. The patient-specific configuration is secured after hardening of the bone cement

Methods

In the first part of the study the intra-operator reliability was investigated. For that purpose the same configuration of the hexapod-based Jig Maker (Fig. 2) was adjusted ten times by the same user. The resulting configurations of the Jig Maker were measured using a portable coordinate measuring machine (CMM, Romer Absolute Arm Compact 7312, Hexagon Manufacturing Intelligence, Wetzlar, Germany). The standard deviation of these measurements was calculated, which is referred to as user error ε_{user} in the following.

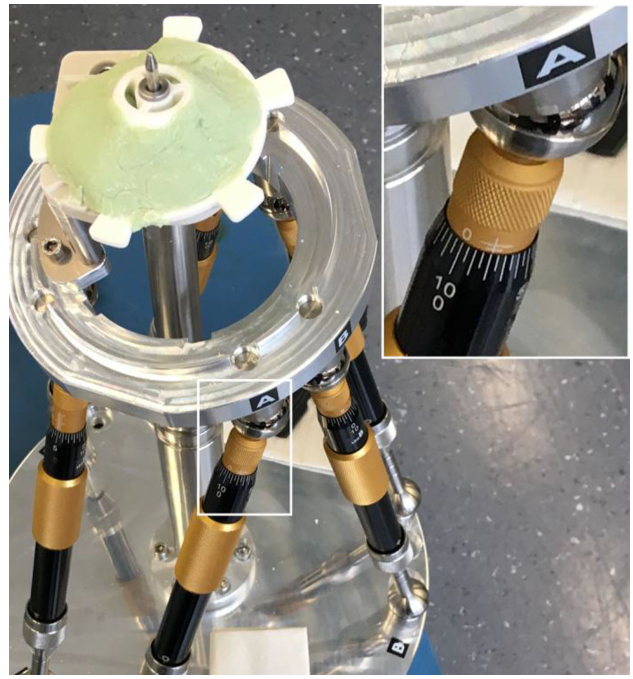

Fig. 2 The Jig-Maker with the surgical template on top of the upper platform. Adjusting the length of all struts enables pose-setting with respect to the alignment pin in the central axis of the device, which represents the planned trajectory

In the second part, half-skull phantoms (Sawbones Europe AB, Malmö, Sweden) made of bone-substitute material and artificial skin (in order to simulate the whole surgical workflow [2]) and corresponding computed tomography (CT) images were used to plan and drill ten bore holes running down to the approximate location of the inner ear. A bone-anchored, unique reference frame ('Trifix') served for both image-to-patient registration after CT imaging and rigid fixation of the surgical template to the artificial skull (Fig. 1). For each trajectory the corresponding lengths of all six struts of the Jig Maker were calculated, afterwards set and finally controlled. After length setting, the struts of the Jig Maker were measured again using the portable CMM in order to get insight into which inaccuracies of the final jig were contributed by the kinematic of the Jig Maker (e.g. manufacturing tolerances) and also the users interaction. This error caused by imperfectly adjusted struts is referred to as ε_{struts} in the following.

Afterwards, the surgical template was fabricated (Fig. 2) and, after hardening of the bone cement, it was mounted on top of an accuracy test bench [1] in order to determine the positioning error (ε_{pos}). Finally, the template was fixed to the reference frame still attached to the artificial skull (Fig. 1) and the initially planned hole was drilled. A second CT scan was used to compare the actual position of the drill canal with the desired one at the target point (ε_{total}).

Results

The precision of the manual length setting of the struts was found to be $\varepsilon_{user} = 0.04$ mm, which is in the range of the accuracy of the CMM ($\pm$ 0.025 mm). The mean strut length setting error ε_{struts} was ($-$ 0.09 $\pm$ 0.09) mm, which indicates a systematic error in the kinematic of the hexapod. However, we also detected a maximum error of 0.65 and 0.35 mm for one single strut in trial #2 and #10, respectively. Reviewing the photo documentation of the adjusted legs showed that these errors stem from a mix-up of two digits when setting the micrometre screw. The mean positioning error ε_{pos} at the target point was found to be 0.35 mm with a standard deviation of

0.09 mm for all ten experiments. In case of the drilling in artificial bone material, the planned target point was reached with a deviation (ε_{total}) of (0.35 ± 0.30) mm.

Conclusion

Manual length setting is feasible with high precision; however, the current design of the hexapod's leg with an integrated micrometre screw is a source of individual errors. In order to increase patient's safety additional security measures (e.g. multi-user readings, sensors) are desirable to detect fatal errors in manual length setting before the surgical template is built. Based on the results the calibration of the Jig Maker was improved which significantly decreased the strut length setting error to (0.01 ± 0.09) mm. This improved calibration will be used in following studies.

Acknowledgment

This work has been supported by the start-up grant for young researchers HiLF of Hannover Medical School, by the German Federal Ministry of Education and Research (BMBF, FKZ 13GW0019E) and by the German Research Foundation (DFG, Cluster of Excellence EXC 1077/1 Hearing4all). Responsibility for the contents of this publication lies with the authors.

References

[1] Rau TS, Lexow GJ, Blume D, Kluge M, Lenarz T, Majdani O (2017): Micro-stereotactic frame utilizing bone cement for individual fabrication. An initial investigation of its accuracy. In Proc. SPIE Medical Imaging 2017: Image-Guided Procedures, Robotic Interventions, and Modeling, 101350P. https://doi.org/10.1117/12.2254304.

[2] Lexow GJ, Kluge M, Majdani O, Lenarz T, Rau TS (2017): Phantom-based evaluation method for surgical assistance devices in minimally invasive cochlear implantation. In Proc. SPIE Medical Imaging 2017: Image-Guided Procedures, Robotic Interventions, and Modeling, 101352 N. https://doi.org/10.1117/12.2254381.

Endoscopic neurosurgery using operation supporting robot "iArmS": preliminary clinical application

T. Ogiwara[1], T. Goto[1], A. Nagm[1], T. Hasegawa[1], K. Hongo[1]
[1]Shinshu University School of Medicine, Neurosurgery, Matsumoto, Japan

Keywords Neurosurgery · Endoscopic neurosurgery · iArmS · Robotic surgery

Purpose

As neurosurgery takes a relatively long time and requires delicate manipulations, hand tremble among neurosurgeons becomes a considerable obstacle to precise microneurosurgery. To resolve this problem, the operation supporting robot (intelligent arm support system "iArmS®", DENSO Corporation, Kariya, Japan) has been developed cooperated with medical-engineers. This revolutionary motor-less medical robot was designed to support the surgeon's forearm to prevent hand trembling and alleviate fatigue during microneurosurgery. It follows and fixes the surgeon's arm at an adequate position automatically. Here, we report the application of this robotic device in endoscopic neurosurgery including endoscopic endonasal approach (EEA) and endoscopic intraventricular surgeries (EIVS), along with an evaluation of our initial experiences.

Methods

The study population consisted of 43 patients with pituitary adenoma (*n* = 29), meningioma (*n* = 3), Rathke's cleft cyst (*n* = 3), craniopharyngioma (*n* = 2), chordoma (*n* = 2) and others (*n* = 4). All patients underwent surgery via the EEA with a rigid endoscope. During nasal and sphenoid phases, iArmS® was used to support the surgeon's non-dominant arm that held the endoscope (Fig. 1). Besides, four patients underwent EIVS including endoscopic third ventriculostomy with flexible endoscopy. To perform EIVS easily, in which the angle of the surgeon's elbow is different from that in EEA and microscopic neurosurgery, a special distinctive attachment (ARIZONO ORTHOPEDIC SUPPLIES CO., LTD., Kitakyusyu, Japan) that fits between robotic arm and handstand, has been developed. This study has evaluated the effectiveness of robotic devices in EEA and EIVS (with special attachment) based on the surgeon's subjectivity. The surgical outcome including tumor removal rate, complication rate, operative time and blood loss were not included in this study.

Fig. 1 Intraoperative photograph showing endoscopic endonasal transsphenoidal surgery during the nasal phase with iArmS®. The system supports the surgeon's non-dominant hand, which holds the endoscope

Results

We used iArmS® easily due to the sufficient knowledge of its characteristics and the familiarity with its manipulation before surgery. The iArmS ® followed the surgeon's arm-movement automatically. It reduced the surgeon's fatigue and stabilized the surgeon's hand during the EEA. Shaking of the video image decreased due to the stabilization of the surgeon's scope-holding hand with iArmS®. There were no complications related to the usage of iArmS®. Although, the fatigue reduction of the surgeon's arm may lead to improvement of the surgical outcome indirectly, it seems to be difficult to prove the direct effectiveness of iArmS® for EEA with a preliminary and initial experience-based study. The iArmS® was also utilized for EIVS due to development and application of special attachment as well as the EEA.

Conclusion

The details of the iArmS® and clinical results were presented and we reported our initial experience with iArmS® in endoscopic neurosurgery. The iArmS®, which is considered a breakthrough operation support robot, enables both stability of the surgeon's hand and excellent operability not only in microsurgery but also endoscopic neurosurgery. Sufficient knowledge of the characteristics of iArmS® makes it a useful new modality for EEA and EIVS. It is expected that it will lead to the development and widespread application of robotic neurosurgery. While robotic platforms have the potential to greatly enhance the performance of endoscopic neursurgery, there is a strong rationale for research into next-generation robots that are better suited to endoscopic neurosurgery. Continued advances in not only surgical technique and instruments but also robotics will ensure continued brisk evolution in this expanding field.

Current experiences and future perspectives for augmented reality visualization in navigated neurosurgical interventions

A. Roethe[1,2], J. Rösler[1], P. Vajkoczy[1], T. Picht[1,2]
[1]Charité-Universitätsmedizin Berlin, Neurosurgery, Berlin, Germany
[2]Humboldt-Universität zu Berlin, Image Knowledge Gestaltung—An Interdisciplinary Laboratory, Berlin, Germany

Keywords Augmented reality · Surgical information · Clinical evaluation · Neurosurgery

Purpose

Augmented reality (AR) visualization of surgically relevant information provides a virtual manifestation of the surgeon's mental projections applied to the surgical area. Thereby, the technology can reduce intraoperative cognitive load and make visual representations more precise and explicit for the surgical team. While several types of AR technology have been explored by clinicians over the past decade [1, 2], the general clinical availability and comfort of heads-up display (HUD)-based systems in combination with improved quality of image injection especially for display of volumetric and depth information marks the beginning of a new and more detailed clinical evaluation phase. Aside from technological advancements and their integrability into both existing operative systems and workflows, the demand for identification of suitable pathologies, optimal display modes and comprehensive intraoperative information visualization (including 2D/3D reconstructions, complexity, overview vs. direct visual guidance) becomes an important focus of investigation.

Methods

Following an initial literature review, we developed a prospective study protocol for comparative evaluation of AR and non-AR cases in clinical routine. All navigated cases (neurovascular, neurooncological, spinal) with compatible imaging data are included and randomly assigned to one group. In AR cases, microscope (ZEISS Pentero 900) and navigation (Brainlab Cranial Navigation, Brainlab Elements) streams are recorded. Type of view, quality, accuracy, complexity and duration of image injection in the heads-up display (HUD) are matched with the corresponding surgical task and surgical outcome. In non-AR cases, planning data, navigation interaction and surgical outcome are documented.

Results

We clustered our preliminary results into four different categories (a. clinical, b. workflow, c. technical, d. visualization quality). (a) All initial cases have been brain tumors (WHO grade I–IV), of which 78.5% were AR cases (n = 11). AR has been utilized in 15% of total resection time. Frequently used HUD display modes were navigation view (75%) and target volume mode (30%). In navigation view, standard ACS injection (axial, coronal and sagittal sectional imaging) has been primarily used as continuous orientation display. Compared to external neuronavigation systems, a combined display of different MRI sequences is currently not possible. All participating surgeons (n = 4) used tumor segmentation in AR visualization with additional anatomical (35%) and functional (50%) structures, requesting especially under initial tumor resection more detailed topographical information. In target volume mode, the average overlay accuracy of tumor margins and adjacent structures of interest (e.g., optic nerve or vessels) has been rated 65% (1–7 mm offset range, accuracy range 60–90% per object) by the surgeons before and during early resection, thus being significantly lower than reported for previous software versions in the literature [2]. In all deep-seated tumors, AR visualization proved acceptably useful as a tool for trajectory planning and intrasurgical decision-making. (b) Planning, preparation and calibration of the microscope-navigation connection added a total of 15 min. surgical time per case. Workflow facilitations, such as pointer-free navigation and fade-in display of surgical infomation, were accompanied by partial blocking of the surgical field and impaired depth assessment. This also extends to brain surface structures used for anatomical orientation. During later resection phase, surgeons switched back to conventional navigation (50%) or used it in addition to AR overlay (100%) for position verification and brainshift estimation. In non-AR resection cases, pointer-based navigation checks were associated with frequent workflow interruptions (4–7 per case). In addition, all surgeons preferred a peripheral display of information over AR visualization in the focus level, due to reported distraction effects. (c) While current generation visualization software introduced 3D volume injection in navigated microscopes, any conveyed object depth information (e.g., of adjacent white matter fibertracking) has still been rated unintuitive by the surgeons. A combination of fluorescence-guided surgery for detection of tumor remnants and AR information overlay with the purpose of further validation turned out technically impossible at this stage. d) A larger number of objects (n > 3) for AR overview cannot be recommended, while green and blue colorizations should be preferred over red scale tumor and object segmentations. In general, AR visualization quality directly depends on the quality of the underlying MRI scan: in case of interpretation difficulties or barely demarcatable anatomical structures in the sectional imaging data, there is no added benefit with AR display.

Conclusion

Aside from a clearly improved navigation management, our preliminary study results underscore the relevance of a continuous critical case evaluation. While the technical workflow is at large compliant with daily surgical routine, the visualization quality still impacts surgical cognitive load and surgical performance, leading to the consultation of conventional radiological imaging and additional use of traditional neuronavigation in over 90% of documented cases. Known restrictions of the technology are primarily due to the overlay of working and viewing area. In cases with critical overlay offset larger than 5 mm, effects caused by perspective distortion require further investigation. Future subgroup analyses and case–control matches will be used for detailed quantification of results, correlation with surgical outcome and practice-based recommendations for AR visualization in neurosurgical routine.

References

[1] Meola A, Cutolo F, Carbone M, Cagnazzo F, Ferrari M, Ferrari V (2016) Augmented reality in neurosurgery: a systematic review. Neurosurg Rev 40: 537–548.

[2] Mascitelli JR, Schlachter L, Chartrain AG, Oemke H, Gilligan J, Costa AB, Shrivastava RK, Bederson JB (2017) Navigation-linked heads-up display in intracranial surgery: early experience. Operative Neurosurgery https://doi.org/10.1093/ons/opx205.

Automatic segmentation of deep brain electrodes used in stereotactic electroencephalography (SEEG)

A. Higueras-Esteban[1,2], J. Ojeda[1], I. Delgado-Martínez[1,3], C. Pérez Enríquez[3], L. Serrano[3], A. Principe[4], M. A. Gonzalez Ballester[2,5], R. Rocamora[4], L. Serra[1], G. Conesa[3]
[1]Galgo Medical, Neuro, Barcelona, Spain
[2]Universitat Pompeu Fabra, SIMBioSys group, Barcelona, Spain
[3]IMIM-Hospital del Mar, Neurosurgical Department, Barcelona, Spain
[4]IMIM-Hospital del Mar, Department of Neurology, Barcelona, Spain
[5]ICREA, Barcelona, Spain

Keywords Epilepsy surgery · SEEG · Automatic segmentation · Electrode segmentation

Purpose

SEEG is a surgical procedure designed to help locate the epileptogenic zone in drug-resistant epileptic patients. It consists on the placement of several intracranial electrodes (typically 7–22) [1] containing several contacts each (5–18). The electrical information retrieved from these contacts is key to determine which area of the brain should be resected or disconnected to stop epileptic seizures.

To locate these contacts, it is common clinical practice to perform a postoperative CT scan which reveals the final position of the implanted electrodes. Segmenting these contacts manually for each patient is a tedious task [2].

Several efforts have been made to automatize this procedure, sometimes requiring user input to select the coordinates of the entry and target points [2]. These points could be obtained from the surgical plan, but this plan is sometimes modified intraoperatively. Sometimes the number of expected contacts for each electrode is also a required input further complicating automatization, as electrodes with different numbers of contacts may be implanted on each patient.

The purpose of this work is to provide an automatic segmentation procedure to segment intracranial electrodes and their contacts from a post-operative CT scan not requiring other inputs nor user interaction. The only prior knowledge required by the algorithm consists in the geometrical parameters of the electrode.

Methods

The algorithm is implemented using the ITK library, and is composed of the following steps:

Removal of outer wires and contacts: A binary volume mask of the air voxels surrounding the head of the patient is obtained with a threshold value of − 500 Hounsfield units (HU). After that, a grow/shrink/grow morphological operation is performed which removes wires but retains the shape of the head. An inverse of the described air mask is then multiplied by the original postoperative CT, effectively removing false positives located outside of the brain.

Binarization, median filtering and label map generation: The masked image is then binarized with a threshold of 2000 HU, leaving mostly metallic elements. A 3 × 3 × 3 voxels median filter is then applied to separate the contacts from each other. Separated binary blobs are identified using connected-component labeling [3] to obtain a list of points computed as the center of mass of each blob.

Geometric constraints: First we remove points obtained from labeled blobs whose size is outside the physical specification of the contact. Then, for each point, we search for others at the expected distance defined for consecutive contacts in an electrode and reject the isolated ones.

Electrode identification: For each point, we search for others in the inter-contact range. When found, we attempt to search for others in the same line using a tolerance which accounts for the curvature of the implanted electrode. Once a line of at least four contacts in a row is found, we store it as a segmentation result, remove the points from the set, and continue with the next point. Then we look for gaps of twice the inter-contact distance among candidate electrodes that lay on the same line, and when the image intensity confirms the presence of metal there, we add a new contact in that position and merge the two candidate electrodes into a longer one (Fig. 1).

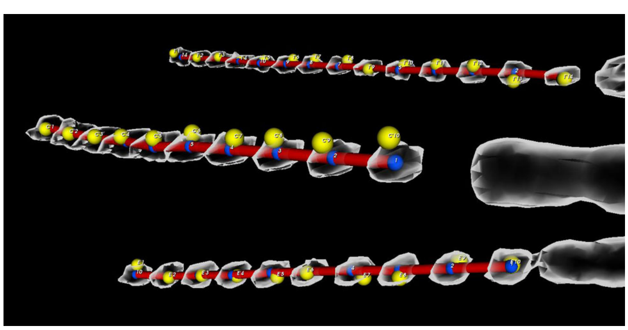

Fig. 1 View of threshold segmented SEEG electrodes (translucent), manually segmented contacts (yellow dots) and automatically detected contacts (blue dots) automatically grouped into electrodes (red lines)

Results

A group of 24 images from 18 patients was used in the quantitative validation of the algorithm. Stereotactic deep electrodes from DIXI medical electrodes of 0.8 mm diameter, 2 mm in length and inter-contact distance of 2.5 mm with 5–18 contacts were used for the implantations. Several different protocols were used for the acquisition of the postoperative CT images of the patient with voxel sizes ranging from (0.4, 0.4, 0.625) to (0.52, 0.52, 1) mm. Manual identification of the contacts was performed by a clinical expert using 3D Slicer (Fig. 2).

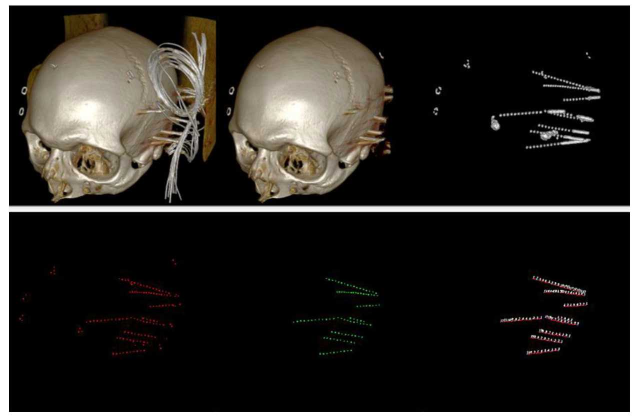

Fig. 2 Segmentation process from top–bottom, left–right: original CT scan, masked CT scan, metal threshold with median filter, all candidate 3D points, points filtered by distance and in line, reconstructed electrodes

From a total of 327 manually segmented electrodes, our algorithm was able to identify 274 with at least four contacts, accounting for an 84%. The total number of manually segmented contacts was 3663, and our algorithm could correctly segment 2422 (66%). Analyzing the different CT protocols, we found that images created with the H31 s reconstruction kernel (7 out of 24) presented poorer results (from 36 to 59%). Removing those images the contact detection ratio rises to 75%.

Performing a sub-analysis on the data, it has been found that 44% of not detected electrodes form an angle smaller than 30 degrees with the axis of less resolution of the image (z), suggesting that this algorithm is not suitable for detection of these vertical electrodes in anisotropic images.

The time required to run the algorithm is approximately half a minute.

Conclusion

We have presented a SEEG electrode segmentation procedure which requires no input from the user apart from the postoperative CT, and which can aid in the localization of the source of electrical data of clinical relevance during the observatory stage of the SEEG procedure.

The procedure presents false negatives, which means a last manual step should be provided to validate and complete the segmentation result. Nevertheless, the automatic detection of 75% of contacts drastically reduces the time required for the segmentation considering that the time required for a manual segmentation may take even hours as described in the literature [4].

Acknowledgements

This work was supported by La Caixa Foundation.

The study received approval by the ethical committee.

References

[1] J. Gonzalez-Martinez, J. Mullin, S. Vadera, J. Bulacio, G. Hughes, S. Jones, R. Enatsu, and I. Najm, "Stereotactic

placement of depth electrodes in medically intractable epilepsy.," *J. Neurosurg.*, vol. 120, no. 3, pp. 639–44, 2014.

[2] G. Arnulfo, M. Narizzano, F. Cardinale, M. M. Fato, and J. M. Palva, "Automatic segmentation of deep intracerebral electrodes in computed tomography scans.," *BMC Bioinformatics*, vol. 16, no. 1, pp. 12–99, 2015.

[3] G. Lehmann, "Label object representation and manipulation with ITK," *Insight J.*, pp. 1–34, 2008.

[4] A. O. Blenkmann, H. N. Phillips, J. P. Princich, J. B. Rowe, T. A. Bekinschtein, C. H. Muravchik, and S. Kochen, "iElectrodes: A Comprehensive Open-Source Toolbox for Depth and Subdural Grid Electrode Localization," *Front. Neuroinform.*, vol. 11, no. March, pp. 1–16, 2017.

Identification and quantification of the acoustic reflex with a digital surgical microscope

A. Schneider[1], A. Bicer[1], K. Ehrt[2], R. Dahl[2], A. Ovari[2], R. Mlynski[2]
[1]Arnold and Richter Cine Technik GmbH & Co. Betriebs KG, BU Medical, Munich, Germany
[2]Universitätsmedizin Rostock, Klinik und Poliklinik für Hals-, Nasen-, Ohrenheilkunde, Kopf- und Halschirurgie "Otto Körner", Rostock, Germany

Keywords ENT, Acoustic reflex · Digital microscope · Measurement

Purpose

Patients with a severe hearing loss can be supported by cochlea implants (CI). These neural prostheses take over the function of the inner ear and restore hearing, using an electrode array which is directly implanted in the cochlea. For postoperative adjustment of the speech processor and to prevent undesired overstimulation electrically evoked stapedius reflex thresholds (ESRT) are used. The stapedius reflex is, in healthy patients, an involuntary mechanism in the middle ear to protect the inner ear in response to high-intensity sound levels. This acoustic reflex leads to a contraction of the stapedius muscles and thus decreases the acoustomechanical coupling of the eardrum with the inner ear, resulting in lower transmission of vibrational energy to the cochlea.

Currently, for postoperative CI processor adjustment, the identification of the electrically evoked acoustic reflex is done optically by the surgeon while observing the stapedius muscle during electrical stimulation. Even if this procedure is currently used as standard, it is, because of the possible small movements after stimulation, still dependent on the subjective assessment of the surgeon. Furthermore, the optical method is only a binary method (reflex yes/no), any quantification is nearly impossible.

Based on the imaging of a digital surgical microscope (ARRISCOPE, Arnold & Richter Cine Technik, Munich, Germany) we developed an algorithm to automatically identify the acoustic reflex and to measure the deflection of the stapedius muscle during ESRT measurement.

Methods

The microscope captures the surgical situs in 3D with an optical system which is directly connected to a high-performance CMOS sensor with a resolution of 3840 × 1920 pixels and a framerate of 60 fps. The captured image is then processed by the attached computer, divided into the images for the left and right eye and displayed on digital OLED binoculars, attached displays and are available for further processing.

The image processing chain for automatic detection of the electrical evoked stapedius reflex is based on several steps: First, the captured image is stabilized to eliminate movements of the complete scene (e.g. heartbeat, ventilation, etc.). In the second step the stapedius muscle is marked with a region of interest (ROI) to define the area to be tracked. Inside this ROI several pixels with a robust discrimination to neighborhood pixels are chosen automatically. The x- and y-position of these marker points are then analyzed frame by frame and the respective motion vector is calculated. If a definable threshold of the motion vector on the stapedius muscle is exceeded, it is rated as an acoustic reflex.

For evaluation, video captures from ESRT of n = 4 cochlea implant surgeries were analyzed. In the audio track of the videos the moment of stimulation was encapsulated by linking the stimulation computer to the microscope which is recording the video. Identified electrical evoked stapedius reflexes by the software were then compared with the intraoperatively visually identified acoustic reflexes by the surgeon.

Results

The software was able to find suitable points for tracking in the ROI in all analyzed videos. Overall 284 electrical stimulations were performed, in n = 142 stimulations an electrical evoked stapedius reflex after stimulation was identified optically by the surgeon, the software identified n = 151 reflexes, respectively.

Additionally, a correlation of the stimulus strength with the length of the motion vector on the stapedius muscle can be demonstrated (Fig. 1).

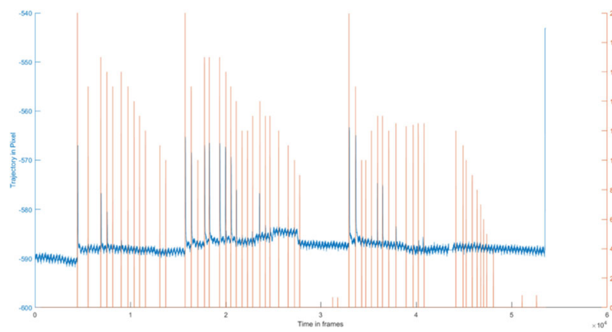

Fig. 1 Correlation of the deflection of the motion vector of the stapedius muscle (blue) in pixels with the strength of the stimulus, however if the stimulus is too low, no electrical evoked stapedius reflex is triggered. Noise in the motion trajectory is remaining heartbeat which was not removed by the stabilization mechanism of the software

Conclusion

It can be shown, that an automated detection of the electrical evoked stapedius reflex is possible with a digital surgical microscope. The automated routine detected 9 reflexes more than the surgeon, however in further studies more surgeons have to rate the videos to verify the surgeon has not overseen reflexes. Nevertheless, with our study we demonstrated, that not only identification of the reflex is possible but furthermore a quantification.

If, in a larger data series, these results can be confirmed, a real-time tracker to analyze intraoperatively the electrical evoked stapedius reflex of the stapedius muscle will be implemented. This would simplify the time-consuming process of post-operative adaption of cochlear implants and enhance the precision significantly.

Adaptive infrared patterns to enhance microscope intraoperative surface reconstruction for varying zoom levels

S. Milosavljevic[1], Z. Bardosi[1], Y. Oezbek[1], W. Freysinger[1]
[1]Medical University Innsbruck, ENT, Innsbruck, Austria

Keywords Stereo reconstruction · Registration · IR pattern · Intraoperative

Purpose

Dense stereo reconstruction of surgical surfaces in stereo microscope views during surgical interventions is challenging due to homogeneous textures like bone or skin, e.g., over-illumination, specular reflections, or occlusion. Accurate stereo reconstructions are hard to achieve without introducing additional visual cues that provide salient features.

Projection of random dot pattern into the surgical scene is proposed [1]. This introduces additional texture features and thus reduces the homogeneity of the visual scene for disparity estimation. Contrary to static patterns that are known only to work well for a specific zoom level this approach can handle different zoom-levels. So far, patterns are used neither in setups where distances are lower than 1.5 m nor for very small structures (nerves, blood vessels, etc.) [3] relevant for the present surgical application.

Accurate three-dimensional stereo reconstructions are of utmost relevance when intraoperative resection margins of the surgical wound should be related to preoperative plans. Segmented 3D model of the region of interest can easily be created from preoperative radiological data (CT or MR, e.g.). In order to monitor the evolution of surgery in relation to the preoperative model, a dense and precise stereo reconstruction is an absolute requirement for correct co-registration and data extraction.

Conventional surface reconstruction techniques for stereo views from a surgical microscope will not provide accurate reconstructions due to lack of texture information in the scene [1].

To overcome these issues an adaptive, scalable infrared pattern is proposed; patterns are projected that are dynamically adjusted to the varying camera parameters to provide optimal dense surface reconstructions across various zoom-levels. This approach is expected to yield more accurate and denser surface reconstructions for a wide range of zoom-levels.

Methods

The pattern generation and surface reconstruction is implemented within a generic navigation framework that provides surgical navigation, segmentation of the medical data, image acquisition, zoom and focus modification, stereo calibration, disparity estimation, surface registration (ICP) and identification of relevant anatomical structures. The framework is built with open-source libraries (ITK, VTK, OpenCV, PCL, QT, IGSTK, CMake). The surgically relevant information, such as segmented reconstructed resection surfaces or nearby important anatomical structures, is presented as an augmented reality view within the eyepiece of the surgical stereo microscope.

The microscope is equipped with two IDS UI-3080CP-M-GL monochrome cameras capable of detecting IR light at 850 nm wavelength (IDS GmbH, Germany). The stereo camera setup was calibrated for each zoom level and data were stored into a zoom-level addressed lookup table. The stereo camera-calibration [2] was performed with a 9×6 checkerboard pattern, with each square having an area of 3×3 mm^2. For each zoom level, 15 pairs of images were taken simultaneously with the two triggered cameras.

To generate the pattern, microscope zoom values were used to define dot dimensions/scale. Knowing the zoom level and the distances between points in the camera space, differences in the back-projection were applied to preserve the distance between the points in the projector space.

The pattern itself was projected into the surgical scene using a modified DLP projector (Aleman, Texas Instruments, Germany), where the micro mirror-array was changed to an IR-LED light source (wavelength 850 nm, power 5 W).

To evaluate the accuracy of the achieved reconstruction the proposed system was run with various zoom-levels on a realistic phantom. A 3D-print of a scanned ear lobe of an anonymized CT data set served as the reference surface. The model was scanned with a high-quality manual optical 3D scanner (Steinbichler GmbH, Germany) to provide a reference surface for evaluating the reconstruction accuracy of the microscopic setup.

The disparity maps within the reconstruction were estimated with semi global block matching (SGBM)[4], followed by a weighted least square smoothing.

In order to provide a colorized 3D depth-map of the scene, each reconstruction required two image acquisitions:

- The first image is taken while the IR pattern projection is active. At this step an IR band high pass filter (LEE 87, 730 nm wavelength and above) was used filter out the visible parts of the light spectrum; this helps avoiding artifacts due to the strong illumination typically used in the operating room.
- The second image is taken in the visible light spectrum to colorize the point cloud.

To evaluate the performance of the microscope surface reconstruction and the effect of applying dynamic pattern projection, reconstructions were performed for 6 zoom levels, with three different cases for each zoom-level:

- Without pattern
- Static random pattern
- With the dynamically scaled pattern

The reconstructed surfaces were registered to the reference surface using point based rigid-body registration between two rigid bodies (microscope surface, defined with four ArUco markers, OpenCV) and the CT segmented object, defined with four markers (X Spot CT marker, 1.5 mm, Beekley Corp.), placed beneath the origin of each ArUco marker, and with active NDI Optotrack certus navigation).

The quality of the surface reconstruction is quantified by the average distance between the reconstructed points and the reference surface (which is approximated as a triangulated mesh of the reference scan).

Results

Qualitative measurements were performed, showing a significant difference between different approaches in favor of the adaptive pattern. Significantly better reconstruction is achieved with pattern for different zoom levels and outlier reduction improvement is viable, while depth perception of the smallest details remains trustful (Figs. 1, 2). Quantitative measurements are ongoing,

Fig. 1 Static pattern with higher zoom showing the external ear and parts of the lateral skull

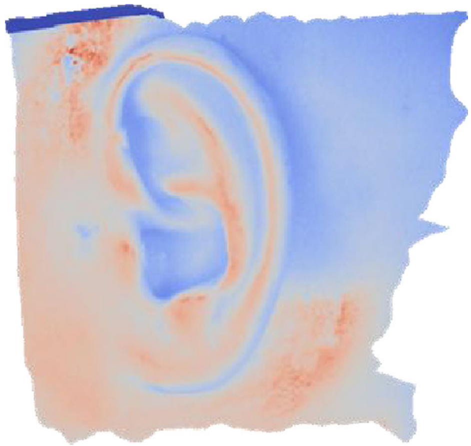

Fig. 2 Same scene imaged with the adaptive pattern

Conclusion

While the quantitative evaluation of the proposed system is still ongoing, the initial results indicate a significant improvement in reconstruction accuracy when dynamic patterns are used. These results suggest that the proposed dynamic patterns will allow to create, high-quality surface reconstructions for stereo views with surgical microscopes under the typical conditions of an ENT surgical scenario.

References

[1] Jeong J, Shin H, Chang J, Lim E, Choi S. M, Yoon K, Cho J (2013) High-Quality Stereo Depth Map Generation Using Infrared Pattern Projection. ETRI 6(35): 1011–1020

[2] Zhang Z (2000) A Flexible New Technique for Camera *Calibration. IEEE 22(11): 1330–1334*

[3] Gonzales-Jorge H, Zancajo S, González-Aguilera D, Arias P (2015) Application of Kinect Gaming Sensor in Forensic Science. Journal of Forensic Sciences 60(1): 206–211

[4] Hirschmuller H (2007) Stereo processing by Semiglobal matching and mutual Information. IEEE Transactions on Pattern Analysis and Machine Intelligence 30(2): 328–341

Intraoperative cone-beam CT navigation for benign bone tumor surgery

T. van Steenbergen[1], I. van der Geest[2], D. Janssen[2], M. Rovers[3], J. Fütterer[1]

[1]Radboudumc, Radiology and Nuclear Medicine, Nijmegen, Netherlands

[2]Radboudumc, Orthopedics, Nijmegen, Netherlands

[3]Radboudumc, Health Evidence, Nijmegen, Netherlands

Keywords Navigation · Hybrid operating room · Orthopedic surgery · Oncology

Purpose

Intralesional curettage is the most common treatment for symptomatic benign bone tumors [1]. The current standard intraoperative imaging technique used to support the orthopedic surgeon is fluoroscopy, which provides two-dimensional (2D) information. Fluoroscopy provides poor visualization of tumors in complexly shaped bones and in the ends of long bones. For these cases, surgical navigation using three-dimensional (3D) images is a potential alternative.

The purpose of this study is to assess the feasibility of navigated benign bone tumor surgery using intraoperative cone-beam CT (CBCT). We describe the workflow, indications for usage of navigation, subjective image quality and registration accuracy, and procedure and set-up times.

Methods

Nine consecutive patients (median age, 36 years; age range, 11–56 years) with different types of benign bone tumors were enrolled in this study. As bone tumors can occur in every bone of the body, a preoperative position planning of patient, optical camera (Curve, Brainlab, Munich, Germany) and reference base was acquired for every patient (Fig. 1). A dedicated technician ensured the execution of this planning and operated the navigation system.

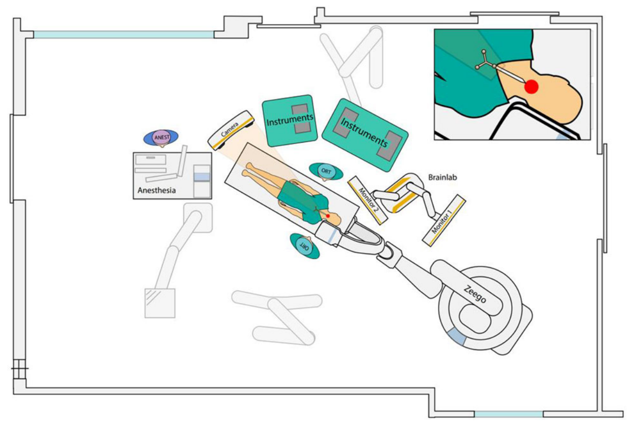

Fig. 1 The preoperative position planning for a patient with an osteoid osteoma in the C7 vertebra. This depicts how to position the patient, where to place the navigation system and camera and where to place the reference base. The red circle indicates the lesion

After attaching the reference base to the affected bone, the intraoperative CBCT was acquired with a floor-mounted multi-axis robotic C-arm system (Artis Zeego, Siemens Healthcare, Forchheim, Germany). The scan was automatically registered to the patient. Registration was visually verified using a tracked pointer. Navigation was used both as a confirmation of position and to assess direction. In case of uncertainty about entire tumor removal, a control CBCT scan was acquired with the possibility of directly continuing navigation based on the current anatomy.

We wanted to define clear indications for the use of CBCT navigation that can be applied to all variations in benign bone tumors. For this the surgeon was asked to list the reasons for the use of navigation per patient, if navigation indeed brought added value, and the reasons for this added value. CBCT image quality for each of the patients was subjectively scored by a radiologist and the treating orthopedic surgeon on a five-point scale (very poor, poor, acceptable, good, very good). The orthopedic surgeon scored the registration accuracy using the same five-point scale. Surgical time was extracted from the anesthesiology logs. The time to set up navigation was split into acquiring the CBCT and verifying the registration accuracy. The verification time also included moving all instrument tables and monitors back into place, as well as properly visualizing the CBCT. These times were extracted from the navigation system log files.

Results

Intraoperative CBCT navigation was properly set up and available throughout the procedure for all of the nine patients. The surgeon reported added value of CBCT in all cases, except for a patient with an ulnar deformation due to multiple osteochondroma. The deformation made it difficult to appreciate the osteochondroma in all planes of the 3D scan. Reasons to use navigation in the surgery of benign bone tumors were: closeness to vital structures (e.g. epiphysis, joint cartilage, spinal cord), expected poor visibility of the tumor and bone on fluoroscopy and repeated surgery.

Both the radiologist and orthopedic surgeon gave the tumor visibility and tumor delineation a median score of "good". The orthopedic surgeon gave the vital structure visibility and registration accuracy a median score of "very good". The median procedure time was 85 min (range 54–104 min). The median scan time was 5 min (range 2.5–15.5 min) and the median verification time was 3 min (range 2–5.5 min). One case of improper initial patient positioning increased the scan time, because the C-arm could not perform a rotation. No complications were observed during surgery.

Conclusion

According to the literature, preoperative CT navigation did not significantly increase surgical time for curettage of atypical cartilaginous tumor as compared to non-navigated surgery [2]. Due to the heterogeneity in benign bone tumor patients, it was not possible for us to compare procedure times to a historical cohort to provide a realistic estimation of the extra time needed to set up intraoperative CBCT navigation. We found the current set-up time acceptable given the benefits of navigation.

In conclusion, intraoperative CBCT navigation for benign bone tumor surgery seems feasible and safe. Indications for navigation in daily clinical practice are an expected poor visibility on fluoroscopy, closeness to vital structures or repeated surgery.

References

[1] Hakim DN, Pelly T, Kulendran M, Caris JA (2015) Benign tumours of the bone: A review. J Bone Oncol 4(2): 37–41

[2] Gerbers JG, Stevens M, Ploegmakers JJW, Bulstra SK, Jutte PC (2014) Computer-assisted surgery in orthopedic oncology: Technique, indications, and a descriptive study of 130 cases. Acta Orthop 85(6): 663–669

Computed analysis of the hindfoot alignment in 3D after a medializing calcaneal osteotomy using a pre- and post-operative weightbearing CT

M. Peiffer[1], A. Burssens[1], A. Barg[2], T. Leenders[3], S. Clockaerts[4], M. Richter[5], J. Victor[1]

[1]University Hospital of Ghent, Department of Orthopaedic Surgery and Traumatology, Gent, Belgium

[2]University Hospital of Utah, Department of Orthopaedics, Salt Lake City, United States

[3]AZ Monica, Department of Orthopaedics and Traumatology, Antwerpen, Belgium

[4]Az Groeninge, Department of Orthopaedics and Traumatology, Kortrijk, Belgium

[5]Hospital Nuremberg/Rummelsberg, Department of Orthopaedic Surgery and Traumatology, Nuremberg/Rummelsberg, Germany

Keywords Hindfoot deformity · 3D Analysis · Re-alignment surgery · Weight bearing CT

Purpose

An adult acquired flat foot (AAFD) is a progressive disabling condition characterized by a complex 3D deformity [1]. The diagnostic work up to differentiate the pathological stages is made clinically and by medical imaging. The latter currently consists of plain radiographs, but the interpretation is hampered by superimposition of the bony structures due to the 2D projection. This causes inaccurate measurements, which make it difficult to propose uniform surgical treatment guidelines, when conservative measurements fail. A medializing calcaneal osteotomy (MCO) is one of these surgical procedures frequently performed to correct the valgus hindfoot in a stage II AAFD. This stage is caused by a posterior tibial tendon (PTT) dysfunction and the goal of this procedure is to unload the PTT by the medial translation of the calcaneus [2]. However currently little is known on its accurate influence regarding the hindfoot alignment (HA), due to a lack of structural 3D insights. The aim is therefore to assess the influence of a MCO on the 3D HA using automated computer aided design (CAD) analysis of the images retrieved from a weightbearing CT (WBCT).

Methods

Twelve patients with a mean age of 49.4 years (range 18–67 years) were prospectively included in a pre-post study design. Indications for a surgical correction by a MCO with a solitary translation of the calcaneus consisted of an adult acquired flat foot stage II (N = 10) and a posttraumatic valgus deformity (N = 2). Fixation of the osteotomy was performed either using a step plate or double screw. A WBCT was obtained pre- and post-operative. Images were subsequently segmented to allow a 3D assessment of the HA (HA3D) by a computed angle between the anatomical tibia axis and the axis connecting the inferior calcaneus point and the centroid of the talus in the coronal plane using 3-matic software (Materialise, Leuven, Belgium (Fig. 1). The tibia in the HA3D was separately assessed by computed best-fitted anatomical tibia axis (TAX 3D) and the axis to determine the tibial rotation (TR3D) by connecting the computed most outer point of the anterior and posterior tubercle of the incisura fibularis (Fig. 1). The difference in pre- and post operative angles and displacements could be obtained from an automated custom Matlab script (MathWorks, Natick, MA, USA) after the pre- and post-operative foot were fitted on top of each other. This was performed according to the part of the calcaneus anterior to the cutting plane of the osteotomy, because this is the fixed part of the calcaneus during surgery. The computed centroid of the anterior calcaneus part served as an origin of the Cartesian coordinate system and was determined according to the method of Kuo et al. [3] (Fig. 2). The computed centroid of the posterior calcaneus part in the pre- and post-operative foot was used to calculate the medial translation. Linear regression analysis was performed to determine if the amount of calcaneal translation could predict the postoperative change in hindfoot angle by calculation of the R-square and visualization of the corresponding linear regression model (Tables 1, 2).

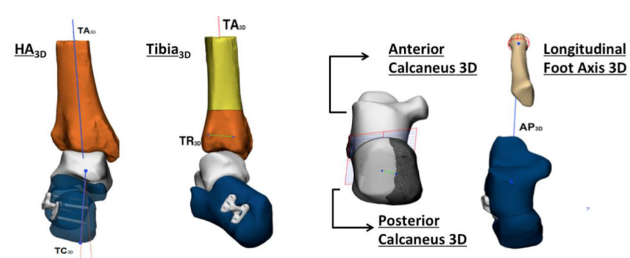

Fig. 1 Computer aided design (CAD) operations to sequentially determine the HA3D, TAx3D and TR3D. The posterior and anterior part of the calcaneus were determined in 3D to respectively calculate the medial translation, to fit both feet on top of each other and to configure the Cartesian coordinate system based on the longitudinal foot axis

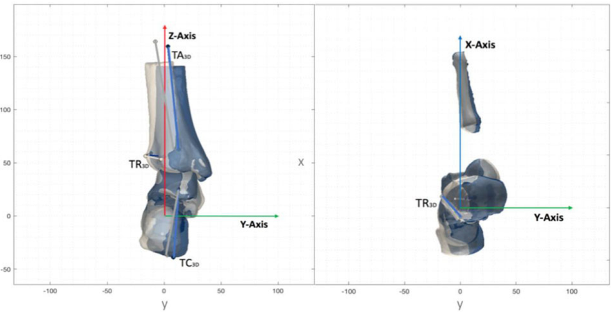

Fig. 2 Computed 3D analysis of the pre- and post-operative correction superimposed on top of each other after a Medializing Calcaneal Osteotomy (MCO). Depiction of the Cartesian coordinate system in the coronal and axial plane

Table 1 Pre-and post-operative difference after a MCO

	PREOP		POSTOP		Change		
	Mean	(SD)	Mean	(SD)	Mean	95% CI	*p* value
HA3D	18.21	− 6.6	9.31	− 6.18	8.89	[5.99, 11.80]	< 0.001
TC3D	11.41	− 6.43	5.31	− 6.54	6.11	[4.14, 8.07]	< 0.001
TA3D	6.8	− 3.38	4.11	− 2.77	2.69	[1.79, 3.59]	< 0.001
TR3D	− 27.11	− 4.77	− 28.8	− 5.89	1.69	[0.41, 2.97]	0.016

Table 2 Results of linear regression analysis

	HA3D		
	Coefficient	95% CI	*p* value
Amount of MCO intercept	2.15	[1.68, 2.62]	< 0.001
	− 3.39	[− 6.16, − 0.61]	0.023

Results

The mean medial translation of the calcaneal osteotomy during surgery was 5.72 mm (SD = 3.9). The mean HA3D pre-operatively equaled 18.21 degrees of valgus (SD = 6.6) and post-operatively 9.31 degrees of valgus (SD = 6.18). The Paired Student's *t* test showed a significant correction of 8.89 degrees (95% CI [5.99, 11.80], $P < 0.001$). The mean TAX 3D pre-operatively was 6.80 degrees of valgus (SD = 3.38) and post-operatively 4.11 degrees of valgus (SD = 2.77), with a significant difference of 2.69 degrees (95% CI [1.79, 3.59], $P < 0.001$). The mean TAXR 3D pre-operatively was − 27.11 degrees (SD = 4.77) and post-operatively − 28.80 degrees (SD = 5.98) and showed a significant difference of 1.69 degrees (95% CI [0.41, 2.97], $P = 0.016$). Linear regression analysis demonstrated a significant relationship ($R^2 = 0.934$, $P < 0.001$) with following equation: Change in hindfoot angle (degrees) = 2.15 × Amount of MCO (mm) − 3.39.

Conclusion

This study shows an effective correction of the 3D valgus hindfoot alignment in an AAFD. It appears that the correction is not only situated in thecalcaneus but also to a lesser extent in the tibia and this resulted in 15% of the achieved HA correction. The overall HA correction is demonstrated by a linear relationship with a formula that can be of use to plan the amount of medial calcaneus translation needed during the osteotomy to obtain the desired change in hindfoot alignment. This linear relationship is in accordance with previous research based on plane 2D radiographs [4]. The main limitation of this study is the small patient cohort. Future pre- and post-operative research could therefore be aimed at validating the obtained formula in clinical practice using large-scale prospective cohort studies. Future peroperative studies could use the 3D computed axes described in this study integrate them on the images of an intraoperative CT to allow a computer assisted surgical correction in realtime as shown previously for other pathologies in the foot and ankle by Richter et al. [5]

References

[1] Brockett CL, Chapman GJ (2016) Biomechanics of the ankle. Orthopaedics and trauma 30 (3): 232–238

[2] Nyska M, Parks BG, Chu I-T, Myerson MS (2001) The contribution of the medial calcaneal osteotomy to the correction of flatfoot deformities. Foot & ankle international 22 (4): 278–282

[3] Kuo CC, Lu HL, Leardini A, Lu TW, Kuo MY, Hsu HC (2014) Three dimensional computer-graphics based ankle morphometry with computerized tomography for total ankle replacement design and positioning. Clinical Anatomy 27 (4): 659–668

[4] Chan JY, Williams BR, Nair P, Young E, Sofka C, Deland JT, Ellis SJ (2013) The contribution of medializing calcaneal osteotomy on hindfoot alignment in the reconstruction of the stage II adult acquired flatfoot deformity. Foot & ankle international 34 (2): 159–166

[5] Richter M, Geerling J, Frink M, Zech S, Knobloch K, Hankemeier S, Krettek C (2006) Computer-assisted surgery (CAS) based correction of posttraumatic ankle and hindfoot deformities—Preliminary results. Foot and ankle surgery 12 (3): 113–119

Computed templating of syndesmotic ankle lesions by use of 3D analysis in weightbearing and non-weight bearing CT

A. Burssens[1], H. Vermue[1], A. Barg[2], F. Lintz[3], C. de Cesar Netto[4], J. Victor[1], K. Buedts[5]
[1]University Hospital of Ghent, Department of Orthopaedic Surgery and Traumatology, Gent, Belgium
[2]University Hospital of Utah, Department of Orthopaedics, Salt Lake City, United States
[3]Clinique de l'Union, Department of Orthopaedic Surgery and Traumatology, Toulouse, France
[4]Hospital for Special Surgery, Department of Orthopaedic Surgery and Traumatology, New York, United States
[5]ZNA Middelheim, Department of Orthopaedic Surgery and Traumatology, Antwerpen, Belgium

Keywords Syndesmotic ankle lesion · 3D analysis · Weight bearing CT · Pre-operative planning

Purpose

Syndesmotic lesions of the ankle have shown to be challenging injuries towards diagnosis and surgical treatment. This could be mainly attributed to the limitations of 2D imaging. These make it difficult in the diagnostic process to accurately determine the extent of the lesion and are hampered by numerous manual measurement methods [1]. During the surgical process it is difficult to verify if an anatomical reduction is achieved due to the absence of 3D insights concerning the tibiofibular congruence [2]. The aim of this study is therefore to develop a reproducible method to quantify the displacement of a syndesmotic lesion in all six degrees of freedom based on computed 3D imaging.

Methods

Eighteen patients were retrospectively included having a unilateral syndesmotic lesion. N = 12 sustained a high ankle sprain and a bilateral weightbearing conebeam CT was obtained because of positive clinical syndesmotic tests. N = 6 presented with a fracture associated syndesmotic lesion and were imaged by a bilateral non-weightbearing CT. The non-affected ankle was used as template after being mirrored and matched on the contralateral ankle containing a syndesmotic lesion (Fig. 1). The distal fibula was marked by computer calculation of the most outer point of the anterior tubercle, posterior tubercle and apex malleolis lateralis. The change of the coordinates attached to these landmarks towards the unaffected fibular position was used to quantify the syndesmotic lesion (Fig. 2). A Cartesian coordinate system was defined based on the tibia [3]. The origin was defined in the coordinate were the tibial shaft axis intersected of the tibial joint surface. The tibial axis (TAx) was defined as the z-axis and dermined by connecting the computed centroid of the plane 5 and 10 cm above the tibial joint surface. The y-axis was defined to run perpendicular on to the z-axis and the axis connecting the most anteromedial (AMP) and anterolateral point (ALP) on the distal articular surface of the tibia. The x-axis was defined as the cross-product of the y- and z-axis. Intra- and interobserver variability was assessed as the distance between the mean position of a landmark to the observed position of the landmark. For the obtained coordinates an inter class correlation coefficient (ICC) was calculated. A control group of seven patients (N = 7) was used to see if these changes differed from the normal variation in tibio-fibular congruency (Fig. 2).

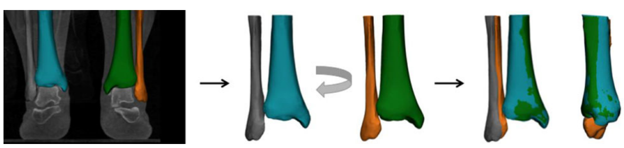

Fig. 1 Sequential 3D analysis of a syndesmotic ankle lesion. CT image slices were segmented towards a 3D volume, the non-affected left ankle (green orange) was mirrored and fitted on top of the right ankle based on the tibias. This points out an increased medio-lateral displacement of the fibula (difference orange-grey)

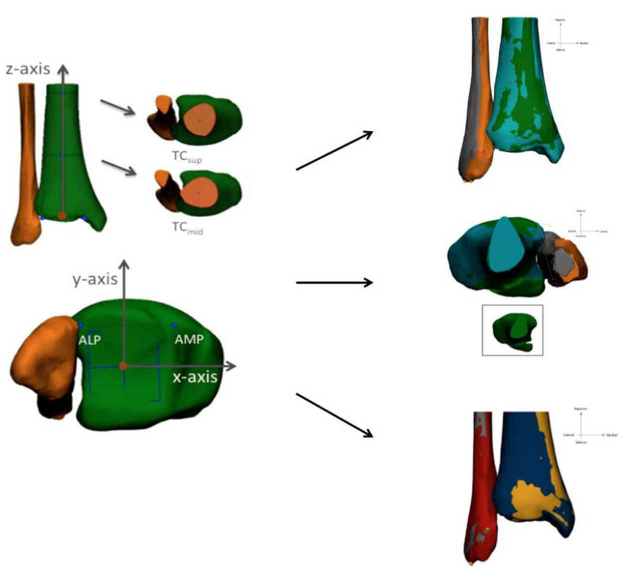

Fig. 2 Displacement in the sprained-, fracture associated—and control group according to the Cartesian coordinate system based on the computed anatomical landmarks

Results

The main findings showed a statistical significant difference in the mean mediolateral diastasis of both the sprained group (M = 1.60 mm, SD = 1.02) and the fracture group (M = 1.69 mm, SD = 0.62) compared to the control group (P < .001). The mean exorotation was statistically different when comparing the sprained group (M = 4.68°, SD = 2.74) and the fracture group (M = 6.97°, SD = 3.02) towards the control group (P < .05). The mean antero-posterior translation was only significantly different when comparing the fracture group (M = − 4.73 mm, SD = 4.53) towards the sprained group (M = − 0.91 mm, SD = 1.26) and the control group (M = − 0.26 mm, SD = 1.53) (P < .05). The intra observer variability (range 0.65–1.52 mm) was better than the inter observer variability (range 0.6–1.91). This tendency was also seen when comparing the computed points (range 1.52–1.87 mm) towards the manually selected points (range 0.6–1.16 mm) (Table 1). The ICC values of the automatic computed coordinates were assessed and showed to be excellent with a range from 0.98 to 0.99.

Table 1 Overview of the mean fibular deviations in all six degrees of freedom and subsequent

Image modality	a. Control (n = 7) WBCT	b. Sprain (n = 12) WBCT	c. Fracture (n = 3) non-WBCT	p value
ANOVA testing with post hoc Tukey analysis				
Translations (mm)				
Anterior/posterior	− 0.26 ± 1.53	− 0.87 ± 1.26	− 4.73 ± 4.53	**< .05**[b, c]
Lateral/medial	− 0.22 ± 0.41	1.60 ± 1.02	1.95 ± 1.02°	**< .001**[a, b]
Superior/inferior	− 0.45 ± 1.15	− 0.69 ± 0.72	0.61 ± 1.65	0.12
Rotations (°)				
Axial (exo/endo)	0.22 ± 1.73	4.80 ± 3.00	6.97 ± 7.11	**< .05**[a, b]
Sagital (ante-/recurvatum)	− 0.21 ± 0.90	− 0.53 ± 1.00	− 2.47 ± 1.57	**< .05**[b, c]
Frontal (valgus/varus)	− 0.41 ± 0.63	0.10 ± 1.14	0.55 ± 0.56	0.2

WBCT weightbearing computed tomography

[a]The sprained group shows significant difference compared to the control group

[b]The fracture group shows significant difference compared to the control group

[c]The fracture group shows significant difference compared to the sprained group

Conclusion

This study shows an effective method to quantify a unilateral syndesmotic lesion of the ankle. The pathological measurements differed from the normal distal tibio-fibular configuration in the syndesmotic complex. This sequential analysis is of use for an accurate diagnosis and a pre-operative planning to know in advance which correction needs to be achieved to have the fibula at proper length correctly rotated, and reduced into the syndesmosis with no anterior, posterior or lateral displacement. The main limitation of this study is the absence of cut off values to differ a normal from a pathological syndesmotic congruence of the ankle. Based on the current literature a mediolateral diastasis of 1.5 mm between sides tended to have worse functional results [4]. However this is currently under debate and gives no information regarding other types of displacements. Future anatomical research could therefore be aimed at investigating the normal range of the 3D distal tibiofibular congruence in a large-scale cohort study. Future peroperative studies could use the anatomical landmarks described in this study could be marked with surgical navigation tools and integrate them on the images of an intraoperative CT to allow a computer assisted surgery as shown previously for other pathologies in the foot and ankle by Richter et al. [5]

References

[1] Krähenbühl N, Weinberg MW, Davidson NP, Mills MK, Hintermann B, Saltzman CL, Barg A (2017) Imaging in syndesmotic injury: a systematic literature review. Skeletal radiology: 1–18

[2] Rammelt S, Zwipp H, Grass R (2008) Injuries to the distal tibiofibular syndesmosis: an evidence-based approach to acute and chronic lesions. Foot and ankle clinics 13 (4): 611–633

[3] Yamaguchi S, Sasho T, Kato H, Kuroyanagi Y, Banks SA (2009) Ankle and subtalar kinematics during dorsiflexion-plantarflexion activities. Foot & ankle international 30 (4): 361–366

[4] Wikerøy AK, Høiness PR, Andreassen GS, Hellund JC, Madsen JE (2010) No difference in functional and radiographic results 8.4 years after quadricortical compared with tricortical syndesmosis fixation in ankle fractures. Journal of orthopaedic trauma 24 (1): 17–23

[5] Richter M, Geerling J, Frink M, Zech S, Knobloch K, Hankemeier S, Krettek C (2006) Computer-assisted surgery (CAS) based correction of posttraumatic ankle and hindfoot deformities—Preliminary results. Foot and ankle surgery 12 (3): 113–119

Tracking of spinal curvature using a hybrid navigation system and interpolation method

M. Kunz[1], B. Chan[1], A. Kashigar[2], R. E. Ellis[1], D. Borschneck[2]
[1]Queen's University, School of Computing, Kingston, Canada
[2]Queen's University, Department of Surgery, Kingston, Canada

Keywords Image-guided scoliosis surgery · Electromagnetic tracking · Patient-specific instruments · Interpolation

Purpose

Scoliosis is a medical condition that describes abnormal curvature of the spine, in which surgical correction is recommended for more severe cases. The surgical intervention involves two major steps: (1) Screws are inserted into the vertebrae to allow the rod to be attached; (2) The curvature of the spine is corrected by manipulating hooks between the screws and the rod.

A number of studies have shown an improved accuracy of screw insertion using image-guidance [1, 2]. However, there has been little work on the use of image-guidance to support the spinal realignment. A previous study has shown that a hybrid tracking system in which electromagnetic (EM) tracking, combined with patient-specific templates, can accurately register spinal alignments [3]. In the proposed method, patient-specific templates which had parts of the anatomical surface of a vertebra integrated, allowed for an ad-hoc registration between an EM sensor (attached to the template) and the anatomical images. Preliminary results of this study showed a tracking accuracy of 1.67 mm (RMS error). However, the proposed method relied on the direct tracking of all relevant 17 vertebrae (L5–T1). The translation of this method into clinical applications would therefore require instrumentation of all 17 vertebrae with an EM sensor. The number of required sensors, as well as the number of cables in the surgical field, would decrease the clinical feasibility of the proposed method.

The hypothesis for this study was that interpolation methods can be used to model vertebra alignment between non-adjacent tracked vertebrae. The purpose of this study was to investigate if by interpolating vertebrae alignments, the number of directly tracked vertebras can be reduced by maintaining the tracking accuracy of the spinal alignment.

Methods

The study was performed on a spine model no. 1323-4 (Sawbones, Vashon Island, Washington, USA). A preoperative CT scan was obtained and 3d models for all vertebrae were created. For each vertebra, a custom-made registration template was created which allowed to securely fix a 6 degree of freedom electromagnetic sensor to the vertebra. Position and orientation of the sensor with respect to the 3d vertebra model were preoperatively determined and stored as registration information.

During the study, an EM tracker with a midrange transmitter was installed and the spine model was secured in three different scoliosis alignments. For each alignment, a 3D model of the spinal alignment was captured using a structured light scanner with a reported 3d point accuracy of 0.05 mm. This scanned model was used as the gold standard model for the spinal curvature.

For each of the three spinal alignments, the position and orientation of each relevant vertebra was tracked by attaching an EM sensor to the corresponding vertebra template and fitting the template to the vertebra.

In a simulation study, three different subsets with 9, 7 and 6 tracked vertebrae were used (Fig. 1). In each configuration, for the remaining (non-tracked) vertebra, position and orientation was determined by interpolation of the tracking information of the surrounding vertebra. For interpolation of the vertebra position, we implemented a spline curve fitting method, in which the position of the tracked vertebras were used to fit the curve. Position of the non-tracked vertebras were interpolated on the curve at a proportional distance. Orientation of the non-tracked vertebrae were determined using a spherical linear quaternion interpolation (SLERP) method.

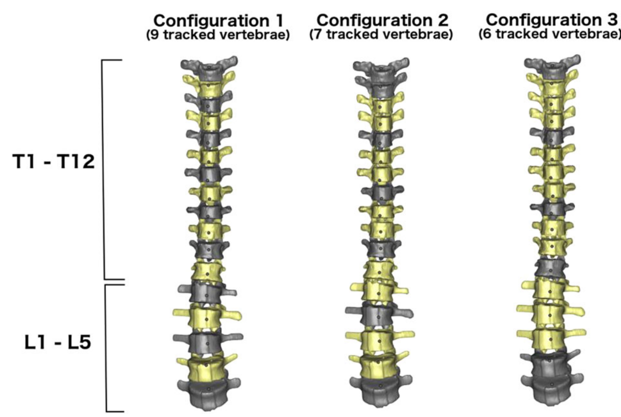

Fig. 1 Configurations for tracking of subsets of vertebrae. Tracked vertebrae are marked in dark grey, non-tracked vertebrae are marked in yellow

Accuracy of spinal alignment for each configuration was measured by determining the position, orientation and RMS error between the interpolated and the tracked vertebra alignment. The accuracy of the overall spinal alignment was determined by comparing it to the gold standard alignment model. RMS error as well as the deviation of Cobb, Lordosis and Kyphosis angles between the two models were determined. All differences were statistically compared using a paired *t* test.

Results

On average, the interpolated positions of the vertebrae differed by 2.7 mm (SD 0.12) from the tracked position in configuration 1, by 3.2 mm (SD 0.27) in configuration 2 and by 4.2 mm (SD 0.64) in configuration 3. Compared to configuration 1, the position interpolation for both other configurations had significantly higher errors ($p < 0.05$).

On average, the interpolated orientation differed by 3.35 deg (SD 0.7) from the tracked orientation in configuration 1, by 4.2 deg (SD

1.05) in configuration 2, and 6.25 deg (SD 3.05) in configuration 3. None of these errors were not significantly different.

Compared to the gold standard alignment models, the model in which all vertebrae were tracked had an average RMS error of 1.99 mm. For configuration 1 the average RMS error was 2.25 mm, for configuration 2, 2.51 mm and for configuration 3, 2.82 mm. For all three configurations, the RMS errors were significant higher compared to the all-tracked model.

Table 1 shows the deviation in the Cobb, Kyphosis, Lordosis and Rotation angle between the all-tracked spinal alignment model and the model for all three interpolation configurations.

Table 1 Deviation between clinical parameters between tracked and interpolated alignments

	Configuration 1	Configuration 2	Configuration 3
Cobb	0.63 (SD 0.2)	1.3 (SD 0.8)	9.3 (SD 9.1)
Kyphosis	3.1 (SD 0.8)	5.2 (SD 0.9)	8.7* (SD 2.8)
Lordosis	2.2 (SD 3.5)	8.1 (SD 11.7)	9.1 (SD 14.3)
Rotation	4.3 (SD 4.7)	7.6 (SD 5)	8.4 (SD 5)

All values are given in degree. *Significant deviation ($p < 0.05$)

Conclusion

Our simulation study showed an increase in RMS errors for the spinal alignment from 1.99 mm with 17 sensors to 2.82 mm with only 6 sensors. When evaluating the results for each vertebra we found that although the position error increased significantly by reducing the number of sensors, we did not see the same significant increase in the angular error. Similarly, we did not see a significant increase of errors for the clinical alignment errors, except for the kyphosis angle with only 6 sensors.

Based on our results, we believe the reduction of sensors from 17 to 7, combined with the proposed interpolation methods, might provide clinical relevant models for the tracking of the spinal curvature.

References

[1] Kotani Y, Abumi K, Ito M, Takahata M, Sudo H, Oshima S, Minami A (2007) Accuracy analysis of pedicle screw placement in posterior surgery: comparison between conventional fluoroscopic and computer-assisted technique. Spine, vol. 32, no. 14, pp. 1543–1550

[2] Gelanlis ID, Paschos NK, Pakos EE, Politis AN, Arnaoutoglou CM, Karageorgos AP, Xenakis TA (2012) Accuracy of pedicle screw placement: a systematic review of prospective in vivo studies comparing free hand, fluoroscopy guidance and navigation techniques. Eur Spine J, vol. 21, no. 2, pp. 247–255

[3] Ellis RE, Kunz M, Chan B, Kashigar A, Boschneck D (2017) Minimally invasive image-guided scoliosis method—A hybrid tracking approach. Int J CARS, 12(Suppl 1)

Accurate wrist immobilization for percutaneous scaphoid navigation

R. Ellis[1], P. St John[1], M. Armstrong[2], R. W. Sellens[3], D. R. Pichora[2]
[1]Queen's University, School of Computing, Kingston, Canada
[2]Queen's University, Surgery, Kingston, Canada
[3]Queen's University, Mechanical Engineering, Kingston, Canada

Keywords Surgical navigation · Wrist immobilization · Scaphoid fixation · Radiological assessment

Purpose

Fractures to the scaphoid bone in the wrist are one of the most commonly reported fractures in emergency clinics. The scaphoid is a small irregularly shaped bone that is the most commonly fractured carpal bone in the wrist. Optimal treatment often requires surgical fixation of scaphoid fractures, usually by placement of a cannulated screw under fluoroscopic guidance. Navigation of percutaneous scaphoid fixation has been reviewed and recommended for reducing radiation exposure while maintaining technical accuracy and precision [1]. Navigation also offers the potential of improving accuracy and precision of screw placement, reducing the number of drilling passes needed to attain satisfactory placement.

Navigated scaphoid fixation has been performed using preoperative CT images, intraoperative fluoroscopy, and intraoperative cone-beam CT; most methods use an immobilization device to hold the forearm and hand in relative stability, in part because of the difficulty in directly tracking the small scaphoid that is surrounded by other carpal bones. Accuracy of navigation in cadaver studies [2, 3] is unclear at best. Recent use of ultrasound for registration has found substantial motion between the target scaphoid and the tracked immobilizer [4] that required manual correction prior to navigation. Other studies have also observed wrist deformations under load during navigation testing.

The purpose of this study was to quantify the motion of the scaphoid relative to an immobilizer. If the relative motion is within a clinical "safe zone" of 1.8 ± 0.8 mm [5], then the immobilizer can be used as a geometric proxy for the target bone.

Three tasks were studied in cadaveric models: simulated scaphoid drilling, simulated ultrasound acquisition at a low contact load, and simulated ultrasound at a high contact load. Two states were studied to simulate immobilization, one that approximated that of previous work and a proposed state that was more geometrically stable but easily achieved intraoperatively.

Methods

The study was conducted with the approval of the relevant Institutional Review Board and respected the provisions of the Helsinki declaration. Materials included tantalum beads of 0.8 mm diameter, a custom forearm immobilization device instrumented with beads, 5 soft-embalmed cadaver forearms, a custom force-sensing load applicator, and a flat-panel fluoroscope. Each scaphoid was instrumented with 4 tantalum beads for radiographic tracking.

Each forearm specimen was tested in 2 states, unwrapped and wrapped. The unwrapped forearm was secured with two self-adhesive straps and the four fingers were secured with small plastic straps. The wrapped forearm and hand were additionally secured with Coban^{TM}; the states are shown in Fig. 1.

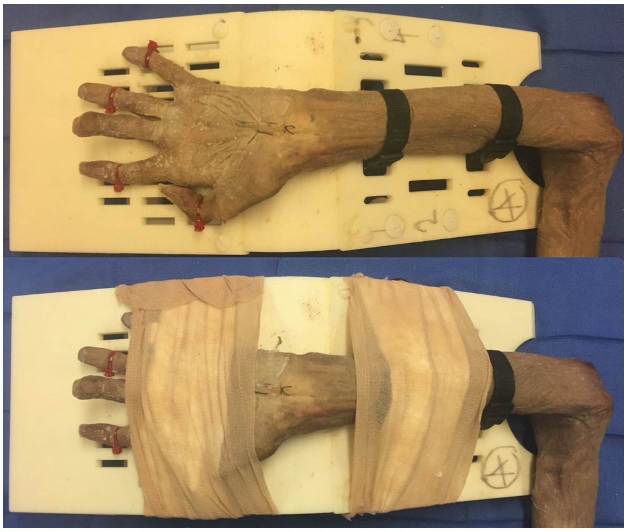

Fig. 1 Photographs of a representative cadaveric specimen in the custom immobilization device. Above: unwrapped, held with simple tapes. Below: wrapped with Coban adhesive wrap

In each state, each forearm was tested with 3 loads. The first load simulated scaphoid drilling; the second load simulated gentle ultrasound acquisition in the volar aspect, applied and verified by the loading device; and the third load simulated a more aggressive ultrasound acquisition, also volar and verified. These provided 6 testing scenarios for 5 forearm specimens.

Two fluoroscopic images were acquired in each scenario, one prior to loading and one during loading, from both the AP and ML views. The images were analyzed using custom software. In each image, the beads for the immobilizer and the scaphoid were used to compute the relative motion of the scaphoid beads in the pre-loading coordinate frame, recorded as the translation magnitude and the angle of rotation. In one scenario, full bead detection was not achieved.

For each scenario, the specimens were pooled by wrapping state. Accuracy was assessed using Student's t test in a 2-sided heteroscedastic analysis. Precision was assessed using the F test on the pools. Statistical significance was $p < 0.05$ for each test.

Results

Pooled data values are in Table 1. Comparing accuracy to the clinical safe zone of 1.8 ± 0.8 mm [5], specimens in the unwrapped state had translatory motion that equalled or exceeded the safety criterion. Specimens in the wrapped state were within the safe zone, statistically significantly for low-load ultrasound ($p < 0.05$) and trending lower at other loads.

Table 1 Means (μ) and standard deviations (σ) for test scenarios. Translation was in millimeters (mm) and rotation was in (degrees) for motion of each cadaver scaphoid relative to the immobilizer, measured from anterior–posterior (AP) and medial–lateral (ML) digital fluoroscopic radiographs of tantalum beads. Loads were for simulated drilling and for simulated ultrasound (US) acquisition

	Simulated Drilling, high load		Simulated US, low load		Simulated US, high load	
	Trans (mm)	Rot (deg)	Trans (mm)	Rot (deg)	Trans (mm)	Rot (deg)
Unwrapped AP, μ ± σ	2.8 ± 1.5	3.3 ± 2.3	1.7 ± 1.3	2.5 ± 2.2	2.4 ± 1.6	3.7 ± 2.5
Unwrapped ML, μ ± σ	1.3 ± 1.1	1.7 ± 1.4	1.9 ± 1.2	3.5 ± 2.6	2.3 ± 1.4	4.7 ± 2.5
Unwrapped, μ ± σ	2.0 ± 1.5	2.5 ± 2.0	1.8 ± 1.2	3.0 ± 2.4	2.3 ± 1.4	4.2 ± 2.4
Wrapped AP, μ ± σ	1.5 ± 0.6	2.9 ± 1.7	1.0 ± 0.3	2.0 ± 1.6	1.5 ± 0.4	2.2 ± 1.7
Wrapped ML, μ ± σ	0.4 ± 0.1	1.0 ± 0.5	0.7 ± 0.2	2.2 ± 0.5	0.9 ± 0.5	3.2 ± 1.6
Wrapped, μ ± σ	1.1 ± 0.7	2.1 ± 1.7	0.9 ± 0.3	2.1 ± 1.2	1.2 ± 0.5	2.7 ± 1.6
p value, T test (μ)	0.1	0.7	**0.04**	0.3	**0.04**	0.2
p value, F test (σ)	0.06	0.7	**0.001**	0.06	**0.01**	0.34

Comparing accuracy of the wrapped and unwrapped states, for high-load drilling the wrapped specimens trended lower in translatory motion ($p = 0.1$) and were not different in rotation. For low-load ultrasound the wrapped specimens were statistically significantly lower in translatory motion ($p = 0.04$) and trended lower in rotation. For high-load ultrasound the wrapped specimens were also statistically significantly lower in translatory motion ($p = 0.04$) and trended lower in rotation.

Comparing precision of the states, for high-load drilling the wrapped specimens trended lower in translatory motion ($p = 0.06$) and were not different in rotation. For low-load ultrasound the wrapped specimens were statistically highly significantly lower in translatory motion ($p = 0.001$) and trended lower in rotation. For high-load ultrasound the wrapped specimens were also statistically significantly lower in translatory motion ($p = 0.01$) and trended lower in rotation.

Verification using post-operative imaging did not show significant residual motion in any scenario.

Conclusion

Direct application of a forearm immobilizer produced translational and rotational motion that is comparable to values reported for ultrasound-registered scaphoid fixation [5]. The motions produced scaphoid displacements exceeding the clinical safe zone, suggesting that simple application could lead to poor clinical results in navigated scaphoid fixation.

Our relatively simple additional step was to wrap the forearm and hand using a conventional intraoperative elastic bandage, which is both conceptually appealing and clinically acceptable. In our radiological study, the motions produced by sample tasks were well within the clinical safe zone. There were statistically significant improvements in the accuracy (less mean motion) and the precision (less motion variance) produced by wrapping the specimens. There was no significant residual motion of the forearm, implying that the soft-tissue and fixation deformations were primarily elastic and quickly recovered to the original state.

For navigated scaphoid fixation that tracks an immobilization device, wrapping the anatomy onto the immobilizer is recommended for improved physical stability. Future work is needed to verify the application accuracy during cadaveric navigation, prior to clinical use.

References

[1] Smith EJ, Ellis RE, Pichora DR (2013) Computer-Assisted Percutaneous Scaphoid Fixation: Concepts and Evolution. *J Wrist Surg* 2(4): 299–305

[2] Liverneaux PA, Gherissi A, Stefanelli MB (2008) Kirschner wire placement in scaphoid bones using fluoroscopic navigation: a cadaver study comparing conventional techniques with navigation. *Int J Med Robot* 4(2): 165–173

[3] Citak M, O'Loughlin PF, Kendoff D (2010) Navigated scaphoid screw placement using customized scaphoid splint: an anatomical study. *Arch Orthop Trauma Surg* 130(7): 889–895

[4] Menapace KA, Larabee L, Arnoczky SP, Neginhal VS, Dass AG, Ross LM (2001) Anatomic placement of the Herbert-Whipple screw in scaphoid fractures: a cadaver study. *J Hand Surg* 26(5): 883–892

[5] Anas EMA, Seitel A, Rasoulian R, St John P, Ungi T, Lasso A, Darras K, Wilson D, Lessoway VA, Fichtinger G, Zec M, Pichora D, Mousavi P, Rohling R, Abolmaesumi P (2015) Registration of a statistical model to intraoperative ultrasound for scaphoid screw fixation. *Int J Comput Assist Radiol Surg* 11(6): 957–965

20th International Workshop on Computer-Aided Diagnosis and Artificial Intelligence

Chairman: Hiroyuki Yoshida, PhD (USA)

Deep volumetric residual learning for differentiating colorectal masses from ileocecal valves in CT colonography

J. Näppi[1], T. Hironaka[1], H. Yoshida[1]
[1]Massachusetts General Hospital, Radiology, Boston, United States

Keywords Computer-aided detection · Deep learning · CT colonography · Residual learning

Purpose

Although the clinical consequences of a missed colorectal cancer far outweigh those of a missed polyp, there has not been much effort to develop computer-aided detection (CADe) methods for colorectal masses in CT colonography (CTC) despite the fact that false negatives do occur and commercial CADe systems are known to miss certain types of masses [1]. One of the problems of CADe for mass detection is that normal ileocecal valves (ICVs) tend to imitate the visual appearance of colorectal masses (Fig. 1) [2]. Therefore, ICVs cause recurring false-positive (FP) CADe detections that frustrate radiologists who use CADe. It is not evident how to manually design features that could differentiate between ICVs and masses. However, deep learning has been shown to be able to determine effective discriminating features for image-based classification tasks. The purpose of this study was to perform a pilot evaluation of the performance of volumetric deep learning in differentiating colorectal masses from ICVs in CTC.

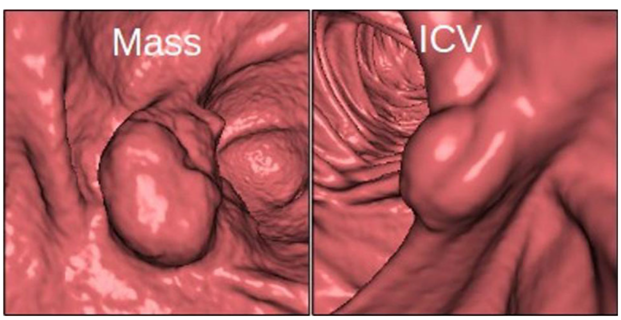

Fig. 1 Normal ICVs tend to imitate the visual appearance of colorectal masses in CTC

Methods

An 18-layer 3D-convolutional residual network (3D-ResNet) was constructed to classify 64 × 64 × 64-voxel volumes of interest (VOIs) by stacking together modular residual network unit blocks with skip connections and 3D-convolutional operators. We used the ResNet architecture because it has been recentlyshown to address the practical problems of constructing very deep (up to 1000 layers) convolutional networks that may be desirable for optimizing the performance of deep learning [3]. The 3D-ResNet was implemented using the Keras neural network application programming interface. To train and evaluate the 3D-ResNet, we sampled 196 CTC cases from our clinical CTC trial case collection. There were 115 biopsy-proven cases with biopsy-confirmed colorectal masses as defined by the CTC Reporting and Data System (C-RADS) [4], and 81 normal cases with no reported CTC or colonoscopy findings. There were two CTC scan volumes (supine, prone, or decubitus) per case. The CTC scan volumes were interpolated to a 1-mm^3 spatial resolution. A total of 700 VOIs that represented volumetric images of masses, ICVs, haustral folds, and rectal tubes were split randomly into 560 (80%) training samples and 140 (20%) test samples. The training samples were further split into 448 (80%) actual training samples and 112 (20%) validation samples. We also calculated an enriched training set of 100,000 actual training samples by volumetric data augmentation based on random volumetric deformations of the VOIs. The accuracy of the training was evaluated using the validation set. We trained three versions of the 3D-ResNet: one that classified the samples using all four object categories and the augmented training set (3D-ResNet-A4), one that classified the samples using all four categories without the augmentation (3D-ResNet-4), and one that classified the samples using only the binary categories of masses and non-masses without the augmentation (3D-ResNet-B). The training was performed on a Tesla P-100 graphics processing unit (NVIDIA Corporation, Santa Clara, CA) with the Adam optimization method. After training for 100 epochs, the classification performances of the 3D-ResNet models with highest validation performance was evaluated by use of the independent test samples.

Results

The test samples included 46 masses, 32 ICVs, 32 haustral folds, and 30 rectal tubes. The 3D-ResNet-A4 classified correctly all but ten samples, including one mass that was misclassified as a fold and one ICV that was misclassified as a mass. The categorical classification accuracy (A_c) was 0.92. For discrimination between masses and non-masses, the area under the receiver-operating characteristic (ROC) curve (A_z) was 0.996 (95% confidence interval (CI) [0.990, 1.000]). For the 3D-ResNet-4, A_c was 0.89 and A_z was 0.977 (95% CI [0.957, 0.997]) ($p < 0.05$). For the 3D-ResNet-B, A_c was 0.81 and A_z was 0.966 (95% CI [0.939, 0.992]) ($p < 0.02$). Figure 2 shows the ROC curves of the three 3D-ResNets.

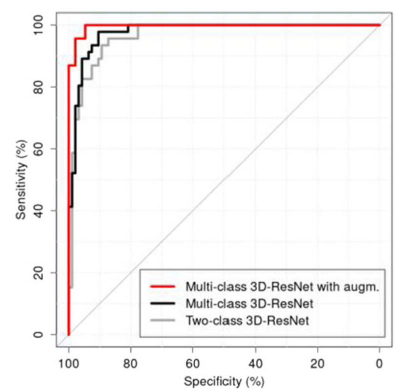

Fig. 2 Illustration of the ROC curves of the 3D-ResNets: multi-class 3D-ResNet trained with data augmentation (3D-ResNet-A4), multi-class 3D-ResNet trained without data augmentation (3D-ResNet-4), and two-class 3D-ResNet trained without data augmentation (3D-ResNet-B)

Conclusion

The results of this pilot study indicate that it is feasible to train a moderately deep volumetric 3D-ResNet for differentiating colorectal masses from ICVs in CTC at a high accuracy. The use of data augmentation and multiple target object categories yielded a statistically significant improvement in the classification accuracy. Therefore, deep learning appears to be an effective approach for improving the detection accuracy of CADe for colorectal masses in CTC.

Acknowledgements

This work was supported partly by the NIH/NCI grants of EB022747 (PI: J.J.N), CA203730 (PI: H.Y.), and EB023942 (PI: H.Y.).

References

[1] Robinson C, Halligan S, Iinuma G, Topping W, Punwani S, Honeyfield L, Taylor SA (2011). CT colonography: computer-assisted detection of colorectal cancer. Br J Radiol 84: 435–440
[2] Silva AC, Beaty SD, Hara AK, Fletcher JG, Fidler JL, Menlas CO, Johnson CD (2007). Spectum of normal and abnormal CT appearances of the ileocecal valve and cecum with endoscopic and surgical correlation. Radiographics 27: 1039–1055
[3] He K, Zhang X, Ren S, Sun J (2016). Deep residual learning for image recognition. IEEE Conference on Computer Vision and Pattern Recognition, 770–778

[4] Zalis ME, Barish MA, Choi JR, Dachman AH, Fenlon HM, Ferrucci JT, Glick SN, Laghi A, Macari M, McFarland EG, Morrin MM, Pickhardt PJ, Soto J, Yee J (2005). CT colonography reporting and data system: a consensus proposal. Radiology 236: 3–9

Colon CAD with a 3D CNN approach

Z. Cao[1], O. Masoud[1]
[1]Vital Images, Minnetonka, United States

Keywords Colon CAD · Deep learning · CNN · Polyp detection

Purpose

Colon cancer is one of the most common and deadly cancers in the United States [1]. Early detection and prevention of colorectal cancer is very important. Virtual colonoscopy through CT scans provides a less invasive way of testing, especially for people that do not want to or cannot have tests done such as colonoscopy. However, the reading of the CT images is time consuming and challenging. Colon CAD algorithms have been proposed in the past to facilitate radiologists in reading colon CT scans with some success. These traditional methods usually use hand crafted features and have their limitations in dealing with diverse nature of the colon scans. Recent advancements in deep learning technology especially convolutional neural networks have provided a new way of crafting algorithms. Through learning techniques, no hand-crafted features are needed and the algorithms learn to distinguish between polyps and non-polyps through native CT images. New colon CAD algorithms based on these technologies have also been proposed and shown promising results. However, these new algorithms mainly focus training and testing on 2D/2D images [2–4]. Here, we propose an end to end 3D convolutional neural network that works on CT colon images directly.

Methods

The proposed CAD system is consisted of candidate generation/augmentation, training and inferencing steps. The colon of each CT volume is extracted in its entirety. Once the colon is segmented, the surface of the colon tissue/air interface is extracted. The CT volume is reformatted into 1 mm^3 isotropic volume. A candidate generation process is done to create 30 mm^3 cube of sub-volumes of the original CT scan centered along the surface of the colon tissue/air interface. For each candidate, an augmentation process is also done by randomly rotating and shifting around the center of the sub-volume cube. To balance out the positive and negative instances (most of the colon surface is free of polyps and thus is a negative example), each positive instance is augmented with 10 random perturbations and each negative instance is augmented with 5 random perturbations. Furthermore, for each CT volume, every positive instance is included while 1% of all negative instances are.

Once all the candidates are generated, they are trained through a 3D convolutional network. The network is consisted of two 3D convolutional layers with max pooling and ReLu layers in between and with two fully connected layers at the end (Fig. 1). Batch normalization is performed after each convolution step and dropout is also applied at the fully connected layer. The first convolutional layer is consisted of sixteen $5 \times 5 \times 5$ kernels, and the second convolutional layer is consisted of eight $5 \times 5 \times 5 \times 16$ kernels. The final two layers are 64-node fully connect layer followed by a 2-node fully connected layer.

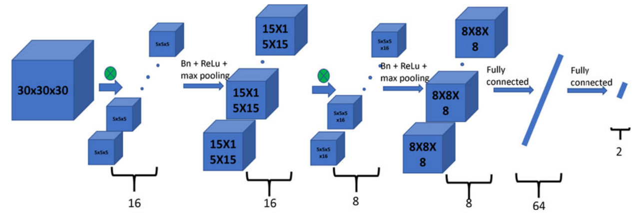

Fig. 1 Schematic of the 3D convolutional network

The training candidates are randomly group into 100/batch and iterated through the network for 500 epochs. After the network is trained, it will be used to inference on the test sets that the network has never seen before. During the testing phase, a similar candidate generation process is done for all the volumes. In this process, all the candidates are included and all the candidates are augmented 5 times. Similar to random view aggregation [3], every candidate and its five-random augmentation are scored through inferencing and the final score is the average of those for each candidate.

Results

The network has been trained on 102 patients and tested on a totally separate set of 46 patients. The scans of these patients include scan thickness ranging from 0.625 to 3 mm. The sensitivity of the system is 85.7% for all polyps that are greater or equal to 6 mm with a 3.5 FP/Vol. The sensitivity of the system is 95% for polyps that are greater than 9 mm with 3.5 FP/vol. To test the potential of the network, we also trained the network with 20, 50, 80% of all the training data and tested on the same set of 46 patient testing set. The performance of the system improves with more training data as shown in Table 1.

Table 1 System performance with different amount of training data

	20% training data	50% training data	80% training data	100% training data
Sensitivity at 3.5FP/Vol for all polyps	66	69	82	85
Sensitivity at 3.5FP/Vol for polyps > 9 mm	76	80	93	95

Conclusion

We developed an end to end CAD system for colon with a novel true 3D CNN network. The approach achieves performance in line with the state of the art with the potential to improve with more training data.

References

[1] American Cancer Society (2017) Cancer Facts & Figures: 13–16
[2] Tulum G, Bolat B, Osman O (2017) A CAD of fully automated colonic polyp detection for contrasted and non-contrasted CT scans. Int J CARS 12: 627–644
[3] Roth H, Lu L, Liu J, Yao J, Seff A, Cherry K, Kim L, Summers R (2016) Improving Computer-Aided Detection Using Convolutional Neural Networks and Random View Aggregation. IEEE TMI 35(5): 1170–1181
[4] Umehara K, Nappi J, Hironaka T, Regge D, Ishida T, Yoshida H (2017) Deep ensemble learning of virtual endoluminal views for polyp detection in CT colonography. Medical Imaging: Computer-Aided Diagnosis 10134: 101340G

3D deep residual convolutional networks for computer-aided detection of polyps in CT colonography

T. Uemura[1], H. Lu[1], H. Kim[1], R. Tachibana[2], T. Hironaka[3], J. Näppi[3], H. Yoshida[3]
[1]Kyushu Institute of Technology, Kitakyushu, Japan
[2]Institute of National Colleges of Technology, Oshima, Japan
[3]Massachusetts General Hospital, Boston, United States

Keywords Computer-aided detection · Deep learning · Colorectal polyp · CT colonography

Purpose

Although the use of computer-aided detection (CADe) yields a significant improvement in the polyp detection sensitivity of CT colonography (CTC), current CADe systems tend to produce many false-positive (FP) detections [1]. Therefore, it is desirable to improve the differentiation of true polyps from FPs for reducing the number of FPs in CADe while maintaining a high detection sensitivity.

Deep convolutional neural networks (CNNs) have recently gained substantial popularity by demonstrating a state-of-the-art classification performance in two-dimensional (2D) natural images. For classification of medical three-dimensional (3D) data, 3D convolutional kernels were introduced to improve the classification performance [2]. In 2D/3D-CNNs, increasing the depth of a CNN model tends to increase the classification performance of the model. However, it is known that, when many convolution layers are stacked together, the proper training of a CNN becomes challenging and the classification performance of the CNN tends to decrease. Residual network (ResNet) models [3] was introduced for obviating the above problem in achieving high performance in a deep CNN model.

In this study, we developed a novel 3D-ResNet model with 3D convolution kernels and 3D residual blocks, and evaluated its performance in classifying true polyps from FPs detected by our CADe system.

Methods

3D-ResNet

Figure 1 shows our proposed 3D-ResNet model. The model consists of two 3D-convolutional layers and three residual blocks with batch normalization. The 3D-convolutional layers are an extension of conventional 2D-convolutional layers, where the weights and convolution kernels have a 3D tensor form for performing convolutional operations on volumetric data such as CTC images. In our 3D-ResNet, we employed two 3D-convolutional layers to capture small- to middle-scale volumetric features in the CTC images.

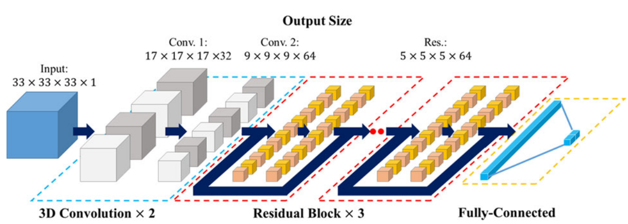

Fig. 1 The architecture of the proposed 3D-ResNet model. The 3D-ResNet consists of 2 convolutional layers, 3 residual blocks, and 2 fully connected layers

Residual Block [3] is a technique for building deeper CNN models than what was possible with the traditional approach of stacking convolutional layers. The residual block was originally developed for 2D-CNNs [3]. To develop a 3D-ResNet, we replaced the 2D convolutional kernels of the residual blocks with 3D kernels, and added three residual blocks of size $5 \times 5 \times 5$ to the first two convolutional layers to capture large-scale variations in the input data (Fig. 1). Also, conventional 2D/3D-CNNs with the same depth as that of the 3D-ResNet were developed for performance comparison.

Evaluation database

The above three types of CNN models were evaluated based on the 40 CTC datasets obtained from the supine and prone CT scans of 20 patients. These CTC datasets contained 65 biopsy-confirmed polyps $\geq$ 6 mm. Polyp candidates were detected from these CTC datasets by use of the initial candidate detection module of our CADe system [4], which generated a total of 6519 FPs (163 FPs per case on average). We extracted volumes of interest (VOIs) from the center of each polyp candidate, and augmented them by scaling and rotating around the y- and the z-axes. As a result, our database contained 21,021 VOIs of polyps and 19,557 VOIs of FPs. We evaluated the performance of the CNN models based on these VOIs by use of a 5-fold cross-validation and receiver operating characteristic (ROC) analysis. The area under the ROC curve (AUC) was used as the figure of merit for the classification performance.

Results

Figure 2 shows the ROC curves indicating the performance of the CNN models in the classification between polyps and FPs. The proposed 3D-ResNet model showed the highest performance (AUC = 0.963) among the three CNN models. The AUC of the 3D-ResNet was 0.168 and 0.018 greater than that of the 2D- and 3D-CNN models, respectively. A two-tailed t-test showed that the differences of the AUCs were statistically significant: 3D-ResNet vs. 2D-CNN: $p = 2.2 \times 10^{-16}$; 3D-ResNet vs. 3D-CNN: $p = 7.86 \times 10^{-7}$. These results indicate that the classification performance of the 3D-ResNet was statistically significantly higher than that of the 2D- and 3D-CNN models. Moreover, the AUC of the 3D-CNN model was 0.15 greater than that of the 2D-CNN model (two-tailed t test, $p = 2.2 \times 10^{-16}$), indicating that the classification performance of the 3D-CNN model was statistically significantly higher than that of the 2D-CNN model.

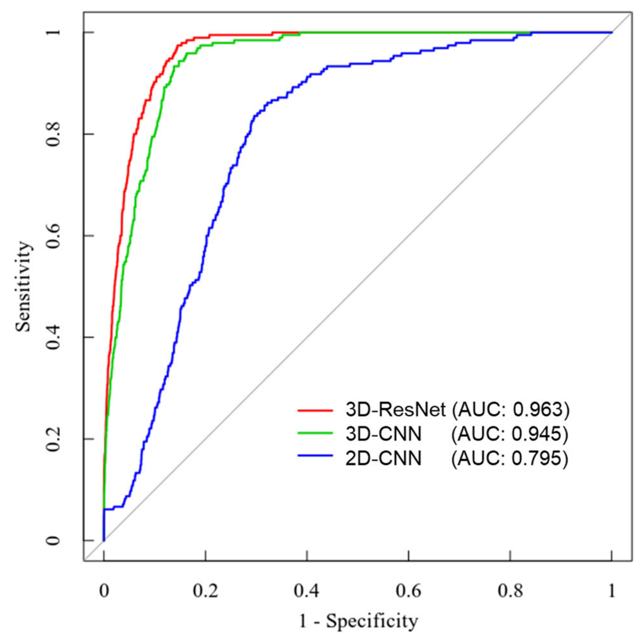

Fig. 2 ROC curves indicating the classification performance of the 3D-ResNet (red), conventional 3D-CNN (green), and the 2D-CNN (blue)

Conclusion

We developed a 3D-ResNet model to classify between polyps and FPs detected by our CADe system for CTC. The classification performance of the 3D-ResNet was compared with those of conventional 2D/3D-CNN models. Our preliminary results show that the 3D model outperforms the 2D model, and that the 3D-ResNet outperforms both 2D- and 3D-CNNs in the classification task. Thus, our 3D-ResNet can reduce the number of FPs with a marginal reduction in sensitivity of CADe, and has potential to substantially improve the detection performance of CADe for polyps in CTC.

Acknowledgments
This work was supported partly by JSPS (17K14694), NIH/NCI grants of UH2CA203730, R01EB023942, and R01CA212382.

References

[1] Yoshida H, Näppi J (2007) CAD in CT colonography without and with oral contrast agents: Progress and challenges. Comput. Med. Imaging Graph. 31(4–5): 267–284
[2] Dou Q, Chen H, Yu L, et al. (2017) Multi-level contextual 3D CNNs for false positive reduction in pulmonary nodule detection. IEEE Transactions on Biomedical Engineering 64(7): 1558–1567
[3] He K, Zhang X, Ren S, Sun J (2016) Deep residual learning for image recognition. In: IEEE Conference on Computer Vision and Pattern Recognition (CVPR) 2016, pp. 770–778
[4] Uemura T, Lu H, Kim H, et al. (2017) Classification of polyp candidates on CTC based on 3D-CNN. In: International Forum on Medical Imaging in Asia 2017, pp. 103–105.

Tumor detection for automated breast ultrasound using 3-D convolutional neural network

R. F. Chang[1], T. C. Chiang[1], Y. S. Huang[1], R. T. Chen[1], C. S. Huang[2]
[1]National Taiwan University, Department of Computer Science and Information Engineering, Taipei, Taiwan
[2]National Taiwan University Hospital, Department of Surgery, Taipei, Taiwan

Keywords Convolutional neural network · Automated breast ultrasound · Tumor detection · Multi-scale lesion detection

Purpose
2-D handheld breast ultrasound (US) was used as an adjunct modality to the mammography. Nevertheless, the handheld US is time-consuming, operator dependent, and has poor reproducibility. To overcome these limitations, the automated whole breast ultrasound (ABUS) has been proposed to scan the whole breast automatically. The ABUS produces 2-D images that can be reconstructed to 3-D volume for further review. Reviewing hundreds of slices produced by the ABUS, however, requires a large amount of time even for expert physicians. Therefore, in this study, a fast and effective computer-aided detection (CADe) system based on 3-D convolutional neural networks (CNN) is proposed to accelerate this reviewing.

Methods
The algorithm involves three main stages: the VOI extraction, tumor likelihood estimation with the 3-D CNN, and the candidate aggregation. At first, an efficient 3-D sliding window method is used to extract the VOIs. Then, the 3-D CNN is used to estimate the likelihood being tumor of each VOI, and the VOIs with tumor likelihood greater than a threshold are selected as tumor candidates. However, some of the candidates may overlap each other. Hence, a candidate aggregation method based on the hierarchical clustering is used to combine the overlapped candidates into a single tumor box, and each candidate is scheduled with different priority for alleviating the over-aggregation problem. Finally, to detect lesions of different sizes, the aforementioned steps are performed multiple times at different scales, and a simple scheme is adopted for multi-scale tumor VOI aggregation.

Results
ABUS images used in this study were acquired between January and September 2015 in the Breast Center of National Taiwan University Hospital from an ACUSON S2000 Automated Breast Volume Scanner (Siemens Medical Solutions, Mountain View, CA, USA) with a 14L5BV linear array transducer ranging from 5 to 15 MHz. The ABUS scanner produced 318 2-D images with 0.5 mm thickness. There are 273 pathology-proven lesions from 187 patients in our dataset, including 124 benign and 149 malignant lesions. The first 25 passes are assigned to the training set, the next 25 passes to the validation set, and the rest 137 passes to the testing set. The proposed CADe system achieves sensitivities of 95% (184/194), 90% (175/194), 85% (165/194), and 80% (155/194) with 2.9, 2.0, 1.3, and 0.8 FPs per pass, respectively. The execution time is 21 s for each pass. The results demonstrate the feasibility of our method.

Conclusion
A CADe system based on 3-D CNN for lesion detection of ABUS images is proposed in this study. An application-independent sliding window detector is adopted for VOI extraction. Then, a 3-D CNN is used for tumor likelihood estimation of each VOI, and VOIs of likelihood higher than a threshold are considered as tumor candidates. The overlapped candidates are combined with a novel aggregation scheme. Finally, the same process is executed multiple times with different target sizes for multi-scale lesion detection.

Acknowledgements
This work was supported by the Ministry of Science and Technology (MOST 107-2634-F-002-013) of the Republic of China for the financial support.

Segmentation of lung nodules on MDCT images by using 3D Conv-DeconvNet

S. Kidera[1], S. Kido[1], Y. Hirano[1], S. Mabu[1], N. Tanaka[2]
[1]Yamaguchi University, Graduate School of Sciences and Technology for Innovation, Ube, Japan
[2]Saiseikai Yamaguchi General Hospital, Department of Radiology, Yamaguchi, Japan

Keywords Deep learning · Image segmentation · Lung nodule · MDCT image

Purpose
Semantic segmentation for lung nodules found by CT examinations is important for calculating image features in recently radiomic analysis. However,segmentation accuracies of conventional methods is not sufficient. In this study, we proposed a segmentation model for lung nodules on three-dimensional (3D) CT images. We used 3D Conv-DeconvNet [1] which combines two deep learning techniques; convolution network and deconvolution network.

Methods
In this study, we used 330 CT images of patients with a lung nodule scanned at Saiseikai Yamaguchi General Hospital in Japan (slice thickness: 0.7 mm, pixel size 0.6 mm). We also used manually segmented images of lung nodules from 3D CT images under the guidance of a radiologist as gold standards. $112 \times 112 \times 56$ voxel size of volume of interests (VOIs) were cut out from CT images. We augmented these VOIs by 42 times in total with rotation, reflection and translation. We used these VOIs as training data and trained our model of Conv-DeconvNet with them. Convolution network in our model extracted image features of lung nodules. From these image features, deconvolution network generated probability maps whose size is same as the input images. The probability maps indicate the likelihood that each voxel on the CT image belongs to the lung nodule or not. Of the data not used for training, 66 VOIs were used as testing data which are not included in the training data. The performance of our method was evaluated by five-fold cross-validation. We compared the performance of our method with that of the conventional method using watershed algorithm [2]. We used Jaccard index and Dice coefficient for evaluation.

Results

In our segmentation method, the median of Dice coefficient was 0.795 ± 0.002, and the mean of Jaccard index was 0.610 ± 0.011 (Table 1). And, in segmentation of the watershed algorithm, the median of Dice coefficient was 0.673 ± 0.016, and the mean Jaccard index was 0.457 ± 0.013 (Table 2). The segmentation results obtained by our model were significantly superior to those obtained by the conventional watershed algorithm ($p < 0.01$). Figure 1 shows examples of segmentation results of lung nodules. In the segmentation of lung nodules with round shapes, our model tended to be superior to the conventional watershed method (Fig. 1a). On the other hand, in the segmentation of lung nodules with complicated margins, the conventional watershed method tended to be superior to our model (Fig. 1b).

Table 1 In our segmentation method, the median of Dice coefficient was 0.795 ± 0.002, and the mean of Jaccard index was 0.610 ± 0.011

	Jaccard index Mean ± SD	Dice coefficient
Average	0.610 ± 0.011	0.737 ± 0.013
Median	0.660 ± 0.003	0.795 ± 0.002

Table 2 In the segmentation of the watershed algorithm, the median of Dice coefficient was 0.673 ± 0.016, and the mean Jaccard index was 0.457 ± 0.013

	Jaccard index Mean ± SD	Dice coefficient
Average	0.457 ± 0.013	0.596 ± 0.012
Median	0.508 ± 0.018	0.673 ± 0.016

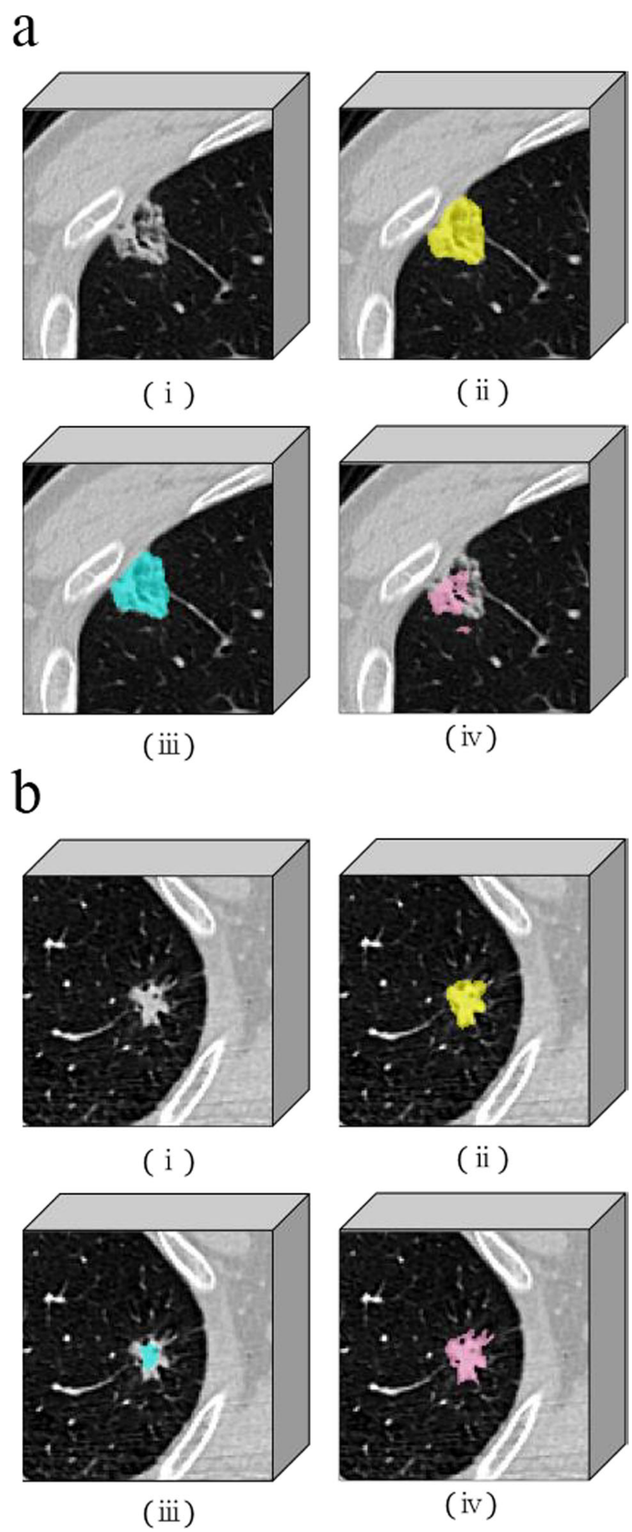

Fig. 1 Examples of segmentation results of lung nodules. (i) original image (ii) manually annotated image (gold standard) (iii) segmentation result of the our model (iv) segmentation result of the watershed algorithm

In our model, MaxPooling layers were used for down-sampling. Therefore, the detailed shape information might be discarded.

Conclusion

The performance of segmenting lung nodules on 3D CT images by our method was superior to that of the conventional watershed algorithm. Even for the lung nodules with complicated margins, it is expected that the segmentation performance will be improved by adjusting the parameters of our model. Our method of segmentation may be useful for computer-aided analysis of lung nodules in the areas of such as radiomics.

References

[1] Noh H, Hong S, Han B (2015) Learning Deconvolution Network for Semantic-Segmentation. Proceedings of the IEEE International Conference on Computer Vision

[2] Tachibana R, Kido S, Matsumoto T (2004) Segmentation of small pulmonary nodules on thoracic CT images. Trans. the Institute of Electronics, Information and Communication Engineers, J87-DII(1): 228–236 (in Japanese)

Polyp detection in colonoscopic videos by using spatio-temporal feature

H. Itoh[1], H. Roth[1], M. Misawa[2], Y. Mori[2], M. Oda[1], S. E. Kudo[2], K. Mori[3]

[1]Nagoya University, Graduate School of Informatics, Nagoya, Japan
[2]Showa University Northern Yokohama Hospital, Digestive Disease Center, Yokohama, Japan
[3]Nagoya University, Information Technology Center, Nagoya, Japan

Keywords Colonoscopic video · Polyp detection · Scene classification · Deep learning

Purpose

This paper proposes a method for polyp detection in colonoscopic videos. Colonoscopy still missed some polyps in colon cancer screening even though the colonoscopy is the gold standard method for the screening. Computer-Aided Detection (CAD) system for the detection of polyps is strongly required for early disease detection and treatment [1, 2]. Furthermore, CAD system must not mislead the diagnosis in colonoscopy. Therefore, our proposed method detects only existence of polyps in each frame of colonoscopic video without the detection of location of polyps. For the validation of our proposed method, we also construct data set that consists of 73 colonoscopy videos where polyp frames are annotated by expert endoscopists. Experimental results show the validity of our proposed method.

Methods

We adopt scene classification approach for the detection of existence of polyps in each frame. In this approach, CAD system classifies colonoscopic video frames into two categories of scenes. The first category represents video frames where polyp exists. The second category represents video frames where polyp does not exist. This scene classification requires the extraction of spatio-temporal feature from videos while image classification usually extracts only spatial feature from two-dimensional images. A video is a sequence of frames, that is, two-dimensional images. The successive video frames include similar objects for the same category of scenes. In particular, for the first category, a polyp should appear in successive frames. Therefore, scene classification has to deal with temporal structure in addition to spatio structure of two-dimensional images.

We use three-dimensional convolutional neural network (C3DNet) [3] for extraction and classification of spatio-temporal features for polyp detection. Figure 1 summarizes the architecture of the C3DNet for polyp detection. The input of the c3d net is a set of successive 16 frames of colonoscopic videos. We set all of three-dimensional convolution filters are $3 \times 3 \times 3$ with $1 \times 1 \times 1$ stride. All three-dimensional pooling layers are $2 \times 2 \times 2$ with $2 \times 2 \times 2$ stride except for the first pooling layer which has kernel size of $1 \times 2 \times 2$. The output of the c3d net are probabilities for the two categories. If the output probability of the first category is larger than the criterion, the CAD system concludes that the input frames represent the scene where polyps exist. Note that before the classification, we preliminarily search the best parameters of the c3d net for polyp detection by using our dataset as a training procedure.

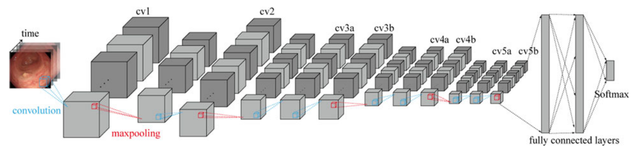

Fig. 1 Architecture of three-dimensional convolutional neural network (C3DNet). Input is a sequence of 16 frames

Results

We constructed a new dataset for the validation of the proposed detection method. We collect 73 colonoscopic videos, which captured by CF-HQ290ZI (Olympus, Tokyo, Japan), with IRB approval. Each frames of these videos are annotated by expert endoscopists. The total time of these videos is about 16 h 37 min. The total time of the frames where represent 155 polyps exist is 4 h 55 min. These videos are captured under the different observation condition such that white light, narrow band imaging, and staining.

We extracted only the polyp frames that are captured under the white light. As non-polyp frames, we extracted frames where polyps do not exist under several observation conditions. We divided these extracted frames into training data and test data. The training data consist of polyp frames of 30 min 30 s and non-polyp frames of 24 min 12 s. The test data consists of polyp frames of 18 min 1 s and non-polyp frames of 18 min 23 s. These training and test data including different 105 and 37 polyps, respectively. The training data is used for searching of parameters of the C3DNet with Adam. The test data is used for validate the accuracy of the classification of polyp and non-polyp frames. In both training and test data, frames are rescaled into 112×112 pixels. Therefore, the size of input data for the C3DNet is $112 \times 112 \times 16$.

Figure 2 summarises the results of validation with the test data. The square on the ROC curve in Fig. 2 represents the result for using criteria of 0.5 where accuracy, sensitivity and specificity are 74.7, 88.1 and 61.7%. The result shows that the specificity is smaller than sensitivity. This implies the wide variety of patterns in non-polyp frames. By setting criteria 0.7, we obtained the highest accuracy 75.1% where sensitivity and specificity are 76.3 and 74.0%, respectively.

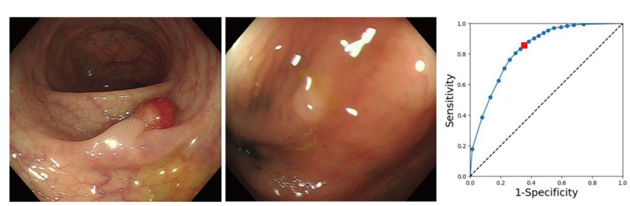

Fig. 2 Left and middle show the detected polyp frames with probabilities 92 and 65%, respectively. Right shows receiver operating characteristic curve for detection of polyps. The curve is obtained by changing criterion from zero to one. The square represents the case with the criterion of 0.5

Conclusion

This paper proposed and validated the polyp detection method that is based on spatio-temporal feature of colonoscopic videos. This paper also reported new dataset that consists of colonoscopic videos of 16 h 37 min. The experimental results with the new dataset showed that our proposed method correctly detects the polyp frames by using spatio-temporal feature. The proposed method achieves 88.1% sensitivity. By adding more non-polyp frames to training data, we focus on the improvement of specificity as the future works. Parts of this research were supported by the Project on Utilizing High-Definition Medical Imaging Data up to 8 K Quality from the Japan Agency for Medical Research and Development, Research on Development of New Medical Devices from Japan Agency for Medical and development, and MEXT KAKENHI (No. 26108006, No. 17H00867).

References

[1] Bernal J, Sanchez J, Vilarino F (2012) Towards Automatic Polyp Detection with a Polyp Appearance Model. Pattern Recognition 45(9): 3166–3182

[2] Bernal J., Tajkbaksh N, Sanchez FJ, Matuszewski BJ, Hao Chen, Lequan Yu, Angermann Q, Romain O, Rustad B, Balasingham I, Pogorelov K, Sungbin Choi, Debard Q, Maier-Hein L, Speidel S, Stoyanov D, Brandao P, Cordova H, Sanchez-Montes C, Gurudu SR, Fernandez-Esparrach G, Dray X, Liang J, Histace A (2017) Comparative Validation of Polyp Detection Methods in Video Colonoscopy: Results From the MICCAI 2015 Endoscopic Vision Challenge. IEEE Transactions on Medical Imaging 36(6): 1231–1249

[3] Tran D, Bourdev L, Fergus R, Torresani L, Paluri M (2015) Learning Spatiotemporal Features with 3D Convolutional Networks. Proc. IEEE International Conference on Computer Vision: 4489–4497

A preliminary study of the computerized detection of nodular liver lesion in Gd-EOB-DTPA-enhanced magnetic resonance images with 4D CNN

T. Takenaga[1], S. Hanaoka[2], Y. Nomura[1], T. Nakao[3], M. Nemoto[4], M. Murata[1], S. Miki[1], T. Yoshikawa[1], N. Hayashi[1], O. Abe[2,3]
[1]The University of Tokyo Hospital, Department of Computational Diagnostic Radiology and Preventive Medicine, Bunkyo-ku, Japan
[2]The University of Tokyo Hospital, Department of Radiology, Bunkyo-ku, Japan [3]University of Tokyo, Radiology and Biomedical Engineering, Graduate School of Medicine, Bunkyo-ku, Japan
[4]Kindai University, Department of Biomedical Engineering, Kinokawa, Japan

Keywords Computer-assisted detection · Gd-EOB-DTPA-enhanced MRI · Nodular liver lesion · Four-dimensional convolutional

Purpose

Several studies reported that Gd-EOB-DTPA-enhanced MRI tends to show higher diagnostic accuracy compared to other modalities. However, in a diagnosis of nodular liver lesions, Gd-EOB-DTPA-enhanced MR generates a huge number of images in five phases. Radiologists may be exhausted from detecting and diagnosing lesions in Gd-EOB-DTPA-enhanced MR. Computer-assisted detection (CAD) in contrast-enhanced multiphase abdominal MR images is challenging because of image registration, intensity inhomogeneity problem, and intensity standardization. In this study, we developed a CAD scheme for the detection of lesions in Gd-EOB-DTPA-enhanced MRI with four-dimensional convolutional neural network (4D CNN) technique.

Methods

165 contrast-enhanced MR images including 299 metastatic liver tumors, 280 hepatocellular carcinomas (HCC), and 11 hemangiomas were used in this study. 3-Tesla MR scanners (Siemens Skyra, GE Signa HDxt) and 1.5-T MR scanners (Siemens Avanto, GE Signa HDxt/EXCITE) with a T1-weighted 3D gradient echo sequence were employed for acquisition of MR images. Images were reconstructed with a matrix size of 240–512 × 210–512 (pixel size of 0.7–1.3 mm) and slice thickness of 2.5 or 3.0 mm. Each case includes 1–74 lesions, and the effective diameter of these legions was ranged from 3.0 to 97.7 mm. Each region of the lesion was painted manually by radiological technologists, and checked by a board-certified radiologist. Among the 165 cases, 84 cases were used for CNN training, 36 cases were used for CNN validation, and remaining 45 cases were used for evaluation. The input image was 4D (three spatial dimensions and one time dimension).

Figure 1 shows the overall scheme to detect lesions. Firstly, the image in hepatobiliary phase was selected as a target image, and images in remaining four phases were non-rigidly registered to the target image by using DROP 3D registration software. Secondly, the liver region was extracted by using temporal subtraction images. Thirdly, we detected lesion candidate voxels by 4D CNN. Positive samples for CNN were extracted so that the center of a sample was a lesion. Negative samples were extracted randomly in an extracted liver region without positive samples. We extracted image patches of size 5 × 31 × 31 × 31 or 5 × 15 × 15 × 15 in five phases. Our network consists of three or less convolutional layers, the same number of max-pooling layers, and two fully-connected layers. The output layer has two units, and the softmax function is applied to the output to convert it into the probability of being positive. We employ a rectified linear unit (ReLU) function as the activation function for all layers except the output layer. Batch normalization is performed before each ReLU function. We utilize the Adam method to optimize the network weights. The number of layer (1, 2, or 3), the number of each convolutional filter (1–31), the size of the fully-connected layer (1–100), negative patch images per case (2500, 5000, 10,000, or 20,000), and a learning rate (10-1–10-6) in Adam method were optimized by random search for each image patch size (5 × 31 × 31 × 31 or 5 × 15 × 15 × 15). Finally, we determined lesion candidate by using the probability of the local maximum in the lesion. In the performance evaluation, if the lesion candidate point was contained with the painted region, the lesion candidate point was judged as a true positive. These processings were done in the GPU cluster system in our university.

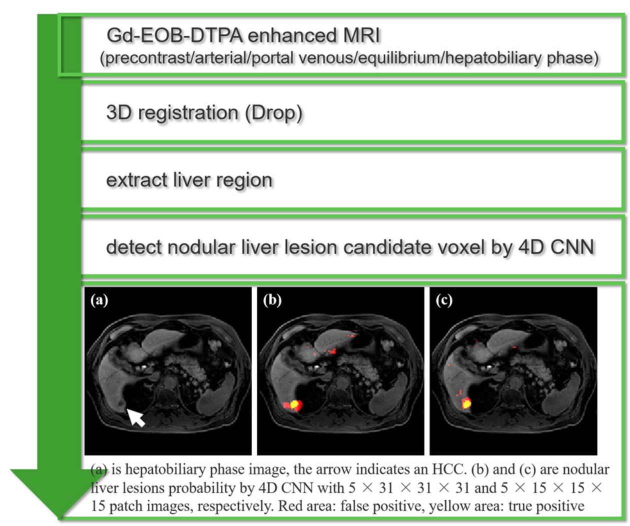

Fig. 1 Summary of the nodular liver lesions detection

Results

Figure 2 shows two free-response receiver operating characteristic (FROC) curves for lesions detection by two CNN. The number of false positives per case at 50.0% sensitivities were 22.3 by CNN with 5 × 31 × 31 × 31 and 13.1 by CNN with 5 × 15 × 15 × 15 patch image. We couldn't detect 34 lesions in 9 cases due to the failure of the liver region extraction. Figure 1b, c shows examples of results by CNN with two kinds of patch images. Both CNN could detect the HCC. It is necessary to improve liver extraction and to combine CNN with image patch of different size.

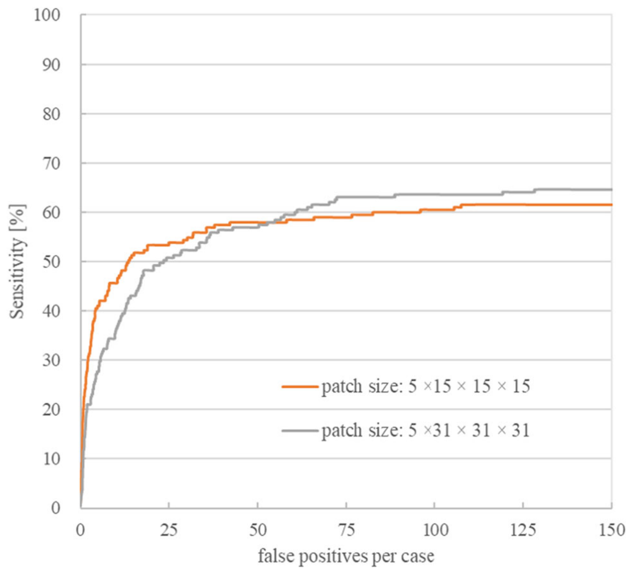

Fig. 2 FROC curves for detection of nodular liver lesions

Conclusion

We had developed a CAD scheme for the nodular liver lesions in Gd-EOB-DTPA-enhanced MRI with 4D CNN. The sensitivity for detection of lesions was 50.0% with 13.1 false positives per case by CNN with 5 × 15 × 15 × 15 patch image. It is necessary to improve detection accuracy.

Plaque classification in coronary arteries from IVOCT images using convolutional neural networks and transfer learning

N. Gessert[1], M. Heyder[1], S. Latus[1], M. Lutz[2], A. Schlaefer[1]
[1]Hamburg University of Technology, Institute of Medical Technology, Hamburg, Germany
[2]Universitätsklinikum Schleswig–Holstein, Klinik für Innere Medizin III, Kiel, Germany

Keywords IVOCT · Plaque classification · Deep learning · CNN

Purpose

Advanced atherosclerosis in the coronary arteries is one of the leading causes of deaths worldwide while being preventable and treatable. In order to image atherosclerotic lesions (plaque), intravascular optical coherence tomography (IVOCT) can be used. The technique provides high-resolution images of arterial walls which allows for early plaque detection by experts. Due to the vast amount of IVOCT images acquired in clinical routines, automatic plaque detection has been addressed. For example, attenuation profiles in single A-Scans of IVOCT images are examined to detect plaque [3]. We address automatic plaque classification from entire IVOCT images using deep feature learning. In this way, we take context between A-Scans into account and directly learn relevant features from the image source without the need for handcrafting features.

Methods

We built a new database of IVOCT images using in vivo patient data acquired with a St. Jude Medical Ilumien OPTIS. A trained expert with daily application experience with IVOCT provides the ground-truth labels for the images. Each image is assigned a binary label of "plaque" or "no plaque". In total, the dataset contains 41 patients with 2868 labeled images. We split off a test set of 6 patients with 509 images.

In contrast to previous approaches [3], we do not apply extensive pre-processing for lumen segmentation and flattening or guide-wire artifact and catheter removal. Therefore, we force our models to be robust towards all kinds of artifacts which will often appear in clinical practice. This allows our models to deal with any raw data without having to rely on an automatic segmentation procedure which might fail if the artery wall is not consistently visible, as shown in Fig. 1.

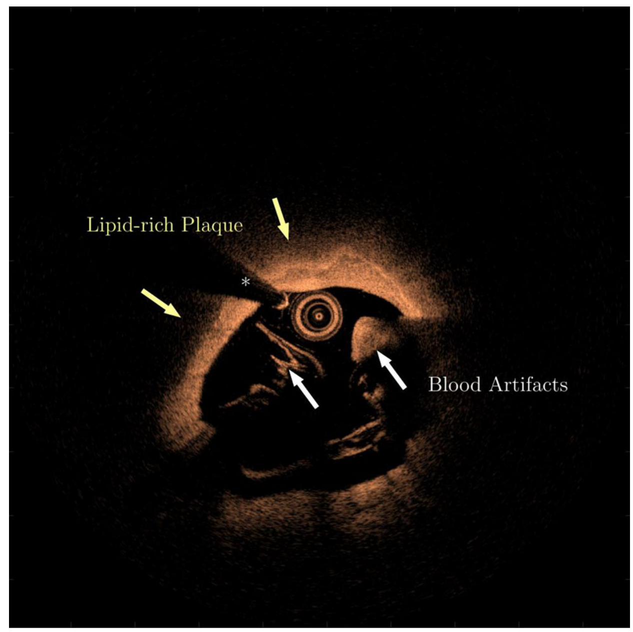

Fig. 1 A cartesian IVOCT image with lipid rich plaque is shown. "*" denotes the guide-wire artifact

We employ convolutional neural networks (CNNs) to directly learn relevant features for plaque classification from the IVOCT images. We make use of standard architectures for image classification in non-medical settings. The architectures are Resnet50, Resnet101, InceptionV3 and Inception-ResnetV2 [4]. Moreover, we apply transfer learning which can help with the adaptation to new problem domains where data is limited [2]. Therefore, we pretrain the models on the ImageNet dataset.

The images that are fed into the model can be represented either in polar or cartesian form. In polar form, the acquired A-Scans are aligned next to each other in temporal acquisition order. The polar image can be transformed into cartesian space by mapping the A-Scans to their respective angle and applying interpolation in between, see Fig. 1. This representation provides a more intuitive cross-sectional view of the artery and is therefore used by practitioners. We investigate whether either representation is more advantageous for deep feature learning.

Results

The resulting prediction performance of our models on the test set is shown in Fig. 2 and Table 1. The sensitivity and 1-specificity of each model for classification of an image as "plaque" is shown. The 4 models were each trained on polar and cartesian images, both with and without transfer learning. Models in the upper left corner perform better as they have a higher sensitivity and specificity.

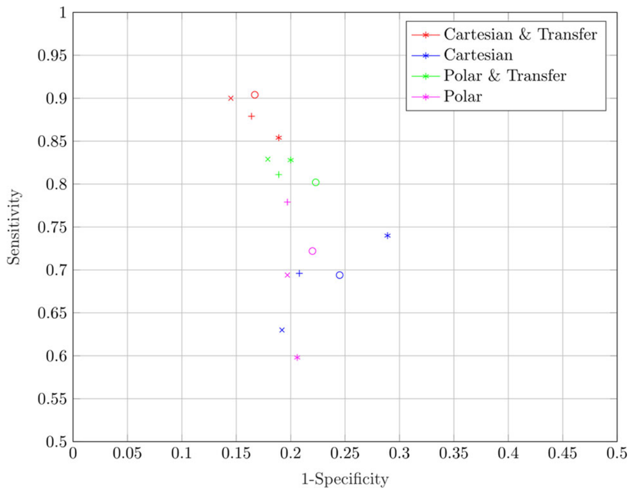

Fig. 2 The sensitivity and 1-specificity of 16 different models is shown. "*" refers to ResNet50, "x" refers to ResNet101, "o" refers to InceptionV3 and "+" refers to Inception-ResnetV2

Table 1 Accuracy, sensitivity, and specificity for all models are shown

	Accuracy	Sensitivity	Specificity
Transfer learning			
Cartesian			
Resnet50	0.835	0.854	0.811
Resnet101	0.88	0.9	0.855
InceptionV3	0.872	0.904	0.833
Inception-ResnetV2	0.844	0.879	0.836
Polar			
Resnet50	0.818	0.828	0.8
Resnet101	0.828	0.829	0.821
InceptionV3	0.79	0.802	0.777
Inception-ResnetV2	0.811	0.811	0.811
No transfer learning			
Cartesian			
Resnet50	0.727	0.74	0.711
Resnet101	0.754	0.63	0.808
InceptionV3	0.726	0.694	0.755
Inception-ResnetV2	0.74	0.696	0.792
Polar			
Resnet50	0.717	0.598	0.794
Resnet101	0.775	0.694	0.803
InceptionV3	0.766	0.722	0.78
Inception-ResnetV2	0.789	0.779	0.803

Overall, pretraining on ImageNet appears to improve performance significantly as the best model without pretraining shows an overall accuracy of 78.9% with a sensitivity of 77.9% and a specificity of 80.3% while the best model with pretraining shows an overall accuracy of 88.0% with a sensitivity of 90.0% and a specificity of 85.5%. It appears, that meaningful feature transfer from the natural image domain to the IVOCT image domain was achieved.

Also, using cartesian representations results in better classification performance. All models with pretraining achieve both a higher sensitivity and specificity when being trained on cartesian images. For example, the best model with polar images shows an accuracy of 82.8% compared to 88.0% for cartesian images. This indicates that a cartesian real-world image representation helps CNN-based learning when employing transfer learning.

The different models all perform similar with Resnet101 standing out slightly as it performs best for the two pretrained cases. All in all, the choice of image representation and transfer learning has a larger impact on performance than the model choice.

Conclusion

We perform plaque classification from IVOCT images using CNNs for deep feature learning. For this purpose, we built a database with in vivo patient image data that is labelled by a trained expert. We employ various standard CNN models with additional pretraining on ImageNet for transfer learning. Our results show that pretraining significantly boosts performance. Moreover, using cartesian image representations appears to be beneficial for CNN learning. Overall, our best model achieves an accuracy of 88.0% for plaque classification.

References

[1] Litjens G, Kooi T, Bejnordi BE, Setio AAA, Ciompi F, Ghafoorian M, Laak J, Ginneken B, Sánchez CI (2017) A survey on deep learning in medical image analysis. Medical image analysis 42: 60–88

[2] Greenspan H, van Ginneken B, Summers RM (2016) Guest editorial deep learning in medical imaging: Overview and future promise of an exciting new technique. IEEE Transactions on Medical Imaging 35(5): 1153–1159

[3] Rico-Jimenez JJ, Campos-Delgado DU, Villiger M, Otsuka K, Bouma BE, Jo JA (2016) Automatic classification of atherosclerotic plaques imaged with intravascular OCT. Biomedical optics express 7(10): 4069–4085

[4] Szegedy C, Ioffe S, Vanhoucke V, Alemi AA (2017) Inception-v4, inception-resnet and the impact of residual connections on learning. AAAI 4: 12

Assessing breast cancer screening using recent deep convolutional neural networks

X. Lessage[1], M. A. Larhmam[1], S. Mahmoudi[1], I. Nedjar [2]
[1]University of Mons, Computer Science, Mons, Belgium
[2]University, Tlemcen, Algeria, Engineering Laboratory, Tlemcen, Tlemcen, Algeria

Keywords Breast cancer · Digital mammograms · Convolutional neural networks · Classification

Purpose

Breast cancer is one the major causes of cancer death among women in the world. Early screening and diagnosis can significantly reduce the death rate related to this disease. Digital mammography is an efficient imaging modality, which present a convenient and an easy tool usually used for masses, and microcalcification detection in the case of breast cancer diagnosis. Computer aided diagnosis systems (CADx) can assist radiologist when reading mammograms and play a key role in early detection of breast cancer. In addition, deep learning methods, especially convolutional neural networks have achieved a huge progress coming with impressive results in many challenging tasks related to image analysis like object detection and image segmentation. In this paper, we investigate the efficiency of recent and robust deep learning architectures for early breast cancer screening based on digital mammograms. So, we address the problem of digital mammogram classification by using three different architectures of convolutional neural networks (InceptionV3 [1], Xception [2] and MobileNet [3]). We experiment our method on two different publicly available datasets, namely **InBreat** [4], **MIAS** [5].

Methods

Breast cancer diagnosis in mammograms imaging can be reformulated as an image classification problem, a machine learning task which have been largely and successfully tackled using Deep Learning technology. In this work we propose, a classification method based on transfer learning and fine tuning of three recent convolutional neural network architectures (CNNs) namely, InceptionV3, Xception and mobileNet. The goal of our method is to classify the mammograms into (02) classes: normal, or abnormal cases. As a first stage of breast cancer screening in mammograms using MIAS and INbreast datasets. For MIAS images, a pre-processing step that consists of removing the pectoral muscle and all annotations was achieved (Fig. 1). The used CNN architectures have been selected as they achieve state of the art results in image recognition tasks (InceptionV3, Xception), and also they enable an excellent accuracy-Network capacity trade off (MobileNet). Therefore, Inception architecture brings the idea of inception module which consist of factoring convolution task into multiple branches that operate first on channels and then on space. Xception introduced a CNN architecture based on depthwise separable convolution, inception modules and residual connections. Otherwise, MobileNet is based on a streamlined architecture that uses depthwise separable convolutions to build a light weight deep neural network and used efficiently a low number of parameter ($\sim$ 4 M) compared to InceptionV3 and Xception ($\sim$ 23 M). In order to tackle the problem of the reduced volume of the database we used transfer learning approach and data augmentation technique by applying multiple transformation.

Fig. 1 Image from MIAS dataset before and after preprocessing (left), and an image from INbreast dataset (right)

Results

Experimentations have been conducted using two separate datasets. **MIAS** database contains 322 digitized mammograms [5] and **INbreast** database [4] contains 410 mammograms of 115 patients. The mammograms include two views; cranial cardo (CC) and mediolateral oblique (MLO). However, we use each view as a separate instance in order to increase the available data sample for training deep neural networks. In addition, for data augmentation, a common practice is to apply classical transformations such as; shift, shear and rotation. The latter can serve as a regularization technique to prevent overfitting due to small data size. We used a binary classification scheme:

– Negative: **normal case** does not require any further examination;
– Positive: **abnormal case** which requires urgent additional examinations.

Both datasets include annotated ROIs. However, in this study, we focus on the evaluation of the capacity of recent and improved CNN architectures to identify cancerous cases based on only raw mammograms images without any annotations. Indeed, most of large scale public dataset does not include any kind of expert annotations. We splited each dataset into training 80% and test 20%. We also initialized the three CNN architectures with pre-trained imageNet weights using two fine tuning configuration: freezing 100 layers and retraining the others or retraining only bottleneck layer. All models have been trained for 100 epochs. In Table 1, we show the results of test accuracy for both INbreast and MIAS datasets using InceptionV3, Xception and MobileNet CNN architectures. The top test scores have been achieved by InceptionV3 for INbreast and by MobileNet for MIAS with 98 and 90% respectively. We noticed that retraining more layers has a positive impact on the accuracy of the networks especially for InceptionV3 (98 instead of 90). In case of MIAS dataset, we noticed that the score of MobileNet outperforms inceptionV3 and Xception. The architecture of MobileNet is considerably smaller than Inception and Xception. The latter can suffer from overfitting in case of low size datasets.

Table 1 Results of test accuracy for the three used CNN architectures. Fine tuning in yellow and bottleneck layer retraining in gray

Dataset	#Patients	#Images	Inception v3	Xception	MobileNet
INbreast	115	410	**98**	95	89
			90	90	91
MIAS	-	322	85	87	**90**
			83	87	85

Computational environment: Experimentation in this study were carried out on a Linux cluster node with 32 CPU cores using a single NVIDIA GeForce GTX 980 with 4 GB memory. Using Keras 2 with Tensorflow backend as a deep learning framework.

Conclusion

In this paper, we addressed the problem of breast cancer screening from mammograms using three recent and efficient convolutional neural networks architectures. The publicly available MIAS and INbresat databases were used for our experiments. We achieved a high accuracy scores of 98 and 90% on INbreast and MIAS dataset. We demonstrated that, in case of small datasets, fine tuning efficient architectures can yield a high accuracy score compared to the state of the art results. Further investigations can be done using patch classifiers to improve screening results. Also, using a Muti-view analysis of large scale mammograms can bring a realistic and more efficient models.

References

[1] Szegedy C, Vanhoucke V, Ioffe S, Shlens J, Wojna Z (2015) Rethinking the inception architecture for computer vision. arXiv preprint arXiv: 1512.00567
[2] Chollet F (2016) Xception: Deep Learning with Depthwise Separable Convolutions. arXiv preprint arXiv: 1610.02357
[3] Howard AG, Zhu M, Chen B, Kalenichenko D, Wang W, Weyand T, Adam H (2017) Mobilenets: Efficient convolutional neural networks for mobile vision applications. arXiv preprint arXiv: 1704.04861
[4] Moreira IC, Amaral I, Domingues I, Cardoso A, Cardoso MJ, Cardoso JS (2012) Inbreast: toward a full-field digital mammographic database Academic radiology, vol. 19, no. 2, pp. 236–248
[5] Suckling J, Parker J, Dance D, Astley S, Hutt I, Boggis, C, Ricketts I, Stamatakis E, Cerneaz N, Kok SL, Taylor P, Betal D,

Savage J (1994) The mammographic images analysis society digital mammogram database. Exerpta. Medica., 1069, pp. 375–378

Interactive segmentation using real-time fine-tuning of a fully convolutional neural network

M. Braginsky[1], L. Joskowicz[1], D. Link[2,3], D. Ben-Bashat[2,3,4]
[1]Hebrew University of Jerusalem, School of Computer Science and Engineering, Jersualem, Israel
[2]Tel Aviv Sourasky Medical Center, Functional Brain Center, The Wohl Institute for Advanced Imaging, Tel Aviv, Israel
[3]Tel Aviv University, Sackler Faculty of Medicine, Tel Aviv, Israel
[4]Tel Aviv University, Sagol School of Neuroscience, Tel Aviv, Israel

Keywords Interactive · Segmentation · Deep-learning · Fetal MRI

Purpose

Accurate segmentation of complex anatomical structures and pathologies in volumetric images is one of the greatest challenges of medical image processing. Often times, and in particular for structures that show high variability, the segmentation has to either be performed by hand or has to be verified and corrected when generated automatically. Since manual delineation and correction are tedious, error-prone, and time-consuming tasks, it is desirable to have a user-friendly interactive editing tool to assist the clinician perform this task. To be most effective, the interactive editing tool should be tailored to the specific structure and scan at hand. However, hand-tailoring the editor to cover each type of structure and pathology is impractical. Instead, it is desirable to develop a method to automatically customize the editor model while the manual segmentation and/or corrections are performed. During the last few years, machine learning techniques, e.g., Deep Neural Networks, have shown to be highly effective for a variety of machine vision and image processing tasks, including classification, object detection and segmentation. These techniques, which create models that are showing state-of-the-art results in segmentation when trained on large annotated datasets, have a great potential to be used for smart editing. However, the use of these methods in medical image processing are hampered both by the lack of a large database of annotated data and by their computational cost, which prevents interactive use.

Methods

We have developed a method for interactive segmentation of structures in volumetric images using a fully convolutional neural network (FCN) that is fine-tuned in real-time during the interactive segmentation process. First, the baseline FCN network is trained offline on a small set of scans (8, 635 slices in total) ground-truth delineations of the structure of interest. Various data augmentation techniques are used to complement the dataset during the training phase. The training process uses volumetric patches and is monitored with an additional validation set of a few scans (5, 412 slices in total), and stopped early to reduce a chance of overfitting on the small data.

The interactive segmentation of a structure of interest in a new scan proceeds on each slice scan as follows. First, an initial segmentation of the structure of interest is automatically generated on the current slice using the baseline FCN and presented to the user. Next, the user manually corrects the segmentation on the slice by adding/deleting segmentation contours components and by changing the segmentation contours as needed using simple editing tools. Then, the baseline FCN is fine-tuned with the resulting segmentation on the slice using the user approved segmentation as the label for the training. This fine-tuning is performed for every slice in real time during the segmentation both to adjust the baseline FCN to the study and to further decrease its overfit to the original small training dataset. The fine-tuned baseline FCN is then used to produce a segmentation of the next scan slice. The process is repeated until the entire segmentation is performed.

To demonstrate our method, we chose the task of segmenting the fetal body envelope on Coronal MRI scans. This task is particularly challenging for automated methods due to the complexity of the fetal body, e.g., hands, feet, fingers, varying imaging contrasts, and the adjacency of the placenta and other structures. We trained offline a baseline FCN network on manually delineated fetal envelopes in eight fetal MRI scans. The baseline FCN was trained on patches of $64 \times 64 \times 3$ voxels with various types of data augmentation. The validation set for the training consisted of five additional scans.

Results

To evaluate our method, we manually annotated a ground truth dataset of 1539 slices from 21 fetal MRI scans. For each study, we compare the ground truth manual segmentation of the fetal envelope to the segmentation produced with one of the following: (1) a segmentation created using our method, including real-time training on each user-approved slice to predict the next slice; (2) a segmentation created by using a single initialization of the entire study without any fine-tuning, followed by a manual correction of all slices; (3) a manual segmentation created by a second annotator to obtain an estimate of the inter-observer variability (on a third of the studies) (Fig. 1). During all segmentations, we logged every step of the segmentation and every action of the user and recorded the time required for each editing action, the resulting volume overlap difference (VOD) with respect to the ground truth, the time to produce the final segmentation, and the final VOD (Fig. 2).

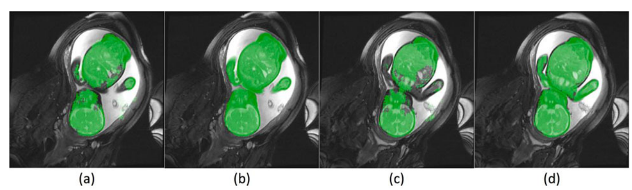

Fig. 1 **a** Baseline FCN initialization segmentation (green) overlaid on a scan slice; **b** segmentation after manual correction on the same slice; **c** automatically generated initial segmentation on the next slice; **d** new initial segmentation generated after fine-tining the baseline FCN overalid on the slice in (**b**)

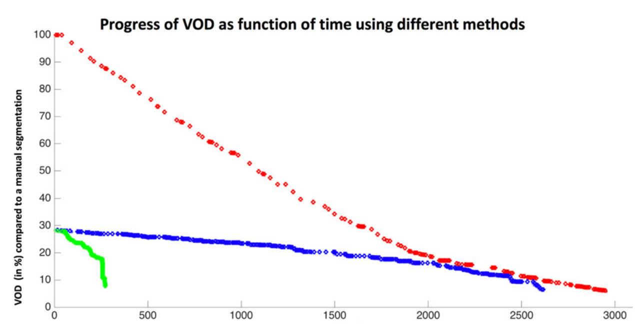

Fig. 2 Change in VOD in % as function of time for the segmentations generated with three different methods. Red: a fully manual annotation. Blue: single initialization with manual corrections. Green

Our measurements show that a fully manual segmentation required an average of 68 min per study. The mean VOD of two annotators is 9.5% (range = 7.9–12.3%, SD = 1.4%), which provides an estimate of the inter-observer variability and an estimated upper bound of the achievable accuracy. Single initialization followed by a manual correction reduced the segmentation time by only 10–15% as compared to fully manual segmentation with the same final accuracy. While the initial segmentation had a VOD of 35% (range = 28–39%, SD = 4%), the nature of segmentation errors was such that it precluded a substantial decrease of segmentation time. With our real-time baseline FCN training method, the mean segmentation time is 4.7 min, a 92% (range 87–94%, SD = 2.4%) time reduction without compromising the accuracy of segmentation.

Conclusion

Our results indicate that interactive segmentation using real-time fine-tuning of Deep Neural Networks is a powerful tool that can be used to decrease segmentation time by up to 20× without compromising the quality of the segmentation. We have shown that the use of Deep Neural Networks is feasible even on small training data by leveraging the interactivity of the system to fine-tune the network on the specific study during the segmentation process.

Fully convolutional network for electronic cleansing in CT colonography

R. Tachibana[1], J. J. Näppi[2], H. Yoshida[2]
[1]National Institute of Technology, Oshima College, Suo-Oshima, Japan
[2]Massachusetts General Hospital and Harvard Medical School, 3D Imaging Research, Department of Radiology, Boston, United States

Keywords Fully convolutional network · CT colonography · Electronic cleansing · Computer-aided detection

Purpose

Early detection and removal of polyps can prevent the development of colon cancer. CT colonography (CTC) provides a safe and accurate method for examining the complete region of the colon, and it is recommended by the American Cancer Society as an option for colon cancer screening. Electronic cleansing (EC) enables computer-aided detection (CADe) systems to detect polyps that are submerged in residual materials by virtual subtraction of the residual materials from CTC images. Previously, we developed a deep-learning (DL) scheme for performing EC in dual-energy CTC (DE-CTC) to overcome the limitations of EC in single-energy CTC [1]. However, the DL-based EC was computationally expensive because it had been designed to analyze 54 cut-plane images at each voxel. Such computations can be made more effective by use of a fully convolutional network (FCN) [2] that provides an instant end-to-end segmentation of an input image volume. In this study, we developed an FCN scheme for performing accurate EC in CTC. The evaluation was performed with an anthropomorphic phantom designed to imitate a human colon in CTC scans.

Methods

Figure 1 shows an overview of the FCN-based EC scheme. An anthropomorphic phantom (Phantom Laboratory, Salem, NY) was filled partially with a diluted iodinated contrast agent to yield average CT values of fecal tagging at 300, 600, and 900 Hounsfield Units (HU). The phantom was scanned using a multi-channel CT scanner (LightSpeed Plus; GE Medical Systems, Milwaukee, WI) with 140 kVp, 50 mA, 1.25-mm collimation and 1.25-mm reconstruction interval. Volumes of interest (VOIs) were extracted from the acquired CT image volumes at the locations of 12 simulated polyps measuring 5–16 mm in size. Figure 2 shows examples of the image patches of the VOIs. A paired training dataset was sampled from the VOIs of CT scans acquired with and without the contrast agent.

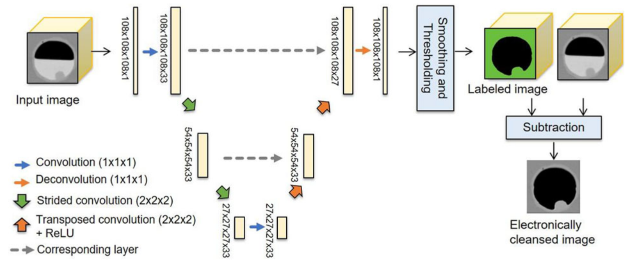

Fig. 1 Overview of the FCN-based EC scheme

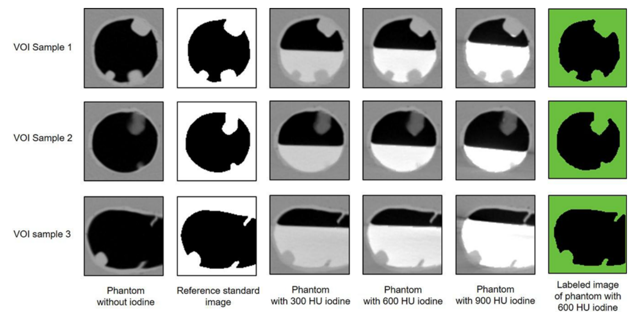

Fig. 2 Examples of VOI samples

We designed a three-dimensional FCN based on the V-Net architecture [3]. The FCN model includes three convolutional/deconvolutional layers. The pooling layers of V-Net were replaced by strided convolutions. The last layer obtains predictions for each voxel. The FCN was trained to learn an end-to-end image mapping from VOIs containing iodinated contrast to their lumen and non-lumen region-label volume images that were derived from the corresponding empty phantom. In our EC scheme, three-dimensional Gaussian filtering is performed for smoothing boundaries, and the input voxels are classified into lumen and non-lumen regions by thresholding. The final electronically cleansed CTC images are generated by subtracting the voxels labeled as lumen from the CTC images and by performing dedicated reconstruction of the virtually cleansed colon surfaces [4].

For evaluation, nine VOIs with a size of 108 × 108 × 108 voxels were prepared from the CT scans of the phantom. The nine VOIs included three set of VOIs with three iodine contrast dilutions corresponding to the observed CT values of 300, 600, and 900 HU. The evaluation was performed by use of three-fold cross-validation, where the performance metric was the mean overlap ratio (OR; 0.0 = no overlap, 1.0 = complete overlap) between the reference standard labels of the empty phantom and the labels generated automatically by the FCN. We also tested the method on a clinical non-cathartic CTC case where the FCN was trained using all nine VOIs.

Results

When images with all three levels of contrast were used to train the FCN, the mean and standard deviation of the overall OR was 0.971 ± 0.924. The mean ± SD of ORs at each sample were 0.973 ± 0.157, 0.978 ± 0.132 and 0.961 ± 1.031, respectively. The mean ± SD of ORs at each level of contrast (300, 600 or 900 HU) were 0.974 ± 0.454, 0.973 ± 0.749 and 0.966 ± 1.452, respectively. The sixth row in Fig. 2 shows the labeled images corresponding to the phantom images with 600 HU iodine contrast dilution on the fourth row. The labeled images provided a satisfactory segmentation for the simulated polyps.

Conclusion

We developed an FCN-based EC scheme for CTC using anthropomorphic phantom datasets. The method yielded a high accuracy in the virtual cleansing of CTC images. The method also showed potential to provide an effective EC for clinical non-cathartic CTC.

Acknowledgements
This study was partly supported by JSPS KAKENHI Grant 16H05913 (PI: Tachibana) and NIH/NCI grants of R21EB024025 (PI: Näppi) and R01CA212382 (PI: Yoshida).

References

[1] Tachibana R, Näppi JJ, Hironaka T, Kim SH, Yoshida H (2016). Deep learning for electronic cleansing in dual-energy CT colonography. Proc SPIE Int Soc Opt Eng 9785
[2] Shelhamer E, Long J, Darrell T (2015). Fully convolutional networks for semantic segmentation. Proc IEEE Conference on Computer Vision and Pattern Recognition 3431–3440
[3] Milletari F, Navab N, Ahmadi SA (2016). V-net: Fully convolutional neural networks for volumetric medical image segmentation. Proc 4th International Conference on 3D Vision 565–571
[4] Zalis ME, Perumpillichira J, Del Frate C, Hahn PF (2003). CT colonography: digital subtraction bowel cleansing with mucosal reconstruction: initial observations. Radiology 226(3), 911–917

Automated ganglion cell detection using fully convolutional networks and evaluation under different training losses

H. Oda[1], K. Chiba[2], H. R. Roth[3], T. Kitasaka[4], M. Oda[1], A. Hinoki[2], H. Uchida[2], K. Mori[3]
[1]Nagoya University, Graduate School of Information Science, Nagoya, Japan
[2]Nagoya University, Graduate School of Medicine, Nagoya, Japan
[3]Nagoya University, Graduate School of Informatics, Nagoya, Japan
[4]Aichi Institute of Technology, School of Information Science, Toyota, Japan

Keywords Fully convolutional network · Pediatric surgery · Spatial dropout · Computer-aided detection

Purpose

We proposed an automated ganglion cell detection method from HE-stained images of colon. 85.3% ganglion cells were detected in normal samples with 2.0 FPs/slice. This performance outperformed the control experiment using the Dice loss. The performance is promising for helping the clinicians to find and count the number of ganglion cells on HE-stained images of the colon, and determining whether the sample is normal or pathological. Future work includes augmentation of ganglion cells that have rare appearance for increasing the detection rate.

Methods

We performed three-fold cross validation of 190 HE-stained images obtained from 24 normal patient samples containing ganglion cells. Parameters were manually chosen as: $t = 0.7$ and $v = 5$ pixels. Detection rate of ganglion cells are computed by the number of ganglion cells that are overlapping with the output. Number of FPs/slice is also evaluated (Fig. 1).

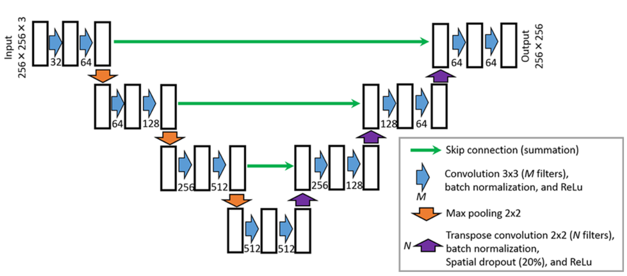

Fig. 1 Network architecture that is similar to U-net [2]. We modified size of input and output as 256 × 256, added batch normalization and spatial dropout layers

Performance using the cross entropy loss was as follows: Among normal samples, detection rate was 85.3%, with 2.0 FPs/slice, by using the cross entropy loss. In evaluation of 16 abnormal patient samples which do not have ganglion cells, only 0.39 FPs/slice were produced. Performance using the Dice loss was: 74.1% of detection rate with 2.0 FPs/slice for normal samples, and 0.81 FPs/slice for abnormal samples.

Figure 2 shows a detection result from a HE-stained image of a normal sample. A ganglion cell whose typical appearance is a white interior with the nucleus clearly shown, can be detected by both the proposed method and the control experiment, because this type of appearance is typical for most ganglion cells. A rarer type of ganglion cells whose entire cell body is purple was often a false negative (FN). One such cell became a FN using the Dice loss, but we could detect it using the cross entropy loss. The performance of the proposed method is already promising for determining between normal and abnormal samples, since markedly less false positives (FPs) were produced on abnormal samples than normal samples.

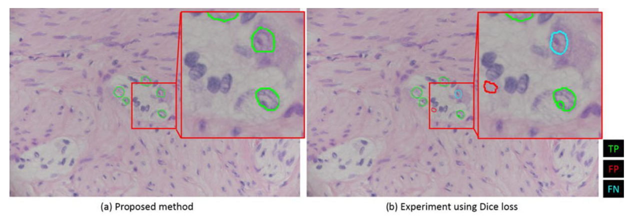

Fig. 2 Detection results on an HE-stained image of a normal sample. Results using cross entropy loss have fewer FPs than result using Dice loss. **a** Result of the proposed method using the cross entropy loss. All ganglion cells on this HE-stained image were detected. **b** Results using Dice loss. One ganglion cell whose entire cell body is purple was not detected, and one FP was produced

Results

Overview: The proposed method detects ganglion cells from input HE-stained images of intestine tissues of Hirschsprung's patients. Pathological samples of intestine tissues are dissected by surgery and cut into several parts. Their images are generated using a built-in camera (DS-Ri2, Nikon, Japan) of a 400-power microscope (ECLIPSE Ni-U, Nikon, Japan), as RGB-color images consisting of 1636 × 1088 pixels with 250 nm resolution. We use these images under ethical approval by Nagoya University. Output is a set of ganglion cell regions.

The proposed method repeats following steps: (1) crop a subimage from a set of training HE-stained images, (2) train the network using the cropped training HE-stained images, and (3) use the trained network for obtaining the ganglion cell regions on testing images. Ground-truth annotations of ganglion cells in the HE-stained images are created manually by a pediatric surgeon using MITK Workbench 2016.11.

Network: We developed a network for pixel-wise semantic segmentation of ganglion cells in HE-stained images, which is shown in Fig. 1. We modified a network proposed by Roth et al. [1], which is inspired by U-net [2]. The size of both input and output of the network are the same, and batch normalization is used throughout the network. Parameters of the network are set empirically as follows. 2D convolutions with the kernel of 3 × 3 are used. The size of input RGB image and output segmentation maps are of size 256 × 256 pixels. Moreover, to prevent overfitting, we add a spatial dropout layer [3] after each deconvolution layer, and set dropout ratio as 20%. The network is implemented in Keras with the TensorFlow backend.

Training phase: Using HE-stained RGB color images and manually annotated ground truths, the network is trained. Subimages containing at least one positive pixel of ground-truth are randomly cropped from several histological slides, and used for as a batch in a mini-batch training scheme (we use a batch-size of 256 × 256 pixels for all experiments). To make sure that positive voxels are around the center of the subimage, we randomly choose a pixel in the ground-truth, set the pixels as the center of the subimage, and crop around 256 × 256 pixels of the pixel. Initial learning rate is 0.0001 and optimized by Adam optimizer. For each subimage, augmentation (rotation, translation, and nonlinear deformation) is performed. We investigate the use of the cross entropy loss and the Dice loss for parameter optimization. We performed 20,000 iterations of training with mini-batch size 12, using 240,000 subimages in total.

Testing phase: Subimages are cropped as grid pattern. Size of each subimage is 768 × 256 pixels, and the network is reshaped for this size. Each subvolume is then fed into the trained model to predict the cropped part. Regions that probability is at least are obtained as candidate regions. The candidate regions which have less than v pixels are removed as false positives (FPs).

Conclusion

Hirschsprung's disease is treated in pediatric surgery, where the convalescence of patients strongly depends on the quality of treatment. In Hirschsprung's disease, peristaltic movements is not functioning in certain segmentations of the colon due to a lack of ganglion cells in the Auerbach's plexus. As a treatment, the abnormal segment of the intestine (from the anus up to the end of the affected some segment) is dissected. To optimize the part to be dissected, pathological samples are obtained from several points along the colon, and pathologists search and count the number of ganglion cells shown on the HE-stained images of each sample. However, the pathological diagnosis and searching of ganglion cells is very difficult since there are many cells looking similar to ganglion cells in the Auerbach's plexus. This makes the detection work difficult for both expert pathologists and computer-aided detection (CADe) systems.

We propose an automated ganglion cell detection method with deep learning to assist diagnosis. To best of our knowledge, this is the first work of automated ganglion cell detection. The proposed method uses a fully convolutional network inspired by U-net. We investigate how the network's performance depends on different loss functions: the cross entropy or the Dice losses.

Acknowledgements

Parts of this research were supported by MEXT/JSPS KAKENHI (26108006, 17H00867, 17K20099) and JSPS Bilateral Joint Research Project "Oncological Diagnostic and Interventional Assistance System Based on Multi-modality Medical Image Processing".

References

[1] Roth HR, Oda H, Shimizu N, Oda M, Hayashi Y, Kitasaka T, Fujiwara M, Misawa K, Mori K (2018) Towards dense volumetric pancreas segmentation in CT using 3D fully convolutional networks, SPIE Medical Imaging 2018: 10574–10610 (accepted).

[2] Ronneberger O, Fischer P, Brox T (2015) U-Net: Convolutional networks for biomedical image segmentation, MICCAI 2015, LNCS 9351: 234–241.

[3] Tompson J, Goroshin R, Jain A, LeCun Y, Bregler C (2015) Efficient object localization using convolutional networks, IEEE CVPR: 648–656.

Preliminary development of training environment for deep learning on supercomputer system

Y. Nomura[1], I. Sato[2,3,4], T. Hanawa[5], S. Hanaoka[4], T. Nakao[4], T. Takenaga[1], D. Sato[4], T. Hoshino[5], Y. Sekiya[5], S. Ohshima[6], N. Hayashi[1], O. Abe[4]

[1]The University of Tokyo Hospital, Dept. of CDRPM, Tokyo, Japan
[2]The University of Tokyo, Graduate School of Frontier Sciences, Tokyo, Japan
[3]RIKEN, Center for Advanced Intelligence Project, Tokyo, Japan
[4]The University of Tokyo Hospital, Department of Radiology, Tokyo, Japan
[5]The University of Tokyo, Information Technology Center, Tokyo, Japan
[6]Kyushu University, Research Institute for Information Technology, Fukuoka, Japan

Keywords Deep learning · Computer-assisted detection · Supercomputer · Bayesian optimization

Purpose

Recently, deep learning has been exploited in medical image analysis, and many research groups reported computer-assisted detection (CAD) using deep learning. However, deep learning requires large amounts of computational power including graphics processing unit (GPU). Moreover, numerous hyper-parameter optimization has great influence on the performance of deep learning. In our institution, a new supercomputer system (Reedbush-H) which consists of 120 compute nodes equipped with two GPUs (Tesla P100, NVIDIA Corporation, Santa Clara, CA) has been in operation since March 2017. If a framework for training deep learning with hyper-parameter optimization on the supercomputer system can be realized, it is expected to accelerate development of CAD using deep learning. In this study, we described our environment for training deep learning on the supercomputer system.

Methods

Figure 1 shows a configuration of our environment. We configured a virtual private network (VPN) between the supercomputer system and the clinical site. Each registered personal computer (PC) at the clinical site can be connected to the dedicated login node of the supercomputer system via the relay server. The dedicated login nodes can't be accessed by other users using the supercomputer system to ensure security. Anonymized image data were transferred from the clinical site to the storage area of the dedicated login node. The transferred data were copied to the parallel file system in advance of executing a training job on the compute nodes.

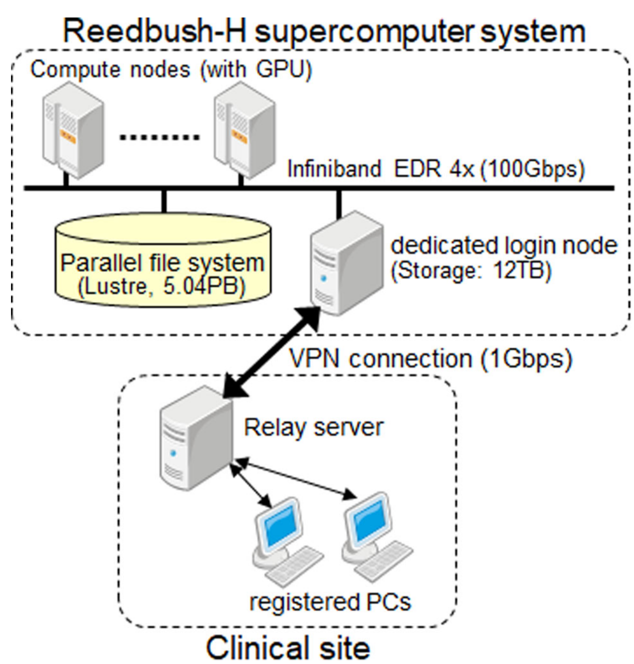

Fig. 1 Configuration of our supercomputer environment

We implemented automated hyper-parameter tuning software into the dedicated login node. The training jobs using the hyper-parameters generated by the software were repeatedly executed at the compute nodes. We utilized Bayesian optimization (BO) [1] as an automated hyper-parameter tuning algorithm. BO is a framework for an optimization of the black-box functions whose derivatives and convexity properties are unknown. In training of deep learning using our framework, the hyper-parameters were chosen by BO so as to maximize the value of evaluation criteria in validation.

Results

We trained CAD using deep learning in the constructed environment. We targeted a computerized detection of cerebral aneurysm in magnetic resonance angiography (MRA) images based on a deep convolutional neural network (CNN) [2]. We utilized 3D time-of-flight unenhanced MRA data sets of 350 cases accumulated from three 3-Tesla MR scanners (two Signa HDxt and one Discovery MR750, GE Healthcare, Waukesha, WI, USA). The acquisition parameters were as follows: echo time, 2.7–3.3 ms, repetition time, 22 or 25 ms; flip angle, 15 degree; field of view, 240 mm; slice thickness/interval, 0.6/1.2 mm; matrix size, 512 × 512. Each case includes at least one aneurysm of 2 mm or more in diameter, which was determined by consensual reading by two experienced radiologists, and areas of aneurysm were defined by pixel-by-pixel painting. We divided the 350 cases into two subsets; 300 cases of training set, and 50 cases of validation set.

In our CAD, we used a CNN classifier that predicts whether each voxel was inside or outside aneurysms by inputting maximum intensity projection images generated from a volume of interest around the voxel. Our network consisted of two convolutional layers, two max-pooling layers, and two fully-connected layers. The output layer had a single unit, and the logistic function was applied to the output to convert it into the probability of being positive (which ranges from 0 to 1). We employed a rectified linear unit (ReLU) function as the activation function for all layers except the output layer. Batch normalization was performed before each ReLU function. We utilized the Adam method to optimize the network weights. The tuned hyper-parameters were: the filter size and the number of filters of each convolution layer, the number of units of the fully-connected layer, the batch size, and three parameters (α, β_1, β_2) of the Adam method. We utilized the area under the curve (AUC) value of the free-response receiver operating characteristic (FROC) curve, with the upper limit of three false positives per case, as an evaluation criterion. In this study, the 40 trials of hyper-parameter tuning with BO were repeated five times.

Figure 2 shows the change in the maximum AUC value with error bar. The value of each trial indicates the maximum value in all past trials. As the number of trials increases, the maximum AUC value has been updated, indicating that the appropriate hyper-parameters were found by BO.

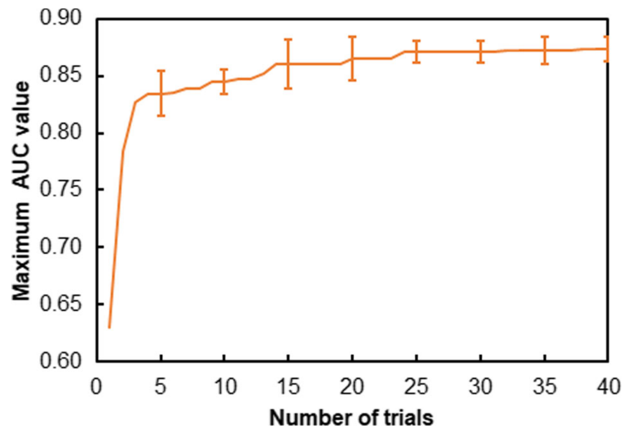

Fig. 2 Change in AUC of validation data where each value is maximum value in past trials

Conclusion

We have built a training environment for deep learning on supercomputer system. The constructed environment enabled to train deep learning model with hyper-parameter tuning. We are planning to validate our environment using other type of CAD, and to implement asynchronous parallel BO algorithm [3] for further efficiency in training.

References

[1] Snoek J, Larochelle H, Adams RP (2012) Practical Bayesian optimization of machine learning algorithms. Advances in neural information processing systems: 2951–2959.

[2] Nakao T, Hanaoka S, Nomura Y, Sato I, Nemoto M, Miki S, Maeda E, Yoshikawa T, Hayashi N, Abe O (2017) Deep neural network-based computer-assisted detection of cerebral aneurysms in MR angiography. J Magn Reson Imaging 2017 Aug 24 (Epub ahead of print)

[3] Kandasamy K, Krishnamurthy A, Schneider J, Poczos B (2017) Asynchronous parallel Bayesian optimisation via Thompson sampling. arXiv: 1705.09236

Features selection analysis to quantify sacroiliitis in magnetic resonance imaging

M. Calil Faleiros[1], J. Raniery Ferreira Junior[1],
A. Priscilla Magalhães Tenório[1], V. Faeda Dalto[1], R. Luppino Assad[1],
M. Henrique Nogueira-Barbosa[1],
P. Mazzoncini de Azevedo-Marques[1]
[1]University of São Paulo, Ribeirão Preto, Brazil

Keywords Feature selection · Machine learning · Sacroiliitis · Imagnetic resonance imaging

Purpose

Spondyloarthritis (SpA) is a group of diseases with common clinical and radiological manifestations. SpA comprises mainly the appendicular skeleton, spine, and the sacroiliac joint. SpA affects mostly young adults and may present the first symptoms at 16 years old, potentially impacting morbidity and socioeconomics [1]. The main technique for early diagnosis of sacroiliitis is magnetic resonance imaging (MRI). Computer-aided classification of sacroiliac joints has showed very promising results, potentially aiding the diagnosis of sacroiliitis using quantitative image features and a classical feature selection method of machine learning [2]. However it still presents results with a high dimensional feature vector, which may contribute to a complex model without relevantly increasing the performance of the classification. Therefore, the aim of this work is to combine different methods of feature selection in order to reach a set of features with low dimensionality and high performance with machine learning classifiers.

Methods

Our institutional research board approved this retrospective study with a waiver of patients' informed consent. MRI exam of 51 patients were used in this study after anonymization. Each MRI exam comprised 6 images, each image was manually segmented and put on a black background. A musculoskeletal radiologist classified each image according to Spondyloarthritis Research Consortium of Canada (SPARCC) score. This classification was the reference standard to evaluate AUC, sensitivity and specificity. The previously classification defined 22 patients positive for sacroiliitis and 29 negative. Images were pre-processed by the warp perspective transform to remove the black background, which causes noise to some features [1]. The features extracted from each image were gray-level statistics, textural based on cooccurrence matrix, textural based on histogram, spectral based on frequency domain, spectral based on wavelets and fractal. Each exam was characterized by the mean and standard deviation of each feature for the 6 images, totalizing 230 features.

Three feature selection methods were combined to filter the final vector, initially composed of 230 features. Mann–Whitney U test is a statistical method that is related to the area under the receiver operating characteristics (ROC) curve [3], giving a p value for each feature according to their statistical significance. ReliefF is a method that assigns a probability of relevance to each feature based on their individual value between multiple nearest instances [4]. Finally, Wrapper is a method that uses classifiers and an incremental learning scheme to select features [5]. The classifiers used to select features with the Wrapper and to classify the images were naive bayes (NB), multilayer perceptron (MLP), decision tree j48 (J48), random forest (RF), and support vector machine (SVM), resulting in a set of features selected by all classifiers.

Due to the class imbalance problem, the dataset samples were balanced using the synthetic minority over-sampling technique (SMOTE) method. Each classifier were evaluated by area under the ROC (AUC), sensitivity, and specificity, using the 10-fold cross-validation method.

Results

The Mann–Whitney U test selected 5 features statistically significant ($p < 0.001$), the ReliefF method selected 6 features with probability threshold of 0.05, and the Wrapper method selected 8 features which is common to the 5 classifiers used.

Using a simple intersection of those three feature sets, we found 4 features that are common to the three methods. These features are 3 energies of high-frequency from Haar wavelet and one gray-level statistic, skewness.

Table 1 presents the results of the classification performed by the NB, J48, MLP, RF and SVM classifiers using those 4 features.

Table 1 Results of each metric for each classifier

	AUC	Sensitivity	Specificity
MLP	0.807	0.793	0.793
NB	0.873	0.828	0.759
J48	0.616	0.655	0.586
RF	0.817	0.793	0.759
SVM	0.828	0.828	0.828

The NB method obtained the highest AUC (0.873), but is less sensitive to predict negative cases than SVM (specificity of 0.759 for NB and 0.828 for SVM). SVM obtained the same value of sensitivity as the NB method (0.828). However, the AUC for SVM (0.828) was close to the AUC of NB (0.873), suggesting the results are statistically the same or very similar.

Conclusion

This work used three methods to select features among a set of gray-level statistical, textural, spectral and fractal. Machine learning analysis was performed to evaluate this feature set efficiency to classify MRI sacroiliitis.

The classification showed that the low dimensional feature vector may be a good approach to classify inflammatory sacroiliitis. Features of gray-level statistics (skewness) and Haar wavelets (3 s level high-frequency energies) have showed efficiency to perform sacroiliitis classification. We propose for future work to use deep learning methods to perform the classification without any previously feature extraction.

References

[1] Costa IP, Bortoluzzo AB, Gonçalves CR, Silva JAB, Ximenes AC, Bértolo MB, Ribeiro SLE, Keiserman M, Menin R, Skare TL, Carneiro S, Azevedo VF, Vieira WP, Albuquerque EN, Bianchi WA, Bonfiglioli R, Campanholo C, Carvalho HMS, Pinto Duarte ALB, Kohem CL, Leite NH, Lima SAL, Meirelles ES, Pereira IA, Pinheiro MM, Polito E, Resende GG, Rocha FAC, Santiago MB, Sauma MFLC, Valim V, Sampaio-Barros PD (2015) Avaliação do desempenho do BASDAI (Bath Ankylosing Spondylitis Disease Activity Index) numa coorte brasileira de 1.492 pacientes com espondiloartrites: dados do Registro Brasileiro de Espondiloartrites (RBE). Revista Brasileira de Reumatologia 55(1): 48–54.

[2] Faleiros MC, Ferreira Junior JR, Jens EJ, Dalto VF, Nogueira-Barbosa MH, Azevedo-Marques PM (2017) Reconhecimento computadorizado de padrões inflamatórios de sacroiliíte em imagens de ressonância magnética. XXXVII Congresso da Sociedade Brasileira de Computação. 17° WIM—Workshop de Informática Médica: 1845–1848.

[3] Mason SJ, Graham NE (2002) Areas beneath the relative operating characteristics (ROC) and relative operating levels (ROL) curves: Statistical significance and interpretation. Quarterly Journal of the Royal Meteorological Society 128: 2145–2166.

[4] Kononenko I (1994) Estimating Attributes: Analysis and Extensions of Relief. European Conference of Machine Learning: 171–182.

[5] Kohavi R, John GH (1997) Wrappers for feature subset selection, Artificial Intelligence 97(1–2): 273–324.

Radiomics association of quantitative CT features with lung cancer patterns

J. R. Ferreira Junior[1], M. Koenigkam-Santos[2], A. Magalhães Tenório[2], M. Calil Faleiros[1], F. Garcia Cipriano[2], A. Todorovic Fabro[2], J. Näppi[3], H. Yoshida[3], P. M. Azevedo-Marques[2]

[1]Universidade de São Paulo, Programa de Pós-Graduação Interunidades em Bioengenharia, São Carlos, Brazil

[2]University of São Paulo, Ribeirão Preto Medical School, Ribeirão Preto, Brazil

[3]Harvard Medical School, Massachusetts General Hospital, Boston, United States

Keywords Lung cancer · Radiomics · Quantitative image analysis · Medical image computing

Purpose

The prognosis of lung carcinoma, the deadliest of all cancers, varies markedly according to tumor staging at diagnosis [1]. One of the most important prognostic factors used to determine therapy is the tumor-node-metastasis (TNM) staging system. Another important prognostic factor is the pathological subtype of the tumor [2]. The two most common lung cancer subtypes are adenocarcinoma (ADC) and squamous cell carcinoma (SCC). Computed tomography (CT) features have also been used as predictive factors, influencing prognosis and response to therapy [1]. Recently, radiomics has emerged as a quantitative imaging approach to improve diagnosis and assessment of prognosis, thereby providing decision support for precision medicine. Radiomics involves computer-based extraction of image features to combine them with other patient data for establishing associations with clinical outcomes [3]. In this work, we aim to extract several quantitative 2D and 3D CT image features, combine them with patient and tumor clinical data, and associate those with tumor pathology and presence of nodal and distant metastases, to potentially aid the pathological diagnosis and treatment decision of lung cancer based on metastases status.

Methods

Our institutional review board approved this retrospective study with a waiver of patients' informed consent. Our lung cancer image cohort has 85 malignant lung tumors with pathology confirmed by biopsy or surgical resection. The presence of metastases was assessed according to the clinical TNM staging system. Patients were imaged using thin-slice contrast-enhanced CT. The lung tumors were semi-automatically segmented from the CT images using the volumetric region growing algorithm GrowCut [4].

Tumors were characterized by 2465 quantitative image features extracted from the segmented CT regions/volumes of interest, including features of gray-level intensity, histogram, cooccurrence matrix, run-length matrix, neighborhood intensity-difference matrix, Tamura texture, Laplacian of Gaussian filters, Gabor filters, Fourier transform, Haar wavelet, fractal dimension, and shape.

The image features were first assessed univariately by the Mann–Whitney *U* test across the different tumor patterns for the pathological subtype (ADC or SCC), presence of nodal metastasis (NM+ or NM−), and presence of distant metastasis (DM+ or DM−). The image features were then normalized and combined with the clinical data of patient's age, gender, smoker status, presence of other primary tumors on patient's body, and the lung lobe location, position, and diameter of the tumor. All combined patient information (quantitative image features and clinical data) were assessed multivariately by a machine-learning algorithm based on the method ReliefF for feature selection and a radial basis function network (RBFN) for image classification [4]. The machine-learning algorithm finds the highest classification performance by determining an optimal combination of x selected features and y neurons for the RBFN single hidden layer, where x was varied in the interval [1, 100] and y was varied in the interval [1, number of samples of the majority class]. The machine-learning algorithm was evaluated using the leave-one-out cross-validation method. Due to class imbalance, the majority class for each pattern was randomly undersampled. Association was assessed by use of the area under the receiver operating characteristic curve (AUC).

Results

Table 1 presents the associative performance of quantitative image features and clinical data for different lung cancer patterns, using the statistical univariate and machine-learning multivariate analyses.

Table 1 Highest AUC values obtained by the univariate and multivariate analyses

	Univariate analysis	Multivariate analysis
Pathology (ADC vs. SCC)	0.66 (COM3D Max Probability)	0.87 (32 features, 14 neurons)
Nodal Metastasis (NM+ vs. NM−)	0.76 (Wavelet HL3)	0.78 (2 features, 2 neurons)
Distant Metastasis (DM+ vs. DM−)	0.70 (Wavelet LH2)	0.92 (13 features, 15 neurons)

Feature or number of features and the number of hidden layer neurons that yielded the highest performance are indicated in parentheses

The Max-Probability feature of the 3D gray-level cooccurrence matrix yielded the highest associative performance for pathologic patterns (p value < 0.05). The level-3 high-frequency HL feature of Haar wavelet yielded the highest associative performance for lymph nodal metastatic patterns (p value < 0.001), and the level-2 low-frequency LH feature of Haar wavelet yielded the highest associative performance for distant metastatic patterns (p value < 0.01). However, the machine-learning algorithm outperformed the univariate statistical analysis in discriminating the pathology and distant metastasis (p value < 0.05). Combining the most relevant features (according to the ReliefF feature selection method) with clinical data and the RBFN increased associative performance with an AUC difference by up to 0.22 units (distant metastasis).

Conclusion

In this work, we associated several quantitative first-order, second-order, and higher-order 2D and 3D CT image features with pathological, nodal and distant metastatic patterns of lung cancer. Statistical and machine learning analyses were performed to assess the associative performance of the features across three different types of malignant lung tumor patterns.

The Max-Probability feature of the 3D gray-level cooccurrence matrix presented a high association with pathological subtypes of lung cancer. The HL3 and LH2 features of Haar wavelet presented a high association with nodal and distant metastases of lung cancer, respectively. However, highest associative performances for pathological and metastatic tumor patterns were obtained by combining several different quantitative CT image features with prognostic clinical data and using the machine-learning algorithm. We propose for future directions to associate quantitative image features with additional types of lung cancer patterns and clinical outcomes, such as tumor recurrence, genomic mutations, and patient survival.

Acknowledgements

We thank CAPES, PDSE (Grant #88881.134004/2016-01), CNPq, FAPESP (Grant #2016/17078-0), and FAEPA-HCFMRP-USP for the financial support.

References

[1] Koenigkam-Santos M, Muley T, Warth A, de Paula WD, Lederlin M, Schnabel PA, Schlemmer HP, Kauczor HU, Heussel CP, Puderbach M (2014) Morphological computed tomography features of surgically resectable pulmonary squamous cell carcinomas: Impact on prognosis and comparison with adenocarcinomas. European Journal of Radiology 83(7): 1275–1281.

[2] Cooper WA, O'toole S, Boyer M, Horvath L, Mahar A. (2011) What's new in non-small cell lung cancer for pathologists: the importance of accurate subtyping, EGFR mutations and ALK rearrangements. Pathology 43(2): 103–115.

[3] Gillies RJ, Kinahan PE, Hricak H (2016) Radiomics: images are more than pictures, they are data. Radiology 278(2): 563–77.

[4] Ferreira Junior J, Garcia Cipriano FE, Todorovic Fabro, A, Koenigkam-Santos M, de Azevedo-Marques PM (2018) Radiomics-based recognition of metastatic and histopathological patterns of lung cancer. Lecture Notes in Computational Vision and Biomechanics 27: 613–623.

Deep-learning combined with radiomic hyper-curvature features for survival prediction of patients with interstitial lung disease

R. Nasirudin[1], M. Matsuhiro[1,2], C. Watari[1], J. Nappi[1], T. Hironaka[1], Y. Kawata[2], N. Niki[2], H. Yoshida[1]
[1]Massachusetts General Hospital/Harvard Medical School, Radiology, Boston, United States
[2]Tokushima University, Tokushima, Japan

Keywords Deep learning · Radiomics · Computer-aided diagnosis · Interstitial lung diseases

Purpose

Rheumatoid arthritis (RA) is the most common connective tissue disease that develops inflammatory synovitis, which affects approximately 1% of people in the United States [1]. Interstitial lung disease (ILD) is one of the major extra-articular manifestations, where 5–10% of patients with RA suffer from clinically significant ILD. Survival after the diagnosis of RA-associated ILD (RA-ILD) has been reported as a median of 3–8 years. Currently, however, there is no established imaging predictor for the survival of patients with RA-ILD.

The purpose of this study was to evaluate the effect of deep-learning-derived radiomic features obtained from CT images, called deep radiomic features (DRFs), and their combination with CT radiomic features called hyper-curvature features, on the prediction of the overall survival of patients with RA-ILD in comparison with an established clinical prognostic biomarker known as the gender, age, and physiology (GAP) index [2].

Methods

We retrospectively identified 70 RA-ILD patients who underwent thin-section lung CT and pulmonary function tests, from the medical records of our institution. An experienced observer (an internist with 15 years of experience in pulmonary disease diagnosis and treatment) extracted approximately 4600 regions of interest (ROIs) from the CT images of all patients, and labeled them as having one of the following five lung texture patterns: normal, consolidated, ground-glass opacity, reticulation, or honeycombing. Then, an image patch of size 24×24 pixels was extracted at each point within these ROIs.

The image patches were subjected to a modified version of a publicly available DCNN (Cifar-10 CNN), which consisted of three layers of convolutional and max-pooling layers, for extracting hierarchical features with increasing levels of abstraction, followed by two fully connected layers for classification of the input images. The top-most layer of the DCNN outputs the probabilities at which the input voxel belongs to each of the five lung texture patterns. A 512-dimensional DRF vector for each patch was identified as an output of the last convolutional layer of the DCNN, and a 5-fold cross-validation method was employed for an unbiased estimate of the DRF vectors. The mean, standard deviation, and maximum of each element of the DRF vectors were computed on the lungs of a patient to derive a 1536-dimensional DRF vector for characterizing the patient.

We also computed CT radiomic features called hyper-curvature features [4] that included 4D principal curvatures, curvedness, blight-sheet, blight-cylinder, blight-blobs, dark-cylinder, dark-line, dark-blob, and the scale thereof on the lungs. Mean of each of these features were calculated on the bronchi and aerated lung regions separately, and used as independent hyper-curvature features.

The above DRF vectors, radiomic hyper-curvature features, and the combination thereof were subjected to a Cox proportional hazards model with an elastic-net penalty (hereafter called elastic-net Cox model) [5] for selecting and combining the elements of the vectors to build a Cox model that optimally predicts the survival of the patient. We used the concordance index (C-index) as a performance metric of the elastic-net Cox model. Bootstrapping with 750 replications was used to obtain an unbiased estimate of the C-index values for the DRFs, hyper-curvature features, and the combination thereof, and they were compared with an established clinical prognostic biomarker for ILD known as the gender, age, and physiology (GAP) index [2] using two-sided t test.

Results

Figure 1 shows the notched box plots of the C-index values obtained by application of the Cox model with the following combinations of features: (a) GAP model: C-index 78.5%, [95% confidence interval (CI) 70.3, 86.8]; (b) radiomic hyper-curvature features (RHC): C-index 86.1%, [CI 79.8, 92.4]; (c) DRF: 90.6% [CI 82.6, 98.7]; and (d) DRF + RHC: 92.1% [CI 84.7, 99.5]. The results indicate that the predictive performance of both the radiomic hyper-curvature features and DRFs are significantly higher than that of the GAP index ($p < 0.001$). Moreover, the combined features, DRF + RHC, outperform either one of these features ($p < 0.001$), indicating that the DRFs and radiomic hyper-curvature features are mutually complementary in their prediction performance.

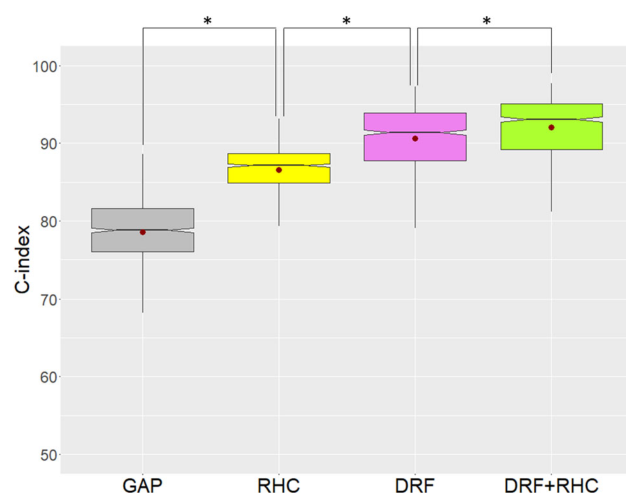

Fig. 1 Notched box plot of the C-index values obtained from the four different radiomic feature combinations. *Two-tailed t test: $P < 0.001$

Figure 2 shows the Kaplan–Meier survival curves of patients who were stratified to low- and high-risk groups of patients based on the combination of DRF and hyper-curvature features. Long-rank test showed that the difference of the survival curves between these two group were statistically significantly ($P < 0.001$).

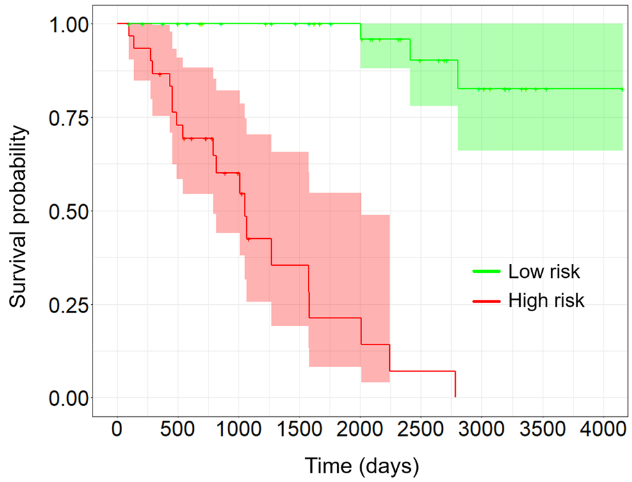

Fig. 2 Kaplan-Meier survival curves of RA-ILD patients stratified to low- and high-risk groups based on the combination of DRF and hyper-curvature features. Log-rank test: $P < 0.0001$. The color shades indicate the 95% confidence intervals of the survival curves

Conclusion

We demonstrated that a combination of DRF and radiomic hyper-curvature features outperformed the GAP, hyper-curvature features, and DRFs in predicting the overall survival of patients with RA-ILD. Thus, the combined features can be an effective prognostic biomarker for overall survival of patients with RA-ILD.

References

[1] Alamanos Y, Drosos AA. Epidemiology of adult rheumatoid arthritis. Autoimmun Rev 2005; 4: 130–136.
[2] Ryerson CJ, Vittinghoff E, Ley B, Lee JS, Mooney JJ, Jones KD, Elicker BM, Wolters PJ, Koth LL, King TE, Jr, Collard HR. Predicting survival across chronic interstitial lung disease: the ILD-GAP model. Chest 2014; 145: 723–728.
[3] Haralick RM, Shanmugam K, Dinstein I. Textural features for image classification. IEEE Trans Syst Man Cybern 1973; 3: 610–621.
[4] Watari C, Matsumoto M, Näpp JJ, Nasirudin RA, Hironaka T, Kawata Y, Niki N, Yoshida H. Deep radiomic prediction with clinical predictors of the survival in patients with rheumatoid arthritis-associated interstitial lung diseases. 2018; 10579.
[5] Simon N, Friedman J, Hastie T, Tibshirani R. Regularization Paths for Cox's Proportional Hazards Model via Coordinate Descent. J Stat Softw 2011; 39: 1–13.

Quantitative prediction capability of 3D CADv with pulmonary nodule component evaluation for malignancy and postoperative recurrence

Y. Ohno[1,2], A. Yaguchi[3], K. Aoyagi[4], S. Kaminaga[4], Y. Kishida[5], S. Seki[1,2], T. Yoshikawa[1,2]
[1]Kobe University Graduate School of Medicine, Division of Functional and Diagnostic Imaging Research, Department of Radiology, Kobe, Japan
[2]Kobe University Graduate School of Medicine, Advanced Biomedical Imaging Research Center, Kobe, Japan
[3]Toshiba Corporation, Corporate Research and Development Center, Kawasaki, Japan
[4]Canon Medical Systems Corporation, Otawara, Japan
[5]Kobe University Graduate School of Medicine, Division of Radiology, Department of Radiology, Kobe, Japan

Keywords Lung · CT · Nodule · Volumetry

Purpose

Lung nodule evaluations by computer-aided volumetry (CADv) such as volume measurement and doubling time assessment have been suggested as useful for differentiation of malignant from benign nodules. Solid component size within total nodule is considered as one of the predictors for non-small cell lung cancer (NSCLC) patients who are considered as candidates for surgical treatment, and assessed for T-factor classification in routine clinical practice. The software is now clinically available, and also developed for automatic differentiation and measurement of nodule component such as ground-glass and solid components within each nodule. No one reported the utility of CADv software with automatic measurement of nodule component for management of pulmonary nodule as well as prediction of postoperative recurrence in NSCLC patients. The purpose of this study was to evaluate the quantitative capability of newly developed 3D computer-aided volumetry (CADv) with pulmonary nodule component assessment for predicting malignancy and postoperative recurrence on thin-section CT.

Methods

59 consecutive patients (32 men, 27 women; mean age 68 years) who suspected lung cancer at nearby hospital and visit our clinic with 101 pulmonary nodules underwent repeated thin-section CTs, pathological examination, surgical resection and/or more than 2-years follow-up examination. All patients were diagnosed as patient with malignant nodule (n = 47) and patient with benign nodule (n = 12) groups. All nodules were also divided into malignant (n = 64) and benign (n = 37) nodule groups according to pathological and follow-up examination results. All patients with malignant nodules were operated and underwent equal to or more than 5 years follow-up examination, and divided into postoperative recurrence (n = 12) and non-recurrence (n = 35) groups. In this study, CADv automatically assessed solid, ground-glass opacity, cavity and total nodule volumes from two serial CT data. Then, total volume change per day (TV change/day), solid to total volume change ratio per day (S/T ratio change/day) and doubling time (DT) were determined. Student's *t* test was performed to compare all indexes between malignant and benign groups, and between recurrence and non-recurrence groups. Then, ROC analyses were performed to compare capabilities for differentiation of malignant from benign nodules and of recurrence from non-recurrence groups among all indexes as having significant difference between two groups, and determined all feasible threshold values. Finally, each diagnostic performance was compared by McNemar's test. A p value less than 0.05 was considered as significant at each statistical analysis.

Results

TV change/day and DT had significant differences between malignant and benign nodule groups ($p < 0.05$), although TV change/day and S/T ratio change/day had significant difference between recurrence and non-recurrence groups ($p < 0.05$). On distinguishing malignant from benign groups, area under the curves (Azs) of TV change/day (Az = 0.94) was significantly larger than that of DT (Az = 0.62, $p < 0.001$). In addition, specificity (SP) and accuracy (AC) of TV change/day (SP: 86.5 [32/37] %, AC: 91.1 [92/101] %) were significantly higher than those of DT (SP: 51.4 [19/37] %, $p < 0.001$; AC: 78.2 [79/101] %, $p < 0.001$). For distinguishing recurrence from non-recurrence groups, Az of S/T ratio change/day (Az = 0.92) was significantly larger than that of TV change/day (Az = 0.68, $p = 0.006$). Moreover, AC of S/T ratio change/day (80.9 [37/47] %) was significantly higher than that of TV change/day (59.6 [28/47] %, $p < 0.001$).

Conclusion

Newly developed 3D CADv system has quantitative capability for prediction of malignancy and postoperative recurrence on thin-section CT. When distinguishing malignant from benign nodules, TV change/day measurement has better potential than DT evaluation. For differentiating recurrence from non-recurrence groups, S/T ratio change/day assessment was more useful than TV change/day measurement (Fig. 1).

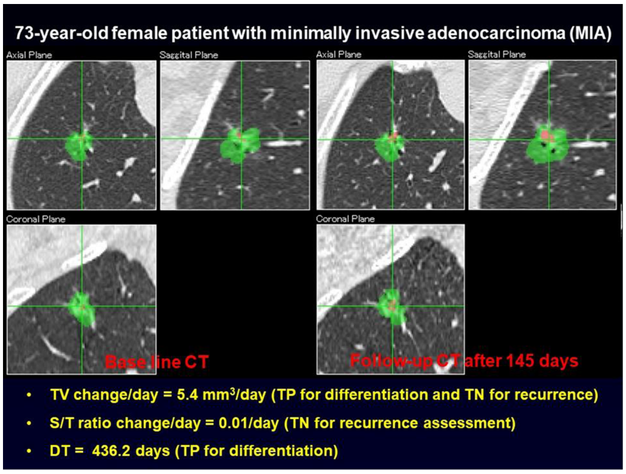

Fig. 1 73-year old female patient with minimally invasive adenocarcinoma (MIA)

On base line and follow-up CTs, a part solid nodule is detected. CADv system demonstrate ground glass component as green and solid component as pink. TV change/day was evaluated as true-positive (TP) for differentiation of malignancy and true-negative (TN) for postoperative recurrence assessment. Moreover, S/T ratio change/day was assessed as TN for recurrence assessment. In addition, DT was determined as TP for differentiation of malignancy.

24th Computed Maxillofacial Imaging Congress

Chairman: Christos Angelopoulos, PhD (USA),
Co-Chair: Yoshihiko Hayakawa, PhD (J)

Evaluation of cone beam computed tomography accuracy in surgical treatment plan of upper airway in OSA patients

W. Aboelmaaty[1], M. Isaac[2], M. Elewa[1], A. Elsobky[3]
[1]Faculty of Dentistry, Mansoura University, Oral medicine, Periodontology and Oral Radiology, Mansoura, Egypt
[2]Faculty of Dentistry, Delta University for Science and Technology, Oral and Maxillofacial Radiology, Mansoura, Egypt
[3]Faculty of Medicine, Mansoura University, ENT, Mansoura, Egypt

Keywords CBCT · Virtual endoscopy · OSA · Airway constriction leveling

Purpose

Obstructive sleep apnea (OSA) is sleep disorder where apnea or hypopnea episodes occur during sleep resulting in airway collapse and so Apnea–Hypopnea Index (AHI) is considered the parameter that classify the disease severity. Today OSA represents a major public health issue with a lot of potential consequences as: Cardiovascular and neurocognitive sequalae [2].

Due to complex airway morphology, (2D) imaging as cephalometric radiographs will lack necessary information to make a proper evaluation. To represent patient's airway anatomy more accurately, (3D) imaging is preferred. Although, computed tomography (CT) and magnetic resonance imaging (MRI) can depict the true 3D-airway morphology; however, their use is limited by high radiation dose, and noisy scan. Cone beam computed tomography (CBCT) scan the entire head with low radiation levels and provide true (3D) anatomically accurate views [1]. The aim of this study to evaluate the accuracy of detection of level of collapse in upper airway using CBCT virtual endoscopy and airway analysis tools versus drug induced sleep endoscopy (DISE).

Methods

This study consists of 40 patients who were selected from outpatient sleep clinic in Mansoura university hospital. Comprehensive clinical evaluation is performed; including assessment of patient risk factors such as: Body Mass Index (BMI) and a detailed sleep history including assessment of signs and symptoms of OSA such as presence of snoring or gasping during sleep, total sleep amount, morning headaches and memory complaints. Only patients who are refusing medical treatment and continuous positive airway pressure (CPAP) "surgical candidates" were selected for this study. Patients were divided into two groups: Group I consists of 20 patients who undergone surgical treatment without CBCT scanning, while group II consists of 20 patients who were exposed to pre-surgical radiographic evaluation by CBCT with quick scan imaging protocol of 23 cm × 17 cm FOV and 0.3 mm voxel size using iCAT FLX V17-Series machine (Imaging Science International, ISI, PA, USA).

Group II patients were scanned twice; once at the end of inspiration and the other at the end of expiration. To detect disease severity; AHI was performed. To evaluate upper airway anatomy to detect the possible levels of airway collapse; DISE was performed.

Raw Dicom data form CBCT scanning were transferred to a specific image analysis software. Linear and volumetric measurements were done including: total airway volume and narrowest cross-sectional area (CSA) which was also used to determine the level of the collapse whether it is retropalatal or retroglossal or hypopharyngeal or at the level of epiglottis. Also, the morphology of retropalatal space was determined (Fig. 1).

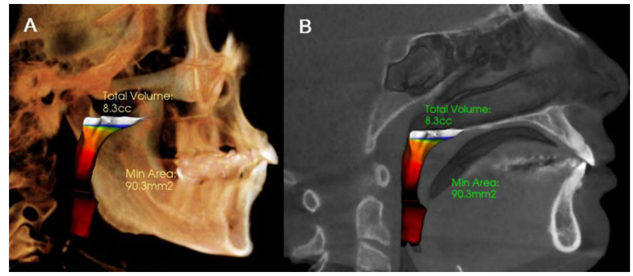

Fig. 1 Showing the total airway volume and minimum area measured by InVivo6 Dental software: **A** Teeth volume rendered view and **B** sagittal view

Virtual endoscopy was performed via Curved Planner Reconstruction (CPR) through the upper airway and compared with DISE. After clinical and radiographic assessment, ENT surgeon determined the proper surgical treatment plan (Fig. 2).

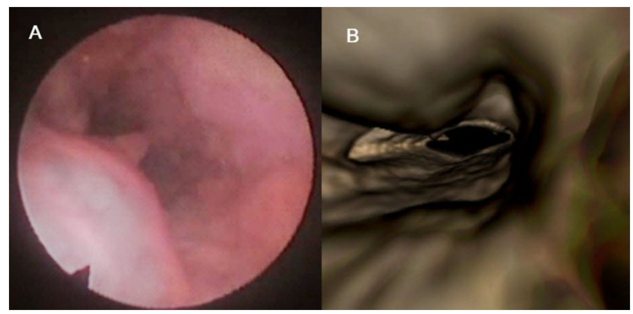

Fig. 2 Showing endoscopy shots: **A** DISE, **B** virtual CBCT endoscopy

Post-surgical clinical evaluation was performed to both groups after 6 months of the surgery to evaluate the success or failure of surgical procedure in both groups.

Results

Group II showed significant difference over group I in accuracy of surgical treatment of OSA. Also, group II showed more clinical superiority over group I in terms of patient satisfaction. The virtual endoscopy shows no significant difference in comparison with DISE.

Conclusion

CBCT is considered an impressive tool in diagnosing, evaluating and leveling upper airway collapse in OSA patients. Virtual endoscopy is considered an easy noninvasive tool that provide true (3D) anatomically accurate view of upper airway.

References

[1] Momany SM, AlJamal G, Shugaa-Addin B, Khader YS (2016) *Cone Beam Computed Tomography Analysis of Upper Airway Measurements in Patients With Obstructive Sleep Apnea*. Am J Med Sci 352(4): pp. 376–384
[2] Mannarino MR, Di Filippo F, Pirro M (2012) *Obstructive sleep apnea syndrome*. Eur J Intern Med, 23(7): p. 586–593

Accuracy improvement of facial soft tissue prediction following orthognathic surgery using geometrically-detailed FE mesh

D. Kim[1], T. Kuang[1], W. Xi[1], P. Yuan[1], S. G. F. Shen[2], X. Wang[2], M. F. Huang[1], J. Gateno[1,3], M. A. K. Liebschner[4], J. J. Xia[1,2,3]

[1]Houston Methodist Research Institute, Department of Oral and Maxillofacial Surgery, Houston, United States
[2]Shanghai Jiaotong University School of Medicine, Department of Oral and Craniomaxillofacial Surgery, Shanghai, China
[3]Weill Medical College of Cornell University, Department of Surgery, New York, United States
[4]Baylor College of Medicine, Houston, United States

Keywords Orthognathic surgery · Soft tissue prediction · Finite element method (FEM) · Lip accuracy

Purpose
It is important to accurately predict facial soft tissue changes following orthognathic surgery during surgical planning. However, the prediction accuracy for critical regions, such as the lips, remains poor [1, 2]. We hypothesized that independent sliding movement of the upper and lower lips can improve the prediction accuracy. In this study, we developed a new patient-specific mesh modeling technique and a new finite element method (FEM) to improve the prediction accuracy in critical regions.

Methods
Our new prediction method incorporates two significant improvements in lip modeling and FEM simulation. In the improved FE mesh modeling, the upper and lower lip surfaces are accurately modeled separately so that their movements can be independently simulated. After the lip geometry of the initial FE mesh is generated using our previously published method [3, 4], the inner and outer lip surfaces are defined by a set of points on the parasagittal planes. The new positions of mesh nodes on the lip surface are interpolated from the points. The lip surfaces are thus separated in the resulting mesh (Fig. 1).

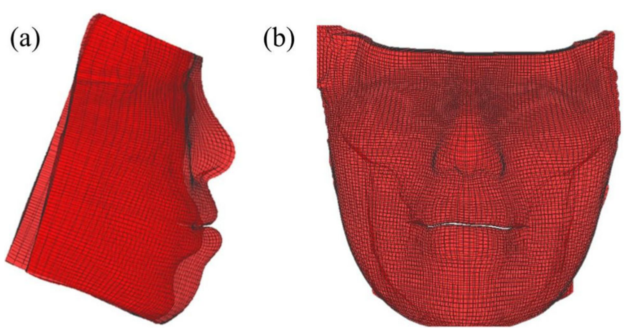

Fig. 1 Lateral (**a**) and frontal (**b**) view of an example of a patient-specific mesh with detailed lip geometry. Clear separation of the upper and lower lips is shown in the mesh

The improved FEM simulation is implemented in two steps. In the first step, facial soft tissue change is simulated with mucosa sliding effect according to the bony movements. Three types of nodes are defined on the mesh inner surface: fixed, moving, and free node. First, the regions that do not change during the surgery is assigned as fixed nodes. The movement of the moving node corresponds to that of the bony segment. In this study, the sliding movement is efficiently simulated by designating nodal movement only to the selected moving nodes and allow the other nodes to move freely. For the maxilla, the superior part of Le FortImaxillary segment above the mucosa and, for the mandible, retaining mandibular ligament attachments are selected as the moving nodes. The remaining nodes are spatially unconstrained (free nodes).

In the second step of the FEM simulation, compensation of lip penetration and mesh inner surface geometry are implemented to ensure geometric integrity of the final mesh. Because the upper and lower lips move independently in the first step, the upper and lower lips may penetrate each other in the resulted mesh. In order to solve this, the amount of vertical penetration of the lower lip surface into the upper lip is calculated. The opposite vector of vertical penetration is applied to the upper and lower lip surfaces to eliminate penetration. Finally, the inner surface of the mesh is projected onto the planed bony segment surface to match the mesh inner surface with the bone surface.

Ten patients who underwent double-jaw orthognathic surgery were randomly selected from our data archive. Accuracy evaluation was completed by comparing the predicted results to the actual postoperative result. Both new and traditional [5] methods were used for simulation. The postoperative CT was registered to the preoperative CT data. Then, facial change prediction was performed based on the bony movements. In the traditional method, the FE mesh was generated without the lip geometry enhancement and the inner surface of the mesh was assumed to be attached to the bone surface. Thus, no sliding movement or lip compensation was performed in the traditional method.

The qualitative evaluation was performed by a CMF surgeon. The surgeon visually compared the predicted results using both our new method and the traditional method to the actual postoperative soft tissue. The surgeon was blinded from the method used for the prediction. Since our algorithm was focused on improving the prediction quality of the lips, only upper and lower lips were evaluated.

Results
The qualitative evaluation results showed the prediction accuracy of our method was significantly better than the traditional method for the lower lip (Fig. 2, Table 1). The result of our new method was at least as good as the result of the traditional method.

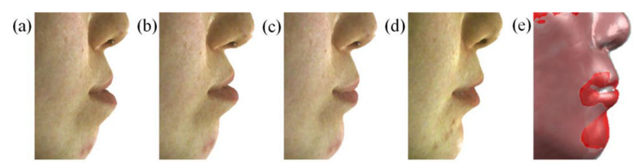

Fig. 2 A randomly selected example of simulated result with color texture mapped. **a** Preoperative soft tissue. **b** The traditional method resulting in large errors. **c** Accuracy improvement using our simulation method in the lips. **d** Actual postoperative soft tissue. **e** Superposition of the simulation result mesh (red) on the actual postoperative soft tissue (grey)

Table 1 Qualitative evaluation of our simulation method compared with the traditional method

Region	Our approach better	No difference noticed	Our approach worse
Upper lip	4	6	0
Lower lip	8	2	0

Conclusion
Our previous mesh modeling method had a limited lip geometrical accuracy, in which the upper and lower lips were not appropriately separated and the inner lip surface was not accurately modeled [3, 4]. Our new FE mesh significantly improves the geometrical accuracy for individual lip surfaces with separated upper and lower lips. The new FEM simulation also extends the application of sliding movement to the lips to enable independent lip movement. As a result, the prediction accuracy of our study is significantly improved compared to the traditional prediction method.

References

[1] Kim D, Ho DC, Mai H, Zhang X, Shen SGF, Shen S, Yuan P, Liu S, Zhang G, Zhou X, Gateno J, Liebschner MAK, Xia JJ (2017) *A clinically validated prediction method for facial soft-tissue changes following double-jaw surgery.* Medical Physics 44(8): 4252–4261

[2] Kim H, Jürgens P, Weber S, Nolte LP, Reyes M (2010) *A new soft-tissue simulation strategy for cranio-maxillofacial surgery using facial muscle template model.* Progress in Biophysics and Molecular Biology 103(2–3): 284–291

[3] Zhang X, Kim D, Shen S, Yuan P, Liu S, Tang Z, Zhang G, Zhou X, Gateno J, Liebschner MAK, Xia JJ (2017) *An eFTD-VP framework for efficiently generating patient-specific anatomically detailed facial soft tissue FE mesh for craniomaxillofacial surgery simulation.* Biomechanics and Modeling in Mechanobiology 17(2): 387–402

[4] Zhang X, Tang Z, Liebschner MA, Kim D, Shen S, Chang CM, Yuan P, Zhang G, Gateno J, Zhou X, Zhang SX, Xia JJ (2016) *An eFace-Template Method for Efficiently Generating Patient-Specific Anatomically-Detailed Facial Soft Tissue FE Models for Craniomaxillofacial Surgery Simulation.* Annals of Biomedical Engineering 44(5): 1656–1671

[5] Koch RM, Gross MH, von Büren DF, Fankhauser G, Parish YIH, Carls FR (1996) *Simulating facial surgery using finite element models. In: Proc. of SIGGRAPH* 421–428

An approach for 3D-visualization of bone metastases with focus on the craniofacial skeleton, applicable to CT and CBCT

C. Kober[1], P. Jürgens[2], H. F. Zeilhofer[2], B. I. Berg[2]
[1]HAW Hamburg, Hamburg, Germany
[2]HFZ Basel and University Hospital Basel, Mund-, Kiefer- und Gesichtschirurgie, Basel, Switzerland

Keywords Skeletal metastasis · 3D-visualization · CBCT · CT

Purpose

Bone is the third most common location for metastasis, after lung and liver. As estimation of osteolytic lesions, imaged with low contrast in spiral computer tomography (CT) and cone beam computer tomography (CBCT), is still a challenge in clinical diagnosis, a visualization approach of skeletal metastases was developed aimed at a clear display of the lesion's extent in 3D. As CBCT is characterized by high resolution, good bone contrast, and often less radiation compared to CT, applicability to both, CT and CBCT, is an additional focus of the research.

Methods

If necessary, image data are upsampled to less than 0.5 mm voxel side length. As preprocessing, kind of envelope around the considered bone, f.i. the mandible, is segmented from CT- or CBCT-data plus about 2 mm axial rim. Additionally, segmentation of an envelope covering trabecular bone plus some (smaller) axial rim through cortical bone is performed. Thereafter, two new image stacks are generated by isolation of the segmented voxels from the original data sets.

Bone metastases can be osteolytic, weakening the bone and imaged with low contrast, and/or osteoblastic, linked to sclerotic processes and imaged with high contrast. Based thereon, special transfer functions for slice oriented direct volume are defined, f.i. for two-tone direct or indirect visualization of kind of "micro-geometry" of the organ including full 3D-extent of the lesion (Figs. 1, 2) or applying a physical color scale for visualization of the distribution of the Hounsfield values displaying tissue inhomogeneity, especially skeletal destruction and/or sclerosation. The considered region is rendered in the foreground whereas the original anatomy is transparently displayed in black and white in the background.

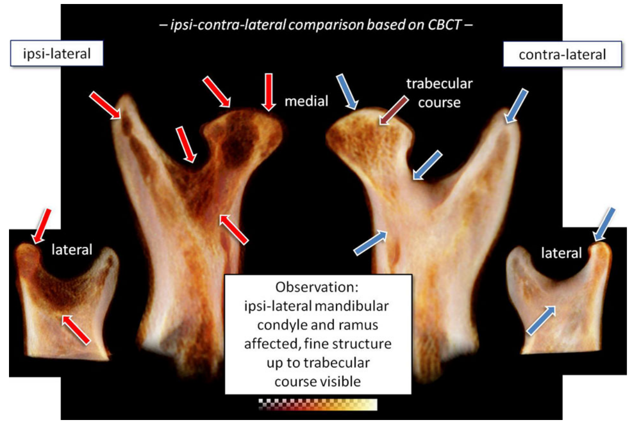

Fig. 1 Application based on CBCT to extended metastasis in condylar head and neck, ipsi-/contra-lateral comparison

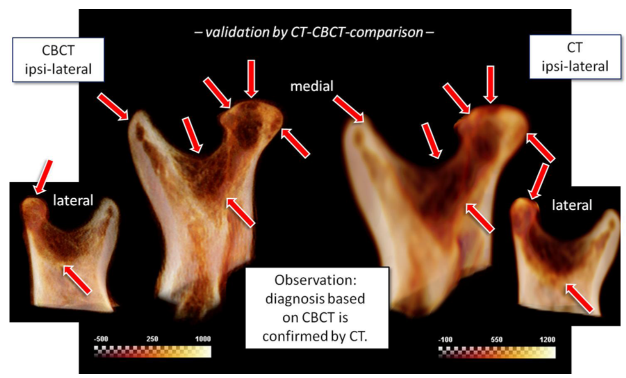

Fig. 2 Application based on CBCT and CT to extended metastasis in condylar head and neck, comparison of rendering of the lesion

If several CT-follow-up's are available or ipsi-/contra-lateral comparison is possible, quantitative evaluation via histogram analysis is possible. So, interpretation of inverse relative cumulative histograms of the trabecular segmentation allows for estimation of asymmetric trabecular loss, f.i. for osteolytic lesions of mandibular condyles.

Results

Exemplarily, the approach was applied to a clinical oncological case with CT and CBCT accquisition available with 2 days delay for diagnostic reasons. In the context of mamma-carcinoma, osteolytic skeletal metastasis in the right mandibular condyle was found. Application to both, CT and CBCT, delivered equivalent results, namely 3D-display of the lesion's extent (two-tone visualization, see Figs. 1, 2) or information about tissue inhomogeneity by multi-color visualization inter alia indicating fracture risk. With regard to its high resolution, CBCT turned out as well suitable for fine structure rendering, up to trabecular course. Quantitatively, ipsi-lateral trabecular loss in the condylar head and neck was confirmed based on CT and CBCT.

Conclusion

A CT/CBCT-based method for 3D-rendering of skeletal metastases is presented with clear results especially for osteolytic lesions which are characterized by low contrast in CT/CBCT and thereby usually harder to be found by conventional diagnosis. By the 3D-visualization, the physician can examine the lesion on the screen at several glances. Therefore, the approach endorses diagnosis efficiency. Additionally, the equivalent results based on CT and CBCT contribute, on the one hand, to the ongoing discussion of application of CBCT in comparison with conventional CT and, on the other hand, a validation of the approach itself as it delivered same results by different modality.

Acknowledgement

The presented results were partially supported by the MIRACLE Project, University of Basel, funded by the Werner Siemens-Stiftung, Switzerland. The first author cordially acknowledges H.-C. Hege, ZIB Berlin, and R. Brandt, Thermo Fisher Scientific, Berlin, Germany, for the Amira license.

Pathological mandibular biomechanics: quantitative estimation of pathological fracture risk by finite element analysis

C. Kober[1], C. Hellmich [2], A. Gurin[3], V. S. Komlev[4], G. Kjeller[5], R. Sader[6], H. F. Zeilhofer[7], B. I. Berg[7]

[1]HAW Hamburg, Hamburg, Germany

[2]TU Vienna, Institut für Mechanik der Werkstoffe und Strukturen, Vienna, Austria

[3]Central Scientific Research Institute of Oral and Maxillofacial Surgery, Moscow, Russian Federation

[4]A.A. Baikov Institute of Metallurgy and Material Science, Russian Academy of Sciences, Moscow, Russian Federation

[5]The Sahlgrenska Academy, Department of Oral and Maxillofacial Surgery, Gothenburg, Sweden

[6]University Frankfurt am Main, Mund-, Kiefer- und Plastische Gesichtschirurgie, Frankfurt am Main, Germany

[7]HFZ Basel and University Hospital Basel, Mund-, Kiefer- und Gesichtschirurgie, Basel, Switzerland

Keywords Mandible · Finite element · Marginal mandibulectomy · Mandibular cyst

Purpose

Mandibular pathologies as oral cancer, septic or aseptic osteonecrosis due to radiation or medication therapy, or severe atrophy cause progressing skeletal compromise with the risk of pathological mandibular fracture (PMF). In a recent clinical study, PMF was reported for 4 out of 44 cases after marginal mandibulectomy related to oral cancer [1]. Motivated by the question about the necessity of surgical stabilization of the jaw, either diagnostic concerning the patient's current situation or prognostic as regards a planned configuration, an approach for quantitative PMF risk estimation, respecting the patient's individual anatomy, bone quality, and biting capacities, was developed.

Methods

Based on patient's CT-data, a finite element (FE) model is built respecting the patient's anatomy, skeletal tissue coefficients, and directions of muscular traction according to [2–4]. Bite forces, f.i. molar or incisal biting, are either clinically measured e.g. by an occlusal force meter or estimated from the literature according to the pathology, notably mostly much lower rather than for healthy subjects.

Individual muscular forces are either highly varying and hardly measurable or fundamentally unknown in case of retro- or prospective analysis. For definition of load cases representing the patient's pathology-related load carrying behavior, data for maximal masticatory activity from the literature are adapted to the patient's (reduced) biting force using tools described in [3, 4]. Referring to scaling factors of electro-myographic measurements from the literature, a bundle of load cases can be computed reflecting the patient's individual reduced biting capacity.

As classical failure indicator, von Mises equivalent stress is evaluated for PMF risk estimation. In [5], 60 MP is reported as threshold for micro-damage in compact adult bone, presumably much lower for compromised bone.

Results

Exemplarily, retrospective results for a case after marginal mandibulectomy with severe osteoradionecrosis (ORN) (Case 1), same patient but with standard (healthy) skeletal tissue coefficients (Case 2), a partially edentulous case with cystic lesion (Case 3), same patient but the cyst filled with trabecular-like material (Case 4) are compared.

Patients with unilateral mandibular pathology tend to contra-lateral biting. Therefore, for all cases, ipsi-lateral stress at the lesion due to contra-lateral molar biting was tested (Fig. 1, Bite 1 and 2). For Cases 3/4, additionally virtual ipsi-lateral biting was analyzed (Fig. 1, Bite 3 and 4).

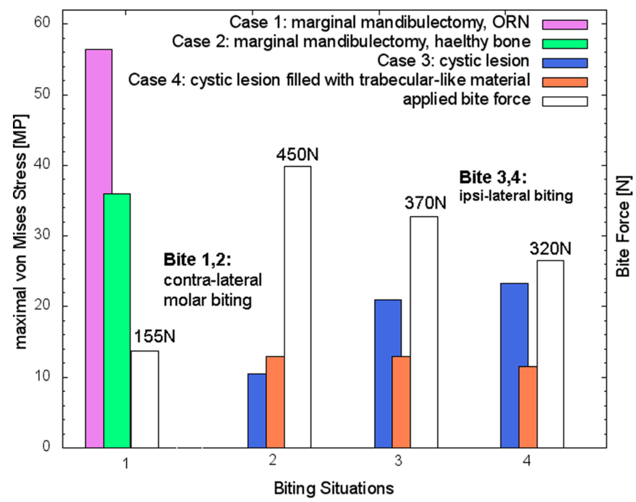

Fig. 1 Ipsi-lateral maximal von Mises equivalent stress for selected biting situations, ipsi-lateral: mandibular half with the lesion, contra-lateral: mandibular half opposite to the lesion

For Bite 1 and 2, biting forces from the literature are applied. Biting forces for Bite 3 and 4 are adapted by the own procedure accordingly. Muscle forces for Bite 2–4 are about at the same level. In the opposite, muscle forces for bite 1 are about one-third of the muscle forces for Bite 2.

For the cystic case (Case 3), the stress due to contra-lateral molar biting with 450 N (Bite 2) is about at the same level as for the cyst filled with trabecular-like material (Case 4). However, for both mandibulectomy cases (Cases 1 and 2), contra-lateral molar biting produces immense ipsi-lateral stress especially at the distal resection margin (Fig. 2, left) which, for the ORN case, nearly achieves the threshold of 60MP though very moderate biting force (Fig. 1, Bite 1). In the opposite, contra-lateral molar biting exhibits comparably moderate ipsi-lateral stress around the cystic lesion though higher bite forces (Fig. 2, right). Besides Bite 2, stress levels with pathology exceeded the ones with healthy tissue coefficients. Generally, increased stress levels for Cases 3 and 4 are also due to partial edentulism.

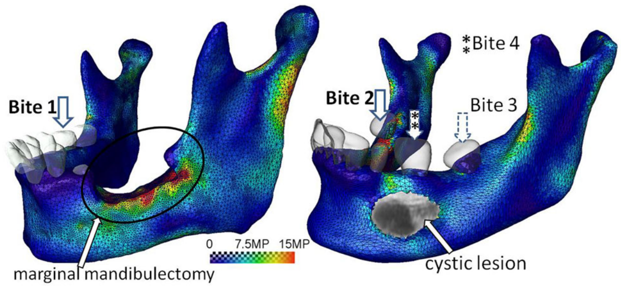

Fig. 2 von Mises equivalent stress due to contra-lateral molar biting, left: high stress in the distal resection margin after marginal resection with ORN (Case 1, Bite 1), right: comparably moderate stress for the cystic lesion (Case 3, Bite 2), dotted arrows indicate load for Bite 3 respectively Bite 4

The results are in good agreement with simulations and experiments from the literature [5].

Conclusion

A computational approach for quantitative PMF risk estimation based on FE simulation was presented respecting individual anatomy, tissue quality, and biting capacity. In case of a cystic lesion, the results endorse contra-lateral molar biting. However, for mandibulectomy patients, even moderate contra-lateral molar load produces dangerous ipsi-lateral stress which is consistent with the high PMF prevalence reported in [1]. Notably, especially patients with good contra-lateral muscular and dental status are at risk for too high masticatory activity. The approach is aimed at support of clinical diagnosis and therapy mainly for estimation of the necessity of surgical stabilization by plates or screws, but also recommendation of soft diet at least for some time or further conservative means of craniofacial therapy.

Acknowledgement

The presented results are part of a detailed project about mandibular biomechanics, partially supported by the MIRACLE Project, University of Basel, funded by the Werner Siemens-Stiftung, Switzerland, and the Theme FP7-2008-SME-1, 7th Framework Programme of the European Commission, Grant No. 232164, BIO-CT-EXPLOIT. The authors acknowledge the Department of Oral and Maxillofacial Radiology, Institute of Odontology, Sahlgrenska Academy, Gothenburg University, Sweden, for provision of the radiological data. Finally, the first author cordially acknowledges H.-C. Hege, ZIB Berlin, and R. Brandt, Thermo Fisher Scientific, Berlin, Germany, for the Amira license.

References

[1] Okuyama K, Michi Y, Mizutani M, Yamashiro M, Kaida A, Harada K (2016) Clinical study on mandibular fracture after marginal resection of the mandible. J Oral Maxillofac Surg 121(5): 461–467.

[2] Hellmich C, Kober C, Erdmann B (2008) Micromechanics-based conversion of CT data into anisotropic elasticity tensors, applied to FE simulations of a mandible. Ann Biomed Eng 36(1): 108–122.

[3] Kober C, Hellmich C, Stübinger S, Zeilhofer HF, Sader R (2015) "Anatomical simulation" of the biomechanical behavior of the human mandible. Int J Comp Dent 18(4): 333–342.

[4] Kober C, Hellmich C, Gurin A, Komlev VS, Kjeller G, Sader R, Zeilhofer HF, Berg BI (2017) Pathological mandibular biomechanics: finite element analysis based on partial dentition, cystic lesion, and partial resection. Int J CARS 12(Suppl 1): S169-S171.

[5] Murakami K, Sugiura T, Yamamoto K, Kawakami M, Kang YB, Tsutsumi S, Kirita T (2011) Biomechanical analysis of the strength of the mandible after marginal resection. J Oral Maxillofac Surg 69(6): 1798–1806.

Importance of quantitative evaluation of jaw bones

A. Katsumata[1], H. Fujita[2], H. Hayashi [3]
[1]Department of Oral Radiology, Asahi University School of Dentistry, Gifu, Japan
[2]Department of Intelligent Image Information, Graduate School of Medicine, Gifu University, Gifu, Japan
[3]College of Medical, Pharmaceutical and Health Sciences, Kanazawa University, Kanazawa, Japan

Keywords Intraoral radiography · Panoramic radiography · Osteonecrosis · Bone mineral density

Purpose

The development of computer-aided detection/diagnosis (CAD) systems for dental imaging is progressing [1]. One expected use of CAD technology is in the quantitative evaluation of jaw bones. Firstly, as the osteoporosis alters the morphology of the inner surface of the mandibular cortex, we developed a CAD system to detect radiological signs of osteoporosis in the dental panoramic radiography. Secondly, mineral density measurement of alveolar bone may be useful to predict possible patients who will occur bisphosphonate-related osteonecrosis of the jaw (BRONJ) or medication-related osteonecrosis of the jaw (MRONJ). Because these osteoporosis medicines affect the mineral density of alveolar bone significantly. It has been reported that alveolar bone with BRONJ and/or MRONJ appeared radiopaque findings. Finally, A newly developed photon-counting semiconductor X-ray detector acquires transparent X-ray beams by dividing them into several energy bands. The energy divided photon counting can be used to evaluate hard tissue quantitatively [2].

Methods

We developed a computer analysis system of mandibular cortex morphology for screening of osteoporosis. It is known that an altered morphology of the mandibular cortex on panoramic radiographs is significantly correlated with osteoporosis. Our computer program scans the mandibular inferior cortex and defines the mandibular cortical index (MCI) automatically. We have reported that, automatic MCI classification concomitant with manual compensation revealed the best accuracy. The overall diagnostic sensitivity to detect possible osteoporosis was 95%, and the specificity was 95%. Clinical trial of this computer program was performed in collaboration with regional dental clinics.

To establish a simple method for evaluating the mineral density of the alveolar bone and teeth. We developed a computer assisted image analysis system based on conventional microdensitometry technique. The proposed system measures bone mineral density (BMD) by means of image density of the intraoral radiograph (Fig. 1). The software measures the image density of the reference object automatically and calculates the BMD value of the arbitrary region of interest (ROI). The value of alveolar bone density was compared between dual-energy X-ray absorptiometry (DEXA) and the proposed system.

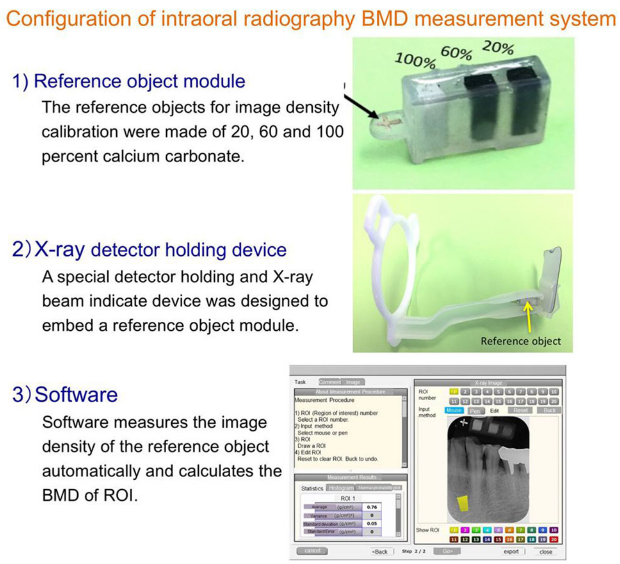

Fig. 1 Configuration of intraoral radiography BMD measurement system

Development of energy divided photon counting system is progressing. A preliminary study to evaluate the effective atomic number (Z-eff) and BMD of mandible body, teeth and cervical vertebra was performed.

Results

Clinical trial of mandibular cortex morphology analysis system discovered 25 new osteoporosis patients out of 830 panoramic X-ray examinations.

As the results from testing of BMD measurement system, high correlation coefficient (r = 0.92) was revealed between the proposed method and the DEXA measurement. Several clinical trials are in progress to evaluate the BMD of alveolar bone in patients who are undergoing medication for osteoporosis. The other hand, mineral density measurement of teeth may useful to diagnose early stage dental caries or weak part of tooth enamel and dentin in each tooth.

The new photon counting detector based proposed method can be used to extract Z-eff of hard tissue anatomical structure. Proposed method also enables to measure BMD of mandible body and cervical vertebra. Intraoral imaging system using new photon counting detector must be useful in dental practice.

Conclusion

The quantitative evaluation techniques of jaw bones are important for dentistry to screen the both new osteoporosis patient and possible patients of BRONJ/MRONJ. In addition, BMD measurement of jaw bones are useful in dental implant and periodontitis treatment. Because the success of dental implants depends largely on the quality and quantity of the available bone in the recipient site. And the periodontitis involves progressive loss of the alveolar bone around the teeth.

References

[1] Katsumata A, Fujita H (2014) Progress of computer-aided detection/diagnosis (CAD) in dentistry. Japanese Dental Science Review. Volume 50(3), 63–68

[2] Langlais R, Katsumata A, Naidoo S, Ogawa K, Fukui T, Shimoda S, Kobayashi K (2015) The cadmium telluride photon counting sensor in panoramic radiology: gray value separation and its potential application for bone density evaluation. Oral Surg Oral Med Oral Pathol Oral Radiol. 120(5), 636–643

Efficient 3D rigid registration of large micro CT images

P. Rösch[1], K. H. Kunzelmann[1,2]

[1]Augsburg University of Applied Sciences, Faculty of Computer Science, Augsburg, Germany

[2]Dental School of the Ludwigs-Maximilians University, Munich, Department of Restorative Dentistry and Periodontology, München, Germany

Keywords 3D Image registration · Image fusion · Micro CT imaging · Optimisation

Purpose

The ever increasing sizes of 3D micro and nano CT images challenge established image registration approaches that require images to fit into random access memory (RAM). The aim of this work is to overcome this limitation by using modern solid-state disks (SSD) in combination with a novel image encoding scheme and on-the-fly compression thus allowing for the efficient registration of very large data sets even on notebook computers.

Methods

Registering images not fitting into RAM requires data stored in files while subsequent blocks are loaded into memory for processing. Although current SSDs are faster than conventional hard disks, file access is still the main bottleneck of the proposed algorithm. Performance can be improved by applying lossless block-based data compression reducing disk load. The achievable compression ratios can be increased by filling volumetric image elements (voxels) not relevant for registration with zeros. Which parts are relevant depends on the chosen similarity measure quantifying the degree of spatial correspondence between images [1]. The major contributions to the local correlation coefficient (LCC) measure [2] applied here originate from corresponding edges which are in turn related to strong gradients. Thus, only voxels at locations with large absolute gradient values are kept together with their neighbours required for LCC calculation while all other voxels are filled with zeros. Binary masks used to exclude e.g. sample holders can be incorporated by setting masked out regions to zero yielding combined, highly compressible images specifically tailored to LCC calculation. LCC derivatives with respect to transformation parameters can be calculated analytically [3] and the Levenberg–Marquardt method is applicable [4] allowing for efficient optimisation.

A class representing compressed on-disk images as well as high-level processing functionality have been implemented in Python using numpy, scipy and a fast compression library [5]. For LCC calculation and other time critical tasks, parallelised cython code has been developed. To increase both robustness and speed, standard multi resolution optimisation progressing from coarse to fine [1] is applied where an initial estimate is provided in terms of a transformation matrix. Settings are stored in configuration files allowing for batch processing and reproduction of previous runs. The algorithm determines the transformation matrix establishing spatial correspondence between image locations. Furthermore, one image can be resampled into the voxel space of the other for direct comparison.

Results

The software has been successfully applied to several dental micro CT images acquired e.g. before and after preparation. Registration accuracy has been assessed qualitatively by inspecting overlay and difference images. One typical experiment is discussed below.

An extracted molar tooth has been imaged using a Micro-CT 40 device (Scanco Medical AG) with an isotropic resolution of 10 µm at different stages of restoration. Image sizes are 2048 × 2048 × 2381 and 2048 × 2048 × 2271 voxels. Restoration material has been segmented using ITK-SNAP and binary masks excluding the restoration have been created. Overall input data amounts to 55 GiB, almost seven times the RAM size of the computer used. Multi resolution representations of the masked data sets with isotropic resolutions up to 320 µm have been created. For each resolution level, local absolute grey value gradients were calculated and voxels corresponding to the top one percentile of gradient values as well as their neighbours were kept. Filling the remaining voxels with zeros, compression ratios around 10 could be achieved for the highest resolution levels. Longitudinal slices are shown in Fig. 1 where areas actually used for registration appear red. Note that the high density of the restoration led to noise-induced gradients in the image shown on the right. However, as these artefacts are not present in the left image and only corresponding edges contribute to LCC, registration was not affected. The identity transform has been used as initial estimate for iterative optimisation. On a notebook with a dual core 2.6 GHz Core i5-3320M CPU, 8 GiB of RAM and a standard SSD reading up to 500 MB/s, total execution time was 192 min if the original images were used at the final resolution level. Overall calculation time could be reduced to 13 min by restricting optimisation to images with minimum isotropic resolutions of 40 µm at the cost of somewhat lower accuracy. Results of the low-resolution run are shown in Fig. 2 where the absolute values of local grey value differences before and after registration at the original resolution are shown. Apparently, registration was accurate even for the low-resolution run as almost all undesired differences resulting from displacement could be removed. In this case, a longitudinal shift by about 300 µm is dominant while rotation angles are below 0.2 degrees. This is typical for such experiments because forces applied during restoration in longitudinal direction often result in sample displacements within the holder.

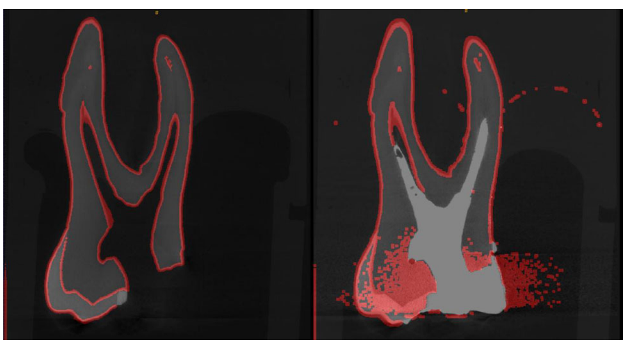

Fig. 1 Longitudinal slices of sub sampled 3D micro CT images acquired before (left) and after (right) restoration. Only voxels close to edges (red) are used for registration. Note that spurious edges resulting from noise in the right image do not affect registration accuracy as explained in the text

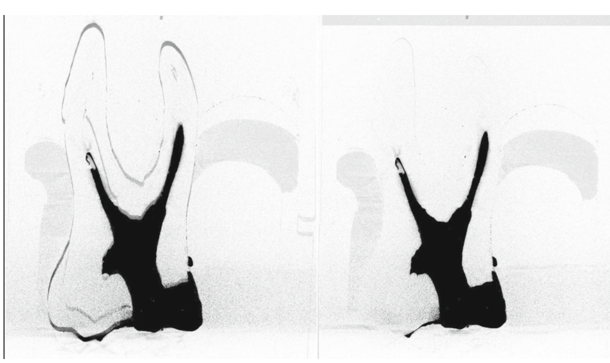

Fig. 2 Longitudinal slices of absolute grey value difference between fixed and moving images before (left) and after (right) 3D registration. Images have been inverted to improve visibility so that dark areas correspond to large absolute differences

Conclusion

Combining an SSD with a novel image encoding scheme specifically tailored to the local correlation similarity measure, an efficient 3D registration software for images that do not fit into random access memory has been created and successfully applied to register two micro CT volumes with sizes above 2048^3 voxels on a notebook computer with 8 GiB of RAM in 13 min. Currently, run-length-encoding is being incorporated to speed up image traversal. Furthermore, a quantitative evaluation of registration accuracy is under way.

Acknowledgements

This work benefited from the use of ITK-SNAP, an open-source software for image segmentation and visualisation. For quaternion computations the module transformations written by Christoph Gohlke has been applied.

References

[1] Hajnal JV, Hill DLG, Hawkes DJ (Eds.): Medical Image Registration, CRC Press (2001)
[2] Rösch P, Blaffert T, Weese J: Multi-Modality Image Registration using Local Correlation. In: H. U. Lemke, M. W. Vannier, K. Inamura, A. G. Farman (Eds.): Proceedings of CARS'99, Elsevier Science (1999) 228–232
[3] Netsch T, Rösch P, v. Muiswinkel A, Weese J: Towards Real-Time Multi-Modality 3-D Medical Image Registration. Eight IEEE International Conferences on Computer Vision, ICCV 2001, 718–725
[4] Kabus S, Netsch T, Fischer B, Modersitzki J: B-Spline Registration of 3D Images with Levenberg–Marquardt Optimization. Proceedings of SPIE 5370 (2004), 304–313
[5] Alted F, et al.: bcolz documentation, http://bcolz.blosc.org (2017)

Do ASIR and MBIR aid in dose optimization for dental implant imaging?

A. Al-Ekrish[1], A. Alabdulwahid[1], S. Alfadda[2], W. Alfaleh[1], R. Al-Shawaf[1], R. Hörmann[3], W. Puelacher[3], D. Tamimi[4,5], G. Widmann[3]
[1]King Saud University, Oral Medicine and Diagnostic Science, Riyadh, Saudi Arabia
[2]King Saud University, Department of Prosthetic Dental Sciences, Riyadh, Saudi Arabia
[3]Medical University of Innsbruck, Innsbruck, Austria
[4]Private Practice, Orlando, United States
[5]University of Texas Health Science Center, San Antonio, United States

Keywords Multidetector computed tomogra · Algorithms · Radiation dosage · Dental implants

Purpose

The iterative reconstruction techniques (IRTs) of Adaptive Statistical Iterative Reconstruction (ASIR) and Model Based Iterative Reconstruction (MBIR) have been advocated as a means for dose optimization in multidetector computed tomography (MDCT) because, compared to the traditionally used filtered backprojection reconstruction (FBP), they lead to the production of images with less noise when ultra-low radiation doses are used. However, the usefulness of ultra-low doses and IRTs in dental implant imaging needs to be assessed prior to their implementation in clinical practice. Dental implant imaging involves several diagnostic and therapeutic tasks, all of which must be validated when performed using ultra-low MDCT doses and IRTs, before such protocols may be considered useful for implant imaging. The diagnostic tasks include measurement of ridge dimensions, objective localization of the inferior alveolar canal (IAC), and subjective classification of bone quality. Thus, the purpose of the study was to compare the following parameters recorded from a reference dose CT examination reconstructed with FBP with those recorded from test examinations obtained using ultra-low doses reconstructed with FBP, ASIR, and MBIR:

1. Linear dimensions of the edentulous ridge.
2. Linear dimension of the height of the ridge above the IAC
3. Subjective bone type classification.

Methods

Complete cadaver heads were imaged with a standard dose reference MDCT examination (100 mA, 120 kV, CTDIvol: 29.4 mGy) and 5 ultra-low dose (LD) test examinations: LD1 (35 mA, 100 kV, CTDIvol: 4.19 mGy), LD2 (40 mA, 80 kV, CTDIvol: 2.64 mGy), LD3 (15 mA, 80 kV, CTDIvol: 0.99 mGy), LD4 (10 mA, 80 kV, CTDIvol: 0.53 mGy), and LD5 (10 mA, 80 kV, CTDIvol: 0.29 mGy). All the examinations utilized a pitch of 0.53, except LD5 which was performed with a pitch of 0.97. The reference examination was reconstructed with FBP and each test examination was reconstructed with FBP, ASIR 50, ASIR 100, and MBIR, for a total of 20 test protocols.

The following parameters were recorded from the images:

1. Linear dimensions of the edentulous ridge (height and width) (recorded from the test protocols LD4 and LD5 only).
2. Linear dimension of the height of the ridge above the IAC.
3. Subjective bone type classification using the revised CT-based Lekholm and Zarb (L&Z) jawbone quality classification.

The results from each test protocol were compared to those from the reference protocol. For the linear dimensions, the test and reference values were compared using One-sample *t* test, Bland–Altman plots and regression analysis. For the bone type classification, Kappa statistic was used to analyze the level of the agreement between the reference and test protocols, and the clinical significance of the differences was analyzed by the Wilcoxin signed ranks test.

Results

Ridge dimensions: The ridge dimensions recorded from the following three protocols were comparable to the those from the reference: LD4/FBP, LD4/ASIR 50, and LD5/FBP. Thus, a 99% reduction in dose combined with FBP provided comparable measurements to the reference dose.

Ridge height above the IAC: In addition to the reference protocol, only three protocols allowed the identification of the IAC on all the sample sites: LD1/FBP, LD1/ASIR 100, and LD2/FBP. The ridge dimensions recorded above the IAC from all three protocols were comparable to those from the reference.

Bone quality classification: The agreement between the reference and test protocols varied slightly by examiner. Examiners 1 and 2 found moderate to strong agreement, while Examiner 3 found strong to almost perfect agreement between the reference and test protocols. For the results of all three examiners, the Wilcoxin signed ranks test did not demonstrate a clinical significance of the differences between the reference and test protocols.

Thus, a 91% reduction in dose did not adversely affect identification of the IAC, and a 99% reduction in dose provided comparable results for linear ridge measurements and subjective bone quality classification.

Conclusion

Dose optimization for implant imaging may be achieved with 91% reduction in dose and use of FBP. The use of ASIR and MBIR does not appear to provide an advantage over FBP. Currently used MDCT protocols need to be re-evaluated to ensure dose optimization is achieved.

Robust digital dental articulation for one-piece maxillary orthognathic surgery

J. Li[1], W. Xi[1,2], F. C. Afonso[1], P. Yuan[1], C. F. Yao[1], M. Huang[1], D. M. Alfi[1], J. Gateno[1], J. J. Xia[1]
[1]Houston Methodist Research Institute, Oral and Maxillofacial Surgery, Houston, United States
[2]Affiliated Stomatological Hospital of Nanchang University, Nanchang, China

Keywords Digital dental articulation · Midline-guided occlusion · Optimization · Configurable constraints

Purpose

One of the critical steps in orthognathic surgery is to establish a correct dental occlusion (the relationship between the upper and lower teeth, or the bite) [1, 2]. When doctors use stone dental models to establish occlusion, the act of articulating maxillary and mandibular models into a desired occlusion is relatively easy and accurate. The visual and tactile feedback together with the cognitive insight for stone models makes dental articulation straightforward. An experienced operator can complete this task in a matter of seconds. The same is not true in the virtual world, where digital dental arches are represented by two three-dimensional (3D) images that lack collision constraints, i.e., the computer software does not stop the two images from moving through each other once the model surfaces are in contact. In addition, there's no tactile feedback for the operator while articulating the models. It's a complex task to virtually articulating 14 upper teeth (3rd molars are usually extracted) against 14 lower teeth into their best possible occlusion. Therefore, the purpose of this study is to develop a midline-guided occlusion optimization with configurable constraints (MGOO-CC) approach for robust digital dental articulation in one-piece maxillary orthognathic surgery.

Methods

The MGOO-CC approach consists of five major steps (Fig. 1). The first step is to extract feature points for occlusal surfaces between the maxillary and mandibular dental arches [3]. These feature points represent the curves for maxillary and mandibular dental arches. The second step is to transform both maxillary and mandibular models to the working space in the leveling position. The third step is the initial (coarse) alignment using an ergodic midline match algorithm [4]. Clinical rules are used to guide this initial alignment, i.e., upper and lower midline alignment, and appropriate overbite and overjet. It is a challenge to determine a definitive combination of overbite and overjet, since the clinical normative value of each measurement is age- and gender-specific and presented in mean and standard deviation [5]. Therefore, in our algorithm, we performed an ergodic search to generate a series of midline-match transformations by using a range of overbite (0.9–3.0 mm, 0.3 mm per step) and overjet (1.5–3.0 mm, 0.3 mm per step), resulting in a total of 48 possible sets of occlusion. Based on clinical requirement for canine and molar Class I relationship, the algorithm automatically ranks the top 8 combinations for the next step. The fourth step is the final (fine) alignment using an improved iterative surface-based minimum distance mapping (ISMDM) optimization algorithm [3]. It combines the configurable constraints, i.e., midline match and the weights of canine and molar Class I relationship. The top 4 final alignments selected from the initial 8 combinations are selected based on clinical occlusal rules. In addition, a 5th occlusion in maximum intercuspation (MI) is also generated regardless of the clinical rules. This is useful for orthodontically optimized patients. In the final step, each of the aligned maxillary and mandibular models is transformed back to the original space for clinical use.

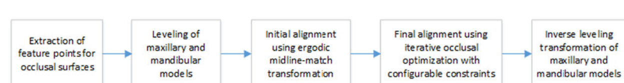

Fig. 1 Overview of the procedure for digital dental articulation

Our MGOO-CC approach was validated using 16 sets of randomly selected patient dental models who underwent one-piece maxillary orthognathic surgery [IRB(2)#1011-0187x]. Each patient dataset included a set of hand-articulated maxillary and mandibular models, which were achieved using the current standard-of-care method [1]. The models were scanned together using a high-resolution cone beam computed tomography scanner and was used for the actual surgery. These models served as ground truth. The maxillary digital models were then disrupted from articulation, repositioned in 6 degrees-of-freedom using a random number table, and re-articulated using our MGOO-CC approach. These served as the experimental group.

Results

The results showed that all dental arch alignments achieved with our automatic MGOO-CC approach were at least as good as the surgeon hand-articulated alignments. There was only a small degree of surface deviation (< 0.5 mm) between the occlusion generated by our MGOO-CC approach and the ground truth. Such a small degree of deviation does not have any clinical significance. It is important to note that the ground truth models were hand articulated by surgeons using the eyeballing method, and thus do not necessarily represent ground truth. Figure 2 shows one randomly selected example of the articulated models.

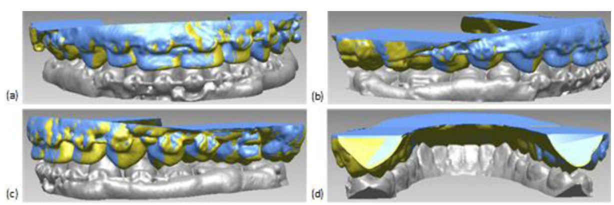

Fig. 2 A randomly selected example of algorithm-generated articulation. Yellow: reference model; Blue: experimental model. **a** Anterior view; **b** right oblique view; **c** left oblique view; **d** posterior view

Conclusion

The results showed that our MGOO-CC approach is a robust method for automated 1-piece digital dental articulation. This is far superior to the original ISMDM optimization algorithm [3] that we previously developed for the same purpose. Although the original algorithm has solved the mathematical problem of aligning the maxillary and mandibular dental models into MI, it does not take into account any clinical rules, including midline alignment overbite, and overjet, which are clinically more relevant. Our other previously developed midline-guided occlusion optimization (MGOO) approach [4] has solved the aforementioned problems. However, it was designed for a 3-piece dental articulation, in which the maxillary dental arch is osteotomized into three individual pieces then realigned back together. Our new MGOO-CC approach possesses the advantages of both ISMDM and MGOO for robust 1-piece dental articulation. In addition, it incorporates configurable constraints in order to meet different requirements of the treating surgeons and orthodontists depending on the various deformities of the dental arches and facial skeleton. Once it has been thoroughly validated with a larger sample size, it will be used in daily clinical practice.

References

[1] Bell WH (editor): Modern practice in orthognathic and reconstructive surgery: Volume 1. W B Saunders Co, 1992
[2] Xia JJ, Gaeteno J, Teichgrae JF: New clinical protocol to evaluate craniomaxillofacial deformity and plan surgical correction. J Oral Maxillofacial Surg, 67(10): 2093–2106, 2009
[3] Chang YB, Xia JJ, Gateno J, Xiong ZX, Zhou XB, Wong STC.: An automatic and robust algorithm of reestablishment of digital dental occlusion. IEEE Transactions on Medical Imaging, 29(9): 1652–1663, 2010
[4] Li JF, Ferraz F, Shen SY, Lo Y-F, Zhang XY, Yuan P, Tang Z, Chen KC, Gateno J, Zhou XB, Xia JJ: Automated Three-Piece Digital Dental Articulation. MICCAI, 2015
[5] Bhatia SN: A manual of facial growth: a computer analysis of longitudinal cephalometric growth data. Oxford: Oxford University Press, 1993.

Evaluation of surgical planning software for mandibular reconstruction using fibular free flap

S. Park[1], T. G. Son[1], H. Kim[1], H. Cho[1], J. W. Lee[2], Y. Kim[1], S. Park[1]
[1]Korea Institute of Science and Technology, Center for Bionics, Seoul, South Korea
[2]Kyung Hee University, School of Dentistry, Seoul, South Korea

Keywords Computer assisted surgery · Mandibular reconstruction · Fibular free flap · Virtual surgical planning

Purpose

Recently, three-dimensional (3D) virtual surgical planning (VSP) techniques have been widely used to improve surgical output and reduce required time and effort of traditional surgical procedures for mandibular reconstruction using fibula free flap. However, there are few indices to evaluate the result of preoperative VSP quantitatively. Most of the evaluations for mandible reconstruction were performed through pre- and post-operative comparative study. Although Nakao [1] has introduced a shape descriptor to quantize the automatic surgical planning system, but it also has limitation that only applicable to the relatively normal and symmetrical mandible. In this paper, we propose an improved reconstruction error metric with inspiration from Nakao's shape descriptor. We also evaluated our surgical planning system developed with optimized functions and a user-friendly interface [2].

Methods

The reconstruction error metric is calculated by measuring the distance difference between the original mandible and the fibula segments located in the preoperative planning. In our evaluation process, a special step which creates a reference mandible has been added. The reference mandible can replace a portion of a mandible that is deformed or lost significantly due to disease or other reasons (the left top of Fig. 1). The reference mandible is created by mirroring the mandible of the normal part and aligning it with the normal region on the opposite side (the right top of Fig. 1). After preparing the reference mandible, we evaluate with the reconstruction error metric fully automatically through a series of steps such as definition of mandibular tangent plane, creation of sampling curve, calculation of the distance between the placed fibula segments and mandible (Fig. 1c). In this paper, we assess our surgical plan in comparison with the surgical plans that clinical experts created using commercial planning software, Mimics (Materialise Inc., Belgium). The planning process of our system consists of automatic planning and manual correction. In manual correction step, the user can easily modify the fully automatically generated surgical plan reflecting the user's preference. Five cases were used, and as the evaluation index, the time taken for the planning and the reconstruction error of the established plan were used.

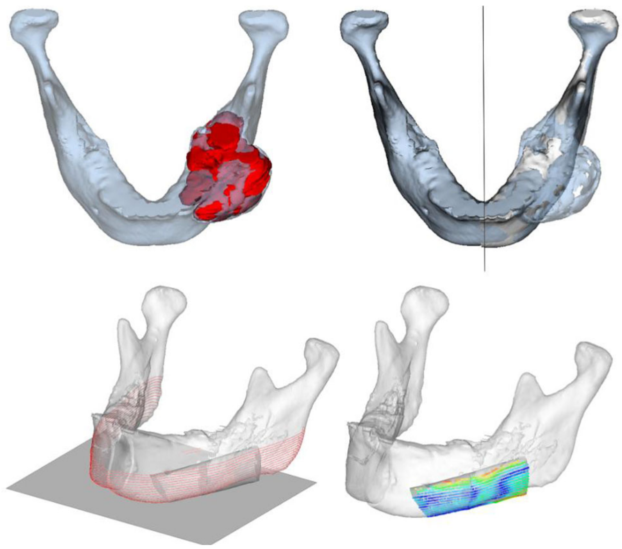

Fig. 1 Generation of reference mandible for significantly deformed case (the top row) and calculation process and result of reconstruction error (the bottom row)

Results

The time taken for the preoperative planning was 38 m 11 s ± 12 m 35 s on average for experts and 3 m 58 s ± 1 m for our system, respectively. Figure 2 shows the reconstruction error metric of plan performed by expert, automatic planning of our system, and automatic planning with user correction. The average difference of reconstruction error metric with the experts of automatic planning and correction are 1.52 ± 1.09 and 0.15 ± 0.18 mm, respectively. The evaluation results show that our system can make a surgical plan of expert-level in a shortened time. In addition, it shows that standardized automatic planning can significantly reduce the individual variation of users.

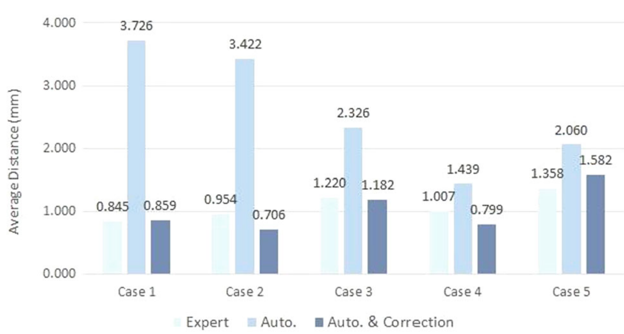

Fig. 2 Evaluation results of our planning system with reconstruction error metric

Conclusion

We presented an evaluation method of 3D surgical plan itself for mandibular reconstruction using fibular free flap which can be used also for abnormal case. We also verified the accuracy and efficiency of our surgical planning system through the proposed evaluation metric. We will improve our system so that it can be reliably applied to more various cases.

Acknowledgements

This work has been supported by the KIST Institutional Program (2E27990).

References

[1] Nakao, S. Aso, Y. Imai, N. Ueda, T. Hatanaka, M. Shiba, T. Kirita, and T. Matsuda, Automated planning with multivariate shape descriptors for fibular transfer in mandibular reconstruction, IEEE transactions on biomedical engineering, vol. 64 (8), pp. 1772–1785, 2016.

[2] Y. Kim, H. Kim, H. Cho, J. Charton, D. Lee, J. W. Lee, L. Kim, Development of surgical planning software for mandibular reconstruction using fibular flap, Proceedings of the 31st International Congress and Exhibition on CARS 2017, Int. J CARS, vol. 12 (Suppl. 1), pp. S285-S286, 2017

The indication and application of computer-assisted navigation in oral and maxillofacial surgery

H. Yu[1], S. Shen[1]

[1]Ninth People's Hospital, Shanghai Joao Tong University School of Medicine, Oral and Craniomaxillofacial Surgery, Shanghai, China

Keywords Navigation · Oral and Maxillofacial Surgery · Surgical accuracy · Indication

Purpose

Requiring functional and esthetic consideration, surgery in oral and maxillofacial region remains intellectually and technically challenging for even the most experienced surgeons. The surgical results can be compromised despite of well-planned operations. Image-guided navigation has shown great potential for clinical applications, particularly when precise location of any instrument or bony anatomic landmark is required. With real-time instrument positioning and clear anatomic identification, computer assisted navigation system (CANS) is exceptionally helpful in maxillofacial surgery. This study introduced our experience with the use of CANS and summarized its indication and advantages in oral and maxillofacial surgery.

Methods

1. Patients

115 patients including 40 zygomatic-orbital-maxillary fractures, 32 unilateral temporomandibular joint (TMJ) ankylosis, 30 craniofacial fibrous dysplasia, 5 cartilage/bone tumors of jaw and 8 cases with facial foreign bodies. The patients (53 males and 62 females) had a median age of 29 years (range 16-47). All the lesions or deformities were unilateral. This study was approved by hospital ethics committee.

2. Preoperative planning and simulation

Five position titanium screws as navigation markers were implanted in maxillary alveolar bone, a preoperative thin-cut (0.625 mm), spiral computed tomography (CT) (Light speed 16, GE, Gloucestershire, UN) scan DICOM data was obtained individually. The data was then transferred to a Windows-based computer workstation with Accu-Navi software (Multifunctional surgical navigation system, Shanghai, China). The software converts DICOM data into a proprietary format; compiles the 2-D axial images; and presents the data in axial, coronal, sagittal, and 3-D reconstructions. Patients individual anatomy was assessed in multiplanar and 3-D views.

For those patients presenting unilateral diseases or deformities, median sagittal plane used as reference plane, normal anatomic structures and contour of the target area were mirrored from the unaffected side. Thus the normal contour of the affected side, the line and amount of osteotomy, the anatomic position for fractured bone reduction and the marginal boundary for tumor resection were ascertained. In side-to-side comparison, the virtual and real anatomic structure was defined and displayed on 3-D reconstruction model by different color. Reference points were set on the designed osteotomy line and the reduced position for fractured bony segments. After the preoperative planning and simulation was completed, both the original CT dataset and the virtual reconstruction model were transferred to intraoperative navigation system.

3. Intraoperative navigation

Acc-Navi system (Multifunctional surgical navigation system, Shanghai, China) was used in this study. With infrared cameras tracking the navigation pointer and trackers, intraoperative navigation was carried out by frameless stereotaxy. The patient and instruments position was identified with Digital Reference Frame (DRF), which fixed rigidly to the patients forehead and surgical instruments respectively. Five position screws, which implanted in maxillary alveolar bone preoperatively, were used as registration markers. Intermaxillary fixation was needed for patients with mandibular operation. Tracking information was processed by the Acc-Navi system and merged with 3D craniomaxillofacial model, providing surgeons with continuous 3D positioning of their instruments.

TMJ arthroplasty, fracture reduction with/without orbital floor reconstruction, craniomaxillofacial recontouring, tumorectomy, and removal of foreign body were performed under the guidance of navigation. Surgical results were checked immediately with the probe to ensure the coincidence with surgical planning.

4. Postoperative evaluation

Postoperative evaluation consisted of CT scans (3–5 days after surgery) and clinical examination. Quantitative postoperative evaluation of the intervention was performed using image mirror method. The postoperative CT reconstruction models were compared with those of preoperative planning using image fusion. The maximal deviation of the operation between the virtual plan and the achieved results was analyzed.

Results

Preoperative planning, simulation and intraoperative navigation were performed successfully in all 115 patients. The navigation system error measured by computer was less than 1 mm after registration. The osteotomy lines, amount and range of tumor resection, the reduction position of bony segments and reconstruction morphology was displayed on the screen. TMJ arthroplasty, anatomic reduction of fractured bone with/without orbital floor reconstruction, craniomaxillofacial recontouring, tumorectomy, and removal of foreign body were performed according to preoperative planning. The navigation systems provided continuously updated information on the position and movement of surgical instruments in the operating field in relation to the preoperative imaging data set.

All patients healed uneventfully and their function and profile was improved obviously. No serious complications occurred in all patients. Facial morphology was improved significantly in 5–65 months of follow up. A mean 33.5 mm interincisor mouth opening was achieved in patients with TMJ ankylosis. For the patients with zygomatic-orbital-maxillary fractures, normal ocular movement was rehabilitated in all patients. Diplopia in 17 patients was eradicated and that in the other two patients was alleviated. Good coincidence with preoperative planning was achieved for osteotomy lines, resection amount and fracture reduction. Using image fusion, the postoperative CT reconstruction models were compared with those of preoperative planning. The mean deviation between the preoperative design and actual surgical results was 1.46 ± 0.24 mm.

Conclusion

At present, the applications of CANS in oral and maxillofacial surgery can be summarized in the following areas: localization of pathological lesions or foreign objects; fracture reduction; bone tumor resection; surgical corrections of maxillomandibular malformations or facial asymmetries. Using this system, different surgical procedures can be simulated and individualized optimal surgical planning can be made. Therefore, as long as surgeons are aware of the limitations and advantages of the system and regularly perform a recalibration using anatomic landmarks, the navigation system will prove to be a useful supplement in oral and maxillofacial surgery.

References

[1] Yu H, Shen G, Wang X, Zhang L, Zhang S. (2013) The indication and application of computer-assisted navigation in oral and maxillofacial surgery-Shanghai's experience based on 104 cases. Journal of Cranio-Maxillofacial Surgery 41(8), pp 770–774

[2] Schramm A, Gellrich NC, Gutwald R, Schipper J, BlossH, Hustedt H, Schmelzeisen R, Otten JE: Indications for computer assisted treatment of cranio-maxillofacial tumors. Comput Aided Surg 2000, 5: 343–352

[3] Yu HB, Shen GF, Zhang SL, Wang XD, Wang CT, Lin YP: Navigation-guided gap arthroplasty in the treatment of temporomandibular joint ankylosis. Int J Oral Maxillofac Surg 2009, 38: 1030–1035

Computer Assisted Radiology and Surgery

Chairs: Leonard Berliner, MD (USA), Makoto Hashizume, MD, PhD (J), Heinz U. Lemke, PhD (D), Yoshihiro Muragaki, MD, PhD (J)

Machine intelligence and CARS

H. U. Lemke
International Foundation of Computer Assisted Radiology and Surgery (IFCARS), Kuessaberg, Germany

Purpose

Contrary to the popular and general term Artificial Intelligence, the more neutral expression Machine Intelligence (MI) is used at CARS as an umbrella term for this very significant information technology. In general, MI is presented and discussed at CARS in the specific context of assisting medical diagnostic and therapeutic procedures in radiology and surgery. Machine learning, deep learning and clinical decision support systems are typical examples of MI in sessions of past CARS congresses. Within this specific medical focus, MI is providing new technical and clinical capabilities using advanced mathematical methods and innovative information technology tools. The CARS 2018 Special Session on Machine Intelligence addresses 5 critical questions relating to the substance, relevance, applications, impact and implications of mathematical methods and algorithms of MI:

1. What qualifies a mathematical method or an information technology tool to be considered as machine, artificial or computational intelligence (or any other synonym or near-synonym) for radiology or surgery?
2. Which mathematical method or information technology tools are of particular relevance for applying MI in radiology and surgery?
3. How can these mathematical method or information technology tools for MI be applied to improve clinical work flow and/or patient outcome?
4. When can results and impact of MI be expected for improved clinical workflow and patient outcome?
5. What are the potential economic, social and ethical implications of MI in radiology and surgery specifically, and in health care generally?

The potential answers to these questions are likely to be of a very divergent nature. A group of experts at CARS will endeavor to converge the answers to reproducible and actionable insights. These should also serve as guidelines for future research in MI for computer assisted radiology and surgery.

Methods

Something to be assigned "intelligent" in the context of CARS, could be defined to imply a system which has an adequate representation/model of the present situation, an adequate representation/model of a desired future situation, and an executable plan (process model) to proceed from the present situation in an optimal way to the desired future situation [1]. For example in the context of machine intelligence in the digital operating room (DOR), this implies the availability of appropriate models of the patient and the systems/environments in the DOR as well as the interventional processes to be followed. The IT architecture of a medical information and model management system (MIMMS) and specifically a therapy imaging and model management system (TIMMS) [3] for the OR environment (Fig. 1) have been designed to fulfill such requirements and are in development at various R&D centers.

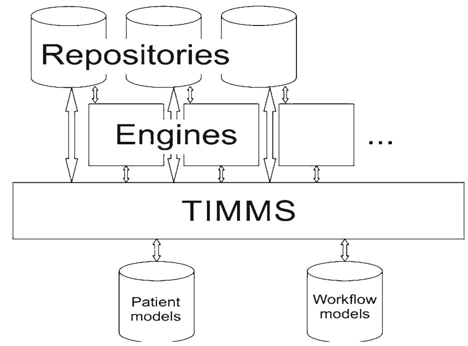

Fig. 1 Therapy imaging and model management system (TIMMS), courtesy R. Stauder [3]

In the language as found in the classic artificial intelligence literature [4], the engines made available to fulfill the required functionalities are agents of various characteristics such as Simple Reflex, Model-based, Goal-based, Utility-based or Learning Agents.

In the context of clinical decision making, for example in the complex decision-making cycles involved in monitoring the progress of a procedure, this may imply usage of software agents at various positions of the surgical workflow, see Fig. 2 [5].

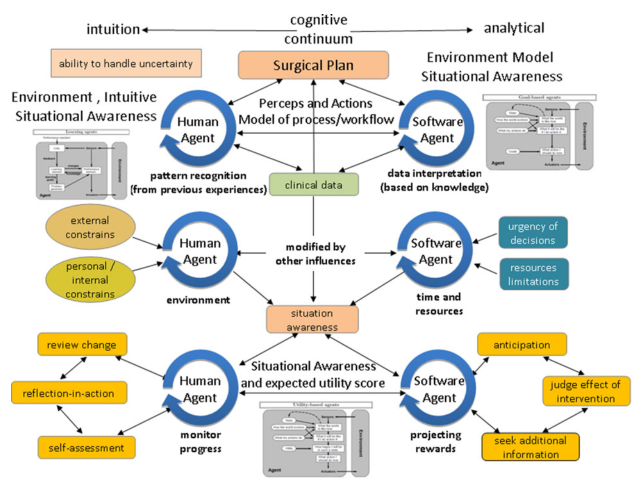

Fig. 2 The complex clinical decision-making cycles involved in monitoring the progress of a procedure and possible positioning of human and software agents, adapted from [5]

As presented by W. Crebbin et al. in [5] and shown as an extract of the surgical process in Figure 2, "clinical decision making is a core competency of surgical practice. It involves two distinct types of mental processes best considered as the ends of a continuum, ranging from intuitive and subconscious to analytical and conscious". These types of processes may best be presented by human and software agents, respectively, as the state-of-the-art in machine intelligence may support.

Results

Different stages of maturity have been identified in the development of the DOR for the first quarter of the twenty-first century [2]: Current research on the DOR suggests that the following machine intelligence driven features can be expected to be realized during the next 10 years:

- Knowledge and decision management
- Patient specific models
- Surgical cockpit systems
- Model-Based Medical Evidence (MBME)

- Real time access to P2P surgical process repositories
- Intelligent real time data mining
- Full voice/gesture control
- Medical TIMMS architecture
- Real time CAD integration
- Intelligent (situation aware) robotic devices

A relatively comprehensive set of models and algorithms (mathematical methods and information technology tools) for intelligent (learning) behavior have been developed in recent years. They can serve as enablers of the above features expected for the digital operating room of the future.

Discussion

Trust in this form of "intelligence" and in the right record keeping and subsequent management of interventional process information for patient outcome evaluation, are new dimensions of concern when machine intelligence moves into therapeutic activities within the context of a DOR. The other dimensions relate to economics and ethics.

In particular, how do we define the measures of goodness or success regarding outcome for the patient, physician and healthcare at large, when applying advanced IT methods, including machine intelligence, in specific clinical domains. One of the real human intellectual challenges ahead (something which cannot be done by the machine!) is to find the right balance between success and resources in the design, implementation, application and evaluation of MIMMS like architectures.

References

[1] Lemke HU (2013) Machine intelligence in the OR: optimizing the effectiveness of surgeons with IT tools, International Hospital, Viewpoints, May/June 2013, pp. 22–24.
[2] Lemke HU, Berliner L (2011) DOR Maturity Levels (2005–2025 and beyond): Evolutionary growth path. Int J CARS 2011; 6(Suppl 1): June 2011, Springer Verlag, Heidelberg, Germany.
[3] Stauder R (2017) Context Awareness for the Operating Room of the Future, PhD Thesis, Technical University Munich, Germany
[4] Russell S, Norvig P (2010) Artificial Intelligence: A Modern Approach (3rd ed.), Prentice Hall, ISBN 0-13-790395-2
[5] Crebbin W, Beasley SW, Watters DAK (2013) Clinical decision making: how surgeons do it, ANZ Journal of Surgery 83(6): 422–428, https://doi.org/10.1111/ans.12180

Convolutional properties and their applications in a neural networks setting—data correlation learning or deep learning?

S. Lo[1], S. K. Mun[1], M. Freedman[1]
[1]Virginia Tech, AIC: Health Research, Arlington, VA, United States

Keywords Convolutional neural networks · Convolution kernal · Data correlation learning · Isotropic CNN

Purpose

Many investigators have raised questions about how to construct an effective convolutional neural networks (CNN) for a given application since it has attracted considerable attention in computer vision and data sciences globally. In this paper, key processes of CNN are reviewed in terms of mathematic properties in various types and kernel sizes of convolution operation which would lead to assist the user in CNN application design particularly in number of layers required, kernel size design, and convolution filtering characteristics.

Methods

Single convolutional layer: In a traditional pattern recognition approach, differentiable features are necessary to be extracted followed by a feature analysis to separate one category from another in order to form an effective machine learning system. To understand how a CNN works, a simplified structure can be used as a model: one input layer, one hidden convolution layer, and one output layer. In a course of pattern recognition, there are two steps for signals to pass by: (1) each node on the hidden convolutional layer receives a composed signal through fan-in networking modulated with shared convolutional weights from adjacent nodes on the input layer; (2) each node on the output layer receives an independent weight from the connected node on the previous layer. After a successful training, we cannot exactly identify which step perform what function. But it is clear that step (1) performs feature extraction more than step (2) and step (2) performs classification more than step (1). This is because convolution process has been proven to be versatile in analyzing correlated data. However, small convolution kernel size would be unable to extract feature with a distant correlation in the input data string. Therefore, a sufficient large kernel size is needed for the convolutional process to extract potential features in distant data correlation. Nevertheless, feature existed within distant data may not be a factor for the classification task (i.e., not a differentiable factor when compared to other categories). In such case, this intra-data correlation feature serves no purpose to the classification task. But it may be an essential factor in another classification task.

Multiple convolutional layers: The most CNN structures used in diversified applications so far are constructed with multiple convolutional layers. Mathematically speaking, a large convolution kernel can be made by multiple convolution processes with smaller kernels. Since convolutional process with a large size kernel takes much more computation time and power than two or a few smaller size kernel computations, if the added small sizes is not larger than the large size of kernel. Hence, the implementation of multiple small convolution layers has its advantage in terms of computational effectiveness.

Results

Simulated data sequences with defined distant correlation were generated to perform the study. The study showed that the smallest kernel size required in the single convolutional layer for the CNN to be effective is approximately the longest distance of differentiable intra-data correlation in the input layer. However, the differentiable intra-data correlation is categorization dependent in the output layer.

As evidenced by previous investigators, the use of a large convolutional kernel can be replaced by composing multiple convolutional processes with small kernels [1, 2]. The relationship between the effective size of composed large convolutional kernel (L) and multiple small length (Si) of convolution kernels is given by:

$$L = S1 + S2 + \cdots + Sm - (m - 1),$$

where "m" is the total number of convolution processes (or layers) and i = 1, 2, … m.

Conclusion

The observation of multiple convolutional layers in a CNN structure is considered as a type of deep learning since ~ 2009 in the field of computer science. However, the truth is the resultant of composed multiple small kernel convolutional processes is a large kernel convolutional process.

Historically, the authors were the first team who named the neural networks with convolution process "convolution neural networks (CNN)" in 1993. This paper further clarifies that the convolutional neural networks is a type of data string (data for short) correlation learning (DCL) no matter number of layers is used. Deep or multilayer learning is observed as an equivalent computational approach of data correlation learning in the internal CNN process.

Two things worth mentioning regarding the properties of convolution process in CNN are: (1) If the data string is correlated somewhat evenly or from beginning to the end, a mirrored data can be padded on the boundary and the convolution kernel can be made isotropic so that a smaller kernel size can be effectively applied for the application. (2) If correlation inside the data string is clearly broken into several regions, individual convolutional process for each region (e.g., through segmentation as preprocessing) can be used for the optimization of the CNN work [3, 4].

References

[1] Simonds RM (1988) "Reduction of large convolutional kernels into multipass applications of small generating kernels." J Opt Soc Amer A, 5(7): 1023–1029.

[2] Lo SB, Xuan J, Li H, Wang Y, Freedman MT, Mun SK, (1997) "Dyadic Decomposition: A Unified Perspective on Predictive, Subband, and Wavelet Transforms", SPIE Proc Med Imag, 3031: 286–301.

[3] Lo SB, Lin JS, Freedman MT, Mun SK (1993) "Computer-Assisted Diagnosis of Lung Nodule Detection using Artificial Convolution Neural Network" SPIE Proc Med Imag, 1898: 859–869.

[4] Lo SB, Chan HP, Lin JS, Li H, Freedman MT, Mun SK (1995) "Artificial Convolution Neural Network for Medical Image Pattern Recognition." Neural Networks, 8(7/8): 1201–1214.

Battery-less power source of intelligent medical IoT instruments and devices

M. Daniol[1,2], L. Boehler[1,2], A. Keller[1], R. Sroka[2]

[1]Aesculap AG, Tuttlingen, Germany

[2]AGH University of Science and Technology, Metrology and Electronics, Krakow, Poland

Keywords Energy harvesting · Internet of things · Medical instruments · Digitalisation

Purpose

Medical internet of things (IoT) is becoming more and more popular in several different areas like patient monitoring, wearables, hospital logistics, etc. One of the possible applications of such technology is surgical container management and logistics. Moreover, it is very important to know the sterile status of the container due to infection threat during the operation procedure [1]. Nowadays most of the facilities use containers with analogue sterile indicators and tracking system based on documentation and labelling. This may be easily replaced by using the electronics for tracking and automated documenting the containers and instruments flow. However, one of the main problems in digital container surveillance is the steam sterilisation. In the standard Aesculap sterilisation process the temperature reaches 135 °C and the pressure inside the autoclave varies from − 1 to 2 bars. The whole procedure takes 32 min. Available power solutions such as primary or secondary batteries have either short lifetime, either either they cannot stand high temperature of steam sterilisation because of thermal runaway which causes the explosion of the cell. This would lead to the power source failure making the whole container out of service and possible dangerous for medical staff. The alternative to standard power sources is using the thermoelectrical generators (TEG). TEG is usually constructed in the form of a plate and generates the electrical power from the temperature gradient across its sides. Their application areas are typically industrial wireless sensors, automotive, marine, and renewable energy (solar panels, wind turbines) [2]. In medical industry, most of the applications are focused on powering wearable sensors or implantable devices while there is no application intended for instrument or container surveillance [3]. The lack of reliable power source is the crucial issue in current development of so called smart surgical instruments. Thus our aim was to create the TEG-based power source for medical IoT devices which can handle standard steam sterilization and become a reliable power source.

Methods

The overall scheme of the energy harvesting module is presented in the Fig. 1.

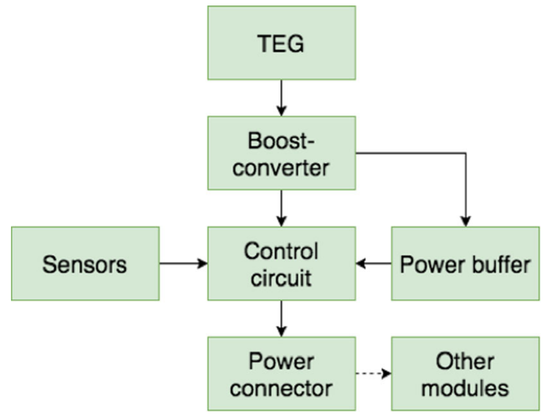

Fig. 1 General scheme of the energy harvesting module

The TEG is connected to the boost converter to increase and stabilize the output voltage. The power generated is then used by sensors or other modules i.e. Bluetooth low energy. It can be also stored in power buffer, like high-temperature supercapacitor, in the case it is not fully used by the sensors. The switching between power buffer and sensors is made using control circuit. The whole module is insulated using the aerogel based insulation. The TEG is connected to the heatsink exposed outside the insulation and to the heat bank inside the insulation. Extreme low thermal conductivity of the aerogel (27) allows to create temperature gradient through TEG during the sterilisation process and maximize the generated power. The selection of the TEG needs to be done according to working conditions. It is worth to mention that in the case of low temperature gradients the Peltier cooling modules can be used as generators. To choose the right module from the manufacturer the thermal coefficient of the heatsink, estimated temperature difference and the ambient temperature needs to be known [4]. The supercapacitor, used as the energy storage device, needs to hold the energy for long time—this implies choosing the model with lowest leakage current possible.

The testing procedure was divided into two phases, in the first phase the temperature differences inside and outside the insulation of TEG was recorded. The average temperature difference during the sterilisation procedure was approx. 35 °C. In the second phase, this temperature gradient was applied as a step to the test circuit comprising TEG, heatsink, boost converter and the load. The additional tests were performed with the Bluetooth module to estimate the possible energy balance of the whole application.

Results

The results of the tests are shown in the Fig. 2 below. TEG was able to provide up to 2.1V (blue line) with the temperature difference of 35 °C. The whole circuit generated 3.0 V (red line), 1.5 mA which gives 4.5mW overall. As it is shown on the diagram, 0.7 V is enough to start the boost converter and provide the output voltage of 3.0 V. The average energy consumption of the Bluetooth Low Energy module used in the experiment is 0.011 mA.

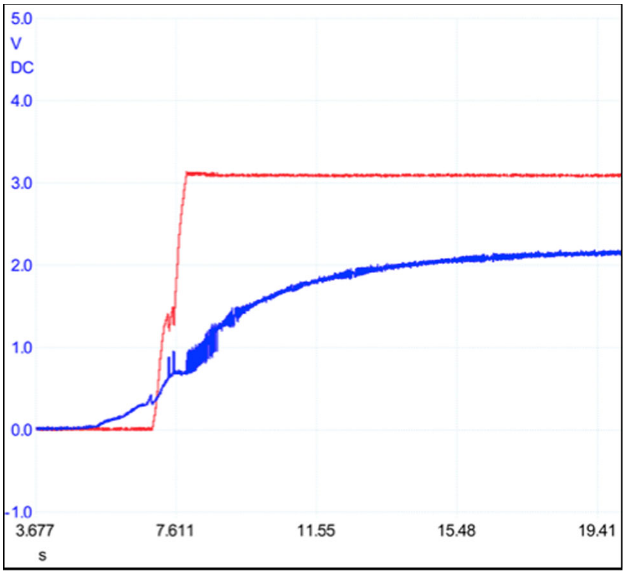

Fig. 2 results of the TEG power generation, the voltage generated by the TEG is marked as a blue line and the red line indicates the voltage after boost converting

Conclusion

The prototype tests showed that it is possible to generate up to 4.5 mW of power with TEG based energy harvesting module. The total power collected during the single sterilization procedure can charge the 2.0 mAh battery. This is enough to run the sensor module for at least 5 days. As some authors suggest, the efficiency of the whole sys-tem may be increased by using multiple TEG modules or optimizing the module arrangement, type (like using the thin organic TEG) or its internal design [5]. Other further possible improvements include using phase changing materials as a heat storage to improve TEG power generation. This combined with the newest cutting-edge Bluetooth low energy chips, which uses only 3.3 mA for broadcasting, gives us very promising possibilities for further optimizations and design enhancements. Possible applications of our idea involve not only the surgical container surveillance and tracking but also powering the smart surgical instruments equipped with sensors, sterilisable smart beacons which can be used in hospital logistics, monitoring the status of surgical power tools, and finally the augmented reality applications bridging the world of physical devices with digital interface for the operating room of the future.

References

[1] Chu NS, Chan-Myers H, Ghazanfari N, Antonoplos P (2015) Levels of naturally occurring microorganisms on surgical instruments after clinical use and after washing. Am J Infect Control, 1999; 27: 315–319.

[2] Champier D (2017) Thermoelectric generators: A review of applications, *Energy Conversion and Management,* vol. 140. pp. 167–181

[3] Boehler L, Daniol M, Kleinhans L, Keller A, Sroka R (2017) Heat resistant electronic modules for intelligent medical sterile containers, in *EPiC Series in Health Sciences, CAOS 2017. 17th Annual Meeting of the International Society for Computer Assisted Orthopaedic Surgery*, pp. 100–103.

[4] Lineykin S, Ruchaevsky I, Kuperman A, (2014) Analysis and Optimization of TEG-Heatsink Waste Energy Harvesting System for Low Temperature Gradients, pp. 1–10

[5] Twaha S, Zhu J, Yan Y, Li B (2016) A comprehensive review of thermoelectric technology: Materials, applications, modelling and performance improvement, *Renew. Sustain. Energy Rev.,* vol. 65

Development of a maturity model for supporting the digitalization in the perioperative area of hospitals

D. Junger[1], O. Burgert[1]

[1]Reutlingen University, School of Informatics, Research Group Computer Assisted Medicine (CaMed), Reutlingen, Germany

Keywords Maturity model · Digitalization · Process optimization · Digital operating room

Purpose

The digitalization in hospitals affects processes, information distribution, devices and other objects. For many core areas of the hospital, digitalization plays a big role. [1] Especially in the perioperative area, there is a lack of digital systems supporting the whole workflow and covering all relevant aspects from hospital management to patient care. Furthermore, there are no guidelines, which systems should be available and how they should interact to optimally support the clinical workflow.

Analysis and evaluation of processes and IT-infrastructure can reveal the current state of digitalization in hospitals. By defining digitalization levels, the next steps towards a more effective organization could be supported.

Maturity models (MM) are tools used to assess the maturity of organizations to investigate various aspects such as processes or technologies to reach the goal of developing and improving skills, structures or other aspects [2]. An analysis in the context of digitalization in hospitals, where different models are applied to areas such as infrastructure or information systems, showed that no MM exists for the operation theatre and the perioperative field [3]. The perioperative field is on one hand the most cost intensive area of a hospital, but on the other hand crucial for the wellbeing of the patient. The perioperative staff has to work under stress and is bothered with administrative side-activities.

The aim of this work is the development of a maturity model to cover the perioperative area. This should map the stages of a digital operating room as well as relevant perioperative processes. The MM can be used within the hospital to measure the current digitalization level in the perioperative field and gives guidelines about sensible enhancements.

Methods

For the conception of the maturity model, its general properties with regard to its focus and scope were defined. In the subsequent literature review and focus group discussions, relevant requirements for assessing the digitalization of the perioperative area relating to digitalization were collected and categorized. Aspects included in the initial categorization were technologies and systems, infrastructure and interfaces as well as perioperative processes.

Based on these digitalization-relevant aspects, possible maturity levels, dimensions and goals were developed which have been analyzed in further discussions. A multi-dimensional model of digitalization aspects has been derived. Expert interviews were used to discuss the first results and to identify further aspects of requirements and options. Furthermore, challenges could be identified which had to be considered in the design of the MM.

Based on the expert interviews, the concept of the maturity model regarding to perioperative processes and their management was further elaborated and refined. The practices of the Capability Maturity Model (CMM), which is used for the optimization of software engineering, [4] were transferred to the MM, adapted and expanded to ensure the process focus. In addition to the process-oriented view, technological as well as networking-specific aspects were added to enable an extensive coverage of different subareas. Further focus group discussions within pre-tests were conducted to evaluate the content and the maturity model was adapted to their results.

Results

Overall, the resulting model consists of five maturity levels (see Fig. 1) and three dimensions (pre-, intra- and postoperative). It contains 24 practices including e.g. the process planning, the group coordination and the management of changes as well as a variety of must and can criteria (prerequisites and optimization goals). The evaluation of the digitalization takes place via a checklist for each dimension and is used for all core processes of the perioperative area to determine their maturity by checking the points of the checklist step-by-step. The checklist covers all practices and other prerequisites like required technologies. The associated roadmap can be used to implement previously unmet criteria and practices of the used checklist and thereby shows sensible enhancements for the optimization of the perioperative field.

Fig. 1 Maturity levels of the maturity model

The highest degree of maturity focuses on continuous process optimization using key figures like the cutting-suture-time. The digitalization is supported via the MM in form of the mandatory and optional criteria. The practices in combination with the criteria allow a processed-focused view with object-specific aspects.

The final evaluation took place within two different operating rooms in the visceral surgery in which high standardized operations are performed. Therefore, the checklist was applied to the operating rooms based on their core processes for evaluating the maturity of the digitalization. The fulfilled points in the checklist were decisive for the maturity of the perioperative area. The result of the evaluation showed the different maturity levels and improvement possibilities. In addition, this evaluation showed that the MM can be applied to different operating rooms to determine the maturity of the perioperative field while gaining traceable results.

Conclusion

The focus of the developed maturity model was set on processes. The concept of the widespread CMM and its practices has been transferred to the perioperative domain and the concept of the new maturity model. Additional optimization goals and technological as well as networking-specific aspects enable a process- and object-focused view of the maturity model in order to ensure broad coverage of different subareas. The evaluation showed that the model is applicable to the perioperative field. Adjustments and extensions of the maturity model are future steps to improve the rating and classification of the new maturity model.

References

[1] Fraunhofer-Institut für Software- und Systemtechnik ISST (2015): Digitalisierungs-Check für Krankenhäuser.

[2] Blondiau A, Mettler T, Winter R (2016): Designing and implementing maturity models in hospitals: An experience report from 5 years of research. *Health informatics journal* 22, 3, 758–767.

[3] Junger D (2017): Analyse von Reifegradmodellen zur Unterstützung der Digitalisierung von Krankenhäusern. *Tagungsband der Informatik-Konferenz Informatics Inside 2017 Digital Future, ISBN* 978-3-00-056455-0.

[4] Dymond, KM (2002): *CMM® Handbuch. Das Capability Maturity Model® für Software*. Xpert.press. Springer, Berlin, Heidelberg.

Strategies of multidisciplinary collaboration for development and implementation of computer-assisted technology in neurosurgery

A. Roethe[1,2], R. Lauer[2], P. Vajkoczy[1], T. Picht[1,2]
[1]Charité-Universitätsmedizin Berlin, Neurosurgery, Berlin, Germany
[2]Humboldt-Universität zu Berlin, Image Knowledge Gestaltung - An Interdisciplinary Laboratory, Berlin, Germany

Keywords Technology development · Multidisciplinarity · Usability · neurosurgery

Purpose

Neurosurgical working environments started to change significantly due to the amount of implemented technological support. Computer-assisted surgery (CAS) and image-guided therapy (IGT) enable neurosurgeons to perform complex interventions more safely, faster, with better control and updated intraoperative information. New devices also introduce different procedures or redefine existing workflows. From an industry perspective, both recent and pioneering developments in the field of CAS/IGT in neurosurgery entail condensed periods of user recruitment, training and workflow implementation. From early to late adopters, clinical teams perform evaluation studies of novel devices following their market introduction; resulting publications primarily address aspects of feasibility, safety and cost–benefit relation. However, in daily surgical practice users are frequently confronted with ongoing training demands, insufficient support by vendors as well as incompatibilities with existing workflows or current standards of care. Numerous technical innovations are rarely or never in use, or limited to standard functions, while updates and technical upgrades are costly. Considering product and market release cycles, clinical user experience and commercial technology development are inevitably asynchronous. On the other hand, many scientific research projects in computer science and bioengineering anticipate future technical advancements in early stages, introducing more tailored yet less sophisticated solutions to single institutions and end users, with the objective of proof of concept. Surgeons who participate in such research endeavors expect concrete improvements in assistance technologies and, ultimately, patient treatment. Yet, productive longterm collaborations between surgeons and engineers or industry and surgical teams are demanding and expensive, thus rare. Inadequate assessment of actual clinical demand as well as consideration of device usability and interoperability in particular are typical shortcomings of many projects. With the extended and accelerated technology transfer to clinical practice, we see a strong demand for systematic evaluation and adjusted forms of collaboration and institutionalization.

Methods

In a multidisciplinary team of medical professionals, designers and multi-background researchers associated with a large university hospital, we performed a series of clinical observation studies, followed by interviews, cross-specialty surveys, pre-clinical lab studies and international workshops (2014–2017). Starting with the analysis of perioperative standard workflows in computer-assisted procedures, we assessed comparatively established and novel devices in daily use, focusing on implementation routines, individual skill development, utilization of technological possibilities, domain-specific knowledge, team language and multidisciplinary communication, as well as user expectations toward computer-assisted surgery. Based on the procedure analyses, follow-up interviews and structured surveys have been focusing on existing collaboration strategies, multidisciplinary team experiences and unmet demands.

Results

There is a general consensus among cross-specialty experts that successful implementation of technological devices in surgical routine requires continuing efforts regarding team training, maintenance, system upgrade and evaluation of efficiency. In complex environments such as modern operating theaters, a minimum interoperability of systems and devices increases frequency and extent of technology use. Early and repeated expert exchanges of developers and clinicians are vital, in both research and industry constellations. Domain-specific knowledge can only be achieved through frequent on-site visits, context analysis and case discussions. Multidisciplinary teams create new forms of cross-domain expertise; mutual transparency in disciplinary methods and work objectives is an important prerequisite for successful collaborations. Grant-supported projects generally center innovative technology development and feasibility studies over considerations of usability, intuitivity and interaction. Accordingly, few designers are permanent members of clinical lab constellations or considered essential for product development and/or evaluation. While only single tools are adopted by standard care in the long term, we registered a broad overall interest in the introduction of best practice models for collaborative technology development. In an accompanying online survey, 98.7% of the participating surgeons (n = 77) voted for close exchange with engineering colleagues, 85.7% demanded even stronger cooperations for the future. Especially operating room infrastructure (85.5%), intraoperative imaging modalities (84.2%) and neuronavigation systems (85.5%) have been indicated as focus interests of surgical professionals, requiring an early and consistent integration of clinical user feedback. In contrast, only 60.5% of the clinicians surveyed confirmed pre-existing industry collaborations at their institutions. Temporal (77%) and financial (68.9%) constraints are major obstacles for active clinical involvement in technology development. Nevertheless, focused hub and community spaces and hackathons as first introduced by some surgical labs in the US established expandable working models for future multidisciplinary expert exchange.

Conclusion

For improved development of CAS devices and IGT procedures in neurosurgery, we recommend an advanced multi-perspective assessment of demand through systematic observation, interviews, preclinical and clinical pilot studies. This includes published guidelines for use case-sensitive methodology and outcome correlation (» added clinical benefit «). In support of productive hospital-industry relationships, we propose in particular a) a reinforced joint research strategy and b) periodic and formalized user feedback surveys. Neurosurgical tool development in CAS and IGT requires structured and close multidisciplinary and multiprofessional collaboration, underscoring the relevance of dedicated clinic-based labs instead of short-term research projects; furthermore, expert communities need to be better connected on the basis of joint events, publication organs, funding opportunities and scientifico-clinical societies. Medical education and continuing education curricula for future surgeons should early introduce methodological and technological basics to build upon during later years of clinical training.

From passive tool to active guidance: requirements for navigation intelligence in computer-assisted endoscopic ENT surgery

R. Bieck[1], K. Heuermann[2], M. Hofer[2], T. Neumuth[1]
[1]Innovation Center Computer Assisted Surgery/Universität Leipzig, Faculty of Medicine, Leipzig, Germany
[2]University Hospital Leipzig, ENT Department, Leipzig, Germany

Keywords Intraoperative navigation · Computational intelligence · Surgical cognition · Situation awareness

Purpose

The digital operating room (OR) is a high outcome- and cost-driven environment where personnel and hospital providers are continuously challenged to improve operation quality and efficiency. As a result, the focus of new intraoperative technologies is to unburden staff while increasing the underlying level of automation [1]. For non-obtrusive functions such as monitoring and documentation, the automation approach is reasonably unproblematic. In minimally-invasive navigation, however, significant challenges arise due to conventional interactive systems. Automating the interaction behaviour with the surgeon is immensely complicated due to patient-, user- and procedure-individuality. Additionally, the orientation process of the surgeon is unknown and leaves any navigation assistance in a strictly passive-reactive state [2]. As a consequence, a paradigm shift in computer-assisted surgery surfaced, investigating the potential of the surgical cognition to understand and translate the knowledge of the surgical domain into intelligent navigation functions [3]. Resulting applications should then be able to adapt to the surgeon and the surgical situation, leading to a cooperative navigation process. However, the intended intelligence itself changes the surgeon's perception of the surgical situation and this influences his cognition and decision making. To which extent the overall surgical workflow is affected remains yet unknown. The aim of this work was twofold: (1) Requirements needed to develop an intelligent form of minimally-invasive endoscopic navigation were identified and (2) Found requirements were translated into the first concept for a system architecture that follows the surgeon's cognition process of navigation.

Methods

We conducted a survey of ENT surgeons (n = 10) to identify the potential for intelligent navigation assistance. Surgeons were then asked to name types of information the system should provide at prominent landmarks in the nasal sinus. Additionally, a mock-up setup simulated the ideal navigation behaviour with the presentation of the current landmark information. Surgeons were then questioned to assess the quality of presented information and assistance. Based on the study output, we identified functional requirements for data management, information presentation and prioritisation as well as user requirements for interaction behaviour and assistance functions. Based on the requirements, a concept for an intelligent navigation system in minimally-invasive endoscopic surgery was developed. The central aspect was to adequately consider the principle of cognition-guided surgery to let the new navigation system ideally mimic the orientation and navigation behaviour of the surgeon. Lastly, user requirements were used to define a set of navigation heuristics for the orientation in endonasal cavities.

Results

The preliminary studies concluded that a more intelligent navigation system would be a critical asset to the OR. The demand for navigation information is highest for the endoscope position, followed missing or next work steps to perform. Furthermore, a proximity alert to current risk structures and prospective work steps was called for. With increasing in situ depth the need for contextual information also increased, while the amount of displayed information (visual, audible) was decreasing. Audible short signals were preferred over textual information, as long as the source of presented information was known. The following requirements were identified to be critical for an intelligent intraoperative navigation system and:

- Situational response to surgical activities with corresponding navigation tasks
- Navigation function planning and adaptation
- Time- and resource-constrained scheduling of presented navigation information
- Internal domain knowledge representation and management
- Internal modelling of the surgeon's spatial and surgical cognition
- Data origin and function plausibility

Since the critical requirement for intelligent navigational assistance was to directly respond to changes in the surgical environment our model approach was based on a situation awareness model (SAM) used in aerospace navigation [4]. The model is extended so that the surgeon is incorporated as a central component throughout the data processing step (Fig. 1). The respective levels of situation awareness are translated into inference steps performed by the navigation system to perceive, comprehend and project the ongoing procedure. The SAM is essentially an inference loop considering the environment, data acquisition and comprehension (Level 1 & 2) as well as task planning and execution steps (Level 3). Preliminary studies on navigation task composition were included to define, how navigation functions are planned and provided. Concerning automotive driver-assistance, the cognitive load theory was introduced to constrain the presented navigation information in modality, time and complexity [5]. The formulated navigation heuristics are centred around the changes in perceivable information based on the observable scene of the inspected anatomical structures. The primary rules are: (1) Increasing task complexity with increasing in situ depth and decreasing in situ cavity diameter, (2) Increasing presentation complexity with reducing visual image quality and presentability of anatomical features and (3) Increasing task complexity and risk with proximity to and the number of anatomical risk structures. As a result, navigation information is adapted with regards to the overall manoeuvrability of the endoscope through the nasal cavities.

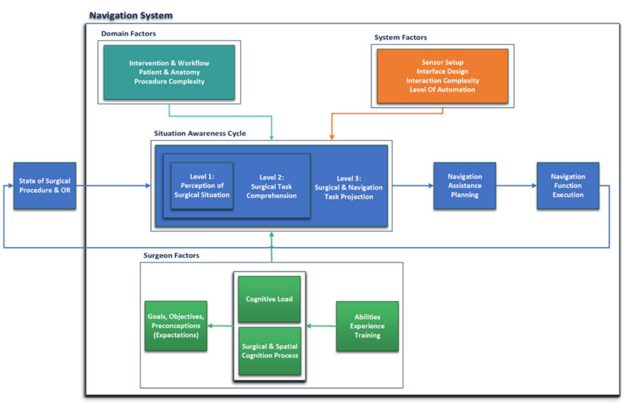

Fig. 1 Design approach for an intelligent intraoperative navigation system including surgeon, system and domain perspectives

Conclusion

We investigated the potential for more intelligent functions in intraoperative navigation for minimally-invasive endoscopic surgery. Based on questionnaires and simulated navigation functions, essential requirements could be identified. Our preliminary modelling approach to meet these requirements in a system design considered main aspects of situation awareness, cognitive load, cognition-guided surgery and the presentation management of navigation information. Additionally, the navigation heuristics are essentially describing the surgeon's cognitive strategies to react to specific anatomical variations and are therefore considered to be essential for future learning strategies. Lastly, understanding the influences of the apparent surgical task and the patient-individual characteristics on the surgeon's orientation and thought the process is the prerequisite to achieve real intelligent system behaviour in a cooperative setup. We consider the first modelling results as the means to approach a possible definition of computational navigation intelligence in the operating room. Only then is shifting from active and passive roles between the navigation system and surgeon conceivable. One significant unpredictability, however, is to which extent such an intelligent system is accepted by the surgeon in daily use and how the surgical outcome is influenced by its assistance capabilities.

References

[1] Kranzfelder M, Staub C, Fiolka A, Schneider A, Gillen S, Wilhelm D, Friess H, Knoll A, Feussner H (2013) Toward increased autonomy in the surgical OR: needs, requests, and expectations. *Surgical endoscopy* 27(5): 1681–1688.
[2] Hegarty M, Keehner M, Cohen C, Montello D, Lippa Y (2007) The role of spatial cognition in medicine: Applications for selecting and training professionals. *Applied spatial cognition* 285–315.
[3] Kenngott H. G, Apitz M, Wagner M, Preukschas A, Speidel S, Müller-Stich B (2017). Paradigm shift: cognitive surgery. Innovative Surgical Sciences, *2*(3): 139–143.
[4] Endsley M (1995) Toward a theory of situation awareness in dynamic systems. *Human factors* 37(1): 32–64.
[5] Engström J, Johansson E, Östlund J (2005) Effects of visual and cognitive load in real and simulated motorway driving. *Transportation Research Part F: Traffic Psychology and Behaviour* 8(2): 97–120.

A novel 3D-CNN approach for ejection fraction classification in transthoracic echocardiography

J. M. Silva[1], A. Guerra[1], J. F. Silva[1], C. Costa[1], S. Matos[1]
[1]IEETA, Universidade de Aveiro, Aveiro, Portugal

Keywords 3D-CNN · Ejection fraction · Transthoracic echocardiography · Cardiology

Purpose

Cardiovascular diseases (CVDs) are the leading cause of death worldwide, with approximately 17.7 million deaths in 2015 [1]. CVDs are highly correlated with left ventricle (LV) function indexes, namely ejection fraction (EF). To assess patient condition, physicians mostly use transthoracic echocardiography (TTE) as a first line of diagnosis due to its availability, portability and reduced cost [2].

The typical pipeline for EF classification with TTE, presented in the top row of Fig. 1, requires a manual segmentation of LV before any analysis can be made. In this process, physicians select a systole and diastole frame, and manually delineate the LV's walls. Then, they compute the LV area and determine EF. This is a user dependent time-consuming task, that must be performed for every exam, with the limitation that different point positioning can lead to a significantly different EF. Furthermore, some exams do not have ECG, which decreases physicians' precision in determining the exact diastole and systole frames, impacting on computed results. It is thus useful to have a CAD system that automatically provides physicians with a second opinion.

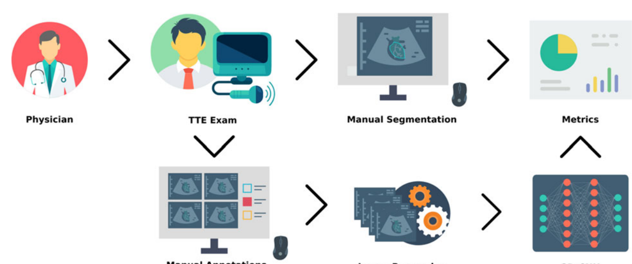

Fig. 1 Existing and proposed pipelines to extract information from TTE exams

Although there are solutions that perform an automatic LV segmentation in TTE, EF estimation and patient classification has only been performed using MRI [3] or 3D Echocardiography data [4]. These two techniques have higher costs, and thus are not used as a first line of diagnosis. Nonetheless, these papers demonstrate a recent trend in cardiology imaging: the use of deep learning to extract metrics from cardiac images. Herein, we propose a pipeline that processes ultrasound images from TTE exams and combines them with exam meta-data in a customized 3D-Convolutional Neural Network (3D-CNN) to classify patients' health based on EF.

Methods

Exams were obtained from a cardiology reference center. All exams should have three types of information: TTE cineloops, annotated information (e.g. EF) and a free-text report. Exams without annotations or cineloops were discarded. The Apical 4 Chambers view was manually selected since it is usually acquired in TTEs and is the most common one for EF computation.

The final dataset contains 8715 exams. From each, 30 sequential frames were randomly extracted to capture a cardiac cycle. Moreover, an automatic process was created to segment each frame's region of interest. For classification purposes, EF data was extracted from exam meta-data and the dataset was divided in 4 classes based in medical expertise: 1-unhealthy (EF < 45%), 2-further analysis recommended (45% < EF < 55%), 3-healthy (55% < EF < 75%), 4-abnormally high EF (EF > 75%). Since Class 3 had higher support, only 5600 TTE exams were used to balance class distribution, which were divided in train and test splits with 4000 and 1600 cases. Class distribution in both splits is presented in Fig. 2.

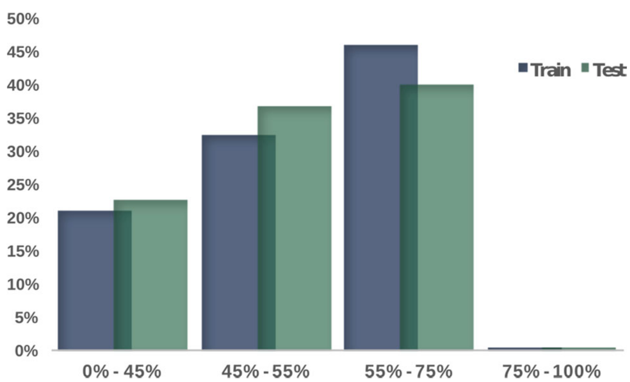

Fig. 2 Class distribution in train and test datasets

A custom 3D-CNN was built using 3D convolutions with asymmetric kernels and integrating 3D convolutional layers in residual learning blocks. Hyper-parameter tuning was performed with random grid search.

The methodology is depicted in the lower part of Fig. 1. The classification process was evaluated using accuracy (global) and F1 Score (class-specific).

Results

The classifier obtained an accuracy of 70.01% and the F1 score for each class was: Class 1—71.3%, Class 2—63.3%, Class 3—72.3% and Class 4—54.6%.

Notice that some values provided in meta-data could be incorrect since we observed discrepancies between values from meta-data and from the free-text report. Despite being a minor problem, this can partly explain class misclassifications.

Furthermore, the low F1 Score for Class 4 can be explained by the reduced class support. Besides, Classes 1 and 3 have higher F1 scores than Class 2 since Class 2 is a transitional class that should contain exams both from unhealthy and healthy patients. The F1 score from Classes 2 and 4 corroborates that these classes have an impact on global model accuracy, penalizing its value. Further class balancing could be explored.

Conclusion

CVDs are the leading cause of death worldwide. The first line of diagnosis is often TTE, where EF is a fundamental metric in diagnosis. To determine EF, physicians resort to manual annotations to segment the ventricle in systole and diastole. This is time-consuming and user-dependent. The authors propose a second opinion solution for physicians. To do so, we created a dataset from real patient TTE exams comprising 5600 annotated studies, that contains 30 sequential frames from the Apical 4 chamber view for each study. The dataset was used on a novel 3D-CNN to classify EF in TTE exams, with the best model obtaining a classification Accuracy of 70.01%. These results are promising and show that CNNs can be applied to this domain. Furthermore, it will serve as a foundation for future works where other relevant cardiac metrics will be determined.

Acknowledgments

This work is financed by the ERDF—European Regional Development Fund through the Operational Programme for Competitiveness and Internationalisation—COMPETE 2020, and by National Funds through Fundação para a Ciência e a Tecnologia within project PTDC/EEI-ESS/6815/2014.

References

[1] World Health Organization. (2017). Cardiovascular diseases (CVDs). [online] Available at: http://www.who.int/mediacentre/factsheets/fs317/en/[Accessed 4 Jan. 2018].
[2] Pagán, R., Parikh, P., Mergo, P., Gerber, T., Mankad, R., Freeman, W., Shapiro, B. (2015). Emerging role of cardiovascular CT and MRI in the evaluation of stroke. American Journal of Roentgenology, 204(2), 269–280.
[3] Luo, G., Sun, G., Wang, K., Dong, S., Zhang, H. (2016). A novel left ventricular volumes prediction method based on deep learning network in cardiac MRI. In Computing in Cardiology Conference (CinC), 2016 (pp. 89–92). IEEE.
[4] Dong, S., Luo, G., Sun, G., Wang, K., Zhang, H. (2016). A combined multi-scale deep learning and random forests approach for direct left ventricular volumes estimation in 3D echocardiography. In Computing in Cardiology Conference (CinC), 2016 (pp. 889–892). IEEE.

Accuracy of mitral valve imaging in dynamic CT

C. Vannelli[1], J. Moore[1], A. So[1], W. Xia[1], T. Peters[1]
[1]Robarts Research Institute, Imaging, London, Canada

Keywords Cardiac computed tomographyvValidation · Ground truth · Image processing

Purpose

With significant increase in life expectancy over the past century, valvular heart disease (VHD) has been identified as the next cardiac epidemic [1–3]. A recent study estimates the prevalence of VHD to be 2.5%, progressively increasing with age up to 13.2% at 75 years of age. Transesophageal echocardiography (TEE) is widely recognized as the standard of care evaluation technique to diagnose mitral valve disease (MVD). In most cases, TEE imaging is adequate for identifying pathology, however due to limitations such as signal dropout, limited resolution and user-variability in interpreting images, the diagnostic value of TEE is often limited. A study of 242 patients who had undergone TEE-guided mitral valve repair for degenerative MVD found the rate of recurrence of mitral valve regurgitation (MVR) to be 5% after 1 month and 40% after 4 years; use of dynamic CT imaging to capture a complete picture of the valve and subvalvular apparatus could enable surgeons to personalize their approach to intervention and reduce the rate of recurring MVR. In addition, the emerging availability of beating-heart valve replacements necessitates pre-operative volumetric data used to size the valve stent; this motivates the use of CT to augment TEE in the clinical workup of MVD for quantification of patient anatomy. Dynamic cardiac computed tomography (CT) is emerging as a valuable tool for diagnosis and assessment of cardiac diseases. However, application of dynamic CT to mitral valve imaging is particularly challenging due to the large and rapid motion of the mitral valve leaflets. Therefore, it is important to investigate the level of precision with which dynamic CT captures mitral valve morphology throughout the cardiac cycle. CT has the potential to provide a high quality rendering of the mitral valve apparatus and subvalvular anatomy, which is lacking in other cardiac imaging modalities. In this work, we propose a method to assess the accuracy of dynamic CT imaging of the mitral valve, validated through comparison with a static but movable ground truth phantom. The results from this work can inform the use of dynamic CT in the clinical workflow for patients with valvular disease—, as well as assess the efficacy of trans-esophageal ultrasound for accurately capturing valve morphology and dynamic motion.

Methods

The morphology and behavior of the mitral valve is dependent on hemodynamics which cannot easily be replicated in a static environment. To address this, we have created a valvular model which mimics normal mitral valve morphology and motion patterns but can be arrested at precise cardiac phases. Valve motion is achieved by pulling on the chordae tendinae, controlled by a servomotor. To assess the accuracy of gated, dynamically acquired mitral valve images, we use a static valvular model against which we can compare the dynamic data. CT images of the valve are acquired in air, both with the valve in motion and at predefined static positions.

Phantom design and construction: The static phantom consists of a silicone mitral valve, chordae and adjustable papillary muscles supported by a flange angled to mimic a patient lying supine. Using a motorized system to control the papillary locations, we can both mimic the full range of cardiac motion from diastole to systole and arrest the phantom at any point in the cardiac cycle.

Acquisition of a proof-of-concept ground truth and dynamic datasets: Static valve images which comprise the ground truth are acquired with a dynamic CT (GE Revolution Cardiac CT http://www3.gehealthcare.com/en/products/categories/computed_tomography/revolution_ct). A system of motors adjusts and arrests the papillary muscles in six positions corresponding to distinct valve locations correlated with the ECG wave. The time points are selected to depict a complete cardiac cycle: pre-, mid- and end-diastole (opening valve) and pre-, mid- and end-systole (closing valve). The dynamic dataset is acquired with retrospective gating of the valve motion at 60 bpm actuated by motorized, continuous papillary movement. Both datasets are reconstructed at 0.625 mm slice thickness (Fig. 1).

Fig. 1 3D volume rendering of silicone mitral valve arrested at the first time point (pre- to mid- P wave)

Comparison and validation of dynamic CT to ground truth: The static, ground truth CT dataset consists of six volumes corresponding to distinct time points in the cardiac cycle. Phase-matched time points from the dynamically-acquired scan are aligned to the corresponding static volumes with homologous-point landmark based registration. The valve leaflets and chordae are segmented in MATLAB using continuous max flow, the static flanges registered using iterative closest point and the segmented volumes compared using the average Euclidean surface distance (Table 1, Fig. 2). Further analysis will be subsequently performed to evaluate the registration, segmentation and quantify motion artifact introduced through dynamic acquisition.

Table 1 Evaluation of phase-matched static and dynamic datasets with mean Euclidean distance observed between the two models

ECG time point		Mean Euclidean surface distance (mm)
1	Pre- to mid-P wave	1.80
2	Mid- to post-P wave	2.91
3	Q wave	2.93
4	RST waves	3.21
5	Post-T wave	3.52
6	Pre-P wave	1.97

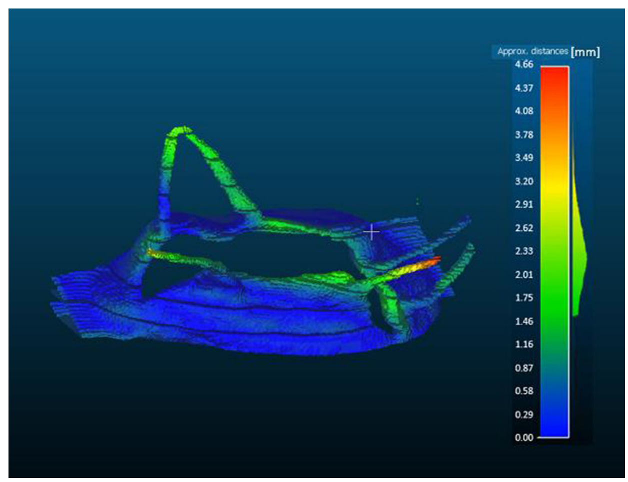

Fig. 2 Cloud comparison of segmentation maps from static and dynamic datasets at the first time point (pre- to mid- P wave). Chordae can be visualized protruding outward from the leaflet

Results

See Table 1.

Conclusion

Dynamic cardiac CT is emerging as a modality well suited to provide high quality images capturing subvalvular anatomy and valve morphology over many cardiac phases. In order to assess the accuracy of dynamic CT for mitral valve imaging, we propose a workflow to compare gated, static CT images with dynamically-acquired images. Preliminary results from a proof-of-concept study demonstrate the need for further analysis and quantification of dynamically-acquired scan motion artifacts and image quality. Ongoing work includes a second iteration of the motorized phantom with an excised porcine valve for improved robustness and physiological-relevance. Additional applications of the ground truth dataset will include evaluating the use of transesophageal echocardiography for capturing dynamic valve behavior. Results from this work will assist in evaluating the potential of dynamic CT as a diagnostic tool in cardiac applications.

References

[1] d'Arcy J, Prendergast B, Chambers J, Ray, S, Bridgewater, B (2011) Valvular heart disease: the next cardiac epidemic. Heart 97(2): 91–93

[2] Lindroos M, Kupari M, Heikkilä J, Tilvis N (1993) Prevalence of aortic valve abnormalities in the elderly: an echocardiographic study of a random population sample. Journal of the American College of Cardiology 21(5): 1220–1225

[3] Choo W, Steeds R (2011) Cardiac imaging in valvular heart disease. Journal of Radiology 84(3): 245–257

Random forest based surgical phase recognition in minimal invasive surgery

F. Meeuwsen[1], F. van Luyn[1], M. Blikkendaal[2], F. W. Jansen[2], J. van den Dobbelsteen[1]

[1]TU Delft, BioMechanical Engineering, Delft, Netherlands

[2]LUMC, Gynaecology, Leiden, Netherlands

Keywords Surgical phase recognition · Workflow · Instrument tracking · Laparoscopic hysterectomy

Purpose

The Operating Room (OR) complex is a cost-intensive part of the hospital, as it typically accounts for more than 40% of a hospitals total revenues and a similarly large proportion of its total expenses [1]. Thus, efficient usage of OR capacity is crucial. To ensure sufficient organisational capacity, it is of utmost importance that the OR scheduling is well planned and managed timely. Delays in the OR planning are generally unwelcome. If an operation takes longer than predicted, subsequent procedures have to be postponed or cancelled. On the other hand, when operations run short, the operating rooms are unutilized at the end of the day. To keep the schedule updated as the day progresses, OR schedulers typically use visual inspection to check the status of a procedure. An alternative is making phone calls or actually entering the OR, which is a disturbance of the surgical team.

There are still huge improvements to make when it comes to real-time progress monitoring. With the use of intelligent algorithms a model can be build to autonomously detect and identify different steps in the surgical procedure [2]. To do so it needs intra-operative data as input for a surgical process model, like instrument use. With this information, phases during a procedure can be recognized and clinical progress can be monitored [3]. Through automatic recognition of different phases during a procedure, we can predict how long the procedure will take and thus optimize our schedule.

So far, many have studied relative short and standardized procedures, such as the laparoscopic cholecystectomy. However, to add more challenge to the phase recognition system and to extend the range of applications, more diverse and complex procedures that are characterised by a high variability in procedure time have to be studied. By this rationale we choose to analyse the more complex laparoscopic hysterectomy, the minimal invasive removal of the uterus. With over 600,000 hysterectomies performed yearly in the US, it is the second most common gynaecological surgical procedure [4]. The aim of this study is to determine to the potential of automated phase recognition for long and complex procedures. Therefore we monitor the instrument use and investigate the accuracy reached in clinically relevant tasks, like surgical end-time prediction and surgical phase extraction.

Methods

The dataset used contains 40 cases of video-recorded laparoscopic hysterectomy (LH), which were performed between November 2010 and April 2012 in the Bronovo Hospital in The Hague, The Netherlands. The procedure was separated into 10 surgical phases and 36 surgical steps. For each phase and step the use of a total of 12 surgical instruments and devices was registered through manual annotation. A Random Forest Model was trained and evaluated on two tasks relevant with respect to clinical practice in the OR: the automatic prediction of surgical end-times and the automatic generation of training material by clipping endoscopic video based on the phase prediction.

Results

The average surgery time was 128 min (± 27 min SD), with the individual surgical phases also showing a high variance in duration between cases (Fig. 1). Overall, the Random Forest model reaches an accuracy of 77% in identifying the surgical phase. The patterns of used instruments and devices differ per surgical phase. Tracking only a few key instruments (the bipolar coagulation device, ultrasound coagulation device, grasper/forceps and needle driver) is sufficient to generate a solid prediction.

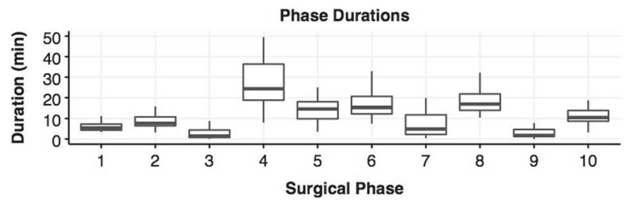

Fig. 1 The duration of surgical phases is different per phase, but also varies strongly between procedures. The fourth phase, exposing the uterine arteries, takes the longest time to complete on average (29 min ± 13 min SD), whereas the ninth phase—final check and irrigation—has the shortest time span (3 min ± 3 min SD)

Evaluation of the clinical relevant tasks shows that on the basis of phase extraction reliable results can be obtained for procedure end-time prediction. The model predicts surgical time using surgical time passed, the detected phase, duration within the phase and the cross terms between the phase and duration within the phase. Using 10-fold cross-validation, a mean average error (MAE) of 15.6 min (± 12.9 min SD) was found for individual phases. At 30 min before the end of the surgery the error drops to MAE = 12.6 min (± 13.2 min SD), as seen in Fig. 2. In the phase extraction task seven out of ten phases can be distinguished with an average error smaller than four minutes.

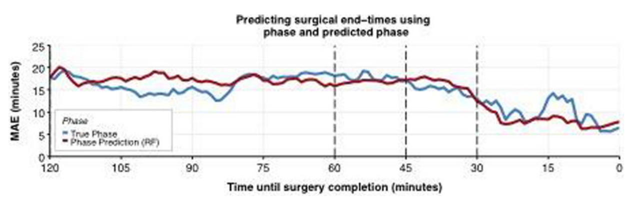

Fig. 2 Mean absolute prediction errors of the surgical end-time prediction models as a function of time until surgery completion. The models based on the true phase and the phase prediction show similar performance. Vertical lines highlight the performance at 60, 45 and 30 min before surgery completion

Conclusion

We conclude that a phase recognition model, based on the Random Forest method, the procedure end-time can be predicted with an accuracy of about 16 min. If one considers the high variability in procedure time in LH, the ability to automatically monitor progression throughout the procedure provides sufficient accuracy to support dynamic OR planning and workflow management. Moreover, we find that only a subset of instruments needs to be tracked to generate viable results. This study has paved the way to in vivo application of intra-operative monitoring of complex surgical procedures.

References

[1] Veen-Berkx EV, Elkhuizen SG, Logten SV, Buhre WF, Kalkman CJ, Gooszen HG, Kazemier G (2015) Enhancement opportunities in operating room utilization; with a statistical appendix. Journal of Surgical Research. https://doi.org/10.1016/j.jss.2014.10.044

[2] Katić D, Julliard C, Wekerle AL, Kenngott H, Müller-Stich BP, Dillmann R, Speidel S, Jannin P, and Gibaud B (2015), Lapontospm: an ontology for laparoscopic surgeries and its application to surgical phase recognition, International Journal of Computer Assisted Radiology And Surgery 10, 1427.

[3] Bouarfa L, Jonker P, Dankelman J (2011) Discovery of high-level tasks in the operating room. Journal of Biomedical Informatics 44: 455–462. https://doi.org/10.1016/j.jbi.2010.01.004

[4] Wu JM, Wechter ME, Geller EJ, Nguyen TV, Visco AG (2007) Hysterectomy Rates in the United States, 2003. Obstetrics & Gynecology 110: 1091–1095. https://doi.org/10.1097/01.aog.0000285997.38553.4b

IEEE 11073 SDC and HL7 FHIR: emerging standards for interoperability of medical systems

M. Kasparick[1], B. Andersen[2], H. Ulrich[2,3], S. Franke[4], E. Schreiber[4], M. Rockstroh[4], F. Golatowski[1], D. Timmermann[1], J. Ingenerf[2,3], T. Neumuth[4]

[1]University of Rostock, Institute of Applied Microelectronics and Computer Engineering, Rostock, Germany

[2]University of Lübeck, Institute of Medical Informatics, Lübeck, Germany

[3]University of Lübeck, IT Center for Clinical Research, Lübeck, Germany

[4]University of Leipzig, Innovation Center Computer Assisted Surgery (ICCAS), Leipzig, Germany

Keywords IEEE 11073 SDC · HL7 FHIR · Integrated operating room · Systems interoperability

Purpose

Manufacturer-independent interoperability is fundamental to meet the challenges of clinical environments, which consist of an increasing number of medical devices (MD) and clinical information systems (CIS). Communication paradigms and protocols have been developed to address their specific needs and are currently being standardised. For digital operating rooms (ORs) and intensive care units (ICUs), the most important current evolutions are IEEE 11073 SDC and HL7 FHIR. Although these emerging standards have different core objectives, they partly overlap in functionality—particularly concerning the accessibility of measurements and parameters of medical devices (Fig. 1). This overlap motivates the analysis of the differences between the two standards that is given in this article. Resulting from a comparative classification of the advantages based on different common component interaction scenarios, it provides suggestions as to which standard should be used for which purpose.

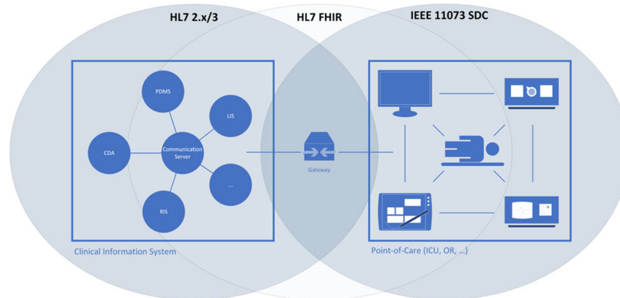

Fig. 1 Schematic representation of the intended fields of application of IEEE 11073 SDC, HL7 FHIR, and HL7 v2

Methods

The established IEEE 11073 family of standards aims for manufacturer-independent interoperability of medical devices. Its original series on Point-of-Care Medical Devices (PoCD) focused on single point-to-point communication. As the transport mechanisms are not suitable for multi-point connections, the IEEE 11073 Service-oriented Device Connectivity (SDC) sub-family has since been developed. It is based on contemporary web service technologies and an extended domain information model [1]. SDC targets the interoperability gap in device-to-device communication and does not aim to compete with or replace standards like HL7 or DICOM, which have different foci, but rather to interact with them meaningfully at system boundaries.

HL7 Fast Healthcare Interoperability Resources (FHIR) [2] is a new draft standard for the exchange of healthcare information. Based on modern design patterns like RESTful communication and the concept of *Resources*, FHIR covers a broad range of clinical use cases by providing modular building blocks that can be combined without jeopardising information integrity. The built-in methods for extending a Resource allow FHIR to provide flexibility and adaptability in the clinical environment. Due to the support of multiple communication paradigms, FHIR can cover various interactions that are insufficiently supported in other HL7 standards, for example medical device communication. Thereby FHIR helps to bring together domains that were previously separated.

Both emerging integration technologies differ in their networking approach. The service-oriented medical device architecture (SOMDA) of SDC [1] implements a SOAP-based communication with service discovery and peer-to-peer messaging. In contrast to SDC, FHIR supports multiple communication paradigms, especially RESTful environments. Usually, one or multiple repository server components, which distribute and may persist Resources, structure the integration architecture.

The suitability of the integration technologies highly depends on the addressed technical use case and needs to be assessed with regard to the targeted application.

Results

In an integrated clinical environment, communication takes place between multiple MDs, multiple CISs, and between both MDs and CISs. Herein, the suitability of FHIR and SDC is discussed for these three interaction scenarios. Table 1 provides an overview.

Table 1 Comparison of properties and features of IEEE 11073 SDC and HL7 FHIR

	IEEE 11073 SDC	HL7 FHIR
Web service realisation	SOAP	(Typically) RESTful
Communication topology	End-to-end	(Typically) centralised repositories
Dynamic discovery	WS-Discovery	Not intended
Synchronous communication	Request–response	Request–response
Asynchronous notifications	WS-Eventing	Yes
Semantic annotations	Coded values	Coded values
Remote control	Built-in	Not intended
Safety mechanisms	Medical DPWS: SafetyContext, DualChannel	Not applicable
Data compression	Optional (EXI)	Optional (gzip for RESTful)
Data streaming	Medical DPWS: Streaming	Not intended
PHR management	Not intended	Built-in
Data traceability	Optional (distributed)	Built-in (repository-based)

Regarding *MD-to-MD communication* in dynamically changing environments, such as ORs or ICUs, the discovery of devices and provided services is crucial. SDC therefore uses the well-known WS-Discovery functionalities provided by the underlying communication standard Devices Profile for Web Services (DPWS). Whereas both SDC and FHIR provide suitable mechanisms for a machine-interpretable exchange of medical data including alerts and notifications, remote control functionality is currently out of scope for FHIR. One conceptual reason is the typically repository-based communication architecture. SDC, in contrast, explicitly defines mechanisms for safe remote control, enabling both a safe flexibility in a multi-manufacturer environment and an effective risk management of the controlled MDs.

Regarding *CIS-to-CIS communication*, where complex information systems exchange data over various message-based interfaces, the environment is rather static. Therein, an extensive amount of personal health records (PHR) must be managed efficiently. SDC is not designed to store or manage PHRs. In contrast, FHIR's repository approach offers a suitable solution to govern and transfer large amounts of PHR data. The functionality of referencing Resources in other repositories reduces both the quantity and the payload of the messages compared to HL7 version 2. Furthermore, the built-in history feature allows for each change to be tracked and thereby to fulfil the requirements of data persistence and traceability.

The *communication between MDs and CISs* used to be intrinsically complicated as most devices, especially if resource-constrained, would not implement an HL7 v2 stack in addition to the IEEE 11073 communication. It was therefore necessary to transform e.g. patient demographics and order data from a CIS before it could be transferred to an MD. In the same way, device observations needed to be transformed before they would be useful for a CIS [3]. Due to the fundamentally different data structures, a loss of detail and/or contextual information could easily occur.

With the introduction of FHIR, however, the complexity of mediating between both worlds decreased significantly. The mutual influence FHIR and SDC had on one another during development as well as the flexibility that is inherent to both standards allow for consistent expression of information in SDC *and* FHIR [4]. Therefore, devices can use FHIR for communication with a CIS just as well as a CIS component can fetch data from devices via SDC.

Conclusion

HL7 FHIR and IEEE 11073 SDC both have their respective areas of excellence. For each use case, it should therefore carefully be evaluated which standard is to be applied. In addition, the interoperability between both data structures will enable seamless data flow between the medical device domain and clinical IT systems. In order to leverage the full benefit of this interoperability, we intend to extend existing mappings into an *implementation guide* that allows for fully automatic conversion of a device containment tree into a set of Resources.

References

[1] Kasparick M, Schmitz M, Andersen B, Rockstroh M, Franke S, Schlichting S, Golatowski F, Timmermann D (2018) OR.NET: A Service-Oriented Architecture for Safe and Dynamic Medical Device Interoperability. Biomedical Engineering/Biomedizinische Technik, DOI: https://doi.org/10.1515/bmt-2017-0020

[2] Bender D, Sartipi K (2013) HL7 FHIR: An Agile and RESTful approach to healthcare information exchange. Proceedings of the 26th IEEE International Symposium on Computer-Based Medical Systems (CBMS), DOI: https://doi.org/10.1109/CBMS.2013.6627810

[3] Andersen B, Kasparick M, Ulrich H, Franke S, Schlamelcher J, Rockstroh M, Ingenerf J (2017) Connecting the Clinical IT Infrastructure to a Service-Oriented Architecture of Medical Devices. Biomedical Engineering/Biomedizinische Technik, DOI: https://doi.org/10.1515/bmt-2017-0021

[4] Andersen B, Kasparick M, Ulrich H, Schlichting S, Golatowski F, Timmermann D, Ingenerf J (2016) Point-of-Care Medical Devices and Systems Interoperability: A Mapping of ICE and FHIR. Proceedings of the IEEE Conference on Standards for Communications and Networking (CSCN), DOI: https://doi.org/10.1109/CSCN.2016.7785165

A method for modeling and identification of surgical processes based on the clinical data of each patient in awake surgery for glioma

T. Nagai[1], I. Sato[1], K. Ohshima[1], Y. Fujino[1], H. Yamada[2,3], M. Tamura[2], Y. Muragaki[2], K. Masamune[2]
[1]Future University Hakodate, Hakodate, Japan
[2]Tokyo Women's Medical University, Tokyo, Japan
[3]Murakumo Corporation, Tokyo, Japan

Keywords Surgical process analysis · Surgical process model · Machine learning · Awake surgery for glioma

Purpose

During glioma resection, identification and analysis of surgical processes can be used to understand the processes involved and their progress, on a patient-by-patient basis. Studies on the surgical workflow have been previously reported for surgical process analysis and modelling [1, 2]. However, during surgery for glioma, an expert surgeon will resect a glioma based on experience and technique, by considering tumor position, brain function and surrounding structure. Therefore, the experience and technique of an expert surgeon is implicit knowledge; the visualization of this implicit knowledge is important for improvement and educational support to increase the quality of medical care. Therefore, we aim to visualize implicit surgical knowledge by the identification and analysis of surgical processes, based on previous research [3]. In our method, improving the accuracy in identifying surgical processes is necessary. Thus, we used microscope videos to improve the surgical process model and associated machine learning method.

In this study, we propose to identify surgical processes using pre- and intra-operative magnetic resonance (MR) images, surgical instrument positional information, and microscope videos from awake glioma surgeries.

Methods

Figure 1 shows a method for identification of surgical processes that includes four steps: (1) Definition of the surgical process model; (2) Feature extraction using segmentation and deformation; (3) Feature extraction using the Gaussian mixture model (GMM) and convolutional neural network (CNN); (4) Identification of a surgical process using the Hierarchical Hidden Markov Model (HHMM).

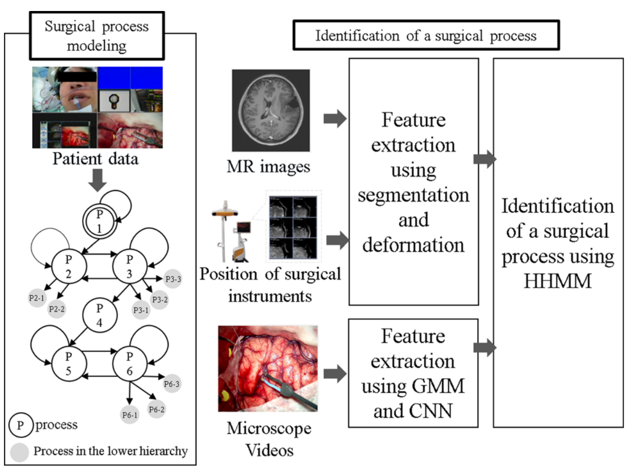

Fig. 1 Methodology for modeling and identification of surgical processes

(1) Definition of a surgical process

In this step, we define surgical processes. Target surgical processes are confined to post-craniotomy glioma resection. We defined 13 surgical processes based on input from expert clinicians. These surgical processes were used in the context of an awake surgery of glioma, during treatment of four patients with similar pathology. The surgical process varies with the location and type of the tumor. Therefore, the surgical process was clustered, and model was reconstructed. We then manually extracted features of surgical processes (types of surgical instruments, positional relationships of surgical instruments, and anatomical information from MR images) based on surgical process definitions. In this study, the number of hierarchies was two. The upper hierarchy consisted of six surgical processes, and the lower hierarchy consisted of seven surgical processes. The defined surgical process is as follows: P1) Verification of the tip position of the surgical instruments, P2) Cortical mapping, P3) Intraoperative rapid diagnosis, P4) Coagulation and approach to the tumor, P5) Resection of glioma, P6) White matter mapping. The hierarchical surgical processes are P2, P3, and P6: P2-1) Cortical mapping to the brain surface, P2-2) Electric discharge wait on cortical mapping, P3-1) Coagulation P3-2) Meninges incision P3-3) sampling lesion of glioma, P6-1) White mapping to the cavity of resection, P6-2) White mapping to the cavity of resection, P6-3) Electric discharge wait on white mapping.

(2) Feature extraction using segmentation and deformation

In this step, we automatically extract the features of surgical processes, using segmentation and deformation. During pre-processing of feature extraction, a sulci image is created from pre-operative MR images using BrainVISA. The sulci image is subsequently deformed to an intra-operative MR image by non-rigid registration. The positional information and types of surgical instruments (e.g., bipolar forceps and bipolar probe) are acquired from a Brainlab navigation system (Curve, Brainlab AG). Subsequently, we extract sulci from the positional information of the surgical instruments. This feature extraction step enables us to ascertain the positional relationships of surgical instruments and sulci on MR images.

(3) Feature extraction using GMM and CNN

In this step, we use GMM and CNN to extract the features of surgical processes from microscope videos, to enable interpolation of information on the types of surgical instruments (e.g., bipolar forceps, bipolar probe, and dura scissors). During pre-processing of feature extraction, an image is captured from the microscope videos. We extract three surgical instruments from microscope images, using a GMM. Extracted surgical instruments are then discriminated using CNN, which is composed of supervised learning; approximately 750 images are used as sources for extraction of these surgical instruments. This feature extraction step enables us to discriminate the instruments used in a surgery.

(4) Identification of a surgical process

In the final step, surgical processes are identified using the outputs from (2) and (3). During pre-processing, we create a surgical process model based on the output from (1). Then, the outputs from (1) and (2) are treated as observations for the HHMM. Finally, the surgical process is identified using the Viterbi algorithm. Identification of a surgical process is performed once per second.

Results

To verify our method, we applied it to past data from awake surgeries for glioma. We identified a surgical process from past surgical data that was recorded over 100 min until the completion of glioma resection following craniotomy. Table 1 shows the results of attempts to identify a surgical process, using our methods. The surgical process identified as 91.4% (P1–P6), and the Lower hierarchy process identified as 68.1% (SP2, SP3 and SP6).

Table 1 Results of the attempts to identify a surgical process

Process	Lower hierarchy process	Percentage of successfully identified surgical processes (%)
P1		66.2
P2		72.4
	P2-1	77.5
	P2-2	95.2
P3		50.4
	P3-1	20.1
	P3-2	33.3
	P3-3	83.1
P4		78.4
P5		97.4
P6		99.5
	P6-1	94.8
	P6-2	97.5
	P6-3	43.5

Table 1 continued

Process	Lower hierarchy process	Percentage of successfully identified surgical processes (%)
P1_P6		91.4
	SP2-1_SP2-2	86.4
	SP3-1_SP3-3	45.5
	SP6-1_SP6-3	78.6

Conclusion

We proposed a surgical process identification method for awake surgery for glioma, based on intra- and pre-operative data. To verify our method, we applied it to past log data, with a 91.4% success rate. On the other hand, the hierarchy process identified as 68.1%. This suggests that there is a problem in extraction of feature quantity using machine learning. The results of this method will enable further analysis of the surgical process. We plan future work to visualize implicit surgical knowledge.

This research and development work was supported by the MIC/SCOPE #162101001.

References

[1] Neumuth T, Jannin P, Schlomberg J, Meixensberger J, Wiedemann P, Burgert O (2011) Analysis of surgical intervention populations using generic surgical process models, IJCARS, vol.6, no.1, pp. 59–71.

[2] Nakamura R, Aizawa T, Muragaki Y, Maruyama T, Tanaka M, Iseki H (2010) Intraoperative analysis of task progress and performance of glioma surgery using navigation information. International Congress on Computer Assisted Radiology and Surgery (CARS2010), 5(1): S405–S406.

[3] Nagai T, Sato I, Nogchi T, Fujino Y, Yamada H, Yoshimitsu K, Muragaki Y, Masamune K (2017) Proposal for identification and modeling of surgical processes using pre-operative and intra-operative information in awake surgery for glioma, International Journal of Computer Assisted Radiology and Surgery; Vol. 12, no. 1, pp. S110–S111.

Ventricular tachycardia ablation assisted by multimodal images fusion

N. Courtial[1,2], A. Simon[1,2], M. Lederlin[1,3], S. Bruge[1,2], R. Martins[1,3], M. Garreau[1,2]

[1]Université Rennes 1, LTSI, Rennes, France

[2]INSERM, U1099, Rennes, France

[3]CHU Rennes Pontchaillou, Rennes, France

Keywords Ventricular tachycardia · Guidance · Multimodal images fusion · Multimodal images registration

Purpose

Radiofrequency catheter ablation is an important therapeutic option for patients with recurrent ventricular tachycardia (VT) resistant to antiarrhythmic drugs. The procedure aims at cauterizing ventricle's regions responsible for VT initiation and maintenance. Depending on the patient condition, an endocardial or an epicardial ablation gesture can be considered. Ablation of ventricle's regions raises important questions to proceed safely and efficiently. During the procedure, the physician has to know (i) the catheter's position relative to the VT sources, (ii) which spots to avoid (arteries, phrenic nerve), (iii) which regions could be potential targets, and (iv) what constraint can be applied on the catheter (myocardium thickness). To answer these requirements, electroanotomical mapping systems have been recognized as a powerful assistance tool for VT ablation. Previous studies have shown the benefit of visualizing structures at risk [1]. A multimodal model integration providing scar locations to the physician has confirmed the potential of such information to guide the gesture [2]. We propose here a process allowing to create patient-specific multimodal model compatible with the clinical procedure, regarding processing time and its integration in the operating room. The model is built from multiphase computed tomography (CT) and late gadolinium-enhanced MRI (LGE-MRI) images. It contains the left ventricle (LV) cavity, and structures at risk in case of an epicardial ablation, segmented on CT, and fibrosis and myocardium thickness segmented on LGE-MRI. The goal of this study is to show the feasibility and the relevance of such a workflow.

Methods

The process workflow, presented in Fig. 1, relies on CT, LGE-MRI, and Cine-MRI sequences.

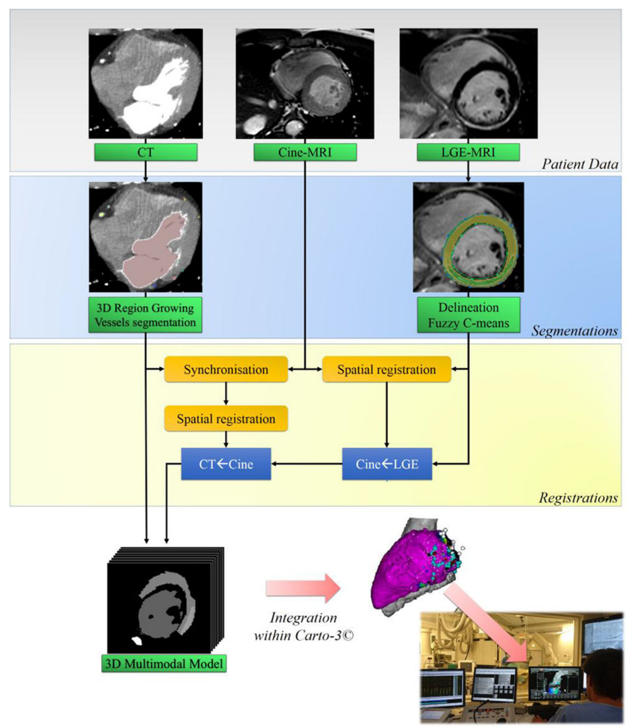

Fig. 1 Process workflow overview

It is divided in three main parts: *segmentation*, *registration*, and *model generation*. The extracted information are represented in the CT's referential, as this is the modality with the highest spatial definition.

(1) Segmentation

LV cavity and structures at risk (coronary vessels, phrenic nerve) are segmented on CT images.

The LV cavity is segmented by using a 3D region growing, followed by a morphological closing operator. Seed points are manually defined. The vessels are segmented using a three steps process. First, the user clicks a vessel along the slices. Then a 2D region growing is performed on each slice. Finally, the result is refined by an interpolation process, considering vessels regularity. The phrenic nerve is segmented manually.

Myocardium and fibrosis are segmented on LGE-MRI images. The LV endocardial and the epicardial contours are delineated using a spline, whose control points are defined by user on each available slice in short axis view. An average of 6 and 10 points are needed to define endocardial and epicardial contour respectively. The healthy parts and the fibrosis are classified using a fuzzy C-means algorithm [3] within the defined myocardium annulus.

(2) Registrations

LGE-MRI and CT images are registered. Cine-MRI is used as an intermediate step to improve the registration robustness, using its temporal dimension to perform a multi-images registration with CT sequence, and its closeness to LGE-MRI in terms of acquisition characteristics.

CT and Cine-MRI sequences are temporally and spatially aligned. The non-linear temporal distortions existing between the two sequences, acquired during different medical exams, are considered. Temporal synchronization is performed with a Dynamic Time Warping (DTW) using the global cardiac dynamic, estimated on each sequence by the Normalized cross correlation computed between the first image and each image of the sequence. The algorithm associates each CT time indexes to Cine-MRI indexes in regards of the dynamic descriptors [4]. The spatial alignment is performed with a rigid transform using a normalized mutual information (NMI) globally optimized on the defined pairs of images.

LGE-MRI and Cine-MRI are acquired during the same medical exam, but are commonly misaligned. A rigid registration is performed between LGE-MRI and the closest phase in Cine-MRI, neglecting the temporal distortion between the two sequences [5]. The similarity measure is the NMI.

(3) Model Creation

The model is created in the CT space. The label values are higher following their considered criticality: Endocardium, Myocardium, Fibrosis, and vessels in ascending order. The LGE-MRI labelled image is resampled using the LGE/Cine-MRI and the Cine-MRI/CT registrations. Both label images are then fused, keeping the highest value for each voxel. A DICOM series is then produced and used as a synthetic exam within Carto-3©, extending its capability to import segmentations obtained from CT images to multimodal models.

All the methods have been merged in a single software solution, making the process quicker, and easy to use for any user. Additionally, if any registration or segmentation had to be wrong, it can be modified manually.

Results

This study has been conducted on a 5 patients' dataset. Considering the MRI analysis, patients with defibrillators and no available MRI sequences were excluded. Both segmentations and registrations were visually validated by a clinician, except a Cine-MRI/CT registration, manually refined due to particularly poor MRI image quality.

The images processing per patient has a total duration of about 10 min for endocardial procedure, 30 min for epicardial, including:

- LV cavity segmentation (CT): 2 min
- Coronaries segmentation (CT): 20 min
- Endocardium and Epicardium delineation (LGE-MRI): 2 min
- Automated registrations: 5 min

This processing time makes this workflow compatible with the clinical schedule.

Amongst the 5 produced models, one has been considered retrospectively as a test case, and four have been used during the procedure of ablation (2 endocardial, 2 epicardial cases). An obtained model can be seen in Fig. 2.

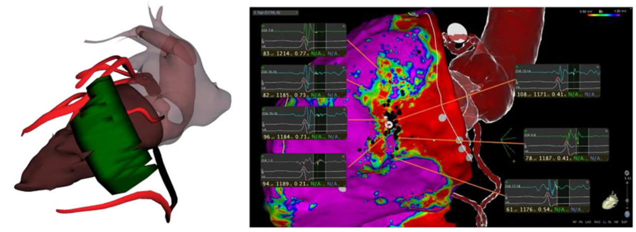

Fig. 2 3D Model (Arteries red, Fibrosis Green) compared to low potential zones ablated during the procedure (Screenshot from Carto-3©)

During the interventions, fibrosis and critical structures have confirmed their relevance, and thickness information confirmed to be a driver of clinician's confidence when ablating, as the risk of perforating cardiac wall was well assessed. Moreover, the clinician's validation lead to a planning phase.

Conclusion

The proposed workflow has shown its compatibility and relevance to plan and assist ventricular tachycardia ablation. Our future aim is to include more patients to evaluate the contribution to procedural efficacy. We will consider also the automatic extraction of myocardium thickness from the CT images. This would allow to consider more patients. As well, additional features could be considered in the model, such as a mechanical descriptor.

References

[1] Yamashita S, Sacher F, Mahida S, Berte B, Lim HS, Komatsu Y, Amraoui S, Denis A, Derval N, Laurent F, Montaudon M, Hocini M, Haïssaguerre M, Jaïs P, Cochet H (2015) The Role of High-Resolution Image Integration to Visualize Left Phrenic Nerve and Coronary Arteries during Epicardal Ventricular Tachycardia Ablation. Circulation: Arrhythmia and Electrophysiology 8(2): 371–380

[2] Yamashita S, Sacher F, Mahida S, Berte B, Lim HS, Komatsu Y, Amraoui S, Denis A, Derval N, Laurent F, Sermesant M, Montaudon M, Hocini M, Haïssaguerre M, Jaïs P, Cochet H (2016) Image Integration to Guide Catheter Ablation in Scar-Related Ventricular Tachycardia. Journal of Cardiovascular Electrophysiology, 27(6): 699–708.

[3] Kachenoura N, Redheuil A, Herment A, Mousseaux E, Frouin F (2008) Robust assessment of the transmural extent of myocardial infarction in late gadolinium-enhanced MRI studies using appropriate angular and circumferential subdivision of the myocardium. European radiology 18(10): 2140—2147

[4] Betancur J, Simon A, Langella B, Leclercq C, Hernandez A, Garreau M (2016) Synchronization and Registration of cine Magnetic Resonance and dynamic Computed Tomography Images of the Heart. IEEE Journal of Biomedical Health Informatics 20(5): 1369–1376

[5] Betancur J, Simon A, Halbert E, Tavard F, Carré F, Hernández A, Donal E, Schnell F, Garreau M (2016) Registration of dynamic multiview 2D ultrasound and late gadolinium enhanced images of the heart: application to hypertrophic cardiomyopathy characterization. Medical image analysis 28: 13–21.

Operating room integration using OPeLiNK technology

J. Okamoto[1], G. Mukumoto[2], H. Okuda[2], Y. Kasuya[3], K. Masamune[1], I. Hiroshi[1], Y. Muragaki[1]
[1]Tokyo Women's Medical University, Institute of Advanced Biomedical Engineering & Science, Tokyo, Japan
[2]Denso Corporation, Kariya, Japan
[3]Tokyo Women's Medical University, Department of Anesthesiology, Tokyo, Japan

Keywords Digital operating room · Middleware · Networking · Surgical strategy desk

Purpose

Surgical navigation devices are no longer a rarity and are now routinely used in the fields of neurosurgery, otolaryngology and orthopedics. Furthermore, with the appearance of intraoperative MRI operating rooms and hybrid operating rooms, development of new treatment methods utilizing intraoperative diagnostic imaging is now underway. Similarly, the equipment used within surgery also shown remarkable development and change. However, the same cannot be said for the role of the treatment room itself; remaining solely a space for equipment to be used and surgery or treatment carried out. With the exception of the automatic anesthesia recording system, no data coordination or system coordination yet exists between the equipment used within the treatment room.

This means that during times of medical error occurrence due to systematic defect (personnel, organization, equipment, etc.) in the medical field, utilization of such data for causal investigation, finding the source of and solutions to complications arising from surgery, or extraction of potential solutions is particularly difficult. The same is also true for usage of such data in the creation of composite information based decision support system.

Since 2014 we have been developing the Smart Cyber Operating Theater (SCOT), the next generation treatment room. This has been done through the AMED project; "Research and development into advanced medical devices and system for the realization of future medical care/development of smart treatment rooms compatible with improvements in safety and medical efficiency".

Methods

Within the SCOT project we developed a treatment room communication interface, "OPeLiNK[(1)]", allowing online uniform management of devices within the treatment room and enabling time synchronization and relocation of their data. Using OPeLiNK we are able to collect various data, such as images obtained from intraoperative modalities and surgical instrument position from surgical navigation systems, as well as surgical field images and biometric patient data. Surgically relevant information from these sources can then be sent through an application and displayed to the surgeon and surgical staff.

By using OPeLiNK, we are integrating many devices. Medical equipment in the operating room (patient monitor, anesthesia machine, surgical navigation system, intraoperative flowcytometer, surgical table, surgical microscope, cautery knife, infusion pump, shadowless lamp, intraoperative monitor, surgical drill and surgical support robot iArms), medical information system (HIS: hospital information system, PACS: picture archiving and communication system), medical image (surgical view from microscope, intraoperative MRI image, C-arm image and angiography image) and operating room facilities (room light, room camera, air conditioner, room door and insulation monitoring system). Figure 1 shows the concept diagram of the integrated operating room in the SCOT project.

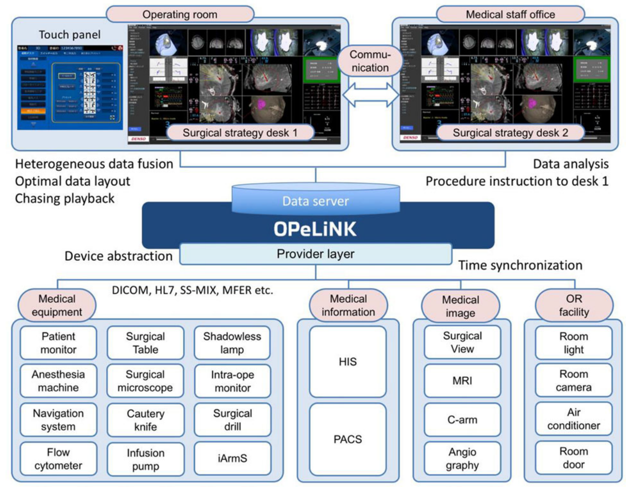

Fig. 1 Operating room integration using OPeLiNK middleware in the SCOT project

Results

We have verified the connection between each device and OPeLiNK and developed a Surgical strategy desk to display the data collected by OPeLiNK in 70 in. 4 K monitor. Surgical strategy desk has function of time synchronous data preservation, data chasing playback and video conference. By installing in the operating room and the medical office respectively, intraoperative conference is possible. We already started to use a small version Surgical strategy desk in the clinical case at intraoperative MRI operating room in Tokyo Womens Medical University Hospital. In this room, OPeLiNK collects data from a surgical navigation system (Curve, Brainlab), an intraoperative monitor (Neuromaster MEE-2000, Nihon Kohden) and an intraoperative flowcytometer (FCM-2200, Nihon Kohden). Surgical strategy desk displays the fusion data from these devices and supports the decision making of a neurosurgeon.

Conclusion

We have been developed an integrated operating room using OPeLiNK system. We plan to conduct a clinical trial for testing a full version Surgical strategy desk (more than 20 devices connected) at Shinshu University Hospital in 2018.

References

[1] Okamoto J, Masamune K, Iseki H, Muragaki Y (2018) Development concepts of a Smart Cyber Operating Theater (SCOT) using ORiN technology. Biomedical Engineering/ Biomedizinische Technik, Vol.63-No.1, (2018), pp.31–37.

Micro-focus X-ray CT of the heart: A comparison with X-ray refraction-contrast CT

H. Oda[1], H. Roth[2], N. Sunaguchi[3], D. Shimao[4], T. Sugino[2], M. Oda[2], T. Akita[2], Y. Narita[3], S. Ichihara[5], T. Yuasa[6], M. Ando[7], K. Mori[2]
[1]Nagoya University, Graduate School of Information Science, Nagoya, Japan
[2]Nagoya University, Graduate School of Informatics, Nagoya, Japan
[3]Nagoya University, Graduate School of Medicine, Nagoya, Japan
[4]Hokkaido University of Science, Department of Radiological Technology, Sapporo, Japan
[5]Nagoya Medical Center, Clinical Research Center, Department of Pathology, Nagoya, Japan
[6]Yamagata University, Graduate School of Engineering and Science, Yonezawa, Japan

[7]Tokyo University of Science, Research Institute of Science and Technology, Noda, Japan

Keywords Cardiac fiber imaging · Phase contrast CT · Helical heart · Cardiac anatomy

Purpose

The muscle fibers in the heart have a complicated structure. More detailed anatomical or pathological investigation may allow us to understand mechanism of cardiac diseases and find efficient ways to treatment. Although diffusion tensor imaging is commonly used for analyzing fiber structures, it has limitations regarding low resolution and high imaging cost. Instead, we have been working on micro-focus X-ray CT (μCT) imaging. It can obtain high-resolution 3-dimensional images of the whole heart [1] if small hearts (e.g. rabbit hearts) are used. Nevertheless, μCT has not yet become common for cardiac imaging due to difficulty in confirming the correct imaging of fibers in the heart. There is another modality named X-ray refraction-contrast CT (refraction CT) [2], which has good soft tissue contrast to conventional X-ray absorption imaging [3]. Both of μCT and refraction CT have great potential to capture fiber structures in the heart, which enables detailed microstructure analysis. Figure 1 shows the images of both modalities. We investigate fiber orientation statistics on a refraction CT volume and three μCT volumes of two rabbit hearts, and compare the results.

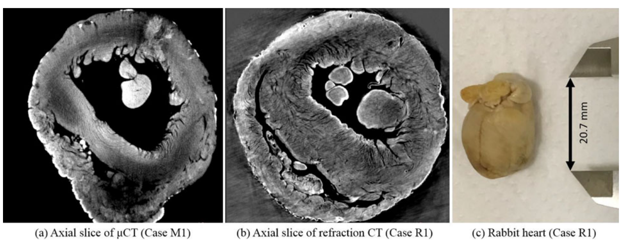

Fig. 1 Imaging of rabbit heart. Axial slices from **a** μCT and **b** refraction CT volumes, and **c** picture of prepared rabbit heart. Rabbit heart is around 20 mm of length

Methods

Creation of materials: Four male rabbits of 10 weeks are used under ethical approval of Nagoya University. Euthanasia is conducted by intravenous KCl injection, and their hearts are harvested. Formalin fixation with contrast enhancement with iodine solution is useful for μCT imaging [1]. Three hearts (Cases M1, M2, and M3) for μCT imaging are immerged in 10% neutral formalin. To enhance the contrast of the μCT volume, M1, M2, and M3 are moved to a 7.5% iodine-potassium iodide (I_2KI) solution, stained for one day, and rinsed by 10% neutral formalin for several seconds. One heart (Case R1) is immerged in 80% ethanol for refraction CT imaging as suggested by [4].

μCT scanning: Cases M1, M2, and M3 are scanned by a cone-beam μCT device: inspeXio SMX-90CT Plus (Shimadzu, Japan). Tube voltage is 90kVp and tube current is 110μA. 12 projections are performed for 1200 angles, and responses are averaged. The entire 3D images had sizes of 1024 × 1024 × (2162–2166) voxels resulting from stacking four individual scans.

Refraction CT scanning: Case R1 is scanned by refraction CT scanner in KEK (High Energy Accelerator Research Organization), Tsukuba, Japan. The refraction CT volume consists of 1600 × 1600 × 1240 voxels with a voxel size of 15^3 um^3. The entire left and right ventricles are included in the volumetric image.

Preprocessing: Now we have three μCT volumes (Cases M1, M2, and M3) and one refraction CT volume (Case R1). For each volume, we manually align Z-axis of the CT volume with the major axis of the left ventricle (LV) from the apex to the atrium parallel. Furthermore, the LV regions are segmented manually and used as a target region of interest.

Estimating fiber orientation: We apply structure tensor (ST) analysis for each voxel of the input volume for estimating the fiber orientations around the voxel. The ST $T(\boldsymbol{x})$, which is computed for a point $\boldsymbol{x}$ and represented as a 3 × 3 tensor matrix, is written as

$$T(\boldsymbol{x}) = \sum_{\boldsymbol{x}' \in \mathrm{N}(\boldsymbol{x})} \mathrm{w}(||\boldsymbol{x} - \boldsymbol{x}'||)\, \mathrm{g}(\boldsymbol{x}')\, \mathrm{g}^{\mathrm{T}}(\boldsymbol{x}')$$

where $\boldsymbol{x}'$ represents one of a point around $\boldsymbol{x}$, $\mathrm{g}(\boldsymbol{x}')$ represents the first-order intensity gradient around $\boldsymbol{x}'$ in the input volume, and $\mathrm{w}(\|\boldsymbol{x} - \boldsymbol{x}'\|)$ represents the response at $\|\boldsymbol{x} - \boldsymbol{x}'\|$ of the Gaussian function with a standard deviation of σ_G [voxels].

Eigenvalues λ_1, λ_2, λ_3 ($\lambda_1 \geq \lambda_2 \geq \lambda_3 \geq 0$) of $T(\boldsymbol{x})$ represent the strength of intensity difference with respect to the corresponding eigenvectors. The eigenvector $\mathbf{e}_3$ corresponding to the smallest eigenvalue λ_3 can be treated as running parallel to the fibers.

Fiber orientation: We define the scalar value of fiber orientation α ($-90 < \alpha \leqq 90$) as the angle between and its orthogonal projection to the axial slice. This represents the fiber angle between the axial slice in a similar fashion to [3]. $\alpha > 0$ means that the fiber is running from upper-right to lower-left, andα

Statistics: We manually select an axial slice in the basal part of each case. On the slice, we perform radial search from a central point (geometrical center of the target region on the axial slice). The angleθ [degree] (θ = 0, 5, 10, …, 355) represents the direction of a radial search and is defined as the clockwise angle between the vector (-1, 0)T in the axial plane and the radial search. In the region of interest, we compute fiber orientation α. We define the measure the distance from inner LV wall [%] similar to [2], that inside wall of LV is 0% and outside wall is 100%. Values of α from inside (endocardium) to outside (epicardium) of the LV are averaged among angles θ.

Results

We performed fiber orientation statistics using Cases M1, M2, M3, and R1. σ_G is empirically set as 16 voxels. Table 1 and Fig. 2 show fiber orientation on μCT and refraction volumes, and the statistics obtained from each case.

Table 1 Mean and standard deviation of fiber orientation estimation results around endocardium, myocardium, and epicardium

Case distance from inner LV wall (%)	M1	M2	M3	R1
20% (endocardium)	16.9 ± 49.3	32.1 ± 37.1	30.2 ± 32	23.7 ± 32.5
50% (myocardium)	8.0 ± 21.6	7.4 ± 25.6	0.7 ± 19.4	9.9 ± 15
80% (epicardium)	− 11.4 ± 24.7	− 10.2 ± 23.9	− 12.1 ± 22.6	-8.9 ± 19.4

We compute the fiber orientations at a position from the inner LV wall defined with respect to the LV wall thickness

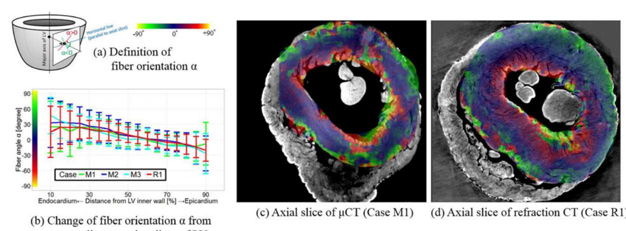

Fig. 2 Results of the experiments. **a** Definition of fiber orientation α. **b** Statistics of fiber orientation α, and values shown on axial slices by color in **c** μCT and **d** refraction CT volumes

The majority of fiber orientations in the inside (endocardium) and outside (epicardium) of the LV are similar in both modalities. They are tending to be positive in the inside and negative in outside of the LV, which follow the anatomical structure of the heart well [2]. Refraction CT achieves more stable fiber orientation estimation results in that slightly smaller standard deviation. Nevertheless, μCT volumes and refraction CT volumes produced similar results. These results indicate that μCT, which is easier to use with low cost, can be used to obtain fiber orientation as well as refraction CT.

Conclusion

We compared fiber orientations of the LV on the hearts scanned by μCT or refraction CT. Fiber orientations are similar and fit the anatomical knowledge. Although refraction CT provides a higher imaging quality of the fibers and stable estimation of fiber orientation, μCT is also useful to analyze fibers in the heart.

Acknowledgements

Parts of this research were supported by MEXT/JSPS KAKENHI (26108006, 17H00867, 17K20099, 16H05427, 17H05288) and JSPS Bilateral Joint Research Project “Oncological Diagnostic and Interventional Assistance System Based on Multi-modality Medical Image Processing”.

References

[1] Aslanidi OV, Nikolaidou T, Zhao J, Smaill BH, Gilbert SH, Holden AV, Lowe T, Withers PJ, Stephenson RS, Jarvis JC, Hancox JC, Boyett MR, Zhang H (2013) Application of micro-computed tomography with iodine staining to cardiac imaging, segmentation, and computational model development, IEEE TMI 32(1): 8–17.

[2] Sunaguchi N, Yuasa T, Huo Q, Ichihara S, Ando M (2010) X-ray refraction-contrast computed tomography images using dark-field imaging optics, Appl Phys Lett, 97: 153701

[3] Streeter DD, Spotnitz HM, Patel DP, Ross J, Sonnenblick EH (1969) Fiber orientation in the canine left ventricle during diastole and systole, Circ. Res. 24(3): 339–347.

[4] Kunii T, Shirai R, Yoneyama A, Maruyama H, LWIN TT, Takeda T (2013) Visualization of rat myocardial layers in phase-contrast X-ray imaging with ethanol fixation, Med Imag Tech, 31(2): 132–135 (in Japanese).

Development of a National Electronic Interval Cancer Review for breast screening

M. Halling-Brown[1], M. Patel[1], W. Matthew[2], K. Young[1]

[1]Royal Surrey County Hospital, Medical Physics, Guildford, United Kingdom

[2]Cambridge University Hospitals NHS Foundation Trust, Cambridge Breast Unit, Cambridge, United Kingdom

Keywords Interval cancer · Review system · Breast screening · Automation

Purpose

The review of interval cancers (cancers arising between screens) is a key means for monitoring screening performance. Radiological analysis of the imaging features of prior screening mammograms and retrospective classification are an important educational tool for readers to improve individual performance. The classification of interval cancers takes place at screening unit level. There were a variety of regional models to review selected cases. Where these reviews take place, a selection of readers from each unit read all the prior screening images independently (often reporting onto paper proformas) and then review the screening images again with the annotated diagnostic images. Classification is made on the basis of thenumber of readers prospectively identifying the cancers on the screening images. However, the process lacks appropriate scientific rigour as there is no accurate localisation system available and no record of any false marks can be made.

In order to provide a national electronic Interval Cancer Review process, software and systems have been developed and tested to facilitate the retrieval and anonymisation of images and data from clinical sites, to provide tools to annotate lesion and web-based display and mark-up of images using standard clinical workstations at any site and finally tools to record radiologists' opinions on sets of review cases with location specific detail.

Methods

The eICR toolkit has been developed to provide a comprehensive review system made up of an interval cancer collection tool, a central server and database, a web-service layer for communication between clients and the central server, a web portal for the setup and analysis of results and finally an extensible medical image viewer for annotations and cases mark.

Interval Cancer Case Collection

A semi-automated process, which allows the centralization of interval cancer cases, has been developed. This stand-alone, flexible image collection toolkit provides the extremely important function of bespoke, ad-hoc image collection at sites where there is no dedicated hardware available. This tool fills this requirement by providing a stand-alone system, which does not require installation or setup. Provided the workstation it is deployed upon has a working Internet connection, the system is designed to be executed and provided with a folder of images for collection. It then anonymises or pseudonymises the cases, optionally extracts data from a local associated cancer database (National Breast Screening System—NBSS), optionally allows the definition of ground truth and then transfers all collected information to a centralised server.

eICR Database

The eICR central server and database store the medical images in a miniPACS and the data in a relational database. The imaegDB is made up of the index-able DICOM tags extracted from the images, the annotationDB stores the ground truth and expert opinions about the case as well as the clinical data from the NBSS and finally the reviewDB stores the marks made by the participating reviews.

eICR Web Portal

Web interfaces have been created which allow reviewers to participate in the review process. The same web interface also allows a national or regional administrator to access the interval cancer review system and inspect the reviewed cases. The portal also allows feedback to be given to the organisers, collection sites and participants.

Results

Interval cancers are a key measure to monitor screening performance. Radiological analysis of the imaging features and retrospective classification are an important educational tool for readers to improve individual performance.

We have developed a web based interval cancer review programme (eICR) which provides:-

- retrieval and anonymisation of images and data (from NBSS) from clinical sites
- tools to annotate lesion locations on digital images and storage within the central database
- web-based display and mark-up of images using standard clinical workstations at any site with internet
- tools to record radiologists' opinions on sets of test cases with location specific detail

The eICR:-

- Provide a uniform process for classifying interval cancers across the NHS Breast Screening Programme (BSP)
- Promote greater access and involvement of all mammography readers in interval cancer review

- Improve feedback to individual readers
- Improve opportunities for self-directed learning and research
- Facilitate rapid access to a robust “external” review for patients and their relatives seeking answers about why their cancer was “missed”

In order to achieve this, the eICR acquires and centralises current and previous screening images, associated case data (from NBSS), ground truths (biopsy proven locations of malignancies) and provides remotely accessible tools to allow the participants to view and annotate the cases on their own workstation. The system provides the results of the review to participants in a suitable format (E.g. heat map overlaid images) that can be reviewed locally or at a regional meeting with minimal infrastructure. Finally, common themes can be identified that can be used to direct training and promote research. Figure 1 shows a graphical outline of the eICR workflow.

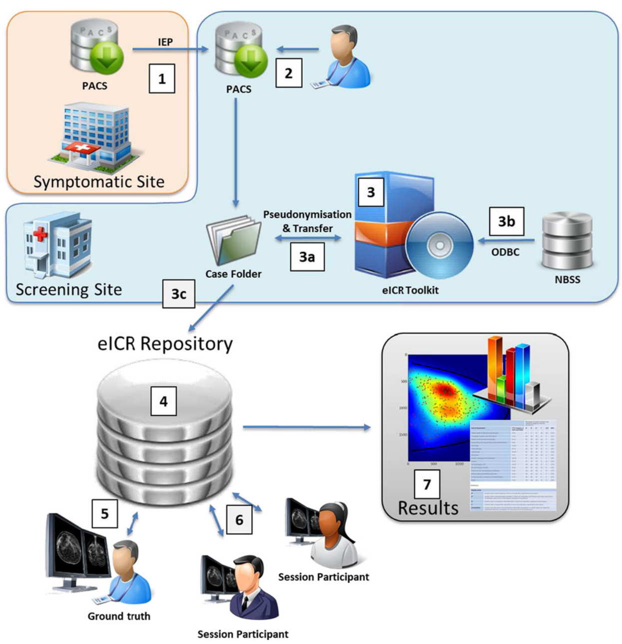

Fig. 1 Overview of the electronic interval cancer review system

Participants are able to read cases that they have not yet read, until there are no cases left in the review. Once complete, they can review the cases they have read and receive immediate feedback including the known ground-truth overlaid with their own mark-up. Once a case has been read by the required number of readers, the case is automatically removed from the review session and the results of that case are then made available to the organisers and collection site. Exportable reports are available on a case or session basis.

Conclusion

An electronic interval cancer review system has been developed to a pilot stage allowing the centralisation of interval cancer cases and subsequent review by clinicians in a remote, collaborative manner utilising the developed eICR toolkit. Web interfaces have been created to setup and administer the review sessions and to view and process feedback to the participants and collection sites.

Examining the utility of clinical, laboratory and radiological data for scoring severity of pulmonary tuberculosis

V. Kovalev[1], V. Liauchuk[1], A. Skrahina[2], A. Astrauko[2], A. Rosenthal[3], A. Gabrielian[3]

[1]United Institute of Informatics, Biomedical Image Analysis, Minsk, Belarus
[2]Scientific and Practical Center for Pulmonology and Tuberculosis, Minsk, Belarus
[3]NIAID Office of Communications and Government Relations, Bethesda, United States

Keywords Pulmonary tuberculosis · Severity · Clinical data · CT

Purpose

Accurate scoring of the severity of pulmonary tuberculosis (TB) is an important problem of quantitative assessment of patients’ state. A number of studies were undertaken in order to introduce a scoring system which provide high diagnostic accuracy and reproducibility of TB diagnosis based on chest radiographs and some additional data (see review [1]). The purpose of this study was to examine the utility of clinical, laboratory, and CT image data for uniform computerized scoring of severity state of TB patients in context of multi-national open-access TB portals [2].

Methods

Materials. Various clinical, laboratory, and CT image data of 214 TB patients (127 males and 87 females, mean age 43.8, STD = 17.3 years) were used in this study. All the data were sampled from one of the national TB sub-portals [2]. Both CT image features extracted by recent image analysis methods and quantitative expert data provided by experienced radiologists were employed. A 5-level score was assigned to each patient by a board of two chief pulmonologists. The score was ranged from 1 (the worst, patient in a critical condition) to 5 (very good, nearly recovered). It happened so that the number of cases with severity levels from 1 to 5 was equal to 16, 17, 63, 98, and 20 respectively. Specific items of clinical and laboratory data being examined are presented in the next section. Figure 1 illustrates typical CT images of patients with extreme score values. The lung component of CT scans was segmented with the help of a thresholding and filtering technique followed by manual correction of lesion regions.

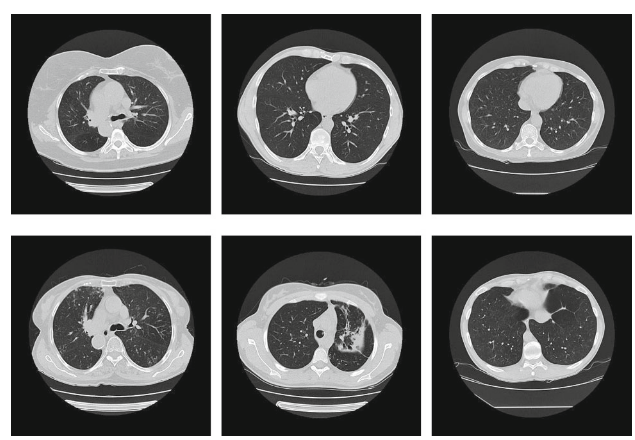

Fig. 1 Characteristic slices of CT images of patients with TB severity scores 5 (top row) and 1 (bottom row)

Methods. Quantitative assessment of the utility of different data types was performed in two stages. At the first stage the clinical and laboratory data, the data provided by radiologist, and computerized CT image features were examined separately. At the second stage they were fused with the hope to get better results. Computerized image features were extracted using Banks of Filters method suggested in [3] and by Principal Component Analysis (PCA, 99% of variance). All kinds of data were correlated with expert scores using significance threshold $p < 0.01$. In addition, the scores were predicted using linear SVM and Random Forest classifiers executed in regression mode.

This case the prediction quality was assessed by correlating non-integer score values produced by classifiers with the integer expert scores as well as by way of a direct comparison of predicted and expert score values and calculating Root Mean Square Error (RMSE).

Results

Clinical and laboratory data. Results of statistical analysis of clinical and laboratory variables revealed that 11 of them have passed the significance threshold. The highest correlation with expert score was observed with Type of drug resistance variable (r = 0.44, p = 2.24e−11), Presence of TB symptoms (r = 0.334, p = 1.14e−6) and Bacillarity (r = 0.322, p = 2.04e−6). The SVM classifier provided correlation between expert and predicted scores of r = 0.584 and RMSE = 0.836 in case of using 11 significant variables and r = 0.593, RMSE = 0.828 obtained on 10 Principal Components (PCs). Corresponding results produced by Random Forest were slightly better on 11 variables (r = 0.607, RMSE = 0.810) but worse on 10 PCs (r = 0.565, RMSE = 0.839).

Radiology data. Analysis of "manual" radiology features suggests that only 7 variables out of 21 were significant. The strongest correlation was observed with the following variables: Number of affected lung segments (r = 0.453, p = 6.61e−12), Prevalence of TB process (r = 0.304, p = 8.23e−6) and Plevritis (r = 0.291, p = 1.43e−5). Contrary to the expectations, the presence/absence of lung caverns was correlating insignificantly with the integral TB severity score assigned by experts. As for the classifiers, this time SVM has demonstrated better TB score prediction on both significantly correlated variables only (r = 0.481, RMSE = 0.897) and PCs extracted from all 21 radiology features (r = 0.484, RMSE = 0.895).

Computerized CT image features alone. Feature extraction step resulted in as many as 786 mutually-correlated variables. First, they were entered into both classifiers. The quality of predicting TB severity was r = 0.414, RMSE = 0.961 achieved by SVM and r = 0.515, RMSE = 0.864 by Random Forest. Same results obtained on 6 PCs were r = 0.422, RMSE = 0.927 and r = 0.442, RMSE = 0.904 respectively.

Combined data. At this stage all the above data were merged and entered into classifiers. As a result, SVM method provided correlation value r = 0.455 and RMSE = 0.920 whereas Random Forest gave the best results of r = 0.619 and RMSE = 0.791 (see also corresponding confusion matrix in Fig. 2).

	1	2	3	4	5
1	1	9	5	0	0
2	0	2	8	7	0
3	0	9	25	30	0
4	0	1	18	78	0
5	0	0	0	20	0

Fig. 2 Confusion matrix of predicting TB severity score using combined patient data

Conclusion

Results achieved with this study allow drawing the following conclusions.

1. The TB severity score depends to a greater extent on the clinical and laboratory data rather than on radiology data provided by CT imaging
2. The computerized CT image features appear to be more powerful predictors of TB severity compared to the traditional radiology findings (r = 0.515, RMSE = 0.864 vs. r = 0.484, RMSE = 0.895 respectively).
3. Combination of clinical, laboratory, radiology, and computerized image features provides the best prediction of 5-level TB severity score considered in this study (N = 214 patients, r = 0.619 and RMSE = 0.791)

References

[1] Pinto LM, Pai M, Dheda K, Schwartzman K, Menzies D, Steingart KR (2013) Scoring systems using chest radiographic features for the diagnosis of pulmonary tuberculosis in adults: a systematic review. European Respiratory Journal, 42: 480–494

[2] Rosenthal A, Gabrielian A, Engle E, Hurt DE, Alexandru S, Crudu V, Sergueev E, Kirichenko V, Lapitskii V, Snezhko E, Kovalev V, Astrovko A, Skrahina A, Taaffe J, Harris M, Long A, Wollenberg K, Akhundova I, Ismayilova S, Skrahin A, Mammadbayov E, Gadirova H, Abuzarov R, Seyfaddinova M, Avaliani Z, Strambu I, Zaharia D, Muntean A, Ghita E, Bogdan M, Mindru R, Spinu V, Sora A, Ene C, Vashakidze S, Shubladze N, Nanava U, Tuzikov A, Tartakovsky M (2017) The TB Portals: an open-access, Web-based platform for global drug-resistant-tuberculosis data sharing and analysis. Journal of Clinical Microbiology, 55: 3267–3282

[3] van Ginneken B and ter Haar Romeny BM (2003) Multi-scale texture classification from generalized locally orderless images, Pattern Recognition, 36: 899–911

Computer-assisted disaster response: benefits for global healthcare

R. Andrews[1,2], L. Quintana[2,3], T. Khan[2,4]

[1]NASA Ames Research Center, Nanotechnology & Smart Systems, Los Gatos, United States

[2]World Federation of Neurosurgical Societies, Nyon, Switzerland

[3]Valparaiso University Medical Center, Neurosurgery, Valparaiso, Chile

[4]Northwest General Hospital & Medical School, Neurosurgery, Peshawar, Pakistan

Keywords Disaster response · Global surgery · Mobile surgical hospital · Telesurgery/drones/robots

Purpose

The United Nations (UN) and World Bank estimate natural disasters have cost over US$500B and 100,000 lives annually; "unnatural disasters" (industrial accidents, terrorism) add to mass casualties. [4]. An estimated 20,000 people died each day from lack of surgical facilities the first week after the 2010 Haiti earthquake. The average number of deaths each year from earthquakes alone is greater than the total number of people killed in traffic accidents in North America and the European Union combined. The *Lancet Commission on Global Surgery 2030* estimates that from 2015 to 2030 the percentage of GDP in low and middle income countries (LMIC) lost to two largely surgical conditions, trauma and cancer, will increase 4-fold—from .15 to .6 of GDP each [2]. Since disaster response (DR) groups including the UN, the Red Cross, and military aeromedical teams all remain separate from ongoing healthcare systems and require authorization before responding, it is a week or more before surgical services are available for disaster victims. [5]. To improve DR morbidity/mortality, all necessary resources (staff, mobile operating rooms, support equipment) must be on-site in 12–24 h—not the current standard of days to weeks.

Methods

Trauma and stroke centers (TSCs) evolved with evidence that immediate "24/7" treatment dramatically improved morbidity/mortality. TSCs and all personnel are part of the ongoing healthcare system—not a separate entity. This is in contrast to current DR resources, e.g. the UN, NGOs, and military resources. Fortunately the universal humanitarian response to disasters suspends the political, cultural, and socioeconomic barriers that hinder response to other global crises: governments and other groups that normally may be at odds with each other come together for the common good during a disaster [1].

Computer-assisted technology has enabled various advances that enhance DR. These begin with disaster mitigation—thanks to novel high-tech early warning systems for hurricanes/typhoons, earthquakes, and even LIDAR-enabled drones for avalanche prediction. Telemedicine advances have not only mitigated loss of life in hydrometerological disasters but also have afforded immediate telesurgical guidance (and in the near future, remotely-guided robotic surgery). Helicopter-portable CT scanners that can be powered by a car battery enable surgical facilities to be present anywhere worldwide within hours. Remote-control drones and robots (aerial, ground, marine) can optimize resource utilization (e.g., identify the living buried in rubble, triage medical resources for the most benefit) [3]. A proof-of-concept demonstration of drone pairs that can "see" through walls (using simple WiFi signals and sophisticated computer programs) may soon enhance our ability to "see" within confined spaces such as buildings.

We propose that DR—like TSCs—be integrated into ongoing healthcare systems worldwide (governmental/nongovernmental, national/international) with the advent of Disaster Response Centers (DRCs) [1]. Each DRC, like a TSC, is a medical center staffed by specialists from all aspects of emergency response—ready for deployment immediately. Each DRC is staffed (faculty and in-training) by local surgeons and staff working side-by-side with developed country surgeons and staff (on a rotating basis) [1].

Results

During 2017, the DRC concept was presented at the National Center for Disaster Medicine and Public Health Symposium (Bethesda, MD, USA), the Aerospace Medical Association Annual Meeting (Denver CO, USA), the European Association for Predictive, Preventive, and Personalized Medicine Congress (Malta), the Healthcare Information Technology Annual Conference (Mumbai, India), the International Workshop on Futuristic Healthcare Technology: Telemedicine and Drones (Chennai, India), as well as at numerous international neurosurgical/neurotrauma conferences. One of the authors (TK), has opened 2 hospitals in Peshawar, Pakistan, in the past 8 years as well as fully accredited medical and nursing schools—and in May 2017 began the first significant ambulance service in the region. Discussions have been held with the Chilean Health Ministry; additional meetings are planned with the Chilean Oficina Nacional de Emergencia del Ministerio del Interior (ONEMI) in February 2018. Additional groups with whom we are communicating/collaborating that can optimize DR include (1) the Apollo Telemedicine Network Foundation (ATNF), based in India and providing daily telemedicine consultation services to over 30 countries (mostly in sub-Saharan Africa), and (2) the Center for Robot-Assisted Search and Rescue (CRASAR), based at Texas A&M University and providing immediate free DR assistance with robots and drones [1, 3]. Initial DRC sites are planned for Iquique (northern Chile) and Peshawar (northwest Pakistan) (Fig. 1).

Fig. 1 Handout on the Disaster Response Center concept from the National Center for Disaster Medicine and Public Health Symposium, Bethesda, MD, USA, September, 2017

In the USA, the National Academies of Sciences, Engineering, and Medicine have recently proposed a National Trauma Care System integrating the civilian trauma system with the military trauma system (Fig. 2)—a concept similar to the DRC.

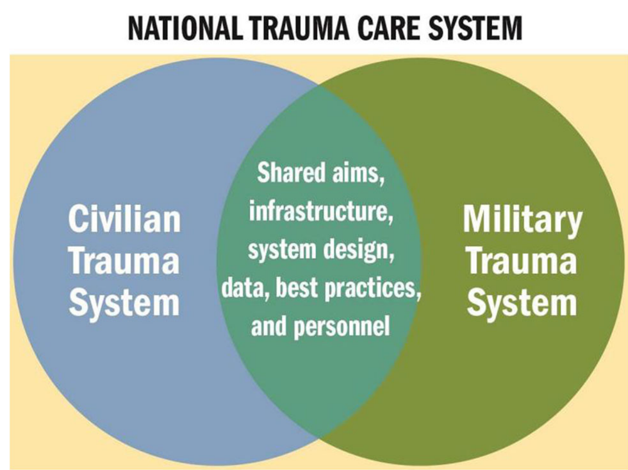

Fig. 2 National Academies of Sciences, Engineering, and Medicine. 2016. A national trauma care system: Integrating military and civilian trauma systems to achieve zero preventable deaths after injury. *Washington, DC: The National Academies Press*

The DRC global "mega TSC system" will dramatically improve disaster DR time, saving countless lives presently lost due to lack of surgical resources for days or more following disasters. DRCs will foster global standards for medical/surgical training, and provide an unmatched universal platform for research. They will also foster camaraderie between physicians and surgeons from various developing and developed countries, and encourage creation of cost-effective but technically sophisticated medical and surgical techniques. DRCs, with multinational staff, will advance healthcare in developing countries—and be a key component to realizing the goals set for global surgery by the recent *Lancet Commission: Global Surgery 2030 [1, 2].*

Conclusion

The technical advances in mobile imaging and surgery, telemedicine/telesurgery, robotics and drones noted above all make not only feasible but economically advantageous the improvement in DR that will not only save countless lives (and hasten recovery/reconstruction after disasters) but also achieve global standards of economic and healthcare parity otherwise impossible.

There are substantial political, cultural, and socioeconomic benefits—beyond the general healthcare benefits—of integrating DR into the ongoing global healthcare system. Integration of DR into the global healthcare system simultaneously addresses important goals such as implementing universal standards for medical/surgical education and training, enhancing medical/surgical research, and improving public health worldwide.

References

[1] Andrews RJ, Quintana LM. Unpredictable, unpreventable and impersonal medicine: global disaster response in the 21st century. *The EPMA Journal* 2015; 6: 1–12.
[2] Meara JG, Leather AJM, Hagander L, et al. Global Surgery 2030: evidence and solutions for achieving health, wealth, and economic development. *Lancet* 2015; 386: 569–624.
[3] Murphy RR. *Disaster Robotics.* The MIT Press, 2014.
[4] UNISDR + WMO: Disaster risk and resilience—thematic think piece. UN System Task Team on the Post-2015 UN Development Agenda, May, 2012. Available from: http://www.unisdr.org.
[5] WHO Emergency Response Framework 2013: WHO performance standards. Available from: http://www.who.int.

In silico and ex vivo validation of a microwave endoscopic system for colon examinations

M. Guardiola[1], J. Romeu[2], G. Fernández-Esparrach[3], M. A. Gonzalez-Ballester[1,4,5], O. Camara[1]
[1]Universitat Pompeu Fabra, DTIC, Barcelona, Spain
[2]Universitat Politècnica de Catalunya, TSC, Barcelona, Spain
[3]Hospital Clínic de Barcelona, Barcelona, Spain
[4]ICREA, Barcelona, Spain

Keywords Microwave imaging · Colorectal cancer · Endoscopy · Diagnosis

Purpose

Colorectal cancer (CRC) is a serious and increasing health problem in countries with a westernized lifestyle. CRC is the second leading cause of cancer mortality in men and the third in women [1] with over 1.3 million new cases annually worldwide. Among CRC screening methods, colonoscopy is the most effective and the only method able to resect neoplastic polyps during the procedure. Nevertheless, the polyp miss rate is 22% and the risk of developing CRC after a negative colonoscopy is 60%. The lack of efficacy is due to visual limitations (limited field of view, occultation by colon's angulation and folds, poor preparation…) and the lack of information on in situ histology to assist medical decisions [2]. MiWEndo is a medical device prototype based on microwave imaging (MI) [3] aimed at complementing conventional colonoscopy to improve polyp detection rate and characterize tissues in situ. MI is a low-cost and safe anatomical and functional imaging method able to create 360° images with a fair trade-off between resolution and light opaque tissue penetration. The working principle of MI is based on the difference between the dielectric properties (i.e. permittivity and conductivity) of biological tissues primarily according to the tissue water content. Due to the higher vascular (and water) content related to tumor angiogenesis, malignant tumors have significantly larger dielectric properties than normal tissues. Here we present in silico validation results and initial ex vivo results of MiWEndo.

Methods

MiWEndo consists of a prototype device composed by a distal unit (to scan the tissue) and an external unit (to generate the electromagnetic (EM) fields, process the data and display). The distal unit is a head attachable to the tip of a conventional endoscope composed by two arrays of antennas that transmit and receive EM fields. From the received fields, MI algorithms reconstruct the dielectric properties of the tissues. A planar version of MiWEndo with 8 transmitting and 8 receiving antennas arranged in two rows was build and simulated. A planar prototype (instead of the final cylindrical one) adapts better to the shape of the ex vivo colon samples. MiWEndo is placed over the sample (separated 20 mm) and moved perpendicularly to the antenna arrays in several steps to simulate the exploration progression. At each step one image is obtained. We computationally modelled and performed EM simulations of a flat colon mucosa with different types of polyps using CST Studio Suite (www.cst.com). The colon mucosa was modelled as a brick of $100 \times 120 \times 10$ mm^3. We also modelled three different histologic types of polyps, i.e. with high grade dysplasia (HGD), with low grade dysplasia (LGD) and cancer; of three different shapes, i.e. pedunculated (Ip, sphere), sessile (Is, cylinder 5 mm high) and flat (IIb, cylinder 2 mm high) of 15 mm of diameter. We assigned the dielectric properties retrieved in our previous ex vivo colon tissue characterization campaign [4] to the modelled geometry. For the experimental validation, an ex vivo fresh colon sample with a flat polyp with HGD was scanned with the planar version of MiWEndo. Frequencies between 5 and 8 GHz were used for both the simulations and the measurement. A simple quantitative bifocusing MI algorithm was used to obtain the results [5]. This algorithm retrieves the areas of highest contrast of the imaged tissues.

Results

Figure 1a shows the received field intensity and Fig. 1b the reconstructed normalized dielectric contrast of the simulated specimens between 5 and 8 GHz. The plots correspond to the cut marked with a dash-dot grey line that goes through the polyp. From the received fields, we can observe that the presence of a pedunculated polyp of 15 mm produces large changes in the received field intensity (5–10 dB). Subtle and small polyps (sessile and flat) produce smaller changes (< 1 dB). The polyp shape produces larger changes than the polyp histology in the received fields. From the reconstruction of the dielectric contrast, Fig. 1b, we can observe that the highest intensity corresponds to the position of the polyp. Pedunculated polyps produce higher intensities followed by sessile and flat polyps. Within each shape, cancer shows the greatest contrast followed by HGD and LGD. Figure 2 shows the experimental imaging results of an ex vivo colon sample with a flat polyp with HGD. The image represents the surface of the sample where the area of higher dielectric contrast intensity corresponds to the position of the polyp.

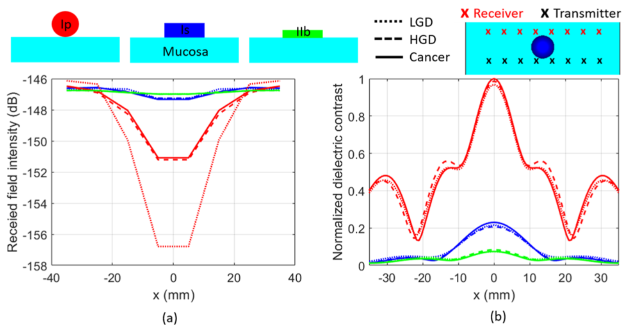

Fig. 1 **a** Received field intensity and **b** normalized dielectric contrast of simulated colon mucosa with a 15-mm polyp of different shapes (I_p = pedunculated, I_s = sessile, II_b = flat) and histology (LGD = low grade dysplasia, HGD = high grade dysplasia and cancer)

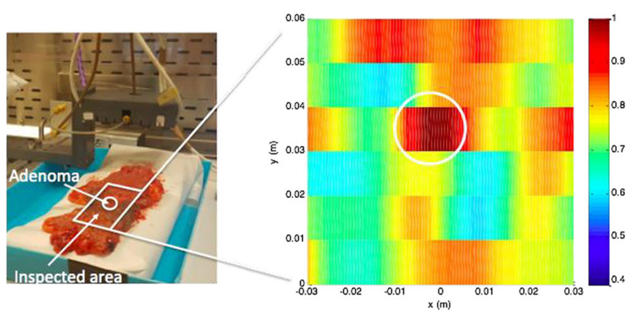

Fig. 2 Superficial image of the reconstructed dielectric contrast of a ex vivo colon sample with a flat polyp with HGD. The area of higher dielectric contrast corresponds to the position of the polyp

Conclusion

A novel, promising concept for in situ endoscopic tissue detection and characterization based on microwaves was presented. The reconstructed contrast reflects the areas of major scattering of the imaged tissue and correlates with the dielectric contrast of the different histologic types of polyps. Thus, based on in silico data, MI can detect and classify colon polyps. Initial ex vivo experiments show promising results.

References

[1] GLOBOCAN 2012 (International Agency for Research on Cancer) http://globocan.iarc.fr
[2] Lee TJ, Rees CJ, Blanks RG, Moss SM, Nickerson C, Wright KC, James PW, McNally RJ, Patnick J, Rutter MD (2014) Colonoscopic factors associated with adenoma detection in a national colorectal cancer screening program. *Endoscopy, 46 (3),* 203–211.
[3] Nikolova, N (2017) Introduction to Microwave Imaging. *Cambridge University Press.*
[4] Guardiola M, Ceresa M, Romeu J, Fernandez-Esparrach G, Gonzalez Ballester MA, Camara O (2017) Microwave endoscopy for colorectal cancer prevention Int J CARS, 12 (Suppl 1): S21.
[5] Jofre L, Broquetas A, Romeu J, Blanch S, Papio Toda A, Fabregas X, Cardama A (2009). UWB tomographic radar imaging of penetrable and impenetrable objects. *Proceedings of the IEEE, 97*(2), 451–64.

A performant and fully DICOM compliant Web PACS for Digital Pathology

R. Lebre[1], T. Godinho[1], L. Silva[2], C. Costa[1]
[1]University of Aveiro, IEETA, Aveiro, Portugal
[2]BMD Software, Aveiro, Portugal

Keywords Whole-slide imaging · DICOM · PACS · Web

Purpose

The focus of pathology is the morphologic anomalies detection, finding out possible relations with functional disorders of tissues. The expected output is the diagnosis of diseases. The identification of such anomalies can be done at macroscopic level using naked eye, or at microscopic level using appropriate devices. The purpose of this specialty has remained intact over time, laying on the analysis and comparison of specimens.

Recently, digital pathology arisen as a new branch of pathology [1]. It refers to the aggregation of hardware and software designed to substitute the traditional devices (e.g. microscope) [2]. In addition, digitalization of specimen provides better conditions of accessibility, cleaning, protection and storage than old glass slides. Moreover, it takes advantage of the decreasing cost of digital storage and distribution.

This article presents a technological solution that brings digital pathology workflows into PACS universe, making use of DICOM standard mechanisms for storage and distribution of data. The system assures a full-stack efficient solution, since the request of the image tiles via the DICOM Web services that follow the principles of RESTful Web services, until the display, by a web viewer application developed to handle the data consumed via those DICOM services.

Proposed Web Pathology PACS is able to store whole-slide imaging (WSI) data in DICOM format. Query and retrieve services are based on the most recent DICOM Web services. A zero-footprint viewer oriented to pathology modality was developed to run in any web-browser. It provides a tiling engine especially suited to deal with the WSI image pyramids and consumes data from PACS archive through DICOM Web services. The solution is capable of achieving better performance than common proprietary solutions based on JPEG2000.

Methods

Digital Pathology workflow starts with the acquisition of the images by the Whole-Slide Scanners. It is performed directly from the glass slides and sent to the PACS Archive. The process of sending must be via DICOM C-Store or STOW-RS. In alternative, DICOMization of proprietary formats is possible since they usually relay in common image formats (e.g. JPEG, JPEG2000, TIFF).

PACS Archive can evaluate the acceptance of the transfer syntax, namely the compression algorithm used and the image pyramid configuration (see Fig. 1). Regarding the compression, the system will try to find the best trade-off between volume data and image quality. The long-term storage capacity of PACS archive is a critical issue in WSI. Our working archive contains 100 studies. The maximum resolution images of this dataset have a combined size of 13.9 GB. Together with the sub-resolution images, the dataset amounts to 19.4 GB. Regarding the image dimensions, the largest images have 26 GPixels, while the lowest image resolution is 16 MPixels.

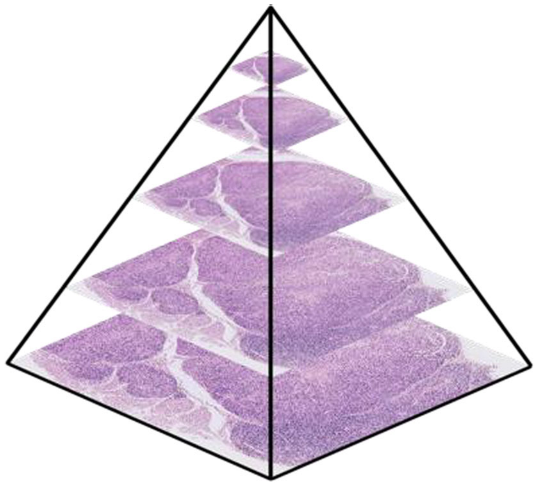

Fig. 1 Pyramid images example

Regarding the image pyramid, the acquisition equipment can operate in two ways: acquiring only the larger resolution image or acquiring the pyramid with sub-resolution images. The sub-resolution images are a key element in the system as they influence the performance of the visualization procedure. In the developed system, it was integrated a module capable of generating sub-resolution images based only on the largest resolution image. It is an intensive process that runs in background to avoid system overloading.

Concerning the visualization of studies, it uses a pure web application developed in JavaScript and HTML5. It starts by searching the image in the archive making use of DICOM QIDO-RS. Developed viewer includes a tile engine and consumes the image pyramids stored in PACS archive DICOM WADO-RS. To retrieve the correct images, some information must be queried, using DICOM QIDO-RS, like, for instance, dimension, resolution, z-planes or image pyramid configuration. Next, the sub-resolution images can be found by querying for "SeriesInstanceUID". For each of the sub-resolution images, the viewer gets the image size (cols vs. rows) to build the pyramid representation at Web client-side. Moreover, it is able to request access to each frame of the relevant image level and display it. Firstly, viewer defines the image level closest to the viewport. Next, it requests the list of frames of the SOP Instance UID desired, using WADO-RS. Once the pixel data has been received, the viewer crops and resizes to fit exactly the viewport. The operations of panning and zooming are also supported in the same way. After the display, some adjustments, like changes in brightness, contrast or color filters are supported in client-side, and therefore, there will be no impact on the solution server-side performance.

Results

Digital pathology laboratories rely on performance of image visualization since it has an impact on the quality of service sensed by pathologists. So, developed viewer [4] focuses not only in the study/tile retrieve time, but also on the displaying usability. For instance, in parameters like panning, zooming, filtering and annotations. The Fig. 2 is a screenshot of the web viewer displaying an image with the resolution of 59,483 × 50,127. Some tools are also visible in the screenshot. In the right side is positioned, above, the thumbnail of the whole image, indicating the relative viewport in the base image. In the middle, information about the handling is presented, namely, zoom applied, rotation and coordinates (on image) of the cursor. Next, below, it is contained all the adjustments available to perform on image. Note that those adjustments are made client-side.

Fig. 2 Web viewer screenshot

The solution supports two types of annotations: the ruler annotation and the area annotation. In both types of annotations, it is possible to write a comment that is stored in the server and made available to every user that requests the SerieInstanceUID of the Whole-Slide Image.

Concerning the architecture performance, we estimate that the proposed viewer is capable of loading around 50 tiles per second, which corresponds to an area of 3620 square pixels. Moreover, it completed the workflow faster than state-of-the-art solutions.

Conclusion

The presented system allows the integration of a Whole-Slide Image viewer in a general PACS [3]. This article describes the workflow of the architecture for supporting digital pathology in a PACS archive alongside with other modalities of medical imaging. The support of DICOM standard for communications and data format associated with the use of pure web technologies is a breakthrough comparatively to the existing proprietary solutions. Regarding the contribution for WSI images, it is also important to refer that the components were designed and developed with focus on performance and usability, demonstrating that these factors are not an issue for the efficiency of DICOM services.

Acknowledgments

This work was supported by the Integrated Programme of SR&TD SOCA (Ref. CENTRO-01-0145-FEDER-000010), co-funded by Centro 2020 program, Portugal 2020, European Union, through the European Regional Development Fund. This work has also received support from the EU/EFPIA Innovative Medicines Initiative Joint Undertaking (EMIF Grant No. 115372).

References

[1] Al-Janabi S, Huisman A, Van Diest PJ (2012) Digital pathology: Current status and future perspectives. *Histopathology* (61): 1–9
[2] Higgins C (2015) Applications and challenges of digital pathology and whole slide imaging. *Biotech. Histochem* (90): 341–347
[3] Godinho T, Lebre R, Silva LB, Costa C (2017) An efficient architecture to support digital pathology in standard medical imaging repositories. *J. Biomed. Inform.* (71): 190–197
[4] demo.dicoogle.com/pathology

How modular technologies and personalized healthcare will influence the design of hospital architecture and care facilities

O. Ratib[1], C. Amato[1,2]
[1]University of Geneva, Radiology and Medical Informatics, Geneva, Switzerland
[2]Cannon Design, Los Angeles, United States

Keywords Hospital design · Patient workflow · Personalised medicine · Architecture

Purpose

Personalized medicine (PM) has been underway for quite some time now, with a rapid evolution in patient management and clinical pathways of patient care. The hospital environment however, has not adapted to the same degree, and continues to react to medical and technologies changes. The industry has not, until now, tried to re-invent the concept of how space should be adapted to advance Personalized Medicine and precision medicine workflow, instead of just being a sidebar or an afterthought.

The goal of our study is to explore alternative and disruptive design concepts that will better accommodate the environment and workspace of care facilities and large hospitals.

Methods

We explored the new advances in technology that allow a shift of design from traditional investigation and interventional suites setups, to bedside point of care. We particularly focused on technical solutions and architectural designs that will enable us to change from traditional workflow of patient moving from a unit to another in a care facility, to the modular design of patient rooms that will host the needed devices for patient monitoring and treatment.

Our research focused on solutions to accommodate the following requirements:

1. The design of multimodality diagnostic and monitoring devices that can allow performing clinical investigations around a single mobile unit that carries the patient with the needed life support environment.
2. The implementation of new point-of-care (POC) technical developments and solutions used to obtain diagnostic results while with the patient or close to the patient.
3. Alternative solutions for improving patient workflow and minimizing patient displacement between different hospital units.
4. The potential pre-fabrication of personal, patient mobile universal modules.

We also analysed solutions that are under development for space travels (such as missions to Mars) to evaluate potential applications in future design of healthcare facilities. This was done to understand and evaluate how extreme scenarios force us to change well established paradigms and challenge traditional healthcare designs.

Results

In our proposed concept the patient room stays and moves with the patient. This enables us to create a controlled environment that can be calibrated to each individual patient. The proposed spatial idea is like a cocoon (or patient envelope) that can move with everything the patient needs.

The architectural design of a hospital that we envision challenges the traditional pre-fabricated hospital concept and downsizes the prefabrication challenge to a much smaller scale and space. This new building type (the new hospital) is conceived as a plug-and-play chassis with robust intelligent infrastructure where these personal patient pods dock in and out with the ability to add the necessary diagnostic and treatment devices around the patient unit instead of moving the patient to a dedicated unit for diagnostic or therapy.

This new healthcare facility design alternative also challenges the concept of specialized departments located in different physical hospital section. Medical specialties become more mobile and move into the patient units. Telecommunication and remote control of diagnostic and treatment devices also allow better utilization of hospital space while concentrating the necessary technology around the patients themselves.

Conclusion

The technical solutions currently in development offer the basic components for a new design of future healthcare facilities.

The new hospital moves with the patient and becomes personalized. Just like medicine becomes personalized.

Bringing technology (real time diagnostics and procedures) to the bedside allows better optimisation of clinical workflow and will contribute to reducing costs and gaining patient management efficiency.

The concepts explored here can also be extended to the Patient-Centered Medical Home (PCMH) healthcare model that is being encouraged by medical authorities in many industrialized countries today as a potential solution for lowering the rapid growth in healthcare costs.

A knowledge-based data entry form for high quality clinical data collection

C. Unger[1], M. Stoehr[2], S. Oeltze-Jafra[1], M. A. Cypko[1]
[1]University of Leipzig, Innovation Center Computer Assisted Surgery, Leipzig, Germany
[2]Clinic of Otolaryngology, Head and Neck Surgery, Department of Head Medicine and Oral Health, University of Leipzig, Leipzig, Germany

Keywords Clinical data collection · Clinical decision support · Tumor board · Bayesian networks

Purpose

Clinical decision support systems (CDSS) based on Bayesian networks (BNs) have the potential to support complex therapy decisions. BNs can represent complex therapy decisions, compute most suitable patient-specific therapy options and potential outcomes, and be used for further analysis, e.g., identifying most relevant decision influences or missing examinations. However, the quality of their output highly depends on the quality of the input patient data.

At the University of Leipzig, a BN based CDSS has been developed for laryngeal cancer consisting of over 1100 decision relevant variables [1], from which a subnetwork has been validated with 303 variables representing the determination of the tumor, lymph node and metastasis staging (TNM staging) [2]. The validation utilized patient data and domain expertise to retrospectively analyze 66 patient cases with given TNM stagings. It identified the quality of the input data as one of the main reasons for incorrect TNM computation. Typical issues in data quality are caused by extensive and unstructured free-text data, among others, describing the reliability of examination results.

We developed and evaluated a form-based tool for model-based data entry to achieve a high-quality input data collection in an adequate time. The tool represents a trade-off between a time-consuming, unguided and unstructured manual entry and a fast, fully automatic entry by computerized retrieval and pre-processing of the data from a hospital information system.

Methods

As a proof of concept, a tool was developed, which extracts all parameters and their possible values dynamically from the available BN and automatically generates structured forms. The tool is a prototype accepting imports of the BN file format XDSL of an open access BN model, inferencing and analysis software GeNIe/SMILE [3].

A workflow of the applying the tool is considered in four steps (Fig. 1). First, from a database of BN decision models a network's XDSL file is selected to be imported into the tool. Second, the tool parses the XDSL file interpreting all tagged items in the section without an "unobservable" property as examination that can be observed and consequently should be entered by clinicians. Third, the data entry forms are automatically generated and presented in the main view for user input. Next, after entering the data, the XDSL file is updated with the new patient data in a separate section. Finally, the file is exported back to the database and can be used to compute the patient-specific therapy recommendations.

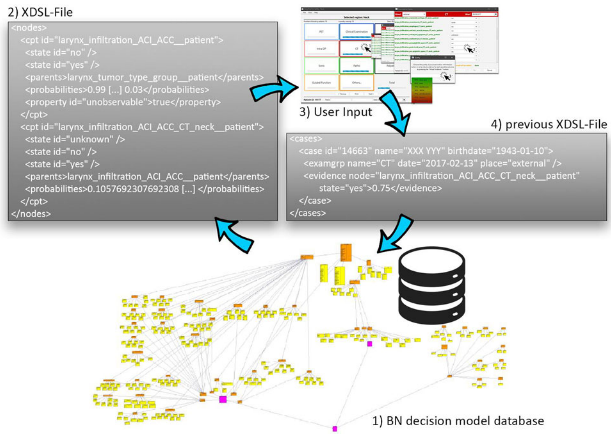

Fig. 1 Workflow of an automatically generated model-based data entry form

In more detail, the main view is divided into several groups for overview purposes (Fig. 2). Each button opens a new view for the respective examination group (Step 1). This view has a list of all variables in that group. By selecting a specific item from the list of possible outcomes (Step 2) the user gets a dialog to choose a certainty for the chosen outcome (Step 3). That is because outcomes may differ in reliability. It is also possible to apply a probability for each possible outcome individually, if there isn't an unambiguously single outcome.

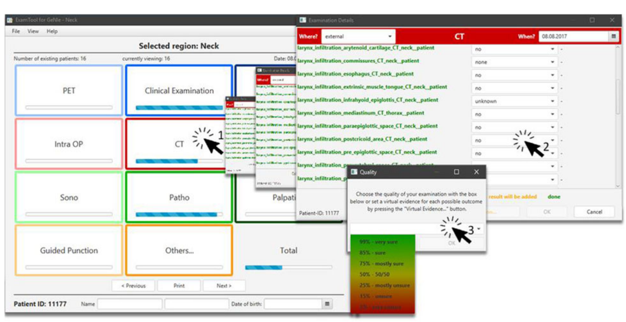

Fig. 2 Form-based tool for model-based data entry, presented in three steps

In an evaluation with one experienced otolaryngologist, the usability of the tool and the quality of the input data were assessed based on 16 retrospective patient cases. The data assessment was time needed for data entry was measured for each examination.

Results

The study identified that (1) the extraction of information from the clinical information system required most of the time in the process and (2) user interface requires too many tasks. The average duration of the data entry process, including information collection, required 7–22 min, with an average of 15 min. Most time-consuming was a frequent search for additional information and the collection of data from different sources being performed for every examination separately. In worst cases, the process required an additional search or difficult information extraction from inconclusive results in the patient's files. Except the search process, the time needed for data entry itself was only a small fraction of the measured time. Furthermore, the study provided considerable feedback for further improvement of simplifying the data input process.

Conclusion

Regarding the extensive searching time during the retrospective data collection, the data entry should take place parallel to a clinical reporting. Additionally, the data collection would benefit from a more structured and standardized reporting with the possibility of additional explanation if necessary. This requires the tool's clinical integration, which is aspired, but further improvements of the tool, as well as evaluation and usability studies on a larger scale (with more domain experts and more patient cases) will be conducted beforehand. Also, for clinical integration, the currently combined information of a decision model and patient information in one XDSL file will be stored separately and only combined for BN reasoning.

Finally, the presented tool for model-based data entry demonstrates the possibilities of optimized high-quality data collection, which can increase the quality of patient-specific decision support, as well as improve the BN decision model. Collecting high quality data will allow future network improvements using learning algorithms in order to re-learn and adjust network parameters.

References

[1] Stoehr M, Cypko MA, Denecke K, Lemke H, Dietz A (2014) A model of the decision-making process: therapy of laryngeal cancer. Int J CARS 9 (Suppl 1): 217–218
[2] Cypko MA, Stoehr M, Kozniewski M, Druzdzel MJ, Dietz A, Lemke HU (2017) Validation workflow for a clinical Bayesian network model in multidisciplinary decision making in head and neck oncology treatment. Int J Comput Assist RadiolSurg 12 (11): 1959–1970
[3] Druzdzel MJ (1999) A development environment for graphical decision-theoretic models (Intelligent Systems Demonstration). Proceedings of the Sixteenth National Conference on Artificial Intelligence (AAAI-99): 342–343

Fully automatic quantification of mean-upper cervical cord area: Agreement with multiple human raters

F. Weiler[1], J. Klein[1], J. Gregori[2], L. Spiess[3], H. Hildebrandt[4,5], S. Heldmann[6]
[1]Fraunhofer MEVIS, Clinical Decision Support/Neuro, Bremen, Germany
[2]mediri GmbH, Heidelberg, Germany
[3]Jung Diagnostics, Hamburg, Germany
[4]Klinikum Bremen-Ost, Bremen, Germany
[5]Universität Oldenburg, Oldenburg, Germany
[6]Fraunhofer MEVIS, Lübeck, Germany

Keywords Multiple sclerosis · Spinal cord · Quantification · Segmentation

Purpose

The relevance of spinal cord pathologies in Multiple Sclerosis (MS) has been studied by different groups in recent years. Current findings suggest that both spinal cord lesions, as well as spinal cord atrophy correlate independently with clinical disability scores. Atrophy of the upper cervical cord around the C2/C3 level showed a stronger correlation with clinical impairment than whole brain atrophy or brain white matter lesion load [1]. Although dedicated spinal cord imaging is not part of many clinical imaging protocols in MS, the upper cervical cord is typically included in 3D T1-weighted MPRAGE scans of the head. We have developed a fully automated method for detection and segmentation of the upper cervical cord from 3D T1w MR-images, with subsequent quantification of the mean upper cross-sectional area. Here, we present results of the fully automated quantification compared to a semi-automated evaluation by three different raters.

Methods

The current work extends our previously developed semi-automatic approach for upper cervical cord quantification [2]. We have automated the process of defining the section to be measured and the following segmentation step. For this purpose, we combine two processing steps: First, an atlas based approach is used for detection of the spinal cord and definition of the area to be analyzed. On the atlas image, the spinal cord is defined by means of its centerline, with additional markers defining each vertebral level. Using a non-linear registration, these markers are transferred into the coordinate system of the patient to initialize the segmentation algorithm. Segmentation is performed using a heuristically steered watershed algorithm, which iteratively places inclusion or exclusion markers in the image, while matching the resulting segmentation with the expected tubular shape of the spinal cord. The quantification itself is equivalent to the method used in the semi-automated process. We use a bi-modal Gaussian Mixture-model fit with explicit partial volume handling. By automating this initial step, we facilitate incorporation of our method into fully automated image processing pipelines. This not only reduces the effort required for image analysis, but also removes potential variation of results induced by rater dependent influences to the segmentation.

We have evaluated our method on a dataset of 116 sagittally acquired MPRAGE images (Siemens Skyra, 3T), from 46 MS patients and 15 age-matched controls, with 42 patients and 13 controls studied at two time-points within approximately 1 year [3]. For each image, we segmented the spinal cord area between C1 and C3, and measured the average mean cross-sectional area (MCSA). For evaluation, we compared the results of the fully automated algorithm with those obtained from three independent human raters using the semi-automatic approach.

Results

Detection and segmentation of the spinal cord area to be measured succeeded in 114 cases, resulting in a success rate of 98.3%. In two cases, the image showed a heavily bent neck, which failed to register to our template image. Subsequent results relate to the 114 images that have been successfully processed.

The average relative standard deviation over the four measurements taken from each image was 0.9%, normalized to the mean MCSA value. In comparison, the average standard deviation over the human raters alone was 0.5%, almost twice as good. Comparing the individual results of the automated approach to the average values of the human operators revealed a systematic under-estimation of the MCSA by the automated algorithm by $\sim$ 1.9%. Correcting the automatic results by this amount resulted in an overall relative standard deviation of 0.56%. Averaged over three raters only, the overall best result of 0.32% was achieved for comparing only human raters A & B, and the algorithm—the automatic approach turned out closer to the average than one of the human experts.

Conclusion

Our study demonstrated an overall inter-rater variability of 0.5% for our quantification method of spinal cord mean cross-sectional area over three human raters. The results of our fully automated algorithm showed a systematic under-estimation of the measured area. Correcting for this effect moved the agreement of the automated technique almost exactly into the range of the human raters. The cause of this effect needs to be further analyzed. A possible explanation for this would be, that the heuristic approach to spinal cord segmentation results in a different distribution of pure tissue and CSF voxels within the segmentation mask, which subsequently might cause slight changes to the Gaussian mixture model fit.

References

[1] Lukas C, Sombekke M, Bellenberg B, Hahn HK, Popescu V, Bendfeldt K, Radue EW, Gass A, Borgwardt SJ, Kappos L, Naegelin Y, Knol DL, Polman CH, Geurts JJ, Barkhof F, Vrenken H (2013) Relevance of Spinal Cord Abnormalities to Clinical Disability in Multiple Sclerosis: MR Imaging Findings in a Large Cohort of Patients. Radiology 269(2): 542–552

[2] Weiler F, Daams M, Lukas C, Barkhof F, Hanh HK (2015) Highly accurate volumetry of the spinal cord. Proc. of SPIE Medical Imaging 2015: 944302–944309

[3] Sander C, Eling P, Hanken K, Klein J, Kastrup A, Hildebrandt H (2016) The Impact of MS-Related Cognitive Fatigue on Future Brain Parenchymal Loss and Relapse: A 17-Month Follow-up Study. Frontiers in Neurology 7: 155

Trans-border telemedicine practices: an institutional experience

S. Mishra[1], R. Daman[1], I. Singh[1], V. Singh[1], K. Pathak[1]
[1]SGPGIMS, Endocrine Surgery, Lucknow, India

Keywords Telemedicine · Distance education · Transborder telemedicine · eHealth

Purpose

Telemedicine, an information and communication technology based tool, holds immense potential to bridge the logistic and geographical barriers in sharing resources between countries across the world. However, non-technical issues are very much relevant as the technical issues in successful outcome of telemedicine practices, more so in trans-border application situation. socio-political, regulatory, language, time zone difference are among few factors which can play significant role in the outcome. Two case studies involving telemedicine co-operation between India, African continent and South Asian countries over a 5-year period are analyzed to find out the management system of such large telemedicine enterprise and its outcome with the objective of sharing the information with the peers, development agencies involved in cross border project implementation.

Methods

Two trans-border telemedicine projects i.e. SAARC (South Asian Association for Regional Co-operation) Telemedicine Network and Pan-Africa e-network deployed by the Government of India in three countries in South Asia (2009–2012) and 48 countries in African continent (2011–2016) respectively were studied at the School of Telemedicine and Biomedical Informatics, Sanjay Gandhi Postgraduate Institute of Medical Sciences (SGPGIMS), Lucknow, India, one of the hospital identified for service delivery using telemedicine system. Telemedicine activities were schedule based and were recorded in log book. Total number of sessions held monthly, participants at remote hospitals and their numbers were collected at the end of the session and recorded in the same register. Activity audit of the record is the main source of outcome analysis.

Results

Pan-Africa e-network project

There were five goals envisioned while setting up the network via satellites and optic fiber deployment- Tele-education, Tele-medicine, Internet, Videoconferencing and VoIP services [1]. Indian scenario in Telemedicine is quite promising and has been expanded to almost all parts of this vast country. The Ministry of External Affairs has started the Pan-African e-network Projects in the year 2010 with Telecommunication Consultant India Ltd. (TCIL), designated as the turnkey Implementing Agency [1, 5]. The Project also covers Continuing Medical Education (CME) to practicing doctors and the nursing staff with a view to updating and enhancing their knowledge and skills.

SGPGIMS, Lucknow provided tele-education and tele-consultation in medical field to 47 countries since 2011. There were six tele-education sessions provided each month through the network to Pan-African countries and in 2012, two more classes with french translator were added each month for francophone countries located in west Africa, taking the number of e-classes to eight per month. The classes covered various topics prepared in advance keeping the needs of the medical students of African countries and the expertise available at SGPGIMS which is tertiary care referral hospital. A total of 409 educational sessions till December 2016 for English speaking countries and 105 sessions for French-speaking countries were held. Consistence and success of sessions as assessed by the number of students attending the classes and growing demand for topic-specific classes has been noted and is the basis of future implementation of the project. However, there have been five consultations through this network, the reason may be that the consultation services are obtained from corporate hospitals empanelled in the network. This project had some specific hurdles such as time-zone difference (language barrier, specific endemic diseases. However, these problems were overcome by use of translators and with store-and-forward mode. On an average 3–5 participants took part in each of the 47 countries hailing from diverse health professional background.

South Asian Association for Regional Cooperation (SAARC) Telemedicine Network

To share knowledge and expertise in the field of medical sciences and healthcare among the SAARC countries, the Government of India has taken the initiative to establish a telemedicine network [2, 4]. The superspecialty hospitals in India include the SGPGIMS, Lucknow and Postgraduate Institute of Medical Education and Research at Chandigarh. Telemedicine centre at SGPGIMS, Lucknow has been successfully conducting tele-education sessions with Indira Gandhi Children Hospital, Kabul, Afghanistan since 1st September, 2009 (183 educational sessions, 5 consultations and 5 CMEs); with Jigme Dorji Wangchuck National Referral Hospital, Thimpu, Bhutan since 16th April, 2009 (64 tele-education sessions, 12 CMEs) and with Patan hospital, Kathmandu, Nepal since 21st January, 2011 (51 tele-education sessions, 12 CMEs) [3]. The SAARC project was implemented by TCIL which installed the hardware, software and provided expert manpower. In year 2012 the project was completed while the infrastructure is in workable condition. The manpower provided by TCIL was withdrawn from the telemedicine centers from SAARC countries. There-after the telemedicine operation is being conducted by locally trained personnel whenever needed.

Conclusion

Advances in telecommunication system combined with information science have brought in newer technology and applications which have steered processes in wide range of sectors, health is no exception. Developing countries has been benefited most. Telemedicine is one such tool, though developed technology wise, but not adopted in health system to that extent as it deserves. As the cost of the technology and network is coming down there is a need of policy makers and healthcare service providers to consider applying this tool in healthcare outreach not only in their work environment but across disparate geographical systems. Many countries have developed bilateral and multilateral co-operation under mutual agreement to develop health system using telemedicine. It is of utmost importance to share such examples for others to learn. In that context the current research study has tried to analyze the design, technology, process, outcome and factors influencing the overall output of such a trans-continental telemedicine project with the objective of sharing the Indian experience.

References

[1] http://www.panafricanenetwork.com/last accessed on 08-03-2017

[2] http://saarctf.org/last accessed on 08-03-2017

[3] Daman R, Pathak K P, Mishra S K (2016) Telemedicine a Tool for International Cooperation; Proceedings of 12th International Conference of Telemedicine Society of India; 10–12 Nov 2016; Bangalore, India

[4] Mishra S K, Singh I P, Chand R D (2012) Â Current Status of Telemedicine in India and Future, Proceedings of the Asia–Pacific Advanced Network 2012 v. 32, pp. 151–163. http://dx.doi.org/10.7125/APAN.32.19 ISSN 2227-3026

[5] Mishra S K, Wakhlu V (2015) International Distance Education Initiatives at SGPGI, Lucknow, India; Proceeding of Med-e-tel 2015; https://www.medetel.eu/?rub=knowledge_resources&page=2015

Micro-CT imaging for intra-operative assessment of surgical resection margins during breast conserving surgery

N. Janssen[1], M. van Seijen[2], C. Loo[3], M. J. Vrancken Peeters[4], I. Ioan[3], J. J. Sonke[1], J. Nijkamp[4]

[1]Netherlands Cancer Institute, Radiation Oncology, Amsterdam, Netherlands

[2]Netherlands Cancer Institute, Molecular Pathology, Amsterdam, Netherlands

[3]Netherlands Cancer Institute, Radiology, Amsterdam, Netherlands

[4]Netherlands Cancer Institute, Surgical Oncology, Amsterdam, Netherlands

Keywords Micro-CT · Breast cancer · Surgical resection margins · Intra-operative

Purpose

Breast conserving surgery and adjuvant radiotherapy, possibly in combination with neo-adjuvant chemotherapy, is the preferred treatment option for patients with breast cancer. Complete tumor removal is achieved when no tumor cells are found in the surgical resection margins, analyzed via a standard pathology procedure several days after surgery. Unfortunately in 10–30% of the patients positive resection margins are found, demanding for an adjuvant radiotherapy boost or a re-operation. A self-shielded micro computed tomography (μCT) is an intra-operative imaging technique that allows resection margin assessment while the patient is still on the operating table. It provides three-dimensional (3D) imaging of the entire excision specimen including the tumor mass and possible calcifications, facilitating 3D analysis of the resection margins. The aim of this study was to evaluate the accuracy of micro-CT for positive resection margin assessment in comparison to the final pathology report. Secondly, the inter-observer agreement for positive margin assessment was evaluated.

Methods

Following excision, fresh specimens were placed in a 3D printed scan container in the appropriate patient orientation and imaged using a table top Micro-CT scanner, Skyscan® 1275B (Bruker, Skyscan, Kontich, Belgium). Specimens were scanned at 50 kV, 200 μA, using 1 mm Aluminium filter, 105 ms exposure time, acquiring 900 projection images at 0.4° increments. Images were reconstructed into 70 μm isotropic voxels with an in-plane resolution of 972 × 972 using Skyscan's NRecon software. Five different observers (1 pathologist in training, 2 radiologists and 2 researchers with prior experience in evaluating micro-CT data) participated in this study but had no precise guidelines for evaluating micro-CT imaging. The observers first evaluated the tumor dimensions, presence of calcifications and implanted tumor markers on the available pre-operative acquired imaging (mainly mammography, ultrasound and in some cases MRI). Subsequently, micro-CT scans were evaluated for positive resection margins using in-house visualization software containing 3 orthogonal views and a 3D maximum intensity projection (MIP) rendering (Fig. 1). Location and extent of the tumor and/or calcifications within the excision specimen and its relation to the borders of the specimen were evaluated. Margins were scored as either tumor free or positive and compared to the final pathology report. Outcome measures were: mean acquisition and reconstruction times, accuracy, sensitivity, specificity and positive predictive value (PPV) for positive margin assessment. Secondly, inter-observer agreement was evaluated by calculating Cohen's kappa using the following interpretation guidelines: poor (0–0.20), fair (0.21–0.40), moderate (0.41–0.60), good (0.61–0.80) and almost perfect agreement (0.81–1.00).

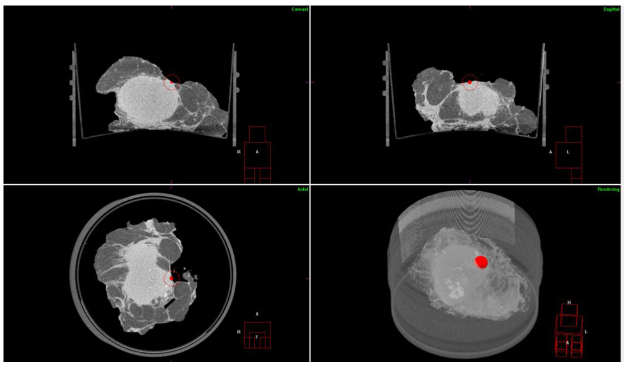

Fig. 1 Visualization of the scanned excision specimen in 3 orthogonal views and a 3-D MIP rendering. The positive margin, as determined by the observer, is annotated with the red circle

Results

A total of 30 excision specimens were scanned deriving from 26 patients that underwent primary breast conserving surgery, including 17 invasive ductal carcinoma, 9 ductal carcinoma in situ and 4 other invasive tumor types. Six of the 30 specimens had positive resection margins, according to the pathology report. Mean ± SD acquisition and reconstruction times were 07:50 ± 00:39 and 04:11 ± 01:16 min. Micro-CT had an average of 61% accuracy, 33% sensitivity, 69% specificity and 19% positive predictive value compared to pathology, over 5 evaluation sessions (Table 1). There were 7 cases in which at least 3 observers reported a positive margin according to the micro-CT while pathology was negative. In 5 of these cases the maximum distance between tumor and resection margin appeared to be only 1 mm or less on pathology. However, the resection margin was still reported as negative according to standard pathological protocol. There was fair agreement among the 5 observers, corresponding to average Kappa value of 0.28 (95% CI 0–0.61). The highest agreement was found between the 2 researchers with prior reading experience: they had evaluated respectively 300 and 100 micro-CT scans before.

Table 1 Sensitivity, specificity, positive predictive value, negative predictive value and accuracy of micro-CT evaluations for positive margin assessment, compared to final pathology

	Accuracy (%)	Sensitivity (%)	Specificity (%)	Positive predictive value (%)
Observer 1	63	17	75	14
Observer 2	53	17	63	10
Observer 3	67	17	79	17
Observer 4	60	50	63	25
Observer 5	63	67	63	31
Average (%)	61	33	69	19

Conclusion

Micro-CT imaging might be a clinically relevant technique for intraoperative assessment of surgical resection margins for breast conserving surgery. Extended training and precise guidelines for evaluating micro-CT imaging might improve the accuracy for positive resection margin assessment. Standard pathological analysis could result in undersampling of the excision specimen, causing an underestimation of positive resection margins by pathology. Further, acquisition and reconstruction times need to be reduced to enable direct feedback to the surgeon and final successful implementation in the clinic.

An only navigation-assisted platform for a multidisciplinary oncological network

S. Catanzaro[1], C. Copelli[1], P. Corsa[1], A. Manfuso[1], L. Cassano[1], K. Tewfik Hanna[1], N. Pederneschi[1], A. Mastromatteo[1], R. Cocchi[1]
[1]Casa Sollievo della Sofferenza-IRCCS, San Giovanni Rotondo, Italy

Keywords Intraoperative navigation · Head and neck cancer · Computer-assisted surgery · Multidisciplinary platform

Purpose

An optimal treatment of head and neck malignant tumours requires an interdisciplinary approach between radiology, surgery, radiotherapy, and pathology, often afflicted by some problems such as: the anatomical complexity of the head and neck area, the complexity of the three-dimensional resections and reconstructions, the difficulty of orienting the specimen by the pathologist and the non-standardized transfer of detailed information among medical specialists. The technological innovations achieved in recent years have provided an important aid to address the above-listed issues and improved the accuracy and quality of oncological treatments performances, starting from the pre-surgical planning till to the adjuvant radiotherapic planning. The purpose is to develop an only interactive platform that can be helpful to exchange important clinical and intraoperative informations between radiologist, surgeon, pathologist and radiotherapist.

Methods

In the first phase, the DICOM data of CT/MRI are imported in planning software iPlan Cranial 3.0 (Brainlab AG, Germany) in order to carry out a surgical planning and define the resection volume. The second phase consists in the intraoperative transposition of surgical planning and in the identification, on the three-dimensional navigation image, of reference landmarks, related both to resection margins and to intraoperative biopsies and to suspected areas for residual involvement that cannot be excised due to the proximity to important structures. The surgical treatment planning with landmarks is used by the pathologist for properly orienting the surgical specimen and to have a better histological definition of resection margins and critical areas. Finally, the pathologist integrates the histological information into the system with specific coordinates about resection margins. The complete information for the tumor (initial tumor volume, resection volume, exact location, and histological evaluation of the intraoperatively acquired biopsies) is available for the radiotherapist in order to perform a correct adjuvant radiation planning, minimizing the irradiation of adjacent healthy structures.

Results

In this study, we found unchanged operative times, a reduced rate of errors in the surgical specimen orientation and an increased distance of the tumor from the margins of resection, an optimal definition of irradiation volume. An important precondition for the feasibility of this image-assisted multidisciplinary network is an efficient common computer system that provides remote access to data from any workstation, at any time. This common system coordinates different components and their software applications: a preoperative 3D image dataset (CT and MRI), a planning and navigation software with a 3D interactive reconstruction image and often a real-time imaging source (portable CT). The reliability of the method is highly related to the accuracy of intraoperative navigation (greater for upper and middle facial thirds) and the ease of use of these different softwares that allow to define on a common map the regions of interest with specific spatial coordinates.

Conclusion

An only navigation-assisted platform allows the interactive exchange of data in ready-to-use formats by radiological examinations, surgical planning, intraoperative navigation, as well as radiotherapy planning software.

2D geometric hip stability in the osteoarthritis initiative dataset

R. Ellis[1], C. DesRoche[1], B. Jiang[1], J. Rudan[2]
[1]Queen's University, School of Computing, Kingston, Canada
[2]Queen's University, Surgery, Kingston, Canada

Keywords Hip osteoarthritis · Hip biomechanics · Radiograph · Osteoarthritis initiative

Purpose

Recent 3D studies suggest that the hip translates as well as rotates. Previous work on hip translation from images has used invasive CT scanning or expensive MRI scanning. A minimally invasive, inexpensive, and accurate way of measuring hip motion may be useful in basic science and clinical application.

Previous work has used 2D plain radiographs to show that an individuals hip translates as various leg poses are imaged [1]. Recent work has shown that, as hip osteoarthritis (OA) progresses, the changes are evident in MRI scans [2] and plain radiographs. An open question is whether significant bone remodeling occurs over a multi-year duration in patients with slowly progressing hip OA.

We propose that 2D geometric models can quantify the progression of radiographic hip osteoarthritis overtime.

This study aimed to geometrically evaluate the progression of radiographic hip osteoarthritis using semiautomatic ellipse fitting. The null hypothesis of this study was that the geometric center of the femoral head is not stable in osteoarthritic hips. It was expected that there would be differences in the position of the femoral center of more than 1.5 mm from the baseline center.

Methods

Data for these analyses are from the Osteoarthritis Initiative (OAI) public use data set(s). Plain AP pelvis radiographs from a cohort of 163 patients with identified radiographic hip osteoarthritis, unilateral (n = 123) and bilateral (n = 40) at baseline were analyzed at three time intervals; baseline or 00 months, and at 48 and 96 months follow up [3].

Radiographs taken at 48 and 96 month follow up were scaled such that the distance between the left and right radiographic teardrops matched that of the baseline measurements. The hips were in the pelvic coordinate frame, which compensated for rotation about the anterior–posterior axis [4]. Circles were fit to the femoral head and ellipses to the acetabulum of each hip radiograph using existing software and methods [1]. The femoral circles of radiographs taken at 48 and 96 months were translated to the baseline radiograph. The translation vector for the femoral centers at 48 and 96 months to the baseline femoral center was computed for each patient. The magnitude of this translation vector was taken as a measurement for hip center stability.

The translations were compared to a magnitude of 1.5 mm, rather than 0 mm,to account for the anticipated errors of X-ray projection and fitting.

The data were analyzed for statistical comparisons using the students t test. P values for the normally distributed error model were computed using a one-sided pooled t test, with alpha = 0.05 to reject Type I errors.

Results

There was no significant shift in the geometric center of the femoral head at 46 and 98 months follow up compared to baseline.

A representative patient image is shown in Fig. 1. This shows the right hip at baseline, with the femoral fits at 48 and 96 months follow up superimposed. Visually, the centers of the superimposed fits at 48 and 96 months overlap with the baseline center. Numerically, the centers at follow-up were less than 1.5 mm from the center at baseline.

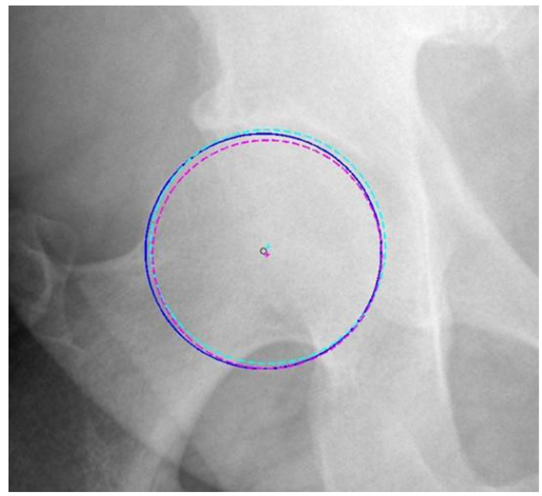

Fig. 1 Plain radiograph of a representative hip at baseline, with fits superimposed. The solid blue line is the baseline fit. The dashed magenta and yellow circles are the fits from the 46 and 98 month radiographs respectively. Fits were translated to the base coordinates

Conclusion

This study found that the hip center was geometrically stable over a period of 8 years in a cohort of 163 patients with hip OA, Table 1. The finding is remarkable because OA is commonly known as a progressive degenerative disease, with short-term changes evident in MRI scans [2]. The same technical methods have previously found hip translation as an individual patient moves, which suggests that the

Table 1 Summary of translations of geometric hip centers over an 8-year follow-up

Data set	Mean	SD	CI(L)	CI(R)
Unilateral, OA Hip (48 months)	1.14	0.48	1.04	1.27
Unilateral, OA Hip (96 months)	1.21	0.81	1.05	1.36
Unilateral, Opposite Hip (48 months)	1.20	0.70	1.05	1.32
Unilateral, Opposite Hip (96 months)	1.40	1.30	1.24	1.63
OA bilateral (48 months)	1.09	0.70	0.91	1.25
OA bilateral (96 months)	1.33	0.80	1.18	1.52

Radiographs were categorized as unilateral and bilateral OA; the contralateral hip in unilateral cases is as an internal control. Data columns are the mean translation from baseline, standard deviation of translation, and the lower and upper 95% confidence intervals methods are powerful enough to distinguish geometric stability from geometric translation.

A key difference between this study and previous studies is the patient cohort. Of the > 1000 patients in the OAI database, these 163 had radiographic signs of hip OA and did not proceed to hip replacement surgery. The presumption is that the OA was slowly progressing in these patients, which our method detected as geometric stability over time.

The findings are both clinically and technically interesting because of the wide availability of plain AP hip radiographs. Geometric analysis of such radiographs is an inexpensive and potentially sensitive way of screening for hip changes. Future work could include a patient cohort with more rapidly progressing hip OA to determine geometric hip stability over time.

References

[1] DesRoche C, Rudan J, Ellis E (2016) Gradient weighted models for planar hip kinematics. In *Proc Comput Assist Orthop Surg*: 355–358

[2] Kamimura M, Nakamura Y, Uchiyama S, Ikegami S, Mukaiyama K, Kato H (2016) The pathophysiology and progression of hip osteoarthritis accompanied with joint pain are potentially due to bone alterations—follow-up study of hip OA patients. *Open Rheum J:* 8: 46–53

[3] Shah A, Palmer A, Rhys Thomas GE, Hunter DJ, Edwards K, Arden NK, Lane NE, Glyn-Jones S, Nevitt M, Javaid KM (2016) The association between hip morphology variations and progression of radiographic hip osteoarthritis using data from the osteoarthritis initiative. *Osteoarthritis Cartilage* 2016; 24: S299

[4] Foss O, Klaksvik J, Benum P, Anda S. The rotation ratios method: a method to describe altered pelvic orientation in sequential radiographs. *Acta Radiol* 2007; 48(9): 1011–1019

Biomechanical simulation of respiratory system for lung cancer surgery

F. Jiang[1], X. Chen[1], K. Ueda[2], J. Ohgi[1]

[1]Yamaguchi University, Department of Mechanical Engineering, Graduate School of Sciences and Technology for Innovation, Ube, Japan

[2]Yamaguchi University, Department of Surgery and Clinical Science, Graduate School of Medicine, Ube, Japan

Keywords Respiratory system · Finite element method · Lung cancer surgery · Numerical simulation

Purpose

Lobectomy and stereotactic radiotherapy are performed as treatments for lung cancer. In the former case, the problem is the reduction of respiratory function after treatment. In the latter case, deformation of the lung due to respiration causes tumor migration and results in difficulty in focusing irradiation only on tumor cells. In recent years, simulation approaches of lung deformation due to respiration have been proposed. However, in previous researches, the lung deformation was represented by shape reconstruction using medical images or by prescribing boundary conditions, rather than represented based on physiological phenomena. The purpose of this work is to develop a biomechanical simulation of respiratory system for predicting the respiratory function after lobectomy and tracking the movement of the tumor during respiration.

Methods

A voxel dataset of the chest was segmented from CT slices of a male volunteer. Based on this dataset, we first constructed a finite element model of the normal respiratory system including lung, trachea, rib cage, intercostal muscles and diaphragm. The intercostal muscles were created by connecting the muscle attachments between upper and lower rib bones, and diaphragm was generated as to attach the lung bottom. Then we performed biomechanical simulation of respiratory system by contracting intercostal muscles and diaphragm based on the physiological phenomena. The behavior of muscle contractions is described by a Hill-type transversely isotropic hyperelastic continuum material model, while the lung including the airflow was characterized as porous hyperelastic materials based on a multiphasic model using mixture theory. The lobectomy operation was numerically reproduced by virtually removing a lobe of the lung from the constructed respiratory system. By simulating the behavior of respiratory system after virtual operation, reduction of respiratory function can be evaluated.

Results

The proposed numerical respiratory system is able to reproduce the data in terms of thorax displacement, diaphragm movement as well as the lung deformation by introducing contraction of the respiratory muscle. The results were validated by comparing the thorax deformation with the four-dimensional computed tomography (4D-CT) images during normal quiet breathing. Furthermore, simulation results for the variations of alveolar, pleural pressures and lung volume during normal breathing are compared with the reference data [1] for the validation of the proposed multiphasic model for lung parts. To estimate the respiratory function decrease, we performed a virtual lobectomy on the developed respiratory system. The flow rates inside the bronchus are calculated and compared by coupling a fluid dynamic simulation into the numerical respiratory system.

Conclusion

This work provides a platform for establishing an integrated computational mechanics model of the human respiratory system. Based on this developed platform, the chest deformation modes were obtained compatible with the conventional inference, and the intrathoracic and intrapulmonary pressures were obtained consistent with clinical observation. The effectiveness of the proposed computational model was demonstrated. In addition, the respiratory function can be evaluated by the proposed virtual lobectomy simulation. The developed numerical respiratory system has great potential for not only providing useful information in terms of predicting accurate lung tumour position for the radiation therapy, but also estimating the respiratory function for post-operative period of lobectomy.

References

[1] Guyton AC (1991). Textbook of Medical Physiology (8th ed.). Philadelphia: W.B. Saunders. ISBN 0-7216-3994-1.

Unsupervised deep learning based registration for aligning micro CT and histology images

K. Nagara[1], S. Nakamura[1], H. Roth[1], M. Oda[1], K. Mori[1]

[1]Nagoya University, Nagoya, Japan

Keywords Registration · Deep learning · Micro CT · histology

Purpose

This paper presents a registration method for a micro CT image and a HE stained image by using unsupervised deep learning. HE stained images are used for pathological diagnosis because of its very high resolution, but it is necessary to destroy the specimen due to slicing for preparing microscopic imaging. The destruction of specimens makes it difficult to observe the sample in three dimensions, and the understanding of the anatomical structure may be shallow. Therefore, micro CT images attract attention. The micro CT image is capable of observing a specimen in three dimensions at high resolutions. It is useful for classification and analysis of microstructure and might be a valid support or alternative to histological imaging. Its effectiveness needs to be confirmed by comparing it with the currently used HE stained histology images. For that, it is necessary to register micro CT images and HE stained images and compare them at the same position. In this study, we examined a new method to perform non-rigid registration using deep learning for aligning micro CT images and HE stained images.

Methods

Recently, deep learning based registration showed some promise in learning direct transformation mappings between images via unsupervised regression of deformation parameters [1, 2]. They can potentially work well for multi-modality image data and perform fast registration during inference after training on many examples in an unsupervised fashion [1, 2].

In this work, we extend the non-rigid deep learning based registration method proposed by Vos et al. [1] which is built on the idea of spatial transformer networks (STN) [3] to output deformation parameters for aligning the source and target images. Vos et al. [1] used an unconstraint deformation model only based on normalized cross correlation (NCC) as similarity metric for optimization and training the networks:

$$L_{NCC} = 1/n * \sum_{\mathbf{x}} 1/(\sigma_A \sigma_B) * (A(\mathbf{x}) - \mu_A)(B(\mathbf{x}) - \mu_B),$$

where A and B are images, μA and μB are the average values, σA and σB are the variance values and n is the number of voxels. Since there is no term to consider the degree of deformation, large and physically implausible deformations can occur. In order to suppress unrealistically large deformations, we add a spatial smoothness term to our cost function:

$$L_{smooth} = 1/n * \iint \left[\left(\partial^2 \mathbf{T}/\partial x^2\right)^2 + \left(\partial^2 \mathbf{T}/\partial y^2\right)^2 + 2 * \left(\partial^2 \mathbf{T}/\partial xy\right)^2 \right] dxdy$$

where T is deformation field. The total loss is then computed as the sum of both terms with some tradeoff parameter α:

$$L = \alpha * L_{NCC} - (1 - \alpha) * L_{smooth}$$

In this formulation, the loss has to be maximized in order to achieve an optimum alignment. Moreover, in order to consider more of the global structure of the image, we introduce a network structure inspired by U-net [4]. Because of the large size of our input images, we extend the downsampling path of the network via max-pooling in order to increase the receptive field of later layers of the network. This approach allows the network to capture more global features which might be useful for image registration. An overview of the network structure is shown in Fig. 1. The network takes pairs of micro CT slice and HE stained image as input, and predicts the deformation on a grid of B-spline control points. After several 3 × 3 convolution layers and 2 × 2 average pooling layers, we perform upsampling via transposed convolutions until the desired control point grid size is achieved.

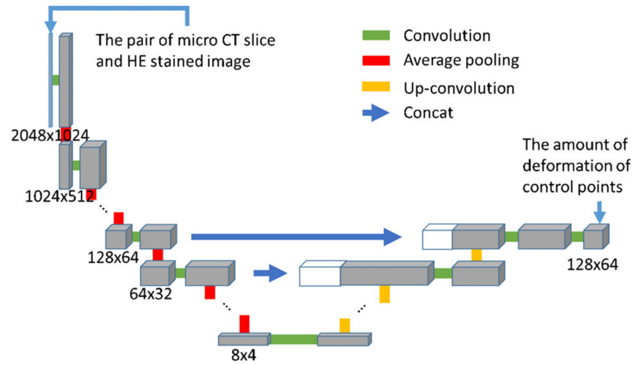

Fig. 1 Structure of our deep learning based registration model

Results

We applied the proposed method to 70 pairs of micro CT slices and HE stained images. These images were taken from one specimen and we applied an initial rigid registration by using [5].

The registration results were shown in Fig. 2. It clearly shows the proposed method correctly registered a micro CT slice and a HE stained image. Registration with the smoothness term can be done while preserving image information, while the transformed image collapsed under folding without the smoothness term. Moreover, an average value of NCC was improved from 0.643 to 0.707 with the smoothness term and only achieved 0.661 without the smoothness term.

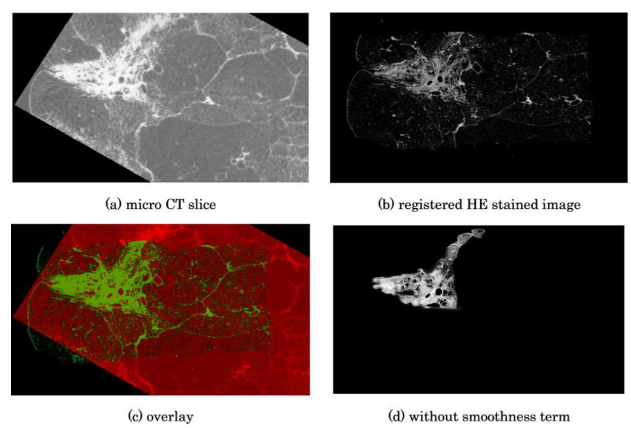

Fig. 2 The registration results of the experiments. **a** One micro CT slice, **b** shows registered HE stained image at the same position as (**a**) and (**c**) shows the image of (**b**) overlaid on (**a**). **d** The result of applying our method without smoothness term

Conclusion

In this work, we proposed a deep learning based non-rigid registration method using a new network architecture in order to learn more global features useful for estimating the deformation. In the future, evaluation of other networks might improve computational efficiency.

References

[1] Vos B, Berendsen F, Viergever M, Staring M, Išgum I (2017) End-to-End Unsupervised Deformable Image Registration with a Convolutional Neural Network. Deep Learning in Medical Image Analysis and Multimodal Learning for Clinical Decision Support: 204–212

[2] Yang, X., Kwitt, R., & Niethammer, M. (2017). Quicksilver: Fast Predictive Image Registration-a Deep Learning Approach. arXiv preprint arXiv: 1703.10908.

[3] Jaderberg, M., Simonyan, K., & Zisserman, A. (2015). Spatial transformer networks. In Advances in Neural Information Processing Systems (pp. 2017–2025).

[4] Ronneberger, O., Fischer, P., & Brox, T. (2015, October). U-net: Convolutional networks for biomedical image segmentation. In International Conference on Medical Image Computing and Computer-Assisted Intervention (pp. 234–241). Springer, Cham.

[5] Nagara K, Roth H, Nakamura S, Oda H, Moriya T, Oda M, Mori K (2017) Micro-CT Guided 3D Reconstruction of Histological Images. Patch-Based Techniques in Medical Imaging: 93–101

Robotically assisted arthrography under MR imaging

R. Monfaredi[1], I. Talati[2], K. Sharma[1,2], K. Cleary[1]
[1]Children's National Health System, Washington, United States
[2]Georgetown University Medical Center, Washington, United States

Keywords Robotics · MRI · Arthrography · Radiology

Purpose

This abstract presents our work in developing a robotic system for MRI-guided arthrography. Arthrography is the evaluation of joint condition using minimally invasive techniques. In a typical procedure, a needle is advanced to the joint under fluoroscopy or CT imaging and contrast is injected to visualize the joint. At our institution, the next available MRI time is then taken to obtain diagnostic quality images and evaluate joint condition. Our goal is to enable the entire procedure to be done under MRI using an MRI-compatible robot.

Methods

The MRI-compatible robotic device is shown in Fig. 1. The device holds the needle and has four degree of freedom: two for positioning the needle anywhere in a circle of 10 cm diameter and two for orienting the needle to any angle. In the envisioned clinical workflow, the robot will position and orient the needle but the Interventional Radiologist will then drive the needle to the center of the joint.

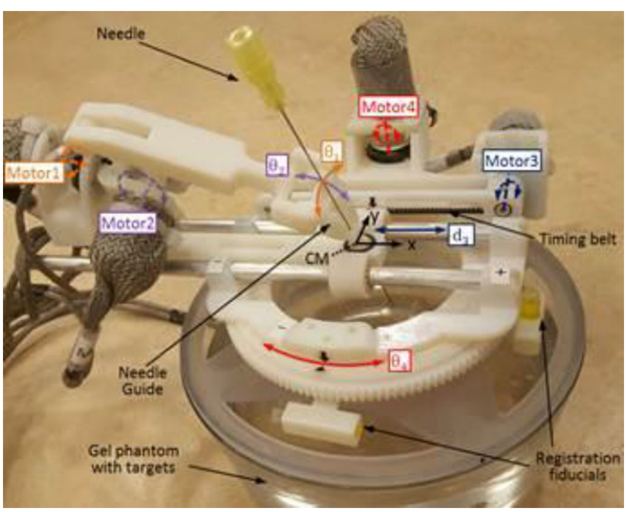

Fig. 1 Robot with 4 degrees of freedom. Color code is used to show each degree of freedom with its associated piezoelectric motor

To investigate the current clinical practice, we started an observational study of arthrography procedures done at our hospital. For this IRB-approved study we gathered the following data: (1) patient age; (2) patient sex; (3) date of procedure; (4) procedure time; (5) fluoroscopy time; (6) success rate; (7) number of needle passes; and (8) needle placement accuracy. Needle placement accuracy was measured by comparing the actual needle placement from the fluoroscopic image with target needle placement as selected by the radiologist. A Matlab script was written to register the two images and compute placement accuracy.

Results

The robotic device was placed in the MRI scanner and no significant issues were found. The geometric distortion is defined by the NEMA standard MS 2-2008 as the maximum percent difference between measured distances in an image and the corresponding ground truth dimensions. The maximum distortion was found to be 2.57% which was deemed acceptable for the proposed clinical application. A quantitative signal to noise (SNR) experiment based on the same EMA standard, using a cylindrical water phantom, showed that SNR changes only 2.3% for T1 weighted images and 1.3% for T2 weighted images when the robot is powered off and is placed on top of the water phantom. A gel phantom study showed targeting accuracy of 1.64 mm to a series of plastic spheres.

For the observational study, we collected data on 4 cases to date. The cases included two right shoulders, one left hip, and one bilateral hip. The age range was 13–16 years. Three patients were male and one was female. We found the mean fluoroscopy time to be 20.5 min, the mean MRI time to be 68 min, and the mean total procedure time, which included fluoroscopy, MRI, and the transfer times to be 104.75 min. There was an average of 1.5 needle adjustments, and a needle targeting accuracy of 3.09 mm. A typical fluoroscopy image is shown in Fig. 2.

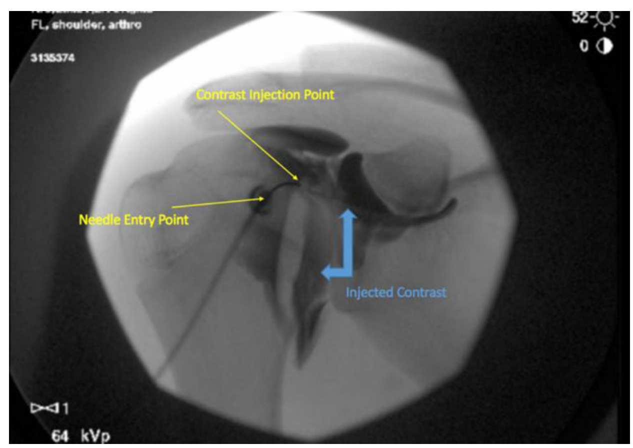

Fig. 2 Fluoroscopy image of hip injection

Conclusion

This abstract presented our progress in developing an MRI-compatible robot for shoulder arthrography. We have received FDA approval for a clinical study using the robot and plan to start the clinical trial this year. This work is a first step towards offering radiation free procedures under MRI at our children's hospital.

Intravascular optical coherence tomography to validate finite-element simulation of angioplasty balloon inflation

H. Azarnoush[1], B. Boulet[2], G. Lamouche[3]
[1]Amirkabir University of Technology (Tehran Polytechnic), Biomedical Engineering, Tehran, Iran, Islamic Republic Of
[2]McGill University, Centre for Intelligent Machines, Montreal, Canada [3]National Research Council Canada, Optical Techniques, Boucherville, Canada

Keywords Angioplasty · Optical coherence tomography · Finite element simulation · Validation

Purpose

We explored the potential of intravascular optical coherence tomography (IVOCT) to experimentally validate results obtained from finite-element simulation of angioplasty balloon deployment [1–5]. So far, concrete methods are lacking to examine simulation results. High resolution of IVOCT could help improve designs that are based on mechanical models of devices used in angioplasty.

Methods

Experimental IVOCT monitoring procedures comprised three scenarios. In the first scenario, the diameter of an inflating semi-compliant balloon was characterized. In the second scenario, inner and outer diameters of three artery phantoms with various mechanical properties were characterized during balloon inflation. In the third scenario, inner and outer diameters of a phantom were characterized during balloon unfolding and inflation. In order to simulate each experimental scenario, IVOCT images were processed to create initial geometrical models for the balloon and the phantoms. An Ogden constitutive model was tuned in an optimizer to fit the IVOCT balloon inflation monitoring results from the first scenario. This model was used to simulate the balloon's response in simulations involving phantoms corresponding to the second and third scenarios. The mechanical models of the phantoms in the second and third scenario were obtained through uniaxial tensile tests. Diameter values were calculated both from processing of images and simulation results. These values were then compared for each scenario.

Results

Related to Scenario 1, the optimization procedure provided values of $\mu = 4.5$ and $\alpha = 4.6$ for the balloon Ogden model. These values corresponded to a residual norm of 0.04 mm in the optimizer and a good fit to the experimental results

In Scenario 2, the inner and outer diameters of the 3 phantoms were measured using image processing techniques and were compared with those obtained from simulation results in the range 0–4 atm. The largest diameter error between simulation and experiment was 4%.

In Scenario 3, the balloon was initially in a folded state. The phantom surrounding the balloon was deformed in 2 phases, i.e., during the balloon unfolding phase at pressures of smaller than 2 atm and during the balloon expansion phase at pressures in the range 2–4 atm. Considering that a semi-compliant balloon was used the diameter increase rate was higher during the balloon unfolding in comparison with the balloon expansion phase. The FEM simulation results captured this 2-phase deformation. The largest diameter error between simulation and experiment was 13%.

Conclusion

IVOCT monitoring of balloon inflation, presents new opportunities and new challenges. The first goal of this paper was to present IVOCT as a high-resolution imaging technique to characterize deformation during angioplasty balloon inflation. In the IVOCT monitoring results difference in mechanical properties of the structures surrounding the balloon could be distinguished. This could potentially provide an insight into the composition of plaque in atherosclerotic arteries. The results could also provide information about tissue response during the balloon unfolding. Although, we used phantoms, the proposed approach is not limited to phantoms. It could be used to study the response of arteries to different interventional procedures, applying different balloons, balloon folding methods, stents, or pressurization strategies. It is thus a great tool to optimize interventional procedures and devices. The second goal of the paper was to establish the relevance of IVOCT monitoring for the validation of simulation models. In this preliminary study, we obtained good agreement between simulation and experimental results. The proposed technique could be beneficial in the modeling of angioplasty procedures, which is generally a challenging task. The need for reliable simulation results requires a validation strategy. We presented a comparison of cross-sectional monitoring and 2D simulation of balloon inflation inside phantoms. Future work may address a 3D scenario. A pullback of the IVOCT probe can provide the geometry of the structure in 3D which could be compared with 3D simulation results. IVOCT monitoring may also be used to validate the simulations corresponding to stent deployment and in vitro angioplasty procedures involving real arteries.

References

[1] Azarnoush H (2012). *Modeling and control of angioplasty balloon deployment based on intravascular optical coherence tomography*. McGill University (Canada).

[2] Azarnoush H, Vergnole S, Bourezak R, Boulet B, Lamouche G (2010). Optical coherence tomography monitoring of angioplasty balloon inflation in a deployment tester. *Review of scientific instruments, 81*(8), 083101.

[3] Azarnoush H, Vergnole S, Boulet B, DiRaddo R, Lamouche G (2012). Real-time control of angioplasty balloon inflation based on feedback from intravascular optical coherence tomography: preliminary study on an artery phantom. *IEEE Transactions on Biomedical Engineering*, *59*(3), 697–705.

[4] Azarnoush H, Vergnole S, Pazos V, Bisaillon CÉ, Boulet B, Lamouche G (2012). Intravascular optical coherence tomography to characterize tissue deformation during angioplasty: preliminary experiments with artery phantoms. *Journal of biomedical optics, 17*(9), 096015–096015.

[5] Azarnoush H, Vergnole S, Boulet B, Sowa M, Lamouche G (2012). Real-time control of angioplasty balloon inflation based on feedback from intravascular optical coherence tomography: experimental validation on an excised heart and a beating heart model. *IEEE Transactions on Biomedical Engineering, 59*(5), 1488–1495.

Training a deep learning network to assess breast cancer risk

K. Höeg Dembrower[1,2], H. Azizpour[3], K. Smith[3], E. Konuk[3], F. Strand[1,4]

[1]Karolinska Institutet, Stockholm, Sweden

[2]Capio Sankt Görans Sjukhus, Stockholm, Sweden

[3]Royal Institute of Technology, Stockholm, Sweden

[4]Karolinska University Hospital, Thoracic Radiology, Solna, Sweden

Keywords Breast cancer · Risk prediction · Deep learning · Mammography

Purpose

Breast cancer is one of the most common forms of cancer worldwide and the incidence is rising. It is crucial to identify more women with the disease at an early stage in order to decrease morbidity and mortality. One approach is to select certain women to undergo magnetic resonance imaging (MRI) in addition to screening mammography. MRI is more sensitive, but also more costly and time-consuming compared to mammography. In practice, this would require an optimized risk assessment in order to accurately select the women most likely to benefit in terms of earlier breast cancer detection. A traditional approach to mammogram analysis has been to estimate mammographic density (MD) which has been shown to be strongly correlated with breast cancer risk (1). MD is defined as the area, or volume, of pixels in the image that has an intensity level above a threshold corresponding to dense breast tissue. However, MD measurements do not entirely capture all risk-relevant information in an image (2). In our study, we have trained a state of the art deep learning network to distinguish between tumor-free negative mammograms from women who developed breast cancer and those women who remained healthy. The aim was to evaluate the performance of the deep learning risk predictions (DLR), and compare with MD, in terms of identifying women at high risk of breast cancer. In this abstract we report interim results based on the first version of our deep learning network.

Methods

The mammograms originated from a population-based cohort of women invited to breast cancer screening in Stockholm, Sweden, between 2008 and 2014. The women were screened every 1.5–2 years between the age of 40 and 74. The follow-up time to ascertain absence of breast cancer diagnosis for healthy women ended on December 31, 2015. We included all women with breast cancer and a random sample of healthy controls at approximately a 1:20 ratio, and analyzed their tumor-free negative full-field digital mammograms. To avoid confounding due to presence of tumor, ipsilateral images from the time of breast cancer diagnosis were not included. The women were randomly divided into a training set, which was used for deep learning network development, and a test set which was analyzed after all training was finished. In the test set, to ensure a balanced comparison between women with and without breast cancer, we included one randomly selected image per woman from the latest date of mammography. A deep learning network based on the Inception-Resnet architecture (3) was pre-trained on the ImageNet dataset (4). Then, the network was fine-tuned on the mammograms and breast cancer outcomes described above. The mammograms were down-sampled to 299×299 pixels. Image augmentations included cropping and changing the aspect ratio of the input mammograms. RMSprop optimization was adopted with a fixed learning rate of 0.01. Binary cross-entropy was used for the loss function. After network training was finished, the test set was used to evaluate the performance of the breast cancer risk predictions. Area Under the Curve (AUC) and Odds Ratio (OR) per quintile were calculated for women with breast cancer compared to healthy women. The predictors were age, MD and DLR. MD was calculated by a publicly available validated software package (5). We estimated four regression models with breast cancer as the outcome and the following predictors: (i) DLR, (ii) DLR and age, (iii) MD, (iv) MD and age.

Results

The training set consisted of 20,542 healthy women and 526 women who developed breast cancer. The corresponding numbers for the test set were 8238 and 219 respectively. The mean age was 55 and 58 years for healthy women and women with breast cancer respectively. The AUC was 0.62, 0.61, 0.56 and 0.63 for model (i), (ii), (iii) and (iv) respectively. Table 1 shows the estimated ORs for all models and quintiles. The OR for the top quintile in each model was 5.32 (95% CI 2.93–9.69), 2.79 (95% CI 1.75–4.44), 1.96 (95% CI 1.23–3.11) and 3.77 (95% CI 2.29–6.21) respectively.

Table 1 Odds ratios for the association between the top quintile of risk estimates and breast cancer outcome, estimated by logistic regression modelling

Model	Predictor	OR	95% CI
1	Deep learning risk	5.32	(2.93–9.69)
2	Deep learning risk and age	2.79	(1.75–4.44)
3	Mammographic density	1.96	(1.23–3.11)
4	Mammographic Density and age	3.77	(2.29–6.21)

Conclusion

Using deep learning to assess breast cancer risk shows promising results. The deep learning risk predictions had better ability to identify the top quintile of women at highest breast cancer risk compared to the more established measure of mammographic density. Since there are several avenues for improving this first deep learning network, we believe that a deep learning approach will be the preferred breast cancer risk prediction method in future clinical applications.

References

[1] Boyd NF, Guo H, Martin LJ, Sun L, Stone J, Fishell E, Jong RA, Hislop G, Chiarelli A, Minkin S, Yaffe MJ (2007) Mammographic density and the risk and detection of breast cancer. N Engl J Med. 2007; 356(3): 227–236

[2] Gastounioti A, Conant EF, Kontos D (2016) Beyond breast density: a review on the advancing role of parenchymal texture analysis in breast cancer risk assessment. Breast Cancer Res. 2016; 18(1): 91

[3] Szegedy C, Ioffe S, Vanhoucke V, Alemi AA (2017) Inception-v4, Inception-ResNet and the Impact of Residual Connections on Learning. Proceedings of the Thirty-First AAAI Conference on Artificial Intelligence

[4] Deng J, Dong W, Socher R, Li L-J, Li K, Fei-Fei L (2009) Imagenet: A large-scale hierarchical image database. Computer Vision and Pattern Recognition, CVPR 2009 IEEE Conference on; 2009: IEEE

[5] Keller BM, Chen J, Daye D, Conant EF, Kontos D (2015) Preliminary evaluation of the publicly available Laboratory for Breast Radiodensity Assessment (LIBRA) software tool: comparison of fully automated area and volumetric density measures in a case–control study with digital mammography. Breast Cancer Res. 2015; 17: 117

Poster Session

Computer Assisted Radiology and Surgery—
32nd International Congress and Exhibition

Obtaining the precise required irradiation time for radiotherapy of liver tissue using medical imaging

S. A. Mousavi Shirazi[1]
[1]Islamic Azad University, South Tehran Branch, Department of Physics, Tehran, Iran, Islamic Republic of

Keywords Dose · Irradiation time · Liver · Neutron therapy

Purpose

During radiotherapy by any radiation, it is always essential to stop absorbing the excess dose by a tissue. To better treat cancerous tissues and to make more precise irradiation for cancerous tumor, there needs the accurate irradiation time to be estimated. The neutron radiation therapy can be put into operation on a patient through two kinds of neutrons. One kind of neutron radiation therapy is Boron Neutron Capture Therapy (BNCT) that applies epithermal neutrons. Another technique is Neutron Capture Therapy (NCT) that is relative to fast neutrons. In that case, it is supposed that the mono-energy neutrons be used. In this research, the main aim is to obtain the required irradiation time for the course of neutron radiation therapy of liver tissue.

Methods

For this purpose, first, the constituent materials of any of existing organs in abdominal tissue are extracted and defined in MCNPX code. Then, every organ in the abdominal tissue is voxelized by MATLAB software, and a large number of voxels are made. Each of voxels is defined according to CT number or Hounsfield unit (HU) of the related organ based on the level of grayness and CT number of all pixels in DICOM images in a way that there is a correlation between the Haunsfield Unit scale and every voxel. In the MATLAB programming, there are a large number of voxels as lattice to build up the geometry of tissue. There is a big lattice specified so that it can be divided into very small lattices. The resolution of small lattices might be arbitrary. In this research, the resolution of every small lattice has been considered 1mm3, because the minimum resolution of clinical X-ray imaging machine which has been applied in this project is 1 mm^3. Then, the existing voxels in the area of liver, which are quite homogeneous, are filled up with the constituent materials of the liver tissue. In order, the abdominal tissue is entirely homogeneous filled up with the related material which has self-radiodensity, and after that the liver tissue is segmented among the abdomen from other tissues located in the abdominal region. This contouring is carried out by filling up the rest of existing materials in the other tissues and sections with air. Then, the geometry of the segmented liver tissue is generated as input data, and this data is transferred into the MCNPX code. Then, the absorbed dose is computed for the liver tissue (Fig. 1).

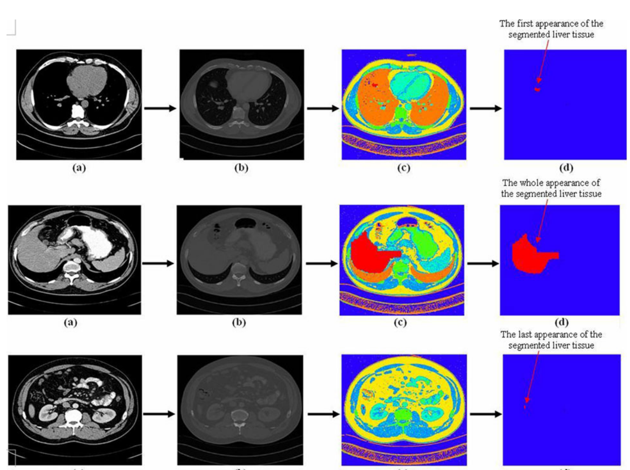

Fig. 1 The image of abdominal tissue converted in four stages

Results

After obtaining the values of absorbed doses in liver tissue per each of incident neutron energies, the required irradiation time is obtained in second (*s*) by an advanced software module (designed in this research using Delphi 7 programming language) based on the required dose (in *Gy*) and various activities (in *Bq*), neutron energy of neutron source and the required treatment dose (in Gy) which is recognized by the related expert like radiobiologist (Fig. 2). In this research, a relationship is considered between absorbed dose, neutron source activity and incident neutron energy. Thus, absorbed dose is proportional to irradiation time multiplied by neutron source activity. As the obtained absorbed dose is actually per irradiation of one neutron, after obtaining absorbed doses per each of energies of incident neutrons, the value of activity is multiplied by. In order to determine the required irradiation time, the values of absorbed doses obtained in liver tissue are divided by neutron activity in an arbitrary neutron energy (Table 1).

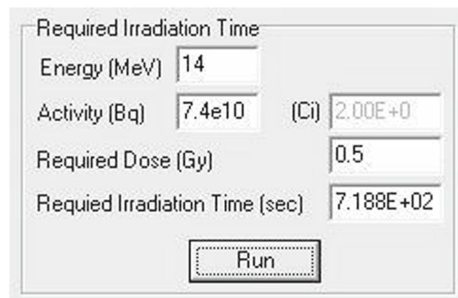

Fig. 2 Obtaining required irradiation time in second (s) by the software module based on required dose (in Gy) and various activities (in Bq) and neutron energies of neutron source (MeV)

Table 1 The obtained absorbed dose per each of incident neutron energies

Energy group	Absorbed dose (MeV/g)	Energy group	Absorbed dose (MeV/g)
Energy of incident neutron: 1.0E−9 MeV			
1.00E−09	4.37E−16	6.00E−03	0.00E+00
5.00E−09	1.90E−16	8.00E−03	0.00E+00
1.00E−08	1.23E−15	1.00E−02	0.00E+00
2.00E−08	3.16E−16	2.00E−02	0.00E+00
4.00E−08	8.45E−15	4.00E−02	0.00E+00
6.00E−08	2.75E−14	6.00E−02	0.00E+00
8.00E−08	3.85E−15	8.00E−02	0.00E+00
1.00E−07	1.99E−16	1.00E−01	0.00E+00
2.00E−07	0.00E+00	2.00E−01	0.00E+00
4.00E−07	0.00E+00	4.00E−01	0.00E+00
6.00E−07	0.00E+00	6.00E−01	0.00E+00
8.00E−07	0.00E+00	8.00E−01	0.00E+00
1.00E−06	0.00E+00	1.00E+00	0.00E+00
2.00E−06	0.00E+00	2.00E+00	0.00E+00
4.00E−06	0.00E+00	4.00E+00	0.00E+00
6.00E−06	0.00E+00	6.00E+00	0.00E+00
8.00E−06	0.00E+00	8.00E+00	0.00E+00
1.00E−05	0.00E+00	1.00E+01	0.00E+00
2.00E−05	0.00E+00	1.10E+01	0.00E+00
4.00E−05	0.00E+00	1.20E+01	0.00E+00
6.00E−05	0.00E+00	1.30E+01	0.00E+00
8.00E−05	0.00E+00	1.40E+01	0.00E+00
1.00E−04	0.00E+00	1.50E+01	0.00E+00

Table 1 continued

Energy group	Absorbed dose (MeV/g)	Energy group	Absorbed dose (MeV/g)
2.00E−04	0.00E+00	1.60E+01	0.00E+00
4.00E−04	0.00E+00	1.70E+01	0.00E+00
6.00E−04	0.00E+00	1.80E+01	0.00E+00
8.00E−04	0.00E+00	1.90E+01	0.00E+00
1.00E−03	0.00E+00	2.00E+01	0.00E+00
2.00E−03	0.00E+00	Total	4.22E−14
4.00E−03	0.00E+00		
.			
.			
.			
Energy of incident neutron: 2.0E+1 MeV			
1.00E−09	1.95E−15	6.00E−03	1.40E−07
5.00E−09	3.81E−14	8.00E−03	1.60E−07
1.00E−08	8.81E−14	1.00E−02	1.63E−07
2.00E−08	4.70E−13	2.00E−02	8.72E−07
4.00E−08	1.94E−12	4.00E−02	2.07E−06
6.00E−08	2.25E−12	6.00E−02	2.19E−06
8.00E−08	1.95E−12	8.00E−02	2.42E−06
1.00E−07	1.38E−12	1.00E−01	2.48E−06
2.00E−07	4.16E−12	2.00E−01	1.58E−05
4.00E−07	4.20E−12	4.00E−01	1.07E−05
6.00E−07	4.08E−12	6.00E−01	1.20E−05
8.00E−07	3.29E−12	8.00E−01	1.29E−05
1.00E−06	3.40E−12	1.00E+00	1.25E−05
2.00E−06	1.84E−11	2.00E+00	7.48E−05
4.00E−06	3.73E−11	4.00E+00	1.92E−04
6.00E−06	4.31E−11	6.00E+00	2.01E−04
8.00E−06	4.47E−11	8.00E+00	1.93E−04
1.00E−05	3.99E−11	1.00E+01	1.90E−04
2.00E−05	2.54E−10	1.10E+01	1.02E−04
4.00E−05	5.99E−10	1.20E+01	9.69E−05
6.00E−05	6.51E−10	1.30E+01	1.20E−04
8.00E−05	6.33E−10	1.40E+01	1.02E−04
1.00E−04	6.91E−10	1.50E+01	7.93E−05
2.00E−04	3.82E−09	1.60E+01	1.03E−04
4.00E−04	8.94E−09	1.70E+01	7.38E−05
6.00E−04	1.01E−08	1.80E+01	1.19E−04
8.00E−04	9.51E−09	1.90E+01	2.21E−04
1.00E−03	9.47E−09	2.00E+01	1.77E−02
2.00E−03	5.77E−08	Total	1.96E−02
4.00E−03	1.26E−07		

Conclusion

After determination of required dose by radiobiologist, this value is held up as input data to the software module, and this value is interpolated in the obtained values of absorbed doses. Therefore, based on the required treatment dose, activity and energy of clinical neutron source, the required irradiation time is calculated to reach the desired dose during neutron radiation therapy. The required irradiation time will be inferred to reach the desirable dose for each patient during neutron therapy course for the therapy of similar liver tissues accordingly. In so doing, from clinical viewpoint, this method might also be generalized and carried out for other soft tissues.

References

[1] Hounsfield G (1980) Nobel lecture, Computed medical imaging. J Radiol 61 (6–7): 459–468.

[2] International Atomic Energy Agency (IAEA-TECDOC-1223) (2001) Current status of neutron therapy. Austria (Vienna): International Atomic Energy Agency.

[3] Mousavi Shirazi S. A, Sardari D (2012) Design and simulation of a new model for treatment by NCT. Sci Technol Nucl Ins 2012 (2012): 1–7. https://doi.org/10.1155/2012/213640

[4] Reeves T. E, Mah P, McDavid W. D (2012) Deriving Hounsfield units using grey levels in cone beam CT: a clinical application. Dentomaxillofac. Radiol. https://doi.org/10.1259/dmfr/31640433

[5] Zhang R, Wang H, Zeng G, Li J (2015) Computer Tomography Scanning and Modeling of Ostrich Foot., J. Med. Imaging Health Inf. 5 (4): 848–854

Overranging and overbeaming for volume helical scanning in computed tomography: a novel method for simultaneously measurement

A. Urikura[1], T. Hara[2], T. Yoshida[3], E. Nishimaru[4], T. Hoshino[5], Y. Nakaya[1], M. Endo[1]

[1]Shizuoka Cancer Centre, Diagnostic Radiology, Shizuoka, Japan

[2]Nakatsugawa Municipal General Hospital, Gifu, Japan

[3]Shizuoka Cancer Center, Shizuoka, Japan

[4]Hiroshima University Hospital, Hiroshima, Japan

[5]Ishinkai Yao General Hospital, Osaka, Japan

Keywords Computed tomography · Overbeaming · Overranging · Radiation dose

Purpose

Advances in multi-row detector computed tomography (MDCT) has made it easy to perform the high-speed scanning. In order to avoid radiation sensitive organs while attaining diagnostic objectives, the operator can set the scan length with an accuracy of millimeter unit at the scanner console. However, X-ray exposure of helical scanning is extended to the outside of the set scan range along to the longitudinal direction. The exposure length extension of helical scanning called overranging tends to increase due to larger detector coverage and pitch selection [1–3]. To reduce the increasing of overranging in MDCT, dynamic z-collimator has installed in advanced CT scanners [4].

The longitudinal X-ray flux of MDCT contains the penumbra called overbeaming for homogenizing the X-ray intensity incident on the detector [4]. The influence of overbeaming in MDCT varies depending on the number of detector configuration. Since overbeaming of MDCT depends on beam width and geometry, denotes scanner specific.

Generally, to quantify the overranging and overbeaming, performing individual measurements. In this study, we propose a novel method to quantify the overranging and overbeaming by one helical scanning. To our knowledge, there is no report of the overranging and overbeaming measurements by one helical scanning.

The aim of this study was to assess the effect of reducing longitudinal exposure range by a dynamic z-collimator by use of a novel method we proposed.

Methods

Overbeaming measurement

In a novel measurement method we proposed, five imaging plates for computed radiography (FCR, Fujifilm Medical, Japan) were placed at a cylindrical shape. By developing the scanned cylindrical IP, it was possible to acquire a "stripe image".

For overbeaming measurements, the profile in the perpendicular direction to a single stripe was plotted. The beam profile at the rotation centre was estimated using full width at half maximum of the profile curve (eFWHM). The eFWHM was calculated using the following equation:

$$\mathrm{eFWHM} = \mathrm{mFWHM} \times \mathrm{FSD/FID},$$

where, mFWHM was the measured FWHM at the stripe image. FSD and FID was the focus surface distance and focus iscentre distance corresponding to the geometrc arrangement of the CT scanner [5]. The dose efficiency (DE) was calculated by deviding nominal beam width by eFWHM. Further, to verify the accuracy of the calculated overbeaming obtained by our method, we compared the values measured by the current method and a conventional method.

Overranging measurement

To measure the overranging, a rectangular region of interest (ROI) containing the entire stripe image was placed. Overranging was calculated from the profile along to the longitudinal direction obtained form the ROI. The overranging was calculated by follows equation:

$$\mathrm{Overranging} = \{(\mathrm{FWHM} - d) + \mathrm{OB}\}/2,$$

where, d was the scan range, and OB was width of the overbeaming. In addition, overranging was compared between with and without dynamic z-collimator at the same scan parameters.

Data acquisition was performed with conventional (32-mm width) and volume (80-mm width) helical scanning. Pitch was set at 0.83, 1.49 for 32-mm, and 0.87, 0.99 for 80-mm of beam collimation, respectively. Further, the overranging reduction by a dynamic z-collimator (Active Collimator, Canon Medical Systems, Japan) was assessed. All examinations were performed with a 320-row area detector CT scanner (Aquilion ONE, Canon Medical Systems, Japan).

Results

Table 1 shows the results of overbeaming and DE with respective beam width and pitch factor setting. The eFWHM were approximately 40 mm (DE: 0.8) and 90 mm (DE: 0.9) at 32-mm and 80-mm collimation, respectively. The results of two different method showed good agreement for overbeaming measurement.

Table 1 Results of overbeaming and dose efficiency obtained by various beam width and pitch factor. eFWHM: Estimated full width at half maximum

Beam width (mm)	Pitch factor	eFWHM (mm)	Dose efficiency
32	Conventional method	39.96	0.80
	0.828	39.71	0.81
	1.484	39.96	0.80
80	Conventional method	84.38	0.95
	0.869	89.49	0.89
	0.994	90.46	0.88

Overranging increased corresponding to the pitch and nominal beam width and was up to 75.8 mm (Fig. 1). Relative overranging reduction by Active Collimator were 24.1 and 15.3% at 32-mm and 80-mm collimation, respectively.

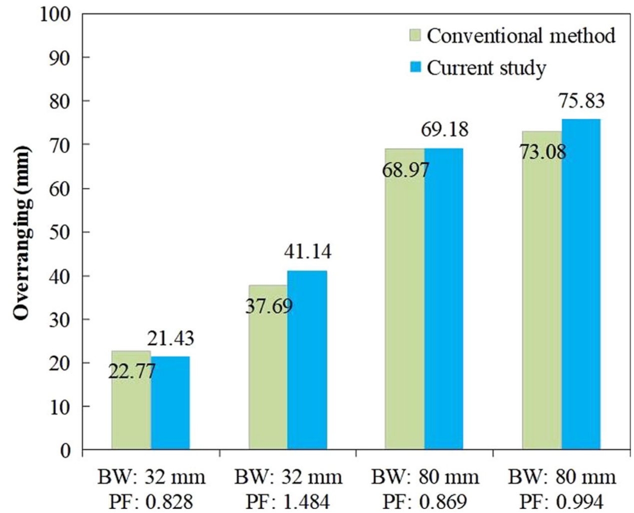

Fig. 1 Overranging for various beam widths and pitch factors. Maximum overranging were 41.14 and 75.83 mm for the beam widths of 32 and 80 mm, respectively

Conclusion

The novel measurement method we devised made it possible to simultaneously measure overbeaming and overranging. The result demonstrated that the current method was not only effective for accurate measurement but also easy-to-measure. The large caliber phantom we used allowed measure with the pitch setting of 1.0 or less.

Since the overbeaming determined by the relative penumbra to the nominal beam width, it was reduced in volume helical scanning than that of conventional helical scanning with narrow beam width. On the other hand, overranging was increased due to the beam width and pitch. Figure 2 shows the stripe images acquired with Active Collimator. The nominal beam width was set at 80 mm. The stripe image depicts that the shade is tapered at the beginning and the end according to the action of Active Collimator. Although Active Collimator reduced overranging up to 24%, wider beam width and higher pitch settings in short scan range would be increased exposure dose outside of the scan range.

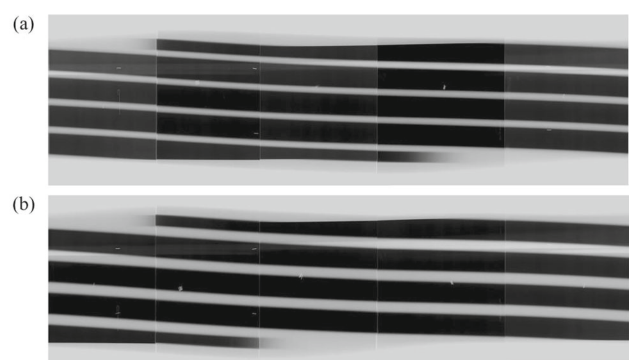

Fig. 2 Stripe images acquired with active collimator. The nominal beam width was set at 80 mm. The stripe image depicts that the shade is tapered at the beginning and the end according to the action of active collimator

References

[1] Tzedakis A, Damilakis J, Perisinakis K, Stratakis J, Gourtsoyiannis N. (2005) The effect of z overscanning on patient effective dose from multidetector helical computed tomography examinations. Medical Phys 32(6Part1): 1621–1629

[2] Schilham A, van der Molen AJ, Prokop M, de Jong HW (2010) Overranging at multisection CT: an underestimated source of excess radiation exposure. Radiographics. 30(4): 1057–1067

[3] Tsalafoutas IA. (2011) The impact of overscan on patient dose with first generation multislice CT scanners. Physica Medica: European Journal of Medical Physics. 27(2): 69–74

[4] Hsieh J, editor (2009) Computed tomography: principles, design, artifacts, and recent advances 2009: SPIE Bellingham, WA

[5] The ImPACT group. Comparative specifications: (2009) 128 to 320 slice CT scanner technical specifications. CEP08028

Visualizing CT 3D model section with USG image plane for hepatic applications

A. Kumar[1], S. L. Yan[1], S. W. Huang[1], Y. Y. Wang[1,2], L. S. Chen[1], K. C. Liu[1], Y. C. Lee[1], W. C. Hung[1]

[1]Chang Bing Show Chwan Memorial Hospital, IRCAD-Taiwan, Medical Imaging, Changhua, Taiwan

[2]National Changhua University of Education, Changhua, Taiwan

Keywords USG CT model fusion · USG · CT · Image fusion

Purpose

Ultrasonography (USG) is widely used for interventional procedures of liver because it has: realtime capability, no radiation hazard, low cost and easy accessibility [1]. In USG-guided interventional procedures, the surgeons need to mentally register the reference data set (computed tomography [CT] or magnetic resonance [MR] images) with the working data set of USG (real-time). However, such mental registration is a challenging step in performing interventional procedure, that can be more challenging when the deep lesions of liver cannot be scanned in USG. Moreover, the radiofrequency (RF) needle, used in several hepatic interventional procedures, is not easy to track in USG image. Fusion imaging is a technique that fuses two different imaging modalities [2]. It can help surgeons in conducting interventional procedures with higher confidence and accuracy. This study presents a system to combine real time USG information with preoperative 3D CT virtual model. The future goal of this system is to apply for radiofrequency needle tracking during the surgery.

Methods

CT and 3D model of Phantom:

An intraoperative abdominal ultrasound phantom (IOUSFAN, Kyoto Kagaku Co. Ltd., Kyoto, Japan), made specifically for ultrasound and laparoscopic applications, was used in this study.

CT scan:

The CT scan images of the human torso phantom was acquired with radiopaque markers placed on it. Segmentation of the CT images and a 3D virtual model reconstruction of the segmented regions was done using ITK-SNAP.

The tracking system:

An NDI Polaris tracking system was used to track the TO (Target object, the real time USG image), VO (virtual object, 3D CT model) and the USG probe location. The NDI Polaris consists of an infra-red camera system and tracking tools which are mounted on the objects to be tracked. The tracking tools are made up with infra-red reflecting spherical balls arranged in a specific geometrical shape. The Polaris emits infrared light to wirelessly detect and track tool's position and orientation in six degrees of freedom.

The visualization software:

The software uses the Visualization toolkit and Insight toolkit C++ libraries. The software interface provides a visualization of the CT 3D model (VO), the real time USG image (TO), and the movements of USG probe.

Combined visualization

A landmark registration technique was used to register 3D CT model. A tracking tool was mounted on the USG probe. The USG image was visualized in the software as image plane with physical dimension of the image in millimetre. The transformation (*T*) between the mounted tool (*ToolPose*) and the image plane was also calculated with a landmark registration technique. The USG probe's position in the visualization software was updated as *T* x *ToolPose*. A section (*SectionModel*) of the 3D model parallel to the USG image plane (*USGPlane*) was calculated. The *SectionModel* and *USGPlane* was visualized in a single image (Fig. 1).

Fig. 1 NDI tracking system (left) and USG probe with tracking tool (right)

Results

A C ++ with CUDA based software for the system was run in a computer with Intel® Core™ i7 960 @3.20 GHz, 6.00 RAM 64 bit Windows 7 and graphics card of NVidia TESLA C2075. The tracked USG image with the 3D CT model and a section from CT model is shown in Fig. 2.

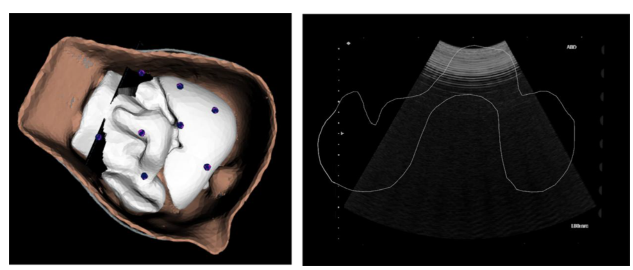

Fig. 2 A 3D model of phantom displayed with an USG image (left) and a section of 3D model parallel to the plane of USG image (right)

Conclusion

This work presents a system to combine the information from 3D CT model and the USG image. In future study a radiofrequency tracking system would be included and visualized. The completed system would be examined and used for radiofrequency ablation of hepatic tumors.

References

[1] Rhim H, Lee MH, Kim YS, Choi D, Lee WJ, Lim HK (2008) Planning sonography to assess the feasibility of percutaneous

radiofrequency ablation of hepatocellular carcinomas. AJR Am J Roentgenol 2008; 190: 1324–1330.
[2] Park HJ, Lee MW, Lee MH, Hwang J, Kang TW, Lim S, Rhim H, Lim HK (2013) Fusion imaging-guided percutaneous biopsy of focal hepatic lesions with poor conspicuity on conventional sonography. J Ultrasound Med; 32: 1557–1564.

Improving image resolution of whole heart coronary magnetic resonance angiography using 3-dimentional super-resolution technique

S. Takahashi[1], R. Nakayama[1], M. Asao[1], A. Hizukuri[1], M. Ishida[2], K. Kitagawa[2], H. Sakuma[2]
[1]Ritsumeikan University, Graduate School of Science and Engineering, Kusatsu, Japan
[2]Mie University School of Medicine, Department of Radiology, Tsu, Japan

Keywords Super-resolution technique · Magnetic resonance angiography · Image resolution · Coronary

Purpose
Coronary artery stenosis causes ischemic heart disease such as angina pectoris. Therefore, it is important to detect early coronary artery stenosis. Whole-heart coronary magnetic resonance angiography (MRA) permits noninvasive assessment of coronary artery stenoses without exposing the patient to radiation. However, several technological constraints restrict image resolution of whole-heart coronary MRA. In brain MRI, a learning-based super-resolution (SR) technique has emerged as a method to increase image resolution and improve image quality. The purposes of this study were to develop a three-dimensional (3D) learning-based SR technique optimized for whole-heart coronary MRA, and to evaluate the usefulness of 3D SR technique for improving the image quality of whole-heart coronary MRA.

Methods
Our database consisted of free-breathing whole-heart coronary MRA images were obtained in 40 patients with known or suspected coronary artery disease by using a 1.5 T MR system and 32-channel cardiac coils, with acquisition resolution of $1.2 \times 1.2 \times 1.5$ mm and reconstruction resolution of $0.6 \times 0.6 \times 0.75$ mm. The training dataset included 20 patients data whereas the test dataset included the other 20 patients data. A learning-based SR technique consists of two steps including the generation of a dictionary and the construction of high-resolution images. In the generation of a dictionary, the low-resolution (LR) images and the high-resolution (HR) images were first constructed by down-sampling the whole-heart coronary MRA images in the training dataset. The dictionary was consisted of pairs of LR image patches with $5 \times 5 \times 5$ matrices and the corresponding HR image patches with $10 \times 10 \times 10$ matrices. In the construction of high-resolution images, the input images were divided to patches with $5 \times 5 \times 5$ matrices. For each input patch, SR patch was generated by embedding optimal patches selected from millions of patch-pairs in the dictionary. The SR images with high resolution for the input images were constructed by applying this process to all input patches. For evaluating the advantages of the 3D SR technique, whole-heart coronary MRA images with $0.6 \times 0.6 \times 0.75$ mm resolution were reconstructed from the down-sampled whole-heart coronary MRA images ($1.2 \times 1.2 \times 1.5$ mm) by using the 3D SR technique and a 3D bicubic interpolation. The original whole-heart coronary MRA images with $0.6 \times 0.6 \times 0.75$ mm resolution were used as reference standard to evaluate the fidelities of those reconstructed images.

Results
Figure 1 shows the comparison of the constructed images by the 3D SR technique and the 3D bicubic interpolation. The image quality of whole-heart coronary MRA images was substantially improved with the 3D SR technique. The root mean square error, the peak signal to noise ratio and the structural similarity index between the SR images and the original images were 11.7 ± 4.01 and 51.3 ± 2.97, 0.993 ± 0.03, being significantly greater than those values for the 3D bicubic interpolation (12.5 ± 4.62, $50.8 \pm 3.11/0.992 \pm 0.01$, $P < .0001$). The 3D SR technique also exhibited significantly improved SNR (4.6 ± 3.64) and CNR (6.7 ± 6.33) as compared with the 3D bicubic interpolation ($4.4 \pm 3.82/5.3 \pm 6.51$, $P < .0001$).

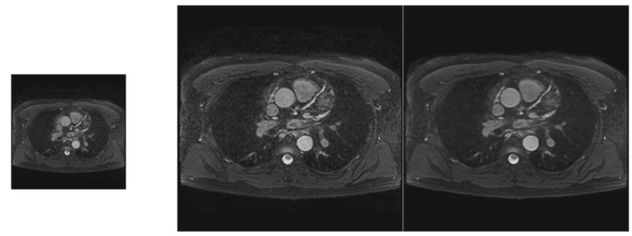

Fig. 1 Comparison of the constructed images by the 3D bicubic interpolation and the 3D SR technique

Conclusion
The 3D SR technique optimized in this study can provide whole-heart coronary MRA images with improved fidelity and image quality compared with the 3D bicubic interpolation. Improved spatial resolution and higher image quality achieved by the 3D SR technique may help to improve the detection of coronary artery stenoses with whole-heart coronary MRA.

A method for generating synthetic mammograms using information from digital breast tomosynthesis (DBT) images

S. H. Chae[1], J. W. Jeong[1], J. H. Choi[2], E. Y. Chae[3], H. H. Kim[3], Y. W. Choi[4], S. Lee[1]
[1]ETRI, Bio-Medical IT Convergence Research Department, Daejeon, South Korea
[2]Ewha Womans University, Division of Mechanical and Biomedical Engineering, Seoul, South Korea
[3]Asan Medical Center, College of Medicine, University of Ulsan, Seoul, South Korea
[4]KERI, Ansan, South Korea

Keywords Digital breast tomosynthesis · Synthetic mammogram · Visualization · Thin plate spline

Purpose
Synthetic mammograms are two-dimensional (2D) breast images obtained through DBTs. A synthetic mammogram is a modality that complements the disadvantages of DBTs, which include significant reading times. In addition, as synthetic mammograms are generated through DBTs, no additional scans are required. A number of studies aimed to improve the conspicuity of synthetic mammograms. Thin plate spline (TPS) is a synthesis method that uses lesion information and that was used in the studies [1]. However, single-layered TPS has disadvantages; for example, the conspicuity of lesions in synthetic mammograms depends on the locations and numbers of lesions. Therefore, this paper proposes a robust multi-layered TPS method regardless of the number and location of the lesions.

Methods
When generating synthetic mammograms, forward projection, maximum intensity projection (MIP), and regional conspicuity methods are used. However, these methods result in poor conspicuity in regards to

lesions in synthetic mammograms because they do not use the locations of the lesions. TPS uses location information after lesions are detected in DBTs. Single-layered TPS generates a single spline containing all lesions and weighs a slice passing through the spline. When a forward projection is applied to a weighted DBT, synthetic mammograms have improved lesion conspicuity. In the single-layered TPS method, when the locations of the lesions overlap on a z axis, dramatic spline changes can distort lesions or weaken their conspicuity. This paper proposes a robust multi-layered TPS technique in which more than one spline can be generated. The technique analyzes the locations of the lesions and generates splines, and it generates additional splines if the lesions overlap on a z axis. It prevents the disadvantages of single-layered TPS by weighing one or more splines and performing forward projections. A phantom was used for a performance analysis of the multi-layered TPS technique. The phantom was made of rice and calcium pieces to create fake lesions. The locations of the lesions were set to overlap on a z axis. Synthetic mammogram images based on single- and multi-layered TPSs were compared while lesion location information was added sequentially.

Results

There were no differences between single- and multi-layered TPS when location information for only one lesion was included. However, differences in the conspicuity of the lesions on synthetic mammograms occurred when overlapping lesions were added. With single-layered TPS, the conspicuity of the lesions changed according to the locations of the added lesions, but with multi-layered TPS, there were robust results in regards to the locations of the added lesions (Fig. 1).

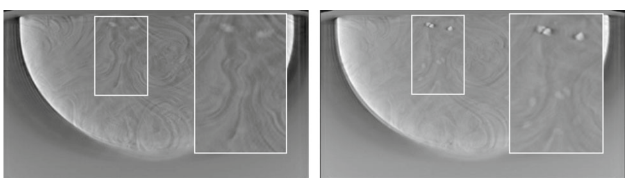

Fig. 1 The results of TPS-based synthetic mammograms with overlapping lesions. In the left image, single-layered TPS was used. In the right image, multi-layered TPS was used

Conclusion

The proposed multi-layered TPS technique improved the conspicuity of lesions in TPS-based synthetic mammograms using lesion location information. The phantom confirmed the improvement using lesion locations. Future quantitative analyses and observations will be conducted to analyze the performance of the multi-layered TPS technique in detail.

Acknowledgment

We would like to acknowledge the financial support from the R&D Convergence Program of NST of Republic of Korea (Grant CAP-13-3-KERI).

References

[1] Schie G, Mann R, Imhof-Tas M, Karssemeijer N (2013) Generating systhetic mammograms from reconstructed tomosynthesis volumes. IEEE Trans. Medical Imaging 32(12): 2322–2331

Polyp detection benchmark in colonoscopy videos using GTCreator: a novel fully configurable tool for easy and fast annotation of image databases

J. Bernal[1], A. Histace[2], M. Masana[1], Q. Angermann[2], C. Sánchez-Montes[3], C. Rodríguez de Miguel[3], M. Hammami[2], A. García-Rodríguez[3], H. Córdova[3], O. Romain[2], G. Fernández-Esparrach[3], X. Dray[2,4] and F. Javier Sánchez[1]

[1]Computer Vision Center and Universitat Autònoma de Barcelona, Barcelona, Spain

[2]ETIS lab, ENSEA, University of Cergy-Pontoise, CNRS, Cergy, France

[3]Digestive Endoscopy Unit, Hospital Clínic de Barcelona, Barcelona, Spain

[4]St. Antoine Hospital, APHP, Paris, France

Keywords Annotation tool · Benchmark · Colonoscopy · Polyp detection

Purpose

Method evaluation for decision support systems for health is a time consuming-task. To assess performance of such support systems, clinicians must deal with the annotation of thousands of images. Current existing tools such as RatSnake [1] could be improved in terms of flexibility and usability, especially with respect to image browsing speed, GUI and ease of use of the generated annotation data.

Methods

We introduce GTCreator, a flexible annotation tool for providing image and text annotations to image datasets. Our tool keeps the main functionalities of other similar tools while extending other capabilities such as allowing multiple annotators to work simultaneously on the same task. Contrary to other tools, the user can freely determine the number and type of annotations to be made for each image. The way our tool is designed makes its use possible in all stages of system evaluation, from dataset generation and annotation to performance assessment. Finally, the output of the annotation process has been designed for an easy use by the most commonly used software suites (Matlab, C++, Microsoft Office, STATA).

Results

The proposed tool allows a fast and precise annotation of image datasets. When compared to other, our tool offers the best balance between annotation capability and quality (see Table 1). Our tool has been used by clinicians to annotate CVC-ClinicVideoDB, the largest fully annotated public database of colonoscopy videos. The database contains 29,657 frames, 21,813 of them (73.55%) with a polyp in the image. With it, the first benchmark on this database is presented. We compared several polyp detection methods, from hand-crafted [2], to pure machine-learning [3], and including recently popular Convolutional Neural Networks (CNNs) [4]. Evaluation on this benchmark shows that CNNs are the current state-of-the-art (see Table 2), showing the benefit of using pre-trained networks, use of data augmentation techniques and network compression [5] to provide performance levels and computation time suitable for a potential use in a clinical environment.

Table 1 Qualitative and quantitative comparison between annotation tools

Feature/tool	RatSnake	LabelMe	VIA	VIAT	ImageJ	GTCreator
Qualitative comparison						
Annotation types	Masks	Masks, semantic labels	Masks, formatted text	Masks, unformatted text	Masks	Masks, formatted text
Image mask annotation types	Polygon	Polygon	Polygon	Polygon	Polygon, freehand	Polygon, freehand
Output format	Masks	XML file	CSV file	XML file	Text file	Masks, CSV files
Database browsing	Image	Collection	Collection	Image	Image	Collection

Feature/tool	RatSnake	LabelMe	VIA	VIAT	ImageJ	GTCreator
Extra features	Semantic ontology	Semi-automatic segment.	Image zooming	MPEG-7 descriptors	Image processing suite	Filtering-based browsing
Quantitative comparison (time metrics are measured in s)						
Mean total annotation time	979.3	459.3	437.6	807.6	652.0	531.33
Mean image annotation time	51.3	34.3	32.6	41.1	31.1	34.8
Mean browsing time	24	1	1	21	22	1
Segmentation accuracy	0.881	0.922	0.917	0.925	0.919	0.938

Table 2 Performance of polyp detection methods in CVC-ClinicVideoDB dataset

Method	Precision	Recall	Specificity	Accuracy	MRT	MPT
WM-DOVA	80.2	64.7	**67.2**	65.1	0.53	10.50
ALCAPOD	**81.4**	78.4	63.2	73.4	0.12	**0.020**
CNN (FT)	79.6	86.9	54.4	76.3	0.06	0.038
CNN (FT) + C	80.0	**91.4**	53.2	**78.8**	**0.05**	0.034
CNN (FT, DA)	80.4	85.6	57.3	76.3	0.06	0.038
CNN (FT, DA) + C	80.5	88.9	55.9	78.1	**0.05**	0.028
CNN (S)	75.6	74.7	50.6	66.8	0.23	0.038
CNN (S) + C	75.5	79.9	46.9	69.1	0.21	0.033
CNN (S, DA)	74.1	86.3	38.0	70.5	0.07	0.038
CNN (S, DA) + C	73.4	89.2	33.6	71.0	0.06	0.033

MRT stands for mean reaction time (in s), MPT for mean processing time (in s), FT for fine-tuned, S for from scratch, DA for data augmentation and C for compression

Conclusion

Our proposed annotation tool has been proven to be efficient for large image dataset annotation, offering a good balance between capabilities, ease of use and annotation quality.

Acknowledgements

This work has been funded by Spanish Government projects iVENDIS (DPI2015-65286-R), DeepMTL (TIN2016-79717-R) and HISINVIA (PI17/00894) projects, Catalan Government through SGR-2017-1669, Région Île de France through SATT funding “iPolyp” (Project 184). A. Histace and J. Bernal acknowledge the Institute of Advanced Studies from UCP (Invited Prof. Position grant). M. Masana acknowledges 2017FIB-00218 grant of Generalitat de Catalunya, and its CERCA Programme. We acknowledge the GPU support from NVIDIA.

References

[1] Iakovidis DK, Goudas T, Smailis, Maglogiannis I (2014) Ratsnake: a versatile image annotation tool with application to computer-aided diagnosis. The Scientific World Journal Jan 27

[2] Bernal J, Sánchez FJ, Fernández-Esparrach G, Gil D, Rodríguez C, Vilariño F (2015) “WM-DOVA maps for accurate polyp highlighting in colonoscopy: validation vs. saliency maps from physicians” Computerized Medical Imaging and Graphics, 43 pp. 99–111

[3] Angermann Q, Bernal J, Sánchez-Montes C, Hammami M, Fernández-Esparrach G, Dray X, Romain O, Sánchez F, Histace A (2017) Towards Real-Time Polyp Detection in Colonoscopy Videos: Adapting Still Frame-Based Methodologies for Video Sequences Analysis. Proceedings of MICCAI CARE 2017 Workshop (pp. 29–41), 2017.

[4] Bernal J, Tajkbaksh N, Sanchez FJ, Matuszewski BJ, Hao Chen, Lequan Yu, Angermann Q, Romain O, Rustad B, Balasingham I, Pogorelov K, Sungbin Choi, Debard Q, Maier-Hein L, Speidel S, Stoyanov D, Brandao P, Cordova H, Sanchez-Montes C, Gurudu SR, Fernandez-Esparrach G, Dray X, Jianming Liang, Histace A (2017) Comparative Validation of Polyp Detection Methods In Video Colonoscopy: Results From The MICCAI 2015 Endoscopic Vision Challenge. IEEE Transactions On Medical Imaging, 36(6), 1231–1249

[5] Masana M, van de Weijer J, Herranz L, Bagdanov AD, Alvarez JM (2017) Domain-adaptive deep network compression. In the IEEE International Conference on Computer Vision (ICCV)

Automatic techniques for registering tracked ultrasound to CT volume sets—a comparative study on a full pelvic phantom

P. Pandey[1], P. Guy[2], A. J. Hodgson[3], R. Garbi[1]
[1]Department of Electrical and Computer Engineering, University of British Columbia, Vancouver, Canada
[2]Department of Orthopaedics, University of British Columbia, Vancouver, Canada
[3]Department of Mechanical Engineering, University of British Columbia, Vancouver, Canada

Keywords Ultrasound · CT · Registration · Pelvic fracture

Purpose

Ultrasound (US) is a safer alternative to X-rays in medical imaging, and its popularity for orthopedic navigation is growing. To enable routine use of intraoperative US imaging for surgical guidance, fast, accurate and automatic alignment of tracked US to preoperative computed-tomography (CT) patient data is often necessary. Our group has previously investigated segmentation [1] and subsequent registration techniques [2] to align untracked US to preoperative CT images of the partial pelvic anatomy. In this paper we study the performance (accuracy and runtime) of these techniques over the complete pelvic field-of-view in a tracked US framework to characterize their suitability in realistic clinical scenarios. Secondly, we propose and evaluate a segmentation and registration method for accurate and efficient tracked US-CT alignment.

Methods

We built a pelvis phantom suitable for ultrasound scanning, and acquired a CT image as the preoperative model. We measured the registration errors of previously-published Phase Symmetry segmentation [1], Gaussian Mixture Model registration (GMM) [2] and Coherent Point Drift registration (CPD) [3] methods on 22–37 steel fiducial markers embedded around the whole pelvis model in the phantom.

To overcome the observed limitations of Phase Symmetry segmentation (namely the high false-positive rate and high runtimes), we designed and evaluated Shadow-Peak (SP) segmentation—a real-time 3D bone segmentation technique to process both tracked freehand US and preoperative CT volumes. SP segmentation is capable of rapid mapping of acoustic shadows and peak intensities, which are used to accurately detect bone surfaces (full segmentation pipeline is illustrated in Fig. 1). We paired this with a novel intensity registration pipeline that optimizes the normalized cross-correlation (NCC) between distance maps of the segmented US-CT images.

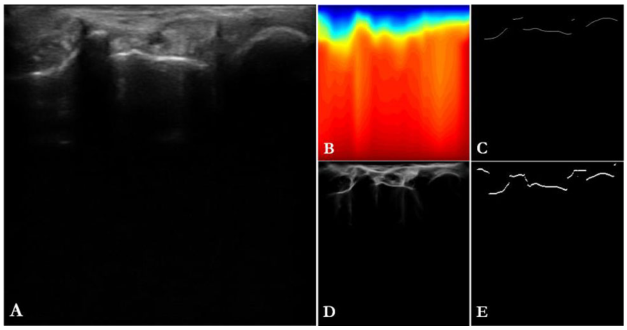

Fig. 1 **A** 2D slice from a 3D US volume of the human radius and ulna. **B** Shadow confidence map of (**A**). Hotter colors represent a higher confidence in shadow presence than cooler colours. **C** Final SP segmentation after peak detection, automatic population thresholding and connected-component analysis. **D** Phase symmetry analysis of (**A**) [1]. **E** Final phase symmetry segmentation after thresholding and ray casting

Results

SP segmentation provides more specific and faster US bone segmentation (median RMS error of 2.0 mm) when compared to Phase Symmetry (median RMS error of 14.0 mm), measured over 110 images. SP segmentation had a mean runtime of 1.80 s (SD 0.57 s) and Phase Symmetry had a mean runtime of 36.50 s (SD 5.24 s) per 3D image.

When combined with SP segmentation, CPD and NCC based registration successfully aligned tracked US volumes of the phantom to the reference CT model in all trials, with a median target registration error (TRE) of 3.59 mm (maximum: 5.32 mm) using CPD and 3.80 mm (maximum: 4.91 mm) using NCC, and a mean runtime of 11.7 and 27.3 s respectively. Figure 2 plots the TRE for the most successful segmentation and registration combinations.

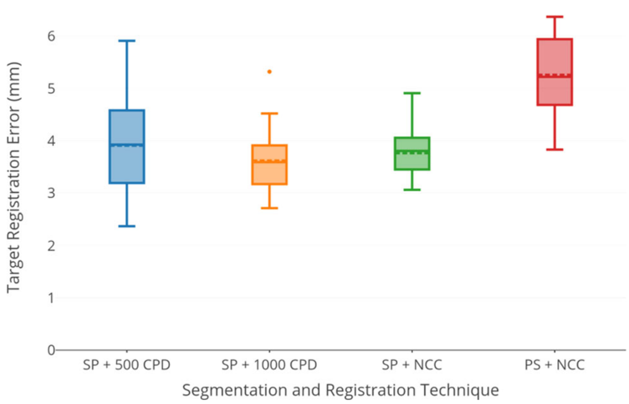

Fig. 2 Target registration errors (TRE) for all segmentation and registration combinations which had a greater than 50% success rate (24 volume pairs in total)

Conclusion

We demonstrate an automatic image-processing pipeline for intra-operative alignment of US-CT over the full pelvis, and show that in the phantom scenario it can repeatedly achieve acceptable accuracies for orthopedic surgeries. The proposed methods are amenable to clinical implementation due to their low runtimes.

References

[1] Hacihaliloglu I, Abugharbieh R, Hodgson AJ, Rohling RN (2009). Bone Surface Localization in Ultrasound Using Image Phase-Based Features. Ultrasound in Medicine & Biology, 35(9), 1475–1487.

[2] Brounstein A, Hacihaliloglu I, Guy P, Hodgson A, Abugharbieh R (2015). Fast and Accurate Data Extraction for Near Real-Time Registration of 3-D Ultrasound and Computed Tomography in Orthopedic Surgery. Ultrasound in Medicine & Biology, 41(12), 3194–3204.

[3] Myronenko A, Song X (2009). Point-Set Registration: Coherent Point Drift. Advances in Neural Information Processing Systems 19, (September), 1009–1016.

Prostate segmentation in MRI using a convolutional neural network architecture and training strategy based on statistical shape models

D. Karimi[1], G. Samei[1], C. Kesch[2], G. Nir[3], S. E. Salcudean[1]
[1]University of British Columbia, Department of Electrical and Computer Engineering, Vancouver, Canada
[2]British Columbia Cancer Agency, Vancouver, Canada
[3]University of British Columbia, Department of Urologic Sciences, Vancouver, Canada

Keywords Statistical shape models · Prostate segmentation · Convolutional neural networks · Deep learning

Purpose

Image segmentation is essential to many tasks in medical image analysis and image-guided intervention. Most of the existing Convolutional Neural Networks (CNN)-based medical image segmentation methods are based on methods that have originally been developed for segmentation of natural images. Therefore, they largely ignore the differences between the two domains, such as the smaller degree of variability in the shape and appearance of the target volume and the smaller amounts of training data in medical applications. In this work, we proposed and evaluated a CNN architecture and training strategy for segmentation of the prostate in magnetic resonance imaging (MRI) that addresses these issues. Our method aims at exploiting the limited variability in the shape of the prostate and simultaneously addressing the scarcity of training data.

Methods

Our training dataset consisted of 49 T2-weighted axial MR images. The prostate was manually segmented in these images by an expert clinician. Our test set included 26 images not used during training. We developed a principal component analysis (PCA)-based shape model from the training images. The parameters that define the prostate surface key-points in our model include the location of the prostate center, coefficients of the PCA-derived shape modes, and prostate rotation. The network consists of a series of blocks of 3D convolutional layers. The final feature maps are then used to estimate the location of the prostate center and the parameters of the shape model, which determine the position of prostate surface keypoints. We adopt a stage-wise training strategy by first training the network to predict the prostate center and subsequently adding modules to the network for predicting the parameters of the shape model and prostate rotation. This strategy leads to shorter training time and better segmentation performance. This is because if there is a large error in the estimation of the prostate location, changes in the shape model coefficients or rotation will have little or no effect on the cost function. Similarly, because in most cases the rotation of the prostate is small, it is best to train the rotation head after an initial training of the position head and the shape model head. To cope with the limited training data, we use a data augmentation method whereby the training images and their prostate surface keypoints are deformed according to the displacements computed based on the shape model.

Results

Our proposed method achieves a mean Dice score of 0.86 on the test images. As shown in Table 1, compared with a standard CNN-based method, our method shows better segmentation performance on the prostate base and apex. Our experiments also show that data augmentation using the shape model significantly improves the segmentation results. As shown in Table 2, the proposed data augmentation approach results in an increase in the mean Dice score of 0.04 in the mid-gland, base, and apex.

Table 1 Comparison of the proposed segmentation method with a fully convolutional CNN in terms of the Dice similarity coefficient computed separately for mid-gland, base, and apex sections

	Dice score—mid-gland	Dice score—base	Dice score—apex
Proposed method	0.86	0.79	0.81
Fully convolutional CNN	0.90	0.76	0.80

Table 2 Impact of shape model-based data augmentation on the performance of the proposed segmentation method in terms of the average Dice score achieved on the test images

	$n_{train} = 49$	$n_{train} = 40$	$n_{train} = 30$
With data augmentation	0.84	0.83	0.81
Without data augmentation	0.80	0.79	0.77

Conclusion

In medical image analysis, the amount of labeled training data is small and this is likely to remain a limiting factor in the foreseeable future. Moreover, the variation in the patterns of interest is usually rather limited. Given such limitations and opportunities, we think that the knowledge that was accumulated over the years prior to the resurgence of deep learning methods can be very useful in boosting the power of these new methods. The results of this study indicate a great potential for integrating the prior knowledge about the variability in the prostate shape into a CNN-based segmentation framework. Our experiments also showed that the knowledge about the expected shape variations can be used to synthesize additional informative training data that can boost the performance of the trained model. A major challenge in the proposed method was the very large number of parameters in the model. Future works can suggest network architectures with more manageable number of parameters. An alternative may be to use a fully convolutional network (which will have a substantially smaller number of parameters) and to inject the knowledge about the expected shape in the network design, training strategy, or in a post-processing stage.

Quantitative analysis of segmented colon in CT Colonography using geometrical features

M. K N[1], S. P C[1], G. Prabhu[1,2]
[1]Manipal Institute of Technology, Computer Science and Engineering, Manipal, India
[2]Manipal University Jaipur, Research and Development, Jaipur, India

Keywords Colon segmentation · Quantitative analysis · Volumetric overlap · Spatial features

Purpose

CT Colonography (CTC) is a radio-diagnosis procedure used to find the polyps in the colon. Measurement of polyp relies completely on how accurately the colon is segmented. Validating the segmented volumes have many solutions at present where accuracy is less [1]. The objective of this study was to provide alternate methods to measure the segmented volumes more accurately using image processing techniques. In this work, three approaches are discussed through qualitative and quantitative analysis

Methods

In this retrospective study, CTC images were downloaded from National Cancer Institute, USA [2]. Three quantitative measurement techniques are implemented in which the distances are randomly measured on DRR (Digitally Reconstructed Radiograph) images of the unsegmented and segmented colon (Volume Of Interest—VOI) and through volumetric overlap computation between two volumes. The block diagram of the proposed technique is shown in Fig. 1. The 3D volume is reconstructed using linear interpolation technique. The colon is segmented using a semi-automatic boundary based segmentation technique [3] which uses adaptive smoothing for denoising the colonic lumen, canny operator for boundary detection, Connected Component Labelling for boundary delineation and recognition of colonic segments using the knowledge of colon distention grading. The relationship between original patient volume and the VOI is given by Eq. (1), where S is the original 3D volume (V_g), S_o is VOI (V_b), f, f_0 are the voxel intensities and c is the scene domain. The methodology is implemented using object based visualization images like DRR, MaxIP and surface rendered image. The image moments are computed from the VOI and these moments are compared using statistical analysis and qualitatively by an expert radiologist.

$$S = (c,\ f) \rightarrow S_o = (c,\ f_o) \qquad (1)$$

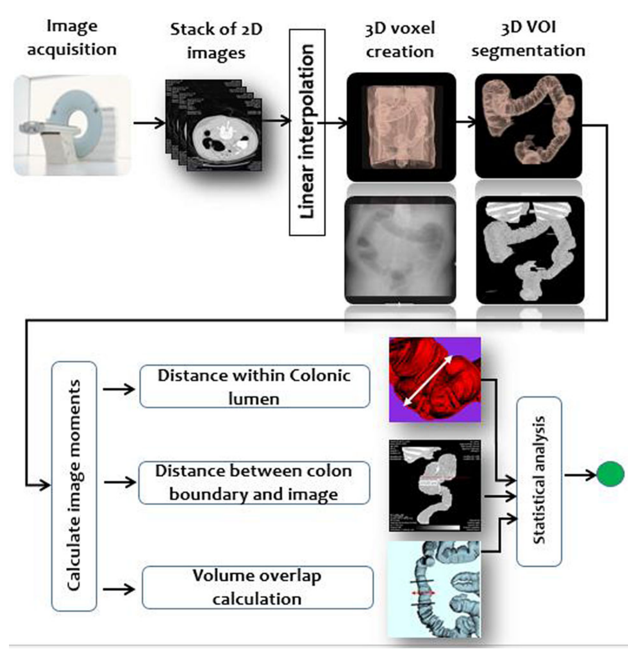

Fig. 1 The block diagram of the proposed technique

Method 1: Measuring the distance within the colonic lumen

The distance between opposite edges of colon interior is manually measured using the electronic calipers (Fig. 2b). This measurement is compared with the automatically calculated width (the geometrical feature) of the colonic segment. Both measurements were compared using paired *t* test to know significant difference. Statistically, the measurements were same.

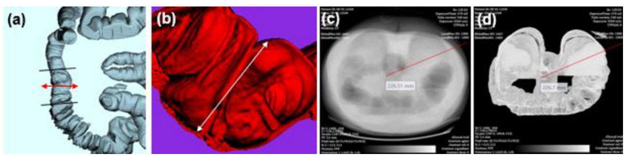

Fig. 2 Measurements under different approaches. **a** Volumetric overlap computation, **b** the distance between the opposite edges of the colon, and **c**, **d** the distance measured between the boundary of the image and the colonic segment on the unsegmented colon (**c**), segmented colon (**d**)

Method 2: The distance between the boundary of the image and the colonic segments

The distance d (u, v) is manually measured from the boundary of the slice and the colonic segments using DRR of the unsegmented (Ground Truth—x_i) and segmented colon (y_i). This feature helps the radiologist to know at what position the colonic segment falls from the periphery of the abdomen (Fig. 2c, d). paired *t* test is applied to test for the difference between x_i and y_i. With n = 30, the mean of differences = 0.0123. In group 1 (i.e. x_i), $\mu_1 = 159.6587$, $\sigma_1^2 = 88.4087$, SEM = 16.1412. In group 2, (μ_2) = 159.6463, $\sigma_2^2 = 16.1672$. The statistic value t at DOF = 29, is t = 0.1026, the *p* value is 0.9190. Since $p > 0.0001$, the minor variation in the measurement is considered to be not significant at $\alpha = 5\%$.

Method 3: Computing the volume overlap

The contour points of the automatically segmented colon and the manually drawn boundary points (GT) are compared using volumetric overlap method. This is an example of Image moments. Due to bulk data, the overlap is computed for a subset of volume (Fig. 2a, only for 20 slices out of 500). Considering subset is acceptable as defining GT is time-consuming for the entire volume [4]. Accuracy is calculated using Eq. (2), where A and B denotes the set of boundary points of VOI and GT respectively. The mean of overlap was $\bar{x} = 94.615\%$ with $\sigma = \pm 0.7754\%$. The average accuracy of 94.614 ± 0.7754% was achieved. Other methods like, average symmetric absolute surface distance, symmetric RMS surface distance and relative absolute volume difference [5] are not applicable as these methods are computationally expensive for the entire volume.

$$\text{Accuracy} = (A \cap B)/(A \cup B) * 100 \tag{2}$$

Results

Thirty samples (n = 30) were used for empirical testing and was tested on Intel Xeon® CPU E52620 2.0 GHz, Windows 2012 Server 64 bit, 48 GB DDR3 RAM, NVIDIA CUDA GPU). The images were acquired with the ACRIN 6664 CTC protocol. The imaging parameters were, 4, 8 slices MDCT images, FFS and FFP position scans, ST = {1.25, 2.5} mm, mA = {200–300}, and 120 kVp.

Conclusion

In this alternate approach, the image moments are used to measure the segmented volumes through statistical analysis. This approach has given good results. The key findings were, the manual measurements and automated measurements were same. It is good to use multiple validation techniques to claim the robustness of the segmentation technique. This method can even be applied to other anatomies and other medical imaging modalities based on the clinical need. The exact comparison with the existing solutions cannot be made here as the software and the dataset used is completely different.

References

[1] Kagadis GC, WalzFlannigan A, Krupinski EA, Nagy PG, Katsanos K, Diamantopoulos A, Langer SG (2013) Medical imaging displays and their use in image interpretation. Radiographics 33(1): 275–290. https://doi.org/10.1148/rg.331125096

[2] Clark K, Vendt B, Smith K, Freymann J, Kirby J, Koppel P, Moore S, Phillips S, Maffitt D, Pringle M, Tarbox L, Prior F (2013) The Cancer Imaging Archive (TCIA): Maintaining and Operating a Public Information Repository. Journal of Digital Imaging 26(6): 1045–1057. https://doi.org/10.1007/s10278-013-9622-7

[3] Manjunath KN, Prabhu GK, Siddalingaswamy PC (2015) A knowledge-based approach for colon segmentation in CT colonography images. International Conference on Signal and Image Processing Applications (ICSIPA), Kuala Lumpur 65–70. https://doi.org/10.1109/ICSIPA.2015.7412165.

[4] Song B, Zhang G, Lu H, Wang H, Zhu W, Pickhardt PJ, Liang Z (2014) Volumetric texture features from higher-order images for diagnosis of colon lesions via CT colonography. Int J Comput Assist Radiol Surg 9(6): 1021–1031. https://dx.doi.org/10.1007%2Fs11548-014-0991-2

[5] Gerig G, Jomier M, Chakos M (2010) Valmet: A new validation tool for assessing and improving 3D object segmentation. Proceedings of International Conference on Medical Image Computing and Computer-Assisted Intervention (MICCAI), Utrecht 516–523. https://doi.org/10.1007/3-540-45468-3_62

Super resolution of a lung CT volume using a generative adversarial network

K. Tozawa[1], A. Saito[1], S. Kido [2], K. Inai [3], H. Kimura[3], A. Shimizu[1]
[1]Tokyo University of Agriculture and Technology, Institute of Engineering, Koganei, Japan
[2]Yamaguchi University, Graduate School of Engineering, Ube, Japan
[3]University of Fukui, Faculty of Medical Sciences, Fukui, Japan

Keywords Super resolution · SRGAN · Lung CT · Micro CT

Purpose

Computed tomography (CT) and magnetic resonance imaging (MRI) have emerged as key tools in diagnosis and therapy. New technologies have been developed to speed up the imaging process and reconstruct high-resolution images. For example, state-of-the-art high-resolution CT (HRCT) has a submillimeter resolution and is proven to be effective in diagnosing interstitial lung diseases, e.g. pulmonary fibrosis, and other lung diseases, e.g. emphysema. It is expected that higher resolution imaging will help in diagnosing diseases at the early stages.

Super resolution (SR) technologies, which have been developed in the field of computer vision, have been demonstrated to be effective in many applications. A conventional approach of single frame SR is a dictionary-based method [1], which can be applied to a CT volume to generate an SR-based HRCT volume. However, the generated high resolution (HR) volume shows blurring and distortion, because of the linear combination of sub-volumes in a dictionary. In addition, the computational cost is high, which would be unacceptable for clinical use. Recently, an SR convolutional neural network [2] was applied to chest CT images to achieve four-fold magnification. However, the method used a two-dimensional network and consequently reconstructed clinical chest CT images that were not of a high resolution.

This paper proposes a novel SR method to generate an HRCT volume from a low resolution (LR) CT volume, in which the voxel size of LRCT is comparable to that of clinical CT and voxel size of

HRCT is less than 100 µm. An SR generative adversarial network (SRGAN) [3] is extended to be applicable to three-dimensional (3D) images in this study. We demonstrate the effectiveness of the proposed method using a lung CT volume scanned by a micro CT (nanotom®; GE).

Methods

The architectures of the discriminator and generator of 3D SRGAN are presented in Fig. 1, where "k" is kernel size, "n" is the number of feature maps, and "s" is stride in each convolution layer. Inputs of both networks are 3D patch images, because of the limitation of memory size in a GPU for training. Outputs of the generator are 3D HR patch images, which are tiled to generate a whole HRCT volume. The generator is trained to decrease the difference between true HR images and the corresponding reconstructed ones as well, so as to increase the error rate of the discriminator. The discriminator is trained to differentiate between true HR images and ones reconstructed by the generator. To this end, SRGAN iteratively optimizes the following loss functions of Eqs. (1) and (2).

$$\max_{\theta D}\left[E_I^{HR}{}_{\sim ptrain(I^{HR})}\left[\log D_{\theta D}(I^{HR})\right] + E_I^{LR}{}_{\sim pG(I^{LR})}\left[\log(1 - D_{\theta D}(G_{\theta G}(I^{LR})))\right]\right], \quad (1)$$

$$\min_{\theta G}\left[l_{MSE}^{SR} + \lambda \cdot E_I^{LR}{}_{\sim pG(I^{LR})}\left[\log\left(1 - D_{\theta D}\left(G_{\theta G}\left(I^{LR}\right)\right)\right)\right]\right], \quad (2)$$

$$l_{MSE}^{SR} = \left(1/r^3 DHW\right)\Sigma_{z=1}^{rD}\Sigma_{y=1}^{rH}\Sigma_{x=1}^{rW}\left(I_{x,y,z}^{ReHR} - I_{x,y,z}^{HR}\right)^2, \quad (3)$$

where I^{HR} and I^{LR} are a 3D HR patch image and a LR image, respectively. Symbols $D_{\theta D}$ and $G_{\theta G}$ denote the discriminator and generator with parameters θ_D and θ_G. l_{MSE}^{SR} is the mean-squared-error between the reconstructed 3D HR patch images and true images. In Eq. (3), r, W,H, D denote the upsampling rate, width, height, and depth in a 3D LR patch image, respectively.

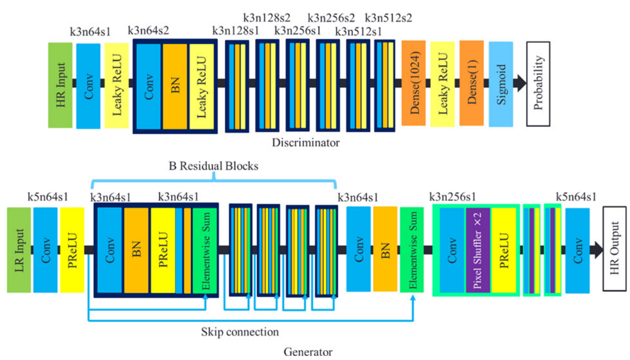

Fig. 1 Network architecture of discriminator and generator

Results

We divided a micro CT volume of human lung specimen of size 2480 × 1299 × 3600 [voxel] into three sets of 3D patch images for training, validation, and testing, none of which overlap each other and which include 95,874, 96,000, and 96,000 3D patch images, respectively. The size of a 3D HR patch image is 32 × 32 × 32 [voxel] whose voxel size is 70 × 66 × 70 [µm]. We simulated 3D LR patch images from 3D HR patch images by using the averaging operation, resulting in 3D LR patch image of 4 × 4 × 4 [voxel], in which voxel size is 0.56 × 0.528 × 0.56 [mm]. The batch size of the generator and discriminator was set to 16, and the Adam algorithm was used in the training process.

Figure 2 shows a part of a true HRCT volume of test dataset as well as the corresponding input LRCT, HRCT interpolated by tricubic, and proposed HRCT volumes, respectively. It is found from the figure that the 3D SRGAN succeeded to reconstruct detailed texture, while the HRCT by tricubic interpolation has blurring. We evaluated the performance by peak signal-to-noise ratio (PSNR), structural similarity (SSIM), and zero-mean normalized cross-correlation (ZNCC). The performance indices of the proposed SR based HRCT were 26.761 [dB] for PSNR, 0.557 for SSIM, and 0.853 for ZNCC, while those of tricubic interpolation were 25.258 [dB] for PSNR, 0.520 for SSIM, and 0.780 for ZNCC.

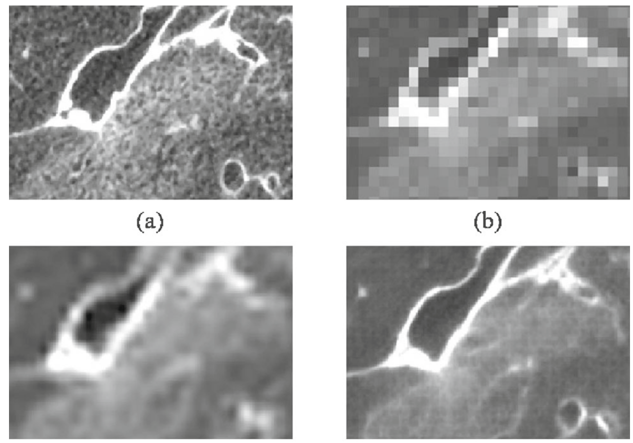

Fig. 2 Part of experimental results of a test volume. **a** True HRCT, **b** corresponding input LRCT, **c** HRCT interpolated by tricubic, and **d** proposed HRCT volumes

Conclusion

We proposed a 3D SRGAN-based super resolution of lung CT, in which a low-resolution CT volume is converted to a high resolution CT volume whose voxel size is eight times smaller than that of LRCT. The effectiveness of the proposed approach was confirmed using a micro CT volume of human lung specimen from the viewpoint of PSNR, SSIM, and ZNCC.

References

[1] Timofte R, Smet VD, Gool LV (2013) Anchored neighborhood regression for fast example-based super-resolution. Proc. of ICCV, pp. 1920–1927. https://doi.org/10.1109/iccv.2013.241

[2] Umehara K, Ota J, Ishida T (2017) Application of Super-Resolution Convolutional Neural Network for Enhancing Image Resolution in Chest CT. J Digital Imaging, pp. 1–10. https://doi.org/10.1007/s10278-017-0033-z

[3] Ledig C, Theis L, Huszar F, Caballero J, Cunningham A, Acosta A, Aitken A, Tejani A, Totz J, Wang Z, Shi W (2017) Photo-Realistic Single Image Super-Resolution Using a Generative Adversarial Network. Proc. of CVPR, pp. 4681–4690. https://doi.org/10.1109/cvpr.2017.19

3D-printed MRI marker for personalized interventional applications through T1 and T2 relaxation time matching

H. Mattern[1], R. Odenbach[2], P. Parsanejad[2], M. Friebe[2]
[1]Otto-von-Guericke-University, Biomedical Magnetic Resonance, Magdeburg, Germany
[2]Otto-von-Guericke-University, Catheter Technologies and Image Guided Therapies, Magdeburg, Germany

Keywords Personalised MRI marker · Relaxation time · 3D-printing · Interventional MRI

Purpose

For magnetic resonance imaging (MRI) guided minimal-invasive procedures the visualization of therapeutical instruments for biopsies, catheter placements, and tissue ablations, is absolutely essential. However, MR safe instruments usually are—depending on the material used—either not visible at all or only indirectly visible due to susceptibility artifacts generated by the device material.

To enable the essential instrument tracking in MRI we presented a fiducial maker which is fully additively manufactured out of a single polymer material [1, 2]. During the stereolithography fabrication process a solid body is printed while the internal z-shaped marker structure remains filled with the unhardened—thus liquid and MR visible—resin.

With prior knowledge of the resins relaxation times, the optimal resin for a given imaging protocol (e.g. liver biopsy) could be determined before marker fabrication. Each resin has a different chemical composition and, thus, potentially different longitudinal (T1) and transversal (T2) relaxation times. The contrast in MRI is largely driven by these relaxation times [3]. Therefore, the visibility of the liquid resin within the marker depends on the used imaging protocol and relaxation properties of the resin.

As a first step to enable MRI markers personalized to a given imaging scenario, this study aims to establish a protocol to determine T1 and T2 relaxation times of the resins used in the stereolithography process.

Methods

T1 and T2 relaxation times were experimentally determined for the initially selected stereolithography resins: VisiJet SL Tough, VisiJet SL Clear both from 3D Systems, Inc., and Formlabs FLGPWH03 from Formlabs Inc. Each of the three resins was stored in separate containers before placing them inside a transmit–receive birdcage head coil of a 3T Skyra MRI system (Siemens Healthineers, Germany).

Measurements were acquired with a spin echo (SE) sequence using a single 4 mm thick slice with 1 mm in-plane resolution), see Fig. 1. For T1 estimation an inversion recovery pulse was included and the inversion time (TI) was varied between measurements (five different TIs between 23 and 2000 ms). For the T2 estimation the echo time (TE) of the SE was varied accordingly (five different TEs between 5.5 and 200 ms).

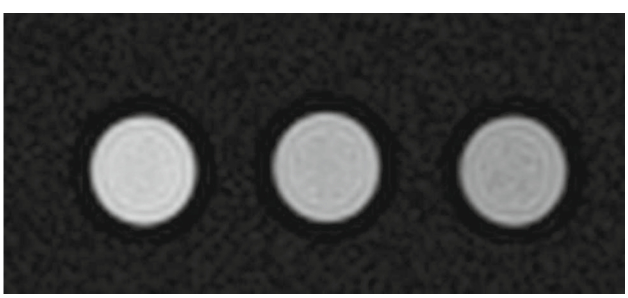

Fig. 1 Measured image slice of the three cylindrical resin containers (left: VisiJet SL Tough, middle: VisiJet SL Clear, right: Formlabs FLGPWH03)

Relaxation times were then calculated for each resin within automatically computed region of interests (based on image thresholding). For each voxel within the region of interest a mono exponential decay was fitted to the signal evolution over TI/TE. The final relaxation time was computed as the mean ± standard deviation over all voxel for a given resin. For the T1 relaxation the following signal equation was used [4]:

$$S(TI) = S_0(1 - 2\exp(-TI/T1))$$

with S(TI) as the mean measured signal at TI and S_0 capturing residual T2 weighting, proton density, and coil sensitivities. For the T2 relaxation time the following signal equation was used [4]:

$$S(TE) = S_0\exp(-TE/T2)$$

with S(TE) as the mean measured signal at TE and S_0 capturing proton density, and coil sensitivities. Goodness of fit was evaluated with the coefficient of determination (R^2).

All processing was done in MATLAB 2015b (MathWorks, USA).

Results

The T1 and T2 relaxation times (see Table 1) of the tested resins were calculated based on the experimental results. Figure 2 shows the mean fitted relaxation time compared to the measured signal. The overall goodness of fit for all estimates was high ($R^2 > 0.99$).

Table 1 Estimated mean ± standard deviation T1 and T2 relaxation times for three different resins

Resin	T1 relaxation time (ms)	T2 relaxation time (ms)
VisiJet SL tough	156.7 ± 2.9	23.2 ± 0.8
VisiJet SL clear	174.0 ± 16.7	20.7 ± 1.0
Formlabs FLGPWH03	162.6 ± 3.6	22.9 ± 1.2

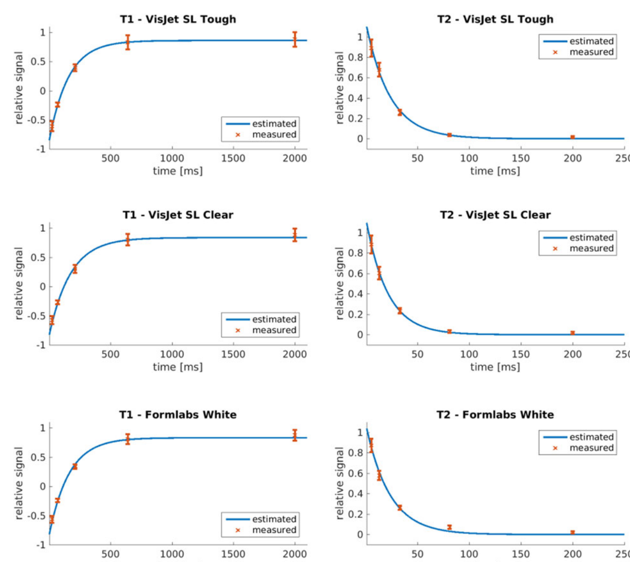

Fig. 2 Comparison of measured and estimated T1 and T2 relaxation times for three different resins. Measured data of the normalized signal intensity is shown as error bars (mean ± standard deviation). After fitting the signal model (using the mean T1/T2 from Table 1) the estimated relaxation curve is overlaid

T1 estimates for all resins differed among each other by up to 9.97% and had an average T1 relaxation time of 164.4 ms, which is considerably shorter than human tissue such as subcutaneous fat (382 ms), liver (809 ms), or the medulla of the kidney (1545 ms) [5].

T2 estimates for all resins differed among each other by up to 10.74% and had an average T2 relaxation time of 22.3 ms, which is shorter than human tissue such as subcutaneous fat (68 ms), liver (34 ms), or the medulla of the kidney (81 ms) [5].

Conclusion

This study determined the MRI T1 and T2 relaxation times for resins used to serve as MRI marker material for the first time. In the future, these results will enable to predict the marker visibility before scanning. Thus, for a given scenario in interventional MRI application (e.g. liver biopsy) the optimal marker can be fabricated with the optimal resin. However, relaxation times for more resins should be estimated in the future as the measured resins do not vary considerably among each other, limiting the potential for personalizing interventional applications through T1 and T2 relaxation time matching. Furthermore, extending the signal equation and MR measurement to account for system imperfections (e.g. imperfect inversion pulses, or transmit and receive inhomogeneities) might improve the estimates.

Acknowledgement

This work was funded by German BMBF 03IPT7100X and by the NIH, Grant No. 1R01-DA021146.

References

[1] Odenbach R, Grundmann M, Boese A, Friebe M (2016) Generatively manufactured, passive and safe MRI-marker. In 11th Interventional MRI Symposium, Baltimore

[2] Odenbach R, Chen Y, Sengupta S, Webster R, Barth E, Friebe M (2017) 3D-printed Z-frame marker for MRI-guided interventions. In 16. Jahrestagung der Deutschen Gesellschaft fuer Computer- und Roboterassistierte Chirurgie, Hannover

[3] Bloch F (1946) Nuclear induction. Physical review 70(7–8): 460.

[4] Tofts P (2005) Quantitative MRI of the brain: measuring changes caused by disease. John Wiley & Sons.

[5] De Bazelaire CM, Duhamel GD, Rofsky NM, Alsop DC (2004) MR imaging relaxation times of abdominal and pelvic tissues measured in vivo at 3.0 T: preliminary results. Radiology 230(3): 652–659.

Residual network-based unsupervised temporal image subtraction for highlighting bone metastases

S. Hanaoka[1], T. Masumoto[2], S. Hoshiai[2], Y. Nomura[3], T. Takenaga[3], M. Murata[3], S. Miki[3], T. Yoshikawa[3], N. Hayashi[3], O. Abe[1]

[1]The University of Tokyo Hospital, Dept. of radiology, Tokyo, Japan

[2]University of Tsukuba, Tsukuba, Japan

[3]The University of Tokyo Hospital, CDRPM, Tokyo, Japan

Keywords Bone metastasis · CT · Temporal subtraction · Residual network

Purpose

The purpose of this study is to develop a system to highlight bone metastasis lesions in a couple of time-series CT volumes. Using two time-series of CT datasets, our algorithm maximize the information of the intertemporal differences and highlight the metastases.

Methods

In our previous study, bony landmark detection and landmark-based demons algorithm which can register two bony images had been established. Furthermore, the bony regions (the spine and the pelvis) are automatically segmented. Using these methods, the previous and current CT volumes are registered and segmented. Then, the subtraction is performed by Residual network-based method. Firstly, from every voxel $\mathbf{x}$ in the given previous CT volume, a 15 × 15 × 15 adjacent voxel set $\mathbf{N}_{previous}(\mathbf{x})$ is extracted. This input is processed by a ResNet-based network illustrated in Fig. 1 right. Finally, this network outputs not only the estimated mean of the current CT image $\mu(\mathbf{x})$, but also the estimated standard deviation of the current CT image $\sigma(\mathbf{x})$.

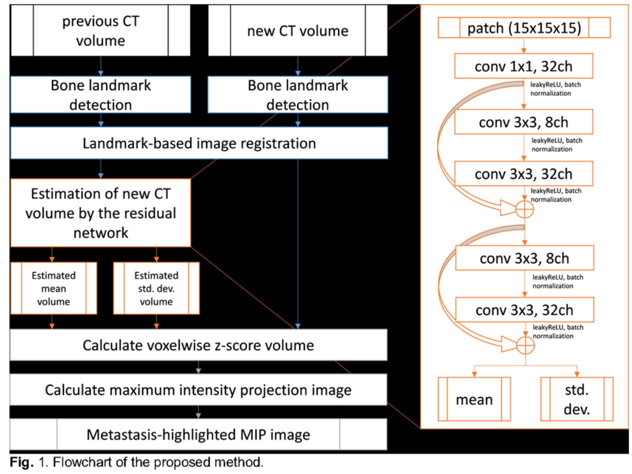

Fig. 1 Flowchart of the proposed method

In the training phase, this network only uses normal temporal pair cases (without bone metastasis). The proposed network estimates $\mathbf{N}_{previous}(\mathbf{x}) \rightarrow \mu(\mathbf{x}), \sigma(\mathbf{x})$. Here, let the CT value of current CT volume (which has been registered to the previous volume) at $\mathbf{x}$ be $I_{new}(\mathbf{x})$. It is assumed that $I_{new}(\mathbf{x}) \sim N(\mu(\mathbf{x}), \sigma(\mathbf{x}))$. Then, the proposed ResNet-based network estimates the best couple of μ and σ by minimizing the loss function $L = -\ln \Pr(I_{new}(\mathbf{x})|\mu, \sigma) = -[-1/2 \ln 2\pi - \ln\sigma(\mathbf{N}_{previous}(\mathbf{x})) - 1/2 \ (\{I_{new}(\mathbf{x}) - \mu(\mathbf{N}_{previous}(\mathbf{x})\}/\sigma(\mathbf{N}_{previous}(\mathbf{x}))^2]$. In other words, our ResNet estimates two functions $\mathbf{N}_{previous}(\mathbf{x}) \rightarrow \mu(\mathbf{x})$ and $\mathbf{N}_{previous}(\mathbf{x}) \rightarrow \sigma(\mathbf{x})$ simultaneously so as to minimize L. Again, note that this loss function minimization is performed only via normal temporal CT pairs in which no metastasis occurred. Thus, this study is a kind of unsupervised learning.

In the test phase, if there is a metastasis at position $\mathbf{x}$ in the current volume, the estimated z score $z(\mathbf{x}) = (I_{new}(\mathbf{x}) - \mu(\mathbf{N}_{previous}(\mathbf{x})))/\sigma(\mathbf{N}_{previous}(\mathbf{x}))$ should be a large positive (e.g. osteoblastic) or negative (e.g. osteolytic) value. Thus, in our implementation, after a sliding window method which makes a 3D z-score volume, both of these positive and negative value are highlighted by using maximum and minimum intensity projection (MIP & MinIP) techniques. Finally, a color map which illustrates both osteoblastic and osteolytic lesions is generated.

The training phase was performed with 50 normal CT temporal pairs. The test was performed with 40 CT temporal pairs in which bone metastases were occurred between the previous and current CT acquisitions. For each test dataset, colored MIP&MinIP images are created in order to grasp the entire bony lesion in one glance.

Results

The exemplar results of the proposed method is illustrated in Fig. 2. As illustrated, the proposed method could highlight both osteolytic and osteoblastic lesions. Among 40 test cases, 12 cases had image distortion/false positive due to large registration errors. However, most of false positives were suppressed due to introduction of the standard deviation. All of the 40 cases, the metastases were clearly highlighted.

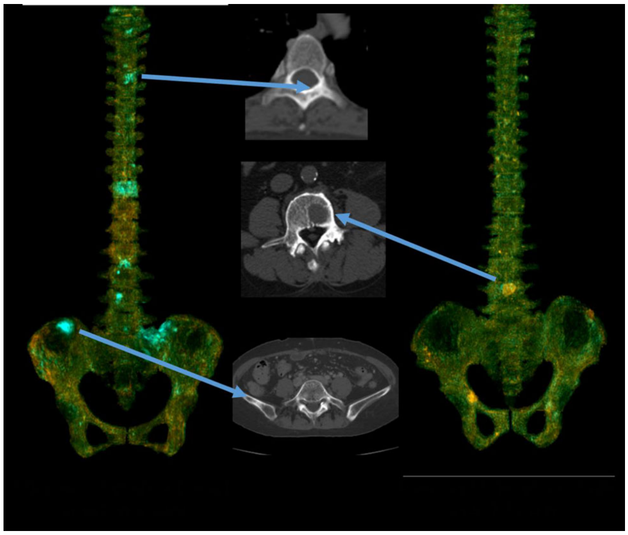

Fig. 2 Anexamplar results of our proposed method

Conclusion
A method to emphasize bony metastatic lesions is presented. Because the proposed method is unsupervised, it can be readily applied to daily clinical environment. Therefore, we consider that the proposed method is beneficial in routine CT examinations for patients with a cancer.

References
[1] Hanaoka S, Masutani Y, Nemoto M, Nomura Y, Miki S, Yoshikawa T, Hayashi N, Ohtomo K, Shimizu A (2017) Landmark-guided diffeomorphic demons algorithm and its application to automatic segmentation of the whole spine and pelvis in CT images. International journal of computer assisted radiology and surgery 12(3): 413–430.

Bi-planar low dose X-Ray method for personalised 3D modeling of the scapula and automated computation of morphological parameters

C. Bascans[1,2], N. Hagemeister[1,2], C. Zhang[1,3], F. Girinon[3], L. Gajny[3], P. Tétreault[4], W. Skalli[3]
[1]Centre de Recherche du CHUM, Laboratoire de recherche en imagerie et orthopédie, Montréal, Canada
[2]Ecole de Technologie Supérieure, Génie de la production automatisée, Montréal, Canada
[3]Institut de Biomécanique Humaine Georges Charpak, Arts et Métiers ParisTech, Paris, France
[4]Centre Hospitalier de l'Université de Montréal, Service d'orthopédie, Montréal, Canada

Keywords 3D modeling · Shoulder · Surgical planning · Validation

Purpose
In the literature, correlation between morphology of the scapula and rotator cuff tears is increasingly discussed. For example, the critical shoulder angle (CSA) is considered as a risk factor of tendinous degeneration [1] and on the success of anatomical total shoulder arthroplasty. Size of the glenoid and humeral head are also important pre-operative parameters for surgery planning. However, measurement of such parameters on a pre-operative X-Ray is not reliable because of out-of-plane errors [2]. Technologies that allow for three-dimensional reconstruction such as CT-Scan or MRI are either irradiating, expensive, or time consuming.

The objective of this study was to assess accuracy and reliability of a method which provides 3D personalized models of scapula and humerus with limited radiation using bi-plane radiography, in order to automatically acquire morphological parameters that are useful for surgical planning.

Methods
3D reconstructions were obtained from simultaneous bi-planar X-Rays taken in standing position with arms along the body and 30o orientation of the body with respect to radiographic plane.

Average models and geometric models
3D surface models of 40 scapula and 19 humerus obtained from CT scan were used in order to construct average models of both scapula and humerus. Two reduced scapula representations were also considered: 1/a so called contour model, constructed with one stereocorresponding contour (SCC) visible on both views, two non stereocorresponding contours (NSCC), only visible on one of them, and two landmarks always visible on at least one image (Fig. 1); and 2/a parametric model composed of geometric primitives associated to morphological parameters and their descriptors.

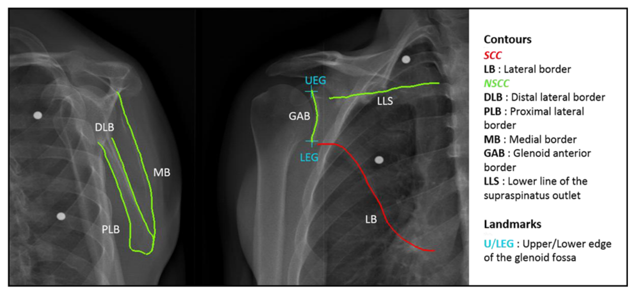

Fig. 1 Identification of contours and points on a set of radiographic images acquired with EOS system

Scapula 3D reconstruction
From contours identification on both X-Rays, the 3D orientation of the lateral border (LB) was computed.

The average contour model was then registered and pre-oriented using Procrustes method and rigid rotation around the LB axis to minimize distance between projected model landmarks and identified contours (NSCC).

Then the parametric model was activated and identified landmarks were used as control points for model deformation using a moving least square method, thus yielding an initial subject specific model.

This initial model was retroprojected on X-ray images, allowing for manual adjustments in order to improve consistency between contours of the model and those of X-Rays.

Humerus 3D reconstruction
Based on the a priori relation between humerus and scapula, the humerus parametric model was pre-positioned, considering humeral head center and the diaphysis axis that resulted from manual segmentation. The humerus model was again deformed using moving least square method.

Computation of the morphological parameters
14 morphological parameters, considered useful for surgical planning, were computed: length and width of the glenoid, morphological and positional glenoid inclination, glenoid version, critical shoulder angle, angle between spine of the scapula and the coracoid root, subacromial distance, humeral head offset with respect to glenoid, distance between acromion and greater tuberosity of the humerus and then between greater tuberosity and deltoid tuberosity (represents a simplified trajectory of the deltoid), humeral head radius and inclination, length of the scapula neck.

Method evaluation: accuracy and reproducibility

Accuracy was estimated on digitally reconstructed radiographs (DRR) from six cadaveric specimens. 3D reconstructions from CT Scan images of these specimens were obtained using AVIZO software (FEI, USA). The 14 above-mentioned morphological parameters were extracted from these reconstructions, and compared with those pertaining from the 3D reconstructions obtained from the DRR. Bias was assessed for each of the six specimens in mm or degrees on the values of the morphological parameters.

Reliability was analyzed by the intra- and inter-operator reproducibility, following recommendations from 5725-2:1994 ISO standards. This has been performed on twelve in vivo subjects: six healthy ones, four with rotator cuff tears, one with glenoid arthritis, one with a reverse shoulder prosthesis. Acquisitions were performed within clinical routine assessment using the EOS low dose biplanar X-Ray system. Two operators repeated the 3D reconstruction twice. A confidence interval at a level of confidence of 95% (95% CI) estimated at $2\times$ SR (reproducibility standard deviation) has been considered as an indicator of the overall reliability uncertainty on the value of the morphological parameters.

Results

The time required to obtain one complete personalised model (Fig. 2) of the scapula and humerus was approximately 10 min. Glenoid version and radius and inclination of humeral head were the 3 most repeatable parameters (95% CI $< 1.5°$ and 1.3 mm).

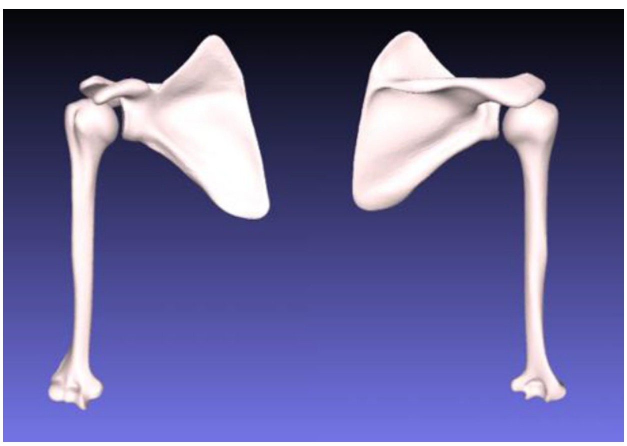

Fig. 2 3D personalized model of a right shoulder with supraspinatus and subscapularis tears (posterior view on the left, anterior view on the right)

Parameters have been divided in two groups with respect to their accuracy/reliability:

Group I: High accuracy/strong reliability

- *|Accuracy | < 1 mm/° and 95% CI < 3 mm/*
- Length, width and version of the glenoid
- Subacromial distance
- Humeral head offset with respect to glenoid
- Radius of the humeral head
- Length of the neck of the scapula

Group II: Acceptable accuracy/lower reliability

- *|Accuracy| < 2 mm/° and 95% CI < 5 mm/°*
- Morphologic and positional glenoid inclination
- Critical shoulder angle
- Angle between spine of the scapula and the coracoid root
- Simplified trajectory of the deltoid
- Humeral head inclination

Conclusion

The 3D reconstructions obtained from the EOS biplanar X-ray system were less time consuming than from CT Scans and much less irradiant. Of the 14 parameters automatically computed, most of them have acceptable accuracy (< 1 mm) and a reproducibility close to what is presented in the literature [3]. Interestingly, the method shows good reliability on healthy, as well as on pathologic and prosthetic patients. A limitation is that the study of accuracy has been made on cadaveric specimen using digitally reconstructed images. Identification of contours and landmarks is also semi-manual. However, image-processing techniques might soon allow for automated landmark identification in the future.

References

[1] Moor BK, Wieser K, Slankamenac K, Gerber C, Bouaicha S (2014). Relationship of individual scapular anatomy and degenerative rotator cuff tears. *Journal of shoulder and elbow surgery, 23*(4), 536–541.

[2] Suter T, Popp AG, Zhang Y, Zhang C, Tashjian RZ, Henninger HB (2015). The influence of radiographic viewing perspective and demographics on the critical shoulder angle. *Journal of shoulder and elbow surgery, 24*(6), e149-e158.

[3] Dumas R, Blanchard B, Carlier R, de Loubresse CG, Le Huec JC, Marty C, Moinard M, Vital JM (2008). A semi-automated method using interpolation and optimisation for the 3D reconstruction of the spine from bi-planar radiography: a precision and accuracy study. *Medical & biological engineering & computing, 46*(1), 85–92.

Measurement of moisture at skin surface with hyperspectral imaging

M. Maktabi[1], C. Chalopin[1], H. Köhler[1], T. Neumuth[1]

[1]Universität Leipzig, Innovation Center Computer Assisted Surgery, Leipzig, Germany

Keywords Hyper spectral imaging · Moisture · Gustatory sweating · Skin surface

Purpose

Hyperspectral imaging (HSI) is a contact-free, non-invasive and non-contrast-agent imaging technology. It is the combination of a spectrometer with a visual camera. An object is illuminated by a light source in the visual range and the light remitted by the object is recorded by the camera and split into single wavelengths. A 3D data cube is generated, consisting of 2D spatial dimensions and the wavelengths as third dimension. HSI technology provides new opportunities to measure essential information. Perfusion parameters like oxygen saturation and tissue haemoglobin concentration can be recorded. These are crucial values to monitor patient state. In several clinical research areas, like monitoring of diabetic foot and skin ulcer [1], tissue perfusion measurements [2], wound analysis [3, 4] and flap monitoring [5] the applicability of HSI was demonstrated.

The moisture volume measurement of skin is a new clinical application. In the clinical area, it could be applied to patients with gustatory sweating. This pathology is caused by the damage of the auriculotemporal nerve that goes to the parotid gland. Pathological sweating occurs immediately after ingesting food and is usually located on one side of the face. Currently, physicians have only a patient-depended grading of the sweating, use iodine and powder to only localize the sweating area. However, the moisture volume at the skin is so far not measured quantitatively. The assessment of severity of the sweating varies a lot according to patients. In this work we want to evaluate HSI for the detection of sweating with the purpose to better assist the physician in the treatment of patients with gustatory sweating.

Methods

1 Data acquisition

We used the HSI camera system TIVITA-Tissue of the company Diaspective Vision GmbH (Germany). Light spectra are measured in the range from 500 to 1000 nm (resolution: 5 nm). The camera unit is a CMOS camera (spatial resolution: 640 × 480 pixels per image). The system includes an illumination unit containing eight 20 W halogen lamps. The camera was positioned at a distance of 80 cm to the object during acquisitions. This distance was chosen to avoid evaporation of water and sweating due to illumination.

The camera parameterization and data acquisition is performed by the software TIVITA Suite (Diaspective Vision GmbH, Germany). The acquired hyperspectral cube was exported in Matlab 2014b to plot and process the recorded spectra. We calculated the absorbance spectra based on the negative decadic logarithm of the signal directly measured by the system. Afterwards, we smoothed the spectra with a Gaussian filter.

2 Study Design

In a first study we examined if moisture at the skin surface can be detected by the HSI system. For that, 0.1 ml water measured using a pipette was dropped on the back of the hand and on the foot on a limited area of 2 × 3 cm^2. This volume of water corresponds to small moisture volume at the skin. We measured the absorbance spectrum once before pipetting and four times after, in the same camera position and at the same subject (totally: 40 acquisitions).

In the second study we studied if sweating can be detected on the skin. For that, two subjects were asked to perform 15 min of sport activity (e.g. jogging, sit ups). Subject foreheads were recorded because many sweat glands are in this face area. Acquisitions were performed before and during the sport activity, every 5 min (totally: 14 acquisitions). After the 5 first minutes of activity the sweating of the subjects was not visible but palpable. After 15 min of activity sweating was visible.

Results

1 Detection of water at skin surface

We calculated the mean absorbance spectra of a region of interest of the skin before and after pipetting. The second derivatives of the spectra point out minor differences in the near infrared area, especially at 960 and 970 nm, for measurements with and without water (Fig. 1). A higher difference was directly after the pipetting of the water. Few minutes later the water at skin surface evaporated and the spectra with water converge to the spectra without water. The spectra of hand showed higher variation than the spectra of feet.

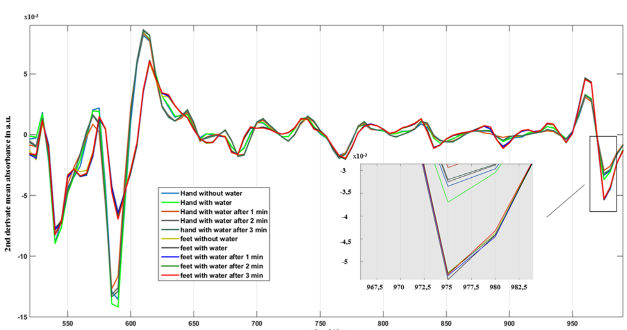

Fig. 1 The curvature of the feet and hand with and without water is shown. Especially the differences of the spectra at 970 nm were depicted

2 Detection of sweating at skin

We calculated the mean absorbance spectra in a region of the forehead. The largest absorbance during sport activity can be explained by an increase of tissue perfusion. The representation of the second derivative (Fig. 2) shows the increase of water content at 830, 875 and 960 nm in the near infrared range of the spectrum during sport activity (black arrow). Especially, differences are depicted already after 5 min of sport activity although no sweat was still visible on the forehead. An explanation could be the ability of the camera in performing measurements in the near infrared range which allows examining the depth of tissue until circa 10 mm.

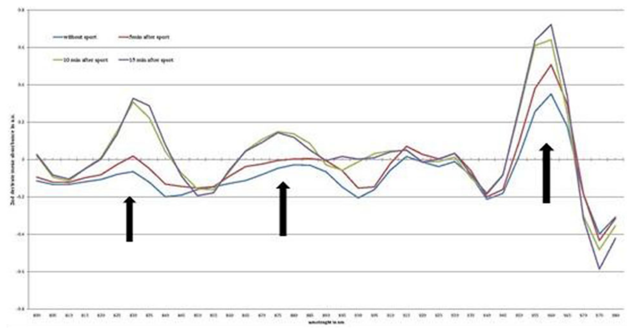

Fig. 2 The representation of the second derivative shows increase of water content at 830, 875 and 960 nm (black arrow) during sport activity

Conclusion

The measurement of water at skin surface was difficult. The applied water volume scattered at the skin surface. However, the experiments could clearly show the impact of the presence of water in the spectra of the hand and foot. In further studies the impact of different water volumes on the skin will be considered.

The measurement of sweating showed changed spectra if the subject performed sport activity. Especially the range between 850 and 950 nm (near infrared range) showed a modified gradient. It means that sweating was measurable before it is external visible at skin surface.

However, the physiological process plays a key role in these experiments and further examinations are necessary. Moreover, a new water index could be defined based on the first observations. The quantitative monitoring of gustatory sweating patients could be a clinical application.

References

[1] Chin MS1, Freniere BB, Lo YC, Saleeby JH, Baker SP, Strom HM, Ignotz RA, Lalikos JF, Fitzgerald TJ (2012) Hyperspectral imaging for early detection of oxygenation and perfusion changes in irradiated skin, *Journal of biomedical optics*, vol. 17, no. 2, p. 26010

[2] Myers, M. McGraw, M. George, K, Mulier, G. Beilman (2009) Tissue hemoglobin index: a non-invasive optical measure of total tissue hemoglobin, *Critical care (London, England),* vol. 13 Suppl 5, S2

[3] Calin MA, Coman T, Parasca SV, Bercaru N, Savastru R, Manea D (2015) Hyperspectral imaging-based wound analysis using mixture-tuned matched filtering classification method, *Journal of biomedical optics,* vol. 20, no. 4, p. 46004

[4] Paul DW, Ghassemi P, Ramella-Roman JC, Prindeze NJ, Moffatt LT, Alkhalil A, Shupp JW (2015) Noninvasive imaging technologies for cutaneous wound assessment: A review. Wound Repair Regen. 2015 Mar-Apr; 23(2): 149–62

[5] Fox M, Zeidler K, Carey J, Lee GK (2013) White light spectroscopy for free flap monitoring *Microsurgery*, vol. 33, no. 3, pp. 198–202

Investigation of local liver strain derived from deformation fields used for radioembolization planning of the liver

N. Spahr[1], S. Thoduka[2], N. Abolmaali[2], A. Schenk[3]
[1]Fraunhofer Institute for Medical Image Computing MEVIS, Lübeck, Germany
[2]Städtisches Klinikum Dresden, Department of Radiology, Dresden, Germany
[3]Fraunhofer Instutite for Medical Image Computing MEVIS, Bremen, Germany

Keywords Image registration · Deformable registration · Liver strain · Radioembolization

Purpose
Transarterial radioembolization is a local radiotherapy used in interventional radiology to treat unresectable liver tumors or metastases. A number of imaging modalities are involved in the patient assessment and radioembolization planning process. For example, liver volume and tumor burden calculations are performed on hepatic venous contrast-enhanced CT or contrast-enhanced T1-weighted MRI. Deformable image registration can be used to combine information from both modalities and the analysis of the resulting deformation field may be helpful to gain new insights about tissue characteristics and local liver strain.

Methods
A variational image registration framework [1] was used for deformable multi-modal hepatic venous CT-MRI registration. The registration model uses normalized gradient fields [2] as distance measure, curvature regularization [3], and volume regularization [1] to obtain smooth deformations. A total of 21 CT-MRI image pairs of patients, who underwent radioembolization at Städtisches Klinikum Dresden, Germany, wereretrospectively analyzed. The anatomical correspondence provided by the fully-automatic image registration was assessed by manually placed landmarks inside the liver volume. Deformation characteristics representing tissue compressibility, regularity, and physical plausibility were determined by a detailed investigation of the deformation fields. The physical behavior of the deformation fields can be described by the determinant of the Jacobian matrix of the deformation field. Positive values indicate transformation consistency. The divergence of the deformation field represents the volume density of outward flux. In addition, the strain tensor can be derived from the deformation gradient. The octahedral shear strain specifies the maximum value of shear strain on any octahedral plane [4]. Local three-dimensional distributions of strain inside the liver were visually inspected. In order to analyze the distribution of local strain, the center of gravity of a semi-automatically defined liver mask was determined. Afterwards, the octahedral shear strain was investigated as a function of distance from the liver center of gravity.

Results
Good anatomical correspondence and plausible deformations were determined by the deformable image registration. The mean landmark distance was 4.49 mm for an average of 8 corresponding landmarks per image pair. The deformation fields showed no foldings. Mean minimum and maximum Jacobian determinant was 0.5 and 1.7 resp., demonstrating volume changes of approximate halving or doubling of single voxel cell volume. The mean average divergence was 0.16. For an exemplary case, the derived octrahedral shear strain inside the liver is visualized in Fig. 1. From visual inspection, low strain values can be determined near the center of the liver increasing towards the liver periphery as expected. This tendency is also shown by the distribution of strain as a function of distance from liver center (cf. Fig. 2).

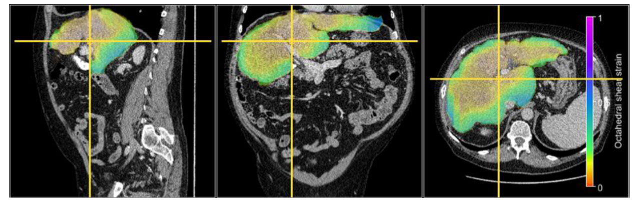

Fig. 1 Overview of octahedral shear strain in cross-sectional slices, sagittal (left), coronal (middle), and axial (right). The cross-hair position indicates the liver center of gravity

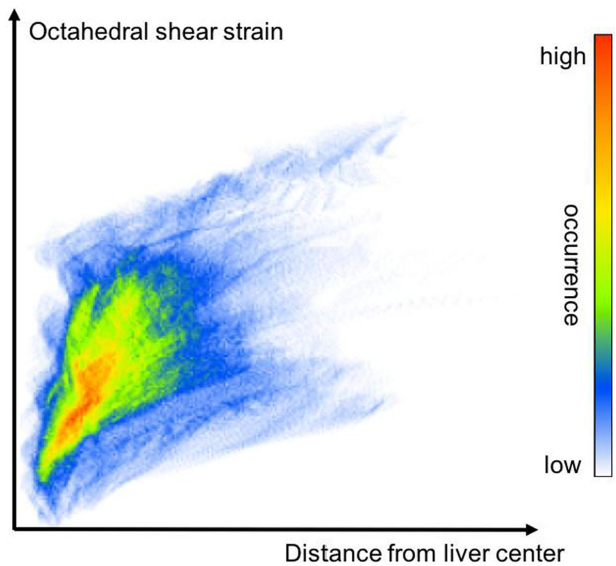

Fig. 2 Distribution of octahedral shear strain as a function of distance from the liver center of gravity

Conclusion
The presented results demonstrate a global tendency of increasing strain from the liver center to the periphery. This leads to the conclusion that local liver strain, derived from deformation fields via deformable image registration, might correlate according to its anatomical position. Further investigation of the three-dimensional distributions of octahedral shear strain including quantitative evaluations and detailed analysis of local deviations with respect to tissue properties and parenchymal liver diseases are planned for the future.

References
[1] Rühaak J, Heldmann S, Kipshagen T, Fischer B (2013) Highly accurate fast lung CT registration. In: SPIE Medical Imaging 2013: Image Processing, Lake Buena Vista, Florida, USA
[2] Haber E, Modersitzki J (2007) Intensity gradient based registration and fusion of multi-modal images. Methods Inf Med 46(3): 292–299
[3] Fischer B, Modersitzki J (2003) Curvature based image registration. J Math Imaging Vis 18: 81–85
[4] McGarry MDJ, Van Houten EEW, Perrinez PR, Pattison AJ, Weaver JB, Paulsen KD (2011) An octahedral shear strain based measure of SNR for 3D MR elastography. Phys Med Biol 56(13): N153-N164

Automatic segmentation of uterus with malignant tumor on MRI using U-net

Y. Kurata[1,2], M. Nishio[1,3], K. Fujimoto[4], M. Yakami[1,3], A. Kido[1], H. Isoda[1,3], K. Togashi[1]
[1]Kyoto University Graduate School of Medicine, Department of Diagnostic Imaging and Nuclear Medicine, Kyoto, Japan
[2]Kobe City Medical Center General Hospital, Department of Diagnostic Radiology, Kobe, Japan
[3]Kyoto University Hospital, Preemptive Medicine and Lifestyle Disease Research Center, Kyoto, Japan
[4]Kyoto University Graduate School of Medicine, Human Brain Research Center, Kyoto, Japan

Keywords U-net · Uterus · Segmentation · MRI

Purpose

Uterine MRI is performed for various kinds of benign and malignant gynecologic disorders. In today's clinical practice, MRI is widely used and useful for the differential diagnosis and clinical staging of malignant tumors. In order to implement computer-aided diagnosis of uterine disorders on MRI, the segmentation of uterus could be essential. For bio-medical image segmentation, a fully convolutional neural network named U-net has recently shown promising results [1]. Original U-net architecture consists of a contracting path for capturing context using convolution and max pooling, and a symmetrical expansive path for localization. In the expansive path, U-net uses many feature filters, and this enables the network to propagate context information to higher resolution layers. In this research, we optimized architecture of U-net for automatic segmentation of uterus with malignant tumor on MRI. To our knowledge, this is the first trial of uterine segmentation on MRI with U-net.

Methods

Uterine MR images of 52 uterine cervical cancer patients (53 studies) were available from The Cancer Genome Squamous Cell Carcinoma and Endocervical Adenocarcinoma data collection in The Cancer Imaging Archive [2, 3]. All patients had visible malignant tumor on MRI. Sagittal T2-weighed images reformatted to 512 × 512 pixels were used for this study, and the input data to our U-net architecture were three consecutive MR images of 512 × 512 pixels. In each scan of MR images, a board-certified radiologist specializing in gynecology manually segmented uteruses including areas with tumor, and these images were used as the reference standard. From 53 studies, 1477 sets of three consecutive image slices were obtained. From these image sets, 996 sets of images from 35 patients and 481 sets of images from 17 patients were used for training of our method and evaluation of its performance, respectively. Before utilizing these MR images, MR signal intensity (SI) was normalized using the mean and SD of SI of the T2-weighted images. A representative example of our U-net architecture employed in this study is shown in Fig. 1. The number of convolution layers in the contracting path was denoted by L, and the number of deconvolution layers in the expansive path was identical to that of convolution layers in the contracting path. The number of filters at the first convolution layers is denoted by F. In our architecture, the size of input images was downsized and upsized by convolution and deconvolution layers, respectively. As shown in Fig. 1, the number of filters at the second and third convolution layers was doubled, compared with the previous convolution layer. To evaluate the effect of L and F, the following values were used: for L, five, seven and nine; for F, two, four, eight and twelve. For improving convergence speed during training phase, batch normalization was adopted after convolution. The output was the predicted segmentation of uterus resulting in three consecutive images of 512 × 512 pixels. As there was a little MRI data available in our study, data augmentation was used during the training phase. The negative Dice coefficient was applied as the loss function.

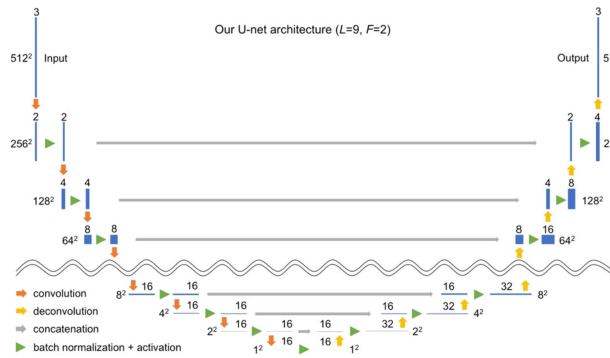

Fig. 1 One representative model of our U-net architecture. This model consists of nine convolution layers and two filters at the first convolution layer

Results

Dice coefficient for evaluation dataset with each parameter is presented in Table 1. The U-net architecture with nine convolution layers and twelve filters at the first convolution layer presented the highest score (0.704). Architectures with deeper layers and more filters at the first convolution layer showed higher Dice coefficient. An actual prediction of uterus segmentation with our architecture is shown in Fig. 2.

Table 1 Dice coefficient of U-net architecture with each parameter

N I F	2	4	8
5	0.478	0.464	0.412
7	0.579	0.494	0.641
9	0.611	0.604	0.655

L number of convolution layers, F number of filters at the first convolution layer

Fig. 2 Left: Sagittal T2-weighted MR image. Right: The prediction result of uterus segmentation corresponding the left image

Conclusion

This study demonstrated the feasibility of automatic segmentation of uterus with malignant tumor on MRI using U-net. Architecture with the deepest layers and the largest number of filters at the first convolution layer yielded the best performance.

References
[1] Ronneberger O, Fischer P, Brox T (2015) U-net: Convolutional networks for biomedical image segmentation. International Conference on Medical Image Computing and Computer-Assisted Intervention. Springer International Publishing
[2] Lucchesi FR., Aredes ND (2016) Radiology Data from The Cancer Genome Atlas Cervical Squamous Cell Carcinoma and Endocervical Adenocarcinoma [TCGA-CESC] collection. The Cancer Imaging Archive. http://doi.org/10.7937/K9/TCIA.2016.SQ4M8YP4
[3] Clark K, Vendt B, Smith K, Freymann J, Kirby J, Koppel P, Moore S, Phillips S, Maffitt D, Pringle M, Tarbox L, Prior F (2013) The Cancer Imaging Archive (TCIA): Maintaining and Operating a Public Information Repository, Journal of Digital Imaging, 26(6): 1045–1057

Deep learning based segmentation of organs of the female pelvis in CBCT scans for adaptive radiotherapy using CT and CBCT data

A. Haensch[1], V. Dicken[1], T. Gass[2], T. Morgas[3], J. Klein[1], H. Meine[1,4], H. K. Hahn[1]
[1]Fraunhofer MEVIS, Bremen, Germany
[2]Varian Medical Systems Imaging Laboratory GmbH, Baden-Dättwil, Switzerland
[3]Varian Medical Systems, Las Vegas, NV, United States
[4]University of Bremen, Bremen, Germany

Keywords Deep learning · Segmentation · Female pelvis · Radiotherapy

Purpose
Radiotherapy (RT) planning involves careful delineation of target organs and organs at risk for dose calculation. Adaptive RT additionally allows for adapting the treatment plan to changes in shape, size or position of organs. Often this will be based on low-dose cone-beam CT (CBCT) scans from a scanner integrated with the RT treatment device. Manual delineation of such data is too time-consuming and thus infeasible, therefore automatic approaches are highly desirable. However, CBCT images can include a variety of artifacts [1], which makes automatic segmentation of CBCT images difficult. A popular approach is to use deformable image registration in order to propagate contours from the initial planning CT to the CBCT scans [2], which is not always an accurate process. We aim to apply deep learning for direct segmentation of the important female pelvic risk structures bladder, rectum and uterus in CBCT images. As the data typically is not manually segmented in the clinic, only a small number of patients with reference annotations is available which is a challenge for deep learning. Therefore, we investigate the use of contoured CT scans in addition to CBCT related contours during training with the idea to increase the anatomical variety in the training set.

Methods

Data
The dataset for training and validation consisted of 124 pelvis CBCT scans from 5 female patients taken at each RT fraction and pelvis CT scans contoured for RT planning from 88 distinct female patients. For testing, an additional patient with 28 CBCT scans was available. All volumes had annotations for bladder, rectum and uterus. Contours were converted to mask images by encoding each structure in a different bit. The data were preprocessed by resampling to 1.5 mm isotropic resolution and by removal of the treatment couch via masking of the patient volume.

Neural network and training
We trained a 3D U-Net with some modifications to the original network described in [3] on an NVIDIA GTX 1080. We implemented only 3 resolution levels which resulted in a receptive field of each output neuron of 44^3 or $(66\ \mathrm{mm})^3$. Furthermore, the network had 4 output channels in order to distinguish background, bladder, rectum and uterus. It was trained using stochastic gradient descent on patches of $60 \times 60 \times 60$ voxels (input patch size) which were drawn from a bounding box with voxel margin 60 around the three target structures. Training batches of size 4 were composed such that each batch contained one patch with background only and 3 patches with at least one foreground voxel to account for low foreground percentage. The loss function was chosen to be soft Dice.

The U-Net was trained multiple times following a leave-one-out scheme for the 5 training CBCT patients. Each training was performed once with and once without including the CT data into training giving a total of 10 trained networks. For each training, the left out patient data was used for validation. During training, we logged the best performing model parametrization based on the highest Jaccard coefficient at the validation steps.

Post-processing and evaluation
Each network was used to segment the three organs on the remaining 6th test patient's 28 CBCTs that were used neither for training nor validation. The output was binarized via thresholding at 0.5 and the largest connected component in each foreground channel was taken as segmentation result. Dice scores were chosen as metric for quantitative evaluation. Statistical significance was determined using the Wilcoxon signed rank test at significance level 0.05.

Results
Figure 1 shows Dice scores obtained on bladder, rectum and uterus on the CBCT data of the test patient. For the sake of clarity, only the mean per case Dice of the 5 associated networks from the leave-one-out training is plotted for training on CBCT versus CBCT plus CT. In the case of bladder and uterus, the mean per case Dice is always higher using models trained also on CT than using CBCT based models only. For the bladder, the median increases significantly from 0.805 to 0.885, for the uterus it increases significantly from 0.600 to 0.757. In the case of rectum, the median increases not significantly from 0.702 to 0.707 when adding CT data to the training. Figure 2 shows segmentation results on a CBCT scan of the test patient. Especially for the uterus, the segmentation quality is clearly improved when CT images are added to the training. The bladder segmentation is improved especially at the anterior part of the structure. The rectum segmentation is similar in both cases. These qualitative observations reflect the quantitative results observed in Fig. 1.

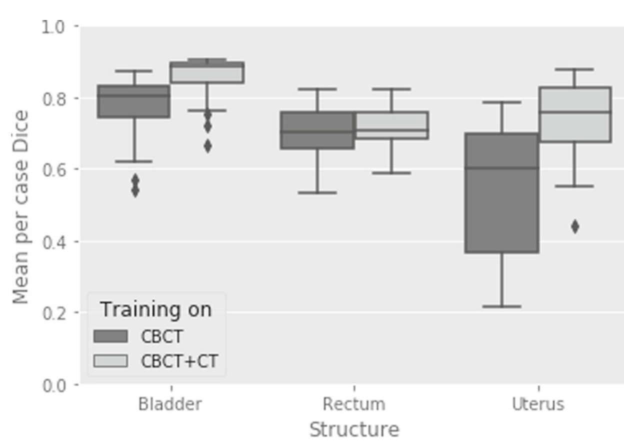

Fig. 1 Boxplot of the per case Dice scores for bladder, rectum and uterus on the independent CBCT test data averaged over 5 models trained with leave-one-out scheme on CBCT data only versus CBCT and CT data

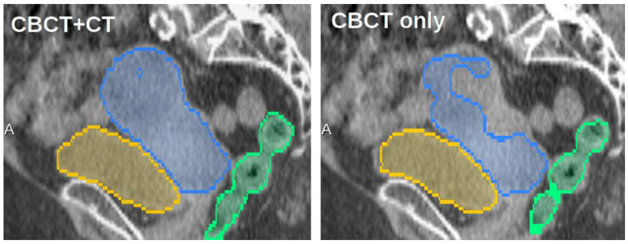

Fig. 2 Sagittal view of a CBCT scan of the testing patient. Including CT data into training improves the network's prediction versus training on CBCT only

Conclusion

Our preliminary results suggest that extending the rather small available training set of contoured female pelvis CBCT scans by additional CT scans is beneficial for the segmentation quality. We suppose that this is due to the increased anatomical variety from just 4 patients to 92 different patients when including the CT data into training as well. In order to confirm the results, we aim to collect more contoured CBCT data from several independent patients. Furthermore, we plan to compare to contours produced by contour propagation using the currently favored methods based on deformable registration.

Acknowledgements

The research was funded by Varian Medical Systems and the Fraunhofer project QuantMed.

References

[1] Schulze R, Heil U, Groβ D, Bruellmann DD, Dranischnikow E, Schwanecke U, Schoemer E (2011) Artefacts in CBCT: a review. Dentomaxillofac. Radiol. 40(5): 265–273

[2] Lim-Reinders S, Keller BM, Al-Ward S, Sahgal A, Kim A (2017) Online Adaptive Radiation Therapy. Int. J. Radiat. Oncol. Biol. Phys. 99(4): 994–1003

[3] Çiçek Ö, Abdulkadir A, Lienkamp S, Brox T, Ronneberger O (2016) 3D U-Net: Learning Dense Volumetric Segmentation from Sparse Annotation. MICCAI LNCS 9901: 424–432

Segmentation of breast from T1-weighted MRI: error analysis

H. Rusinek[1], A. Mikheev[1], L. Heacock[1], A. Melsaether[1], L. Moy[1]
[1]New York University School of Medicine, Radiology, New York, United States

Keywords Medical image analysis · Image segmentation · Breast MRI · Error analysis

Purpose

Our aim was to evaluate the accuracy of a new algorithm to automatically delineate the breast region from the chest on T1-weighted, non-fat-suppressed MR images. This process is also referred to as the chest wall detection. There is a general agreement that this step is very difficult to automate. At the same time it is crucially needed for clinically important processing workflows [1]. These workflows include 3D measurement of breast density and of the breast parenchymal enhancement. Both measures reveal patients at risk of breast cancer [2]. Manually traced chest wall was used as the ground truth when estimating the segmentation errors. Segmentation accuracy was evaluated using the Hausdorff distance and the volumetric error. We also estimated the inter-observer agreement in defining the chest wall surface.

Methods

The program starts by generating the mid-sagittal 2D section by averaging the signal across 20 mm thick mid-sagittal slab. We determine the chest wall boundary on this image by modeling the signal profiles along the antero-posterior direction as a sequence of three tissues: background air, skin and fat layer, muscle.

Non-uniformity correction is then applied to the entire 3D volume. The mid-sagittal boundary, represented as a polyline *P*, is then propagated in two opposite (left and right) directions. At each sagittal section the algorithm adjusts the control points of the polyline received from an adjacent slice. The adjustment is estimated from the weighted sum of six measures that combine specific local and global signal statistics. These include: the local gradient, the signal uniformity, the gradient similarity, the contour-gradient consistency, the global contour uniformity and the normal vector consistency. At each iteration we form a candidate shift vector, we apply it to shift *P* to its new position, and then we smooth the resulting polyline. The process terminates when the magnitude of the shift becomes negligible or when the specified number of iterations is exceeded.

Two metrics were used to estimate accuracy. The conventional volumetric error was obtained by dividing the volume DV of misclassified breast voxels over the true breast volume V. The Hausdorff distance, HD, is the distance between each voxel on the true breast/chest wall border and the closest boundary voxel produced by the algorithm. HD is averaged over the entire chest wall surface.

From a clinical database of screening breast MRIs acquired at our medical center we have randomly selected 16 test exams. The selection was constrained to enforce that there were four exams in each of the four breast density categories [3].

Bilateral breasts were imaged on Siemens 3T Magnetom Trio equipped with a 7-element surface breast coil. The parameters of the T1-weighted non-fat-suppressed sequence were: TR = 4.74 ms, TE = 1.79 ms, FOV = 320 mm2, matrix = 448 × 358 × ∼ 150, 0.7 × 0.7 × 1.1 mm voxels, TA = 2–3 min.

Three experts in breast and chest anatomy drew contours to separate the chest wall from the breast (Fig. 1). The pectoralis fascia and pectoralis muscles were used as reference points for the anterolateral borders. The medial border of the axilla was the posterolateral boundary. The axillary tail was considered as the breast tissue. The ground truth references were constructed by a software designed to perform voxel-based ROI averaging [4].

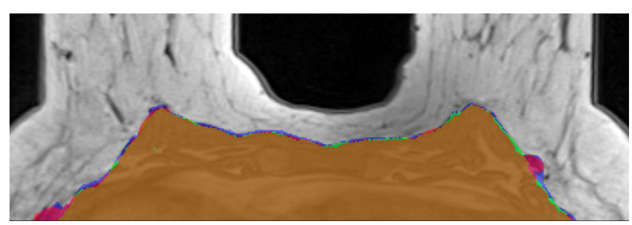

Fig. 1 The masks drawn by 3 experts are shown in different colors: observer 1 only = red, observer 2 only = green, observer 3 only = blue. The area of overall agreement is in brown

Results

The border distance error HD was 0.84 ± 0.8 mm (average ± standard deviation) and ranged from 0.57 to 2.45 mm. The volume error DV/V was 6.43 ± 6.82%. There was no correlation between the HD and DV/V (R^2 = 0.23, p = 0.12). The test cases covered a wide range 411–3439 ml of breast volumes. There was a significant positive correlation (R^2 = 0.40, p = 0.02) between volumetric error and the true breast volume V, but there was no correlation between HD and V (R^2 = 0.08, p = 0.44). The average execution time was under 1.5 min per case on a standard 8-core workstation.

The inter-observer agreement measured in term of HD was 0.56 ± 0.15 mm (average $\pm$ standard deviation). The agreement expressed in terms of volumetric discrepancy (relative to breast volume) was $1.61\% \pm 0.71\%$.

Conclusion

Breast density, defined as fraction of fibroglandular tissue, and post-contrast enhancement, are considered significant risk factors for breast cancer. These MRI measures are recommended for radiologic reports and are promising cancer biomarkers. Radiologists currently visually estimate these measure. Unfortunately, readers agreement for qualitative evaluation is only fair, requiring better standardization and reproducibility.

Computer-assisted quantitative assessment is needed, but the task is challenging due to image nonuniformity (breast coils cause loss of MR signal in remote regions) and to the anatomical complexity of chest wall boundary (Fig. 2).

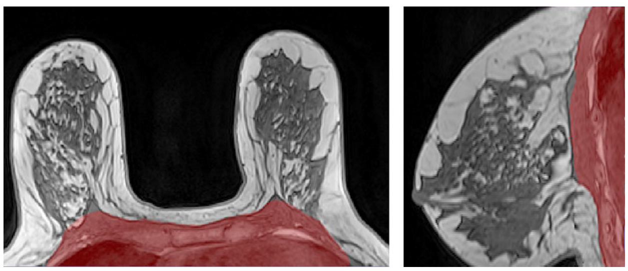

Fig. 2 A representative segmentation result. The chest wall mask, in red, is superimposed on the original T1-weighted MRI

Given its accuracy and speed, our breast segmentation method appears to be ready for clinical use as a part of larger workflow to generate routine diagnostic reports.

References

[1] Milenkovic J, Chambers O, Music MM, Tasic JF (2015) Automated breast-region segmentation in the axial breast MR images. Comput Biol Med 62: 55–64.

[2] Dontchos BN, Rahbar H, Partridge SC, Korde LA, Lam DL, Scheel JR, Peacock S, Lehman CD (2015) Are qualitative assessments of background parenchymal enhancement, amount of fibroglandular Tissue on MRI, and mammographic density associated with breast cancer risk? Radiology 276(2): 371–380.

[3] Morris EA, Lee CH, et al. (2013) ACR BI-RADS® Magnetic Resonance Imaging. In: ACR BI-RADS® Atlas, Breast Imaging Reporting and Data System. Reston, VA, American College of Radiology.

[4] Warfield SK, Zou KH, Wells WM (2004) Simultaneous truth and performance level estimation (STAPLE): an algorithm for the validation of image segmentation. IEEE Trans Med Imaging.: 23(7): 903–921.

Fully automatic segmentation of ischemic stroke lesion in 3D MRI images using deep convolutional neural networks with adversarial training

C. W. Mok[1], C. S. Chung[1]

[1]Hong Kong University of Science and Technology, Computer Science and Engineering, Hong Kong, Hong Kong

Keywords Ischemic stroke · Segmentation · Adversarial training · Deep learning

Purpose

Accurate segmentation of brain stroke regions from medical images is a crucial step in clinical diagnosis, evaluation, and treatment. The success of ischemic stroke treatment is highly dependent on the time delay between its onset and the recanalization of occluded cerebral arteries. Timely and precise decision making, which should be made within several minutes, is therefore important for patients who suffer an ischemic stroke [1].

Although modern magnetic resonance imaging (MRI) techniques can distinguish between acutely infarcted and hypo-perfused lesion tissues, automatic methods are rarely used or too simple to capture the full complexity of a dataset. The classic methods for automatic image segmentation with machine learning involves the use of fully convolutional neural networks (FCNs). However, FCNs fail to produce precise segmentation localized around object boundaries because of the large receptive fields and pooling operations. Therefore, FCNs methods are usually combined with post-processing methods to refine the segmentation results further.

We propose a new segmentation method based on two deep convolutional neural networks (DCNNs) with adversarial training, to enable stroke regions to be delineated reliably and automatically from magnetic resonance images without post-processing.

Methods

This paper presents a fully automatic stroke region segmentation method based on two DCNNs, one acts as the generator and the other acts as the critic (adversarial network). The generator is trained end to end with 3D multi-modal volumes of the whole brain and produces a preliminary segmentation result for the stroke region, while the critic takes the preliminary segmentation result of the generator or the ground truth label of the training data along with the 3D multi-modal volumes as input. It then tries to distinguish whether the input is the corresponding ground truth result of the 3D volumes of the magnetic resonance image or not. We train the critic to maximize the probability of assigning the correct label to the training examples and outputs from the generator. Simultaneously, we train the generator to minimize the segmentation error between the output and ground truth. In other words, the generator and critic play the following min–max game with value function $V(G, D)$.

$$\min_G \max_D V(G, D) = E_{x\sim p(x)}[\log D(y|x)] + E_{x\sim p(x)}[\log(1 - D(G(x)|x))],$$

where G and D represent the generator and critic, represents the probability that label map y originated from the data rather than the generator G, given the input multi-model images x. Considering that critic networks have a field of view that is either the entire image or a large portion of it, mismatches in the high-order label statistics can be penalized by the critic loss term. During the backpropagating of the critic error to the generator, artefacts in the preliminary pixel map will be removed and a more reliable result will be obtained by generator. However, as indicated in [2], training with adversarial networks is unstable and easily suffers from model collapse, which means that either G or D learns much quicker than the other, such that G or D does not converge throughout the entire training phase. We propose to design a new loss function to stabilize the training process. The preliminary change is to replace the classic cross-entropy loss with the Wasserstein loss [3]. The Wasserstein loss can help stabilize the training phase because its scale ranges from [− 1, 1] instead of [0, 1], which provides better feedback to G. Wasserstein loss also helps to diminish the effect of the vanishing gradient when the depths of G and D increase. During the testing phase, only the generator will be used to segment the stroke lesion region from multi-modal images. The proposed architecture of this method is shown in Fig. 1. The automatic 3D segmentations are compared with the ground truths in terms of the Dice coefficient and the Hausdorff distance.

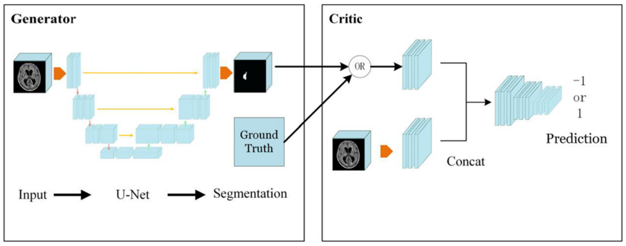

Fig. 1 Proposed architecture for ischemic stroke lesion

Results

Our preliminary experiments were conducted on training data provided by the ischemic stroke lesion segmentation (ISLES) 2017 Challenge [4]. Seven types of pre-processed MRI images, namely, apparent diffusion coefficient, perfusion-weighted image, relative cerebral blood flow, relative cerebral blood volume, mean transit time, time to peak, and time to maximum, are available, as shown in Fig. 2. These databases provide a total of 43 training cases, from which the ground truths for the stroke lesions were acquired. The ground truths of 32 test cases, which have been prepared by two experienced experts, are hidden from the public. The evaluation measurements for stroke lesion prediction were Dices coefficient (DC) and Hausdorff distance (HD). ISLES also provide an online evaluation system that allows participants to upload their stroke lesion segmentation results to evaluate different approaches and provide a platform for researchers to compare different approaches in a fair manner. In the preliminary experiments, the datasets were divided randomly into training and validation sets disjointedly. With the learned discriminative features, the label probability for each pixel in the target image was estimated from a test sample without post-processing operation. Our preliminary result from the proposed approach was submitted to the online benchmark system provided by the ISLES 2017 Challenge, and the results ranked among the top entries, which achieved 0.32 in DC and 131.25 in HD. We also compare our method with FCN and U-Net to validate that our method indeed shows improvement in segmentation accuracy. Table 1 summarizes the result for the networks. Furthermore, intensive experiments will be conducted using publicly available databases provided by the MICCAI 2012 Grand Challenge and the International Stroke Database.

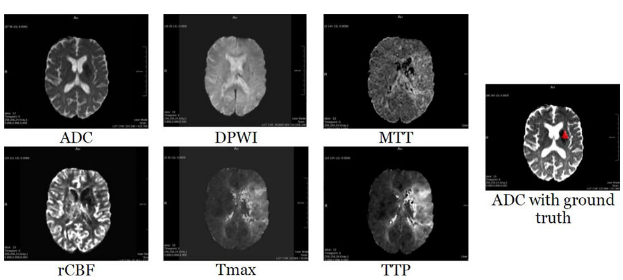

Fig. 2 Multi-modal images of the ISLES dataset

Table 1 Evaluation result with validation set of ISLES dataset

Method	Dice coefficient	Hausdorff distance
FCN	0.25	17.93
U-Net	0.28	15.25
U-Net w/ adv. training (ours)	0.3	14.16

Conclusion

We have proposed a DCNNs-based fully automatic segmentation method for ischemic stroke, including an evaluation by comparing the 3D binary predicted probability maps with the ground truth delineated by experts. Previous approaches for ischemic stroke segmentation have failed to produce precise segmentation localized around object boundaries without post-processing because of the large receptive fields and pooling operations. Our approach introduces the adversarial network in the training phase, which is able to capture the artefacts of the probability label maps and measure the quality of the segmentations, and the results reach the state-of-the-art performance without post-processing. This approach is also easily translated into other clinical practices.

References

[1] Saver JL., Goyal M, Van der Lugt A, et al. (2016) Time to treatment with endovascular thrombectomy and outcomes from ischemic stroke: a meta-analysis. Jama, 316(12): 1279–1288
[2] Luc P, Couprie C, Chintala S, Verbeek J (2016) Semantic segmentation using adversarial networks. NIPS2016
[3] Frogner C, Zhang C, Mobahi H, Araya-Polo M, Poggio TA (2015) Learning with a Wasserstein loss. CoRR, abs/1506.05439
[4] Maier O, Menze BH, von der Gablentz J, et al. (2015) Isles 2015-a public evaluation benchmark for ischemic stroke lesion segmentation from multispectral MRI. Medical image analysis, 35: 250–269

Eye structure segmentation on micro-CT images using 3D fully convolutional network with sparsely-annotated training data

T. Sugino[1], H. Roth[1], M. Oda[1], S. Omata[2], S. Sakuma[2], F. Arai[2], K. Mori[1,3,4]
[1]Nagoya University, Graduate School of Informatics, Nagoya, Japan
[2]Nagoya University, Graduate School of Engineering, Nagoya, Japan
[3]Nagoya University, Information Technology Center, Nagoya, Japan
[4]National Institute of Informatics, Research Center for Medical Big Data, Tokyo, Japan

Keywords Segmentation · Fully convolutional networks · Sparse annotation · Eye structures

Purpose

Recently, elaborate eyeball models [1] have been fabricated for training of ophthalmic surgeries, and thus a database of eyeball segmentation data that is available as design drawings for the eyeball models needs to be constructed. However, because manual segmentation is a time-consuming task, it is desirable to provide a full- or semi-automated segmentation method effective for reducing the burden of segmentation. Additionally, we need to segment smaller structures in the eyeball because ophthalmic surgeries often have a chance to treat minute tissues. Therefore, in this study, we focus on segmenting detailed eye structures including the cornea, the lens, the sclera, and the vitreous from micro-CT images, which have higher resolution and include the information of finer-scale anatomical structures than MR or CT images, by using fully convolutional networks (FCNs) [2]. In particular, we aim to accurately segment eye structures from micro-CT images based on less training data because we have difficulty collecting a large number of samples for training this type of images.

Methods

In the previous study [3], end-to-end segmentation of eye structures from micro-CT images was performed by utilizing a 2D FCN based on sparse annotation. In this study, for further improvement of segmentation accuracy, we apply a 3D FCN (3D U-net) [4] to eye structure segmentation from sparsely-annotated micro-CT images.

We assume that we use the network trained on some images which are sparsely annotated from stacked images to accurately perform eye structure segmentation in the entire stacked images. Figure 1 shows the overview of 3D FCN-based segmentation from sparse annotation. We first apply the filter for removal of ring artifacts and random noises to original micro-CT images and train the 3D FCN based on the preprocessed image data and the sparsely-annotated label data. Although in [4] they used the label data sparsely annotated on three orthogonal image planes for training their network, we utilize only sparsely-annotated axial slices as the label data. The label data can be created by assigning the defined labels to some slices and "Unlabeled" label to the other slices on the axial plane. In addition, for successful training of the network from the sparsely-annotated label data, we use the loss function implemented so as to ignore the loss computation on voxels with "Unlabeled" label, and then we add spatial dropout layer [5] after the convolution layer in the decoder part to avoid or delay overfitting of the network. Finally, we get the eye structure segmentation result from the entire volumetric image by inputting the image data to the trained network.

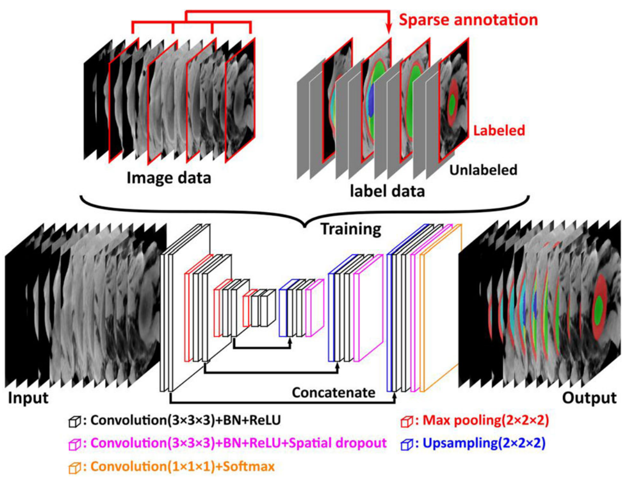

Fig. 1 Overview of 3D FCN-based segmentation from sparse annotation

Results

We validated the 3D FCN-based segmentation performance from sparse annotation by using micro-CT volumes of five pig eyeballs that were scanned by inspeXio SMX-90CT Plus (Shimadzu Co., Kyoto, Japan). Herein, due to the GPU memory restriction, each micro-CT volume was downsampled to 256 × 256 × 137 voxels with a voxel size of 200 × 200 × 200 μm^3 although it originally has 1024 × 1024 × 548 voxels with a voxel size of 50 × 50 × 50 μm^3. We created the preprocessed micro-CT images and the corresponding manually-annotated images (i.e., ground truth) in each volume. In the annotated images, the labels 0–5 were assigned to the following six regions: background, wall and membrane, vitreum, lens, ciliary body and Zinn's zonule, and anterior chamber. We also created sparsely-annotated training data for which the label 6 (i.e., "Unlabeled") was assigned to the remaining slices except for every ten slices in each volume.

We compared the segmentation results of 3D FCN with those of 2D FCN (which was utilized in [3]). Table 1 and Fig. 2 show Dice similarity coefficient (DSC) values and visualization examples of the segmentation results by the networks trained on the sparsely-annotated training data, respectively. The DSC values were calculated on the slices for testing (i.e., the remaining slices except for the slices for training). From the results in Table 1, we found that the 3D FCN-based segmentation could provide higher DSC values than 2D FCN-based segmentation for all the eye structures except for lens. Moreover, as shown in Fig. 2, although 2D FCN provided unsatisfactory segmentation on some slices, 3D FCN got better segmentation even on them. This is probably because 3D FCN could take into account 3D image features in micro-CT volumes, which are effective for volumetric segmentation. Therefore, the 3D FCN has the potential to provide successful eye structure segmentation even based on the training from sparsely-annotated slices on the axial plane.

Table 1 Segmentation results of pig eyeballs (n = 5)

Label	Eye structures	Dice similarity coefficient	
		2D FCN	3D FCN
0	(Background)	99.7 ± 0.0%	**99.9 ± 0.0%**
1	Wall and membrane	82.6 ± 1.6%	**91.1 ± 1.7%**
2	Vitreum	97.2 ± 0.6%	**98.5 ± 0.4%**
3	Lens	**95.3 ± 1.1%**	95.1 ± 1.1%
4	Ciliary body and Zinn's zonule	78.2 ± 6.7%	**84.5 ± 4.8%**
5	Anterior chamber	86.9 ± 2.8%	**90.7 ± 2.0%**
Mean (except for background)		88.0%	**92.0%**
Std (except for background)		8.1%	**5.3%**

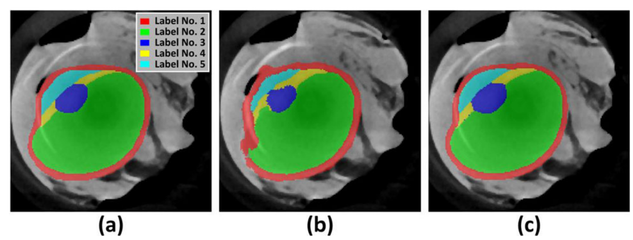

Fig. 2 Example of the segmentation results obtained by **a** manual segmentation (ground truth), **b** 2D FCN, and **c** 3D FCN

Conclusion

In this study, we presented 3D FCN-based eyeball structure segmentation from sparsely-annotated micro-CT images. In the validation results, the 3D FCN outperformed the 2D FCN and provided the high average accuracy of 92.0% for eye structure segmentation from sparse annotation. The results suggested that 3D FCN-based segmentation could be useful for creating a database of ophthalmic segmentation data from less training data.

Acknowledgment

Parts of this research were supported by the ImPACT Program of Council for Science, Technology and Innovation (Cabinet Office, Government of Japan), the JSPS KAKENHI (Grant Numbers 26108006, 17K20099 and 17H00867), and the JSPS Bilateral International Collaboration Grants.

References

[1] Someya Y, Omata S, Hayakawa T, Mitsuishi M, Sugita N, Harada K, Noda Y, Ueta T, Totsuka K, Araki F, Aihara H, Arai F (2016) Training system using Bionic-eye for internal limiting membrane peeling. International Symposium on Micro-NanoMechatronics and Human Science (MHS), 1–3

[2] Long J, Shelhamer E, Darrell T (2015) Fully Convolutional Networks for Semantic Segmentation, IEEE Conference on Computer Vision and Pattern Recognition (CVPR), 3431–3440

[3] Sugino T, Roth H, Oda M, Omata S, Sakuma S, Arai F, Mori K (2018) Automatic segmentation of eyeball structures from

micro-CT images based on sparse annotation. SPIE Medical Imaging, 10578: 105780 V
[4] Çiçek Ö, Abdulkadir A, Lienkamp SS, Brox T, Ronneberger O (2016) 3D U-Net: Learning Dense Volumetric Segmentation from Sparse Annotation. International Conference on Medical Image Computing and Computer-Assisted Intervention (MICCAI), 424–432
[5] Tompson J, Goroshin R, Jain A, LeCun Y, Bregler C (2015) Efficient object localization using Convolutional Networks. IEEE Conference on Computer Vision and Pattern Recognition (CVPR), 648–656

Development of automatic measurement of callosal angle on coronal image in head CT

N. Takahashi[1], T. Kinoshita[1], T. Ohmura[1], E. Matsuyama[2], H. Toyoshima[1]
[1]Research Institute for Brain and Blood Vessels-Akita, Radiology and Nuclear Medicine, Akita, Japan
[2]Int. Univ. of Health and Welfare, Ohtawara, Japan

Keywords Computed tomography · Normal pressure hydrocephalus · Callosal angle · Segmentation

Purpose

Idiopathic normal pressure hydrocephalus (iNPH) is a treatable type of dementia in elderly people. Appropriate cerebrospinal fluid shunt surgery can improve symptoms of patients with iNPH. There are some difficulties in the diagnosis of iNPH, because the clinical symptoms associated with iNPH are presented commonly in elderly people and overlap with other neurodegenerative disorders such as Alzheimer's disease and Parkinson disease. Thus, accurate and early diagnosis of iNPH is needed for appropriate treatment.

Neuroimaging such as CT and MR imaging is essential to diagnose iNPH. Ventricular enlargement is a major imaging finding for iNPH. Other imaging findings for iNPH include enlarged sylvian fissure and tight medial and high convexity CSF space. These findings except the ventricular enlargement are called disproportional enlarged subarachnoid-space hydrocephalus (DESH). The DESH finding is of importance to support the diagnosis of iNPH. Callosal angle (CA) is used as an index of imaging criterion and indirectly represents the DESH finding. The CA serves as a screening tool to assist radiologists differentiate patients with iNPH patients from patients with other neurodegenerative disorders [1]. The CA is defined as the angle of the roof of the lateral ventricles measured on the coronal image through the posterior commissure (PC), perpendicular to the anteroposterior commissure-PC (AC-PC) plane as shown in Fig. 1. iNPH causes a steep CA (less than 90 degree) on the image.

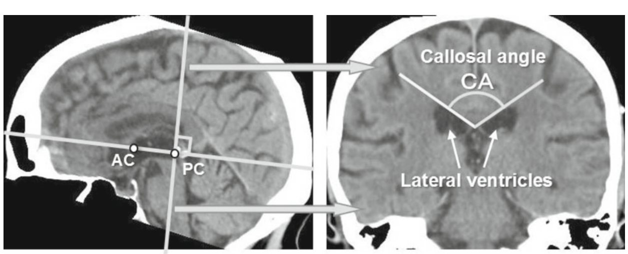

Fig. 1 The callosal angle is defined as the measurement on the coronal section

CT may be superior to MR imaging for evaluation of elderly people with a cognitive complaint, because the high-speed of the scan is an advantage in patients suspected of dementia who can be agitated. However, coronal CT images are not easily obtained, because one has to obtain them from a three-dimensional (3-D) CT images using the process of multi-planer reconstruction. It is a difficult task and a time-consuming process.

In this study, we present an automated method to measure the CA on the coronal CT images.

Methods

The algorithm of the method consisted of standardization to an atlas, determination of the coronal plane in 3-D images, segmentation of lateral ventricles, determination of roof lines of the bilateral lateral ventricles, and measurement of CA.

First, brain CT data are normalized into a standard atlas by using linear affine transformation and non-linear wrapping techniques. For the normalization, areas of the skull are removed from the CT data sets. The matrix size used for normalization was $157 \times 189 \times 68$ voxels (voxel size, $1 \times 1 \times 2$ mm). Second, for the determination of the coronal plane, the coronal plane perpendicular to the AC-PC plane is reconstructed in the normalized data according to the CA definition. Then, 41 continuous images with a slice distance of 1 mm parallel to coronal plane that centered at the image through the PC. Third, lateral ventricle regions are segmented on the coronal images by using a 3-D region growing technique to delineate the contours of the lateral ventricle regions. For employing the 3D region growing technique, a noise reduction filter, adaptive partial median filter [2], which greatly eliminates quantum noise without blurring anatomic structure contours, was applied to the 41 coronal images. Then, bilateral roof lines representing the upper contours of the lateral ventricles are determined on the coronal image through the PC. Finally, the straight lines of the best fit for the pixels of the roof lines of the right and left lateral ventricles, respectively, are determined by use of a least squares method, and the CA is measured from the bilateral roof lines. An example of a computed result is shown in Fig. 2.

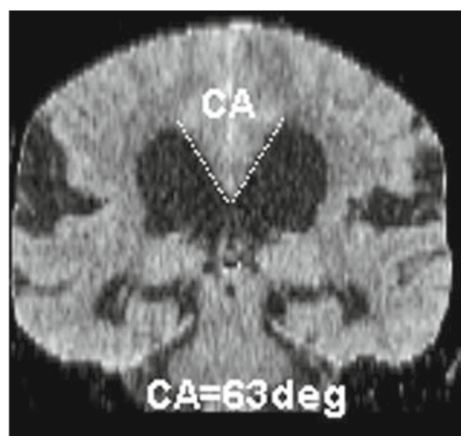

Fig. 2 An examle of a computer result for the callosal angle

CT data from 10 subjects (age range, 62–86 years; mean age, 76.2 years) with CA of varying in angles were obtained. Three patients with iNPH diagnosed in accordance with the Japanese guideline for iNPH [3] were included in the 10 subjects. The automated method was applied to the 10 CT scans, and was evaluated for the performance on measurement of CA.

Results

We compared the CAs computed from the proposed method with the gold standard CAs in order to evaluate the accuracy of this method for measurement of CA. We investigated the relationship between the computed results and the gold standards for the CA. As a result, the correlation coefficient of these data for the CA was 0.985. Also, differences between the computer results and the gold standards were investigated by using Bland–Altman analysis. The average differences in the CAs between the computed results and the gold standards was 3.3° (4.8%; SD, 3.1°). There was no significant evidence of fixed bias ($P = 0.59$) and proportional bias ($P = 0.47$). The computed results agreed well with the gold standards on the original images.

Conclusion

We developed an automated method to measure the CA on head CT images. The correlation coefficient in the CAs between the computerized method and the gold standard was 0.985 for the 10 subjects (three patients with iNPH). Therefore, these results suggest that the automated method has the potential to accurately measure the CA on coronal CT images.

References

[1] Miskin N, Patel H, Franceschi AM, Ades-Aron B, Le A Damadian BE, Stanton C, Serulle Y, Golomb J, Gonen O, Rusinek H, George AE; Alzheimer's Disease Neuroimaging Initiative (2017) Diagnosis of normal-pressure hydrocephalus: use of traditional Measures in the era of volumetric MR Imaging. Radiology 2017; 285(1): 197–205.

[2] Takahashi N, et al. A novel noise reduction filter for improving visibility of early CT signs of hyperacute stroke: evaluation of the filter's performance—preliminary clinical experience. Radiat Med 2007; 25: 247–254.

[3] Mori E, et al. Guidelines for management of idiopathic normal pressure hydrocephalus: second edition. Neurol Med Chir (Tokyo). 2012; 52(11): 775–809.

Social media in remote monitoring of cancer patients: a longitudinal trial in context of a developing country

S. Mishra[1], A. Mishra[1], S. Yadav[1]

[1]SGPGIMS, Endocrine Surgery, Lucknow, India

Keywords Social media · Telemedicine · eHealth · Remote monitoring

Purpose

Over the next decades, cancer burden is expected to reach 20 million new cases annually in low and middle income countries (LMICs) by 2025. The rate of incidence of thyroid cancer has increased more than any other cancer worldwide. In the United States has seen > 300% increase within the past 30 years and few estimates suggest that thyroid cancer couldbecome the third most common cancer diagnosed in women by 2019 [1–4]. Large increase in the prevalence of endocrine cancers means that the absolute number of patients is likely to continue to increase. Health care services therefore need to gear up to provide close clinical follow-up care for people both in primary and specialist care. Information and communication technologies may enable more integrated treatment and care pathways across geographical boundaries. Though, hospital based telemedicine system has been proved to be effective in carrying out continuity of care after primary treatment is over, current usage of social media in such situations are not studied well. The social media based remote monitoring can be done at leisure, convenient to both patients and treating surgeons and does not require costly hospital infrastructure. Therefore, we conducted this study to assess the effect of remote monitoring using tele-follow up on compliance, satisfaction and economic benefit.

Methods

In this longitudinal trial, 32 participants were recruited to traditional hospital follow-up (consultation, clinical examination, and investigations as per hospital policy) or tele-followup based on social media. Outcomes included information needs, participantsâ€™ compliance and satisfaction, post-op complications, clinical investigations ordered, and change in treatment strategy. Data were collected by researcher when patients returned to hospital for their annual follow up. Patient satisfaction with remote monitoring system was measured by a numeric scale ranging from one to five.

Results

A total of 32 patients with diagnosis of thyroid cancer were recruited—12 in hospital follow up group and 20 in remote monitoring based on tele-follow up based on social media. There were no significant differences between groups regarding satisfaction with information received. There was nodifference between groups but at the end of the trial, responses were significantly morepositive in the social media group, with a higherpercentage reporting â€œvery satisfied. Wound evaluation through tele-follow up was on par with OPD follow up as no patient had to report to OPD for wound infection. If all of these 20 patients would have come to our OPD follow-up, they would have travelled on an average 930 Kms per patient, apart from losing work hours. Hence this technology saved 930 Kms of travel per patient and significant financial loss. Compliance was good as all patients reported on the date and time of appointment.

Conclusion

Follow up of cancer patients in developed countries is not a problem-better communication system, transport system and educated patients. A Low and middle income countries need an eHealth revolution using this type of technology to achieve the goal of health for all as availability of health care facilities is a problem in such geographical locations in addition to lack of human resources as compared to patients needing healthcare.

References

[1] United Nations, Department of Economic and Social Affairs, Population Division (2015). World Population Prospects: The 2015 Revision, Key Findings and Advance Tables. Working Paper No. ESA/P/WP.241.

[2] Davies L, Welch HG. Current thyroid cancer trends in the United States. JAMA Otolaryngol Head Neck Surg. 2014; 140: 317–322.

[3] Surveillance, Epidemiology, and End Results. Introduction. http://seer.cancer.gov/. Accessed January 2, 2017.

[4] Pellegriti G, Frasca F, Regalbuto C, Squatrito S, Vigneri R. Worldwide increasing incidence of thyroid cancer: update on epidemiology and risk factors. J Cancer Epidemiol. 2013; 2013: 965212.

Design for artificial anal sphincter with constant force

M. Wang[1,2], H. Yu[1,2]

[1]University of Shanghai for Science and Technology, Institute of Rehabilitation Engineering and Technology, Shanghai, China

[2]University of Shanghai for Science and Technology, Shanghai Engineering Research Center of Assistive Devices, Shanghai, China

Keywords Fecal incontinence · Artificial anal sphincter · Constant force · Shape memory alloy

Purpose

Fecal incontinence is an unresolved problem which has a serious effect on patients, both physically and psychologically. As a treatment for such patients, an artificial sphincter is considered an eventual choice as prosthesis to assist anal continence [1]. The clinically available system is the Acticon Neosphincter (American Medical Systems, Minneapolis, MN, USA), which can not maintain the long-term effectiveness. The crucial problem of this study was to keeping long-term biomechanical compatibility between the artificial anal sphincter (AAS) and the surrounding tissue [2]. This paper presented a design of an AAS with constant force or pressure using superelastic shape memory alloy (SMA) to solve the problem. Its characteristic properties were evaluated by preliminary experiments.

Methods

A schematic drawing of the proposed AAS is shown in Fig. 1. It can be seen that the mechanism consists of two upper claw, two lower claw, two clamping elements, two superelastic SMA sheets and two ropes with position limit. The upper claw connected to lower claw by hinges, and the rope with position limit is a link between clamping element connected and upper claw. The constant force characteristics of AAS is achived by superelastic SMA sheet. A unique characteristic of superelastic SMA is the constant stress during their stress-induced transformation. The geometric dimensions of superelastic SMA sheet are determined by the optimization.

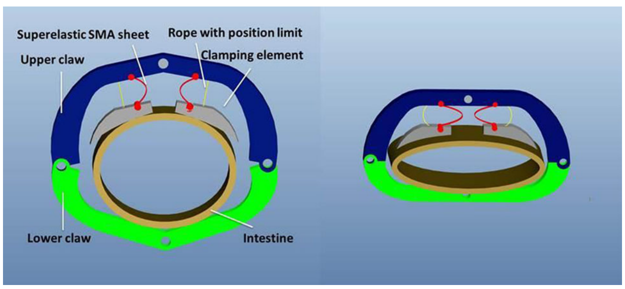

Fig. 1 Schematic drawing of the proposed AAS in its open (left) and closing (right) state

A prototype of the developed AAS with the constant force element was fabricated. Preliminary experiment was conducted to confirm the effectiveness of the device. Single layer artificial intestine, two layers artificial intestine and three layers artificial intestine were prepared to measure the internal pressure of the artificial intestine with various thicknesses. The artificial intestine with soft rubber was installed into the clamping component to test the occlusion pressure to the bowel provided by the device. The occlusion pressure was measured with a gastrointestinal motility measurement system (Solar GI System, MMS) and a pressure catheter (K3104-00-9722-D, Unisensor) connected to the system. The pressure catheter is put into the artificial intestine to measure pressure, and the intestine is installed into the device. The internal pressure of the artificial intestine is monitored and collected simultaneously during the closing state of the device.

Results

The experimental comparison for internal pressure of artificial intestine with three kinds of thicknesses was shown in Fig. 2. It can be seen that the internal pressure of intestine with three kinds of thicknesses is 55 mmHg, 56 mmHg and 54 mmHg respectively. The average pressure of intestine of three kinds of thicknesses is 55 mmHg, and the maximum pressure difference is 2 mmHg. The fluctuation error of constant force is about 3.64%.

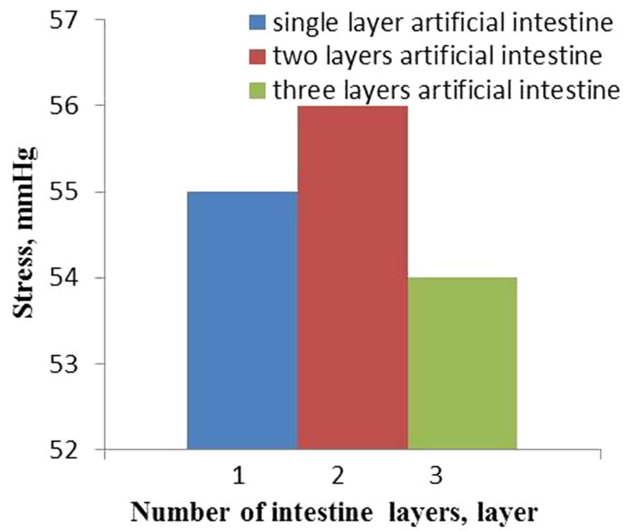

Fig. 2 Comparison of internal pressure of artificial intestines with three kinds of thicknesses

It was demonstrated that the AAS had minimal change in the clamping pressure, even if the thickness of the artificial intestine was changed. This could prevent ischemic necrosis of soft tissues caused by excessive pressure. It was possible that this device would be helpful for patients with fecal incontinence and could have long term effective.

Conclusion

The artificial anal sphincter embedded constant force element has simple and compact structure. The device can make the internal pressure of the intestine with various thicknesses maintaining almost constant force. It is possible that this device will prevent ischemic necrosis of soft tissues and maintain long term effective. The occlusion pressure provided by the device met the requirement of safety for human body. Further experiments will be carried out with animal intestine and faked stool to simulate the process of occlusion and defecation. The work was supported by the foundation from the National Natural Science Foundation of China (61473193) and Science and Technology Committee of Shanghai Municipality (16441905102, 16441905202, 16060502500).

References

[1] Luo Y, Higa M, Amae S, Takagi T, Yambe T, Okuyama T, Tanaka H, Kakubari Y, Matsuki H (2009) Preclinical development of SMA artificial anal sphincters, *Minim. Invasive Ther. Allied Technol*. 15(2006) 241–245.

[2] Luo Y, Takagi T, Okuyama T, Amae S, Wada M, Nishi K, Kamiyama T, Yambe T, Matsuki H (2004) Functional evaluation of an artificial anal sphincter using shape memory alloys, *ASAIO J.* 50, 338–343.

Water-hammer effects after aortic valve replacement with a mechanical valve in aortic regurgitation: wave intensity analysis

K. Niki[1], M. Sugawara[2], S. Takenouchi[1], M. Tanaka[2], I. Takamisawa[3], S. Takanashi[4]
[1]Tokyo City University, Biomedical Engineering, Tokyo, Japan
[2]Himeji Dokkyo University, Medical Engineering, Himeji, Japan
[3]Sakakibara Heart Institute, Cardiology, Tokyo, Japan
[4]Sakakibara Heart Institute, Surgery, Tokyo, Japan

Keywords Wave intensity · Aortic regurgitation · Mechanical valve · Water hammer

Purpose

Water hammer is a well-known phenomenon in a piping system caused by a sudden stoppage of flow accompanying the closure of a valve. It generates a pressure wave which propagates in the pipe, sometimes causing serious damage to the line. This phenomenon could occur when the reverse flow from the aorta to the ventricle near end-systole is stopped by the closure of a prosthetic valve, but the effects on the vascular system are unclear. Wave intensity (WI) is an index which provides information about the behavior of the heart and arterial system. WI is defined as the product of time-derivatives of pressure (P) and velocity (U): WI = (dP/dt)(dU/dt). A WI waveform has two positive peaks in a cardiac cycle (Fig. 1). The first peak (W_1), which is the compression wave generated by the heart, occurs in early ejection and correlates with peak dP/dt, an index of cardiac contractility. The second positive peak (W_2), which appears near end-systole, is the expansion wave also generated by the heart. The aim of this study was to obtain WI in AR patients who underwent mechanical valve replacement and evaluate the effects of water hammer.

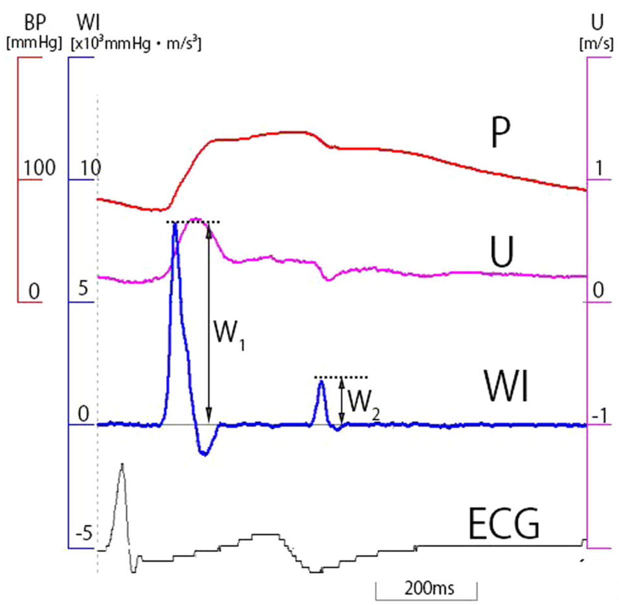

Fig. 1 A WI waveform has two positive peaks in a cardiac cycle

Methods

We measured carotid arterial wave intensity in 36 patients with aortic regurgitation (AR) before and early after surgery of valve replacement (mechanical valve group: n = 19 mean age 57 ± 10 years; biological valve group n = 17, mean age 58 ± 17). WI was measured noninvasively by an ultrasonic system, which simultaneously measures blood flow velocity by a color Doppler system and diameter change by an echo-tracking subsystem with a linear array probe. Arterial diameter waveforms were calibrated by the upper arm blood pressure measured with a sphygmomanometer and used as surrogates for blood pressure waveforms. Five consecutive beats were ensemble-averaged and by imputing systolic and diastolic pressure, WI indices (W_1 and W_2) were calculated automatically, and the waveforms of WI, blood velocity and pressure are digitally recorded at an interval of 1 ms.

Results

There were no differences in W_1 and W_2 before surgery between the groups. After the surgery, W_2 was significantly increased in the mechanical valve group, but not in the biological valve group. The increase in W_2 suggests that the reverse flow velocity before valve closure was greater. Systolic and diastolic pressure and maximum velocity decreased after surgery in both group. Minimum velocity was increased in biological valve group, but not in the mechanical group (Table 1).

Table 1 Minimum velocity was increased in biological valve group, but not in the mechanical group

	Mechanical valve		Biological valve	
	Before surgery	After surgery	Before surgery	After surgery
W_1 [mmHg m/s^3]	11.3 ± 4.6	5.4 ± 3.2$^{\#\#}$	14.3 ± 7.7	3.8 ± 2.2$^{\#\#}$
W_2 [mmHg m/s^3]	1.8 ± 1.1	3.1 ± 1.4$^{**\#\#}$	1.6 ± 0.7	1.6 ± 0.6
Sys P [mmHg]	117 ± 12	103 ± 15$^{\#\#}$	122 ± 13	100 ± 11$^{\#\#}$
Dia P [mmHg]	48 ± 8	58 ± 10$^{\#\#}$	50 ± 10	62 ± 10$^{\#\#}$
Max V [m/s]	0.65 ± 0.18	0.51 ± 0.14$^{\#\#}$	0.67 ± 0.25	0.44 ± 0.16$^{\#\#}$
Min V [m/s]	− 0.01 ± 0.07	0.02 ± 0.07*	0.01 ± 0.04	0.06 ± 0.04$^{\#}$

sys P systolic pressure, *dia P* diasolic pressure, *max V* maximum velocity, *min V* minimum velocity

$^*p < 0.05$ versus biological valve

$^\#p < 0.05$ versus before surgery

Conclusion

The increase in W_2 in AR patients who had surgical treatment with mechanical valve replacement suggests that water hammer effects were enhanced. The enhancement of water hammer effects may affect the integrity of the cardiovascular system.

Carotid artery contrast-enhanced ultrasound can predict development of microembolic signals ontranscranial Doppler during CEA

K. Oikawa[1], T. Kato[2], O. Kazumasa[2], S. Narumi[2], M. Sasaki[3], S. Fujiwara[1], M. Kobayashi[1], Y. Matsumoto[1], J. I. Nomura[1], K. Yoshida[1], Y. Terayama[2], K. Ogasawara[1]
[1]Iwate Medical University, Neurosurgery, Morioka, Japan
[2]Iwate Medical University, Neurology and Gerontology, Morioka, Japan
[3]Iwate Medical University, Institute for Biomedical Sciences, Yahaba, Japan

Keywords Carotid endarterectomy · Ultrasound · Contrast enhancement · Microembolic signals

Purpose

Emboli from the surgical site during exposure of the carotid arteries for carotid endarterectomy (CEA) cause new cerebral ischemic lesions or neurological deficits CEA [1–3]. The emboli can be detected as microembolic signals (MES) on intraoperative transcranial Doppler (TCD) monitoring of the middle cerebral artery. It has been reported that contrast-enhanced ultrasound can identify the neovascularization in vulnerable plaque casing such emboli [4]. The purpose of the present study was to determine whether preoperative contrast-enhanced ultrasound findings of the cervical carotid arteries are associated with the development of MES on TCD during exposure of the arteries in CEA and to compare the predictive accuracy of contrast-enhanced ultrasound findings with that of gray-scale median (GSM).

Methods

Seventy patients with internal carotid artery stenosis ($\geq$ 70%) underwent preoperative cervical carotid artery ultrasound and CEA under TCD monitoring of MES in the ipsilateral middle cerebral artery. Raw data of contrast-enhanced ultrasonography were transferred to the workstation. One investigator, who was blinded to patient information, manually placed multiple circular regions of interest (ROIs) within the carotid plaque on the sagittal section of a coded phase inversion image so that ROIs extended all over the plaque and were located near the lumen of the carotid artery. Time-intensity curves of the intraplaque and lumen ROIs were generated from the raw data using echo analyzing software (VolMap445 ver.1.1.2a2, YD, Ikoma, Nara, Japan). Next, a curve-fitting technique was applied for the smoothed time intensity curves of intraplaque ROIs and of lumen ROIs. The gamma variate curve was used for the fitting because of the bolus injection of the contrast media [5]. All fitting analyses were performed on Curve Fitting Tool of MATLAB R2015b (MathWorks, Natick, MA). A baseline intensity before injection of contrast agent and a maximal intensity after the injection were obtained on the intraplaque and lumen curves after the fitting in each patient. Maximally enhanced intensities on the intraplaque and lumen time-intensity curves, respectively, were obtained from contrast-enhanced ultrasonography data, and the ratio of the maximal intensity (EI_p) of the intraplaque curve to that (EI_l) of the lumen curve was calculated. The GSM value of the plaque was also measured on B-mode image with ROIs corresponding to intraplaque ROIs for the time intensity curves. Relationships between EI_p/EI_l or averaged GSM and the development of MES during exposure of the carotid arterieswere evaluated using the Mann–Whitney *U* test. The accuracy of the EI_p/EI_l or averaged GSM to predict the development of MES during exposure of the carotid arteries was determined using a receiver operating characteristic (ROC) curve, and the ability to discriminate between the presence and absence of MES during exposure of the carotid arteries was estimated using the area under the ROC curve (AUC).

Results

EI_p/EI_l was significantly greater in patients with MES (0.666 $\pm$ 0.209) than in those without MES (0.324 $\pm$ 0.254) ($p < 0.0001$), averaged GSM did not differ between patients with (9.639 $\pm$ 6.301) and without MES (13.034 $\pm$ 8.021) ($p < 0.1537$). AUC was significantly greater for EI_p/EI_l than for GSM ($p = 0.0108$). Multivariate statistical analysis demonstrated that only EI_p/EI_l was significantly associated with the development of MES during exposure of the carotid arteries ($p = 0.0002$).

Conclusion

Preoperative contrast-enhanced ultrasound findings of the cervical carotid arteries are associated with development of MES on transcranial Doppler during exposure of the arteries in CEA, and the predictive accuracy of contrast-enhanced ultrasound is greater than that of GSM.

References

[1] Ackerstaff RG, Moons KG, van de Vlasakker CJ, Moll FL, Vermeulen FE, Algra A, Spencer MP (2000) Association of intraoperative transcranial Doppler monitoring variables with stroke from carotid endarterectomy. Stroke 31(8): 1817–1823.

[2] Wolf O, Heider P, Heinz M, Poppert H, Sander D, Greil O, Weiss W, Hanke M, Eckstein HH (2004) Microembolic signals detected by transcranial Doppler sonography during carotid endarterectomy and correlation with serial diffusion-weighted imaging. Stroke 35(11): e373–e375.

[3] Verhoeven BA, de Vries JP, Pasterkamp G, Ackerstaff RG, Schoneveld AH, Velema E, de Kleijn DP, Moll F (2005) Carotid atherosclerotic plaque characteristics are associated with microembolization during carotid endarterectomy and procedural outcome. Stroke 36(8): 1735–1740.

[4] Saito K, Nagatsuka K, Ishibashi-Ueda H, Watanabe A, Kannki H, Iihara K (2014) Contrast-enhanced ultrasound for the evaluation of neovascularization in atherosclerotic carotid artery plaques. Stroke 45(10): 3073e3075.

[5] Blomley MJ, Dawson P (1997) Bolus dynamics: theoretical and experimental aspects. Br J Radiol.70(832): 351–359.

Projector-based augmented reality applied in CT-guided liver biopsy considering both user's viewpoint and geometric distortion

L. Liang[1], H. Ding[1], G. Wang[1]
[1]Tsinghua University, School of Medicine, Beijing, China

Keywords Projector based AR · Viewpoint · Geometric distortion · CT-guided liver biopsy

Purpose

Projector-based augmented reality (AR) applied in CT-guided live biopsy can provide an intuitive view of navigation information by projecting tumor model and surrounding vessel model onto the patient's body surface.

However, observing the projection from the surgeon's viewpoint, the surgeon may get wrong guidance information, because the surgeon's viewpoint is usually different from the projection orientation. What's more, the projection on the body can also be distorted by the surface geometry. Only a few studies have been found to correct the projection error for projector-based AR [1, 2]. The existing methods just correct the projection in simple situations and are not suitable for the complex situations in surgery where viewpoint deviation and geometric distortion both exists.

This study aims to propose a method to correct the projection considering both surgeon's viewpoint and geometric distortion so that the projector-based AR can provide right guidance information for surgeons in CT-guided liver biopsy.

Methods

Before going into the details of the proposed method, the procedure of a CT-guided liver biopsy integrated withprojector-based AR is described as follows.

A projector is added into the CT system, which is fixed above the CT table and has been calibrated. Before the liver biopsy, the patient is scanned and the surgeon plans the needle insertion trajectory based on the patient's CT images. Besides, the body surface model and internal organ models (tumor and surrounding vessel) are reconstructed. During the liver biopsy, when the surgeon observes the patient body along the planned trajectory, the projector projects the corrected image generated by our proposed method. Thus, the surgeon can see the internal organ models based on the projection.

The proposed method contains four steps, as shown in Fig. 1:

(1) A virtual scene is created based on the reconstructed models. According to the parameters in real surgery space including surgeon's view position P1, view orientation O1, projector's

position P2 and orientation O2, the corresponding parameters P1′, O1′, P2′, O2′ in the virtual space can be calculated.

(2) In the virtual scene, a virtual camera in P1′ with orientation O1′ is created. This camera is used to observe the internal organ model and generates an image. The surgeon's viewpoint is considered in this step.

(3) In the virtual scene, a virtual projector in P1′ with orientation O1′ is created. Then this projector projects the image obtained in (2) to the human body surface. The projection can be implemented using projective texture. The geometric distortion can be corrected in this step.

(4) In the virtual scene, a virtual camera in P2′ with orientation O2′ is created. This camera is used to observe the body surface model with texture. Finally, the pre-warped projection image is generated and is loaded into the projector in real surgery scene.

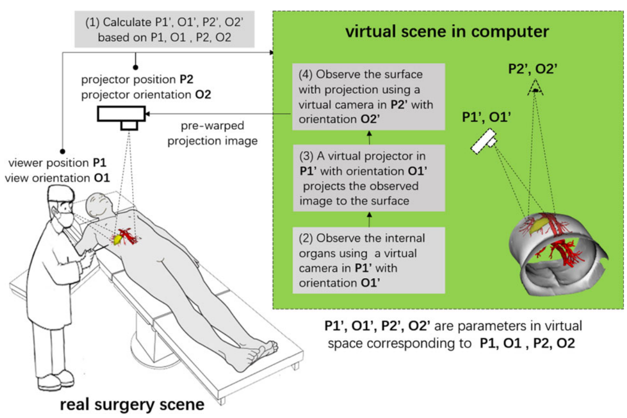

Fig. 1 The proposed method to generate a right pre-warped projection image considering user's viewpoint and geometric distortion for projector-based augmented reality

Results

We performed a simulation experiment to evaluate the proposed method. And we used Visualization Toolkits to create a virtual scene. First, 3D models including liver vessels, tumor and skin were reconstructed from CT images and were loaded into the virtual scene. Then a virtual camera and a virtual projector was created. The camera's viewpoint was set along the planned trajectory. And the projector was set in a proper position above the human body. The pre-warped projection image was generated by using the proposed method and the simulation results are shown in Fig. 2. The results show that the image obtained by observing the internal models is quite consistent with the image obtained by observing the surface model with projection.

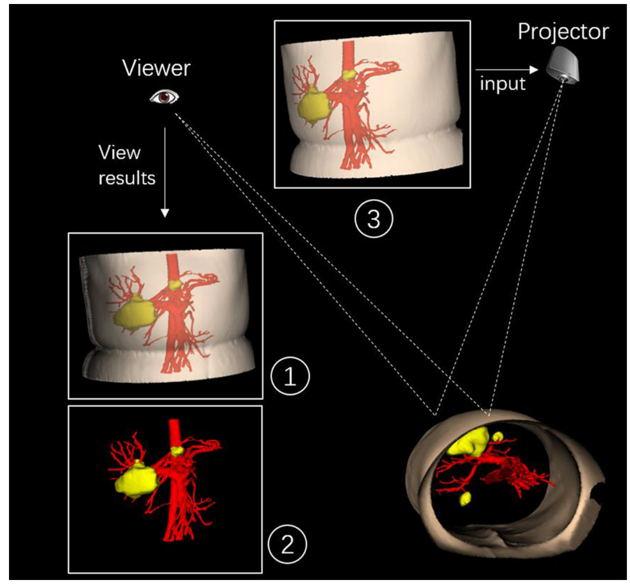

Fig. 2 The simulation experiment results. (1) The image obtained by observing the surface model with projection. (2) The image obtained by observing the internal models. (3) The generated pre-warped projection image using the proposed method

Conclusion

In this study, we have proposed a method to correct the projection image considering both user's viewpoint and geometric distortion. With this method, projector-based AR can provide right projection for surgeons in a CT-guided liver biopsy. The validity of the proposed method was verified by the simulation experiment.

References

[1] Park H, Kang G-C, Lee M-H, Kim S-J, Park J-I (2005). *Direct-projected augmented reality considering user's viewpoint.* Paper presented at the Proceedings of International Meeting on Information Display and Exhibition.

[2] Zeng B, Meng F, Ding H, Wang G (2017) A surgical robot with augmented reality visualization for stereoelectroencephalography electrode implantation. *International journal of computer assisted radiology and surgery, 12*(8), 1355–1368.

Development of a hand–eye calibration method for augmented reality applied to computer-assisted orthopedic surgery

M. Elias de Oliveira[1], H. Galvan Debarba[1], A. Lädermann[2], S. Chagué[1], C. Charbonnier[1]
[1]Artanim Foundation, Medical Research Department, Meyrin, Geneva, Switzerland
[2]La Tour Hospital, Meyrin, Switzerland, and Faculty of Medicine, University of Geneva, Geneva, Switzerland, Division of Orthopedics and Trauma Surgery, Meyrin, Geneva, Switzerland

Keywords Augmented reality · Hand–eye calibration · HoloLens · Computer assisted surgery

Purpose

Recent technology advances in Augmented Reality (AR) is creating an opportunity for a paradigm shift in the field of Computer Assisted Surgery (CAS). In March 2007, Microsoft released the Microsoft HoloLens Development Edition. This platform is a wearable high-definition stereoscopic 3D optical head-mounted system (OHMDs) equipped with near-eye multifocus dichromated-gelatin holographic lenses (AR headset, Microsoft HoloLens). Despite having the potential of being a promising technology in clinical applications, its accuracy, robustness, and performances under specific environmental conditions have not been fully investigated and evaluated. In an attempt to address the limitations and uncertainties that arise from using computer vision in SLAM based algorithms [1] due to the dynamism of clinical environments, we propose a Hand-Eye (HE) based approach to determine an invariant mapping between the HoloLens headset (i.e., rigid body defined by a unique set of passive markers) and the OHMDs virtual camera (user's visual system).

Methods

In order to achieve the required precision for using the Microsoft HoloLens in a surgical application, an invariant mapping was estimated. First, a set of non-collinear retroreflective markers were rigidly attached to the Microsoft HoloLens headset (Fig. 1). Consequently, the OHMDs's intrinsic parameters, as well as their radial and tangential lenses distortion coefficients, were determined by solving simultaneously a set of homogeneous system of equations by using nonlinear optimization techniques. Posteriorly, the extrinsic OHMDs parameters were determined with respect to checkboard pattern by solving a linear homogeneous system of equation [2], and then the invariant transformation was determined by solving the following matrix equation: $\mathrm{T}_{\mathrm{h}}^{\mathrm{c}} = T_{\mathrm{p}}^{\mathrm{c}}\mathrm{T}_{\mathrm{w}}^{\mathrm{p}}\mathrm{T}_{\mathrm{h}}^{\mathrm{w}}$, as graphically represented in Fig. 1.

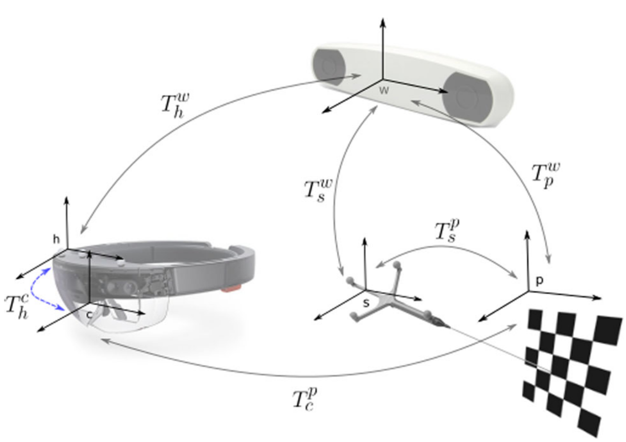

Fig. 1 AR hand-eye calibration based method

The accuracy of the proposed HE based method has been evaluated by using a retro-projection error estimation method. Finally, a full male pelvis model with acetabulum and cancellous inner structures (SKU #1301-1, Sawbones, Pacific Research Laboratories, Vashon, Washington, USA) was used to validate and test the proposed calibration method.

Results

A checkerboard pattern was digitized by using a surgical navigation pointer and therefore, the position of each individual pattern (i.e., internal corners of the checkerboard pattern) was determined with respect to the world reference frame. Based on the estimated invariant transformation $\mathrm{T}_{\mathrm{h}}^{\mathrm{c}}$ shown in Fig. 1, holograms representing these internal edges were created and represented into the physical space. Since these holograms representing the internal edges of the used checkerboard calibration object have their counterparts in the real world, the root mean square error (RMSE) of the 2D representations of these holograms were compared with the acquired OHMDs checkerboard images. RMSEs for ten randomly selected poses and at different radial distances ranging from 0.5 to 1.5 m from the calibration object were considered. A RMSE of 3.2 ± 1.6 mm for a total of 150 different patterns were considered in this analysis (3×5 grid size and 10 poses).

Initially, a surgical frame has been anchored to the organ of interest as shown in Fig. 2. After loading the patient-specific dataset, a hologram of the organ of interest appears in front of the user's initial position. Correspondences between the hologram and the fiducial markers can then be established by using the tracked surgical pointer. Fiducial markers can be defined and then be mapped with respect to the surgical frame. After finishing this process, an orthonormal basis is created in the physical space, which has its counterpart in the image space and, therefore, a transformation can be determined to map the hologram with respect to the surgical frame as shown in Fig. 2.

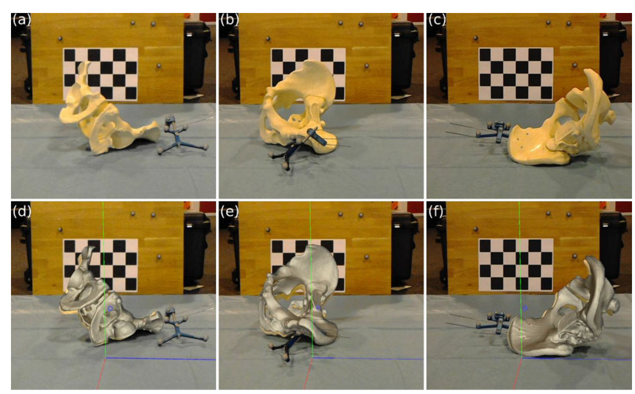

Fig. 2 **a–c** Male pelvis model with acetabulum and cancellous inner structures. **d–f** Superposition between the physical specimen and its corresponding isosurface mesh represented with respect to the surgical frame

Conclusion

Preoperative planning may be an extremely complex and cumbersome task, involving different qualitative and quantitative aspects, such as patient's physical and mental health conditions and records, different image-acquisition protocols, different clinical laboratory results, multiple surgical choices for the same case, and optimal surgical sequences and maneuvers that should ideally be performed during a surgical intervention. It is important to note that surgeons may have several competing responsibilities and multiple patients and surgical procedures to be carried out on the same day and on pre-specified time windows. For these reasons, OHMDs may be able to create an opportunity for a paradigm shift in the field of CAS, since all this detailed information could easily be displayed on virtual and interactive screens in the operating room on the same time and in real time. A very important aspect of using such OHMDs is that it can be very intuitive, especially among inexperienced surgeon, since surgical instruments and maneuvers motions are represented with respect to the surgeon's visual system and, therefore, attention disruptions are more likely to be reduced in terms of the surgeon's gaze, considering that the surgeon would not need to be searching for a conventional display located at static location in the operating room.

References

[1] Thrun S, Probabilistic robotics, *Commun. ACM*, 2002.

[2] Hartley R, Zisserman A, *Multiple View Geometry in Computer Vision*, vol. 2, no. 2. Cambridge University Press, 2004.

Perspective pin-hole model with planar source for augmented reality surgical navigation based on C-arm imaging

Ho-Gun Ha, Sangseo Jeon, Seongpung Lee, Hyunseok Choi, and Jaesung Hong

DGIST, Department of Robotics Engineering, Daegu, Republic of Korea

Keywords Augmented reality · Calibration · Radiography · Surgical navigation

Purpose

For augmented reality surgical navigation based on C-ram imaging, accuracy of the overlaid augmented reality onto the X-ray image is imperative. However, overlay displacement is generated when a conventional pin-hole model describing a geometric relationship of a normal camera is adopted for C-arm calibration [1–3]. Thus, a modified model for C-arm calibration is proposed to reduce this displacement, which is essential for accurate surgical navigation.

Methods

AR surgical navigation with C-arm X-ray images occasionally exhibits significant displacement. Figure 1 shows the displacement between AR and the corresponding X-ray image for bead centers in a 3D phantom, providing a demonstration of the problem. This displacement depends not on spatial location but rather the 3D phantom volume, i.e., depth which is the distance between the object and X-ray source in the C-arm.

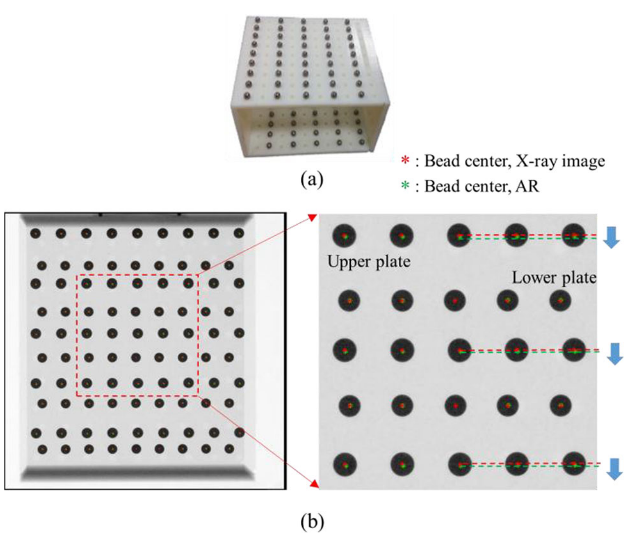

Fig. 1 AR overlay errors due to the object depth: **a** 3D phantom and **b** AR overlay displacement

Based on the analysis of displacement pattern generated for three dimensional objects, we assumed that displacement originated by moving the X-ray source position toward the depth. In the proposed method, X-ray source movement was modeled as variable intrinsic parameters and represented in the perspective pin-hole model by replacing the point source with a planar source. As the depth reduces, the effective source size increases from the plate's point of view. Consequently, as shown in Fig. 2, the equivalent point source of the upper plate is located behind the one of the lower plate, which results in an elongated focal length and shifted principal point. Variation of the equivalent point source can be derived from the planar source shape change according to the depth.

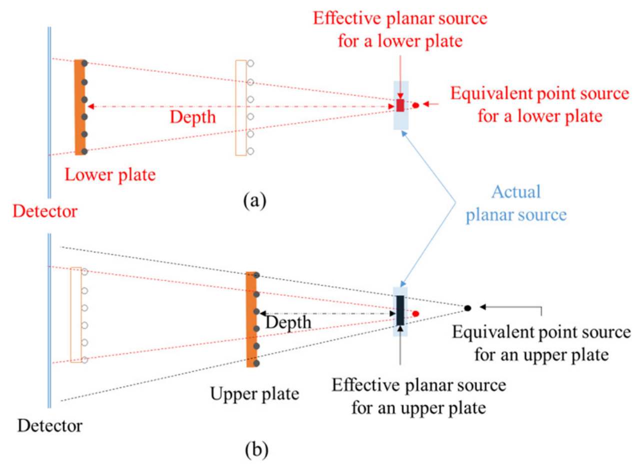

Fig. 2 Proposed planar source model showing the equivalent pin-hole model for **a** lower and **b** upper plate of the 3D phantom

Results

The improvement which represents a reduced displacement was verified by comparing overlay accuracy for augmented reality surgical navigation between the conventional and proposed methods. The proposed method achieved more accurate overlay on the X-ray image in spatial position as well as depth of the object volume.

Conclusion

We investigated the soundness of the calibration model for accurate AR surgical navigation based on C-arm imaging. Through the experimental results, we validated that intrinsic parameters that describe the source position were dependent on depth for a three dimensional object, and showed that displacement can be reduced by using the proposed planar source model.

Acknowledgements

This work was supported by the Technology Innovation Program (10063309, Development of high-precision modular restoration system for fracture reduction and bone deformity correction) funded by the Ministry of Trade, industry & Energy (MOTIE, Korea) and by the Robot industry fusion core technology development project through the Korea Evaluation Institute of Industrial Technology (KEIT) funded by the Ministry of Trade, Industry and Energy of Korea (MOTIE) (NO. 10052980).

References

[1] Hofstetter R, Slomczykowski M, Sati M, Nolte L-P (1999) Fluoroscopy as an imaging means for computer-assisted surgical navigation. Computer Aided Surgery 4 (2): 65–76

[2] Tsai R (1987) A versatile camera calibration technique for high-accuracy 3D machine vision metrology using off-the-shelf TV cameras and lenses. IEEE Journal on Robotics and Automation 3 (4): 323–344

[3] Zhang Z (2000) A flexible new technique for camera calibration. IEEE Transactions on pattern analysis and machine intelligence 22 (11): 1330–1334

Interventional device guidance support with proximal audio emission signal acquisition

A. Illanes[1], A. Boese[1], I. Maldonado[1], A. Pashazadeh[1], A. Schaufler[1], N. Navab[2], M. Friebe[1]
Otto-von-Guericke University, INKA Intelligente Katheter, Magdeburg, Germany
[2]Technische Universität München, Fakultät für Informatik, Munich, Germany

Keywords Acoustic emission · Guided surgery · Interventional device · Autoregressive modelling

Purpose

Targeting and subsequent verification is one of the main issues when medical interventional devices (MIDs) such as needles, catheters and guide wires are used [1, 2]. In combination with the clinician's skills and experience accurate device placement is essential for a successful surgery. Visual feedback from a diagnostic imaging modality as computed tomography, ultrasound or magnetic resonance is helpful to achieve that. However, even with image guidance accurate placement cannot be guaranteed due to image artefacts or in case of preoperative image guidance due to patient motion.

In this work we propose a new approach for MID/tissue interaction monitoring and surgery augmentation using acoustic emission (AE) data acquisition from the proximal end to extract dynamical characteristics of the interaction between the distal tip and the tissue. By applying advanced signal processing techniques to the acquired audio signal it is possible to identify and characterize significant events related to the interaction of the MID distal tip with the tissue, such as penetration friction and puncture dynamics. In contrast with recent papers on Surgical Soundtracks or auditory display [3], which use medical image analysis for sonification, this work aims at acquiring, modifying and amplifying natural sounds of tool/tissue interactions.

Methods

Experimental setups (ES) for two different MIDs, an *18*G *200* mm length biopsy needle with the needle core (ITP, Germany) and a 0.014-in. guide wire (Boston Scientific, US), were implemented. The main objective of the ES for the biopsy needle was to observe audio signal dynamical changes when the needle passes through different tissue layers. In contrast the guide wire ES intended to analyze signal dynamics of perforation in vascular structures. For both experiments AE signals were acquired using a stethoscope connected to a microphone which was directly and firmly attached to the proximal end of the MID via a 3D printed adapter (see Fig. 1). A gelatin phantom filled with different fruits, chicken breast and liver located at 6 cm deep was used for the biopsy needle, and porcine coronary arteries were used for the guide wire.

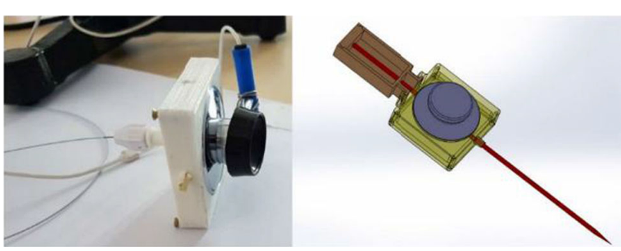

Fig. 1 Connection between the stethoscope and the guide wire and needle respectively

Time-varying auto-regressive (TV-AR) spectral analysis was employed to characterize dynamic changes and to compute the time-varying maximal energy pole (TV-MEP) for subsequent analysis of MID/tissue interaction characterization patterns [4].

Results

Figure 2 shows the obtained audio signal and the TV-MEP signal for needle insertion in persimmon fruit and for guide wire coronary artery perforation. For the needle insertion in persimmon it is possible to observe that in the audio signal it is difficult to observe the time instants when the needle enters and leaves the fruit, while in the TV-MEP signal these time instants are clearly identifiable. In the case of guidewire perforation we can observe that the patterns observed in the TV-MEP signal during a perforation were significantly different to other observed events occurring in a guide wire.

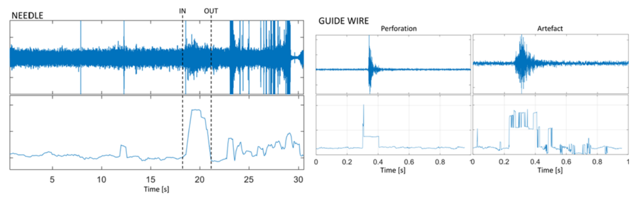

Fig. 2 Examples of obtained results from the audio signal acquisition and processing

Conclusion

The presented research approach shows a novel and relatively simple method to obtain valuable information for MID guidance and tissue/device interactions using an attached microphone that records the propagated sound over the devices shaft for further analysis and evaluation. These interactions starting at the tip of an interventional device, e.g. a needle entering human tissue, can be picked up and detected on the proximal end of a standard clinically used device. Integration of the device sound could enhance and improve device guidance. It could also be used as a quality assurance tool indicating and verifying that a target has been reached. This could prove valuable especially for biopsies and reduce false negative results. It could also prove a valuable correction and verification tool for robotic surgery assistance that relies on preoperative images. This research is clearly at its beginning. We hope that this paper offers a new path for the computer assisted intervention community to elaborate further the hardware and improve the methodology in order finally to validate and transfer CAI solutions including auditory sensing and guidance into clinical practice.

References

[1] Abolhassani N, Patel R, MoallemM (2007) Needle insertion into soft tissue: A survey. Medical Engineering and Physics, 29(4), 413–431.
[2] van Gerwen DJ, Dankelman J, van den Dobbelsteen JJ (2012) Needle–tissue interaction forces–A survey of experimental data. Medical Engineering and Physics, 34(6), 665–680.
[3] Black D, Hansen C, Nabavi A, Kikinis R, Hahn H (2017) A survey of auditory display in image-guided interventions. International journal of computer assisted radiology and surgery, 12(10), 1665–1676.
[4] Thanagasundram S, Spurgeon S, Schlindwein FS (2008) A fault detection tool using analysis from an autoregressive model pole trajectory. Journal of Sound and Vibration, 317(3–5), 975–993.

Development of intraoperative plantar pressure measuring system considering weight bearing axis

Izumu Hosoi[1], Etsuko Kobayashi[1], Song Ho Chang[2], Takumi Matsumoto[2], Qi An[1], Emi Anzai[3], Yuji Ohta[3], Ichiro Sakuma[1]

[1]School of Engineering, The University of Tokyo, Tokyo, Japan
[2]Department of Orthopaedic Surgery, Faculty of Medicine, The University of Tokyo
[3]Biomedical Engineering, Ochanomizu University, Tokyo, Japan

Keywords Treatment for foot deformation · Measurement of the plantar pressure distribution · Physiological load axis · Surgical navigation

Purpose

Hallux valgus is a common foot deformity that may require foot surgery [1]. It reduces the gait balance of the patient because of pain and deformation. Surgical reconstructions in three dimensions are needed for the treatment of foot and ankle deformities to obtain the same sole pressure as that in healthy people. However, the major problem with patient treatment is that surgical performance is influenced by the skill and experience of medical doctors. Intraoperative judgement by surgeons depends on the two-dimensional X-ray images and palpation. To solve these problems and improve surgical outcomes, studies were carried out to measure plantar pressure distribution during surgery [2–3]. However, it is not possible to measure plantar pressure distribution accurately under various postures during operation. Therefore, we proposed the intraoperative plantar pressure measurement (IPPM) device that enable to measure plantar pressure distribution even when the patient is in the supine position.

Methods

To measure the plantar-pressure distribution accurately while the patient is in the supine position, it is necessary to push the pressure sensor of the IPPM device to the affected foot in the same direction as that in which the ground pushes their body while in a standing position. If the pushing direction is inappropriate, the plantar-pressure distribution cannot be accurately measured. Hence it is important to reproduce the physiological load axis that can express the direction of the exact floor reaction force. At first, we assumed that the physiological load axis equals to the floor reaction vector and then performed the following experiment based on the hypothesis that the physiological load axis faces the direction of the femoral head center. The experiment was conducted in two phases: (1) identification of the femoral head center in the human body using pivot calibration algorithm [4] and (2) investigation whether the physiological load axis passes through the femoral head center in four postures. According to this experiment, the distance error between the femoral head center and the physiological load axis vector falls within 3 mm in all postures. As the femoral head size was approximately 40–50 mm (average), the floor reaction force vector was found to pass through the femoral head center in the static standing state.

Second, according to the result of this experiment, we developed the IPPM device (Fig. 1). This device comprises a monitor, a computer, a plantar pressure measurement device, and an optical sensor which was used to track the position of the device and the subject's thigh. The size of IPPM device is 320 × 230 × 90 mm and its weight is 2.5 kg. The PC draws the trajectory of the thigh and the shape of the device at the correct position using the information of the rotation matrix and the translation vector obtaine from the optical sensor. Based on the information displayed on the monitor, the operator aligns the position of the device such that the physiological load axis faces the femoral head center and presses the device in the direction to measure the plantar pressure distribution, thereby reproducing the physiological standing load.

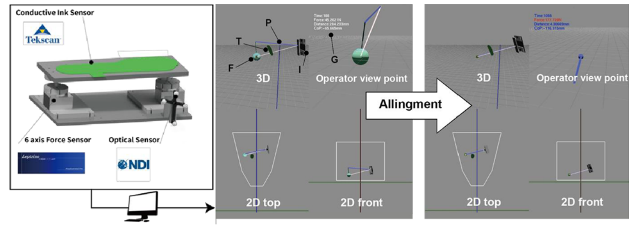

Fig. 1 Overview of the IPPM device (3D F: femoral head center, T: trajectory of thigh; P: physiological load axis, I: IPPM device, operator viewpoint G: Force: pushing force, distance: the distance between the femoral head center and physiological load axis; CoP, center of pressure)

Results

Figure 2 shows the plantar pressure distribution at standing positon, one with the proposed device, one without the device. This result show that using IPPM device, plantar pressure distribution could be measured more accurately to one of standing posture than without using the device. It seems that it became possible to prevent measurement of excessive plantar-pressure distribution by pressing the device so that the physiological load axis passes through the femoral head center.

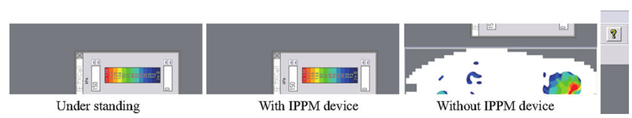

Fig. 2 The plantar pressure distribution at standing position, one with IPPM device, and one without IPPM device

Conclusion

We first investigated the positional relationship between the physiological load axis and the subject's body in a standing position, and clarified that the physiological load axis passes through the femoral head center. We then constructed a navigation device that can extract the physiological load axis by pushing in the direction of the femoral head center, and measure the plantar pressure distribution. The plantar pressure distribution extracted by the proposed device could reproduce the plantar pressure distribution equivalent to one at the standing positon accurately.

This work was partly supported by Terumo foundation for life sciences and arts and JSPS Kakenhi grant number 26108008.

References

[1] Menz HB, Roddy E (2011) Impact of hallux valgus severity on general and foot-specific health-related quality of life. Arthritis Care and Research 63(1): 396–404
[2] Ellis SJ, Hillstrom H (2009) The development of an intraoperative plantar pressure assessment device. Foot & ankle international 30(4): 333–340
[3] Ricther M, Zech S (2009) Is intraoperative pedography helpful in clinical use-Preliminary results of 100 cases from a consecutive, prospective, randomized, controlled clinical study. Foot and Ankle Surgery 15(4): 198–204
[4] Holzreiter S (1991) Calculation of the instantaneous centre of rotation for rigid body. Journal of Biomechanics 4(7): 643–647

Laparoscopic training using a quantitative assessment and instructional system

T. Yamaguchi[1], R. Nakamura[2]
[1]Department of Medical System Engineering, Graduate School of Science and Engineering, Chiba University, Chiba, Japan
[2]Center for Frontier Medical Engineering, Chiba University, Chiba, Japan

Keywords Laparoscopic training system · Surgical skill assessment · Skill evaluation and feedback · Educational support system

Purpose

Laparoscopic surgery requires complex surgical skills. Hence, surgeons require continuing surgical education and training to improve their surgical techniques. Quantitative assessments of a surgeon's skills and provision of feedback are important for conducting effective training. We have developed a laparoscopic surgical training system for routine use [1, 2]. However, this system does not include a tool for adequate feedback. The aim of this study was to develop an inexpensive training system that provides automatic feedback and evaluation of technique.

Methods

We identified the appropriate instrument via image processing of commercial web camera images. We combined a moving object detection method and a straight-line detection method into an algorithm. To quantify performance features, we calculated the Motion Analysis Parameters (MAPs) of the instrument comprising task time, average velocity, work density, and instrument cross time. Based on the results, we developed a method for evaluating a surgeon's skill level. We calculated a performance value, V, and set the target value from the deviation value. V was obtained by applying a leave-one-out cross-validation method, in which one surgeon selected from experimental data was chosen to be a discrimination object, and the other surgeons to be discriminants. The mean of each for all discriminants was defined A, and the standard deviation of each MAP for all discriminants was S. For a surgeon's MAP value, v, the surgeon's performance value V was calculated as:

$$V = (10 \times (v - A)/S) + 50 \quad (1)$$

In calculating individual MAP scores, we used the relationship between a normal distribution curve and the standard deviation. The overall MAPs score, T, was obtained by adding the weighted individual MAP scores. We subsequently made adjustments to the distribution of T. First, we narrowed down the overall MAP distribution to its 99% confidence interval. When the sum of the weighted individual MAP scores for a surgeon was t, the average t for all surgeons was t_A, and the standard deviation of t was S. The upper bound of the 99% one-sided confidence interval, t_M, was calculated using Eq. (2). t_M was defined by a full score of 100 points, and the lower limit was defined as the expected minimum score of 10 points. The value of T after the distribution adjustment, was obtained using Eq. (3).

$$t_M = t_A + S \times 2.58 \quad (2)$$

$$T = (t - 10)/(t_M - 10) \times 100 \quad (3)$$

The feedback system was developed using MAPs-based radar charts and scores for determining skill levels. Additionally, we constructed a system that indicated when an instrument intersection occurred by the position of an orange part. As a result of reviewing several videos, we set thresholds to 100 pixels and extracted surgical instrument crossing times above that threshold only. These methods were evaluated based on the videos of 38 surgeons performing a suturing task, of which 16 were experts and 22 were novices.

Results

There were significant differences in the MAPs among surgeons, therefore, MAPs can be effectively used to quantify a surgeon's performance features. The results of the skill evaluation and feedback differed greatly between skilled and unskilled surgeons, and it was possible to identify areas for improvement for the procedures performed in this study (right and center in Fig. 1). Furthermore, the results obtained for certain novice surgeons were similar to those obtained for skilled surgeons (left in Fig. 1). The results from presenting the conditional instrument cross times are shown in Fig. 2. We found that instrument crossing happened at different times among surgeons.

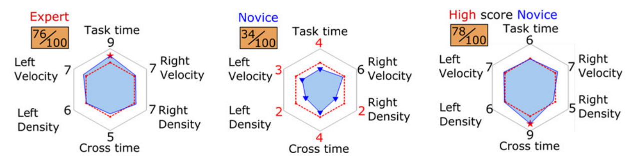

Fig. 1 Example of the radar chart and scoring method

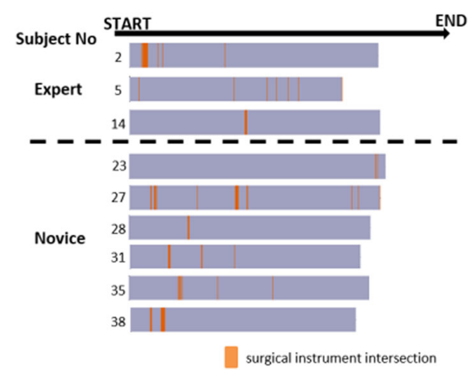

Fig. 2 Presentation of instances in which instrument intersections occurred

Conclusion

In this study, we developed a method for automatically detecting the tip position of a surgical instrument using an image processing method from an inexpensive USB camera image. Furthermore, it was possible to calculate surgical performance scores using MAPs, thereby quantitatively assessing skill level during training on a pad and providing feedback. This system can be used to assess the skill level of surgeons independent of the years of experience. It effectively provides an understanding of the individual's current surgical skill level. This system is inexpensive, simple, and objective as a quantitative assessment and instructional training system for laparoscopic surgery.

Acknowledgments

This research was partly supported by the Japan Science and Technology Agency, PRESTO (No. JPMJPR16D9).
T. Yamaguchi acknowledges financial support from Frontier Science Program of Graduate School of Science and Engineering, Chiba University.

References

[1] Suzuki K, Nakamura R, Sugino T (2014). Surgical Instruments Trajectory Analysis for Training of Endoscopic Surgery. Trans Jpn Soc Med Biol Eng 52 (suppl): O-267–O-268.
[2] Yamaguchi T, Suzuki K, Nakamura R (2016). Development of a visualization and quantitative assessment system of laparoscopic surgery skill based on trajectory analysis from USB camera image. Int J Comput Assist Radiol Surg 11(suppl): S254–S256.

Surface scanning for abdominal surgical interventions

J. Geurten[1], W. Xia[2], U. Jayarathne[2], T.M. Peters[2], E.C.S. Chen[2]
[1]University of Waterloo, Biomedical Engineering, Waterloo, Canada
[2]Robarts Research Institute, Western University, London, Canada

Keywords Surface reconstruction · Laser scanning · Calibration · Intra-operative navigation

Purpose

In the context of multi-port minimally invasive abdominal surgery, we present an active system for 3D scanning organ surfaces endoscopically. The system comprises two surgically tracked surgical instruments: a clinical endoscope camera and a custom plane laser source. The system can be integrated into clinical navigation systems where the endoscope camera and laser subsystem enter the abdomen via separate access ports. Once the internal organ surface has been scanned, it can be used for rigid body registration with preoperative patient data or serve to initialize subsequent deformable registration [1]. The accuracy of the system was validated by means of CT registration with scans derived from the proposed system, where surface target registration error (surface TRE) [2] is reported.

Methods

The scanning subsystem employs a 650 nm red laser generator with a 120-degree plane divergence diffractive lens within a stainless steel tube with an endoscopic form factor. The imaging subsystem uses a hand-eye calibrated stereo laparoscope (Surgical laparoscope, Olympus). An optical DRF was rigidly attached to each of the handles to enable spatial tracking using an optical tracking system (Spectra, Northern Digital Inc., Canada), refer to Fig. 1.

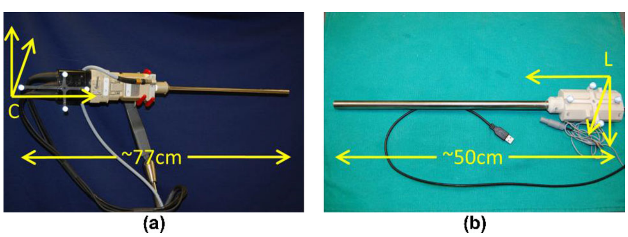

Fig. 1 **a** A stereo surgical endoscopic (Olympus) and **b** a custom laser instrument. Both instruments are spatially tracked using an optical DRF rigidly attached at the handle

The geometry of the laser beam with respect to its DRF was calibrated using a custom calibration phantom. This calibration phantom comprises a metal block with a thin engraved line attached to a DRF where the geometry of the line is known with respect to its DRF by manufacturing. By aligning the laser plane projection to this line, laser beam calibration is formulated as a plane fitting problem, for which the laser plane origin ($\boldsymbol{o}'$) and the plane normal ($\boldsymbol{n}'$) are determined . Collaterally, an optical axis **O** can be defined for the surgical video camera after camera calibration and a hand-eye calibration. Once both tools are calibrated and tracked, surface reconstruction is formulated as the intersection between the line-of-sight ray (Q') and the laser plane beam ($\mathbf{n}', \mathbf{o}'$) :

$$W_q = \frac{(\boldsymbol{o}' - C')\cdot \boldsymbol{n}'}{Q'\cdot \boldsymbol{n}'} Q' + C'$$

where W_q is a point on the surface of the organ intersected by the laser plane, and C' is the camera center. All above points and vectors are specified in the coordinate system of the tracker (**W**).

To assess the accuracy of the proposed scanning system, an ex vivo phantom with a porcine kidney and a lobe of porcine liver was positioned in a torso box. A CT scan of the torso phantom, acquired using an O-Arm (Medtronic, Ireland), served as the ground truth for subsequent analysis.

Results

Two scans of the organ surfaces were derived; one of the liver and one of the liver and kidney. A total of 127 images of the liver were acquired resulting in a total of 33,571 laser scanned 3D points. A subsequent scan of the liver and kidney resulted in 43,910 laser scanned 3D points. Using rigid-body ICP registration, the Euclidean distances between the computed scanline surfaces and the CT scanned liver and liver/kidney were computed and summarized in Table 1. The scans and their associated surface TRE are presented in Fig. 2.

Table 1 Accuracy of the laser surface scanning system validated using an ex vivo porcine model

	Mean surface TRE (mm)	SD (mm)	RMS (mm)	Max (mm)
Liver	0.74	1.04	1.28	13.18
Kidney/liver	0.23	0.31	0.39	7.80

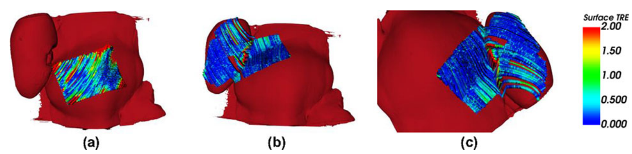

Fig. 2 Surface reconstruction of the kidney and the kidney/liver lobes using two camera views

The ICP registration statistics are presented in Table 1. More than 90% of the vertices exhibited TRE less than 2 mm resulting in sub-millimeter mean surface TRE. The surface reconstruction results demonstrate an accurate means of performing multi-modal patient-specific data registration.

Conclusion

An active 3D surface scanning system for multi-port MIS abdominal surgeries is presented. Using a novel calibration framework, surface scanning was formulated as the intersection between the camera line-of-sight and the scanner laser beam. The camera and laser calibrations require minimal images ($\sim$ 10–12) and user interaction on the order of minutes [5]. Using a single-beam laser allows us to reconstruct a 3D scanline in real-time since the segmentation of a single laser projection is trivial, and the computational requirement for our system is extremely low.

The proposed scanning system provides a viable and accurate means of performing organ scanning endoscopically and subsequently initializing patient data registration. In the ex vivo experiments, our system achieves sub-millimeter surface reconstruction accuracy which is comparable to other systems [3–4]. A commercial endoscope camera was integrated into the system, therefore, minimizing the impact on surgical workflow. Despite the accuracy of the system, we cannot currently account for motion artefacts (respiratory and cardiac motion). This study demonstrates the feasibility of using 3D surface scanners to register subsurface anatomical details to endoscopic video to enable the next generation of minimally invasive endoscopic procedures.

References

[1] Hill DLG, Batchelor PG, Holden M, Hawkes DJ (2001) Medical image registration. Physics in Medicine & Biology 46(3): 1–45
[2] Ma B, Ellis RE (2006) Analytic expressions for fiducial and surface target registration error. In: MICCAI 2006, Part II: 637–644
[3] Maier-Hein L, Mountney P, Bartoli A, Elhawary H, Elson D, Groch A, Kolb A, Rodrigues M, Sorger J, Speidel S, Stoyanov D

(2013). Optical techniques for 3D surface reconstruction in computer-assisted laparoscopic surgery. Medical Image Analysis 17(8): 974–996

[4] Maier-Hein L, et al. (2014) Comparative validation of single-shot optical techniques for laparoscopic 3-D surface reconstruction. IEEE Transactions on Medical Imaging 33(10): 1913–1930

[5] Morgan I, Jayarathne U, Rankin A, Peters TM, Chen ECS (2017) Hand-eye calibration for surgical cameras: a procrustean perspective-n-point solution. International Journal of Computer Assisted Radiology and Surgery 12(7): 1141–1149

3D modeling and 3D printing in surgical planning of cloacal malformations

J. Parthasarathy[1], D. G. Bates[1], D. Halleran[1], A. Gasior[1], M. Levitt[1], R. Wood[1]

[1]Nationwide Children's Hospital, Radiology, Columbus, United States

Keywords 3D printing · Cloaca · Anatomical model · Surgical planning

Purpose

3D modeling and 3D printing have found many applications in cranio maxillo facial, plastic/reconstructive, orthopedic, and cardiac surgeries in the areas of, pre-surgical planning, surgical guides, implantable devices, as well as patient and trainee education [1]. The range of applications is increasing with advancements in image processing and printing processes and materials. We herein describe a process pathway for 3D printing of patient-specific models for cloacal malformations that could be used as an adjunct to surgical planning. A cloaca is a congenital anomaly whereby there is a confluence of vagina, urethra, and rectum into a common channel opening on the perineum. It occurs in 1 in 20,000 live births and is a challenge to pediatric surgeons due a varying nature of the anatomy, the complexity of the structures and their relationships, and a wide spectrum of defects. A pediatric surgeon faces the challenges of trying to achieve urinary control, bowel control, and sexual function for the patients. Surgical planning and prognosis depends on precise measurements of the common channel and urethra. Patients with a common channel less than or equal to 3.0 cm are more common and have a good prognosis compared to patients with a greater than 3 cm common channel which are more challenging and need a more experienced surgeon [2]. Typically a voiding cystourethrogram and 3D rotational fluoroscopy images are used for diagnostic purposes. We hypothesized that 3D color coded virtual models and multicolor 3D printed models could provide the critical information to the surgeon along with the spatial relationship to pelvis and sacrum, and might improve surgical planning.

Methods

Patients with cloacal malformation were evaluated in the department of radiology and in the Center for Colorectal and Pelvic Reconstruction at Nationwide Children's Hospital. Patients underwent general anesthesia and catheter placement into the bladder, mucus fistula (for distal bowel visualization), and vagina (via the common channel or through a vaginostomy, if present). Contrast was injected to distend the bladder, vagina, and distal colon. Once distended, 3D rotational fluoroscopic examination was performed and multi planar images in the axial, coronal, and sagittal planes were acquired. The CT images were imported into MIMICSTM software (Materialise Belgium) in DICOM format. Using the tissue segmentation and region growing tools in MIMICS, the bladder, vagina, colon, rectum, common channel, urethra, vertebral column, and pelvis were segmented as separate masks (layers). Each of the masks is then converted into a 3D model representing the structural anatomy as shown in Fig. 1. The 3D models representing the cloacal anatomy along with the pelvis and vertebral column were exported as a.STL (Stereolithography file or Standard Tessellation Language file) to Geomagic Freeform (3D Systems USA) in preparation for 3D printing. The models were ensured as ready for print and support structures were added and exported as individual.STL files n file format that is accepted by any 3D printer. 3D printing consists of a group of technologies where material (liquid photopolymer) is either jetted (polyjet) or laid one layer at a time and solidified using either UV or laser power. At our institution, we established 3D Printing Lab with dedicated workstations for each of the aforementioned software processes. We use a Stratasys Polyjet CONNEX 3 Objet 350 printer, which has the ability to print 30 micron layers in multiple colors and material types (e.g., hard and flex materials within the same model). Material assignment was critical for proper visualization of the structures. The colors assigned for printing were: (1) clear—bladder, (2) opaque magenta—vagina, (3) opaque pink—colon with rectum, (4) urethra–white, (5) common channel—clear magenta, and (6) pelvis white. Once the print is completed, the model is washed and cleaned to remove support material. The model is then coated with a protective layer that increases the transparency. A final printed model is shown in Fig. 2.

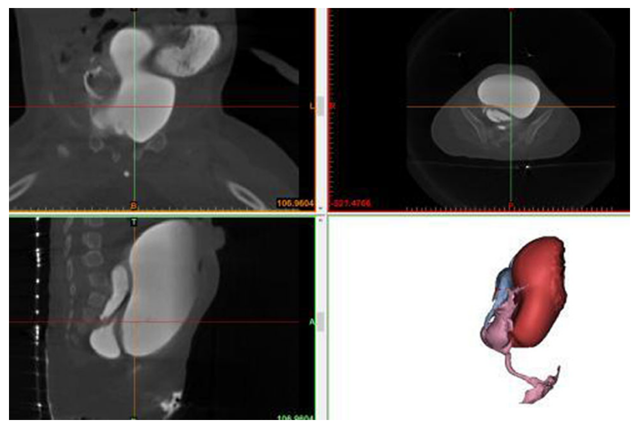

Fig. 1 3D Multiplanar fluoroscopic images and 3D virtual cloaca model

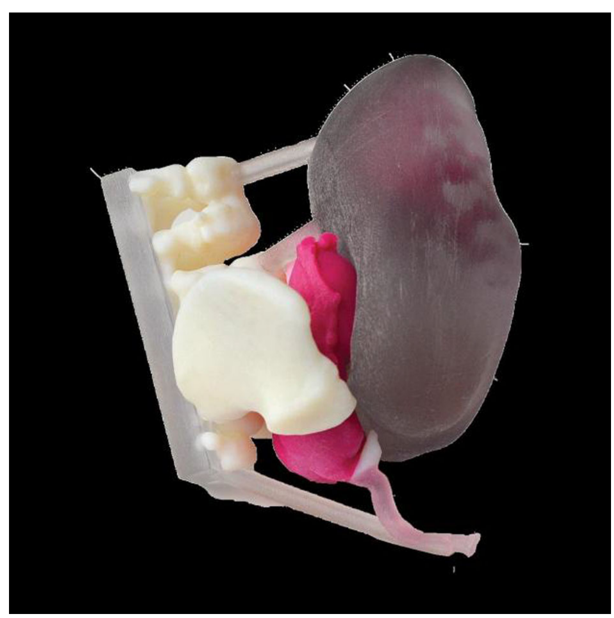

Fig. 2 3D printed multi-color model of cloaca with pelvic and sacral bones

Results

We describe an established process for 3D modeling and printing from cloacagrams depicting the complex anatomy and the spatial relationship of the structures in the region of interest. The urethral length and length of the common channel measured on the 3D reconstructed virtual model and the 3D printed model were within 0.5 mm difference. The models gave the surgeon a tactile perception of the structures and the ability to view spatial relationships of the regional anatomy prior to surgery. Measurements of the urethra and the common channel are critical factors for determining the surgical plan, and were successfully measured with precision using this technology. The models were also found to be very useful in training surgeons and for patient family education of the condition.

Conclusion

Color coded 3D virtual models and multicolor 3D printed models created from 3D rotational fluoroscopic examination was performed and multi planar images. The model provides critical information of the anatomical malformation to the surgeon along with the spatial relationship to pelvis and sacrum, and improves surgical planning.

References

[1] Heller M, Bauer HK, Goetze E, Gielisch M, Roth KE, Drees P, Maier GS, Dorweiler B, Ghazy A, Neufurth M, Müller WE, Schröder HC, Wang X, Vahl CF, Al-Nawas B (2017), Applications of patient-specific 3D printing in medicine, Int J Comput Dent. 19(4): 323–339.

[2] Levitt A M, Peña A (2010), Cloacal malformations: lessons learned from 490 cases, Seminars in Pediatric Surgery 19, 128–138.

Comparison of different kinematic methods for determining the hip joint center

S. S. Hung[1], P. L. Yen[1]

[1]Taipei Tzuchi Hospital, The Buddhist Tzuchi Medical Foundation, Orthopedic Surgery, New Taipei City, Taiwan

Keywords Hip joint center · Motion analysis · Geometric sphere fitting · Hip biomechanics

Purpose

The purpose of this research is to evaluate the different kinematic method for estimating the HJC in vitro in a cadaver study

Methods

A fresh-frozen adult cadaver with no visible pathology to the hip joint was provided in this study. Under supine position, two sets of infrared passive optical markers were firmly fixed onto both right iliac crest and right femur shaft. The coordinates of these markers were collected by NDI optical tracking system (Northern Digital Inc., Canada), at 20 Hz of sampling rate. The pelvic marker was regarded as the origin of the coordinate system, and the trajectories of the femoral movement were all corresponded to the pelvis. Three passive motions of the femur, including flexion–extension (FE), adduction-abduction (AA) and circumduction (CIR), were achieved by moving the lower leg of cadaver. The knee was kept in full extension during FE and AA, while in arbitrary flexion during CIR. Each movement was operated four times, with a 5 min break between each test, in order to allow the soft tissue tension to return back to its original condition.

The results of three motions were compared to the actual center of femoral head which was considered as the standard point. In order to obtain this position, the femoral head was exposed via anterior arthrotomy, and the surface was partially swept by a scanning probe. The center of femoral head was subsequently obtained via the least square sphere fitting method [1].

The algorithm used for assessing the motion of femur was the geometric sphere fitting method. This method has already been proven as one of the standard ways to estimate HJC [2, 3].

Results

The mean value of HJC was (17.52, − 194.64, − 142.88), and the average value of the radius of the femur head was 21.65 mm, which was compatible with the data published in literature of 22.45 ± 1.6 mm [4]. The coordinates of HJC obtained in FE, AA and CIR motions were (16.72, − 193.84, − 142.32), (15.23, − 189.29, − 136.00) and (15.90, − 194.28, − 142.51) respectively. The average distance between the femoral skeletal tracker and HJC in three motions was 264.90 mm with a standard deviation of 4.59 mm. The distance errors from the actual femoral head center to the HJC obtained by FE, AA, and CIR motion were 1.30, 8.20 and 1.77 mm respectively.

Figure 1 presents the motion tracts of the three movements and respective calculated HJCs in relation to the actual femoral head center. The corresponding motion arc zone in mean values are as follows: 57.13 (SD 1.67)° in FE motion, 38.04 (SD 3.39)° in AA motion, and 42.20° in CIR motion. Figure 2 shows the distance error between the estimated HJC calculated from different motion arcs and the actual femoral head center. It is found that the error decreases as the range of arc zone increases. In FE motion, the error under the range of 10° is 44.41 mm and dropped down to 2.34 mm if the arc zone increased to 50°. In CIR motion, the error under the range of 10° was 6.32 mm and decreases to 2.35 mm when the range of arc zone is 50°. FE had a greater error than CIR when the arc of motion was only 10°; however, similar error was noted as the arc zone increases to 50°. For the AA motion, the error in the range of 10° was 85.12 mm and improved to 23.94 mm in 40°, which was still considerably higher comparing to the FE and CIR movement. The CIR motion presented a better accuracy than FE motion regardless of its range of motion, with the most accurate estimation obtained when the motion was performed in circumduction at a range between 10° and 40°.

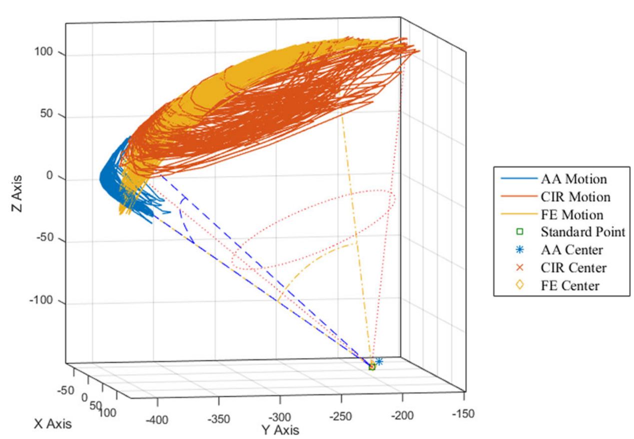

Fig. 1 Trajectories in AA, CIR and FE motion

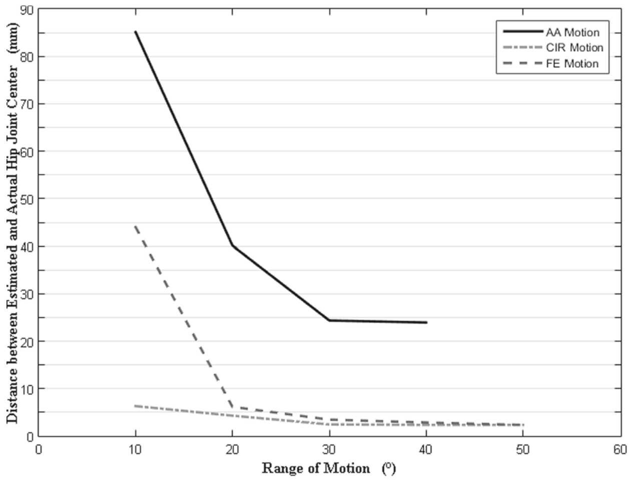

Fig. 2 Distance errors of the three methods at different range of motion

Conclusion

Although a larger range of motion is preferred during the assessment of hip joint center, excessive range of motion may cause unwanted acetabulum clearance, which may subsequently lead to a greater error. We have attempted to identify the optimal value for this range of motion, and the distance error in different range has been calculated as well. As a result, the best accuracy is obtained under an arc zone between 10° and 40° in CIR motion.

This study shows that different types of movement and different ranges of motion may cause significant effect on the evaluation of HJC. The FE and CIR motion can provide a more accurate estimation than AA motion, and the performance is better as the range of arc increased.

References

[1] Ehrig RM, Taylor WR, Duda GN, Heller MO (2006). A survey of formal methods for determining the centre of rotation of ball joints. *Journal of Biomechanics* 39(15): 2798–2809.

[2] Sangeux M, Peters A, Baker R (2011). Hip joint centre localization: Evaluation on normal subjects in the context of gait analysis. *Gait & Posture* 34(3): 324–328.

[3] Piazza SJ, Okita N, Cavanagh PR (2001). Accuracy of the functional method of hip joint center location: effects of limited motion and varied implementation. Journal of Biomechanics 34(7): 967–973.

[4] Lee CK, Kwan MK, Merican AM, Ng WM, Saw LB, Teh KK, Krishnan M (2014). Femoral head diameter in the Malaysian population. Singapore Medical Journal 55(8): 436–438.

Flexible polymeric puncture needle for a nonlinear intervention path

M. AL-Maatoq [1], C. H. Chen[1], A. Boese[1], M. Friebe[1]
[1]Intelligente Katheter, Otto von Guericke University, Medical Engineering, Magdeburg, Germany

Keywords Polymeric biopsy needle · Elasticity performance · Biomechanics · Non-linear path

Purpose

In clinical puncturing procedures (e.g. biopsies or injection of medication), one of the most important steps is the planning of a suitable needle path with least damage which is not always the most direct route. With conventional metal puncture needles, only straight lines between the entry point and the target location are possible. Linear pathways are sometimes not feasible or possible due to sensitive structures or bones on the line. Accessing pathologies on a nonlinear pathway is only possible with proximately bendable and flexible materials. To address the issues of high flexibility for nonlinear accesses, a prototype of fully polymeric needle was developed and tested.

Methods

Puncture needles consist of an inner mandrin and an outer hollow sheet. By removing the mandrin the hollow sheet allows the placement of therapy devices or the collection of biopsy samples. For the polymeric needle, a similar design composed of an inner mandrin and an outer sheet was created. The mandrin is made of Polyether Ether Ketone (PEEK) core (Victrex Company, UK), with an average diameter of 1.21 mm. The sheet is a multilayer design combining different layers of thin wall plastic tubes made of (1) Polyimide (PI), small (S), medium (M), and large (L) with inner diameters of 0.07, 0.073 and 0.077 mm, respectively and (2) PEEK, small (S) and large (L) with inner diameter of 0.075 and 0.085 mm, respectively, (Vention Medical Andorson Company, USA). Groups of prototypes were built. The configurations of these sheet designs are listed in Table 1.

Table 1 Prototype specifications

Needle type	Materials	Outer diameter (OD) mm
Group A	PEEK core + Polyimide tube (S) +Polyimide tube (M)	1.84
Group B	PEEK core + Polyimide tube (S) + Polyimide tube (M) + Polyimide tube (L)	1.86
Group C	PEEK core + Polyimide tube (S) + PEEK tube (S)	2.17
Group D	PEEK core + Polyimide tube (S) + Polyimide tube (M) + Polyimide tube (L) + PEEK tube (L)	2.45

The needle prototypes were tested using a standard bending machine (Z0.5, Zwick Roell, Ulm, Germany), applying an adapted 3-point bending test (plastic ISO 178) to evaluate the flexibility. A commercial puncture needle (ITP GmbH, Bochum, Germany) was chosen as a standard sample for comparison. The test setup was to fix the needle from both sides with the tip of the bending applying force in the middle of the needles with 3 mm deformation at a speed of 1 mm/s. The test was repeated three times for each needle.

Results

The results of experiment are shown in Fig. 1 the metallic comparison needle showed the expected much higher stiffness forces compared to all the PEEK needles. PEEK group A and B, produced very low stiffness force and also did not show large variations between each other. PEEK group C, composed of one polyimide and one PEEK tube as outer layer, showed higher stiffness values. The PEEK tube outer layer causes a higher supporting effect for the needle structure. As we expected, the PEEK group D achieved the highest stiffness force among all PEEK needles, since they have the most layers of polyimide and the PEEK tube at the outmost; however, they are still much more flexible than the metallic comparison needle. To evaluate the performance for non-linear access pathways, a phantom study was performed. The needles exhibited bending capabilities by showing deformations as displayed in Fig. 2.

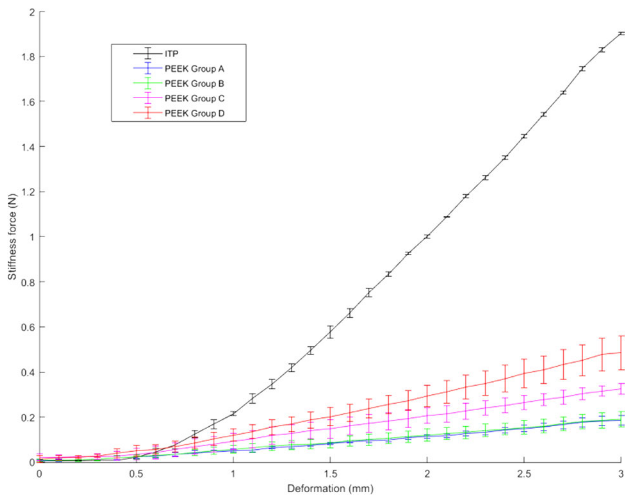

Fig. 1 Comparison for the flexible performance between standard and proposed polymeric needles

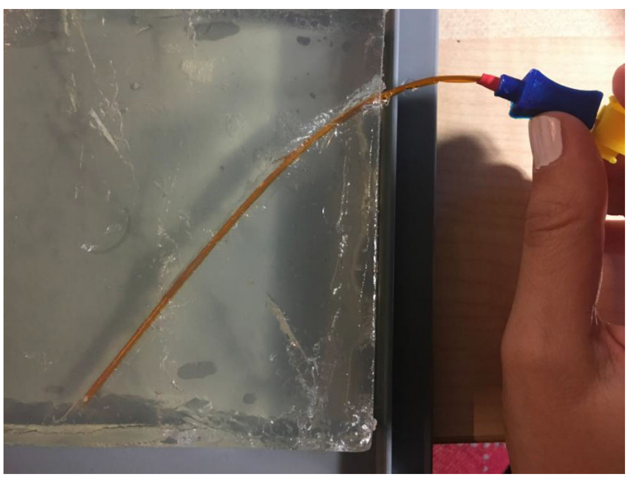

Fig. 2 Needle bending in a gelatin phantom

Conclusion

This study has shown the potential feasibility of a polymer-based MR-compatible biopsy needle with a high flexibility for *in vivo* needle steering. We have checked the flexibility in accordance to the vertical deformation at the center of the needle, and the results indicated that the multiple layer composition of our PEEK needle would have the benefit of better maneuverability and at the same time maintain the stability, which may grant surgeons better control of the needle movement when they steer the needle to avoid critical structures and hit the target inside patient. The next step form this work is to apply to phantom with optimal needle tip shape.

References

[1] Zhao X, Kong L, Ye D, ZhaoY, Wu Z (2014). Flexible tip-steerable needle control with tissue uncertainty. The 26th Chinese Control and Decision Conference (2014 CCDC)

[2] Bui V, Park S, Park J, Ko S (2016). A novel curvature-controllable steerable needle for percutaneous intervention. Proceedings of the Institution of Mechanical Engineers, Part H: Journal of Engineering in Medicine, 230(8), pp. 727–738

[3] Leibinger A, Burrows C, Oldfield M, Rodriguez y Baena F (2015). Tissue motion due to needle deflection. 2015 37th Annual International Conference of the IEEE Engineering in Medicine and Biology Society (EMBC)

Evaluation of breast glandularity using the parametrized mathematical model and mammography

Y. X. Tang[1,2], Y. L. Liu[3], K. M. Lu[1], M. T. Tseng[1], Y. F. Tsai[1], J. Wu[2]

[1]Shin Kong Wu Ho Su Memorial Hospital, Department of Diagnostic Radiology, Taipei, Taiwan

[2]National Yang-Ming University, Department of Biomedical Imaging and Radiological Sciences, Taipei, Taiwan

[3]National Tsing Hua University, Institute of Nuclear Engineering and Science, Hsinchu, Taiwan

Keywords Glandularity · BI-RADS · Mathematical model · Breast density

Purpose

Breast densities can be measured from the levels of X-ray attenuation in dense breast tissues, as obtained from mammography. The risk of breast cancer is highly correlated with the breast density and the clinical classification of breast density is still performed based on a breast imaging-reporting and data system (BI-RADS), the classification results will be affected by the subjective diagnosis of the clinical radiologist and the breast density cannot be accurately quantified. In order to improve the accuracy of quantifying breast tissues, this study uses a parametrized mathematical model to construct the correlation between breast glandularity and photon intensity.

Methods

We used the breast compression thickness and exposure conditions that are typically used in clinics. The equivalent flat phantom of 3–5 cm thickness and glandular/fat ratios of 30/70, 50/50, and 70/30 were used. The exposure conditions were 24, 26, 28, 30, and 32 kVp, and 30, 55, 80, 105, and 130 mAs. The regions of interest (ROIs) of 10×10 mm was selected on the images. The measurements described above were repeated three times, and the mean and standard deviation were estimated. The polynomial fit coefficients were obtained using the multivariable linear regression. Coupled with the physics equations of linear attenuation coefficient, we constructed a parametrized mathematical model to verify the CIRS012A standard breast phantom and breast glandularity obtained from clinical mammograms.

Results

We verified our mathematical model with the standard breast phantom. The parametrized mathematical equation was obtained as $\ln(I) = 13.457–0.12 \times \text{mAs}–0.154 \times \text{kVp}–0.363 \times \text{thickness} + 0.011 \times \text{glandularity} + 0.001 \times \text{mAs} \times x + 0.015 \times \text{kVp} \times x$. The multivariable regression analysis for equivalent flat phantom tests showed a good correspondence, $R^2 = 0.941$ ($p < 0.01$). We found that as the kVp increases, the relative error of the grayscale value increases from -13.46 to -24.09%. The absolute error of the glandular density ratio ranges between 0.08 and 0.28. For CIRS012A phantom, The percent differences of glandularity to the mathematical model were 5.3% (4.5 cm) and 10.3% (5.0 cm) for 21.7% glandularity and 3.8% (6.5 cm) and 5.9% (7.0 cm) for 50.0% glandularity. The average percent differences were 7.9%. Compared with the BI-RADS scale, the breast densities of heterogeneously dense and entirely fat breasts in the mammograms are 0.41 and 0.29, respectively. By converting the mammograms to breast density distribution maps using the parametrized mathematical model, we found that the breast tissue distribution ranges from 21.7 to 31.2%, and that of tumor tissues from 60.7 to 69.3%. Figure 1 shows the craniocaudal view and mediolateral oblique view of the breast density map at 28 kVp and 55 mAs of a 43-year-old female patient.

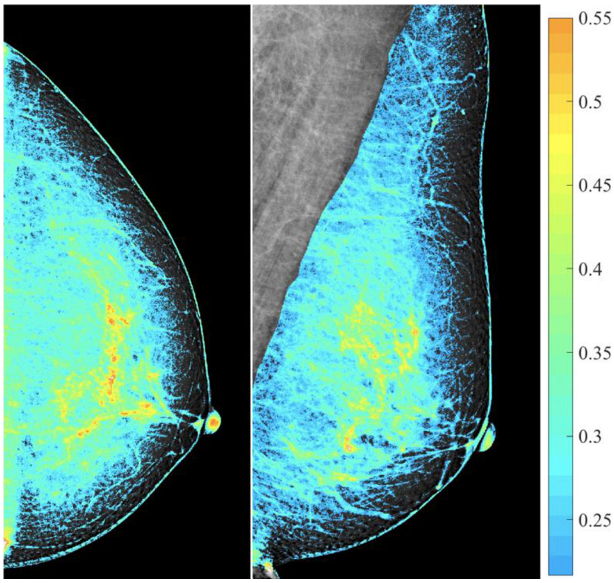

Fig. 1 **a** The craniocaudal view, and **b** mediolateral oblique view calculated using the parametrized mathematical model

Conclusion

The method proposed in this study can quantify breast glandularity effectively and differentiate between different breast tissues and tumor regions. Therefore, it can be used as an auxiliary diagnostic tool by radiologists, further aiding in breast cancer imaging and screening.

Intraoperative stent segmentation in X-ray fluoroscopy for endovascular aortic repair

K. Breininger[1], S. Albarqouni[2], T. Kurzendorfer[1,3], M. Pfister[3], M. Kowarschik[2,3], A. Maier[1,4]
[1]Pattern Recognition Lab, Friedrich-Alexander-Universität Erlangen-Nürnberg, Erlangen, Germany
[2]Computer Aided Medical Procedures (CAMP), Technische Universität München, Munich, Germany
[3]Siemens Healthcare GmbH, Forchheim, Germany
[4]School of Advanced Optical Techniques (SAOT), Erlangen, Germany

Keywords EVAR · Fluoroscopy · Convolutional neural network · Aortic stents

Purpose

Endovascular aortic repair (EVAR) has become the predominant choice for elective repair of abdominal aortic aneurysms (AAAs). In this minimally invasive procedure navigated by intraoperative fluoroscopy, multiple stent grafts are placed in the aorta and visceral arteries to reduce stress on the aneurysm wall and prevent rupture.

Fusion of preoperative data with intraoperative X-ray images has proven the potential to reduce radiation exposure and contrast agent, especially for complex cases requiring branched or fenestrated stents [1]. To provide guidance during EVAR, a segmentation of the aorta from preoperative CT is overlaid onto the fluoroscopic image. However, due to patient movement and introduced devices that deform the vasculature, this fusion can become inaccurate.

In this work, we propose a method to segment the stent graft in fluoroscopic images. A comparison of segmentation and the overlaid preoperative information can then be used to automatically detect a deteriorated fusion without the use of contrast agent and a manual or automatic re-registration can be requested. Previously proposed methods for stent segmentation require either an explicit model of the stent strut configuration [2], or a sequence of images [3], while the approach presented here is model free and works on single X-ray frames to facilitate easy integration into the intraoperative workflow.

Methods

Motivated by the success of convolutional neural networks (CNNs) in related tasks, including segmenting coronary wires in fluoroscopic images [4], we propose a fast, learning-based method to segment aortic stents in single uncontrasted X-ray frames. To this end, we employ a fully convolutional, multiscale network with skip connections (U-net) [5] and residual units. Additionally, we examine whether the incorporation of prior knowledge is able to improve the segmentation. For this purpose, the overlay image or a vesselness image tuned to the expected stent wire width is provided as additional input channels to the network. Furthermore, we investigate whether pretraining with synthetic data helps to converge to a better solution. The parameters of the CNN are optimized using weighted cross-entropy as a loss function.

Results

We trained and evaluated our method on a set of 63 2D X-ray images acquired during 43 EVAR interventions at Heidelberg University Hospital (Heidelberg, Germany) with an angiographic C-arm system. We used 36 X-ray images for training and validation, and tested the segmentation on 27 additional images, splitting the data patient-wise into the different sets. We achieve a Dice coefficient of 0.933 when using X-ray alone, and a Dice coefficient of 0.918 and 0.888 when adding the preoperative model and information about the expected wire width, respectively. Results are presented in Table 1. Exemplary results for the network trained only with fluoroscopic images are presented in Fig. 1. Mean runtime for a single frame was 0.75 s on an NVIDIA GTX 1080.

Table 1 Quantitative results for the stent segmentation for different inputs and pretraining versus random initialization

	Dice coefficient	Precision	Recall	AUC
Fluoro only				
Random	0.933 ± 0.046	0.927 ± 0.032	0.946 ± 0.078	0.996
Pretrained	0.942 ± 0.046	0.943 ± 0.028	0.947 ± 0.077	0.997
Fluoro + overlay				
Random	0.918 ± 0.061	0.915 ± 0.038	0.931 ± 0.099	0.993
Pretrained	0.913 ± 0.051	0.882 ± 0.056	0.954 ± 0.080	0.995
Fluoro + vesselness				
Random	0.888 ± 0.106	0.871 ± 0.092	0.925 ± 0.140	0.990
Pretrained	0.899 ± 0.103	0.885 ± 0.091	0.930 ± 0.133	0.991

Mean and standard deviation over all images over five different random initializations of the networks are shown

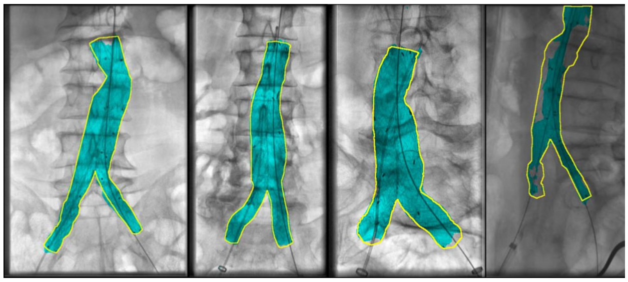

Fig. 1 Exemplary segmentations computed by the network using only fluoroscopic images. The yellow outline represents the ground truth, the cyan overlay shows the computed segmentation. Fluoroscopic images courtesy of Heidelberg University Hospital

Conclusion

The proposed method is fully-automatic, fast, and able to segment aortic stent grafts in fluoroscopic images with high accuracy. Adding additional channels to the input does not show a quantitative benefit, while the effect of pretraining is minor. The performance of the segmentation allows for a comparison with the preoperative model to assess the quality of fusion in an intraoperative environment.

Disclaimer: The methods and information presented in this work are based on research and are not commercially available.

References

[1] Panuccio G, Federico Torsello G, Pfister M, Bisdas T, Bosiers M, Torsello G, Austermann M (2016) Computer-aided endovascular aortic repair using fully automated two and three-dimensional fusion imaging. Journal of Vascular Surgery 64(6): 1587–1594

[2] Demirci S, Bigdelou A, Wang L, Wachinger C, Baust M, Tibrewal R, Ghotbi R, Eckstein H, Navab N (2011) 3D stent recovery from one X-ray projection. MICCAI 2011: 13th International Conference, Proceedings, Part I: 178–185

[3] Volpi D, Sarhan MH, Ghotbi R, Navab N, Mateus D, Demirci S (2015) Online tracking of interventional devices for endovascular aortic repair. IJCARS 10(6): 773–781

[4] Ambrosini P, Ruijters D, Niessen WJ, Moelker A, van Walsum T (2017) Fully automatic and real-time catheter segmentation in X-ray fluoroscopy. MICCAI 2017: 20th International Conference, Proceedings, Part II: 577–585

[5] Ronneberger O, Fischer P, Brox T (2015) U-Net: Convolutional networks for biomedical image segmentation. MICCAI 2015: 18th International Conference, Proceedings, Part III: 234–241

Viewpoint planning for quantitative coronary angiography

A. Preuhs[1], M. Berger[2], S. Bauer[2], T. Redel[2], M. Unberath[1], S. Achenbach[3], A. Maier[1]

[1]Pattern Recognition Lab, Friedrich-Alexander Universität Erlangen-Nürnberg, Germany

[2]Siemens Healthcare GmbH, Forchheim, Germany

[3]Department of Cardiology, Medizinische Klinik 2, Universitätsklinikum Erlangen, Germany

Keywords Coronary angiography · Patient specific imaging · Foreshortening · Desired view

Purpose

In coronary angiography the condition of myocardial blood supply is assessed by analyzing 2-D X-ray projections of contrasted coronary arteries. This is typically done using a flexible C-arm system. Due to the X-ray immanent dimensionality reduction projecting the 3-D scene onto a 2-D image, the viewpoint is critical to guarantee an appropriate view onto the affected artery and, thus, enable reliable diagnosis [1]. Previous work on viewpoint determination systems for quantitative coronary angiography (QCA) [2] require several views of the vessel [4] or a 3-D model [1, 3, 5]. In this work we introduce an algorithm that computes optimal viewpoints for the assessment of coronary arteries without the need for 3-D models.

Methods

We introduce the concept of optimal viewpoint planning solely based on a single angiographic X-ray image. The subsequent viewpoint is computed such that it is rotated precisely around a target vessel, while minimizing foreshortening of that vessel. In the simplest case, the target vessel is in the C-arm iso-center and not foreshortened in the initial X-ray projection. While this assumption will almost never be satisfied in clinical practice, it is a good starting point to grasp on the general idea. First, we estimate the rotation axis of our transformation. In this very simple case, assuming a rotation axis that is simply the backprojection of the vessel to the isocenter, will produce exact results as we know that the vessel of interest is a) in the isocenter and b) not foreshortened. Thus, we can use this axis and rotate the gantry around it.

However, in clinical practice the target vessel is not necessarily in the iso-center, nor is it projected without foreshortening. This makes an exact determination of the rotation axis infeasible as depth cannot be recovered from a single image, but we can make some adjustments to perform substantially better than by just assuming a centered, foreshortening-free vessel.

Assume the vessel is off-centered e.g. 5 mm parallel to the detector. In this case, due to the X-ray cone, we already observe the vessel from an orientation rotated compared to the principal ray. In a first step, we find an intermediate view, that compensates this offset, such that the backprojection-plane of the vessel is parallel to the principal ray. To compute that intermediate view we rotate around an isocenter, that does not necessarily correspond to the center of the vessel. Therefore, in a second step we can minimize the difference between the true isocenter and the isocenter of rotation by translating either the table or the gantry. These two steps can be summarized as iso-center rotation and iso-center offset correction. After applying these two steps the desired angulation is performed with a physician determined angle ξ.

Results

The accuracy of the proposed algorithm is depicted in Figs. 1 and 2, respectively. The shown errors are computed in a worst case scenario and depict the maximal inaccuracy that is to be expected. Our algorithm reduces foreshortening substantially compared to the input view and completely eliminates it for 90° rotations (cf. Fig. 1). Rotations around foreshortening-free vessels passing the isocenter are exact. The precision, however, decreases when the vessel is off-centered in depth-direction or foreshortened (cf. Fig. 2). The evaluated worst case boundaries can be used to design viewpoints guaranteeing desired requirements, e.g. a true rotation around the target vessel of at minimum 30°.

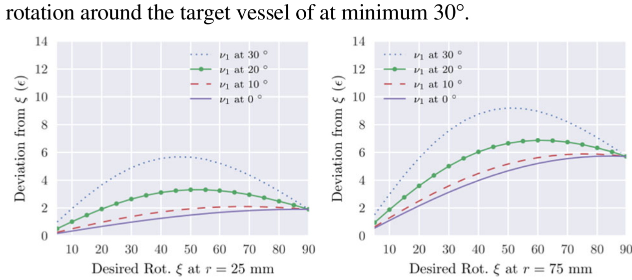

Fig. 1 Accuracy plots depicting the residual rotation ε as a function of the desired rotation ξ. The inaccuracy is depicted for different initial foreshortenings ν_1

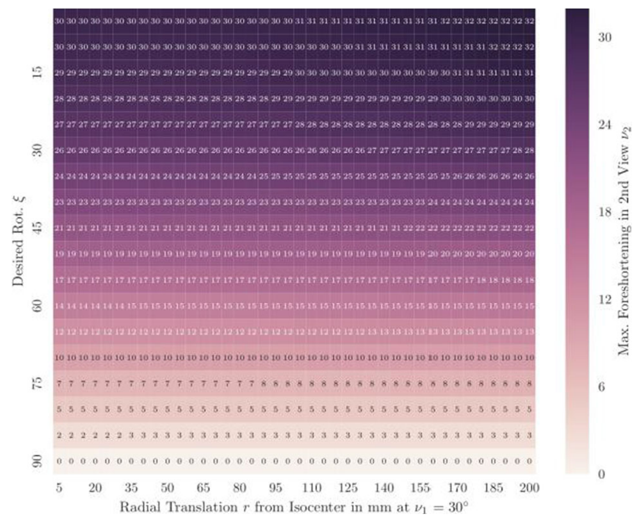

Fig. 2 Heatmap showing the maximal foreshortening in the second view for vessels having an initial foreshortening of $\nu_1 = 30°$. The inaccuracy is depicted for different offsets r of the vessel from the origin and desired rotations ξ

Conclusion

We introduce an algorithm for optimal viewpoint planning from a single angiographic X-ray image. The quality of the second viewpoint—i.e. vessel-foreshortening and true rotation around vessel—depends on the first viewpoint selected by the physician, however, our computed viewpoint is guaranteed to reduce the initial foreshortening. Our novel approach to viewpoint planning uses fluoroscopy images only and, thus, seamlessly integrates with the current clinical workflow for coronary assessment. In addition it can be implemented in the quantitative coronary angiography workflow without increasing user-interaction, making vessel-shape reconstruction more stable by standardizing the viewpoints.

Disclaimer: The concepts and information presented in this paper are based on research and are not commercially available.

References

[1] Sato Y, Araki T, Tamura S (1998) A viewpoint determination system for stenosis diagnosis and quantification in coronary angiographic image acquisition. TMI 17(1): 121–137

[2] Unberath M, Taubmann O, Maier A (2017) Symmetry, Outliers, and Geodesics in Coronary Artery Centerline Reconstruction from Rotational Angiography. Med. Phys

[3] Green N, Chen J, Caroll J (2005) Angiographic views used for percutaneous coronary interventions: A three-dimensional analysis of physician-determined vs. computer-generated views. CCI 64(4): 451–459

[4] Tu S, Koning G, Reiber J (2010) Assessment of obstruction length and optimal viewing angle from biplane X-ray angiograms. Journal of Cardiovascular Imaging

[5] Wink O, Kamkers R, Chen S, Caroll J (2002) Coronary intervention planning using hybrid 3d reconstruction. MICCAI 604–611

Convolutional neural network for automatic detection of X-ray contrast injection in endovascular procedures

T. Leblanc[1], V. Durrmann[1], M. Colleaux[1], F. Lalys[1]
[1]Therenva, Rennes, France

Keywords Endovascular procedures · CNN · Deep learning · EVAR

Purpose

Navigation and deployment of the prosthesis during endovascular procedures such as endovascular abdominal aortic aneurysm (EVAR) can be greatly facilitated with 3D image fusion and augmented reality techniques. Recent developments of 3D/2D registration techniques allow image fusion to be transferred to conventional operating room with mobile C-arm [1], [2]. In this context, and by opposition of hybrid OR, fast and robust automatic detection of injection on X-ray images is essential for automatically triggering the current fusion that align the 3-D model. While automatic classification can be performed using standard histogram-based algorithms [3], [4], these algorithms lack of robustness due to the high heterogeneity of patient images. We present here the use of Convolutional Neural Network (CNN) for automatic and real-time contrast injection detection in X-ray images, and compared it with baseline machine learning approaches, i.e. Random Forest (RF) and AdaBoost classifiers (AB).

Methods

Creation of the CNN

Transfer learning was used to achieve the network. The CaffeNet model, a replication of the AlexNet [5] with 1000 different classes, was preferred. The network takes images of 227 × 227 and contains five convolutional layers, three pooling layers and three fully-connected layers. We chose this architecture since this type of architecture is often used with good results in image detection. The first two convolutional layers were modified with increased stride values to gain detection speed. The output layer (the last fully-connected layer) was modified in order to have two outputs (Table 1). We didnt use data augmentation since structures on X-ray images dont show major differences in zoom or orientation.

Table 1 CNN architecture

Layer	Type	No. of neurons (output layer)	Kernel size for each output feature map	Stride
1	Convolution + Max Pooling + Normalization	96	11 × 11 × 3	6
3	Convolution + Max Pooling + Normalization	256	5 × 5	2
5	Convolution	384	3 × 3	1
6	Convolution	384	3 × 3	1
7	Convolution + Max Pooling	256	3 × 3	1
9	Fully connected	4096	–	–
10	Fully connected	4096	–	–
11	Fully connected	2	–	–

Comparison with baseline approaches

AB and RF are well-adapted to binary classification problems. Both of them were created and trained through OpenCV. To train the RF and AB, 24 histograms were computed per image: one from the original image, the others from gradient obtaining thanks to the convolutional result of a 3 × 3 SOBEL filter with the original image in each direction, and DOG of the original image, resulting in a feature vector of 6144 features. All histograms were normalized.

Data collection

We screened a total of 130 EVAR, 10 Fenestrated EVAR, 5 Thoracic EVAR and 60 lower limb intervention surgeries from 4 different French clinical centers including 6 different types of mobile C-arm: 2 from Siemens Heathcare, Germany; 2 from Ziehm Imaging, Germany; and 2 from GE Healthcare, USA. We finally obtained 18,000 independent images equally distributed with or without contrast injection. Due to the different shapes of input images, we differentiated images of X-ray image intensifier from images of flat panel detectors (Fig. 1). For each approach, we trained three classifiers: one specific to the images from flat panel detectors, one for X-ray image intensifiers and one from both types of C-arms. 6-fold cross-validation was performed for validation.

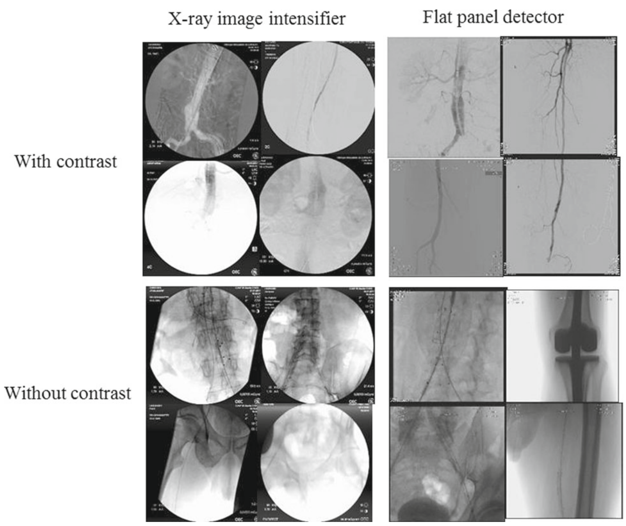

Fig. 1 Example of training images

Results

We can see on Table 2 that even if accuracies are very high for the three methods, the CNN outperforms baseline machine learning methods for the 3 databases. The computation time in CNN is even lower (0.015 s) than AB and RF (0.025 and 0.026 s respectively) on a standard machine. AB has better accuracy on the specific databases than the RF but has a lower accuracy on the global database.

Table 2 Accuracy result of the classifiers

Type of image	CNN	AB	RF	Total images
Digital	0.9985	0.993549	0.993301	18,000
Analogical	0.9988	0.995907	0.995191	9100
Global	0.997	0.979282	0.993356	8900

Conclusion

Our work allowed us to develop a powerful classifier with higher accuracy (99.998 vs. 99.8%) and lower computation time (0.015 vs. 0.95 s) than classical histogram-based algorithms [3], [4]. The convolutional layers of the CNN extract deep features of interest from the large available training database. The network architecture and the number of convolutional layer is well adapted to this application. Thanks to a slight modification on the convolutional layers, the inference time is greatly reduced and can now be used for real-time application. AB reaches better accuracies on specific classifiers since it selects smarter the features to classify the images. The fact that AB performs worse on the global database can be due to the huge variability of our training data. As a result, the randomness of RF outperforms AB. Future work will include an increased training database from other types of endovascular surgery such as transcatheter aortic valve implantation.

References

[1] Duménil A, Kaladji A, Castro M, Göksu C, Lucas A. Haigron P (2016) A versatile intensity-based 3D/2D rigid registration compatible with mobile C-arm for endovascular treatment of abdominal aortic aneurysm, *Int. J. Comput. Assist. Radiol. Surg.*, May 2016, 11(9): 1713–1729.

[2] Kaladji A, Dumenil A, Mahé G, Castro M, Cardon A, Lucas A, Haigron P (2015) Safety and Accuracy of Endovascular Aneurysm Repair Without Pre-operative and Intra-operative Contrast Agent *Eur. J. Vasc. Endovasc. Surg. Off. J. Eur. Soc. Vasc. Surg.*, Jan. 2015, 49(3): 255–261.

[3] Liu Y, Liao R, Lv X (2012) Extended contrast detection on fluoroscopy and angiography for image-guided trans-catheter aortic valve implantations (TAVI), vol. 8316, pp. 831618–831618-9.

[4] Condurache A, Aach T, Eck K, Bredno J (2004) Fast Detection and Processing of Arbitrary Contrast Agent Injections in Coronary Angiography and Fluoroscopy. *Bildverarbeitung für die Medizin 2004*, Springer, Berlin, Heidelberg, 2004, pp. 5–9.

[5] Krizhevsky A, Sutskever I, Hinton GE (2012) ImageNet Classification with Deep Convolutional Neural Networks. *Advances in Neural Information Processing Systems 25*, F. Pereira, C. J. C. Burges, L. Bottou, and K. Q. Weinberger, Eds. Curran Associates, Inc., 2012, pp. 1097–1105.

Computer-aided estimation for surgical margin evaluation of malignant tumor in breast-conserving surgery

Y. C. Chen[1], D. R. Chen[2], H. K. Wu[3], Y. L. Huang[1]
[1]Tunghai University, Department of Computer Science, Taichung, Taiwan
[2]Changhua Christian Hospital, Comprehensive Breast Cancer Center, Changhua, Taiwan
[3]Changhua Christian Hospital, Department of Medical Imaging, Changhua, Taiwan

Keywords Surgical margins · Breast conservative therapy · Deep-learning · Specimen mammography

Purpose

Breast-conserving therapy (BCT) followed by irradiation is the treatment of choice for early-stage breast cancer. A positive margin may result in an increased risk of local recurrences after BCT for any malignant tumor. In order to reduce the number of positive margins would offer surgeon real-time intra-operative information on the presence of positive resection margins [1]. This study proposed a computer-aided margin estimation by using the specimen mammography during BCT. The proposed method utilized the deep-learning image segmentation techniques to segment the cancerous tissue and then to evaluate the margin width of normal tissues surrounding it. With this work, surgeons might have more information to get clean margins when performing breast conserving surgeries.

Methods

Data acquisition: Two full field digital mammography (FFDM) systems were included in the study: GE Senographe Senographe Essential and Hologic Selenia Dimentions system. After wide excision of the tumor, location stiches were made on 12 (0°), 3 (90°), 6 (180°) and 9 (270°) o'clock direction and clipped on the stiches in order to be easily identified on specimen mammogram. There were 1, 2, 3 and 4 clips on each stich and a standard one-dollar coin (20 mm diameter) was put near the specimen as a measuring scale. All obtained images were stored on the hard disk and transferred to a personal computer using a DICOM connection for image analysis. Figure 1 shows an excision specimen picture and its specimen mammogram image with clips and coin.

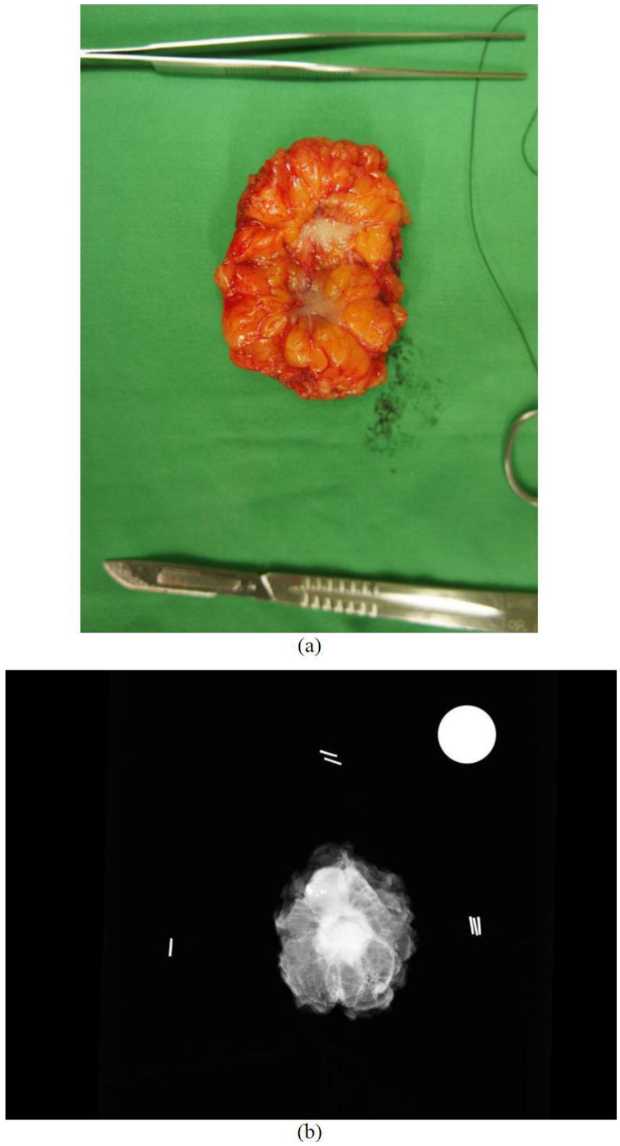

Fig. 1 **a** An excision specimen picture and **b** the specimen mammogram image

Image pre-processing: Pre-processing is a significant step before classification and contouring since the specimen mammogram always include speckles and tissue textures that make segmentation difficult. The effective pre-processing method for segmentation should aim to reduce noises and preserve the useful information. The proposed method performed the block-matching and 3D filtering (BM3D) algorithm to reduce noise and enhance contrast. The BM3D is based on an enhanced sparse representation in transform-domain. The enhancement of the sparsity is achieved by grouping similar 2D image blocks into 3D data arrays. The proposed pre-processing procedure is very practical to subtract noise, but not subtract to major part of the specimen mammogram images.

Deep-learning classification: Convolutional neural networks (CNNs), a major deep-learning model, have been applied successfully to tasks of computer vision. The ability of CNN in semantic segmentation shows their highly feasibility to medical image segmentation [2]. For this purpose, this study utilized a CNN-based method with 2D filters to specimen radiograph. To segment breast tissues, the classifier is applied to each pixel of image in a sliding window manner by extracting a patch around the pixel. The patch is input to the network to classify its central pixel. In order to classify nearby pixels, the network will have to process near identical patches. The hidden layers can be substituted by convolutions to obtain a fully convolutional network. It is trained to predict whether the central pixel is pathology or normal breast tissue, depending on the content of the surrounding patch. The parameters of the kernels are optimized using gradient descent during training, with the target of minimizing the error between the predictions and the desired labels.

Tumor contouring and margin evaluatio: The proposed method utilized an automatic thresholding algorithm (i.e., Otsu's method) to identify the tissue specimen area on mammogram image and then to generate its boundary. The CNN classifier was performed to segment pixels in the tissue specimen area into pathology or normal pixel. The contour of tumor was extracted from pathology pixels by using the morphological operators. The proposed method worked well in practice for an image to be composed of uniform regions of similar intensity or texture. The *Euclidean distance* between tissue specimen boundary and tumor contour was estimated as the margin width.

Results

The data set for this task comprises 10 specimen mammograms from BCT. In resections for breast cancer there appears to be a difference between European and American radiation oncologists, with the former preferring larger margins of over 5 mm. In this study, the desired size of margin around the tumor was set for 10 mm. In the all case, the BM3D algorithm was used as the image pre-processing step to get clear contours of tumor area on image. The thresholding and CNN algorithms were utilized to obtain tissue specimen boundary and tumor contour. Two segmentation examples of proposed method are shown in Fig. 2. Figure 2a, b shows the case without and with positive resection margins warning obtained from the proposed method, respectively. The use of the proposed method on margins from 10 patients indicated that this technology is helpful in discriminating positive from negative margins in the intra-operative setting.

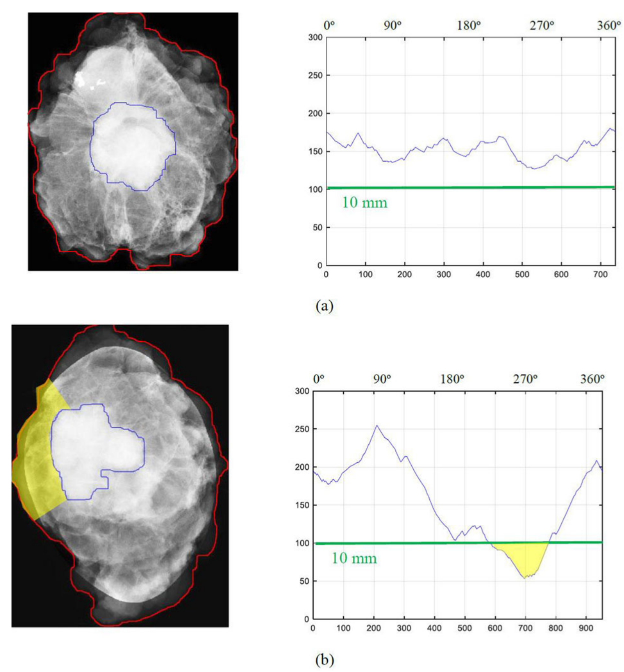

Fig. 2 Evaluation results of the proposed method: **a** an example without positive resection margins and **b** an example suspected positive resection margins (Red: tissue specimen boundary; Blue: obtained tumor contour; Green: 10 mm warning line; Yellow: warning area of positive resection margin)

Conclusion

Tumor resection margin status is important when performing breast conserving surgeries. The proposed method offered surgeon the margin width evaluation of malignant tumor as an opinion. The evaluation results have potential value as an intra-operative modality to get clean margins used in BCT. This work is helpful in improving surgical outcome and reducing the need for re-excision in BCT. Continued refinements to the method should result in a clinically-practical device with potential for widespread clinical application.

References

[1] Chiappa C, Rovera F, Corben AD, Fachinetti A, De Berardinis V, Marchionini V, Rausei S, Boni L, Dionigi G, Dionigi R (2013) Surgical margins in breast conservation. International Journal of Surgery. 11(S1): S69–S72.

[2] Lee JG, Jun S, Cho YW, Lee H, Kim GB, Seo JB, Kim N (2017) "Deep Learning in Medical Imaging: General Overview," *Korean J Radiol*. 18(4): 570–584.

Acknowledgements

This work was supported by the Ministry of Science and Technology, Taiwan, Republic of China, under Grant MOST 106-2221-E-029-029.

Image based connector for the automatic identification of ultrasound parameter values

J. G. Cabal Aragon[1], D. Lindner[2], S. Arnold[3], A. Schmitgen[3], C. Chalopin[1]
[1]Universität Leipzig, Innovation Center Computer Assisted Surgery (ICCAS), Leipzig, Germany
[2]Leipzig University Hospital, Neurosurgery, Leipzig, Germany
[3]Localite GmbH, Sankt Augustin, Germany

Keywords Ultrasound imaging · Parameter recognition · Template matching · Neurosurgery

Purpose

The use of intraoperative ultrasound (iUS) imaging supports the neurosurgeon in the identification of tumorous tissue during brain tumor operations. Especially 3D image data provides a complete overview of the surgical field. The commercial SonoNavigator product (Localite GmbH, Sankt Augustin, Germany) includes a navigation system connected to an ultrasound device and an optical tracking system. It performs the reconstruction of 3D iUS data based on 2D iUS images acquired with array ultrasound transducers equipped with a tracker (Fig. 1). The reconstruction step requires the previous calibration of the system using a phantom. The calibration depends on different parameters: the US device model, the transducer, the image depth, shape and orientation. In the current SonoNavigator system, the user manually selects the calibration file which corresponds to the parameter values used during the acquisition. The selection of the wrong file leads up to incorrect 3D reconstruction. Therefore, the automation of this step would make more safety and reliable the use of 3D iUS imaging during surgery.

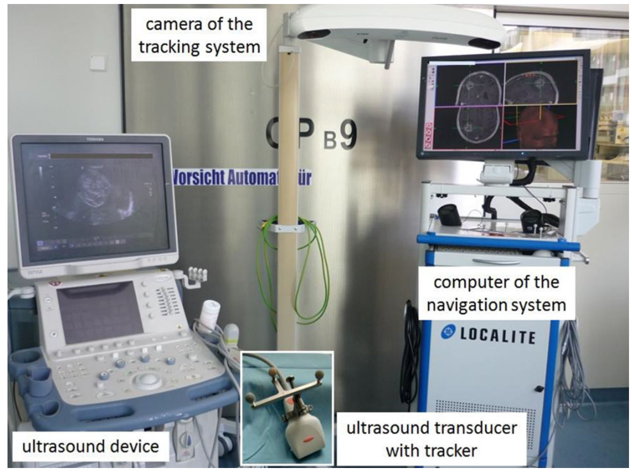

Fig. 1 Neuronavigation system composed by US device, tracking system and a computer

In commercial US devices the parameter values are generally only available through the US image data visualized on the monitor. Therefore the goal of this project is the development of an image processing tool, called connector, for the automatic identification in real time of the parameter values in the US image data. The applications are the automatic selection of the calibration data file and the documentation of further US parameters for clinical research.

Methods

A common method in digital image processing for the identification of features in images is the template matching. It is a technique for finding the areas within a source image *I* that match or are similar to a template image *T* whose size is generally lower than *I*. For that, *T* is moved through *I* and for each position a similarity metric is calculated between *T* and *I*. The position of *T* with the highest similarity score indicates the position of the searched feature in *I*. This method requires the constitution of a database of templates representing the features which have to be identified in the source images.

Therefore, the implemented image based connector includes two parts. The first part is a tool for the creation of a database of template images including the parameter values that are commonly used during brain tumor operations. The second part is the tool for the automatic identification of the parameter values in the life iUS images by performing a matching between the iUS image and the templates of the database.

Database creation. An interface was developed to support the user in the constitution of the data base. The method consists firstly in identifying the different parameters mostly used during image acquisition, secondly in locating them interactively in a set of tests iUS images using regions of interest (ROI), and thirdly in saving the obtained templates in a repository. A new template has to be generated for each different value of the parameters.

Automatic identification of the parameters the iUS images. The in live iUS images are firstly processed with a sigmoid filter to reduce the image noise and thresholded to enhance the parameter values. Then, the algorithm performs the template matching process in real time between the iUS image and the database of templates. The template with the highest improved Pearson correlation score is returned as the identified US parameter value. The connector is able to identify unknown parameter values and returns then a pop up message to the user. The identified parameter values are visualized on the connector interface and stored into a text file (Fig. 2).

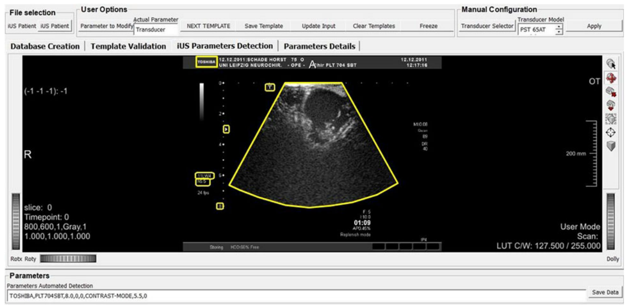

Fig. 2 The identified parameters are shown into the text box on the bottom left corner. They are: the US device model (Toshiba), the transducer (PLT704SBT), the image depth (8.0 cm), shape (0 for trapezoid) and orientation (0 when the marker is on the left), the imaging mode (CONTRAST) and the frequency (5.5 MHz)

Results

The connector tool was implemented with MeVisLab on a laptop connected with a digital video grabber to the US device. It is currently able to identify the seven following parameters: US device model, name of the transducer currently used, imaging modality (B-mode or contrast mode), current used frequency, image depth, shape (rectangular or trapezoid) and orientation (image flipped or not). The template data base was constituted using a couple of test images acquired for this task.

In a second step, the tool was offline evaluated on 71 iUS images acquired in the context of a clinical study during brain tumor operations of patients. A recognition score of 100% was obtained for the parameters US device model, transducer, image depth, orientation and shape. The recognition score of the imaging modality and current frequency was 95.77%. The unsuccessful cases were due to the use of frequencies which were not included in the template database. The connector was able to correctly identify the unknown parameter values by sending a pop up message.

Conclusion

An image based connector was presented to automatically identify the parameter values used for image acquisition during brain tumor operations. The main limitation of the tool is the creation of database of templates representing the parameter values. Since the set of different parameters and values is restricted, an interactive tool to support the creation of the data base was implemented. This step is required for each different US device.

The current version of the connector can be used for the documentation of the parameter values during clinical research project. Next step will be to link the connector tool with the neuronavigation system in order to compare the current identified US parameter values with the configurations stored in the calibration data used for the 3D reconstruction of iUS volumes. Such automatic tool should increase the safety of the use of US imaging in neurosurgery.

Breast volume measurement using three-dimensional surface scan for planning fat grafting for breast reconstruction

R. House[1], A. Lasso[1], M. Kunz[1], T. Ungi [1], J. Rudan[2], G. Martou[2], G. Fichtinger[1,2]
[1]Queen's University, School of Computing, Kingston, Canada
[2]Queen's University, Surgery, Kingston, Canada

Keywords Breast volume measurement · 3D surface scanning · Fat grafting planning · Breast reconstruction planning

Purpose

Breast Cancer is the most frequently occurring cancer in Canadian women. Up to 80% of these patients are candidates for breast-conserving surgery (partial mastectomy). During a partial mastectomy, the tumor is completely excised while preserving as much healthy tissue as possible. Unfortunately, up to one-third of these patients still experience severe breast deformity that requires surgical reconstruction. Fat grafting has been emerging as a safe and suitable modality in breast reconstruction following breast-conserving surgery. The fat, harvested from donor areas of the same patient, is injected into the breast in several fractions, typically 100–150 cc each time. There is always a variable degree of fat resorption in the breast, which leads to repeated fat grafting surgeries until the desired result is achieved. It is imperative to accurately monitor the changes in volume in order to plan and execute the optimal grafting regimen. Minimizing the number of fat grafting sessions decreases risk to the patient and burden to the healthcare system, as each session costs $5000–$7000. Currently, there is no low cost, widely available monitoring tool for the reconstructive surgeon. We aim to provide a system and clinical workflow to accurately compute volume changes of the breast, in a safe and convenient manner during a visit to the clinic.

Methods

Using the Artec Eva (www.artec3d.com) three-dimensional surface scanner a three-dimensional surface of the patient can be obtained in a non-contact manner (Fig. 1). The patient stands up-right with the hands rested on the hips, allowing the surface scan to be easily captured in under 1 min. The surface scan is imported into 3D Slicer (www.slicer.org) where a module has been created for processing and visual rendering. To compute the breast volume the breast must be isolated from the rest of the chest using specific anatomical landmarks. The volume of the isolated breast can then be computed. To assist in planning the total graft volume, volume difference between the two breasts are computed by mirroring the healthy breast onto the reconstructed side. To monitor the retention of graft volume between implanting fractions, the volume difference between two consecutive scans of the same breast is computed and compared to the graft volume. Three-dimensional distribution of the volume differences over the breast is visualized on the computer display using semi-transparent surfaces and surface-to-surface distance maps (Fig. 2) after two scans from different times within the treatment process are aligned. These visualizations will allow the reconstructive surgeon to monitor breast sites that have signification volume differences.

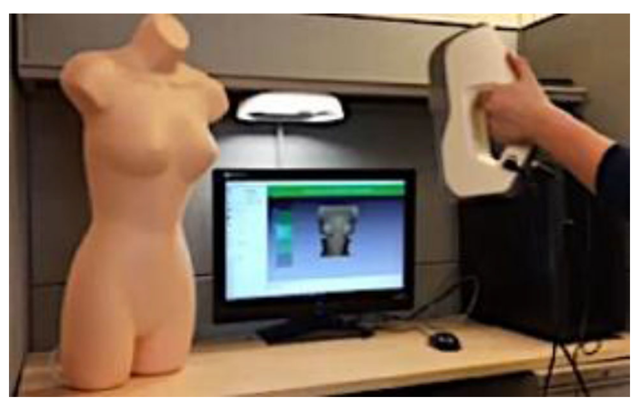

Fig. 1 Mannequin being scanned using Artec Eva

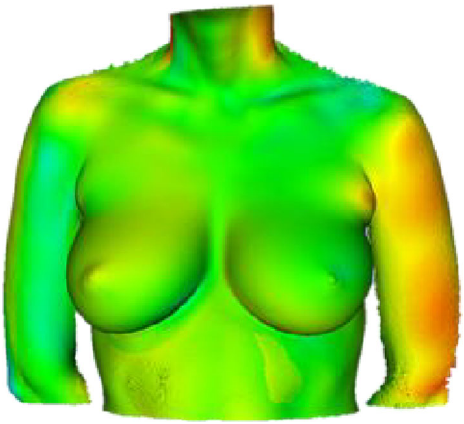

Fig. 2 Surface-to-surface distance map of two scans of a volunteer after alignment

Results

We demonstrated the ability to measure volume differences in the breast in three (3) female volunteers. Each volunteer was scanned three (3) times. Between each scan, the volunteer was asked to relax for a few seconds and reposition herself for the next scan. The breast volume of the same breast for each volunteer was computed for each of the three scans. The average difference between three consecutive measurements of the same breast was 1.1 cc (Table 1). In addition, we also demonstrated the ability to measure the absolute volume of the breast. To this end, a mannequins breast volume was first measured by water displacement and compared to the volume measured by our system. Having repeated each measurement five (5) times for the same breast, the average difference between the measurements was 4.1 cc. A surface-to-surface distance map (Fig. 2) was also created for one volunteer using two of the three scan and as expected the distance map illustrated very little difference between the two scans. The small differences in the two scans can be accounted for by the volunteer not resuming the exact same scanning position and the registration error.

Table 1 Computed breast volume for three volunteers

Volunteer	Breast volume (mean ±)
1	341.2 ± 0.5 cc
2	165.0 ± 1.7 cc
3	211.4 ± 1.2 cc

Conclusion

Considering the typical volume of a graft injection fraction (100–150 cc), our accuracy in measuring breast volume changes (1.1 cc) is highly promising for clinical use. Further testing will be conducted to assess the accuracy when scanning and measuring breast volume of post partial mastectomy patients. Research Ethics Board approval has been sought to commence clinical evaluation in 25 post breast-conserving surgery patients.

A preliminary study on disease annotation from unstructured electronic medical records using recurrent neural network

C. Lee[1], J. Jang[2], Y. Kim[3], Y. S. Kim[1]
[1]Hanyang University, Institute of Innovative Surgical Technology, Seoul, South Korea
[2]Kyushu University, Center for Integration of Advanced Medicine Life Science Innovative Technologies (CAMIT), Fukuoka, Japan
[3]Hanyang University, Department of Orthopedic Surgery, Seoul, South Korea

Keywords EMR · Text classification · RNN · Sequence to sequence

Purpose

Electronic medical records (EMRs) contain significant amounts of unstructured text that pose a challenge to their secondary use as a research data source. To utilize the data efficiently, EMR text data is necessary to be converted to outcome label which contains the type and extent of the disease. However, categorizing EMR text with key annotation is very difficult because it contains ambiguous word and has free-text format.

We would like to develop a fully automated disease annotation system or which it would be necessary only to supply radiology reports. The system would generate label that correspond to the type and extent of the disease. As a preliminary study, we evaluated the performance of the annotation method based on RNN describing the database of free-text X-ray reports as fracture and non-fracture.

The purpose of this study is (1) to present a classifier with high accuracy based on RNN (2) to evaluate the performance of the classifier.

Methods

We assembled an NLP system that uses RNNs within free-text narrative musculoskeletal X-ray reports to automatically identify fracture and non-fracture cases (Fig. 1). We trained and tested the system using the reports that had been classified by expert at our institution.

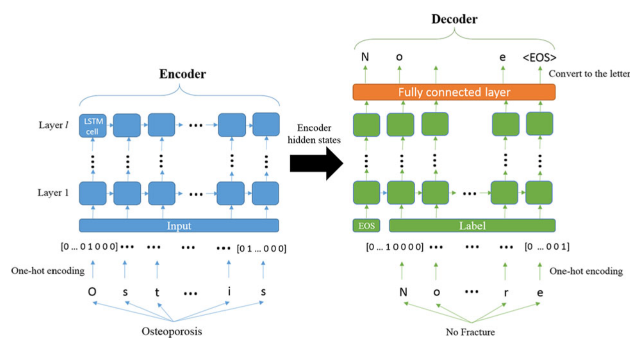

Fig. 1 RNN based model to classify the X-ray reports

X-ray reports

The reports of musculoskeletal radiographs were exported from medical database of our institution into a text file and after excluding the sentences not written in English, and containing typos, 3032 sentences were included. After then, experienced orthopaedic surgeon classified the sentences according to the presence or absence of the meaning of fracture (Table 1).

Table 1 Examples of X-ray reports and the labels

X-ray reports	Labels
'Degenerative irregularities in bilateral SI joints'	'Non-fracture'
'Synovitis at left hip joint'	'Non-fracture'
'No gross interval change since 2016-08-23'	'Non-fracture'
'Fracture of Lt. acetabulum'	'Fracture'
'S/P Intramedullary nailing in the right femoral shaft'	'Fracture'
'Interval increased callus formation'	'Fracture'
'Fracture at coccyx'	'Fracture'

Deep learning for Natural language processing

To build our NLP system, we randomly partitioned the radiology reports into a training set with 2274 (75%) of the reports and a test set with the remaining 758 (25%) of the reports.

We used sequence to sequence model (seq2seq) [1], which is a sequence learning model used for chatbot, translation, and image captioning (Fig. 1). The seq2seq model is comprised of an encoder and a decoder, each consisting of several vertically stacked layers. The Long short-term memory (LSTM) recurrent layer with depth l consists of l vertically stacked LSTM blocks. The characters of each sentence were separated one by one and one-hot encoded values are inserted into the encoder cell of the seq2seq.

Statistical analysis

We evaluated the system in two ways. The first was its performance as a binary fracture classifier. To this end, the output sentence of each character was compared with the label sentence; if it had more than 50% agreement, it was determined that the output corresponded to the meaning of the label. Based on the correspondence, we calculated standard evaluation metrics, such as accuracy, precision, recall, and F1 score, for each layer. The second evaluation method was the word error rate of the output of the model, which is based on the Levenshtein distance, a sequence similarity metric that calculates the number of additions, deletions, or substitutions of sequence elements needed to convert one sequence to another.

Results

Figure 2a shows the precision, recall, accuracy, and F1 score for each number of layers in the model. The three-layered model demonstrated the highest overall performance; we obtained the highest recall (0.966), accuracy (0.979), and F1 score (0.962) in three-layered model.

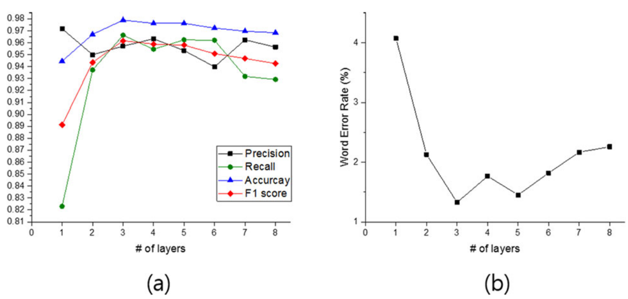

Fig. 2 **a** Classification results for the number of layers. **b** Word error rate results. The three-layered model showed the highest overall performance

The word error rate using the Levenshtein distance also exhibited the best performance in the three-layered model, at just 1.327% (Fig. 2b). The maximum word error rate yielded by the models was less than 4.07%. It means that almost all X-ray reports could be interpreted. In other words, all output sentences could be distinguished by "fracture" and "non-fracture".

Conclusion

The high accuracy classifier that reduce the need for manual chart review to identify pertinent radiology reports are critical to support retrospective studies. We have demonstrated that standard ML and NLP methods may address this challenge when supported by human expert guidance.

We developed the automatic annotation tool that can help standardize medical data and reduce unnecessary diagnostics. This classifier showed high accuracy and extendibility to other diseases without modification of the model.

The results showed excellent accuracy for radiology reposts relative to the other research. Our classifier shows the performance difference according to the layer depth. These results show a clue of overfitting in the systems over than three layers. It might come from the output property which was actually close to two dimensional (i.e. "fracture" and "non-fracture"), even though the system output one hundred fifty-six 76-dimensional vectors.

As future works, we plan to adapt our system to annotate not only the presence of the disease but also the anatomical location and extent of disease using other institutions with no label.

References

[1] Sutskever I, Vinyals O, Le QV (2014) Sequence to sequence learning with neural networks. In Advances in neural information processing systems (pp. 3104–3112).

[2] Hassanpour S, Langlotz CP, Amrhein TJ, Befera NT, Lungren MP (2017). Performance of a machine learning classifier of knee MRI reports in two large academic radiology practices: a tool to estimate diagnostic yield. American Journal of Roentgenology, *208*(4), 750–753.

Comparative analysis of unsupervised representation learning methods for concept detection in medical images

E. Pinho[1], C. Costa[1]

[1]University of Aveiro, DETI/IEETA, Aveiro, Portugal

Keywords Representation learning · Unsupervised learning · Deep learning · Medical image retrieval

Purpose

The subject of representation learning has been rapidly evolving during the last decade [1]. The discovery of more powerful representation learning techniques opens up tremendous prospect for decision support systems, and further unlocks the potential of content-based image retrieval (CBIR) in this domain. A significant part of this progress comes as a consequence of the latest breakthroughs in deep learning, which has already made its way to medical imaging analysis [2]. In this work, we present an assessment of unsupervised feature learning approaches for images in the biomedical literature, which can be applied in cases where additional information is unavailable.

Methods

We have considered a set of six unsupervised representation learning techniques, both more traditional and based on deep learning, for the scope of images in the biomedical domain. These representations were subsequently used for the task of biomedical concept detection.

Two of the approaches are based on the Bags of Visual Words (BoWs), for two different visual keypoint extraction algorithms (SIFT and ORB). For each one, the keypoints were extracted and their respective descriptors computed. From the training set, 3000 files were randomly chosen and their respective keypoints collected to serve as template keypoints. A visual vocabulary (codebook) of size $k = 512$ was then obtained by performing k-means clustering on all template keypoints and retrieving the centroids of each cluster. Once the visual vocabulary was available, we constructed each image's BoW by determining the closest visual vocabulary point and incrementing the corresponding position in the BoW for each image keypoint descriptor.

With the use of modern deep learning approaches, we have also designed and trained four deep neural network architectures, each of them named and identified below. The models were composed of sub-networks with a similar number of layers and parameters to promote fairness among the models. More specifically, encoders and discriminators used a network with 5 convolutional layers of stride 2 and an exponentially increasing number of kernels and rectified linear unit

(ReLU) activations which could include a *leaking* factor depending on the particular model, ending with a global average pool and a fully connected layer. Generators and decoders were composed of a fully connected layer after the latent (or prior) code vector and 5 layers of transpose convolutions of increasing dimensions, until an output of 3 channels is obtained.

- The sparse denoising autoenoder (SDAE) is a common autoencoder, which learns to minimize the mean squared error of reconstructing a sample with synthetically induced noise after passing through an encoder-decoder process. An absolute penalization loss over the bottleneck vector was used to impose sparsity.
- In the variational encoder (VAE), the encoder of the model learns instead a stochastic distribution which can be sampled from, by minimizing the Kulback-Leibler divergence with a unit-variance normal distribution.
- The bidirectional generative adversarial network (BiGAN) is a redesign of the basic GAN that includes an encoder, thus learning the inverse process of the generator. Rather than only observing data samples, the BiGAN discriminator's loss function depends on the code-sample pair.
- Lastly, the adversarial autoencoder (AAE) is an autoencoder in which a discriminator is added to distinguish latent codes in the autoencoder from codes sampled from a stochastic prior.

Each image from the training and validation folds of the ImageCLEF 2017 data set for biomedical concept detection [3] was mapped to its respective feature vector for each representation. Afterwards, two types of simple classifiers were trained in a supervised fashion over the learned feature spaces: logistic regressors and k-nearest neighbors.

Results

Each representation was scored by the best mean F_1 score of multiple previously defined thresholds (0.05, 0.075, 0.125, and 0.25). For the logistic regressors, the area under the ROC curve (AUC) was also retrieved. The linear classifiers (Table 1) were trained for the 1000 most frequent concepts in the data set. Among the representations learned, 0.075 was the threshold which would better optimize the mean F_1 score. The AAE obtained the best single-model representation F_1 score of 0.15166 and AUC of 0.78670, followed by the SDAE with an F_1 score of 0.14258 and AUC of 0.76984. The combinated representation of concatenating the feature spaces of the SDAE and AAE have resulted in even better classifiers. The representations based on BoWs were the least effective for the task, with ORB slighly outperforming SIFT. With k-nearest neighbors (Table 2), the best mean F_1 score of 0.07995 was obtained with the SDAE, for $k = 2$. Overall, these methods have outperformed our previous participation [4] and are on par with other techniques in the concept detection challenge.

Table 1 The best F_1 scores, and respective area under the ROC curve, obtained from logistic regression for each representation learned, where *Mix* is the feature combination of SDAE and AAE

Type	F_1 score	AUC	Threshold
ORB	0.12904	0.68050	0.075
SIFT	0.12027	0.70800	0.075
SDAE	0.14258	0.76984	0.075
VAE	0.13483	0.75187	0.075
BiGAN	0.13044	0.77111	0.075
AAE	**0.15166**	0.78670	0.075
Mix	**0.15588**	0.78869	0.075

Table 2 The best F_1 scores obtained from vector similarity search for each representation learned

Type	F_1 score	k
ORB	0.04275	4
SIFT	0.05983	3
SDAE	**0.07995**	2
VAE	0.03569	4
BiGAN	0.04702	3
AAE	0.07213	2

Conclusion

This work takes unsupervised representation learning techniques from state-of-the-art, evaluating them with the ImageCLEF 2017 concept detection task. Results are presented for six different approaches, where two of them rely on visual keypoint extraction and description algorithms, and other two of them are based on generative adversarial networks. We conclude that it is possible to obtain more powerful representations with modern deep learning approaches, in contrast with previously popular computer vision methods such as bags of visual words. Deep learning techniques based on GANs can provide good results, but the additional complexity, the difficulty of convergence, and the possibility of mode collapse can significantly cripple their performance in representation learning. It is also important that these approaches are augmented with non-visual information. In particular, a medical imaging archive should take the most advantage of the available data beyond pixel data. Future work should consider semi-supervised learning as a means of building more descriptive representations from known categories and other annotations. Subsequently, these representations are to be evaluated in a medical information retrieval scenario, as well as with other data sets in the medical imaging domain.

Acknowledgements

This work is financed by the ERDF—European Regional Development Fund through the Operational Programme for Competitiveness and Internationalisation—COMPETE 2020 Programme, and by National Funds through the FCT—Fundação para a Ciência e a Tecnologia, within project PTDC/EEI-ESS/6815/2014. Eduardo Pinho is funded by the FCT under the grant PD/BD/105806/2014.

References

[1] Bengio Y, Courville A, Vincent P (2013) Representation learning: A review and new perspectives, *Pattern Analysis and Machine Intelligence, IEEE Transactions on*, vol. 35, no. 8, pp. 1798–1828

[2] Litjens G, Kooi T, Bejnordi BE, Setio AAA, Ciompi F, Ghafoorian M, van der Laak JAWM, van Ginneken B, Sánchez CI, A survey on deep learning in medical image analysis. *Medical Image Analysis,* vol. 42, pp. 60–88, 2017.

[3] Eickhoff C, Schwall I, de Herrera A, Müller H (2017) Overview of ImageCLEFcaption 2017—the image caption prediction and concept extraction tasks to understand biomedical images, *CLEF working notes, CEUR*

[4] Pinho E, Silva JF, Silva JM, Costa C (2017) Towards Representation Learning for Biomedical Concept Detection in Medical Images: UA. PT Bioinformatics in ImageCLEF 2017. *Working notes of conference and labs of the evaluation forum*

Knee joint goniometry using MARG low-cost sensors

D. García-Mato[1,2], E. León-Román[2,3], M. García-Sevilla[1,2], P. Sanz-Ruiz[2,3,4], R. Pérez-Mañanes[2,3,4], J. A. Calvo[2,3,4], F. Forriol[5], M. Desco[1,2,6,7], J. Vaquero-Martín[2,3,4], J. Pascau[1,2]
[1]Universidad Carlos III de Madrid, Departamento de Bioingeniería e Ingeniería Aeroespacial, Madrid, Spain
[2]Instituto de Investigación Sanitaria Gregorio Marañón, Madrid, Spain
[3]Hospital General Universitario Gregorio Marañón, Servicio de Cirugía Ortopédica y Traumatología, Madrid, Spain
[4]Universidad Complutense de Madrid, Facultad de Medicina, Madrid, Spain
[5]CEU-San Pablo University School of Medicine, Madrid, Spain
[6]Centro de Investigación Biomédica en Red de Salud Mental (CIBERSAM), Madrid, Spain
[7]Centro Nacional de Investigaciones Cardiovasculares Carlos III (CNIC), Madrid, Spain

Keywords Knee · Joint goniometry · Inertial sensor · Optical tracking system

Purpose

Joint goniometry is an essential tool for clinical assessment in many disciplines. Measurement of joint angle can be used to determine the presence or absence of dysfunction, to quantify treatment effectiveness or to guide treatment interventions [1].

Although many different technologies have been proposed for angle measurement, universal goniometers (UG) are the tool most commonly found in clinical practice. They are cheap, easy to use, easily accessible and portable. Several studies have reported a good intra- and inter-tester reliability of UG, but reliability varies according to the joint and range of motion being measured [2]. The main disadvantage of UG is that an incorrect positioning of the device with respect to bony landmarks and center of rotation of the joint can affect reliability and validity. Some studies report an accuracy in UG angle measurements of 4°, while others found errors of up to 10° [3].

In this work we present the development and validation of a new system for knee joint goniometry based on two low-cost inertial sensors and open-source software. For the validation, the proposed system is used to measure flexion–extension and tibial rotation movements of several human cadaveric knees using an optical tracking system as gold-standard.

Methods

Several technologies enable the measurement of orientation, e.g., optical, mechanical and inertial sensory systems. However, inertial sensing has the advantage of being completely independent of the environment or location since no external reference is required. Within inertial sensory systems, MARG (Magnetic, Angular Rate, and Gravity) sensors can provide a full estimation of orientation by combining the information of tri-axis gyroscope, accelerometer and magnetometer using an orientation estimation algorithm (e.g., Madgwick). Since magnetometer measurements are affected by artificial magnetic field distortions, MARG sensors need to be calibrated according to the local magnetic field intensity.

Our system is composed of two MARG sensors (Phidgets Inc.). One sensor is attached to the femoral component and a second sensor to the tibial component of the knee joint. Sensors can be attached using elastic and adjustable straps, or directly screwed to the bones (femur and tibia). This system does not require an exact placement of the sensors.

An application was developed in 3D Slicer, a free open-source platform for the analysis and visualization of medical images, that receives the angular data acquired by both MARG sensors using PLUS open-source toolkit. The application enables to record flexion–extension and tibial rotation movements by computing the angle between both MARG sensors. The rotation profile is displayed on the screen in real-time (Fig. 1).

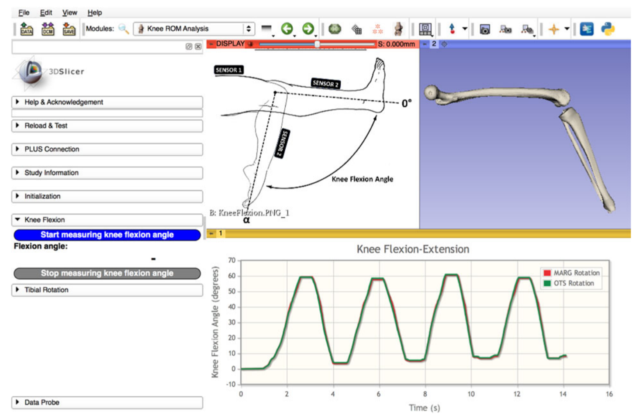

Fig. 1 Application developed in 3D Slicer for recording and real-time visualization

For the validation of the joint angle measurements provided by the described system, a dual-camera optical tracking system (NaturalPoint Inc., OR, USA) was used as a gold-standard. In this study, two rigid-bodies composed of 4 optical markers were used: one attached to the femoral component and other to the tibial component. The optical tracking system (OTS) is able to infer accurately the position and orientation of these rigid-bodies in real-time.

A total of 8 human cadaveric knees were used in this study. MARG sensors and OTS rigid-bodies were fixed to the femur and the tibia using screws to ensure an accurate measurement of the knee joint motion. Knee flexion–extension and tibial rotation movements were evaluated by performing four complete oscillations. Each repetition consisted on four continuous flexion–extension cycles (flexion, and then extension) and four continuous tibial rotation cycles (left, and then right). A total of 6 repetitions were performed in each cadaveric knee.

The performance of the proposed system was evaluated by comparing the recorded measurements with those provided by the gold-standard (OTS). The correlation between measurements of both systems was calculated using the Pearson correlation coefficient (r). The error was also computed for every individual sample and for the range of motion estimation in each movement.

Results

Estimated angles were highly correlated ($r > 0.99$) with OTS measurements. The average difference and standard deviation for every individual sample in all the 48 repetitions of the experiment performed on 8 cadaveric knees was 0.83° ± 0.73° for flexion–extension and 0.31° ± 0.31° for tibial rotation.

Regarding the range of motion estimation, an error of 0.98° ± 0.74° was found for flexion, 0.96° ± 0.83° for extension, 0.37° ± 0.35° for left tibial rotation and 0.23° ± 0.19° for right tibial rotation (Fig. 2). The average range of motion of the movements performed during the experiment was 45.72° for flexion–extension and 5.18° for tibial rotation.

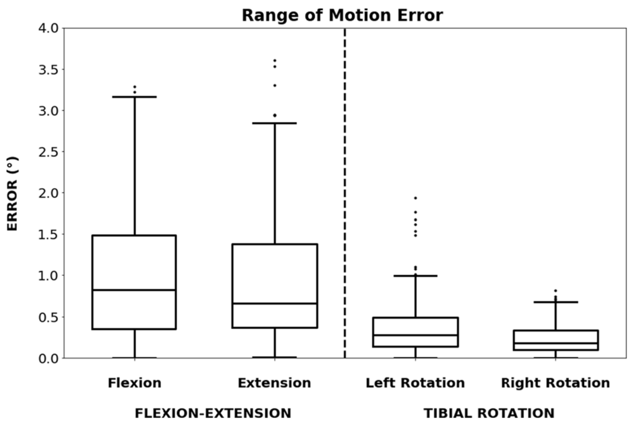

Fig. 2 Error in range of motion estimation for flexion–extension and tibial rotation movements

Conclusion

This technical report provides an initial evaluation on the viability of using low-cost MARG sensors for knee joint goniometry. Measurements provided by a system composed of two MARG sensors were compared with a gold-standard (OTS), obtaining an average error below 1°. These results demonstrate an accurate estimation of orientation as a function of time which enables a precise analysis of the temporal evolution of knee joint motion.

The proposed system presents higher accuracy than UG. In addition, while reliability of UG measurements is affected by correct positioning of the device on the joint, the performance of this system is independent on the location of sensors. Also, this system is connected to a computer and allows users to record knee joint motion with an approximate frequency of 100 Hz.

To conclude, this validation study has demonstrated the feasibility of using low-cost MARG sensors for the measurement of the knee joint motion overcoming some of the drawbacks presented by previously described approaches. This development has been possible thanks to the use of existing open-source toolkits.

References

[1] Ferriero G, Vercelli S, Sartorio F, Muñoz Lasa S, Ilieva E, Brigatti E, Ruella C, Foti C (2013) Reliability of a smartphone-based goniometer for knee joint goniometry. International Journal of Rehabilitation Research 36(2): 146–151

[2] Rothstein MJ, Miller PJ, Roettger RF (1983) Goniometric reliability in a clinical setting. Elbow and knee measurements. Physical Therapy 63(10): 1611–1615

[3] Crowford P, Jones K, Barker K (1998) Inter-tester comparison between visual estimation and goniometric measurement of ankle dorsiflexion. Physiotherapy Theory and Practice 14(2): 107–113

3D printed phalangeal prosthesis and bone tumor models: Presenting personalized advantage in operative outcome

S. Pairojboriboon[1], T. Punyaratabhandhu[1], P. Liacouras[2,3]
[1]Phramongkutklao College of Medicine, Orthopaedic, Bangkok, Thailand
[2]Walter Reed National Military Medical Center, 3D Medical Application Center, Department of Radiology, Bethesda, United States
[3]Uniform Services University of the Health Sciences, Radiology and Radiological Services & Naval Postgraduate Dental School, Bethesda, United States

Keywords 3D printing · Orthopaedic · Bone tumor · Phalange prosthesis

Purpose

The objectives of this study are to present in vivo surgical outcomes of the procedures where

1. 3D printed models were used as a 3D virtual surgical simulator and resources in preoperative planning. For most of the models in this report, the 3D printed anatomical models can aid in effective preoperative planning by helping to determine the appropriate acetabular supporting ring, reducing the surgical incision and defining the bony resection plane, and in the determination of intraoperative procedures, methods of resections, and reconstructive technique.
2. Titanium printed phalangeal prosthesis was used for reconstruction after bone tumor resection.

Methods

6 complicated cases were selected, reconstructed and printed. Theses 6 cases were then classified into four groups of 3D printed models and prosthesis.

Group 1 consisted of basic 3D abnormal anatomy.

Group 2 consisted of a bone tumor with major arterial implications.

Group 3 consisted of an extracompartmental bone tumor in which the cortical outline was destroyed, thus requiring CT and MRI images fusion to properly reconstruct.

Group 4 consisted of titanium printed prosthesis of phalangeal bone.

Each of them were measured in quantitative analysis such as operative time, blood loss, incision length and implants selection depend on cases.

Results

Three-dimensional models of group 1–2 were created by orthopedists in using standard segmentation techniques. Post-surgery, Parosteal osteosarcoma, the clinical outcome found a reduction in the operative time, estimated patient blood loss and length of surgical incision by 208 min, 250 ml and 12 cm (medial), 4 cm (lateral), respectively. This reduction was seen when this case was compared with 2 previous distal femoral osteosarcoma cases with a similar diagnosis, the identical surgeon and within the same year. These values were consistant to other research found where the use of 3D models can significantly decrease the operative time and the operative blood loss [1]. In case of acetabular metastasis, by utilizing the real-size patient's 3D hemipelvis model, we were able to measure the diameter of acetabular cup as 44 mm and the superoinferior length of supraacetabular defect as 24 mm. From this data, surgeon could select the most appropriate implant pre-operatively. This implant was found to be the Gantz ring, size 44 (Fig. 1).

Fig. 1 The 3D pelvic with external iliac artery model showed large peri-acetabular bone defect as a preoperative virtual simulator assisted for implant selection between Burch–Schneider Cage and Ganz ring

Since group 3–4 required complex techniques, an engineer assisted during the digital model construction. These models helped to guide in orthopedist in the creation of a a personalized preoperative plan and as a virtual simulator. In group 3, the surgical team tried to perform initially with a CT scan containing 2 mm thickness and combining with MRI images after that postoperative validation of accuracy was assessed between our 3D model and gross tumor resection [2]. However, the resulting model was not satisfactory. By utilizing phalangeal prosthesis (Fig. 2) in group 4, it could be choice of reconstruction in difficult area where there is on off the shelf prosthesis [3].

Fig. 2 3D printed titanium prosthesis of fifth proximal phalange

Conclusion

The 3D models proved to be benificial and assisted with all 5 cases. Models impacted implant selection and screws positioning in case of severe acetabular defect and minimally invasive limb sparing surgery. The models also helped to decreased blood loss and make smaller incisions, in group 2, when compared to past cases. The phalangeal prosthesis is proved to be a choice of reconstruction in the difficult area such as finger. Qualitatively, utilizing 3D printing, in the tumor cases, provides personalized advantages for the various characteristics of each bony tumor.

References

[1] Giannetti S, Bizzotto N, Stancati A, Santucci A (2017) Minimally invasive fixation in tibial plateau fractures using an pre-operative and intra-operative real size 3D printing. Injury.; 48(3): 784–788.

[2] Dong Y, Dong Y, Hu G, Xu Q. (2011) Three-dimensional reconstruction of extremity tumor regions by CT and MRI image data fusion for subject-specific preoperative assessment and planning. Comput Aided Surg; 16(5): 220–233.

[3] Punyaratabandhu T, Lohwongwatana B, Puncreobutr C, Kosiyatrakul A, Veerapan P, Luenam SA (2017) Patient-Matched Entire First Metacarpal Prosthesis in Treatment of Giant Cell Tumor of Bone. Case Rep Orthop 2017: 4101346.

Tongue coating analysis via machine learning using texture and color features

Y. Ota[1], T. Nakaguchi[2], V. Bochko[3], P. Fält[4], M. Hauta-Kasari[5]

[1]Graduate School of Science and Engineering, Chiba university, chiba-shi, Japan

[2]Center for Frontier Medical Engineering, Chiba University, chiba-shi, Japan

[3]University of Vaasa, Department of Electrical Engineering and Energy Technology, Vaasa, Finland

[4]University of Eastern Finland, Joensuu, Finland

[5]University of Eastern Finland, School of Computing, Joensuu, Finland

Keywords Tongue coating · Fluorescence imaging · Tongue diagnosis · Machine learning

Purpose

Tongue diagnosis is one practical diagnostic method of the traditional Japanese herbal medicine called Kampo medicine. It diagnoses a physical state called “Qi, Blood, Fluid”, which indicates the progress of an illness and the state of the blood and bodily fluids via the condition of the tongue color, form, and moisture and the tongue coating. One serious problem with tongue diagnoses is that they depend on the ability and experience of a doctor. This problem can be solved with a quantitative diagnosis taking a picture of the tongue and analyzing the image. Studies of computer-aided quantitative tongue diagnoses are in progress [1]. However, their objects are primarily the tongue color and there are few studies quantitatively measuring the tongue coating, which is a mossy layer attached to the tongue surface. The tongue coating is an important factor in tongue diagnoses. For example, there are reports describing the relationship between excess tongue coating and gastrointestinal disorders and diabetes [2]. In a previous tongue coating study, the effectiveness of measuring the tongue coating was indicated by fluorescence imaging using light sources with a peak wavelength of 405 nm. However, there is a versatility problem for special imaging using light sources close to ultraviolet light [3]. Therefore, in this study, we propose extracting the tongue coating area via machine learning from a general RGB tongue image. The RGB image is taken by a tongue image analyzing system called TIAS with an integrating sphere light source. The light source repeatedly reflects in the integrating sphere to irradiate the tongue surface widely and uniformly. In addition, the integrating light source removes directional irradiation from the light source. Therefore, it enables tongue imaging without gloss.

Methods

We classify the tongue coating area via machine learning using feature values and ground truth data. A plurality of feature values is calculated from the RGB tongue image taken by TIAS and input into the classifier. The fluorescence intensity is extracted as the ground truth data from the tongue fluorescence images taken by the fluorescence imaging system developed in a previous study [3]. The size of the RGB image and the fluorescence image is 5184 × 3456 pixels.

First, to extract the feature values and the ground truth data from the corresponding regions in the RGB image and the fluorescence image, it is necessary to perform a registration of the tongue form between the two images. The tongue contour of each image is selected manually. Then, the transformation of the tongue form is performed using a thin plate spline method [4] using the gravity center and 24 edge points of the tongue, that is, the intersection points of the tongue contour and a line drawn radially every 15° from the gravity center.

Next, the area of the tongue surface is divided into patches with sizes of 100 × 100 pixels. Then, 20 feature values related to the texture and color of the tongue are calculated from each patch of the RGB image and input into the classifier. The 20 feature values include the RGB values, HSV values, CIELAB values, fractal dimension, output of the Gabor filter, average of the Fourier spectrum, and statistics of the pixel intensity. The fluorescence intensity is extracted from each patch of the fluorescence image as the ground truth data. To verify the effectiveness of the proposed method, which extracts the tongue coating area, the experiment was performed on 11 subjects. In the experiment, the RGB tongue image and the fluorescence tongue image were taken using TIAS and the fluorescence imaging system, respectively.

Results

The tongue images of all the subjects were evaluated using the leave-one-patient-out cross validation method. First, to verify the effectiveness of the proposed method, the correlation between the output of the machine learning and the fluorescence intensity of each patch was calculated. Next, the accuracy of the tongue coating extraction was evaluated using a Receiver Operating Characteristic (ROC) curve and a confusion matrix. The tongue coating area and the no tongue coating area were respectively denoted by positive and negative values.

As a result of the correlation analysis, the average correlation coefficient of the 11 subjects was 0.74. This suggests that the proposed method is effective. The area under the ROC curve (AUC) was 0.925 and the sensitivity was 88.1%, confirming the high accuracy of the tongue coating extraction. The ROC curve and the confusion matrix are shown in Fig. 1 and Table 1, respectively.

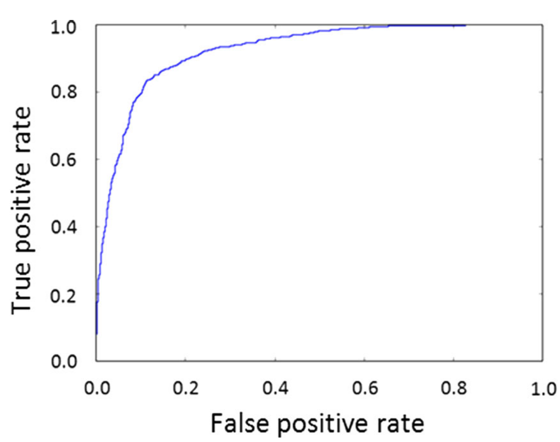

Fig. 1 ROC curve of estimation of tongue coating area

Table 1 The example of extraction of tongue coating area

	Machine learning	
	True	False
Label		
True	88.1	11.8
False	16.0	84.0
Correct rate	85.8	

Conclusion

In this study, feature values were extracted from an RGB image taken by TIAS and ground truth data were extracted from a fluorescence image taken by a fluorescence imaging system. We proposed a system to extract the tongue coating area via machine learning using this data and verified its effectiveness via a validation experiment. A high correlation between the output of the machine learning and the fluorescence intensity was confirmed, suggesting the effectiveness of the proposed method. In addition, the AUC and sensitivity show the high accuracy of the tongue coating extraction.

References

[1] Yamamoto S, Ishikawa Y, Nakaguchi T, Ogawa-Ochiai K, Tsumura N, Kasahara Y, Namiki T, Miyake Y (2012) Temporal Changes in Tongue Color as Criterion for Tongue Diagnosis in Kampo Medicine, Forsch Komplementmed 2012, 80–85

[2] Ojima K (1985) Clinical Studies on the Coated Tongue, Japanese Journal of Oral and Maxillofacial Surgery, 31(7), 1659–1678 (in Japanese)

[3] Ota Y, Iino S, Ichihashi T, Chiba A, Naito S, Nakaguchi T (2016) Proposal and Evaluation of Fluorescence Imaging System for Non-Contact Tongue Coating Measurement and Tongue Protrusion Guide, JAMIT2016, PP-48

[4] Bookstein, FL (1989) Principal Warps: Thin-Plate Splines and the Decomposition of Deformations, IEEE Transactions on Pattern Analysis and Machine Intelligence, 11(6), 567–585

Robustness of trabecular bone parameters for small CT volumes

S. G. Ryan[1], G. Venne[1], J. F. Rudan[2], R. E. Ellis[1]
[1]Queen's University, School of Computing, Kingston, Canada
[2]Queen's University, Surgery, Kingston, Canada

Keywords Bone density · Computed tomography · Trabecular bone · Statistical equivalence

Purpose

Three-dimensional microarchitectural morphometric parameters have been used to study trabecular bone in the mandible, spine, osteoarthritic hips, and many other anatomical sites. The literature is unclear on whether there is a minimum acceptable volume size for accurate measurements, and for what morphological parameters. We selected the 6 morphological parameters of Parkinson [2].

We used femoral head samples from surgical patients, acquiring high-resolution computed microscopic tomography (μ-CT). Two regions in the femoral head were subsampled at volumes typical for a small structure: the primary compressive group and the overall trabecular bone in the femoral head. We used methods of statistical equivalence to determine whether each of these 6 morphological parameters were robust to changes in volume size.

Methods

With approval from the relevant IRB, 15 femoral head and neck samples were collected from patients who had total hip arthroplasty.

μ-CT images were acquired with 50 μm isotropic voxels reconstructed at 100 μm (eXplore speCZT scanner, GE Healthcare).

Microarchitecture analysis

The two regions are depicted in Fig. 1a. Each main volume was subsampled with 100 mm3 and 50 mm3 cubes, binarized as depicted in Fig. 1b, and 3D morphometric parameters were calculated. These were the bone volume fraction, connectivity density, degree of anisotropy, structure model index, trabecular number, trabecular separation, and trabecular thickness. Bone fraction was a percentage; other parameters were real numbers. Data were assembled into six groups: compressive full, compressive 100 mm3, compressive 50 mm3, head full, head 100 mm3, and head 50 mm3.

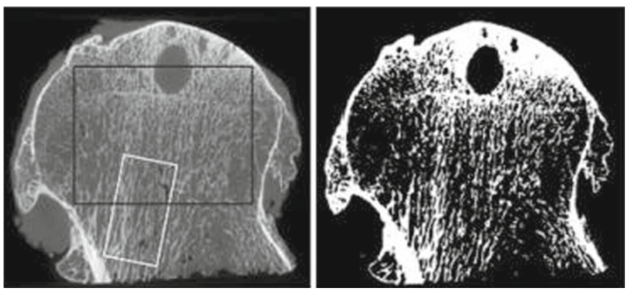

Fig. 1 CT images from a femoral head sample. Left: Representative CT slice, with the compressive region outlined in white and the sampled femoral head in black. Right: Binarization of the same slice

Statistical analysis

Decreasingly smaller sampling volumes were evaluated with three-way comparisons, made separately for data from the compressive region and the femoral head. Differences of means were compared with 2-sided independent *t* tests assuming unequal variances, rejecting Type I errors with $\alpha = 0.01$ as strongly statistically significant. Variances were compared using 2-sided independent F-tests, also with $\alpha = 0.01$. If either of the means or variances were strongly statistically different, groups were taken to be different. Otherwise, the Limentani algorithm [1] was used to determine statistical equivalence with $\alpha = 0.01$ to reject Type I errors, $\beta = 0.01$ to reject Type II errors, and adjusted 95% confidence intervals. The Bonferroni correction was applied. Results were tabulated separately for the compressive region and the femoral head.

Results

Values of the parameters are summarized in Table 1. For the compressive region, which was presumably loaded trabecular bone, most of the parameters were statistically equivalent for the full volumes, subsamples of 100 mm3 cubes, and subsamples of 50 mm3 cubes. The structural model index produced statistically strongly significant results depending on the size of the subsamples.

Table 1 Values of the 3D morphometric parameters, presented as mean ± standard deviation, for the 6 data groups

GROUP	Bone fraction (%)	Connectivity density	Degree of anisotropy	Struct. model index	Trabec. number	Trabec. spacing	Trabec. thickness
Comp., full	39.87 ± 5.52	1.88 ± 0.76	2.75 ± 0.44	0.51 ± 0.43	0.88 ± 0.15	0.74 ± 0.12	0.46 ± 0.08
Comp., 100 mm^3	41.24 ± 6.33	1.79 ± 0.74	2.52 ± 0.41	0.81 ± 0.41	0.97 ± 0.12	0.67 ± 0.09	0.43 ± 0.06
Comp., 50 mm^3	40.98 ± 6.78	1.74 ± 0.76	2.43 ± 0.37	1.00 ± 0.39	0.99 ± 0.13	0.65 ± 0.08	0.42 ± 0.06
Head, full	39.20 ± 4.26	2.25 ± 0.66	1.83 ± 0.16	0.23 ± 0.54	0.83 ± 0.14	0.87 ± 0.16	0.48 ± 0.07
Head, 100 mm^3	41.06 ± 7.78	2.46 ± 0.84	1.95 ± 0.33	0.70 ± 0.55	1.04 ± 0.17	0.66 ± 0.24	0.40 ± 0.05
Head, 50 mm^3	41.06 ± 7.80	2.51 ± 0.92	1.92 ± 0.34	0.90 ± 0.52	1.06 ± 0.18	0.62 ± 0.16	0.39 ± 0.05

For the femoral-head trabecular bone, two of the parameters were statistically equivalent for all sampling volumes: the bone-volume fraction and the connectivity density of the trabeculae. A third parameter, the degree of anisotropy was statistically equivalent for the subsamples but differed statistically from the full femoral heads. The structural model index and the trabecular parameters were statistically different across subsampling sizes for the femoral head and were statistically indeterminate for the compressive region.

The values of the three more robust parameters are shown in Fig. 2 as box plots. Visually, the medians (center lines) and first quartiles (boxed areas) are similar across sizes for each parameter.

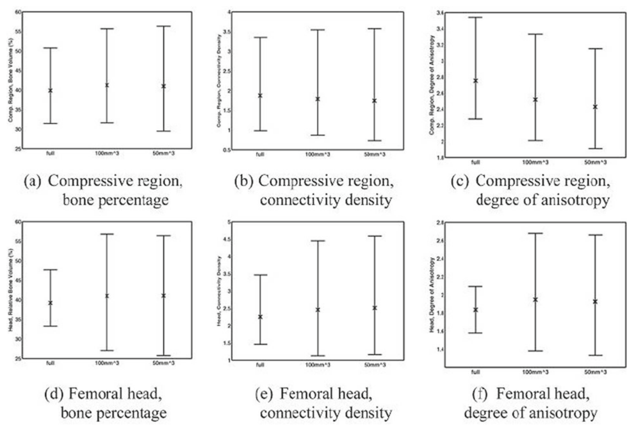

(a) Compressive region, bone percentage
(b) Compressive region, connectivity density
(c) Compressive region, degree of anisotropy
(d) Femoral head, bone percentage
(e) Femoral head, connectivity density
(f) Femoral head, degree of anisotropy

Fig. 2 Plots of selected morphological parameters over 3 physical scales. The center cross is the mean value, whiskers are the 95% confidence interval

Conclusion

We identified 3D morphometric parameters that remain reliable for assessing microstructure of small bone volumes. The bone volume fraction and connectivity density were robust across physical scales from 1000 to 50 mm^3. A third parameter, the degree of anisotropy, was statistically equivalent for volumes of the compressive region; it was also consistent for small volumes of the overall femoral head and differed for larger head volumes. These results may be useful in quantitatively assessing small volumes of bony tissue.

The structure model index performed poorly and the trabecular indices exhibited mixed performance. We would not recommend their use on novel studies of small volumes.

This study was limited by its small sample size and inclusion of only arthritic proximal femurs. The parameters were studied radiographically, with no ground truth from ash contents for bone fractions or histological analysis for the other parameters.

Future work could include the analysis of small volumes of high clinical relevance, such as cancellous and alveolar bone in the mandible and maxilla. Osteophytes appear radiographically to have internal structure [3]; robust morphological parameters may be a useful adjunct to traditional grading systems for osteoarthritis.

References

[1] Limentani GB, Ringo MC, Ye F, Bergquist ML, McSorley EO (2015) Beyond the t-test: statistical equivalence testing. *Am Chem Soc*, 77(1): 221–26.

[2] Parkinson IH, Badiei A, Fazzalari NL (2008) Variation in segmentation of bone from micro-CT imaging: implications for quantitative morphometric analysis. *Australas Phys Eng Sci Med*; 31(2): 160–164.

[3] Venne G, Ryan S, Rudan JF, Ellis RE (2016) Radiological evidence of 3D internal structure in hip osteophytes. *Int J Comput Assist Radiol Surg*; 11(Suppl 1): S35-S37.

Patient specific surgical implants made of 3D printed PEEK—material, technology and scope of surgical application

P. Honigmann[1], N. Sharma[2], U. Popp[3], B. Okolo[3], B. Msallem[4], F. Thieringer[4]

[1]Kantonsspital Baselland Liestal, Hand Surgery, Liestal, Switzerland
[2]University Basel, Medical Additive Manufacturing Research Group, Department of Biomedical Engineering, Basel, Switzerland
[3]Apium Additive Technologies GmbH, Karlsruhe, Germany
[4]University Hospital Basel, Clinic for Craniomaxillofacial Surgery, Basel, Switzerland

Keywords Polyether-ether-ketone · FFF/FDM · Additive manufacturing · Patient specific implant

Purpose

Additive Manufacturing (AM) is rapidly gaining acceptance in the healthcare sector. Three-dimensional (3D) virtual surgical planning, fabrication of anatomical models, and patient specific implants (PSI) are well-established processes in the surgical fields. Poly-ether-ether-ketone (PEEK) has been used, mainly in reconstructive surgeries as a reliable alternative to other alloplastic materials for the fabrication of PSI. Recently, it has become possible to fabricate PEEK PSI with Fused Filament Fabrication (FFF) technology. 3D printing of PEEK using FFF allows construction of almost any complex design geometry, which cannot be manufactured using other technologies.

Methods

In this study, we fabricated various PEEK PSI by FFF 3D printer in an effort to check the feasibility of manufacturing PEEK with 3D printing. Based on these preliminary results, PEEK can be successfully used as an appropriate biomaterial to reconstruct the surgical defects in a “bio-mimicking” design.

Results

The results showed that the 3D printed PEEK PSI fabricated were of a smooth finish without any irregularities. No black specks formation nor discoloration (improper crystallization) were detected in the test parts. All of the 3D printed parts passed a certified sterilization test without any deformation. Thus, these preliminary tests confirm the possibility of fabricating 3D printed PEEK in the desired way (extrusion through nozzle) by FFF.

Conclusion

Personalized medicine is poised to revolutionize the modern practice of medicine where “one size does not fit all” and implants must be tailored to individual patient’s needs are the ultimate goal. The refinement of imaging technologies, coupled with the capabilities to fabricate PSI, has given rise to a proliferation of alternatives to traditional off-the-shelf implants. With the availability of inexpensive compact desktop 3D printers, the surgeons in near future can manufacture medically certified 3D PSI in their own hospitals. This would have a major advantage for surgical planning thereby reducing an enormous amount of time compared with the off-site implant production by third-party providers leading to a more cost-effective healthcare management (Figs. 1, 2).

Fig. 1 3D printed PEEK osteosynthesis plates

Fig. 2 PSI small fragment osteosynthesis plates

Investigation of humeral locking plate system effect on absorbed dose in breast tissue with different radiological energies by using MCNPX

B. Güçlü[1], E. E. Altunsoy[2,3], T. Manici[3], H. O. Tekin[3,4]
[1]Uskudar University Vocational School of Health Services, Department of Physiotherapy, Istanbul, Turkey
[2]Uskudar University Vocational School of Health Services, Department of Medical Imaging, Istanbul, Turkey
[3]Uskudar University, Medical Radiation Research Center (USMERA), Istanbul, Turkey
[4]Uskudar University Vocational School of Health Services, Department of Radiotherapy, Istanbul, Turkey

Keywords Absorbed radiation dose · Ti–6Al–4 V alloy locking plate · Breast · MCNPX

Purpose

Humerus has the most mobile joint in the body. 1% of all body fractures are humerus shaft fractures. Humerus fractures can be treated both conservatively and surgically. Conservative treatment of isolated humerus fractures, particularly those with low energies, may be sufficient. Nevertheless, surgical procedures such as plate-nail osteosynthesis, external fixation, and intramedullary nailing are used to achieve fracture alignment and functional outcome in fractures of high energy intensity [1]. Developments in implant technology, especially the appearance of locking plate systems, have proved to a conservative treatment of many fractures which resulted in limited joint motion. AP and axillary radiographs are routinely used to control condition of pre-operative and post-operative. Lately, the increased use of imaging methods such as computed tomography has upraised concerns about potential cancer risk [2].

Breast cancer is the most common type of cancer in woman. There are many causes of breast cancer, one of which is exposure to ionizing radiation. X-ray radiation is also an ionizing radiation species that can increase the risk of radiation-related cancer in patients. According to the ALARA principle, the total absorbed dose in the breast tissue should be kept as low as possible [3].

Locking plate systems are used as fixation devices in the treatment of humerus shaft fracture. The purpose of this study is to investigate the radiation absorption effects of humeral locking plate system on breast tissue in different radiological energy ranges. The radiation absorption effects of locking plate systems have not been completely studied for the treatment of humerus shaft fracture.

Methods

Ti–Al–7Nb (TAN), Ti–6Al–4 V (TAV) and Ti–6Al–4 V ELI (TAV ELI) titanium alloys are used for various orthopedic and dental implants. These alloys harmonize to the principle of using non-toxic elements in the alloy formulation to optimize the biocompatibility of implant. Ti–6Al–4 V alloy is only exception because of vanadium is considered a cytotoxic element. Animal studies pointed out that although vanadium caused an undesirable biological reaction, the biocompatibility of Ti–6Al–4 V alloy was similar to vanadium-free alloys. In this study, the effect of the Ti–6Al–4 V alloy used as a locking plate system in humeral shaft fractures on the amount of radiation absorption in breast tissue was studied by using MCNP-X (version 2.6.0 Monte Carlo N-particle Transport Code System).

In general, an MCNP-X Monte Carlo code consists of three parts. In the first part of the input file where the geometry definitions are found, the cell identifications of the muscle, fat, skin and humeral bone with a humeral locking plate system placed on humeral fractured patient shown in Fig. 1. In the second part, the surface definitions were made and the dimensions of the phantoms were realized. The simulation geometry was formed with the following information; the humerus bone was 26.3 cm length with 3 cm diameter [4], the thickness of the muscular tissue was 2.1 cm, the thickness of the fat tissue was 0.5 cm and the thickness of the arm skin was 0.5 cm. The Ti–6Al–4 V alloy used for locking plate system after the humerus shaft fracture was included in the simulation by considering the length of 26.3 cm, the width of 1.2 cm and thickness of 0.35 cm and eight threaded screw-holes were arranged in plate system [5]. In addition to geometry, the breast tissue placed with 8 cm in diameter. The source has been defined in this simulation as a point source at radiological photon energies of 0.08, 0.09, 0.10, 0.11, 0.12, 0.13 and 0.14 MeV. The average flux tally F4 is employed in the detector section to measure the amount of absorbed dose. MCNP-X calculations were completed by using Intel® Core ™ i5 CPU 2.71 GHz computer hardware.

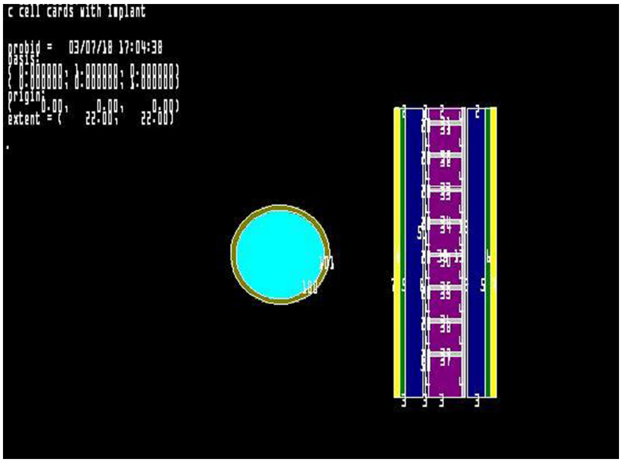

Fig. 1 The screenshot of MCNPX visualization tool for absorbed dose calculation of whole breast tissue on humeral bone fractured patient with Ti–6Al–4V locking plate system

Results

The first simulation has been studied for the investigation of absorbed radiation dose amount in breast tissue without using humeral locking plate system. Afterwards, the next simulation has been studied for the investigation of absorbed radiation dose amount in breast tissue with using humeral locking plate system. Finally, the absorbed radiation dose amount in breast tissue for both situation has been compared. It can be clearly seen from Fig. 2 that, absorbed radiation dose amount in the breast tissue with humeral locking plate system is higher than without humeral locking plate system. This indicates that absorbed dose amount inside of the breast tissue was higher while humeral locking plate system used as the implant material. One can say that, material composition of the humeral locking plate system has a chemical structure that makes the diagnostic X-ray more scattered than bone. In other words, backscattered radiation amount can be change depending on the elemental structure as well as the density of the interacted environment.

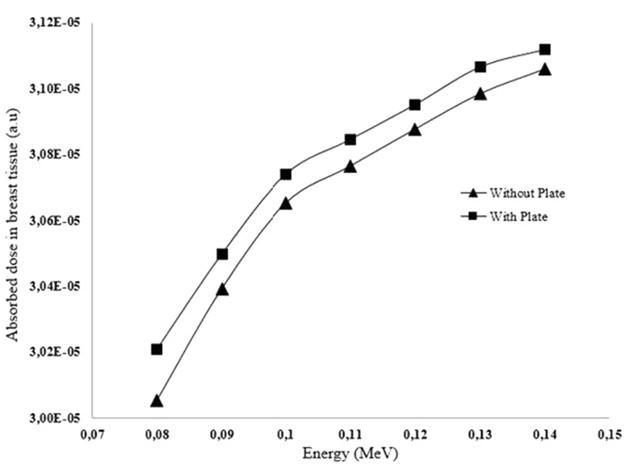

Fig. 2 Comparison of absorbed radiation dose in breast tissue with Ti–6Al–4V alloy plate and without plate

Conclusion

Nowadays, radiographic imaging methods are being used to evaluate the health condition of patients with various medical problems. From this study, it can be concluded that the amount of absorbed dose in the breast tissue strongly depends on backscattered radiation amount from neighboring organs, tissues and material of humeral locking plate system. In this study, it has been shown that the amount of absorbed dose in the breast tissue is related to the humeral locking plate system. In summary, the investigated physical principles of radiation protection and the guidelines of ALARA combined with the dose reduction may further decrease the health risks of low-dose radiation no matter how small that risk might be.

References

[1] Ertem K, Esenkaya İ, İnan M, Taş F, Bora A (2004) Humerus Cisim Kırıklarında Tedavi Yöntemleri. Turgut Özal Tıp Merkezi Dergisi 11(1): 15–17

[2] Brenner DJ, Doll R, Goodhead DT et al. (2003) Cancer risks attributable to low doses of ionizing radiation: assessing what we really know. Proceedings of the National Academy of Sciences 100(24): 13761–13766.

[3] Gholamkar L, Mowlavi AA, Sadeghi M, Athari M (2016) Assessment of Mean Glandular Dose in Mammography System with Different Anode-Filter Combinations Using MCNP Code. Iran J Radiology 13(4): e36484

[4] Anudeep S, Mahindra N, Anil K (2014) An Anthropometric Study of Humerus in Adults. RRJMHS 3(3): 77–82

[5] Karakasli A, Basci O, Ertem F, Sekik E, Havitcioglu H (2016) Dual plating for fixation of humeral shaft fractures: A mechanical comparison of various combinations of plate lengths. ACTA Orthopaedica et Traumatologica Turcica 50(4): 432–436

Classification of thyroid texture in ultrasound images using Bayesian network and adaptive boosting in combination with autoregressive modelling

P. Poudel[1], S. Ghosh[1], T. Suhn[1], A. Illanes[1], M. Friebe[1]
[1]Otto-von-Guericke-Universität Magdeburg, INKA, Magdeburg, Germany

Keywords Ultrasound · Thyroid gland · Segmentation · Classification

Purpose

The thyroid is one of the largest endocrine glands in the human body and is involved in protein synthesis as well as in controlling the human energy sources usage. It is very important to monitor the state of thyroid over time as most of the thyroid diseases like Graves' disease, and thyroid cancer involves change in shape and size of the thyroid [1]. Segmentation and 3D reconstruction are the first steps that are involved to compute the volume of the thyroid. In this work, we propose two methods for classifying the thyroid texture in 2D US image datasets, which can later be used for volume computation by 3D reconstruction.

Methods

Data Collection

We have acquired a total of 4 US datasets from 4 different subjects using a General Electrics (GE) Logiq E9 US system and ML6-15 linear probe with an image resolution of 760 × 500 pixels. The datasets (D1–D4) used for evaluation consisted of between 50 and 96 images with a total over all datasets of 295 images.

Pre-processing and Feature Extraction

In general, US images contain a significant amount of noise and have a low contrast ratio. Simple thresholding-based techniques can therefore not accurately classify thyroid texture [2]. For that, we implemented a more robust technique that would not be affected by the presence of noise and at the same time correctly classify the texture. We divided the individual images belonging to the datasets into small patches of size 20 × 20 pixel. These patches are then converted into two types of signals by taking the pixel information in linear and spiral order. AR modelling [3] is then applied to each resulting signal. A total of 36 preliminary features were computed for each patch from the parametrical AR spectrum and poles at different bandwidths. Finally, Principal Component Analysis and Information Gain techniques were used for computing the four most significant AR features. The advantage of AR modelling is that features are computed not directly from the data (in general corrupted by noise) like in FFT based techniques, but from a parametrical version of the data. This allows computing the robust features in noisy images and with less data. So in summary every US image is divided into 950 texture patches and each patch is characterized by a label (i.e. either thyroid or non-thyroid) and four robust AR features which are based on the frequency and energy components of the signals. These features are used by the bayesian network and adaptive boosting algorithm for characterizing the thyroid texture. The flowchart of the approach we have followed can be seen in Fig. 1.

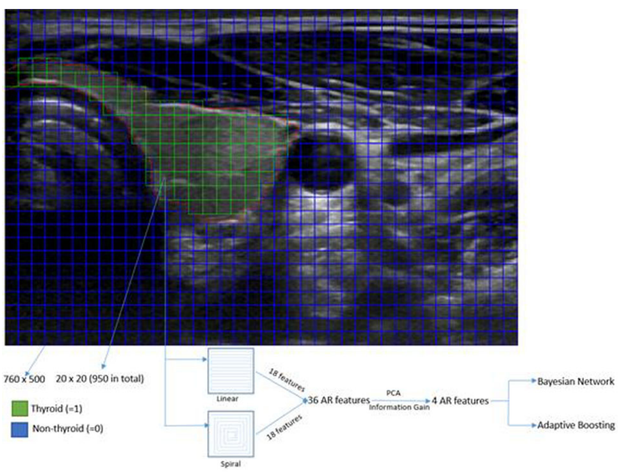

Fig. 1 Flowchart of the approach used

Texture Classification

Bayesian network and adaptive boosting were used to classify the thyroid textures by using the extracted AR features. A bayesian network is a probabilistic model that represents the joint probability distribution of a set of random variables, which in our case are the AR features. Similarly, adaptive boosting is a machine learning based algorithm which is used in conjunction with many other types of learning algorithms for performance improvement. In our case, we have used the decision stump classifier [4] and a software suite called Weka [5] for implementing the two classification procedures.

Results

Testing of these two approaches was carried out in two different formats. First, the four datasets were combined and in a second variation, the test was carried out in each of the datasets individually. In both cases, a 10 fold cross-validation technique was used for the training and testing of the networks. Precision (Pr) and Recall (Re) were computed as the performance measures for the classification of thyroid (= 1) and non-thyroid (= 0) regions. Additionally, the accuracy of the approaches were computed by finding how many texture patches were correctly classified as thyroid and non-thyroid. The classification accuracy of 86.26 and 87.04% show that even with the usage of only four of the AR features, we can achieve a good classification of thyroid texture and we can also predict that, with more significant AR features, the accuracy of the classification would increase. The performance analysis of these two algorithms are presented in Tables 1 and 2.

Table 1 Classification performance using adaptive boosting

Datasets	Combined datasets	D1	D2	D3	D4
Accuracy (%)	87.04	90.84	85.51	91.35	83.32
Pr(1)	0.698	0.782	0.797	0.757	0.657
Re(1)	0.645	0.736	0.470	0.781	0.580
Pr(0)	0.910	0.937	0.864	0.950	0.878
Re(0)	0.928	0.950	0.966	0.944	0.909

Table 2 Classification performance using Bayesian Network

Datasets	Combined datasets	D1	D2	D3	D4
Accuracy (%)	86.26	89.68	82.70	89.68	87.48
Pr(1)	0.626	0.698	0.589	0.667	0.685
Re(1)	0.815	0.830	0.743	0.878	0.847
Pr(0)	0.949	0.957	0.920	0.970	0.951
Re(0)	0.875	0.913	0.851	0.901	0.883

Conclusion

In this work, we have used a novel approach of feature extraction by converting the images into signals and modelling them using AR model. This is a very robust technique of feature selection as it is not affected by the presence of noise in the image and capable of extracting robust features with little amount of data. We have obtained a significant classification accuracy by using only four significant AR features and this accuracy can be increased by computing more significant AR features. Similarly, we have compared two classification techniques and our preliminary results show that adaptive boosting outperforms bayesian network in most of the cases. We have tested the algorithms in only four datasets. More tests have to be carried out in future to improve the accuracy as well as clearly distinguish which algorithm outperforms the other.

References

[1] Ratini M, "Understanding Thyroid Problems—the Basics: Women's Health", WebMD Medical Reference, WebMD, LLC. View.
[2] P. Poudel, A. Illanes and M. Friebe, "Ultrasound thyroid texture classification using a simple texture pattern characterization", In Book of abstracts 51st annual conference of the German Society for Biomedical Engineering, Vol. 62, Dresden, Germany, September 2017.
[3] A. Materka and M. Strzelecki, "Texture analysis methods—a review", Technical University of Ludz, Institute of electronics, COST B11 report, Brussels 1998
[4] C. Sammut and G. I. Webb, "Decision Stump, in Encyclopedia of Machine Learning", Springer US: Boston, MA. P. 262–263.
[5] https://www.cs.waikato.ac.nz/ml/weka/

Optimization design of constant force component using superelastic SMA

M. Wang[1,2], H. Yu[1,2]
[1]University of Shanghai for Science and Technology, Institute of Rehabilitation Engineering and Technology, Shanghai, China
[2]University of Shanghai for Science and Technology, Shanghai Engineering Research Center of Assistive Devices, Shanghai, China

Keywords Optimization · Shape memory alloy (SMA) · Superelasticity · Constant force

Purpose

In clinical application, the clamping instruments for soft tissues of the human body are common, such as the artificial sphincter and hemostatic forceps. The pressure on bowel or urethra caused by the conventional artificial sphincter is hard to control within the safe range. Excessive pressure is usually exerted on the bowel or urethra in order to make it closed, it results in the increasing risk of tissue ischemia or necrosis [1]. Hemostatic forceps also suffered from the same problem [2]. Clamping soft tissues of human body with constant force or pressure within a safe range is considered as an effective solution for this issue. The novel concept that allows the restriction of clamping pressure within a safe range was introduced by Luo [3]. This concept can be realized by embedding superelastic shape memory alloy (SMA) in conventional clamping devices to limit the clamping pressure, which is based on the unique mechanical properties of an SMA during its stress-induced transformation. The structure optimization for superelastic SMA component is required to obtain most constant force.

This paper presented an optimization design for constant force component using superelastic SMA by the combined application of finite element analysis (FEA) with ANSYS and genetic algorithm (GA) in MATLAB. This is followed by the optimization of a *C*-shaped SMA sheet to obtain constant force. The prototypes were fabricated and validated experimentally by comparison with optimization results.

Methods

Due to the unique mechanical properties of superelastic SMA, its structural analysis is a complicated nonlinear problem. Considering the capability of FEA in analyzing problems over complicated domains, it is adopted to analyse the mechanical properties of superelastic SMA. The solution spaces of superelastic SMA are nonsmooth and nonlinear making GA suitable candidates for optimization. The combined application of FEA with ANSYS and GA in MATLAB is desired to achieve the optimization design of constant force structure for superelastic SMA. Performing structural analysis in ANSYS, then the data of calculating result is passed into GA in MATLAB to carry out optimizing.

A C-shaped sheet is selected as the optimization model, as shown in Fig. 1a. The sleeves connected to the pins are designed to simulate for applying load on ends of sheet. Due to the symmetry, only a 1/4 model is considered in optimization. Symmetry constraints are applied on section B, C, D and E while the degree of freedom in Y direction of area A is constrained. The displacement load in X-direction is applied on area A.

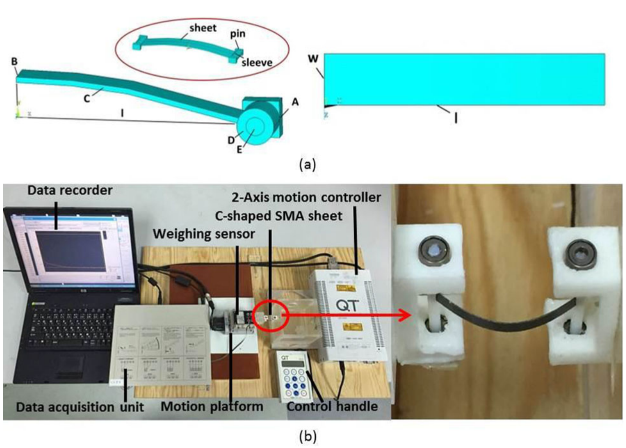

Fig. 1 **a** The C-shaped SMA model and its 1/4 part used in optimization simulation. **b** Experiment setup and prototype of C-shaped SMA sheet

Superelastic SMA of thickness 0.15 mm is used as the material of sheet with Ti–55.9at %Ni. The geometric parameter of initial shape is considered as design variable for optimization, and the optimization process is as follows: the width w is set to be 1 mm. The equation for the initial C-shape curve of the sheetis $y(x) = ax^2 + 1$, x [-l, l], in which $a = -1/l^2$. Different initial shapes of the sheet can be obtained by changing values of l. In this case, l is defined as the design variable with $4 < l$

The result of optimal design is validated by performing the experiments. Figure 1b shows experimental setup for measuring the actual F-D curve.

Results

Based on the proposed optimization method, the obtained optimal solution is *l* = 8 mm. Figure 2a shows several experiment curves, and the curves *C1*, *C2*, *C3*, *C4*, *C5* are force–displacement curves of sheets with the variable *l* of 6, 7, 8, 9 and 10 mm respectively. It can be seen that curve *C3* is the optimal as its slope remains nearly constant within a certain range of displacement. Namely, the best constant force property can be obtained using *C*-shaped SMA sheet with *l* = 8 mm, this is coincident with the result obtained by optimization. The optimal simulation curve obtained by combined optimization was compared with the experimental curve of the *C*-shaped sheet with *l* = 8 mm, as shown in Fig. 2b, clearly show that the experimental curve is roughly 0.06 N higher than its simulation curve in the constant force region. This caused primarily by imperfections in fabrication and machining error. Nevertheless, the shape of experiment curve is similar with optimal simulation curve, and they all show good flatness between displacement of 4 and 14 mm. The constant force region is approximately 71.4% of the entire input displacement. This signifies the constant force property is not sensitive to modeling and manufacturing error. The global solution can be found by the optimization method, and its accuracy can be confirmed by experiments.

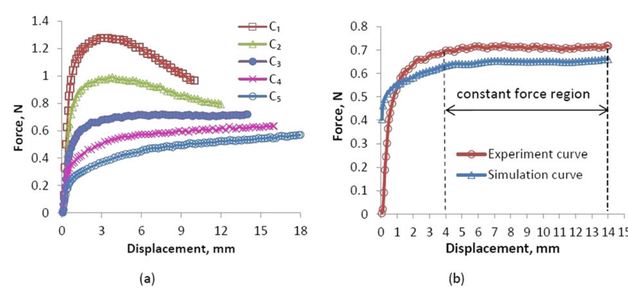

Fig. 2 **a** Several experiment curves at varying parameter *l*. **b** Compared optimal simulation curve (at *l* = 8) with its corresponding experiment curve

Conclusion

This paper proposed an optimization method combining FEA with ANSYS and GA in MATLAB for superelastic SMA to design constant force component. The feasibility of the proposed optimization method has been verified by comparing the optimization and experimental results of the *C*-shaped SMA sheets. It has been demonstrated that constant force can be obtained within a relatively large deformation range by varying the parameters *l*. It has been concluded that large constant force range can be achieved by changing the initial shape of SMA component. Further optimization for width and thickness of *C*-shaped SMA sheet and experimental verification will be carried out in the future work. The work was supported by the foundation from the National Natural Science Foundation of China (61473193) and Science and Technology Committee of Shanghai Municipality (16441905102, 16441905202, 16060502500).

References

[1] Luo Y, Higa M, Amae S, et al. (2006). Preclinical development of SMA artificial anal sphincters. Minimally Invasive Therapy & Allied Technologies. 15(4): 241–245

[2] Luo Y., Higa M., Okuyama T., et al. (2006). Design of safe surgical forceps using superelastic SMAs. International Journal of Applied Electromagnetics and Mechanics 25(1): 571–576

[3] Luo Y., Kodaira S., Zhang Y., Takagi, T (2007) The application of superelastic SMAs in less invasive haemostatic forceps. Smart Materials and Structures. 16(4): 1061–1065

Medical 3D visualization system with gesture-based user interface

L. Yu[1], I. Katramados[2], P. van Ooijen[3]

[1]University of Groningen, Johann Bernoulli Institute for Mathematics and Computer Science, Groningen, Netherlands

[2]COSMONiO, Groningen, Netherlands

[3]University of Groningen, University Medical Center Groningen, Department of Radiology, Center for Medical Imaging (CMI), Groningen, Netherlands

Keywords Human–computer interaction · Medical visualization · Operating room · Image manipulation

Purpose

Hygiene is important for the operating room (OR). All equipment used during surgery needs to be sterilized to prevent contaminations and therefore help prevent infections or serious complications for patients. However, surgeons need access to patient data, medical images and surgery plan during surgeries. The frequently used images include ECG's, CT or MRI scans and X-Ray images which have been recorded prior to surgery and have to be available to the surgeons at all time during surgery.

Currently, the computer systems used to display patients' images require the use of the traditional input tools. Since the computer setup should be separate from the sterile field around the patient and the doctor should not touch any instrument that is not used on the patients, usually there is an assistant or a nurse standing next to the computer screen at the wall of the OR operating a conventional PC using a mouse or touchpad (as shown in Fig. 1). Thus, the surgeon gives oral commands to the assistant who interacts with the interface. However, such oral instructions are inefficient and even if the assistant eventually understands exactly the intended result from the surgeon's instructions, joint computer control may lead to error. It is therefore important to reduce or even completely avoid the necessity for oral instruction and indirect manipulation without compromising the sterility of the surgeon.

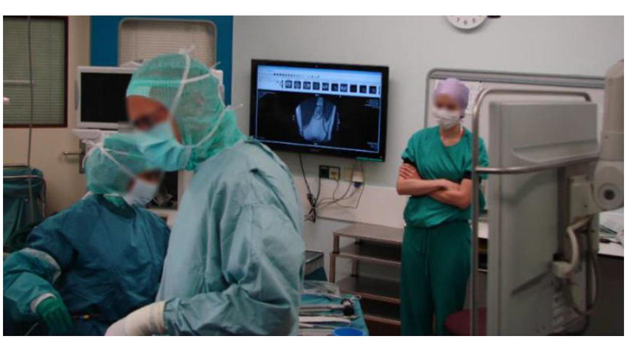

Fig. 1 OR Assistant standing next to the computer used for medical images, a sequential set of images are shown on the screen

Human–Computer Interaction (HCI) in the operating room is gradually becoming commonplace. Image manipulation through gestural devices has been shown to be natural and intuitive and does not compromise the sterility of the surgeon. To overcome the above limitations in the operating room, we developed a gesture-based interface for medical 3D visualization, with which surgeons are able to manipulate 3D images with intuitive gestures. Through our interface, surgeons can load patientss image data/information from an image set, translate, rotate and zoom the data, and change the window level (brightness and contrast of the image) through a set of pre-defined gestures.

Methods

We developed a medical visualization system that allows gestures to control an interface which shows medical images. The major challenge involved in this project is how to provide surgeons with safe means of interaction without affecting the quality of operations. To ensure precise gesture detection, we use Leap motion as our tracking device. The Leap Motion controller is a small USB peripheral device which is designed to be placed on a physical desktop or mounted onto a virtual reality headset. Using two monochromatic IR cameras and three infrared LEDs, the device observes a roughly hemispherical area, which is then sent through a USB cable to the host computer. This is processed to generate 3D position data by comparing the 2D frames generated by the two cameras. According to 3D position of the hand and fingers, we generate the gestures which are further mapped to specific data manipulations. Several data manipulations have been implemented in our system:

1. Load DICOM images from patients' image set: In certain cases, there may be several image sequences used per patient, resulting in many different data sets. In our system, users can scroll and review the data set by moving their palm up and down. Once the desired image is found, users can point to the image with their index finger and open their thumb to have it selected.
2. Navigation of the 3D image: Doctors are able to use free-hand gestures (panning, rolling, two hand gestures) to control different manipulation events. The fundamental manipulation techniques include but are not limited to: translation of 3D volume parallel to the view plane (*x-/y*-translation); rotation of 3D volume around *x*- and *y*- axes (*x-/y*-rotation); translation of 3D volume in *z* and rotation around *z axis* (*z* translation); and scaling. Specific icons associated to the chosen actions are shown to make it easier for users to remember the current interaction.
3. Window level adjustment: doctors can adjust the brightness and contrast of the visualization by using one finger (in the window level adjust mode, pointing to the data with index finger and move the hand up/down or left/right).
4. Adjusting the cutting plane: in the cutting plane adjustment mode, doctors can specify a direction with index finger and thumb and adjust the clipping plane in the selected direction by moving the hand.
5. Hand floating menu and static menu: a gesture-based menu is involved in our interface, so that users can select specific manipulations directly.

Results

Although we have not yet tested our system in the OR, it has been evaluated by medical domain experts in a lab environment (as shown in Fig. 2). Response to the interaction and the 3D projection of medical data is very positive. Doctors can understand and remember gestures after a short introduction and can precisely control the interface and manipulate 3D data with intuitive gestures. If the system works in an effective way, we hypothesize that surgeons should be able to check and manipulate patients' data in a more precise way, compared to asking assistants to interact with data by using traditional inputs. However, most of the traditional input devices have two major benefits, familiarity and precise control, which make people feel that they are easy to use, especially for an urgent task. Therefore, it will be interesting to learn if and how gesture-based interfaces can replace the traditional setup.

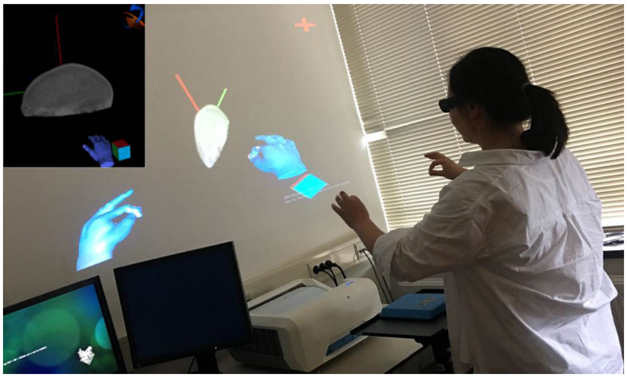

Fig. 2 A user is manipulating 3D medical data with our gesture-based interface

Conclusion

Our touch-free medical 3D visualization system provides the surgeons an effective and efficient way to manipulate patients' images. However, there are other more specific data manipulations that can be extended in the system, such as marking and measuring the size of regions of interests. Therefore, more gestures will be required and formal user validation in the OR has to be performed.

The general operation manager (GOM)—first experiences with process-oriented workflow management system

K. Feige[1], I. Gollnick[2], G. Strauss[1]
[1]Kopfzentrum, Leipzig, Germany
[2]IRDC GmbH, International Reference and Development Centre for Surgical Technology, Leipzig, Germany

Keywords General operation manager · Workflow management · Perioperative logistic · Pre- and postsurgical process

Purpose

The key to a successful operative procedure is not only the technically correct execution but also its optimal implementation in the form of a well-organised workflow of perioperative care [1]. The safety of surgical interventions also depends to a large extent on the error-free procedure of perioperative standards. In particular this applies to: medical indications, processing and checking of admission requirements, identity verification, the transport of patients, the follow-up and the postoperative management. Investigations and studies show that up to one-third of the available operating capacity is not used due to mismatching, first, between perioperative and operative processes [2] and, second, during the single steps of the perioperative process itself.

Therefore, it seems to be necessary to find new ways for optimisation the perioperative management. This could be realised by standardizing these processes with support of a software-based process control. Firstly, this program should guarantee that all decisions that are relevant to safety are queried in a distinct manner. Secondly, it should be orientated towards each user's procedures and be immediately available on all relevant points-of-contact. Thirdly, it should lead to a reduction of adverse events in terms of indication and check-in and check-out processes. Furthermore, this software program should offer an efficient cost–benefit ratio. Such a software program has been developed and been in use at ACQUA Clinic in Leipzig: The General Operation Manager (GOM).

Methods

Between 1st December 2013 and 15th March 2014 (14 weeks) a control group of 200 patients were collected and analysed. In the time from 1st May 2014 and 30th September 2014 (5 month, 120 patients), and 1st January 2017 and 31th December 2017 the GOM-system was evaluated. Regarding the cost–benefit ratio the Patient Handling Time (PHT) was investigated. The PHT includes the total temporal requirement: from the time point of cabin-into the check-out, except surgery time. Additional, a questionnaire about the application of GOM-system was conducted and evaluated, by 22 participating staff members of ACQUA clinic (6 surgeons, 6 technical officers for surgery, 2 receptions, 3 anaesthetists, 3 technical officers for anaesthesia and 2 concierges).

Results

No medically or technically safety-relevant incidence emerged in the studied time 2014 and 2017. From May 2014–Sept 2014 (with GOM) the total PHT amounted to 272 min (+SD: 33 min), in the control group (Dec 2013–March 2014) PHT was 245 min (+SD: 14 min) (data not shown).

The evaluation of time course with GOM is presented in Fig. 1. It shows that the total time in the case of "surgery with stay overnight" has been reduced by at least 124 min, whereas the total time in the event "surgery without stay overnight" is not significantly different. The total time of "surgery with local anesthesia" continued to show strong fluctuation (minimum time: 46 min, maximum time: 149 min) in the period between January and October 2017.

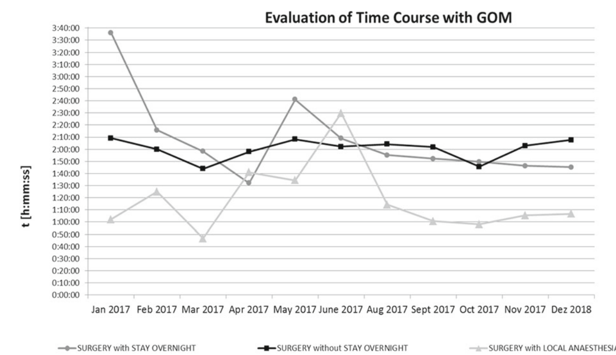

	Jan 2017	Feb 2017	Mar 2017	Apr 2017	May 2017	June 2017	Aug 2017	Sept 2017	Oct 2017	Nov 2017	Dez 2018
SURGERY with OVN	03:36:09	02:15:52	01:58:22	01:32:04	02:41:00	02:09:05	01:55:12	01:52:18	01:49:39	01:46:22	01:45:14
SURGERY	02:09:08	01:59:54	01:43:53	01:57:52	02:08:13	02:02:05	02:04:17	02:01:44	01:45:33	02:02:54	02:07:47
SURGERY with LOC ANA	01:02:03	01:25:02	00:46:32	01:41:01	01:34:19	02:29:47	01:14:18	01:00:33	00:58:07	01:05:26	01:06:44

Fig. 1 Evaluation of time course using GOM-system: surgery with stay overnight, surgery without stay overnight outpatient (OVN) and surgery with local anaesthesia outpatient (LOC ANA); no data of July 2017 due to the company holiday

The analysis of the questionnaires in Fig. 2 revealed that most of the staff members voted "approval" and "parts-parts", i.e. the rate of satisfaction among the users of the GOM-system is relative high.

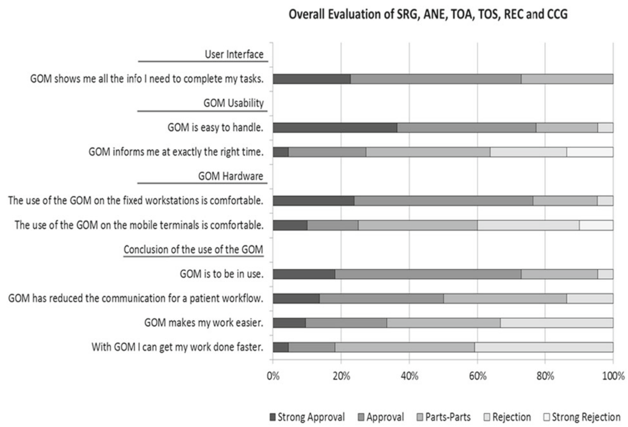

Fig. 2 Evaluation of questionnaires filled in by all participating staff members. The rate of acceptance of the GOM-system is relative high by participants

Conclusion

The current study confirmed that the GOM can be deployed in the clinical routine, without any technical or medical risk for the patient. It can be assumed, that no new systematically risks occur also for treatments other than ENT surgery. Furthermore, it has been shown that the GOM leads to a significant time reduction within perioperative procedures. Additionally, process deviations are perceived earlier.

Finally, the cost–benefit ratio is positive, although at the begin (May–September 2014) the requirement of time is higher, but in the course of years (October 2017) time savings were increasing.

Not only checking a checklist increases patient safety, but also structured communication in transfer processes and situation awareness of all professionals involved in the course of treatment [3]. About 70% of the staff members support the GOM-system. In regard to the user interface, about 70% confirmed that GOM shows them all the information they need to complete their tasks.

References

[1] Madler C, Danner K, Kawach H (1996) Präoperative anästhesiologische Visite, Anästhesieambulanz—Risikoeinschätzung, Patientenvorbereitung und Planung des perioperativen Vorgehens. AINS 31(10): 633–653, https://doi.org/10.1055/s-2007-995999

[2] Tsekos E (2017) KU Gesundheitsmanagement 06/2017, S. 46, https://www.wiso-net.de/document/KU__3143592508

[3] Weckenbrock R, Heid F, Groß-Liebsch D (2017) KU Gesundheitsmanagement 03/2017, S. 46 https://www.wiso-net.de/document/KU__3142781227

Poster Session

22nd Annual Conference of the International Society for Computer Aided Surgery

Biomechanical assessment of custom plates design for the distal radius

G. Caiti[1], J. Dobbe[1], E. Bervoets[2], M. Beerens[3], S. Strackee[4], G. Strijkers[1], G. Streekstra[1]
[1]AMC, Biomedical Engineering and Physics, Amsterdam, Netherlands
[2]Metrotech Engineering and Physics, Farre, Denmark
[3]Xilloc Medical BV, Geleen, Netherlands
[4]AMC, Plastic, Reconstructive and Hand Surgery, Amsterdam, Netherlands

Keywords Patient specific implant · Modelling · Fracture fixation biomechanics · Distal radius malunion

Purpose

When a distal radius fracture heals in a displaced position, often causing pain and functional impairment of the wrist joint, it may be treated with corrective osteotomy surgery. This surgical procedure consists in cutting the bone at the level of the old fracture with subsequent reduction and fixation of the bone parts with plate and screws to restore the anatomical alignment.

Patient-specific implants can be used to fixate the bone segments. These custom implants are designed to fit the individual patient's anatomy and ensure accurate bone repositioning according to the three-dimensional (3D) pre-operative virtual plan [1, 2].

In current patient specific plate designs, biomechanically relevant parameters such as screw configuration, size and thickness have remained essentially similar to standard anatomical plates. However, taking the biomechanics of bone-fracture fixation in plate design into account is important since it has a direct effect on the quality of bone healing, in particular the callus formation which is stimulated by moderate strain at the fracture site (2–10%) [3].

Methods

Patient–Specific implant modelling

For our simulations we used previously acquired bilateral CT-scans of the radii of five patients. For each scan, after segmentation of the image of the affected bone, the distal and proximal bone segments of the affected 3D bone model were registered to the mirrored image of the contralateral image to find the optimal required anatomical alignment. The custom plates were designed with custom software to fit the repositioned bone segments.

We first considered a custom plate of size and screw configuration similar to the standard anatomical distal radius plate (Fig. 1). Nine screw holes were added to the plate. Five screws were positioned on the distal and four on the proximal part of the plate. The initial plate thickness was set to 2.4 mm.

Fig. 1 Patient-specific plate initial design. Screw configuration and plate thickness are similar to standard anatomical plates

Finite Element Analysis

To simulate forces acting on the radius and the osteosynthesis material during daily activity, we separately applied three loading conditions: axial compression (50 N), and bending (1 Nm) and torsion (1 Nm) moments to each radius model. We estimated the interfragmentary strain (ε_{IF}) as the mean relative change in distance between four different corresponding mesh node pairs when load was applied to the bone-plate model.

Stress distributions in the plate, gap strains, and axial screw forces were estimated for the initial custom plate geometry under the three loading conditions. Results of this first analysis were used in order to decide whether screw configuration could be improved. After the improved screw configuration was found, the shape of the plate was changed accordingly. In the second set of simulations, the improved screw pattern and plate shape were applied to four additional patient cases. For four different plate thicknesses (2.4, 1.9, 1.5, and 1.0 mm) we estimated stress distributions in the plate, gap strains, and axial screw forces in the considered plate-bone models.

Results

In the initial custom plate, the stress exceeded the plastic deformation limit at the level of the proximal screw close to the osteotomy gap during torsional loading. Since in the initial plate geometry the proximal screws were directed toward the bone axis with insufficient lever to counteract the exerted torsional moment, we improved this initial configuration by placing three distal and proximal screws in a triangular pattern (Fig. 2).

Fig. 2 The novel patient-specific plate design. Screws are arranged in a triangular pattern to counteract torsional moment

The new screw configuration reduced the maximum stress in the implant in all load cases, especially under torsional load (− 31%). Reduction of the modified plate thickness resulted in an increase in the interfragmentary strains. Under bending load, implants with 1.9 mm thickness induced an average level of strain (median = 2.14% IQR = 0.2) in the recommended range (2–10%) to promote callus formation.

Conclusion

Placing the fixation screws in a triangular configuration in custom distal radius plates reduces the maximum stress compared to a standard screw configuration, which helps reducing the size of the implant. Future mechanical evaluation is needed to experimentally confirm this finding. Choosing the optimal plate thickness allows sufficient strain to enhance callus formation which is expected to improve osteosynthesis.

References

[1] Dobbe JGG, Vroemen JC, Strackee SD, Streekstra GJ (2013) Patient-tailored plate for bone fixation and accurate 3D positioning in corrective osteotomy. Med Biol Eng Comput 51: 19–27. https://doi.org/10.1007/s11517-012-0959-8

[2] Omori S, Murase T, Kataoka T, Kawanishi Y, Oura K, Miyake J, Tanaka H, Yoshikawa H (2014) Three-dimensional corrective osteotomy using a patient-specific osteotomy guide and bone plate based on a computer simulation system: Accuracy analysis in a cadaver study. Int J Med Robot Comput Assist Surg 10: 196–202. https://doi.org/10.1002/rcs.1530

[3] Perren SM (2002) Evolution Of The Internal Fixation Of Long Bone Fractures. J Bone & Jt Surgery, Br Vol 84–B: 1093 LP-1110

Gastric volume reduction surgery using novel endoscopic suturing device on porcine model

S. H. Park[1], B. Kim[1], H. S. Choi[2]
[1]Korea University, Mechanical Engineering, Seoul, South Korea
[2]Korea University Anam Hospital, Gastroenterology, Seoul, South Korea

Keywords NOTES · Bariatric surgery · Endoscopic surgery device Porcine in vivo model

Purpose

Not only dietetic therapy but also surgical method is recommended for patients with morbid obesity. Typical conventional gastrectomy surgery, mainly using the laparoscope to cut most of the stomach. However, it has disadvantages in terms of scarring and recovery period due to its invasiveness. Endoscopic gastroplasty has been proposed as an alternative and surgical instruments have been studied for this purpose. We developed a Successive suturing device (SSD), which is an endoscopic suturing device. We will use this to reduce the stomach. The aim of this study is to confirm the feasibility of SSD in vivo and to see the effects of weight loss.

Methods

Six one-month-old Yorkshire pigs were tested. The initial weight is 35.5 kg. We tested Endoluminal gastroplasty in fundus (EGF) and Sleeve gastroplasty in body (SGB) that is the most commonly perform gastroplasy (Fig. 1). EGF was performed to two pigs and SGB to two other pigs. The other two are controls. Two-channel endoscopy (Olympus GIF-2T100. Tokyo, Japan) and our developed SSD were used. SSD consists of anchor bead, needle tube, suction cap, knotting device and bead transferring device. SSD installs the anchor bead in several places on the gastric wall. Then pulls the wire connecting the anchor beads and gather them to reduce the volume. EGF case, anchor beads were located along the perimeter of the fundus, and at the front of the body on SGB case. Then, fix the state with a knotting device. The pigs were observed for 82 days after the surgery, during which all the meals were supplied with the same and limited amount. Endoscopy and weight measurements were performed eight times to observe the stomach during study period.

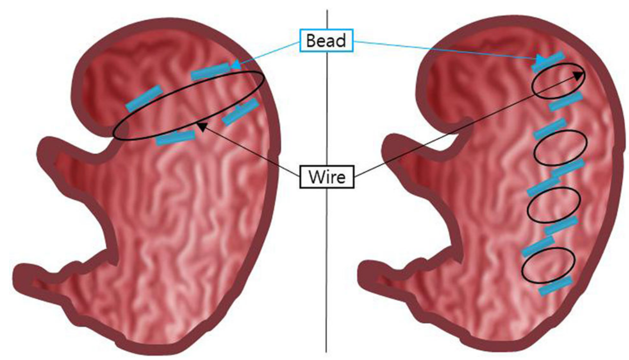

Fig. 1 Endoluminal gastroplasy on fundus (EGF) (left) Sleeve gastroplasy on body (SGB)(right)

Results

The operation time of EGF was 22.8 and 18.7 min, respectively and 28.7 and 22.0 min in case of SGB. All operations were completed without device problems. All pigs survived for 82 days without any complication. No visible inflammation or perforation was found on the in and outside of the stomach when sacrificed at 82 days It showed a body weight gain difference between the EGF group, SGB Group, control group. While the control group increased by 45.1 kg, the EGF group increased by 33 kg and 34 kg, respectively, while the SGB group increased by 26 kg and 27 kg (Fig. 2).

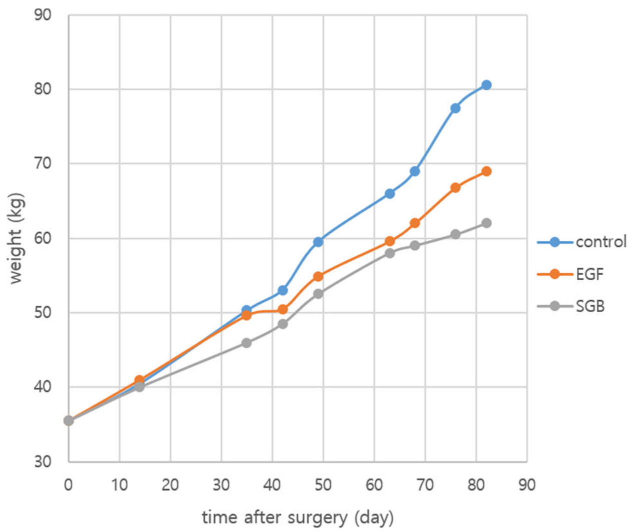

Fig. 2 Weight gain for 82 day after surgery

Conclusion

In terms of feasibility, it was confirmed that there were no fatal problems during surgery or short term after surgery. We also confirmed that the operation was possible in fundus, which was difficult to work with existing equipment. When comparing two surgical methods, the operation time of EGF was faster than that of SGB. The fundus took longer to approach, but the anchor bead installation time was shorter. In terms of weight loss, surgery on the body is more effective. The EGF group was 11 kg less than the control group and the SGB group was 18.6 kg less. This confirmed the possibility of obesity inhibition. However, it was difficult to confirm the statistical significance due to the small number of pigs, and there was no follow up for more than 6 months. Therefore, a follow-up study will be conducted.

Automating end-product assessment of virtual temporal bone dissection

K. Hassan[1], J. Lui[2], J. Dort[2], S. Chan[1]
[1]University of Calgary, Department of Computer Science, Calgary, Canada
[2]University of Calgary, Department of Surgery, Section of Otolaryngology, Calgary, Canada

Keywords Surgical simulation · Performance assessment · Image analysis · Virtual reality

Purpose

Temporal bone dissection is a core component of an otolaryngologist's training. Presently, surgical residents acquire this skill through observation and repeated practice on cadaveric specimens in the environment of a temporal bone dissection laboratory. Competency is assessed by direct expert observation of surgical performance, or by evaluating the end-product of the procedure: a dissected temporal bone. Limited availability of cadaveric specimens, coupled with ethical concerns on their use, has spurred development of virtual reality simulators, with high-fidelity visual, auditory, and force feedback, for temporal bone surgery [1–4]. Virtual reality simulation has been demonstrated to improve surgeon mastoidectomy performance [4].

Performance assessment and providing feedback places a heavy burden on expert surgeons' time, but the use of surgical simulators provides an opportunity to automate evaluation. An instrument for surgical performance assessment must be reliable, valid, and feasible. Among several such instruments that have been proposed for temporal bone surgery, the Welling Scale [5] likely has the widest adoption today. It consists of a 35-item binary checklist designed to assess outcome of a mastoidectomy with a facial recess dissection.

The purpose of our research is to automate the scoring of a mastoidectomy, using the Welling Scale, performed in a virtual surgical environment. While others have demonstrated that metrics can be devised to score virtual temporal bone dissections to distinguish between novices and experts [3], our investigation is focused on automating a well-established and validated assessment instrument. The Welling Scale is a reliable and valid instrument for assessing virtual mastoidectomies [1], though no means of automating the scoring has yet been developed.

Methods

A temporal bone surgery simulator that we developed [2], which enables virtual dissection of virtual models derived from clinical computed tomography (CT) data, was used for this investigation. The output, or end-product, of a virtual temporal bone dissection in this environment consists of the original CT image of the specimen, a segmentation of the critical structures, and a dissected CT image (Fig. 1). Image processing algorithms can be devised and run on these digital outputs to automatically score each of the items on the Welling Scale.

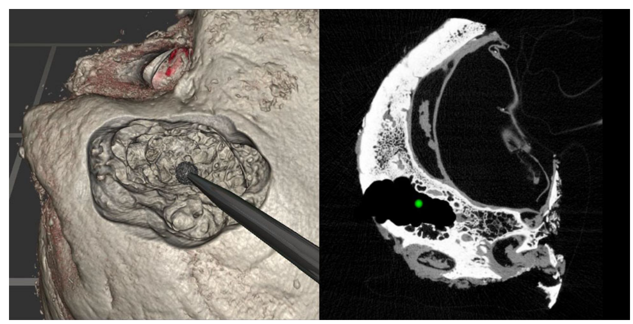

Fig. 1 The end-product of a virtual temporal bone dissection (left) is a dissected CT image (right) with excised bone tissue removed. The green dot shows the position of the virtual surgical drill within the excised cavity

The criteria of the Welling Scale were adapted to facilitate development of methods for automated analysis. Specific requirement groups include identification and exposure (of the tegmen, digastric ridge, facial nerve, facial recess, carotid artery, jugular bulb), skeletonization (of the posterior canal wall, sigmoid sinus, semicircular canals, basal turn of the cochlea), preservation (of the tegmen, sigmoid sinus, external auditory canal, semicircular canal, facial nerve), adequate dissection (bone surrounding the tegmen, sigmoid sinus, sinodural angle, external auditory canal), and other tasks (rounded cortex, complete saucerization, sharp sinodural angle).

The identification and exposure criteria determine whether each critical structure is visible from the surgeon's vantage point. Within the dissected CT image, a ray is cast from the vantage point to each point (voxel) on the surface of a critical structure. Ray marching is used to determine if any tissue obstructs the view of the structure along each ray. A structure is considered exposed if a sufficient proportion of its surface is determined to be visible from the vantage point.

To protect critical anatomy, surgeons skeletonize the structures by leaving a thin protective layer of bone overlying the critical structure. For assessment of these criteria, a signed distance field is first created (using Danielsson's distance mapping algorithm) from the binary segmentation of each structure. Each voxel location in the original CT image with tissue present and a distance marked greater than the desired skeleton thickness (e.g. 0.5 mm) is examined in the dissected CT image to verify that it was properly removed. Similarly, voxel locations marked with a distance less than the desired skeleton thickness are examined to see if they are still intact. These tests take into account the surgeon's vantage point to ensure that the skeletonization requirement is applied only to the visible portion of the structure.

The preservation criterion assesses whether or not the surgeon injured critical structures or dissected anatomy that should have been preserved. Each critical structure's segmentation is tested against the dissected CT image to determine if any part of the structure was incorrectly excised.

Adequate dissection, which means leaving no air cells or bony overhang, requires a more complex geometric analysis of the end product to assess, and is not presently implemented in our prototype. Likewise, proper scoring of the criteria grouped in "other qualities" will likely require specialized algorithms for future development.

Results

A prototype computer application implementing the image analysis algorithms described for automated end-product assessment was developed. The digital product of a virtual temporal bone dissection can be loaded into the application, and assessment of various Welling Scale criteria on the dissection can be driven through a graphical interface. A micro-CT image of a cadaveric temporal bone specimen, with relevant anatomical structures segmented, was dissected in the virtual surgical environment to serve as a test case for this work. Automatic assessment of the virtual dissection was performed in the prototype application, and results of specific criteria are shown visually on the dissected CT image, and optionally on the 3D rendering of the specimen within the simulator itself (Fig. 2).

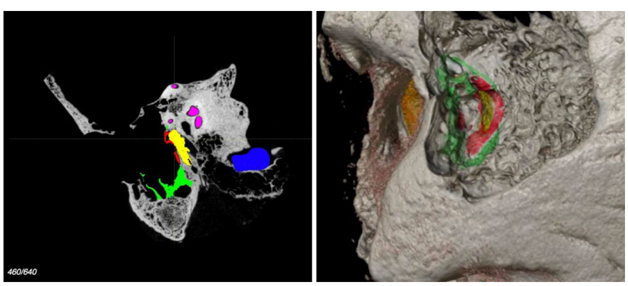

Fig. 2 Algorithms are run on the dissected CT image to score various criteria of the Welling Scale (left). Segmentations are shown as: inner ear in purple, sigmoid sinus in blue, and facial nerve in yellow. Red regions show erroneously dissected bone, while areas that require further dissection appear in green. Results of the assessment can be visualized within the virtual surgical environment (right)

Conclusion

This work demonstrates the feasibility of automating end-product assessment of a virtual temporal bone dissection using the Welling Scale. Scoring of many criteria on this checklist instrument can be automated by use of image analysis algorithms, when coupled with a temporal bone surgery simulator that can export virtual dissections as image data. This has potential to provide otolaryngology residents much richer opportunities for learning and practice, without increasing the time burden on surgical experts.

The research described is an ongoing project where we are striving to develop algorithms to address all assessment criteria on the Welling Scale, and continuing to refine the accuracy of our methods. Ultimately, we must determine the reliability of our automated end-product assessment, as compared to human expert ratings, through formal studies before fully incorporating it into our simulation workflow, and possibly into the education curriculum.

References

[1] Anderson S, Cayé-Thomasen P, Sørensen MS (2015) Mastoidectomy performance assessment of virtual simulation training using final-product analysis. Laryngoscope 125(2): 431–435.

[2] Chan S, Li P, Locketz G, Salisbury K, Blevins NH (2016) High-fidelity haptic and visual rendering for patient-specific simulation of temporal bone surgery. Comput Assist Surg 21(1): 85–101.

[3] Kerwin T, Wiet GJ, Stredney D, Shen H-W (2012) Automatic scoring of virtual mastoidectomies using expert examples. Int J Comput Assist Radiol Surg 7(1): 1–11.

[4] Lui JT, Hoy MY (2017) Evaluating the effect of virtual reality temporal bone simulation on mastoidectomy performance: a meta-analysis. Otolaryngol Head Neck Surg 156(6): 1018–1024.

[5] Butler N, Wiet GJ (2007) Reliability of the Welling Scale (WS1) for rating temporal bone dissection performance. Laryngoscope 117(10): 1803–1808.

Towards a complete simulator of Twin-to-Twin fetal surgery: performance of a cost-effective tracking system

M. Ceresa[1], R. López-Velazco[1], A. Alises[1], J. Torrents-Barrena[1], N. Masoller[2], E. Eixarch[2], E. Gratacós[2], M. A. Gonzalez Ballester[1,3]
[1]Universitat Pompeu Fabra, DTIC, Barcelona, Spain
[2]Fetal i + D Fetal Medicine Research Center, BCNatal—Barcelona Center for Maternal–Fetal and Neonatal Medicine (Hospital Clínic and Hospital Sant Joan de Deu), Institut Clínic de Ginecologia, Obstetricia i Neonatologia, Institut d'Investigacions Biomèdiques August Pi iSunyer, Universitat de Barcelona, and Centre for Biomedical Research on Rare Diseases (CIBER-ER), Barcelona, Spain
[3]ICREA, Barcelona, Spain

Keywords Twin-to-twin transfusion syndr · Surgical planning · Fetal surgery · Tracking systems

Purpose

Twin-to-twin transfusion syndrome is a relatively common pregnancy complication where two monochorionic twins have small fenestrations between vessels called anastomoses. Fetoscopic photocoagulation of the anastomoses is the elective surgical procedure, capable of substantially improving the prognosis of the twins. This is, however, complicated by many factors such as: (i) the variability in localization, size and shape of the placenta [1] (ii) the reduced manoeuvrability and visibility of the fetoscope once inside the uterus (iii) the impossibility to know exactly the localization of the anastomoses ahead of surgery. Additionally, once inside the uterus, there is only a short time window available for the operation [2] and re-intervention is associated with high mortality.

Ideally, surgeons could use a good surgical planning system to simulate the entire intervention, estimate the effect of different insertion points on the manoeuvrability of the fetoscope and confirm the possibility to reach all the anastomoses, which is very important in order to prevent recurrence. However, there is no such system currently available. One of the barriers is the high costs and setup complexity of commercial movement tracking solutions, which are not justified for a purely pre-operative system.

In this paper, we compare a low-cost tracking solution based on optical markers with the more expensive electromagnetic NDI Aurora tracker, to see if the intervals of confidence are good enough to be used to simulate the surgery.

Methods

Our proposed system integrates the "Medical Imaging inTeraction toolKit" (MITK) [3] with a computer vision library called ArUco [4]. MITK is a free open-source software for development of interactive medical image applications. ArUco is a library which uses markers and a RGB camera to perform tracking.

We compare the intrinsic error of the marker tracking system. To this end, we used a square marker with 60 mm length attached to a cardboard to eliminate transparencies. The EM sensor probe was fixed to the back of the cardboard, aligning both the sensor and the marker centers. A precise alignment of both centers is not needed as we are measuring the variability instead of the absolute value. The camera used for the tests is the Logitech C920 webcam with the autofocus disabled. Lighting conditions can impact marker detection and were for this reason kept artificial and constant. The physical setup can be seen on Fig. 1a). The EM field generator was placed in front of the camera. The test recorded the position of the pointer, reported by both the Aruco-based tracker and the NDI's one, in six different points on the surface of a 3D-printed phantom generated with OpenSCAD http://www.openscad.org (see Fig. 1a). We repeated each acquisition five times, each one with a duration of 10 s. Prior to that, both systems were synchronized with a latency inferior to 10 ms.

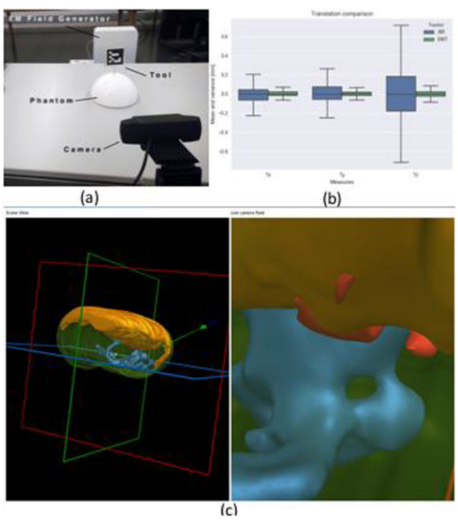

Fig. 1 **a** Setup of the experiment. **b** Comparison of the variability of both the Aruco (blue) and the EMT (green) tracking systems. **c** Example of using the system to test different insertion points

Results

The results of the experiments were analysed using python and matplotlib. In Fig. 1b we show the boxplots of the positions obtained in the experiment. We see that all variables are centered at zero with almost no fixed bias while the variance for the position varies from (0.2; − 0.4) cm for X and Y to (− 1.6; 0.4) cm for Z. The differences in position where not statistically significant w.r.t. the results of the EM tracking.

In agreement with [5], the tracking accuracy varied according to the spatial location and was, in our case, between 5 and 34 mm. The accuracy was better when the markers were closer to the centre of the image and degraded as they got closer to the periphery.

We think that the millimetric errors that we found in our experiments are acceptable for the use of the system in a pre-operative planning simulation setting where the aim is to explore the effect of different insertion points of the fetoscope (see Fig. 1c). Also, this is already a great improvement from the current practice, where the insertion is determined manually using only the MRI images.

Conclusion

In this paper we analyzed the performance of a low-cost tracking system and compared it to the more expensive electromagnetic one. We showed that the limits of agreement are good enough to simulate the insertion of the fetoscope for fetal surgeries. This is important to reduce the uncertainties in complex cases.

Acknowledgements

This work was supported by a project granted by CELLEX foundation.

References

[1] Barker D, Bull AR, Osmond C, Simmonds SJ (1990) "Fetal and placental size and risk of hypertension in adult life." Bmj, vol. 301, no. 6746, pp. 259–262
[2] Ville Y, Hecher K, Gagnon A, Sebire N, Hyett J, Nicolaides K (1998) Endoscopic laser coagulation in the management of severe twin-to-twin transfusion syndrome, BJOG: An International Journal of Obstetrics & Gynaecology, vol. 105, no. 4, pp. 446–453
[3] Wolf I, Vetter M, Wegner I, Bottger T, Nolden M, Schobinger M, Hastenteufel M, Kunert T, Meinzer H-P (2005) The medical imaging interaction toolkit, Medical image analysis, vol. 9, no. 6, pp. 594–604
[4] Garrido-Jurado S, Munoz Salinas R, Madrid-Cuevas F, Marın-Jimenez M (2014) Automatic generation and detection of highly reliable fiducial markers under occlusion. Pattern Recognition, vol. 47, no. 6, pp. 2280–2292
[5] Guler O, Yaniv Z (2012) Image-guided navigation: A cost effective practical introduction using the image-guided surgery toolkit (igstk). Engineering in Medicine and Biology Society (EMBC), 2012 Annual International Conference of the IEEE. IEEE, 2012, pp. 6056–6059. II-B, IV-A, IV-B

Personalized medicine: technological bridge between patient and surgeon by 3D printed surgical guide in rhinoplasty

H. Herrero Antón de Vez[1], J. Herrero Jover[1], R. Comas[1]
[1]CM Teknon, Herrero Jover Médicos, Barcelona, Spain

Keywords Personalized medicine · 3D printing · Rhinoplasty · Patient–physician communication

Purpose

Since the introduction of Evidence based medicine (EBM) in medical decision making, surgeons have tried to standardize procedures, minimize variability from one subject to another and maximize predictability of the outcomes [1]. Standardization of surgery has led to discard or support surgery techniques based on statistical data, so traditionally the best approach to treat a patient has been the one proven better to the majority of them. [2]

As an alternative to the standardization of surgery, surgeon's mindset is shifting from "disease centered medicine" to "patient centered medicine". [3/4/5] The "patient centered" approach in surgery complements EBM with comprehensive Patient specific models (PSM) that manage inter individual variability. [4]

The aim of this article is to introduce the PSM as an instrument of communication with the patient that allows, thanks to technology to build personalized intraoperative instruments that aids the surgeon to deal with patient variability.

The introduction of our workflow in plastic surgery, for conducting the dorsal hump reduction in rhinoplasty using a 3d printing guide, gives to personalized medicine a real application that adjust to results, brings security and predictability, maximize velocity and minimize technical risks, especially in novel hands; moreover, it allows us to transfer the preoperative planning conducted on the Patient specific model (PSM).

Reduction of convexity of nasal profile is the most common request of rhinoplasty patients, also it is one of the most sophisticated, dangerous, and difficult to learn techniques in plastic surgery field. [5] Its technical complexity is justified because the high risk of lateral and vertical deviation while conducting a resection that starts in cartilaginous tissue from the nasal septum and finalize in osseous tissue from the nasal bones and sometimes including the ethmoidal perpendicular plate. The point with the highest risk of deviation is the rhinion (osseocartilaginous junction).

Methods

We have used the surgical guide for the removal of the nasal dorsum in 10 patients, whom we have worked with in the virtual preoperative planning of the surgery conducted on the PSM using 3d CT images, nasal anthropometries and resection objectives.

To achieve the obtainment of a personalized tool, we have designed a general sixth step workflow. First, for guide designing, it is necessary to work on a digital patient model (DPM) that gives us an accurate template of the patient anatomy; therefore, we have built our 3D DPM from preoperative CT images. In second place, we conduct a surgical preoperative planning of the rhinoplasty using a radiological viewer (Fig. 1), this is a key step, because we have to incorporate to our design: patient desires, technical possibilities, surgeon experience and the risk–benefit balance of being too aggressive or too conservative. Next step consists in designing the guide taking into account: structural strength, nasal anthropometric measures and hump resection objectives; then, using CAD software, we adapt the guide attachment part to the nasal bone surface of our patient.

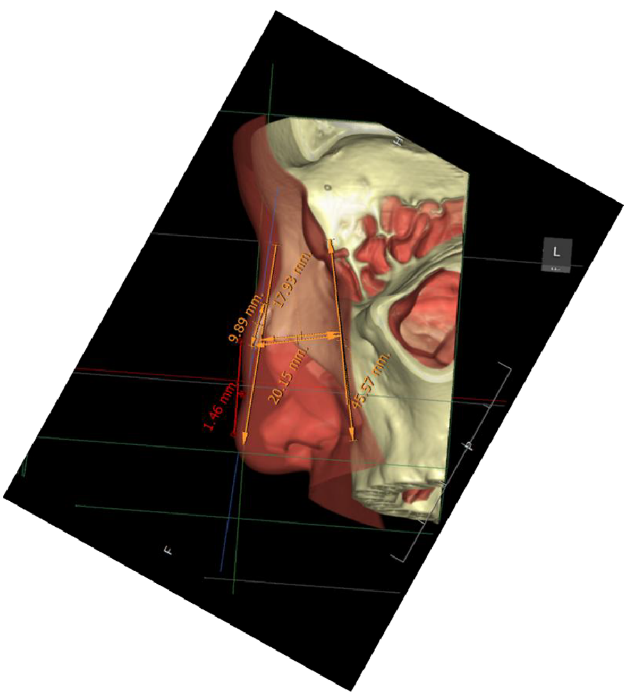

Fig. 1 Surgical planning of dorsal hump reduction

In fourth place, we print the guide using 3D rapid prototyping and we proceed to its sterilization using cold plasma for being able to introduce it in the surgical field.

Lastly, we perform the surgery, using the surgical guide under direct vision of an endoscope to ensure proper colocation and good behavior during use (Fig. 2).

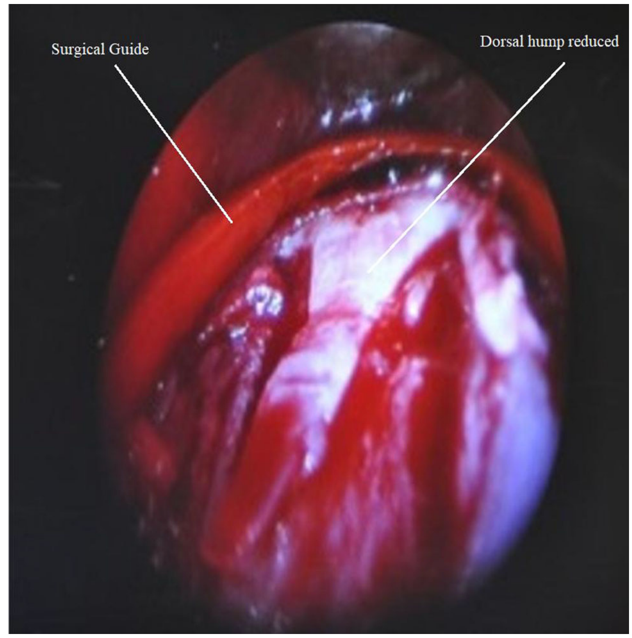

Fig. 2 Osteotomy result with guide attached

Results

Communication with the patient and joint planning have been the most important aspects to highlight in our work. Thanks to that, the patient understanding of the procedure was significant better after showing the 3D model of the surgery.

For all patients have been very instructive to understand their own anatomy, the process to be performed and to be able to share the lasts decisions with the surgeon. For our part, making the exact planning with the patient, has facilitated communication and has helped us to guarantee the autonomy bioethical principle (see Table 1).

Table 1 Patient survey

	Totally disagree	Disagree	NC	Agree	Totally agree
Has the vision of your 3D anatomy been useful?					
Has it given you greater security to be able to discuss with the surgeon the amount of dorsum to be removed from the PSM?					
What is your opinion of the work session?					
Has it given greater security to know that the surgeon used a guide that would guarantee the amount of dorsum to be removed?					
Has it given you greater certainty to know that this guide will prevent the surgeon from deviating from the calculation made?					

Table 1 continued

	Totally disagree	Disagree	NC	Agree	Totally agree
Are you happy with the result?					

The surgical guide, allows to transfer with extreme simplicity this planning to the surgical field, allowing us to remove the amount of dorsum that we decided to remove during the preoperative planning in a quick way and, more important, performing only one step osteotomy instead of the usual multistep.

The use of the guide was technically easier, than the conventional method and reduces the learning curve from years to minutes (once the guide is printed, because exhaustive formation is still needed to plan the surgery).

Conclusion

Technology is bringing us a drastic change in our surgical procedures and planning. It allows us to transform highly standardized technical procedures, in personalized ones, not only technically, but in very specific objectives shared and decided together with the patient.

This increasing trend in personalization of medical and surgical demands, show the importance of walking in that direction.

Greater understanding on the part of the patient, greater understanding of the patient's request by the surgeon, enhanced safety and surgical speed and finally optimization of the results, are aspects that make that the application of 3d printing guide in extirpation of the nasal dorsum is becoming essential for said procedures.

Moreover, we want to highlight again that the surgical guide, allows to transfer with extreme simplicity the pre-surgical planning to the surgical field.

References

[1] Chung KC, Swanson JA, Schmitz D, Sullivan D, Rohrich RJ (2009) Introducing Evidence-based Medicine to Plastic and Reconstructive Surgery. Plast Reconstr Surg. Apr; 123(4): 1385–1389

[2] Armstrong T, Yu D, Frischknecht A, Minter R, Andreatta P, Kasten S (2012) Standardization of surgical procedures for identifying best practices and training. Work. 2012; 41 Suppl 1: 4673–4679.

[3] Moscatiello F, Herrero Jover J, González Ballester MA, Carreño Hernández E, Piombino P, Califano L (2010) Preoperative digital three-dimensional planning for rhinoplasty. Aesthetic Plast Surg. Apr; 34(2): 232–238

[4] Berliner L, Lemke HU (eds.), An Information Technology Framework for Predictive, Preventive and Personalised Medicine, Advances in Predictive, Preventive and Personalised Medicine 8. Springer International Publishing Switzerland 2015.

[5] Hontanilla B, Cabello A, Olivas J (2016) A Predictable Approach for Osteotomy in Rhinoplasty: A New Concept of Open External Osteotomy. Plast Reconstr Surg Glob Open. Jun; 4(6): e764

Heuristic based optimal path planning for neurosurgical tumor ablation

R. Monfaredi[1], H. Fooladi Talari[2], C. Oluigbo[2], K. Cleary[2]
[1]Children's National Health System, Sheikh Zayed Institute, Washington DC, United States
[2]Children's National Health System, Sheikh Zayed Institute, Washington DC, United States

Keywords Neurosurgery · Tumor ablation · Optimal · Path planning

Purpose

In the current workflow for brain tumor ablation, path planning imaging and tumour ablation are done in two subsequent sessions. First the surgeon uses preoperative CT or MR images to do path planning, and then the patient is scheduled for the surgery. Manual planning for brain tumour ablation, based on preoperative CT and MR images, is a time-intensive task. In addition, the preoperative images often do not match the intraoperative images due to brain shift after opening the skull. This shift results in a targeting error. Therefore, path planning adjustment by surgeons often is required during the surgical procedure, this leads to increased anaesthesia and operation time and eventually results in sub-optimal use of hospital resources and surgeon's valuable time. More importantly, it should be noted that increased anaesthesia time is not favourable especially for pediatric and geriatric population [1]. Specifically for MRI-guided tumor ablation, increased time substantially increases the procedure cost, since MRI is a very expensive modality compared with other modalities [2]. In this paper we introduced a new heuristic based search algorithm to find an optimal ablation path to avoid critical structures, while maximizing safe ablation region for a single ablation path.

Methods

Neurosurgeons use 2D or 3D preoperative images to find a straight path to tomur, while avoiding critical structures. For example, Fig. 1 shows a schematic of a biopsy needle that is introduced into the skull and reached the tumor without hitting blood vessels. The target point for biopsy is selected by a surgeon and it could be any point within the canorous lesion. Ablation planning is more complicated, since the ablation tool is a straight tool and it should be introduced in an optimal direction to maximize the ablation zone along its axis. Therefore, manual optimization of the ablation path is difficult if not possible. Figure 1 shows a hypothetical optimal path for ablation which is along the longitudinal axis of the cancerous lesion. In this paper we introduced a heuristic function to optimize the path planning process. Figure 2 shows the planning concept for this problem. As a simplified model, the skull is considered as a spheroid with principle axes: a, b, and c defined as follows:

$$x^2/a^2 + y^2/b^2 + z^2/c^2 = 1,\ a \neq b,\ \text{and}\ b = c \tag{1}$$

We define sate space as (α, β, θ, φ) where α, and β are the rotations of needle about fulcrum point located at entry point and θ, and φ are defined to address a point on the spheroid as follows:

$$x = a\cos(\theta)\cos(\varphi) \tag{2}$$

$$y = b\cos(\theta)\sin(\varphi) \tag{3}$$

$$z = b\sin(\theta) \tag{4}$$

The surgeon selects the start point P_0 = (θ_0, φ_0) on the skin and N points, $\{T_1,\ldots, T_N\}$, along the tumor and M points, $\{O_1,\ldots, O_M\}$, on the obstacle boundary. Search space is defined as $\theta \in [\theta_0-\pi/2, \theta_0 + \pi/2]$, $\varphi \in [\varphi_0-\pi/2, \varphi_0 + \pi/2]$, $\alpha \in [\alpha_0-\pi/2, \alpha_0 + \pi/2]$, $\beta \in [\beta_0-\pi/2, \beta_0 + \pi/2]$, where α_0 and β_0 are Euler angles of the normal vector, $N_{i,j}$, for each state point on the spheroid surface. Vector $N_{i,j}$ is shown in Fig. 2.

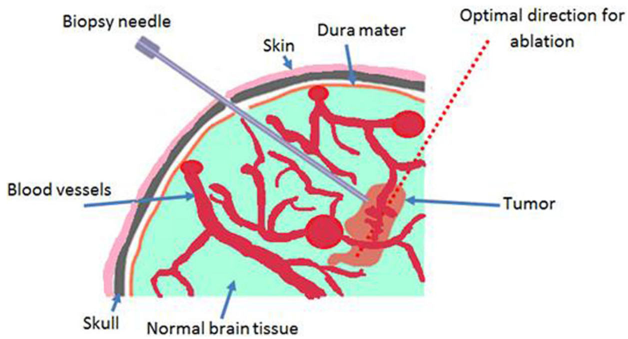

Fig. 1 A schematic of brain critical structures and a possible biopsy path and optimal ablation path

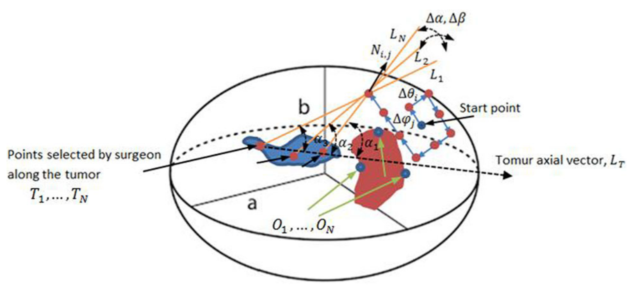

Fig. 2 Diagram of proposed search algorithm concept search along the skull surface with $\Delta\theta$, and $\Delta\varphi$ steps while minimizing the angle between L_T, and $\{L_1, \ldots, L_N\}$

We suggested a cost function, F, and a heuristic function, H, to find the optimal path.

Cost function is defined as:

$$F(\alpha, \beta, \theta, \varphi) = \min\{(A_1 + \cdots + A_N)/N\} \quad (5)$$

where A1, to AN is the angle between each line L_i and L_T.

The goal is cost function is to minimize the cost function so the average angle between $L_1,\ldots, L_N$, and tomur axial vector, L_T is minimized.

Heuristic function is defined as the average Euclidian distance between the entry point and points on the obstacle, i.e. $\{O_1,\ldots, O_M\}$. The goal is to maximize the heuristic function so the distance between the entry point and the obstacle is maximized.

Results

Step size of search algorithm is considered equal to $\pi/180$ in all directions. Breadth First search algorithm requires $(\pi/2 \times 180/\pi)$ ^4 = 65,610,000 iterations to find the optimal path. For each iteration, the depth of needle should be also swept to find the intersection of the extended needle and the cancerous lesion. Considering the maximum needle depth at 10 cm and the resolution at 1 mm, the total number of iteration is in the order of 6.5×10^9. Therefore, for the Breadth First search algorithm the computational time is very high and is not practical for intraoperative path planning. Our suggested heuristic algorithm minimizes the state space domain and decreases the computational cost substantially. By avoiding the search of unnecessary states estimated at 50% of search space, the search algorithm could be 16 time faster. A novel heuristic function is proposed for a weighted A* search algorithm and the results of Breadth First search algorithm and weighted A* is compared.

Conclusion

This method could be used during the intraoperative MRI or CT-guided brain tomur ablation procedure to minimize the planning time and to maximize the ablation zone in single path ablation.

References

[1] Comber D, Pitt EB, Gilbert HB, Powelson MW, Matijevich E, Neimat JS, Webster RJ, Barth EJ, 820179 Optimization of Curvilinear Needle Trajectories for Transforamenal Hippocampotomy. *Journal of Operative Neurosurger,* vol. 13, No. 1

[2] Brunenberg E, Vilanova A, Vandewalle V, Temel Y, Ackermans L, Platel B (2007) Automatic Trajectory Planning for Deep Brain Stimulation: A Feasibility Study. *International Conference on Medical Image Computing and Computer-Assisted Intervention* (MICCAI), pp 584–592

Port placement planning method for assistant surgeon in laparoscopic gastrectomy

Y. Hayashi[1], K. Misawa[2], K. Mori[1]
[1]Nagoya University, Graduate School of Informatics, Nagoya, Japan
[2]Aichi Cancer Center Hospital, Department of Gastroenterological Surgery, Nagoya, Japan

Keywords Port placement · Surgical navigation · Laparoscopic surgery · Stomach

Purpose

This paper presents a method for determining an appropriate port placement for an assistant surgeon in laparoscopic gastrectomy. In laparoscopic surgery, ports are placed on abdominal wall in order to insert surgical tools into the abdominal cavity. Since the configuration of the port location is closely related to ease of laparoscopic surgical procedure, the port placement is important for laparoscopic surgery [1]. In laparoscopic gastrectomy for gastric cancer, surgeons utilize five ports as shown in Fig. 1 [2]. A main surgeon (operator) uses two ports and an assistant surgeon uses two ports to insert surgical tools. A remaining one port, which usually places on umbilicus, is used for inserting a laparoscope. Currently, surgeons plan the port placement based on their knowledges and experiences. Therefore an assistance system for determining the port placement is useful especially for a novice surgeon. A method for computing an appropriate port placement for laparoscopic gastrectomy has been proposed [3]. This method determined the appropriate port placement for only a main surgeon. To assist the port placement planning for all ports, a port placement planning method for an assistant surgeon is desirable. This paper presents a method for determining an appropriate port placement for an assistant surgeon. This is the first trial of the appropriate port placement determination for an assistant surgeon in laparoscopic gastrectomy.

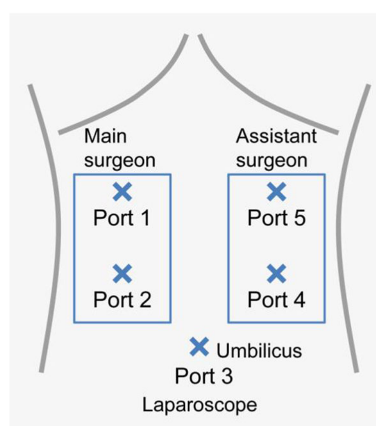

Fig. 1 Typical port placement for laparoscopic gastrectomy

Methods

The proposed method determines an appropriate port placement for an assistant surgeon performing laparoscopic gastrectomy. A main surgeon (operator) utilizes the two ports placed on the right side of a patient (Ports 1 and 2 in Fig. 1). On the other hand, an assistant surgeon utilizes the two ports placed on the left side of a patient (Ports 4 and 5 in Fig. 1). One way of determining the appropriate port placement for an assistant surgeon is that the appropriate port placement for an assistant surgeon and for a main surgeon will be arranged symmetrically about a sagittal plane through umbilicus. The proposed method determines an appropriate port placement for assistant surgeon based on an appropriate port placement for a main surgeon. Before computing the appropriate port placement for an assistant surgeon, we compute the appropriate port placement for a main surgeon using the previous method [3]. This method computes the appropriate port placement using the angle conditions including the angle between the forceps and the laparoscope, the angle between the forceps and the horizontal plane, and the angle between the right and left hand side forceps. This method represents the appropriate port placement by two lines passing through the appropriate positions of Port 1 and Port 2. To obtain the appropriate port placement for an assistant surgeon, we compute the symmetrical arrangement of the appropriate port placement for a main surgeon. Since these lines representing the appropriate port placement are defined in the CT image coordinate system, the x-axis, y-axis, and z-axis represent the patient's the right-to-left, the anterior-to-posterior, and the head-to-foot directions, respectively. Therefore, we transform these two lines to be symmetrical about the plane that is parallel to the yz-plane and through the umbilicus. The line prior to the transformation is defined using a point through the line $\boldsymbol{a}$ and a direction vector of the line d. The point $\boldsymbol{a}'$ and the direction vector $\boldsymbol{d}'$ of the line after the transformation is computed by $\boldsymbol{a}' = \mathbf{T}(\boldsymbol{a} - \boldsymbol{u}) + \boldsymbol{u}$ and $\boldsymbol{d}' = \mathbf{T}d$, where $\mathbf{T}$ is the reflection matrix about the yz-plane and $\boldsymbol{u}$ is the position of the umbilicus, respectively. The transformed lines indicate the appropriate port placement for an assistant surgeon (Port 4 and Port 5).

Results

We evaluated the proposed method using the positional information of the ports and the anatomical structures acquired during laparoscopic gastrectomy in 26 cases. We computed distances between the appropriate port placement obtained by the proposed method and the port locations determined by the experienced surgeons using leave-one-out manner. The averages and standard deviations of the distances were 23.4 $\pm$ 12.1 mm in the left hand side port (Port 4) and 41.3 $\pm$ 12.5 mm in the right hand side port (Port 5), respectively. An example of the appropriate port placement for an assistant surgeon obtained by the proposed method and the port locations determined by the experienced surgeons are shown in Fig. 2. The green and the yellow lines show the appropriate port placement of the left hand side port (Port 4) and the right hand side port (Port 5) computed by the proposed method, respectively. The green and the yellow spheres show the left and the right hand side port determined by the experienced surgeons, respectively.

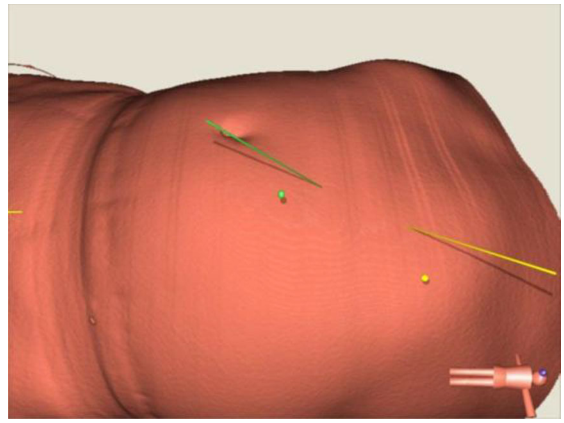

Fig. 2 Example of appropriate port placement obtained by proposed method and port locations determined by experienced surgeons. Green and yellow lines show appropriate port placement of left and right hand side port computed by proposed method, respectively. Green and yellow spheres show left and right hand side port determined by experienced surgeons, respectively

Conclusion

This paper presented a method for generating port placement planning for an assistant surgeon in laparoscopic gastrectomy. This is the first report on the automated determination of the port locations for an assistant surgeon. The proposed method can compute the port placement with an average error of 32.4 mm. In particular, the proposed method demonstrated the error of the left hand side port is about 20 mm, this result is promising with considering there is no method for assisting the port configuration for an assistant surgeon. On the other hand, the error of the right hand side port is larger than 40 mm. We need to reconsider other conditions for determining the appropriate port placement in order to reduce the error of the right hand side port.

References

[1] Hanna GB, Shimi S, Cuschieri A (1997) Influence of direction of view, target-to-endoscope distance and manipulation angle on endoscopic knot tying. Br J Surg 84: 1460–1464

[2] Fujiwara M, Kodera Y, Misawa K, Kinoshita M, Kinoshita T, Miura S, Ohashi N, Nakayama G, Koike M, Nakao A (2008) Longterm outcomes of early-stage gastric carcinoma patients treated with laparoscopy-assisted surgery. J Am Coll Surg 206: 138–143

[3] Hayashi Y, Misawa K, Mori K (2017) Optimal port placement planning method for laparoscopic gastrectomy, Int J CARS 12: 1677–1684

A traction and retraction device with magnet and hook for laparoscopic surgery

Y. H. Jeon[1], K. Y. Lee[2], S. J. Park[2], C. J. Kim[1], S. W. Cho[3], S. C. Yun[3], M. G. Lee[1]
[1]Ajou University, Mechanical Engineering, Suwon-si, South Korea
[2]Kyung Hee University, Surgery, Seoul, South Korea
[3]Soonchunhyang University Seoul Hospital, Surgery, Seoul, South Korea

Keywords Laparoscopic surgery · Magnetic device · Attractee · Cholecystectomy

Purpose

Traction and retraction are important to increase visibility in a dissecting plane during minimally invasive surgery (MIS), such as laparoscopic surgery and natural orifice transluminal endoscopic surgery (NOTES) [1, 2]. However, the procedure is too complicated to be operated by a surgeon unaided; therefore, he or she needs additional aid from an assistant. Some devices have been devised to carry out the procedure without additional aid. However, they still have problems. The devices have insufficient force to pull an organ. They are difficult to be applied to the procedure. Some of them are even harmful to humans.

Methods

In this study, a remote magnetic traction and retraction device consisting of an extra-abdominal handheld magnetic manipulator and an intra-abdominal attractee of a bullet and a flexible wire is proposed to be applied to cholecystectomy. The device is designed to have a sufficient pulling force through magneto-static finite-element (FE) simulations (Fig. 1). The attractee is made of biocompatible materials. The surgeon was able to achieve sufficient exposure in Calot's triangle by dragging the internal attractee using the external manipulator. The cystic duct and artery were ligated using endoscopic clips, two proximal and one distal. Using an IT knife, the cystic duct and artery were transected, and then the GB was dissected from the liver bed.

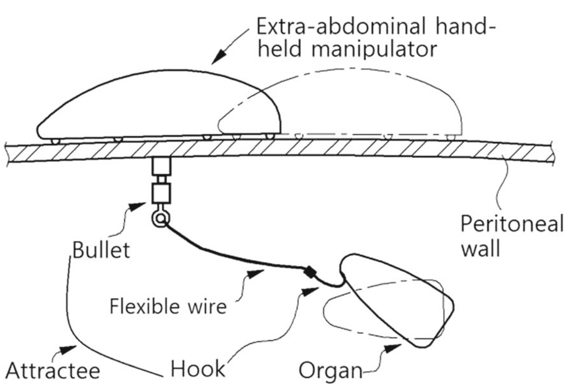

Fig. 1 A new magnetic retraction device

Results

The magnetic manipulator with four magnets and the attractee with a 15-mm-long bullet were implemented to have traction and retraction forces of 0.194 N for attaching the bullet and 0.834 N for holding the bullet and an organ. The targeting peritoneal wall thickness varies within 5–25 mm, which corresponds to a body mass index (BMI) range of 10–30. The towing force and ease of use are experimentally investigated in a non-survival porcine model's laparoscopic cholecystectomy (Fig. 2). The manipulator provides easy and secured traction and retraction because of its large force and handy design; therefore, it can eliminate the need for an assistant.

Fig. 2 GB after cholecystectomy with the device

Conclusion

The proposed device has the potential to be applied to minimally invasive surgery, to improve health recovery for patients, and to save medical costs. However, some improvements are still required so that the hooking procedure can be achieved by the endoscopic tool alone. The operation time have not been accurately evaluated and compared yet. If a single surgeon carries out the operation without assist, the time may be somewhat prolonged because of the traction and retraction only by himself or herself. However, the duration of surgery is comparable to the conventional laparoscopic surgery for the swain model. One of the important goals is to eliminate the aid, therefore, this is acceptable. Several surgeons gave us the opinion that the GB or liver can be punctured or torn. We have performed a series of animal tests, but there is no puncture or tear of organ by the hook. For GB, its outer wall is slippery and flexible but not be torn easily. The hook is very so small that it just hooked shallowly. For liver, the surgeon had to be careful when handling the hook because it is easy to be torn or punctured. Sometimes, there was mislay of the bullet in abdomen, therefore, it could be found and positioned by using the laparoscope and grasper. These problems will be addressed in the next study.

References

[1] Abe N, Takeuchi H, Ueki H, Yanagida O, Masaki T, Mori T, Sugiyama M, Atomi Y (2009) Single-port endoscopic cholecystectomy: a bridge between laparoscopic and translumenal endoscopic surgery. *Hepato-Biliary-Pancreatic Surgery,* 16(5): 633–638

[2] Scott DJ, Tang SJ, Fernandez R, Bergs R, Goova MT, Zeltser I, Kehdy FJ, Cadeddu JA. (2007) Completely transvaginal NOTES cholecystectomy using magnetically anchored instruments. *Surgical Endoscopy,* Dec, 21(12): 2308–2316

A magnetic navigation system development for minimum invasive surgery

Y. S. Li [1], T. Y. Wan[1], C. H. Cheng[2], D. G. Liu[2]
[1]The Hong-Kong Polytechnic University, Hong-Kong, China
[2]Feng Chia University, Taichung, Taiwan

Keywords Magnetic navigation · Magnet positioning · Trilateration calibration · Positioning visualization

Purpose

The objective of the project is to build a magnetic navigation system that can be applied to medical surgery. Currently, there is lack of such safe visualization technique applied. Therefore, doctors cannot easily know the exact position of the instruments when operating in-body surgery for inexperienced surgeons. We would like to build a magnetic positioning system, it is an easy-use, reliable system that can help the doctors to visualize in-body operation.

Methods

With the system, the surgical instruments can be displayed when combined with a magnet. Also, to make to the system more convenient and portable, we have built a wireless system; the data can be transmitted and received using Wi-Fi technology. In order to display the image in real time, we have also developed an application with user-friendly GUI. Lastly, we have applied trilateration technology to enhance the accuracy of the magnet navigation.

As we need to trace the magnet in order to achieve real-time magnetic navigation, it is important to consistently track the magnet position. We have developed an algorithm for that part by applying the 3D positioning formula which shows the relationship of magnetic field and distance. We have integrated the algorithm into the program so it can calculate the relative coordinates with respect to the sensors. When the magnet is attached to the surgical instrument, it is possible to locate the surgical instrument inside the patients' body.

For convenient, only one small magnet is applied to the surgical scalpels. It is depending on the sensing strength, there are one to five magnetometers are reading simultaneously; from these, it can track the position of a magnet. To apply this magnetic navigation technology in surgical use, more precise data is needed. Hence, we tried to apply trilateration in the calculation. This technology is mainly used by the GPS system when the detection object is within the range of three sensors, it is possible to locate it by finding the intersection point of the three circles. The system is developed by using Python; a Visualization Toolkit (VTK) is used to 3D display the surgical tool position.

The WiFi network mesh of the magnetic sensors is built for the accurate positioning requirement. The ESP8266 magnet sensors are adapted for wireless communication. The device contains a low power 32-bit MCU, 10-bit ADC and several SPI, UART, I^2C, I^2S, PWM, GPIO peripheral interfaces. The 802.11 b/g/n WIFI supported. The characteristics of this mesh network are easily adaptable and expandable by the quantities varying of the magnetic sensors. The synchronous clock source for accurate calculates the distance information.

The data packet delay 125 ms between ESP8266 receives each TCP package. This problem is solved by assign one of the sensor as an access-point (AP) mode and use PC as sever to receive the data.

The operation environment needs to prevent the other magnetic fields around the sensor, e.g., magnets, power supply wires. The calibration process needs to consider these factors as offset errors during the measurement process.

The magnet positioning follows the magnetic field strength formula and the calibration is needed from multiple magnetometers. The magnetometer need consider the influences due to hard-iron and soft-iron distortions.

The following calibrating requirements are needed to take into consideration. The MagMaster and MagViewer tools are used for scaling offset errors the ferromagnetic materials around the sensor, such as skew the density of the Earth's magnetic field locally.

The Trilateration process is very important for the proposed system. The Non-Linear Least-Squares minimization and the Levenberg–Marquardt algorithm are utilized to solve the accurate positioning problem. Because of the sensing errors are occurred fromdifferent sensors. The following method is used to regulated and limited positioning within minimum error. The program is stopped when the function executed.

The accurate positioning need to be solved with the LMFIT library in Python is utilized to fit data. Then, the differences between guessed position and real position can be reduced progressively.

Results

Throughout the research, the system development can be divided into four portions.

1. Model Visualization
2. Wireless Communication
3. Magnet Positioning
4. Trilateration calibration

In the real experiments, the detection would be affected by some internal and external electrical noise, e.g., strong electrical field. So, the result would not fit quite exactly on a calibration point. In fact, the calibration process will intersect in a range and tempt to intersect within a minimum error range. To deal with this problem, we set up a regression analysis, fitting the data with least square equation will minimize the data error. An estimated position can be calculated after certain minimizations. However, the maximum error is around 2–3 cm, which is about 8–10% of the detection range. The Model Visualization includes Surface Rendering (Method 1) and Volume Rendering (Method 2) from Ray casting can be well demonstrated.

Conclusion

The proposed project is trying to promote the use of sensing electronics in surgical applications. It helps reduce the risk of hurting patients' organs and improve the success of the surgical operation. A magnetic surgical guiding system is developed to include some tools of OpenCV, Arduino and Unity 3D in this proposed project. The system works fine and the surgeons appreciate our work. One of the current works is to combine the proposed system with a wireless panoramic endoscope [1, 2] for minimum invasive surgery.

References

[1] Zeng J-L, Cheng Y-H, Wu T-Y, Liu D-G, Cheng C-H (2017) "MicroEYE: A Wireless Multiple-Lenses Panoramic Endoscopic System," Recent Advances in Electrical Engineering and Related Sciences: Theory and Application

[2] Shimada J, Itoh K, Yamaguchi S, Nishikawa A, Miyazaki F (2005) Magnetic navigation system for thoracoscopic surgery of the pig lung partial resection with transbronchial marking, CARS 2005: Computer Assisted Radiology and Surgery 1281: 752–755

Locally operated unilateral master–slave control system with portable device and forceps manipulator for laparoscopic surgery

S. Fukui[1], H. Kobayashi[1], T. Kawai[1], Y. Nishizawa[2], A. Nishikawa[3], N. Iwamoto[3], Y. Horise[4], K. Masamune[4]

[1]Osaka Institute of Technology, Graduate School of Robotics and Design, Osaka, Japan

[2]National Cancer Center Hospital East, Department of Colorectal Surgery, Kashiwa, Japan

[3]Shinshu University, Faculty of Textile Science and Technology, Ueda, Japan

[4]Tokyo Women's Medical University, Institute of Advanced Biomedical Engineering and Science, Tokyo, Japan

Keywords Surgical robot · Master–slave control · Locally operated · Third arm

Purpose

By integrating locally operated small surgical robots in a sterilized area, a surgeon can perform safe and accurate robotically assisted laparoscopic surgery using multiple-degree-of-freedom (multiple-DOF) manually controlled forceps, with an intelligent armrest, while controlling an endoscope-holding robot for view stabilization and a forceps robot for grasping and pulling organs.

It is important that manipulation of surgical robots be intuitive. Although endoscope-holding robots, such as the voice-controlled ViKY, the button-controlled SOLOASSIST, and the head-sensor-controlled FreeHand, can provide a simple interface and on/off control system, the master–slave-controlled P-arm has an intuitive interface and control system. We previously developed a mobile locally operated detachable end-effector manipulator (LODEM) as a forceps robot, which is operated via a forceps-mounted button or a pressure sensor sheet placed on the floor. At present, there is no locally operated master–slave-controlled forceps robot that can provide intuitive manipulation.

A new locally operated master–slave control system with portable device and a forceps manipulator for laparoscopic surgery was developed. We previously reported a mechanically separable master device with five DOFs, and a principle master–slave control system between an encoder and a motor. The present study describes the newly proposed sensor-embedded master device, the revised parallel-linkage mobile LODEM, and the unilateral master–slave control system based on the kinematics between the sensor-embedded or separated master device and the revised parallel-linkage mobile LODEM. In addition, we report the performance of the proposed control system using two master devices evaluated while performing simulated laparoscopic surgery.

Methods

A mechanically separable master device (type-1) consisting of a portable mechanical part that can be autoclave sterilized and an encoder sensor connected to driving wires covered with a coiled steel tube are shown in Fig. 1. The dimensions of the mechanical component are 130 mm × 130 mm × 350 mm, and its mass is 1.0 kg. The dimensions of the encoder sensor component are 160 mm × 90 mm × 200 mm, and its mass is 1.4 kg. A sensor-embedded master device (type-2) that can be draped with a sterilized cover is shown in Fig. 1. The dimensions of the master device are 130 mm × 130 mm × 330 mm, and its mass is 0.9 kg. Both five-DOF master devices use a magnetic ball joint and gimbals for the pitch and yaw axes, a linear guide for the insertion axis, a circular dial for the roll axis, and a handle for the grasp axis. The operating ranges for these axes are ± 70°, ± 70°, 100 mm, ± 180°, and 40°, respectively. The maximum mechanical backlash of the type-1 master device is 4.9° for the pitch and yaw axes and 4.7 mm for the insertion axis, due to the wire connection between the portable mechanical component and the encoder sensor component.

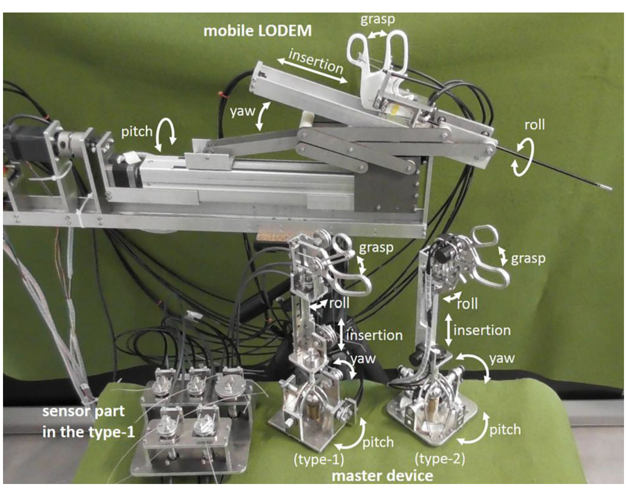

Fig. 1 Prototype of the locally operated master–slave control system

The modified mobile LODEM is shown in Fig. 1. The mobile LODEM, which has five DOFs, consists of a harmonic gear for the pitch axis, a ball screw slider with a parallel linkage crank for the yaw axis, a wire-connected linear guide attached to the forceps for the insertion axis, and wire-driven roll and grasp axes. The dimensions of the mobile LODEM are 360 mm × 80 mm × 800 mm, and its mass is 5.8 kg. The operating ranges of these axes are ± 70°, ± 70°, 200 mm, ± 90°, and 40°, respectively.

The mobile LODEM, which is used as the slave manipulator, is a unilateral master–slave controlled by a master device. The x–y–z position of the handle of the master device and the forceps handle of the slave manipulator are calculated using a homogeneous transformation matrix. Point-to-point (PTP) commands to control the individual axes of the mobile LODEM driven by stepper motors are input by the appropriate axes of the master device rotating encoder, and these commands are processed by a motion control board installed in a PC, which outputs the appropriate signals to the manipulator.

In order to evaluate the new unilateral master–slave control system, two master device prototypes were used in the following experiment. Simulated laparoscopic cholecystectomy was performed on a surgically realistic gall bladder model in a training box by an endoscope specialist. The manipulator, which was attached to the forceps, was positioned at the right-hand side of the surgical table. The endoscope was fixed to the table, and the operator stood at the foot of the table. The operator used scissors in his right hand and forceps in his left hand. The manipulator was controlled by a master device prototype positioned to the right of the operator.

Results

Figure 2 shows a photograph of the simulated laparoscopic cholecystectomy. The forceps manipulator was driven by the motors under the surgeon's master–slave control using the master device. The organ model could be pulled in various directions using the forceps attached to the manipulator. The forceps (held in the left hand) could also be used to grasp and pull the organ model with sufficient tension, while the scissors (held in the right hand) could be used to dissect the organ model. Smooth dissection of the organ model was performed by the endoscope specialist. The unilateral PTP master–slave control between the master device and the mobile LODEM was confirmed for the pitch, yaw, insertion, and roll axes.

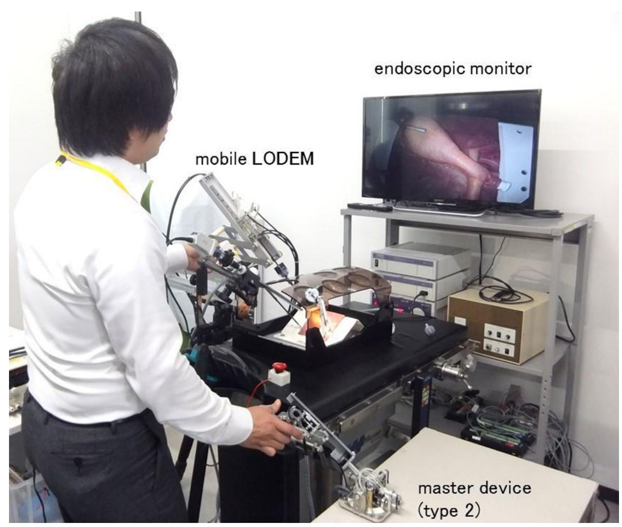

Fig. 2 Simulated laparoscopic cholecystectomy by an endoscope specialist using the sensor-embedded master device (type-2) and the mobile LODEM under master–slave control

Although time delay occurred when using the type-1 master device because of the mechanical backlash, the experimental results indicate that the influence of the air gaps between the wire and the coiled steel tube is not large for the mechanism of the master device used as the assistant. For the purpose of integrating master devices and slave manipulators, this system can provide multiple connection using a middleware ORiN.

Conclusion

We developed a locally operated master–slave control system with portable device and a forceps manipulator for laparoscopic surgery. The unilateral master–slave control system based on the kinematics between the sensor-embedded or separated master device and the revised parallel-linkage mobile LODEM is constructed to facilitate minimally invasive, robotically assisted laparoscopic surgery by a doctor working near the patient. The results of the present study indicate that the proposed system could be used for such applications.

The preset study was supported in part by JSPS Kakenhi (JP15K05917, JP16H01859).

Development of traceability system for surgical instruments in operation room

K. Kusuda[1], K. Yamashita[2], K. Masamune[1], Y. Muragaki[1]
[1]Tokyo Women's Medical University, Faculty of Advanced Techno-Surgery, Tokyo, Japan
[2]Osaka University, Graduate School of Medicine,, Osaka, Japan

Keywords RFID · Surgical instruments · Individual management · Operation room

Purpose

Incidents that surgical items are retained in a patient's body occur once in every 10,000 operations, and 30 percent of the items is surgical instruments [1, 2]. The issues are cumbersome surgical count defect of surgical instruments. Because all surgical count is conducted manually, miscount is happened after surgery. Additionally, because surgical instruments never have been managed individually, factors of the defects do not clear.

To prevent these issues, individual management of surgical instruments is required. In this study, surgical instruments with radio-frequency identification (RFID) tags and system for use in operation room (OR) were developed. With the use of such surgical instruments can be identified automatically. The purpose of this study is to acquire information of surgical instruments during surgery.

Methods

In this study, clinical trials were conducted to evaluate an accuracy of the system. Our system was put on Mayo table that is instrument table in OR. If RFID surgical instruments were put on the table (shown in Fig. 1), our system could automatically detect these tags and get this information.

Fig. 1 Antenna and surgical instrument with RFID tags on mayo table: An RFID tag is attached to a surgical instrument. This is the situation where the RFID tag is perpendicular to the plane of the antenna

In this study, number of these instruments that were used during surgery were counted. Additionally, these were counted visually using video camera at the same time and compare with it. Number of surgery was 10 cases, and the procedure were mastectomy including sentinel lymph node biopsy and lymphadenectomy. Sixty-one surgical instruments that were attached RFID tags were prepared.

Results

As a result, the system accuracy was around 96% and average surgical time was 95.3 ± 43.4 min. The situations that could not get information of instruments were that RFID tags were put on outside of the antenna. Because the accuracy was case of each scanning, the accuracy was decrease. However, because scrub nurse kept to touch instruments during surgery, the system could detect it finally.

Additionally, because RFID tags communicate with an antenna using radio-frequency, the system could get information when tags were covered with blood.

Tendency of surgical instrument that were used during surgery was detected automatically. For example, surgical knife was put on table at the first of surgery, retractor was put on it frequently at the middle of it, and Adoson forceps was prepared on table at the end of it.

Conclusion

Generally, as a function of RFID tag, it can send and receive information when tags and antenna is parallel. Passage of the magnetic flux is difficult when an antenna of reader/writer is perpendicular to the plane of RFID tag, the system cannot detect it. If scrub nurses put instruments on table unconsciously, RFID tags are perpendicular to the plane of the instrument table. So, the magnetic flux from the system cannot pass it. Therefore, to acquire data of surgical instruments in OR, a technical issue should be resolved.

Because the system that was developed in our previous study use multiple antenna, it can detect information of instruments when RFID and antenna were in parallel. In this study, the system could detect RFID tags during surgery, and the accuracy was enough if scrub nurses put it unconsciously.

References

[1] World Health Organization (2009) WHO Guidelines for Safe Surgery 2009.
[2] Gawande A, Studdert D, Orav E, Brennan T, Zinner M (2003) Risk factors for retained instruments and sponges after surgery, N Engl J Med 348(3): 229–235

In situ augmentation of force and torque perception using patient-based forces

G. Stetten[1], R. Klatzky[2], H. Y. Lee[3], S. Satpute[1], N. Loewen[4], N. Amesur[5]
[1]University of Pittsburgh, Bioengineering, Pittsburgh, United States
[2]Carnegie Mellon University, Psychology, Pittsburgh, United States
[3]Carnegie Mellon University, Electrical and Computer Engineering, Pittsburgh, United States
[4]University of Pittsburgh Medical Center, Ophthalmology, Pittsburgh, United States
[5]University of Pittsburgh Medical Center, Radiology, Pittsburgh, United States

Keywords Robotics · Microsurgery · Haptics · Augmentation

Purpose

Our goal is to increase the clinician's touch sensitivity and enable more precise control in situations where tactile or visual feedback is limited, thereby improving procedural outcomes. Microsurgery, or any other manipulation of fragile or flexible tissues, mandates extremely high technical skill, surgical acuity and precision. If tactile feedback could be amplified during such procedures, tissue trauma could be minimized, operator efficacy maximized, and techniques optimized.

We have created designs for a new device to address several such clinical applications, including Difficult Venous Access (DVA). Veins may be difficult to access for a variety of reasons, and we specifically address the tendency for some veins to roll, especially in pediatric patients, where it may prevent as many as 5% of patients from receiving placement of peripheral intravenous lines essential for treatment of dehydration, septic shock, or trauma [1].

Methods

We have previously developed a technology we call the *Hand-Held Force Magnifier* (HHFM) [2, 3]. This technology augments forces detected at the tip of a tool with forces exerted on the tool handle by an actuator connected to a brace on the back of the operator's hand. It does so *in situ*, meaning the operator interprets the augmenting forces as coming from the tip of the tool, superimposed on the original forces [4, 5].

Our innovation falls into the category of *Cooperative Robots*, meaning that, as opposed to telerobotic systems such as the da Vinci Surgical System, the robot directly affects the same tool as the clinician, in our case by exerting forces that augment those already present from contact with the patient.

Prior tactile augmentation systems had used a robotic arm that holds the surgical tool simultaneously with the surgeon, pushing and pulling as appropriate. Because every force needs an opposing force, the robotic arm was mounted on the floor or table-top. The HHFM freed the operator from such an external ground by using the back of the operator's hand as a reference instead.

We now adapt the HHFM approach to use passive forces generated relative to the patient rather than the operator's hand, in what we call the *Patient-Based Force Magnifier* (PBFM). This provides a number of significant improvements:

(1) The augmenting forces now exist outside the hand, so that the operator's upper arm and shoulder also experience actual force augmentation, rather than the illusion of such as in the HHFM.
(2) The platform resting on the patient can be significantly larger and heavier than a typical surgical tool, permitting generation of larger forces and providing a firmer base against which to generate them.
(3) Since forces are now generated nearer the distal end of the tool, leverage problems with non-axial forces and torques in the HHFM are alleviated.
(4) Since the augmenting force and torques need never be greater than those being applied by the surgeon, we may simply impede the intended motion so as to increase the force or torque required by the surgeon to move the tissue. This can be accomplished by a brake or variable-compliance linkage instead of an actuator, and in some cases, a single variable-compliance linkage may replace multiple independent actuators.
(5) Eliminating the brace frees the surgeon to shift his/her grasp on the tool and to switch tools more easily.

In addition, we have replaced the embedded force sensors used in the original HHFM to inform the force augmentation with real-time imaging (ultrasound and optical coherence imaging) to detect tissue motion or deformation. Along with the removal of the hand brace, this frees us to use standard surgical instruments, a significant advantage for introducing the technology into clinical practice.

Results

Figure 1 shows a PBFM device for rolling veins, which rests on the patient, through which the needle passes before reaching the skin. The legs contain variable-compliance actuators, allowing each leg independently to be stiff or to act essentially as a variable-compliance spring. The device also contains a gripper that can engage the needle, or let it pass freely. Initially the needle is allowed to pass freely by the gripper. The legs are both initially stiff. When the needle reaches the vein, the vein may move laterally (roll) rather than submit to puncture. We detect this lateral motion relative to the surrounding tissue by automated analysis of an ultrasound image, at which point the gripper engages the needle and one or the legs becomes compliant while the other remains stiff. Which leg becomes compliant depends on the direction of the roll. Figure 2 shows how having the left leg become compliant causes a shift of the needle (from solid to dashed lines) to track the vein to the right, with the entry point through the skin acting as a fulcrum. The effect of this will be for the operator to feel a tendency for the needle to move in the correct direction to follow the rolling vein, as if finding a soft spot in the vein that guides the needle tip along its path of least resistance. It will feel as if the needle had a rounded tip and were finding a hole whose edges were sloped to guide it in.

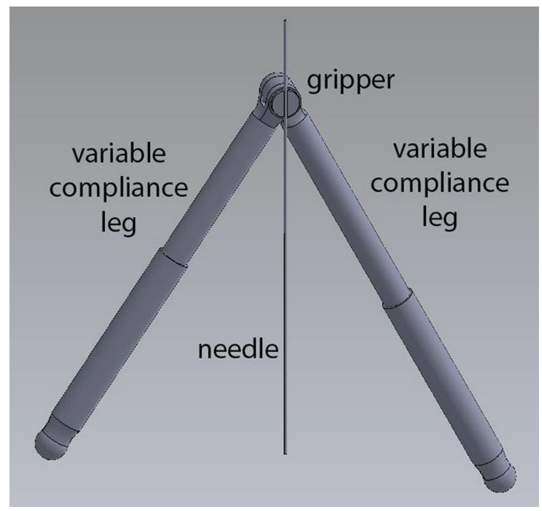

Fig. 1 Patient based force magnifier (PBFM) configuration for difficult venous access (DVA)

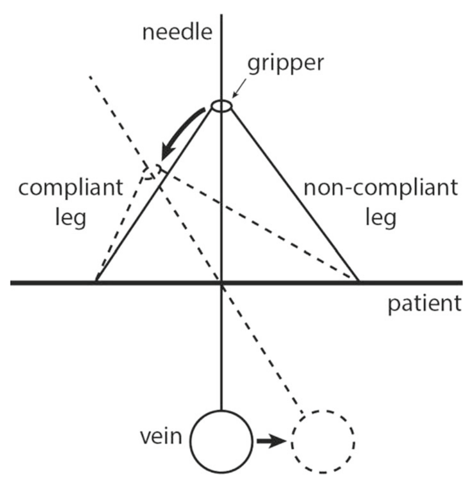

Fig. 2 Patient based force magnifier (PBFM) geometry for following mobile vein

We expect to be able to detect puncture of the proximal wall of the vein in the vertical motion of the vein in the ultrasound image. At that point, with the gripper maintaining its hold on the needle, the PBFM device will lock both of its legs into a non-compliant configuration.

This will present the haptic illusion of a stiff boundary at the distal wall, preventing its puncture and associated vessel damage.

Conclusion

Although our innovation is at an early stage, we believe the underlying concepts are important and novel enough to be of interest to the community. We have submitted a grant proposal to the NIH, as well as a patent application, and hope to be able to report more results in the near future.

References

[1] Hartzog TH, Eldridge DL, Larsen PG, et al. (2008) Putting in the pediatric IV: does confidence and competence make a difference? Presented at the *Annual Meeting of the American Academy of Pediatrics*; October 11–14, 2008; Boston, MA.

[2] Stetten G, Wu B, Klatzky RL, Galeotti J, Siegel M, Lee R., Mah F, Eller A, Schuman J, Hollis R (2011) "Hand-Held Force Magnifier for Surgical Instruments," 2nd International Conference on Information Processing in Computer-Assisted Interventions (IPCAI), June 22–23, 2011, Berlin, Germany, *Lecture Notes in Computer Science*, 6689, pp. 90–100.

[3] Stetten G, (2015) U.S. Patent no. 8,981,914, Portable Haptic Force Magnifier, filed September 27, 2011, issued March 17, 2015.

[4] Wu B, Klatzky RL, Lee R, Shivaprabhu V, Galeotti J, Siegel M, Schuman J, Hollis R, Stetten G (2014), Psychophysical Evaluation of Haptic Perception under Augmentation by a Hand-Held Device, *Human Factors*, published online, Sept. 26, 2014.

[5] Lee R, Klatzky RL, Stetten G, (2017) In-Situ Force Augmentation Improves Surface Contact and Force Control, *IEEE Transactions on Haptics,* April 24, 2017, https://doi.org/10.1109/toh.2017.2696949

Direct design of an individual bone implant on patient-specific CT data in CAx systems

D. Hofmann[1], P. Sembdner[1], S. Holtzhausen[1], R. Stelzer[1]
[1]Dresden University of Technology, Dresden, Germany

Keywords Patient-specific implant · CT data · CAx design process · 3D Modelling

Purpose

In recent years, the integration of computed tomography (CT) data has become increasingly important in product development. Patient-specific CT data is being used more and more frequently, especially in the medical field, to design and manufacture (e.g. by 3D printing) individual bone implants.

However there are currently too many deficits to be able to use this data quickly and specifically in design processes. In addition to numerous processing steps, several programs must be used to obtain a 3D model representation in the form of discrete polygon data. In medicine, for example, the Mimics Innovation Suite from Materialise has been established for this purpose [1]. However, this isosurface representation cannot be used directly in common modelling tools, e.g. CAD systems as part of computer-aided technologies (CAx). Therefore, there is a lack of an end-to-end approach for the processing of CT data in the design engineer's work environment (modelling tool).

The current procedure needs several steps starting with isosurface computation from a stack of CT images (voxel representation) with previous application of several complex segmentation steps. Afterwards, the isosurface representation is processed (e.g. removing artefacts) and the surfaces are reconstructed in order to obtain a solid model with continuously defined surfaces like NURBS (CAD representation). The result of this step is the base for ongoing design process. One disadvantage of this procedure is that the transfer into the corresponding form of representation (from voxel to isosurface to CAD representation) entails losses in accuracy. [2]

Methods

The scientific approach is to develop a consistent concept to use CT data directly in the product development process. To do this, individual layered images or areas (ROI—Region-of-Interest) are used to derive further information from the voxel representation. The basis for this interface is the concept CTinA (**CT** data **in** product development **A**pplications), a modular application that implements a connection between the CT- and the CAx-environment. The implementation of CTinA is based on different software libraries and can be divided into three structural entities (basics, interfaces and visualisation).

The method of operation is carried out using a specified number of queries from the CAx system. CTinA serves as an interface and creates derived information out of the voxel representation in response. The following examples show how the link between queries and their replies can look like:

- 1D: Point (query as geometric information) – > Intensity value (reply as grey scale intensity of a voxel)
- 2D: Plane (query as geometric information) – > a sectional image (reply as set of intensity values on plane)
- 3D: Cuboid (query as geometric information) – > ROI (reply as e.g. sectional images or an isosurface)

In summary, it is possible for the design engineer to create sequentially as many references as needed for the task. Ultimately, the final design can be carried out completely. In doing so, the design engineer uses the available functions from the CAx systems to obtain the desired geometric information without first creating a complete 3D isosurface model.

Results

As a result, the application of the concept CTinA will be shown using the example of designing an individual mandibular implant for additive manufacturing (Fig. 1). The goal of the concept is to design this implant in the CAD modelling tool SolidWorks (version 2016 SP5.0) [3]. To this end, a 3D model of the mandible was first used to define boundary conditions (e.g. section planes, tooth templates) which were planned by a surgeon. A third-party program was used for this purpose [4]. The 3D model was created by simple threshold segmentation using Marching Cubes algorithm [5]. It is not necessary to further refine the model for planning. Thus, existing artefacts are clearly visible at tooth level due to dental restorations. It is no longer necessary to prepare the model in the context of a complex and thus time-consuming segmentation. In the further course of the design process the complete 3D model will not be used. Only some areas are generated as isosurfaces and displayed in the modelling tool to support the design process.

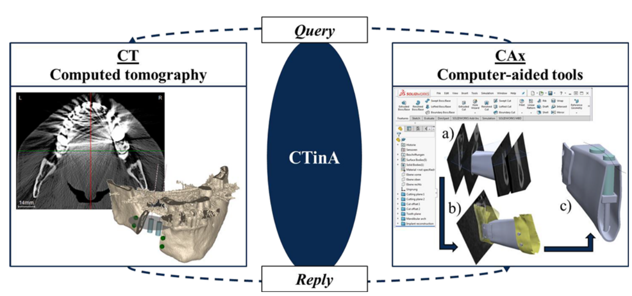

Fig. 1 Concept for using CT data in product development processes; illustrated by modelling an individual mandibular implant; **a** basic implant modelling, **b** modelling of the fixing lugs, **c** modelling additional functions

First, the basic implant body is designed. For this purpose, the sectional images in the intersection area and an offset area as well as a reference tooth plane are transferred. On the sectional images visualised in the modelling tool, a sketch is subsequently created in the form of a spline along the outer contour of the recognisable bone (outer bone shape). These sketches represent the (edge) contours of the implant model in the area to be reconstructed. That step is carried out by means of functions of the modelling tool like a lofted surface (SolidWorks function "Lofted Boss/Base"). The model is then trimmed in height by means of the tooth plane.

This is followed by the modelling of the fixing lugs. Here ROI-isosurfaces are required. Using SolidWorks as an example, these isosurfaces are reconstructed to a continuous surface using the "ScanTo3D"-module. Since the surfaces are only a limited area compared to the entire mandibular model, this step is normally possible without any problems. With the help of the surfaces it is now possible to create a contour-identical mounting strap. The integration of additional functions such as dental implants completes the modelling process. For this case, support elements are designed using defined cylinder features.

Conclusion

An alternative approach to use CT data in product development processes was shown. One focal point is the use and the processing of data from the design engineer's modelling tool. This approach was illustrated using an example from the medical area. The necessary boundary conditions for the design process can be generated on the basis of the presented approach. Finally this approach has the following advantages in contrast to the state of the art process:

- Less high system requirements
- Less time consumption
- Working in the designer's environment
- All functions of the modelling tool can be used directly
- More accuracy
- Work with the original data
- Using additional information (e.g. meta data, material information)

This contribution is funded by the European Social Fund (ESF) with funds from the European Union and the Free State of Saxony, grant number: 100310389.

References

[1] Materialise: Mimics Innovation Suite | Materialise Medical 3D Printing, http://www.materialise.com/en/medical/mimics-innovation-suite (status: 09.01.2018).

[2] Hofmann D; Sembdner P; Holtzhausen S; Schöne C; Stelzer R (2016) Parametric design in Reverse Engineering based on CT data. The e-Journal of Nondestructive Testing 21(2), February 2016, ISSN 1435-4934.

[3] Dassault Systemes SolidWorks Corporation: Introduction SolidWorks, 2016, Waltham, USA.

[4] Sembdner P; Schöne C; Stelzer R (2012) Forming the interface between doctor and design engineer—an efficient software tool to define auxiliary geometries for the design of individualized lower jaw implants. 26th Computer Assisted Radiology and Surgery 2012 (CARS), 27–30 June 2012, Pisa, Italy. Int J CARS 2012/7, Suppl 1: 369, 418–420

[5] Lorensen, William E.; Cline, Harvey E.: Marching Cubes: A high resolution 3D surface construction algorithm, In: Computer Graphics, Vol. 21, No. 4, July 1987, pp. 163–169.

Sacral alar iliac (SAI) Screws insertion through 1st and 2nd dorsal sacral foramen and implications for clinical application

G. H. Jung[1], Y. S. Park[1]
[1]Gyeongsang national university, college of medicine, Gyeongsang national university changwon hospital, Orthopaedic surgery, changwon-si, South Korea

Keywords Pelvis · Sacro alar iliac screw fixation · Three-dimensional modeling · Three-dimensional modeling

Purpose

To assess the possibility of sacral alar iliac (SAI) Screws insertion through 1st and 2nd dorsal sacral foramen by virtually placing two 8.5 mm-sized screws (S1AI and S2AI screw) and introduce the practical landmarks for fluoroscopically guided procedure.

Methods

82 cadaveric pelvises (42 males and 40 females) underwent continuous 1.0 mm slice computed tomography (CT) scans. CT images imported into Mimics® software to reconstruct the 3D model of pelvis. The 8.5 mm-sized pedicle screw was processed into a 3D model using a 3D-sensor at the actual size and optimally placed as SAI screw through transforaminal insertion technique using Mimics® software. The cortical violation along the screw path, intraosseous screw length the relationship with adjacent structures were assessed. If the screw length was shorter than 65 mm, the pelvis was assigned as impossible model.

Results

There was no cortical violation around sacral nerve root canal in all screws and the ideal SAI screw trajectory directed to the anteroinfeior iliac spine (AIIS) (Fig. 1). The average length of S1AI screw was 105.3 mm (range 71.5–115 mm, SD 9.7) and S2AI screw, 90.3 mm (range 47.5–115 mm, SD 22.26). Fifteen models were assigned as impossible model just owing to short S2AI screw (range 47.5–62.4 mm, SD 4.41) and they all had the iliac groove. In the model with iliac groove, the S2AI screw should be directed more outward to avoid the cortical perforation around the groove. Via the transforaminal entry point through the 1st and 2nd dorsal sacral foramen, SAI screws had an easy extensibility from lumbar fixation constructs without cortical violation around the nerve root canal (Fig. 2). Additionally, two SAI screws could be simultaneously fixed by moving the entry point of the S1AI screw upwards from the conventional point even in Asians who had characteristic smaller frame. Thus, for a safe osseous corridor of the conventional S2AI screw, the entry point could be expanded to the area between the 1st and 2nd dorsal sacral foramen if the screw trajectory was directed to the AIIS during the fluoroscopically guided procedure.

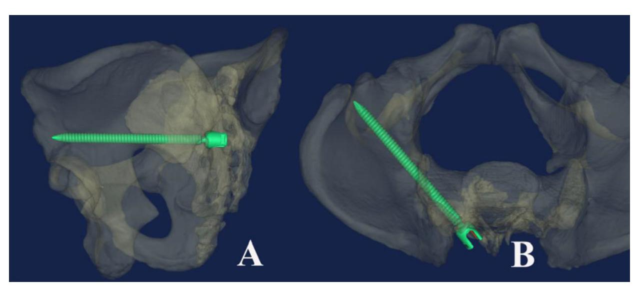

Fig. 1 There was no cortical violation around sacral nerve root canal in all screws and the ideal SAI screw trajectory directed to the anteroinfeior iliac spine (AIIS) in iliac oblique view (**A**) and pelvic inlet view (**B**)

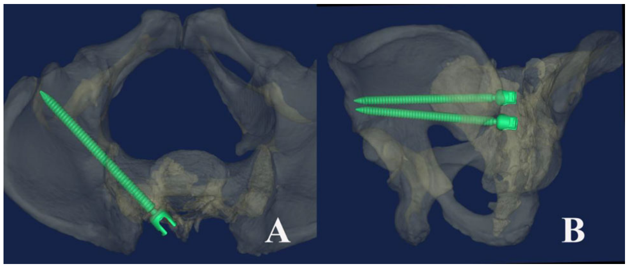

Fig. 2 **A** The ideal S2AI and S1AI screw had the same trajectory in pelvic inlet view. **B** In iliac oblique view, two SAI screws were directed to the anteroinfeior iliac spine (AIIS)

Conclusion

The SAI screw fixation of 8.5-mm-sized S1AI and S2AI screws could be applied safely through the 1st and 2nd transforaminal insertion at the same time and thus, the optimal entry point had a wide tolerance range with respect to the extent of the 1st and 2nd foramen. If there was the iliac groove, the S2AI screw could not reach a sufficient intraosseous length. To assess the possibility of a S2AI screw fixation preoperatively, the iliac grove has to be verified through 3D reconstruction images of CT scans. During a fluoroscopically guided procedure, the AIIS could be used as a consistent intraoperative landmark in the iliac oblique and pelvic inlet views.

Surgery assistance system for continuous resection of brain tumors

T. Koguchi[1], A. Hanafusa[1], F. Shimizu[1], K. Masamune[2], Y. Muragaki[2], H. Iseki[3]
[1]Shibaura Institute of Technology, Bio-Science and Engineering, Saitama, Japan
[2]Tokyo Women's Medical University, Tokyo, Japan
[3]Waseda University, Tokyo, Japan

Keywords Brain tumor · Continuous resection forceps · Flow cytometer · Reflux water

Purpose

Brain tumor is a generic term for neoplasm that occurs in the skull and can be divided into two types, namely, benign and malignant tumors. Because a malignant brain tumor infiltrates the normal brain tissue, surgical treatment is considered to be difficult. It has been reported that the remaining brain tumors have a negative influence on the patient survival ratio due to may recur or malignantly convert [1]. Intraoperative rapid diagnosis, which is used to prepare pathological specimens during surgery and diagnosing tumor malignancy through biopsy, is utilized for determining the extent of brain tumor extraction. However, in this method, it is possible to miss the removal range owing to the lack of varied pathological specimens and the method for obtaining them. This problem can be solved by increasing the number of specimens using continuous resecting method. The purpose of this study is to construct a system that includes forceps for continuous resection and suction function, and a flow cytometer that diagnoses the malignancy of the tumor. By increasing the number of specimens, the accurate boundary of the tumor can be estimated.

Methods

The proposed system consists of forceps for resecting the brain tumor continuously, a separation and dehydration mechanism, cell crushing mechanism, and diagnosis result reflection system (Fig. 1). The separation and dehydration mechanism separates the tumor from reflux water, dehydrates the reflux water, and collects the tumor to the trap. The cell crushing mechanism pulverizes the cell of the gathered tumor to be diagnosed by the flow cytometer. By reflecting the diagnosed results to the navigation system, the resecting range of the tumor is determined and displayed. The flow cytometer carries out a fluorescent staining procedure on the nucleus of the isolated cell and diagnoses its malignancy with its fluorescence amount. The reflux water is required to shed the tumor and resect continuously. However, if the specimens contain large amounts of reflux water, the result of the diagnosis by the flow cytometer may be affected. Therefore, the dehydration mechanism is developed to separate the tumor from the water. The arc shaped dehydration mechanism consists of a recovery passage part through which the tumor passes, a drainage passage part through which the reflux water passes, and a filter which separates the tumor and reflux water. At the lower end of the mechanism, two pipes with different lengths, one long and the other short, and a rubber stopper are installed (Fig. 2). After the tumor and reflux water are separated by the filter, the tumor moves to the trap through the collection channel and the reflux water passes through the dehydration channel to the water trap. The long and short pipe mechanism also assists in the suction of the tumor towards the tumor trap. The dehydration mechanism was manufactured by a stereo lithography machine, and evaluated by separation and dehydration experiments using a tumor alternative.

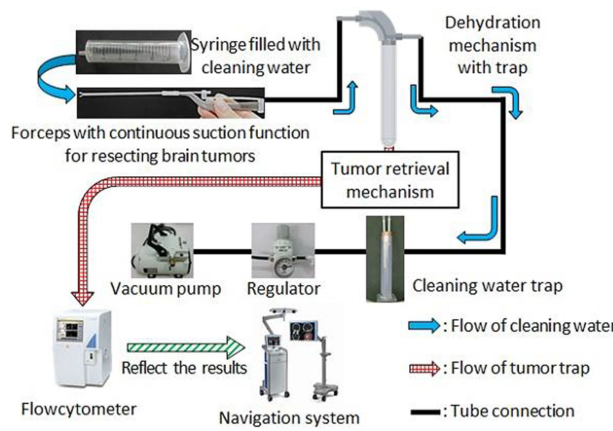

Fig. 1 Configuration of continuous brain tumors resection system

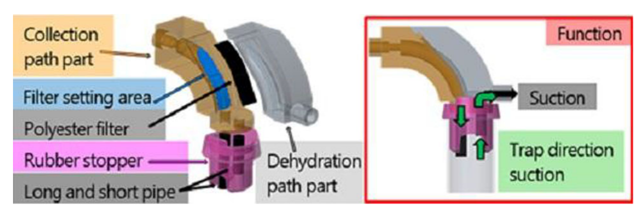

Fig. 2 Filter and trap suction mechanisms

Results

Experiments were performed under three different conditions by changing the area of the dewatering filter installed in the dehydration mechanism and the suction pressure used by the continuous resection forceps. The combinations of area and pressure were 56.78 [mm^2], − 20 [kPa] (case 1), 56.78 [mm^2], − 30 [kPa] (case 2), and 70.76 [mm^2], − 30 [kPa] (case 3). As an experimental method, a forceps and dehydration mechanism, a regulator, a suction pump were connected with a tube, and the suction time was set to 5 [s]. Porcine brain used as a tumor alternative was resected by the continuous resection forceps and separated from water by the developed mechanism. The dehydration ratio and tumor collection ratio were calculated from the amount of reflux water and porcine brain collected in the trap. The target tumor collection amount is the amount collected 10 times without aspiration by the forceps, and this value is used as the target collection ratio of 100%. The average reflux water dehydration ratio, standard deviation, and the tumor alternative collection ratios were 60.59%, 12.24%, 105.79% for case 1, 70.58%, 19.66%, 101.79% for case 2, and 72.87%, 7.16%, 100.82% for case 3. Since the dehydration ratio was improved when the suction pressure condition was − 30 [kPa], it was suggested that the suction pressure had relation to the dehydration ratio. Among the three results, the best result was 72.87, 7.16 and 100.82%. Hence, case 3 had the most suitable conditions for separation and dewatering.

Conclusion

An arc shaped dehydration mechanism was designed and manufactured using a stereo-lithography machine. Experiments on the dehydration of reflux water and collection of a tumor alternative were performed using the developed mechanism. The experiments were performed while changing the suction pressure and filter area. By connecting the dehydration mechanism and continuous resection forceps with a tube, the reflux water dehydration and tumor collection rates were evaluated. It was established that the most suitable condition for the separation and dehydration mechanism was when the suction pressure was 30 [kPa] and the filter area was 70.76 [mm^2]. We intend to create a mechanism that enables 80% dehydration, cell isolation, and a navigation system that reflects the result of malignancy diagnosis in the future.

References

[1] Miyatake S, Kajimoto Y, Aoki A, Kuroiwa T: Glioma Surgery using 5-ALA and Navigation System. Japanese journal of neurosurgery 15(10): 706–714, 2006 [in Japanese]

A comparative accuracy of the ROSA® stereotactic robot towards Frameless and Frame-based stereotaxical systems

R. Kamouni[1], F. Schoovaerts[1], O. De Witte[1]
[1]ULB Hopital erasme, Neurosurgery, Brussels, Belgium

Keywords ROSA® · Stereotactic robot · Frameless · Frame-based · Accuracy

Purpose

During the last recent years, numerous Robots have been developed to achieve accurate stereotactic procedures. The crucial benefits are that robots can procure imaging information (CT, MRI, PET scan, …) from the patient, handle surgical tools with high precision and guide the surgeon to execute accurate surgeries. With six degrees of freedom in the robotic arm, the ROSA® Robot system provides easy access to the surgical area and freedom in selecting trajectories for surgical instruments with high skill.

The objective of this study is to establish the accuracy of this system and compare it with ordinarily used systems like:

Frameless infrared based surgical localisation system.

Electromagnetic system based surgical localisation system.

And frame-based surgical localisation system.

Methods

We discuss and compare accuracy of four systems:

- The ROSA® robot in the frameless configuration.
- The standard stereotactic frame-based approach.
- An infrared tracking system using a standard registration technique.
- An electromagnetic tracking system.

The study was performed with 1-mm section of CT scans.

A dedicated phantom device is used to evaluate the overall accuracy and it was designed so that it could be used with all types of registration and preoperative imaging techniques. In a CT scan, the phantom is easily viewed because of its radiopacity. The phantom device is designed to be used for the Frameless surface registration and for the Frame-Based registration (Fig. 1).

Fig. 1 The phantom device

Infrared and Electromagnetic tracking systems:

Image-guided surgery (neuronavigation) is an operative technique by which correlation between imaging studies and the operative field is provided. This frameless stereotaxy enables safe, accurate surgery and may ultimately reduce complications and improve outcome. Neuronavigation approach is high flexible and may have broad applications in general neurosurgery.

Electromagnetic technology extends the application of neuronavigation to shunt placement and ventricular catheter placement in patients with traumatic brain injury.

Each neuronavigation system involves the intraoperative localization step. There are several methods for capturing the common points needed for registration. The two methods used in this study were infrared and Electromagnetic.

Infrared system

Passive optical trackers. These systems work in the near IR range. Instead of active markers, retro-reflective spheres are illuminated by the camera in the near-IR spectrum. The 2d pattern of the reflective markers, has to be unique for each tracking probe so that unambiguous identification is possible. For this reason, these systems are always equipped with coupled CCD cameras. One big advantage of these systems is that the tracking of the probe's tip is done wirelessly.

Electromagnetic system

Electromagnetic system is a relatively new tracking technology in medical applications. Their main advantage is that they have no line-of-sight limitation, but their disadvantages include susceptibility to distortion from nearby metal sources and limited accuracy compared to optical tracking. These systems localize small electromagnetic field sensors in an electromagnetic field of known geometry.

The ROSA® robot in the frameless configuration

Step motor position sensors are used in robotics for sensing and controlling the *arm movements* with extreme mechanical precision. With six degrees of freedom in the robotic arm, the ROSA® system provides increased access to the surgical area and freedom in selecting trajectories for surgical instruments with high skill. Advanced haptic aptitude of the ROSA® system provides surgeons easy guidance of instruments by hands inside boundaries set up during the planning stage. The ROSA® neuronavigation system is based on a highly accurate laser-controlled distance measurement for localisation during the registration steps.

The standard stereotactic frame-based

The stereotactic approach to intracranial targets involves the rigid application of a stereotactic frame, a localizer and an image data set. The system uses *x, y, z* coordinates to stereotactically localize any point in 3D space. Knowing the relationship between the patient's head and the fiducial localizers, full access to any intracranial area can be reached with accuracy below 1 mm. Despite the development of frameless image guided surgery systems, frame-based systems will remain an important tool in functional stereotactic neurosurgery. Frame-based systems provide a high degree of mechanical stability and accuracy.

Results

To determine whether ROSA® Robot is accurate, three commonly used stereotactic localization systems (stereotactic frame, IR tracking system and EM tracking system) were used to carry out a quantitative comparison.

The results indicate that the accuracy of the frameless ROSA® robot is comparable to that of standard localizing systems, whether they are frame-based or infrared tracked (EM tracked).

Conclusion

ROSA® is a robotic solution designed for neurosurgical applications. For surgical procedures, it can reduce human error and can also save time in procedures including multiple targets and biopsies. In general, robotic systems are less inclined to making mistakes.

This type of robotic arm may prove to be highly useful supporting and stabilizing a variety of dedicated or conventional surgical devices such as biopsy needles and drills.

Many surgeries demand precise manipulation of instruments involving stable and strict positioning with the best orientation accuracy in the 3D patient space. The robot go and stand automatically to a specific position. In some case it is less invasive than the frame in term of comfort for the patient.

Infrared navigators (commonly used nowadays) are more *indicators* of the position of a probe. In return classical navigation systems easily provide augmented reality through the head up display of any microscopes. Each system bringing its own advantages.

Frame-based approaches are more subject to human errors, sometimes more complex in their manipulations. They are occasionally limited in terms of positioning and on what instruments can be mounted. Invasiveness in term of comfort for the patient.

The 2 optical and the electromagnetic systems provided similar accuracy.

Level of accuracy of the ROSA® stereotactic robot is comparable to that of the most accurate standard image guided neurosurgery techniques.

Preliminary application of ultrasound and CT image fusion in craniomaxillofacial soft tissue surgery

C. Yang[1], J. Wu[1], Y. Zhang[1], B. Xu[1], S. G. Shen[1], S. Zhang[1]
[1]Shanghai Ninth People's Hospital, Shanghai Jiao Tong University School of Medicine, Shanghai Key Laboratory of Stomatology, Department of Oral and Cranio-maxillofacial Surgery, Shanghai, China

Keywords Ultrasound · CT · Maxillofacial soft tissue · Image fusion

Purpose

Craniomaxillofacial surgery is anatomically complex and used for special therapeutic purposes [1, 2]. However, surgeons have sought to safely and accurately complete surgical procedures with minor invasion. Due to the inflexibility of bone tissue, which is similar to a rigid body, modern digital technologies such as virtual surgery and surgical navigation have greatly improved the accuracy of cranio-maxillofacial bone surgery. These technologies have wide clinical applications, including surgeries for cranio-maxillofacial fracture, temporomandibular joint arthroplasty, bone tumor resection, and contour trimming [3]. For craniomaxillofacial soft tissue, deformation may easily occur during surgery and cause image drift. This study attempted to solve the challenging problem of intraoperative navigation image drift caused by the deformation of oral craniomaxillofacial soft tissue. A self-developed algorithm was used to establish a fusion imaging technology that integrates ultrasound and CT images based on optical positioning to address the key issue of navigation in cranio-maxillofacial soft tissue surgery.

Methods

(1) Two-dimensional (2D) spatial location was obtained by ultrasound imaging, and three-dimensional (3D) reconstruction was performeded using a nearest-neighbor interpolation algorithm. (2) The CT image data in digital imaging and communication in medicine format (DICOM) and ultrasound data were integrated using a self-developed, diference local directional pattern (dLDP) based image fusion algorithm. (3) The ultrasound and CT image fusion was clinically verified, and the accuracy was evaluated using a scale tool provided by the image processing software.

Results

(1) The dLDP—a self-developed algorithm for multimodal image registration was obtained. (2) The connected and assembled system operated properly, and the time required for the entire operation (including installation and initial settings) was less than 15 min, which could meet the basic requirements of clinical applications under physician supervision. (3) The dLDP-based fusion algorithm achieved the fusion of ultrasound and CT imaging in the craniomaxillofacial region, with an average error of 1.96 mm. The experimental results are shown in Fig. 1.

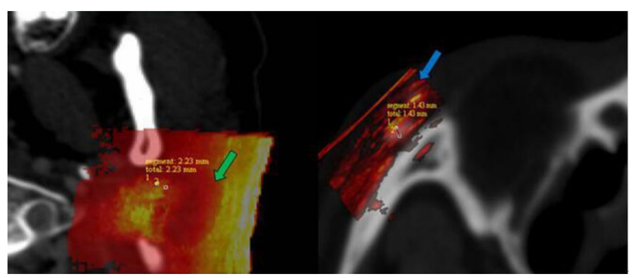

Fig. 1 Accuracy evaluation of ultrasound and CT image fusion

Conclusion

The precision and image display of the dLDP-based image fusion algorithm met basic clinical needs, showing an important guiding significance for this self-developed navigation system in oral and craniomaxillofacial soft tissue surgery.

Acknowledgements

This work was supported by the National Natural Science Foundation of China (81671035 and 81701034); Shanghai Science and Technology Committee (15441906000); the Project from Cooperative Innovation Center of Translational Medicine (TM201717); and the Interdisciplinary Program of Shanghai Jiao Tong University (project number YG2015QN05).

References

[1] Schramm A, Suarezcunqueiro MM, Barth EL, Essig H, Bormann KH, Kokemueller H, Rücker M, Gellrich NC (2008) Computer-assisted navigation in craniomaxillofacial tumors. Journal of Craniofacial Surgery 19: 1067

[2] Juergens P, Beinemann J, Zandbergen M, Raith S, Kunz C, Zeilhofer HF (2012) A computer-assisted diagnostic and treatment concept to increase accuracy and safety in the extracranial correction of cranial vault asymmetries. Journal of Oral & Maxillofacial Surgery Official Journal of the American Association of Oral & Maxillofacial Surgeons 70: 677

[3] Yu H, Wang X, Zhang S, Zhang L, Xin P, Shen SG (2013) Navigation-guided en bloc resection and defect reconstruction of craniomaxillary bony tumours. International Journal of Oral & Maxillofacial Surgery 42: 1409

TTRE and FRE are uncorrelated in a paired-point rigid registration

Z. Min[1], M. Q.-H. Meng[1]

[1]Department of Electronic Engineering, The Chinese University of Hong Kong, Hong Kong, China

Keywords Registration · Image guidance · Anisotropy · Inhomogeneity

Purpose

In image-guided surgery (IGS), registration of pre-operative image space and intra-operative physical space is an essential step. Generally speaking, 1) paired-point rigid registration 2) surface registration can both be used to complete the task. The distinctive characteristic of surface registration is that correspondences between points in two spaces to be registered are not known. Surface registration is deemed to be more robust to noise and outliers. However, paired-point rigid registration is still the most frequently used technique in an image-to-patient registration. The target registration error (TRE) statistic has often been used to evaluate the accuracy of a rigid registration. However, target localization errors (TLEs) in two spaces are not considered in the formulation of TRE. Total target registration error (TTRE) was thus recently formally formulated to include the influence of TLE [1]. On the other hand, fiducial registration error (FRE) is easier to acquire in a rigid registration. In this article, we would like to answer a very useful question in a single paired-point rigid registration (PPRR) as: "Can total target registration error be represented by fiducial registration error?" If the answer is Yes, then we can use FRE to evaluate a rigid registration. If not, we still have to measure the TTRE value or estimate the TTRE statistics using a TTRE statistical model.

Methods

In a paired-point rigid registration (PPRR), the total target registration error $\mathbf{TTRE}(\mathbf{r})$ at a nominal target point $\mathbf{r} \in \mathbb{R}^{3\times1}$ is formally defined as [1]:

$$\begin{aligned}\mathbf{TTRE}(\mathbf{r}) &= \mathbf{R}(\mathbf{r}+\Delta\mathbf{r}_x)+\mathbf{t}+\Delta\mathbf{r}_\mathbf{y}-(\mathbf{R}^{(0)}\mathbf{r}+\mathbf{t}^{(0)})\\ &= \mathbf{R}\mathbf{r}+\mathbf{t}-(\mathbf{R}^{(0)}\mathbf{r}+\mathbf{t}^{(0)})+\mathbf{R}\Delta\mathbf{r}_x+\Delta\mathbf{r}_y\\ &= \Delta\mathbf{R}\mathbf{R}^{(0)}\mathbf{r}+\mathbf{t}-\mathbf{t}^{(0)}+\mathbf{R}\Delta\mathbf{r}_x+\Delta\mathbf{r}_y\\ &= \mathbf{TRE}(\mathbf{r})+\mathbf{R}\Delta\mathbf{r}_x+\Delta\mathbf{r}_y\end{aligned}$$

where $\mathbf{R} \in SO(3)$ and $\mathbf{t} \in \mathbb{R}^{3\times1}$ are the calculated rotation matrix and translation vector using measured fiducial positions, $\mathbf{R}^{(0)} \in SO(3)$ and $\mathbf{t}^{(0)} \in \mathbb{R}^{3\times1}$ are the 'true' rotation matrix and translation vector, $\Delta\mathbf{R} = \mathbf{R}\mathbf{R}^{(0)^T} - \mathbf{I}_{3\times3}$, $\Delta\mathbf{r}_x \in \mathbb{R}^{3\times1}$ and $\Delta\mathbf{r}_y \in \mathbb{R}^{3\times1}$ are target localization errors (TLEs) in X and Y spaces to be registered. The overall idea is to decompose the **TTRE** into three separate parts: **TRE**, $\mathbf{R}\Delta\mathbf{r}_x$ and $\Delta\mathbf{r}_\mathbf{y}$, and show that **FRE** is uncorrelated with all these three vectors respectively. To proceed, we present a few assumptions throughout the methods: a) FLE is small enough; b) first-order approximation in FLE is assumed; c) **FLE**, $\Delta\mathbf{r}_x$ and $\Delta\mathbf{r}_\mathbf{y}$ are independent and obey certain Gaussian distributions; d) the ideal weighting scheme [2] is used in the registration process. It is noteworthy that we do not assume that TLE is small. When the ideal weighting scheme is used, it has been proved in [2] that **TRE** and **FRE** are uncorrelated. With the expression of **FRE** in [2], $\mathbf{R}\Delta\mathbf{r}_x$ and **FRE** can be further verified to be uncorrelated. With the assumption (c), we can also conclude that **FRE** and $\Delta\mathbf{r}_\mathbf{y}$ are independent and thus uncorrelated since **FRE** is a function of only **FLE**.

Results

Numerical simulations are conducted to validate the proposition. Four fiducials' true positions in X space (e.g. CT image space) are set as:

$$\mathbf{x}_1 = [46.08, -42.34, 115.94]^\mathrm{T},$$
$$\mathbf{x}_2 = [-0.98, -69.82, 122.81]^\mathrm{T},$$
$$\mathbf{x}_3 = [-53.40, -51.55, 122.19]^\mathrm{T},$$
$$\mathbf{x}_4 = [-5.37, -65.43, 73.44]^\mathrm{T}$$

The target's true position in X space is the following:

$$\mathbf{r} = [21.48, -49.32, 89.69]^\mathrm{T}$$

For each registration trial, the 'true' rotation matrix were generated randomly by setting the rotated angle being 10, 20, − 30 degrees about the *x, y, z* axes. The 'true' translation vector was set to be $[7, -10, 100]^\mathrm{T}$. The FLE and TLE vectors were generated from certain covariance matrices. Here, FLE and TLE covariance matrices were set to be anisotropic and inhomogeneous with their root-mean-square (rms) values varied from 1 to 70 mm. FLE and TLE vectors were then added to the fiducials' and target's 'true' positions in X and Y (e.g. patient space) spaces to generate the 'disturbed' fiducials and target. Both singular value decomposition (SVD) [1] and the ideal weighting methods [2] were adopted to register the 'disturbed' fiducials in two spaces. In all, 2000 registration trials were conducted using either registration method, and in each trial TTRE and FRE vectors could be computed correspondingly. For either method, CC (TTRE, FRE) was then further calculated using 2000 rms values of TTRE and FRE vectors. We then repeated the above process with certain FLE and TLE rms value for 30 times, respectively. The mean and standard deviation of 30 CC (TTRE, FRE) values were computed for each case with specific FLE and TLE value.

Figure 1 shows the statistics of correlation coefficients between TTRE and FRE (i.e. CC (TTRE, FRE)) for different test cases. In Fig. 1a, SVD method is adopted while the ideal weighting scheme is adopted in Fig. 1b. As can be seen in Fig. 1a, 95% confidence interval (CI) of CC (TTRE, FRE) values is within 0.1 which is negligible. As shown in Fig. 1b, when FLE and TLE are less than 10 mm, 95% CI of CC (TTRE, FRE) is also less than 0.1. When FLE and TLE are equal to or larger than 20 mm, the mean CC (TTRE, FRE) value is less than 0.4. We note that in IGS, the chance of FLE or TLE being larger than 10 mm is small.

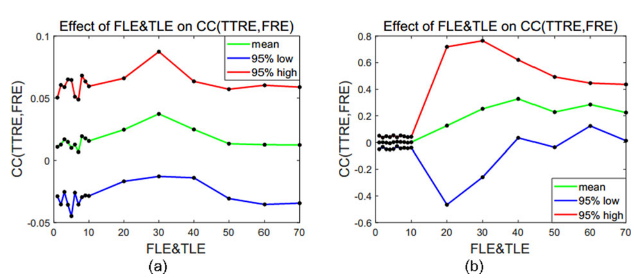

Fig. 1 Correlation coefficients between TTRE and FRE when FLE is anisotropic and inhomogeneous, and TLE is anisotropic. Two registration algorithms are used in the above two plots (**a**) SVD method is adopted (**b**) ideal weighting scheme is adopted

Conclusion

In this work, we have verified that TTRE and FRE are uncorrelated to first order in FLE. We have a) proved that TTRE and FRE are uncorrelated under certain assumptions; b) validated through simulations that the correlation between TTRE and FRE are insignificant under more general conditions. We thus conclude that, in image-guided surgery, it is not suitable to use FRE as a quantifying metric for a paired-point rigid registration. A statistical model of TTRE like that presented in [1] should otherwise be used to evaluate a rigid registration.

References

[1] Min Z, Ren H, Meng MQ, H (2017, September). TTRE: A new type of error to evaluate the accuracy of a paired-point rigid registration. In Intelligent Robots and Systems (IROS), 2017 IEEE/RSJ International Conference on (pp. 953–960). IEEE.

[2] Danilchenko, Andrei, and J. Michael Fitzpatrick. "General approach to first-order error prediction in rigid point registration." IEEE transactions on medical imaging 30(3) (2011): 679–693.

Quantitative evaluation of laparoscopic intestinal suturing by forceps motion analysis from 305 training videos

N. Fukatsu[1], S. Aoki[1], T. Yamaguchi[1], M. Uemura[2], M. Hashizume[2], R. Nakamura[3]

[1]Chiba University, Graduate School of Science and Engineering, Chiba, Japan

[2]Kyushu University, Graduate School of Medical Science, Fukuoka, Japan

[3]Chiba University, Center for Frontier Medical Engineering, Chiba, Japan

Keywords Forceps motion analysis · Surgery training · Quantitative assessment · Forceps detection

Purpose

With endoscopic surgery being increasingly used in highly difficult surgeries, regular training is important to improve its safety. Objective evaluation of the trainee's skill and providing feedback on the results are highly effective in the educational process. Hence, we have developed a suture ligature simulator for the quantitative evaluation of the intestinal suture technique [1]. This simulator evaluates suture skill based on the final suture ligature. However, determining the factors that affect the evaluation results is difficult if only this simulator is used. Therefore, we developed a system that could quantitatively evaluate the parts of suture process based on the forceps motion from a video recorded by a USB camera installed on the simulator [2]. We included 15 videos in previous study; however, in this study, we added 290 videos gathered from a suture ligature contest with 280 doctors participating, which used the suture ligature simulator.

Methods

For automatic detection of forceps motion from the videos recorded by a USB camera on the simulator, we employed motion and straight-line detection method. Next, in order to quantify the features of the procedure, this motion information was used to define skill parameters, namely, task time, work density, forceps cross time, average velocity, relative velocity, size of work area (rectangle and ellipse), path length, and distance between forceps. Work density, average velocity, size of work area, and path length were calculated on the left and right hand individually. Further, work density, average velocity, and path length were also calculated using the center of the forceps' tip motion. Work density is the degree of concentration on the work; average velocity is the operability of the forceps; work area reflects the working range; forceps cross time is the time when the left and right forceps cross each other. Forceps cross time, relative velocity, distance between forceps and density, velocity, and path length of the center of the forceps tip motion reflect the coordination between the hands of the trainee. In this study, we used 305 video recordings and evaluated the difference in surgical techniques between experts and novices using the above mentioned parameters. In this study, an expert classified based on the following categories: (1) good simulator results, (2) a qualified surgeon, and (3) experienced a minimum of 100 cases. In each category, we investigated the parameters that show significant difference between an expert and a novice using Mann–Whitney *U* test. Then, parameters that show significant difference in the three categories were quantitatively evaluated through clustering, and the difference in each skill level was determined by analyzing the procedure features of each cluster.

Results

Based on the result of the investigation of parameters with significant difference between expert and novice using the three categories, work time, work density of the left and right hands, forceps cross time, rectangular area of the right hand, ellipse area of the right hand, path length of the left and right hands, distance between forceps, density, and path length of the center of the forceps tip motion were quantitatively evaluated. Clustering of the parameters resulted in five groups: S, A, B, C, and D (Fig. 1). Detailed information on each cluster is shown in Table 1. The number of experienced cases, percentage of qualified surgeons, and good simulator results were included in the cluster, which showed that the simulator score progressively increased as the groups transitioned from D to S (i.e., S > A>B > C > D). Therefore, we confirmed that skill level is increased in group S. The results of that examination of the characteristics of skill parameters in each group are shown in Fig. 2. We confirmed that work time, cross time, and path length progressively decreased as the groups transitioned to group S (Fig. 2a–e). Therefore, it was suggested that a doctor who has a high skill level tends to have a shorter work time and perform fewer mistake. Additionally, we confirmed that work density tends to increase and work area and distance between forceps tend to decrease as the group transitions to group S (Fig. 2f–k). Thus, it was suggested that a doctor who has high skill level tends to concentrate more on the target area and perform surgical procedure more compactly. However, in group B, parameters such as work density and work area tended to be opposite to those of experts. From this result, it was suggested that there is a time when the motion becomes larger during skilled process; thus, in group B, focusing on the work area will lead to further improvement of skill level.

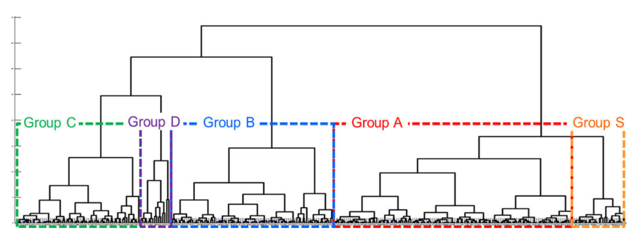

Fig. 1 Result of clustering

Table 1 Detailed information of each cluster

	Qualified surgeon (%)[a]	Good simulator result (%)[a]	Simulator score (25-point scale)	Average case	Average post-graduate year
S (n = 26)	37	40.7	18.7	444	14
A (n = 120)	24.8	30.6	17.4	193	12.7
B (n = 82)	18.3	17.1	17.1	175	12.4
C (n = 62)	9.7	17.7	15.4	151	11.5
D (n = 15)	0	12.5	13.4	58	12.3

[a] Based on the percentage included in each cluster

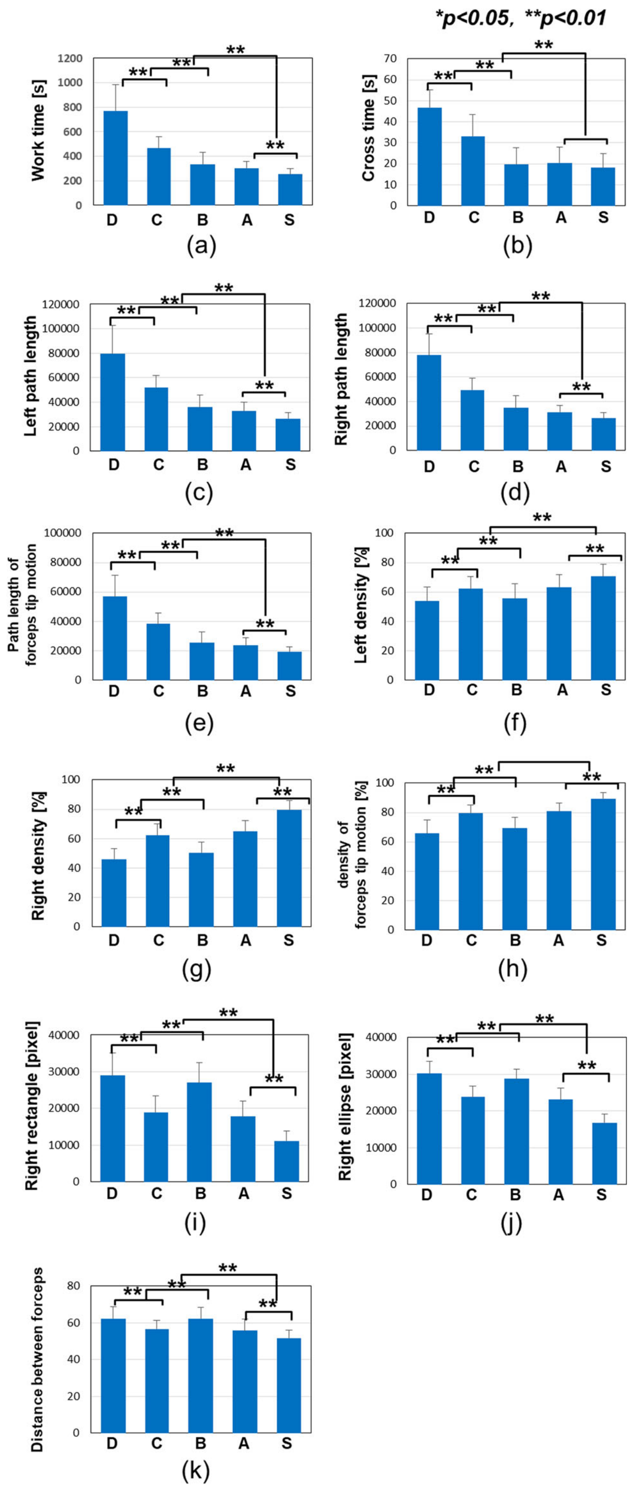

Fig. 2 Results of the examination of the characteristics of each group using skill parameters

Conclusion

In this study, we quantitatively evaluated 305 videos from a suture ligature simulator through forceps motion analysis to evaluate the intestinal suture procedure. This method can determine and evaluate the features of a surgical technique for each skill level, and it shows that experts have fewer mistakes, have better concentration on the target area, and perform a more compact procedure. Furthermore, we confirmed that there is a time when the motion becomes larger during skilled process.

References

[1] Uemura M, Yamashita M, Tomikawa M, Obata S, Souzaki R, Ieiri S, Ohuchida K, Matsuoka N, Katayama T, Hashizume M (2015) "Objective assessment of the suture ligature method for the laparoscopic intestinal anastomosis model using a new computerized system," Surg. Endosc. 29(2): 444–452

[2] Fukatsu N, Aoki S, Yamaguchi T, Uemura M, Hashizume M, Nakamura R (2017) "Quantitative evaluation of training intestinal suturing by examination of forceps movement using image processing of video recording," Int. J. Comput. Assist. Radiol. Surg. 12(Suppl 1): 129–130

Using classifiers to distinguish neurosurgical skill levels in a virtual reality tumor resection task

S. Siyar[1], H. Azarnoush[1,2], S. Rashidi[3], A. Winkler-Schwartz[2], R. F. Del Maestro[2]

[1]Amirkabir University of Technology (Tehran Polytechnic), Biomedical Engineering, Tehran, Iran, Islamic Republic Of

[2]McGill University, Neurosurgical Simulation Research and Training Centre, Department of Neurosurgery, Montreal Neurological Institute and Hospital, Montreal, Canada

[3]Science and Research Branch, The Islamic Azad University, Biomedical Engineering, Tehran, Iran, Islamic Republic Of

Keywords Virtual reality · Skill assessment · Neurosurgery · Classification

Purpose

Virtual reality simulators can be useful tools in training and evaluating neurosurgery residents. An important expectation for a surgical simulator is its ability to distinguish between a skilled operator ("expert") and a less skilled operator ("novice") which is considered constructive validity [1, 2].

This study outlines the first investigation of the application of classifiers to make such distinction among individuals participating in a virtual reality tumor resection task. Traditionally, a neurosurgery resident's skill level has been determined in an apprenticeship model by subjective criteria used by a supervisor. Earlier virtual reality simulation studies attempted to overcome the limitations of the traditional approach by applying basic metrics. However, basic metrics may not be adequate to encompass all complexities related to surgical skill. Therefore, a more sophisticated model with a more comprehensive set of metrics are required to differentiate the skill level. This motivated us to consider the application of classifiers to achieve this task [3–5].

Methods

A total of 115 individuals participated in the trial involving a neurosurgery simulator, including 23 staff neurosurgeons and senior neurosurgery residents in the "skilled" group and 92 junior neurosurgery residents and medical students in the "novice" group. The defined task was removing a virtual brain tumor using a virtual aspirator while causing minimal damage to the surrounding virtual healthy tissue.

Figure 1 shows the 6 scenarios used in the task with each scenario including 3 tumors to be resected. For each tumor 1 of 3 different appearance as well as stiffness models was used. In Scenarios 1–3, the same appearance model was used for all 3 tumors with varying tumor stiffness in each scenario. In Scenarios 4–6, the stiffness of the tumors was the same while the appearance varied in each scenario. Data related to individual performance were recorded.

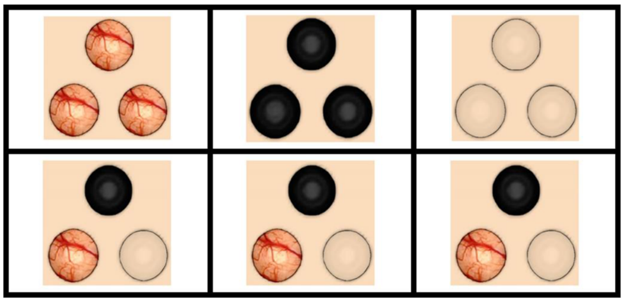

Fig. 1 The 6 scenarios including tumors with various appearance and stiffness models

Figure 2 depicts the processing stages used. In order to apply the classifiers, we initially extracted 150 features from the recorded data. Using statistical t-test analysis, 68 features were selected. The forward feature selection algorithm was used to rank and select best subsets of the previously chosen 68 features. We used 4 classifiers, namely, K-Nearest-Neighbors (KNN), Parzen Window (PW), Support Vector Machine (SVM), and Fuzzy K-Nearest-Neighbors (FKNN).

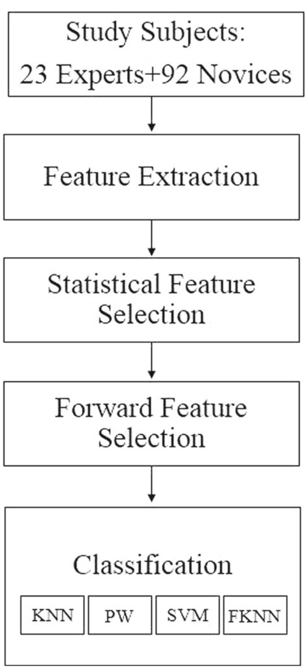

Fig. 2 The applied feature selection and classification procedure

Results

In order to determine an acceptable ratio of train set size to test set size, first, various train and test set sizes were used ranging between 10 and 90% of the feature data. Train sets were randomly chosen in 20 iterations. The obtained average equal error rates (EER) from all 4 classifiers were compared for this range. The obtained average EERs did not significantly decrease once the train set size was increased to values above 50%. Therefore, 50% was chosen as the working point for the train set size. At this working point, FKNN showed an overall better performance with an average EER as low as 9.6% for Scenario 1.

In the next step, performance of classifiers was assessed based on number of the selected premier features and train sets randomly chosen in 20 iterations. Using forward feature selection a range of 5–30 best features were used to compare the performance of the classifiers. In many cases, not only increasing the number of features did not improve the performance of the classifier, but also increased the average EERs. In this assessment, FKNN was again the best classifier overall with average EERs as low as 8.2%.

Conclusion

In this study, we demonstrated a first investigation of application of classifiers in assessing surgical skill level. The importance of our results lies in their potential educational application in neurosurgical resident training and help in further defining of the psychomotor skill set of the expert surgeon. These classifiers can be used not only for evaluation, but also can help formulate the criteria for expert performance which currently do not exist, and eventually shift the educational paradigm from the traditional apprenticeship model to a more objective model based on proven performance standards.

References

[1] Azarnoush H, Alzhrani G, Winkler-Schwartz A, Alotaibi F, Gelinas-Phaneuf N, Pazos V, Choudhury N, Fares J, DiRaddo R, Del Maestro RF (2015) Neurosurgical virtual reality simulation metrics to assess psychomotor skills during brain tumor resection. *International journal of computer assisted radiology and surgery, 10*(5), 603–618

[2] Alotaibi FE, Al Zhrani G, Bajunaid K, Winkler-Schwartz A, Azarnoush H, Mullah MAS, Sabbagh A, Del Maestro RF (2015) Assessing neurosurgical psychomotor performance: role of virtual reality simulators, current and future potential. *SOJ Neurol, 2,* 1–7

[3] Azarnoush H, Siar S, Sawaya R, Zhrani GA, Winkler-Schwartz A, Alotaibi FE, Bugdadi A, Bajunaid K, Marwa I, Sabbagh AJ, Del Maestro RF (2016) The force pyramid: a spatial analysis of force application during virtual reality brain tumor resection. *Journal of neurosurgery*, 1–11

[4] Sawaya R, Bugdadi A, Azarnoush H, Winkler-Schwartz A, Alotaibi FE, Bajunaid K, AlZhrani GA, Alsideiri G, Sabbagh AJ, Del Maestro RF (2017) Virtual Reality Tumor Resection: The Force Pyramid Approach. *Operative Neurosurgery*

[5] Bugdadi A, Sawaya R, Olwi D, Al-Zhrani G, Azarnoush H, Sabbagh AJ, Alsideiri G, Bajunaid K, Alotaibi FE, Winkler-Schwartz A, Del Maestro R (2017) Automaticity of Force Application During Simulated Brain Tumor Resection: Testing the Fitts and Posner Model. *Journal of surgical education*

A novel tracking system for biopsy navigation using a tablet—A feasibility study

M. Rodgers[1], J. Rudan[2], M. Kunz[1,2]
[1]Queen's University, School of Computing, Kingston, Canada
[2]Queen's University, Department of Surgery, Kingston, Canada

Keywords Image-guided surgery · Biopsy · 2D–3D registration · Structured light scanner

Purpose

Image-guided surgery methods have been shown to improve the accuracy and/or precision of various surgical applications. However, often their use in clinical routine is limited due to the need of expensive and technically demanding equipment. In this project, we investigated an alternative approach for image-guided biopsy applications. The hypothesis was that expensive tracking and navigation equipment can be replaced for some applications by a cost-efficient and easy-to-use tablet and a handheld structured light scanner.

Methods
A phantom was created containing a knee model as well as a transparent cylinder attached inferior to the knee. A tumour region of interest in the shape of a torus was created using a prototype printer. Pins attached to the torus were then used to fixate the torus within the transparent cylinder (Fig. 1). A CT scan was obtained and the biopsy target in the center of the torus was planned. In addition, a 3D model of anatomy (including skin) was generated from the CT information (Fig. 1).

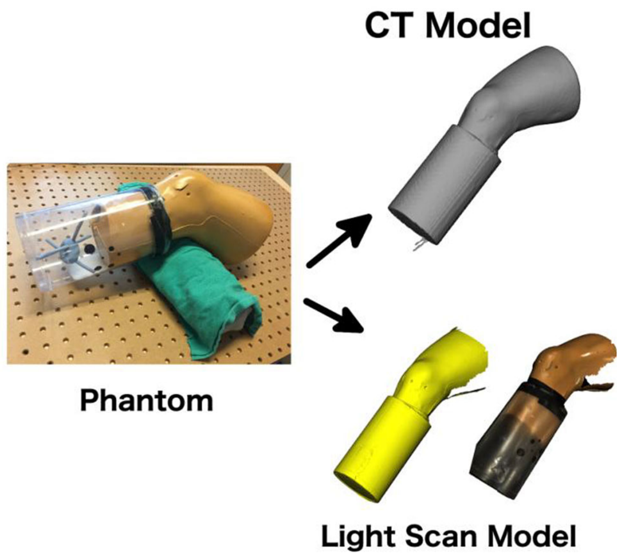

Fig. 1 Knee Phantom and CT and light-scan model of the phantom. Light-scan model contains the geometry information, as well as the texture information

During the trial, the phantom was positioned and 6 circular spots of different sizes were painted on the skin using a sterile marker. The marks created a non-linear pattern in the region of interest of the anatomy. A handheld structured light scanner (Artec Eva, Artec Group, Palo Alto, USA) was employed to capture the 3D surface geometry of the phantom, as well as the texture information (including the circular spots). The light scanned surfaces geometry was saved in a 3D isosurface model (Fig. 1). Furthermore, using the captured texture information, 3D coordinates of the center point for each circular spot were determined and saved in the light scan coordinate system in the order from the largest radius, to the smallest radius of the circular marks.

CT isosurface model of the anatomy was registered to the light scan model using a ICP algorithm and the coordinates of the biopsy target were transformed into the light scan coordinate system.

We captured a series of 2D images of the surgical side using the integrated camera of an iPad. Prior to image acquisition, intrinsic parameters of the camera were determined using a 9×6 checkerboard pattern.

Using a Hough Circle Transform, the 2D coordinates of the center as well as the radius of the circular marks in each image were automatically identified. The 2D centers were sorted from the largest radius to the smallest circular radius.

To determine the pose of the 3D phantom in relation to the iPad camera, the 3D coordinates of the circular spots in the light-scanner coordinate system were paired with the 2D coordinates of the same circular marks in the image. Using the intrinsic parameters of the camera as well as a pinhole camera model, a set of six equations were created with the unknown parameters for the 3D object position and orientation. An approximate solution for the set of parameters was determined using a Direct Linear Transform. This solution was refined with a Levenberg–Marquardt Optimization. With the 3D pose information for the phantom, the 3D coordinates for the biopsy target were projected into the image coordinate system using the pinhole camera model. The information of the biopsy target was then superimposed in the iPad image.

Results
In this preliminary feasibility study, we used a partly transparent phantom which allows a direct visualization of the region of interest (grey torus). Figure 2 shows one of the test images in which the region of interest is visible (in grey) and the center of the biopsy target (the center of the grey torus) was projected as a black cross onto the image. The augmented center point aligned with the visible region of interest.

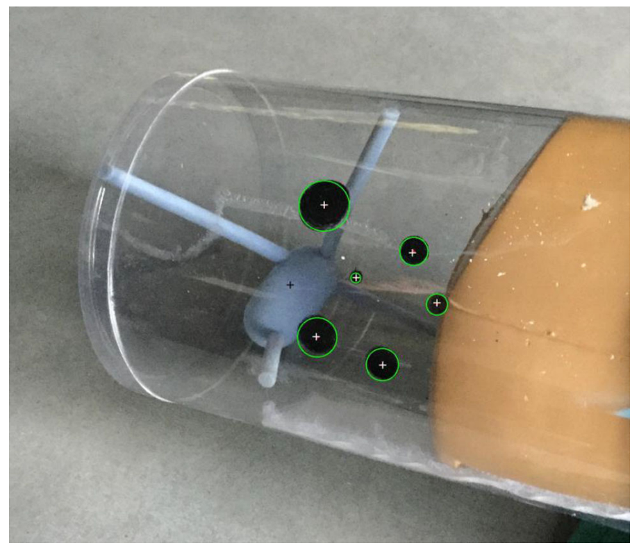

Fig. 2 Augmented iPad image. The green circles mark the result of the Hough Circle Transform. After the phantom pose was determined, the 3D circular spot centers from the light-scan model were projected onto the 2D image plane (white cross). The black cross marks the 2D coordinates of the projected target (center of the grey torus)

Conclusion
In this feasibility study, we registered a preoperative CT skin model to the intraoperative 3D light-scan skin model to transform planning data, such as tumour location and biopsy targets into the intraoperative light-scan coordinate system. Furthermore, we investigated if texture marks on an anatomy can provide registration features to match a 2D image of the anatomy to a 3D light-scan model of the anatomy. The successful two step registration procedure allowed us to use an conventional tablet as a navigation modality in which information from a preoperative CT scan can be augmented in real time onto the 2D image.

The application of a handheld structured light scanner to capture 3D texture and the surface geometry of the anatomy during the intervention, eliminates the need for any special preoperative imaging protocol, such as the additional requirement for external fiducials, etc.

Since the proposed method relies on a registration between two skin models we believe this system might be limited to applications in which the accuracy requirements are within the boundaries of the skin registration limitations. However, many biopsy applications might profit from this user-friendly and fast image-guidance by improving target accuracy and simultaneously reducing intraoperative radiation exposure.

Future studies are needed to determine the quantitative accuracy of the proposed method and to establish optimal augmentation of the CT information onto the 2D navigation image.

The research and implication on key technologies of haptic simulation in virtual bone drilling surgery

Z. Wang[1], T. Cheng[1], Y. Lin[1], H. Chen[1], Y. Zhang[1], W. Yuan[1]
[1]Shanghai Jiao Tong University, School of Mechanical Engineering, Shanghai, China

Keywords Virtual bone drilling surgery · Haptic simulation · Physics modeling of bone tissue · Fast collision detection

Purpose

The traditional method of training young orthopedic surgeons is inefficient and costly, which takes a long time to train in order to grasp the accurate operation feeling [1]. The virtual bone drilling surgical system based on force feedback can precisely simulate the feedback force in the process of drilling bone, provide new training method for young orthopedics with ease, efficiency and low cost. The most important thing in the virtual drilling training system is to accurately simulate the drilling force in the process of drilling the bone.

There are mainly three key technologies that affect the accuracy of the drilling force, namely: the drilling force prediction model, the physical modeling of bone tissue and the rapid collision detection algorithm. This paper mainly studies the bone tissue physics modeling and rapid collision detection algorithm.

Methods

In the material properties of bone tissue, bone mineral density value is the main factor affecting the size of the drill bone strength, so we need to establish the physical model of the bone tissue corresponding to the bone mineral density. Based on the relationship between the gray value and the density of bone tissue [2], the solid physical model of bone that is one-to-one corresponding to the CT scan bone tissue is established based on the voxel. An octree data structure is used to efficiently manage the voxel dataset, and then a fast collision detection algorithm is designed based on the octree data structure and node information.

According to the references paper we choice the drill direct, bone mineral density, drilling speed and feed rate of drilling as the variables using the drill bone empirical force prediction model to calculate the size of the feedback force [3], and then the drill bit is divided into multiple collision points and the direction of the force constraints to the drill on the discrete point [4].

Finally, based on the voxel processing algorithm and tool constraint algorithm after the collision detection time, a continuous and virtual drill bone stability force-haptic interaction and visual interaction are realized by using the dual-thread programming technology.

Results

Based on the above algorithm, a virtual drilling system was implemented, and force Dimension's Omega6 was used as a force feedback interaction tool to achieve a steady and continuous feedback simulation showed as Fig. 1.

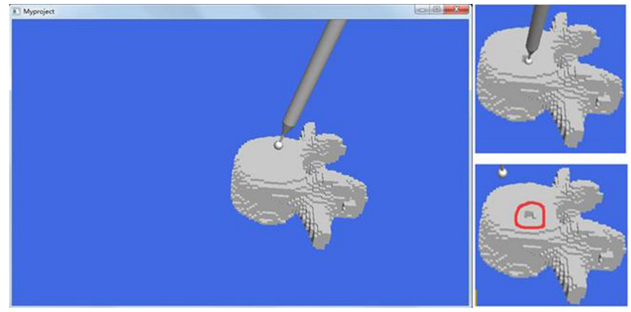

Fig. 1 Drilling bone interaction process

The physical model of bone tissue established in the system can fully express the bone material characteristics. During the operation, drilling different bone tissue layers can feel significant force difference and provide better bone strength tactile interaction, the force curve of the drill bone showed as Fig. 2.

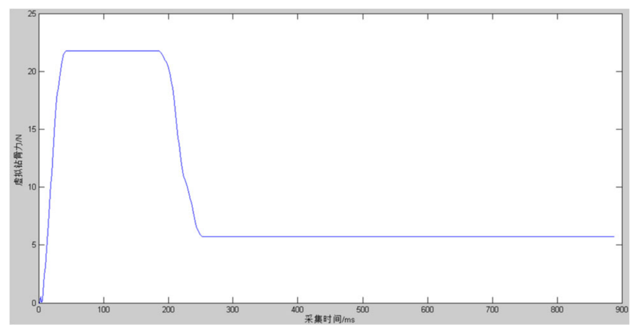

Fig. 2 Virtual drill bone feedback curve

Conclusion

On the one hand, due to the drilling force prediction model is not precise enough, on the other hand tools discrete collision point envelope is not complete, resulting in the accuracy of the force is not enough. However, the physical model and the collision detection algorithm of bone tissue can provide the basic algorithm support for the accurate force-haptic simulation based on the accurate drilling force prediction model.

References

[1] Salisbury K, Conti F, Barbagli F. Haptic rendering: introductory concepts [J]. IEEE Comput Graph Appl, 2004, 24(2): 24–32.

[2] Li D, Mao SS, Khazai B, Hyder JA, Allison M, McClelland R, de Boer I, Carr JJ, Criqui MH, Gao Y, Budoff MJ (2013) Noncontrast cardiac computed tomography image-based vertebral bone mineral density: the Multi-Ethnic Study of Atherosclerosis (MESA) [J]. Acad Radiol, 2013, 20(5): 621–627.

[3] Chi X, Niu Q, Thakker VS, Leu MC (2005) "Development of a Bone Drilling Simulation System With Force Feedback." ASME 2005 International Mechanical Engineering Congress and Exposition 2005: 83–89.

[4] Xing Q, Chen J, Li J, Moshirfar A, Theiss MM, Wei Q (2015) A real time haptic simulator of spine surgeries. ACM Symposium on Virtual Reality Software and Technology ACM, 2015: 121–124.

Finite element modeling and experimentation of lumbar vertebra drilling force

Z. Wang[1], Y. Lin[1], Y. Huang[1], H. Chen[2], Y. Zhang[2], W. Yuan[2]
[1]Shanghai Jiao Tong University, School of mechanical engineering, Shanghai, China
[2]Shanghai Changzheng Hospital, Shanghai, China

Keywords Force prediction model · Finite element analysis · Drilling of lumbar vertebra · Material properties of bone

Purpose

In recent years, the virtual surgery training system with force feedback has provided a new way for young doctors to improve their surgical skills. Precise drilling force of manipulation is crucial in the virtual surgery training, and the accurate simulation of bone drilling of lumbar vertebra depends on the establishment of accurate drilling force prediction model. Our study aims at establishing a 3D finite element (FE) model for the prediction of thrust force and torque during lumbar vertebra drilling operation. The model incorporates the dynamic characteristics involved in the drilling operation. Drilling thrust force and torque are obtained using FE analysis while the bone density, feed rate and spindle speed of the drill were changed.

Methods

In our study, a 3D lumbar vertebra model of a 30-year-old male patient was built from classical CT scans and MR images, and the segment T10 of lumbar vertebra was separated using 3D image segmentation software Mimics. Based on the 3D lumbar vertebra model, a 3D Lagrangian FE model including segment T10 of lumbar vertebra and medical twist drill was developed in FE software ABAQUS/Explicit. The bone model of lumbar vertebra consisted of 92,039 tetrahedral elements while the drill model consisted of 3609 tetrahedral elements. The material properties about the cortical bone were taken from the literature and a Johnson–cook model was adopted to describe the plastic behavior of the cortical bone [1]. Taking into account differences in cancellous bone material properties (density, elastic modulus, yield stress of the bone and so on), the cancellous bone FE model used the density obtained from CT scans and other material properties were defined according to the relationship between these properties and density, as mentioned in literature [2, 3]. The dynamic failure law was used to initiate and propagate the material failure. Contact between the drill and the bone was defined by surface-to-surface contact algorithm and friction coefficient was 0.7 [4]. Boundary conditions were used depending on the drilling of bone in the surgical operation. To validate the developed FE model of bone drilling, we carried out experimental measurements of thrust forces and torque for real bones of lumbar vertebra. The FE model and an experimental setup for measuring the thrust force and torque are shown in Fig. 1.

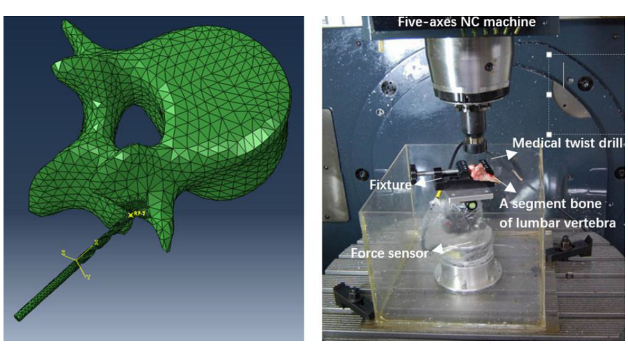

Fig. 1 *Left* FE model in ABAQUS. *Right* Experimental setup for measuring the thrust force and torque

Results

The FE analyses were carried out using these properties obtained from CT scans or their relationship to the bone density to predict the thrust force and torque. Figure 2 shows the FE data of thrust force in the segment bone of lumbar vertebra with different feed rates as well as the comparison of thrust force from FE model and experiment. Feed rate and spindle speed of the drill are the major parameters that are important to the drilling force. The obtained results indicate that both the thrust force and drill spindle speed increase with increasing feed rate and decreasing drill spindle speed. The thickness of the bone was about 5 cm so the bone was drilled through within a few seconds, and a higher feed rate of drill led to a shorter time of drilling. Beyond that, we find that drill feed rate is the most influential factor on the thrust force while drill spindle speed is the most influential factor on the torque in the drilling. Compared to experimental results, the FE model predict the drilling force with reasonable accuracy.

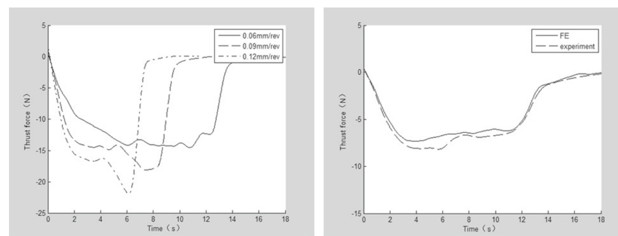

Fig. 2 *Left* The FE data of thrust force in the segment bone of lumbar vertebra with different feed rates at a spindle speed of 5000 rpm. *Right* Comparison of thrust force from FE model and experiment at a feed rate of 0.09 mm/rev and a spindle speed of 4000 rpm

Conclusion

A FE model was developed to predict the drilling force for material properties and various process parameters, such as feed rate (0.06–0.12 mm/rev) and spindle speed (3000–6000 rpm). The FE model was validated through the comparison with the experimental results. Based on the proposed FE model, drilling thrust force and torque during lumbar vertebra drilling operation can be predicted. In the future, we will further validate the FE model, which will take into account the thermal analysis in bone drilling and the material model will be more accurate.

References

[1] Alam K, Mitrofanov AV, Silberschmidt VV. (2009) Finite element analysis of forces of plane cutting of cortical bone [J]. Comp Mater Sci, 2009, 46(3): 738–743
[2] Garo A, Arnoux PJ, Wagnac E, Aubin CE. Calibration of the mechanical properties in a finite element model of a lumbar vertebra under dynamic compression up to failure. Med Biol Eng Comput, 2011, 49: 1371–1379
[3] Helgason B, Perilli E, Schileo E, Taddei F, Brynjólfsson S, Viceconti M (2008) Mathematical relationships between bone density and mechanical properties: A literature review. Clin Biomech, 2008, 23: 135–146
[4] Lughmani WA, Bouazza-Marouf K, Ashcroft I. (2013) Finite element modeling and experimentation of bone drilling forces [C]//IOP. International symposium on dynamic deformation and fracture of advanced materials. Loughborough: IOP, 2013, 451: 012034.

Novel application for prostate cancer localization based on magnetic resonance elastography and haptics

E. Tagliabue[1,2,3], C. Luciano[2], P. Fiorini[3], E. De Momi[1]
[1]Politecnico di Milano, Dept. of Electronics, Information and Bioengineering, Milan, Italy
[2]University of Illinois at Chicago, Dept. of Bioengineering and Urology, Chicago (IL), USA
[3]University of Verona, Dept. of Computer Science, Verona, Italy

Keywords Prostate cancer localization · Haptics rendering · Magnetic resonance elastography · Virtual palpation system

Purpose

One of the main shortcomings of current clinical procedures for early prostate cancer diagnosis is their inability to precisely identify tumor site. Prostate tumors, which are harder than the surrounding healthy tissues, can be identified by Magnetic Resonance Elastography (MRE), an innovative technique that images the 3D tissue stiffness distribution [1]. In this work, we propose an application where visualization of the 3D MRE prostate volume is complemented with haptic feedback. The force feedback relies directly on MRE data and aims at facilitating tumor masses detection within the volume. The goal of the work is to investigate if the tactile feedback is able to improve the localization accuracy, based on the idea that integration between more sensory modalities can enhance the information content [2]. By enabling a more accurate and faster localization of prostate cancer region, the proposed methodology could serve as a non-invasive complementary tool to improve prostate cancer diagnostic process.

Methods

A volumetric model of the gland tissue is obtained by a Magnetic Resonance Elastography, where hard masses (tumors) as well as soft (healthy) tissue are rendered according to a color code. Haptic cues are added to the simulation to support and strengthen the visual cues, and they are aimed to exaggerate the tactile feedback obtained with real prostates, in order to facilitate the identification of tumor masses within the volume. The implemented haptic feedback directly relies on the intrinsic stiffness information provided by MRE images. The proposed method overcomes the other approaches for haptic feedback modelling from elastographic data since it allows to obtain a patient-specific haptic simulation of the whole 3D anatomy, requiring neither the meshing of the volume nor the tuning of mechanical parameters [3], [4]. The total force provided to the user is computed as sum of several contributions: $\boldsymbol{F}_{total}(\boldsymbol{x}_{tip}, t) = \boldsymbol{F}_{volume}(\boldsymbol{x}_{tip}, t) + \boldsymbol{F}_{friction}(t) + \boldsymbol{F}_{damping}(t) + \boldsymbol{F}_{gravity}$, where $\boldsymbol{x}_{tip}$ is the current position of the haptic device, and t represents time. The main contribution to the force $\boldsymbol{F}_{total}$ is provided by the elasticity-dependent force $\boldsymbol{F}_{volume}$, which takes into account both the local stiffness at the cursor tip and the one of the surrounding voxels ($|\boldsymbol{F}_{volume}(\boldsymbol{x}_{tip}, t)| = F_{local}(\boldsymbol{x}_{tip}, t) + F_{surrounding}(\boldsymbol{x}_{tip}, t)$) to obtain a complete representation of volume data by force sensation. Its direction is defined by the device direction of motion. The contribution of local elasticity $\boldsymbol{F}_{local}$ is linearly dependent on the MRE value at the cursor tip ($\boldsymbol{x}_{tip}$) at current time (t), normalized on the maximum MRE value of the considered elastogram. Elasticity of neighboring voxels contributes to the $\boldsymbol{F}_{volume}$ through data gradient in x, y, z coordinates, exploited to obtain the directional derivative at the device position ($\boldsymbol{x}_{tip}$) in the direction in which the device is moving. This contribution is proportional to the extent at which voxel values are changing at the current position in the device direction of motion. In addition to the volume force, friction $\boldsymbol{F}_{friction}$, damping $\boldsymbol{F}_{damping}$ and gravity compensation $\boldsymbol{F}_{gravity}$ contributions are added and empirically set to constant values, to guarantee a perfect trade-off between instability minimization and natural feedback delivery. Experiments were conducted to investigate the role played by the haptic feedback to locate hard masses. The system used for the experiments is shown in Fig. 1. It is composed of a Windows-based workstation (with a NVIDIA TITAN Xp graphics card) and a 3D Systems Touch haptic device. The MRE dataset available comes from excised prostates of patients who underwent radical prostatectomy at University of Illinois at Chicago hospital. Specimens were scanned with a modified 9.4 T ultra-high field pre-clinical scanner, employing the phase constant SLIM-MRE method. We recruited 15 participants, who were asked to explore prostate anatomies through the simulator and place the cursor inside all the hard masses, without and with the help of haptic feedback. We compared localization accuracy in visual-only and visuo-haptic modalities by computing two main parameters. The first one is a percentage accuracy *ACC %*, defined as ratio between the number of high stiffness areas correctly targeted by the user and the total number of positions selected by the same user. The second parameter is the ratio between the percentage accuracy *ACC %* and the percentage time spent in each modality (visual or visuo-haptic). This parameter (called *AT ratio*) increases with increasing accuracy and decreasing time, with the most desirable situation being high accuracy in a small amount of time.

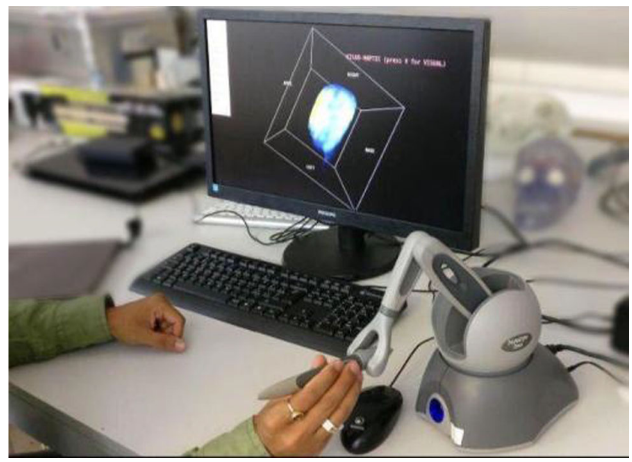

Fig. 1 A participant while testing the application. The monitor is rendering the MRE volume and the graphic cursor, whose movements are mapped to those of the 3D systems touch haptic device

Results

ACC % significantly improved when forces were active, passing from a median value of 0.35 (interquartile range = 0–0.75) in visual mode to 0.83 (interquartile range = 0.28–1) in visuo-haptic mode (sign test, 5% significance level). A statistically significant difference between the two conditions was found also when considering the *AT ratio*, whose values (median and interquartile range) were 0.20 (0–0.43) and 0.53 (0.15–0.64) respectively (sign test, p value < 0.05).

Conclusion

Experimental outcomes demonstrate that participants were able to locate stiff regions with greater accuracy and in a smaller amount of time when forces were active. By complementing a 3D model of the prostate based on MRE with haptic feedback, the proposed method allows for a precise and fast localization of damaged areas. Therefore, it has promising prospects to improve prostate cancer diagnostic process and pre-surgical planning phase.

Acknowledgements

This research is partially funded by the Italian Ministry of International Affairs and Cooperation as a “Progetto di Grande Rilevanza” of the cooperation between USA and Italy.

References

[1] Good DW, Stewart GD, Hammer S, Scanlan P, Shu W, Phipps S, Reuben R, McNeill AS (2014) Elasticity as a biomarker for

prostate cancer: a systematic review. BJU international 113(4): 523–534
[2] Ernst MO, Bulthoff HH (2004) Merging the senses into a robust percept. Trends in cognitive sciences 8(4): 162–169
[3] Li BN, Shan X, Qin J, Huang W, An N (2013) Senseviewer: A unified rendering interface of visual and haptic cues in medical images. In: Robotics and Biomimetics (ROBIO), 2013 IEEE International Conference on, IEEE, pp 2209–2212
[4] Suzuki S, Hamamoto K (2016) Haptic rendering for a virtual palpation system. Electronics and Communications in Japan 99(5): 27–36

Virtual reality in the pre-operative planning and training for oncological treatment using MentorEye system: preliminary results

M. Żuk[1], M. Majak[1], G. Dębowski[1], E. Świątek-Najwer[1], M. Popek[1], P. Pietruski[2], J. Jaworowski[2]
[1]Wroclaw University of Science and Technology, Faculty of Mechanical Engineering, Wroclaw, Poland
[2]Medical University of Warsaw, Warsaw, Poland

Keywords Virtual reality · Preoperative planning · Medical training · Computed aided surgery

Purpose
The main purpose of this work was to develop virtual-reality module for MentorEye system which is a complex computer aided surgery system supporting planning and aiding oncological treatment [1]. Developed system fuses few imaging modalities such as: CT, MRI DICOM formats and intraoperative fluorescence images. Complex oncological treatment is divided into few crucial steps: virtual planning, real surgery and validation phase. Currently, greater attention is devoted to the preoperative stage where personalized virtual plan is created according to the current patient's state. What is more, huge technology advancement in virtual and augmented reality area raises promising potential for improving virtual medical visualization [2–3].

In this work, we present possible applications of zSpace and HTC Vive devices used in MentorEye system. These devices were selected to accomplish two main goals. Firstly, zSpace enriches virtual planning for both biopsy trajectory and resection plane definitions. Secondly, HTC Vive system is used for different surgery scenario simulations.

Methods
For virtual planning, we have applied 3D virtual reality zSpace 200 display. It sequentially presents left and right buffers with the refresh rate equal to 120 Hz. zSpace offers user friendly 3D model interaction and manipulation using stylus tool. Moreover, this device is equipped with tracked oculars which enables the user to look at virtual objects from different perspective and locations. We have adjusted zSpace API into our system, while virtual object presentation was done by OpenGL.

Fully immersive virtual reality system HTC Vive has been used. System consists of headset, two base stations for tracking and two controllers. Tracking system (IMU and IR Laser tracking) covers 360° in area of 5 meters. Tracked controllers provide also haptic feedback. Applied virtual reality system enables natural moving in fully immersive, self-designed virtual environments together with interaction with 3D virtual objects, including simple haptic feedback. Unity engine handles physical simulations and scene generation. Different anatomical models were placed in the virtual scene: models from open libraries, anatomical models reconstructed from DICOMs and models from surface 3D scanner (Artec Space Spider).

Results
In our previous works [4–5], we described base virtual planning on 2D DICOM projections and 3D virtual model preview. Main difficulties were related to resection with proper margin definitions. Currently, zSpace is used for planning biopsy trajectories, and for cutting plane definition after resection area segmentation (Fig. 1). When biopsy is planned, it is very important to properly define entry and biopsy collection points ensuring that a needle does not cross any nerve or blood vessels. Stylus tool can be used for 3D virtual objects manipulation together with biopsy plan definition. Additionally, navigated oculars enable to observe various 3D anatomical structures from different perspectives. Another application of zSpace is involved with cutting planes definition after resection planning. This step is divided into two stages. Firstly, qualified user is responsible for manual (or semi-automatic) tumour segmentation. Tumours located in the maxillofacial area are very specific and in many cases irregular causing problems with proper resection in the operating environment, especially when surgical oscillating saw is used. Due to these constraints, MentorEye supports an additional step for virtual plane definition with proper safety margins. The user can observe 3D skull together with reconstructed tumour model and can define trajectory for virtual cutting planes using stylus tool. Additionally, since resection margins are described by 3D plane, we can navigate surgical saw using optical navigation system and compare its transformation with planned resection planes during real surgery.

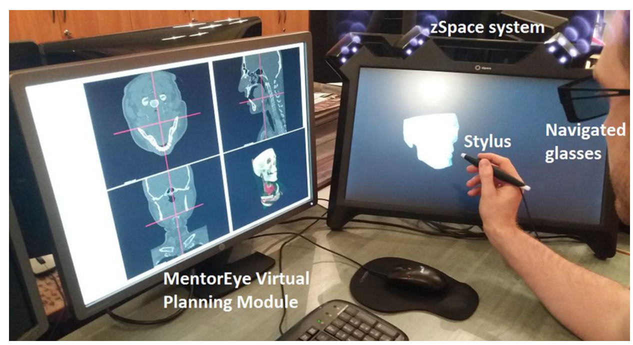

Fig. 1 Virtual planning in MentorEye system

Preliminary developed fully immersive application for HTC Vive enables moving around basically furnished operating room equipped with surgical tools (Fig. 2). Several anatomical models are placed in the scene. Initial module's usability and comfortability was confirmed by test performed on 10 users. Further development of this tool could include faithful reconstruction of the operating theatre equipped with devices built-in MentorEye as: NIR fluorescence system, augmented reality glasses, optical navigations system and detailed surgical instrumentation, as well as presentation and training of surgical procedures developed in cooperation with surgeons working on MentorEye system [1].

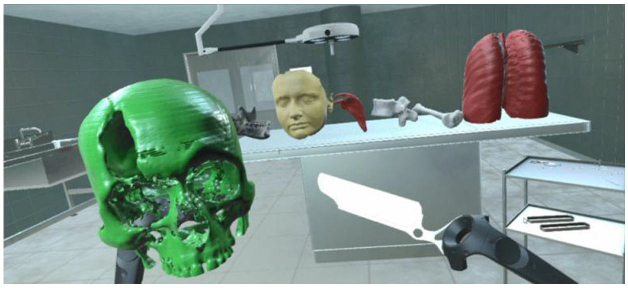

Fig. 2 Preliminary operating room visualisation using virtual reality headset

Conclusion

Either 3D interactive displays or fully immersive virtual reality headset are affordable, versatile and sufficiently developed virtual reality tools, which can be successfully applied in the preoperative planning and medical trainings. In this paper, we have shown general concept of their application in MentorEye system, applied tools and methods together with preliminary results.

Acknowledgements

The work is supported by National Centre of Research and Development in Poland, in frames of the project: "Development of Polish complementary system of molecular surgical navigation for tumor treatment", STRATEGMED1/233624/4/NCBR/201

References

[1] Świątek-Najwer E, Majak M, Zuk M, Popek M, Kulas Z, Jaworowski J, Pietruski P (2017) The new computer and fluorescence-guided system for planning and aiding oncological treatment. J CARS 12 (Suppl 1): S1–S286

[2] Egger J, Gall M, Wallner J, Boechat P, Hann A, Li X, Chen X, Schmalstieg D (2017) HTC Vive MeVisLab integration via OpenVR for medical applications. PLOS ONE 12(3): e0173972

[3] Cutolo F, Meola A, Carbone M, Sinceri S, Cagnazzo F, Denaro E, Eposito n, Ferrari M, Ferrari V (2017) A new head-mounted display-based augmented reality system in neurosurgical oncology: a study on phantom. Computer Assisted Surgery 22(1): 39–53

[4] Pietruski P, Majak M, Świątek-Najwer E, M. Popek M, Jaworowski J, Żuk M, Nowakowski F (2015) Image-guided bone resection as a prospective alternative to cutting templates-a preliminary study. Journal of Cranio-Maxillofacial Surgery 43(7): 1021–1027

[5] Pietruski P, Majak M, Świątek-Najwer E, Popek M, Szram D, Żuk M, Jaworowski J (2016) Accuracy of experimental mandibular osteotomy using the image–guided sagittal saw. International Journal of Oral and Maxillofacial Surgery. 45(6): 793–800

Poster Session

20th International Workshop on Computer-Aided Diagnosis and Artificial Intelligence

Creation of artificial microcalcifications for MMG and verification of effectiveness of CAD development technique that uses no actual cases

K. Abe[1], H. Takeo[1], Y. NAGAI[2], Y. Kuroki[3], S. Nawano[4]
[1]Kanagawa Institute of Technology, Electrical and Electronic Engineering, Atsugi, Kanagawa, Japan
[2]National Cancer Center Hospital East, Kashiwa, Chiba, Japan
[3]Niimura Hospital, Radiology, Kagoshima, Japan
[4]International University of Health and Welfare, Mita Hospital, Tokyo, Japan

Keywords Artificial calcification · CAD development · Microcalcification · Machine learning

Purpose

CAD system development is complicated by a shortage of case images [1]. To compensate for this, efforts are underway to artificially create case images by embedding tumors and other such lesions into lesion-free images. Previously, the authors have demonstrated the effectiveness of creating artificial case images for hepatic and breast tumors and utilizing them in CAD development.

In this study, a CAD development technique using training data comprising 100% artificial cases (that is, no actual cases) is proposed. In addition, this proposal focuses on a new target: breast cancer calcifications. Because calcifications appear in image signals as pulses, compared to past hepatic tumors and the like, their features are easily computed. Also, as opposed to tumor shadows, the original lesion shape information is easy to derive in embedding. These factors suggest that even with 100% artificial cases, detection performance equal to that previously attained can be expected.

Methods

(1) Creating artificial case images

It was determined to create artificial case images using a technique comprising extraction of calcifications from actual cases and the embedding of such calcifications. General process of calcification embedding are shown in Fig. 1. Calcifications to be embedded were first subjected to coarse extraction that was based on threshold value processing. Precision of calcification region extraction was maximized by performing regional expansion while calculating the density gradient based on pixel values from the course extraction. By inculcating not only calcification bright spots, but also surrounding field information, this process makes it possible to create artificial cases having the characteristics of actual cases.

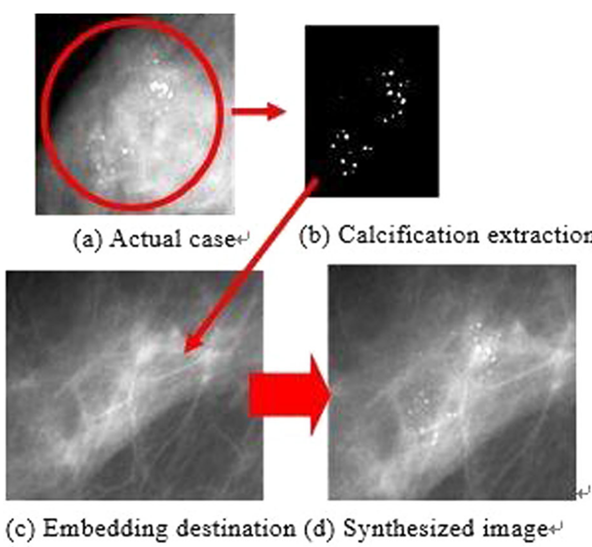

Fig. 1 General process of calcification embedding

(2) Creating breast cancer calcification CAD

Basically, because pulse-shaped projections are smoothed by ordinary smoothing processing, calcification candidate regions can be detected by obtaining the difference between this and the original image.[2] However, with simple smoothing, such linear shadows as mammary glands are also detected, so morphology using line structuring elements is used to limit detection to only point-shaped pulse elements.

(3) Creating an SVM discriminator

A discriminator created using an SVM was used to determine whether or not there was false detection of calcifications among the calcification candidate regions extracted as discussed in section (2). Actual cases for learning and artificial cases created for learning were extracted using candidate region extraction processing, and their features were computed.

Results

Table 1 shows the results of detection for the two cases of learning using exclusively artificial cases and learning using exclusively actual cases. Machine learning used 50 TP cases and 50 FP cases for each discriminator, totaling 100 cases per discriminator. The results in Table 1 show that both learning methods yielded a TP rate of over 90% and a number of FP objects per image of 0.30 or less. In context of current calcification detection CAD detection rates in the high 90 percents, these results indicate that discriminator performance remains unsatisfactory. However, they also affirm that discriminators trained with artificial images can achieve detection equal to that of discriminators trained with actual images.

Table 1 Calcification detection results

CAD learning method	TP rate (%)	FP (objects/image)
Only actual cases used	91	0.3
Only artificial cases used	93	0.28

Figure 2 shows FROC curves for detection performance. These curves are also verification that equal detection performance from both discriminators can be obtained.

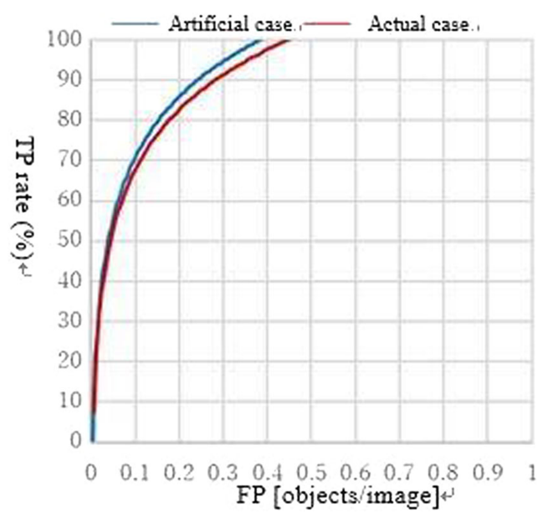

Fig. 2 FROC curve for detection performance

Conclusion

In this study, breast cancer calcifications were applied to detection CAD as a new site for the application of artificial case images. Additionally, as opposed to the previous hepatic and breast cancer tumors studies, CAD development using exclusively artificial cases for training was conducted for a performance comparison with CAD designed using only actual cases for training. The results verified that it is possible to develop CAD using exclusively artificial images for training that has performance equal to that of CAD developed using only actual images for training.

References

[1] Kitasaka T. 5th JAMIT CAD Contest Results Report, 2014, JAMIT News Letter, No. 16, pp. 5–11

[2] Takeo H, Shimura K, Imamura T, Shimizu A, Kobatake H Detection system of Clustered Microcalcifications on CR Mammogram, IEICE TRANS. INF. & SYST., Vol. E88-D, No. 11, pp. 2591–2601, 2005

Automatic differentiation cystic and solid breast lesions at ultrasonic images

I. Egoshin[1], D. Pasynkov[2], A. Kolchev[3], I. Kliouchkin[4], O. Pasynkova[5]

[1]Mari State University, Applied mathematics and informatics, Yoshkar-Ola, Russian Federation

[2]Oncology Clinic of Mari El Republic, Radiology, Yoshkar-Ola, Russian Federation

[3]Kazan Federal University, Yoshkar-Ola, Russian Federation

[4]Kazan State Medical University, General Surgery, Kazan, Russian Federation

[5]Mari State University, Ecology, Yoshkar-Ola, Russian Federation

Keywords Breast · Lesion · Ultrasonography · Image processing

Purpose

Cysts are fluid-filled cavities that in most cases require no future diagnostic work-up. In most cases typical simple breast cysts are easily recognized at ultrasonography due to specific visual characteristics. They have well-defined contour, round or oval shape, homogenous anechoic signal (no internal echoes), thin wall and posterior acoustic enhancement. The specificity of this method for typical cysts reaches 98%, and it is usually considered as a gold standard for their diagnosis [1]. However it is necessary to have all the given above features to conclude the typical cyst. At the same time not every breast cyst is typical. It is especially characteristic for protein (including blood) contained cysts that may have significant internal echoes mimicking the solid component. These masses can be defined as complex cysts. They appear in about 5% of all breast ultrasound examinations [2] and the malignancy rate of such lesions is about 23–31% [3, 4]. On the other hand, some solid lesions (composed of soft tissue, including malignant) may have cystic appearance at ultrasound and may be falsely accepted as cysts (Fig. 1) [5]. Moreover, such difficult to distinguish cases usually require biopsy. Therefore we tried to develop the automatic method of cystic and solid breast lesions differentiation.

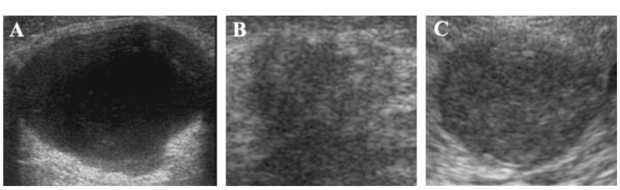

Fig. 1 **A** Typical cyst; **B** solid lesion with irregular margin; **C** atypical cyst

Methods

The input data were the ultrasound digital images with the 256-gradations of gray color (the following ultrasound systems were used: Medison SA8000SE, Siemens X150, Esaote MyLab C). Characterisation of the lesion on these images was performed in two steps. On the first one the region of interest (or contour of lesion) was searched and segmented. Segmentation of such region was carried out by means of the sigmoid filter where the threshold is calculated according to the empirical distribution function of the image brightness and, if necessary, it was corrected according to the average brightness of the image points which have the highest gradient of brightness. Manual segmentation was also possible when necessary. At the second step the identification of the selected region to one of lesion groups based on its statistical characteristics of brightness distribution was made. We tested more than 70 such characteristics based on the pixel brightness values and their derivatives: set of absolute value of gradients, set of gradient directions, histogram of pixel brightness values etc. Moreover, the characteristics were also calculated for separate parts of the selected region, directed from the center of the region to its boundary. Among the whole set of tested characteristics we selected only 10 of them with the least intercorrelation coefficients and greater association with the cyst. The following characteristics were selected: entropy, coefficients of the linear and polynomial regression, quantiles of different orders, average gradient of brightness etc. For determination of decisive criterion of belonging the lesion to one of the groups (cystic or solid) the training set of these brightness distribution characteristics separately for both groups of lesions were used. To test our approach we used a set of 217 ultrasonic images of 107 cystic (including 53 atypical, difficult for bare eye differentiation) and 110 solid lesions. All lesions were cytologically and/or histologically confirmed. Visual identification was performed by trained specialist in breast ultrasonography.

Results

Our system correctly distinguished all (107, 100%) typical cysts, 107 of 110 (97.3%) solid lesions and 50 of 53 (94.3%) atypical cysts. On the contrary, with the bare eye it was possible to identify correctly all (107, 100%) typical cysts, 96 of 110 (87.3%) solid lesions and 32 of 53 (60.4%) atypical cysts. The corresponding overall specificity values were 98% and 87%.

Conclusion

Automatic approach surpasses the visual assessment performed by trained specialist. The difference is especially large for atypical cysts and hypoechoic solid lesions with clear margin. This data may have a clinical significance.

References

[1] Gokhale S. (2009). Ultrasound characterization of breast masses. The Indian Journal of Radiology and Imaging. 19(3): 242–247.

[2] Houssami N., Irwig L., Ung O. (2005). Review of complex breast cysts: implications for cancer detection and clinical practice. ANZ J Surg. 75(12): 1080–1085.

[3] Berg WA, Campassi CI, Ioffe OB. (2003). Cystic lesions of the breast: sonographic-pathologic correlation. Radiology. 227(1): 183–191.

[4] Doshi DJ, March DE, Coughlin BF, Crisi GM. (2006). Accuracy of ultrasound-guided percutaneous biopsy of complex cystic breast masses (abstract). In: Radiological Society of North America scientific assembly and annual meeting program. Oak Brook, ILL: Radiological Society of North America. 655.

[5] Hines N., Slanetz P.J., Eisenberg R.L. (2010). Cystic Masses of the Breast. American Journal of Roentgenology. 194(2): 122–133.

Automated mass detection on digital breast tomosynthesis images using deep learning based localization methods

J. W. Jeong[1], S. H. Chae[1], E. Y. Chae[2], H. H. Kim[2], Y. W. Choi[3], S. Lee[1]
[1]ETRI, Bio-Medical IT Convergence Research Division, Daejeon, South Korea
[2]Asan Medical Center, Seoul, South Korea
[3]Korea Electrotechnology Research Institute, Ansan, South Korea

Keywords Digital breast tomosynthesis · Deep learning · Computer assisted detection · Object localization

Purpose
An automated computer-aided detection (CADe) system for breast masses in three-dimensionally reconstructed digital breast tomosynthesis (DBT) [1] using several deep convolutional neural network (DCNN) based object localization models [2, 3] is proposed. Our framework involves only DCNN-based object localization algorithms to detect region of interest (ROI) containing breast mass. We obtained the False-Positive (FP) rate to be 2.99 per DBT image volume with a sensitivity of up to 91.4% after training two typical DCNN-based models.

Methods
The DBT scans were collected at the Asan Medical Center (Seoul, Korea). An experienced radiologist diagnosed 181 breast masses on the 393 DBT image volumes of 200 breasts. To construct the dataset for the input data of DCNN-based model training, 4367 images were extracted from every 10 slices of the three-dimensional DBT image volumes for the two-dimensional object localization process. The extracted images were againg partitioned 3:1:1 for training, validating, and testing the models. The test subset were used for CAD performance evaluation. The breast mass in each slice was marked by an experienced radiologist with a two-dimensional bounding box as reference standard. For the data augmentation, the input images were randomly distorted photo-metrically, cropped, shifted, flipped horizontally and vertically. All the images were resized 300 × 300 and 416 × 416, respectively to train the DCNN-based network models.

Then, we performed a mass detection step to localize two-dimensional mass candidate ROIs (Region of Interests) using several DCNN-based mass detection systems currently available. In this study, we used the well-known Single Shot MultiBox Detector (SSD) [2] and YOLO (You Only Look Once) [3] models for the localization of breast masses with no modification on the network architectures.

The snapshots of the training models at the minimum validation loss was evaluated to obtain free-response receiver-operating characteristics (FROC) curve. The detection accuracy of our mass detection system based on the DCNN-based object localization algorithms was discussed and compared with the previous results.

Results
Firstly, the SSD model [2] trained on our DBT image data was applied for the breast mass detection, giving the FP rate of 1.49 at 79.3% and 2.99 at 91.4% sensitivity as shown in Fig. 1. Considering that our detection system adapts a DCNN-based object localization algorithm only, we hope to note that those results are in accordance with other researches [4, 5] in this preliminary study, showing the promising results for the clinical use. The another detection system using the YOLO model [3] revealed the similar results of the FP rate of 1.78 at 81.0% and 2.93 at 87.9% sensitivity with those of the SSD model.

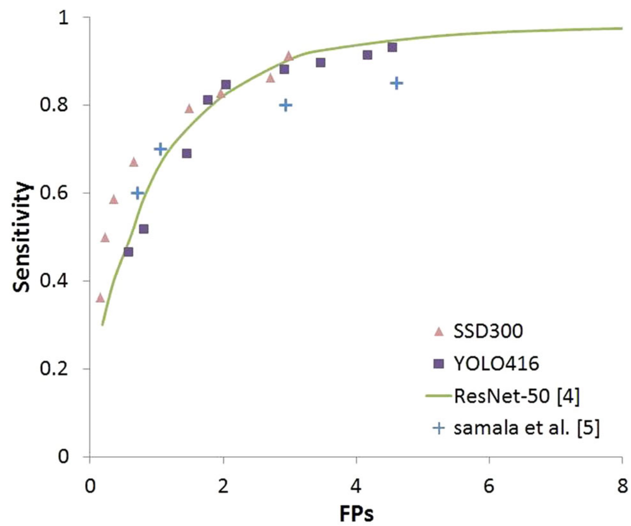

Fig. 1 A FROC curve for our breast mass detection system using SSD [2] and YOLO [3] object localization algorithms. The solid triangles and solid squares are for the detection results using SSD and YOLO models, respectively. A solid line is for the calculational results of our previous detection scheme using a three-dimensional Hough-transform-based mass candidate detection combined with FP screening with ResNet-50 DCNN model [4]. The crosses are for the previous calculational results with the DCNN model [5]

In this preliminary study, we focused on the possibility of constructing the relatively simple detection process using only DCNN-based object localization algorithm without preceeding prescreening and FP-reduction processes [4]. We hope to note that our framework is a fully automated DCNN-based approach with no additional auxiliary bounding box localization algorithm because the typical execution of the testing process using graphics processing unit (GPU) is quite fast in spite of the relatively long training time, enabling the diagnosis of the DBT image volumes in real time.

In the future study, its effect on the detection accuracy on a larger data set and the more finetuned DCNN models will be reported later.

Conclusion
A fully automated breast mass detection system in DBT images using several DCNN-based object localization methods is constructed and compared with the previous algorithms, implying that it may be possible in the near future that a fully DCNN-based and real-time second observer system assists radiologists in breast mass screening.

References
[1] Chan H-P, Wei J, Sahiner B, Rafferty EA, Wu T, Roubidoux MA, Moore RH, Kopans DB, Hadjiiski LM, Helvie MA (2005) Computer-aided detection system for breast masses on digital tomosynthesis mammograms—Preliminary experience, Radiology 237, 1075–1080
[2] Liu W, Anguelov D, Erhan D, Szegedy C, Reed S, Fu C-Y, Berg AC (2016) SSD: Single Shot MultiBox Detector, in European conference on computer vision, pp. 21–37, Springer, Cham
[3] Redmon J, Farhadi A (2016) YOLO9000: better, faster, stronger. arXiv preprint arXiv:1612.08242
[4] Jeong J-W, Chae S–H, Cho YL, Chae EY, Kim HH, Choi Y-W, Lee S (2017) A Deep Convolutional Neural Network Based False Positive Reduction in Mass Detection Algorithm on Digital Breast Tomosynthesis Images. Computer Assisted Radiology and Surgery (2017).
[5] Samala RK, Chan HP, Hadjiiski L, Helvie MA, Wei J, Cha K (2016) Mass detection in digital breast tomosynthesis: Deep

convolutional neural network with transfer learning from mammography, Medical Physics, vol. 43, no. 12, pp. 6654–6666

Application of convolutional neural networks for computer-aided diagnosis and treatment planning in oncology

S. Pröll[1], E. Tappeiner[1], M. Netzer[2], A. L. Simpson[3], J. Chakraborty[3], R. Schubert[1], K. D. Fritscher[1]
[1]UMIT—Private University for Health Sciences, Medical Informatics and Technology GmbH, Institute for Biomedical Image Analysis, Hall in Tirol, Austria
[2]UMIT—Private University for Health Sciences, Medical Informatics and Technology GmbH, Institute of Electrical and Biomedical Engineering, Hall in Tirol, Austria
[3]Memorial Sloan Kettering Cancer Center, Department of Surgery, New York, United States

Keywords Deep learning · Oncology · Texture analysis · Computer-aided diagnosis

Purpose

The increasing number of cancer patients worldwide and the rising costs in healthcare motivate the development of further methodological improvements to prevention, detection and treatment in clinical oncology. Early detection is crucial for a successful treatment of most cancers. Hence, computer-assisted methods are increasingly important for the detection and diagnosis of cancer.

This project explores the utilization of convolutional neural networks (CNNs) for computer-aided diagnosis (CAD) in oncological applications. A CNN is a machine learning method that transforms a high-dimensional input into a lower-dimensional representation of abstract features. This is achieved by a sequence of convolution and pooling operations, where the weights of the filter kernels are trained on sample data. We examine two distinct oncological applications. The first CAD task is concerned with the classification of benign and malignant breast tumors in digital mammograms. The second application is the prediction of hepatic disease-free survival (HDFS) after resection of colorectal liver metastases (CRLMs). For both CAD tasks, the performance of CNNs and radiomics-based methods is evaluated and compared.

Methods

In a series of experiments, different CNN architectures have been implemented and trained on task-specific datasets. For breast tumor classification, a subset of the CBIS-DDSM [1] consisting of 1151 digital mammographies have been used. Based on the provided mass segmentations, regions of interest (ROIs) around each tumor with a fixed size have been extracted and resampled to a lower resolution. 951 of the resulting images have been used to train four differently structured networks (ResNet-50 [2], Inception-v3 [3] and two custom configurations). The ResNet-50 and Inception-v3 models have also been initialized with weights pretrained on non-medical images. The remaining 200 images have been used as a held-out test set.

For HDFS prediction, 121 contrast-enhanced CT images of the liver have been taken from the MICCAI CPM Challenge training set (http://miccai.cloudapp.net/competitions/58). Using the provided segmentations, ROIs have been extracted both around the entire liver tissue and around the primary metastasis. Various combinations of physical ROI sizes and spatial resolutions have been tested. In different experiments networks have been given ROIs extracted either around the entire liver or the tumor and classify patients based on a HDFS threshold. Two CNN architectures have been trained from scratch as the 3D nature of the CT images prohibits the usage of pretrained models.

The training procedure was similar for both tasks. A rudimentary grid-search has been applied to find the best configuration of learning rate and L2 regularization. 5-fold cross validation has been used to achieve more conclusive results. During training, on-line data augmentation has been applied by means of random rotations and cropping.

Results

In breast tumor classification, an Inception-v3 model pretrained on non-medical images achieves a cross-validated accuracy of 74% when evaluating either the cranio-caudal or mediolateral oblique view of a single patient. Figure 1 shows the performance of the ResNet-50 and the Inception-v3 models with and without pretrained weights. The results are shown for different learning rates. Since both cranio-caudal and mediolateral oblique views are available for most patients, the predictions for both views can be combined into a more robust classifier. In two-view evaluation, the best model (ResNet-50) achieves a held-out test accuracy of 84%. Additionally, by combining the predictions for multiple crops, the test accuracy can further be improved to 85%. This performance is comparable with other state-of-the-art solutions based on either deep learning or radiomics [4, 5]. In all experiments, pretrained models outperform models trained from scratch.

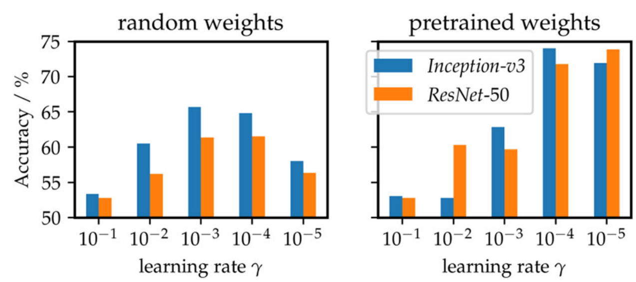

Fig. 1 5-fold cross-validated performance of ResNet-50 and Inception-v3 models with both random and pretrained weights for different learning rates and single-view evaluation. Pretrained networks significantly outperform networks trained from scratch

For the prediction of HDFS, no functional CNN model has been found. A number of different hyper-parameter settings has been tested, with every setting yielding similarly unsatisfactory results (55–60% accuracy). Similar results have been obtained with a feature-based approach.

Conclusion

CNNs achieve state-of-the-art performance in breast tumor classification, while rather poor results have been obtained in HDFS prediction. This could be attributed to a number of aspects. Firstly, the small dataset size and high variability in liver CT images pose a big challenge to data-driven classification approaches. Secondly, 3D-CNNs require substantially more processing power and memory capacity, limiting size and resolution of the input images. Finally, HDFS prediction is an arguably more challenging problem compared to breast tumor classification, as more clinical factors contribute to disease-free survival than are visible in a CT image. Although no exhaustive evaluation of hyper-parameters and model architectures has been performed, the results show the high potential for deep learning methods to further improve CAD tools for diagnosis and treatment planning of cancer.

References

[1] Sawyer R, Gimenez F, Hoogi A, Rubin D (2016) Curated Breast Imaging Subset of DDSM. The Cancer Imaging Archive (https://doi.org/10.7937/k9/tcia.2016.7o02s9cy)
[2] He K, Zhang X, Ren S, Sun J (2015) Deep residual learning for image recognition. ArXiv preprint: 1506.01497

[3] Szegedy C, Vanhoucke V, Ioffe S, Shlens J, Wojna Z (2015) Rethinking the inception architecture for computer vision. ArXiv preprint: 1512.00567
[4] Yi D, Sawyer R, Cohn III D, Dunnmon J, Lam C, Xiao X, Rubin D (2017) Optimizing and visualizing deep learning for benign/malignant classification in breast tumors. ArXiv preprint: 1705.06362
[5] Setiawan AS, Wesley J, Purnama Y (2015) Mammogram classification using law's texture energy measure and neural networks. Procedia Computer Science 58: 92–97

Radiomics association of MRI texture features with spondyloarthritis and sacroiliitis

A. P. Magalhães Tenorio[1], M. Calil Faleiros[2], J. Raniery Ferreira Junior[2], V. Faeda Dalto[1], R. Luppino Assad[1], H. Yoshida[3], M. H. Nogueira-Barbosa[1], P. M. Azevedo-Marques[1]
[1]University of São Paulo, Ribeirão Preto Medical School, Ribeirão Preto, Brazil
[2]University of São Paulo, São Carlos School of Engineering, São Carlos, Brazil
[3]Harvard Medical School, Massachusetts General Hospital, Boston, United States

Keywords Radiomics · Spondyloarthritis · Sacroiliitis · Quantitative image analysis

Purpose

Spondyloarthritis (SpA) comprises a set of diseases sharing common clinical manifestations, such as inflammatory axial pain, enthesopathies, and peripheral arthritis. The Assessment of Spondyloarthritis International Society (ASAS) Group classification criteria for axial SpA introduced sacroiliac joints active inflammation (sacroiliitis) assessed using Magnetic Resonance Imaging (MRI) as one of the most important criteria in the classification of SpA. Furthermore, therapy decision considers, among other factors, the subtype of the SpA, which makes the diagnosis and subclassification of SpA crucial for treatment [1]. Recently, radiomics has emerged as a promising approach to improve diagnosis and to provide therapy decision support for precision medicine. Radiomics consists of the massive extraction of quantitative features from medical images and their association with clinical outcomes [2]. The main objective of this study is to evaluate the use of radiomics to aid the diagnosis and therapy decision of SpA by associating quantitative MRI texture features with the outcomes of presence of sacroiliitis, diagnosis of SpA, and subclassification in axial or peripheral SpA.

Methods

Our institutional research board approved this retrospective study with a waiver of patients' informed consent. MRI exams of 47 patients were used in this study after anonymization. From each MRI exam, we selected 6 consecutive images in the coronal plane acquired with fluid sensitive technique. Each image was manually segmented by a musculoskeletal radiologist and processed by the warp geometric transform to reduce noise [3]. Texture features were extracted from each MRI image and categorized as: gray-level Histogram, Haralick, Tamura, Fourier, Gabor, Wavelet, and Fractal. Each exam was characterized by the mean and standard deviation of each feature for the 6 images, totalizing 230 features.

Quantitative image features were first assessed univariately by the Mann–Whitney *U* test for the association with presence of sacroiliitis (S+ or S−), diagnosis of SpA (SpA or Other Pathology), and subtype of SpA (Axial or Peripheral). Diagnoses were obtained from patient's records using the ASAS criteria [1, 4]. Quantitative image features were also assessed multivariately by a machine learning model based on the ReliefF feature selection method and an Artificial Neural Network (ANN) [5]. This model finds the highest performance for the combination of x selected features and y ANN neurons, where x varied from 1 to all 230 features and y varied from 1 to the number of samples of the majority outcome group. Association was assessed by the area under the receiver operating characteristic curve (AUC) using the leave-one-out cross-validation method.

Results

The univariate analysis showed that the Tamura_D11_SD feature yielded the highest overall performance in distinguishing the diagnostic outcomes with AUC equal to 0.97 (association with axial SpA and peripheral SpA, $p < 0.0001$). Histogram_Skewness_M feature yielded the highest performance to identify the presence of inflammation in the sacroiliac joints with AUC of 0.86 ($p < 0.0001$). Tamura_D11_SD feature also yielded the highest associative performance in differentiating SpA from other pathologies with AUC of 0.80 ($p < 0.001$) (Table 1).

Table 1 Highest AUC values obtained by the univariate and multivariate analyses

Outcome	Univariate analysis	Multivariate analysis
Sacroiliitis presence (S+ vs. S−)	0.86 (Histogram_ Skewness_M)	0.96 (25 n + 59 f)
SpA diagnosis (SpA vs. other)	0.80 (Tamura_D11_SD)	0.83 (18 n + 32 f)
SpA subtype (Axial vs. peripheral)	0.97 (Tamura_D11_SD)	0.99 (5 n + 26 f)

Feature and number of ANN neurons (n) + number of features (f) that yielded the highest performance are shown in the parentheses

On the other hand, the multivariate analysis, using the ANN and the most relevant attributes (according to the ReliefF method), was able to increase the AUC value by 0.10 units (sacroiliitis presence) as shown in Table 1. However, the AUC values were similar to those of the univariate analysis, especially for SpA subtype with a difference of only 0.02.

Conclusion

MRI analysis to SpA diagnosis may be a difficult task. To potentially improve the diagnosis of these pathologies and their therapy decision, this work applied radiomics techniques by extracting 230 quantitative MRI texture features and associate them with clinical diagnostic outcomes of SpA. Statistical and machine learning analyses were performed to assess the associative performance of the features across the different SpA outcomes.

Histogram_Skewness_M feature presented high association with sacroiliitis presence and Tamura_D11_SD feature with SpA diagnosis and subtypes. In contrast, combining several different quantitative MRI texture features into a machine learning model presented highest associative performance for sacroiliitis and SpA diagnostic outcomes. Several different disease patterns from the Other Pathology group may have interfered with the SpA diagnosis association due to the low AUC values. Further investigation is necessary to improve its associative performance and aid the diagnosis and therapy decision of SpA.

Acknowledgements

We thank CAPES, CNPq, FAPESP, and FAEPA-HCFMRP-USP for financial support.

References

[1] Sieper J, Rudwaleit M, Baraliakos X, Brandt J, Braun J, Burgos-Vargas R et al. (2009) The Assessment of Spondyloarthritis international Society (ASAS) handbook: a guide to assess spondyloarthritis. Annals of the Rheumatic Diseases 68(Suppl 2): ii1-ii44.

[2] Gillies R, Kinahan P, Hricak H (2016) Radiomics: Images Are More than Pictures, They Are Data. Radiology 278(2): 563–77.
[3] Faleiros MC, Ferreira Junior JR, Jens EZ, Dalto VF, Nogueira-Barbosa MH, Azevedo-Marques PM (2018) Pattern Recognition of Inflammatory Sacroiliitis in Magnetic Resonance Imaging. Lecture Notes in Computational Vision and Biomechanics 27: 639–644.
[4] Rudwaleit M, Heijde D, Landewé R, Akkoc N, Brandt J, Chou CT et al. (2011) The Assessment of SpondyloArthritis international Society classification criteria for peripheral spondyloarthritis and for spondyloarthritis in general. Annals of the Rheumatic Diseases 70: 25–31.
[5] Ferreira Junior JR, Cipriano F, Fabro A, Koenigkam-Santos M, Azevedo-Marques, PM (2018) Radiomics-based recognition of metastatic and histopathological patterns of lung cancer. Lecture Notes in Computational Vision and Biomechanics 27: 613–623.

Recognition algorithm of anatomical skeleton in a bone scintigram

T. Kanamori[1], A. Saito[1], S. Hanaoka[2], S. Higashiyama[3], J. Kawabe[3], S. Shiomi[3], A. Shimizu[1]
[1]Tokyo University of Agriculture and Technology, Institute of Engineering, Koganei, Japan
[2]The University of Tokyo Hospital, Department of Radiology, Bunkyo, Japan
[3]Osaka City University, Department of Nuclear Medicine, Graduate School of Medicine, Osaka, Japan

Keywords Skeleton · Multi-atlas segmentation · Bone scintigram · Prostate cancer

Purpose

A bone scintigram is effective in detecting bony metastases of prostate cancer [1]. Several papers have proposed computer aided diagnosis (CAD) systems for assisting metastasis detection [2–4], in which precise recognition of an anatomical skeleton is essential for cancer staging. Sadik et al. proposed an algorithm segmenting four skeletons using an active shape model [2]. As the algorithm uses a single model of four skeletons, it might fail in segmentation in a scenario where the skeleton shape differs from the model. Kikuchi et al. [3] presented a method using a nonlinearly deformed skeleton atlas to recognize skeletons of a test case. However, this method, too, suffers from the difference in shape between the atlas and the case with atypical skeleton shape.

This paper proposes a novel method to recognize skeletons in bone scintigrams. The method is multi-atlas based segmentation [5] of multiple bones, in which multiple atlases of 15 bones are used to recognize a skeleton in a scintigram. We apply the proposed method to 103 cases and discuss its effectiveness.

Methods

The inputs are a bone scintigram and a database composed of pairs of a bone scintigram and corresponding manually delineated anatomical labels, named "atlas" in this paper. The proposed algorithm to recognize 15 bones in a bone scintigram is as follows.

<u>Spatial standardization</u>
The algorithm spatially standardizes the input scintigram and those in the database simultaneously. The process consists of three steps: body axis correction, affine transformation, and free-form deformation, to align all scintigrams in the database to the input one.

<u>Deformation of multiple atlases based on the spatial standardization</u>
All anatomical labels in the database were deformed using the results of the spatial standardization.

<u>Removal of hot spots</u>
Given that hot spots with high accumulation make the next atlas matching process fail, we estimated hot spot regions approximately and removed such regions from the input scintigram.

<u>Atlas matching for each bone</u>
All anatomical labels in the database were aligned to the input scintigram. To this end, template matching between the input scintigram and those in the database was employed. The evaluation value used in the template matching was normalized mutual information (NMI). The location with the maximum NMI was identified. The multiple anatomical labels of each bone in the database were transformed based on the template matching. This process works well for large bones, such as a cranial bone and ribs, but fails for small bones, e.g., cervical vertebrae. Therefore, we proposed a conditional template matching for small bones, in which conditional labels are generated based on the results of template matching of neighboring large bones, e.g., a skull for cervical vertebrae.

<u>Probabilistic atlas based recognition</u>
Pixel-wise recognition of an anatomical skeleton was carried out by a weighted majority vote based on the aligned anatomical labels.

<u>Inverse transformation of spatial standardization</u>
Inverse transformation of the spatial standardization was applied to obtain the results corresponding to an original scintigram.

Results

We applied the proposed algorithm to bone scintigrams of 103 cases and evaluated the performance as the Jaccard Index (JI) between a segmented region of each bone and its manually delineated true label. The size of a scintigram is 512 $\times$ 1024 pixels and the pixel size is 2.8 mm.

Figure 1 shows an example of skeleton segmentation with true labels of bones. As shown in the subtraction image between the segmentation result and corresponding true labels, the difference is small enough for cancer staging. The average JI of 15 bones in this case was 0.847. Figure 2 presents JIs of 103 cases evaluated by a leave-one-out method. The average was 0.800, which was satisfactory on average, because the inter-observer variation of JIs of true labels was approximately distributed from 0.7 to 0.8. However, the results of several bones, such as scapula and humerus, indicate low JIs, which will be tackled in the near future.

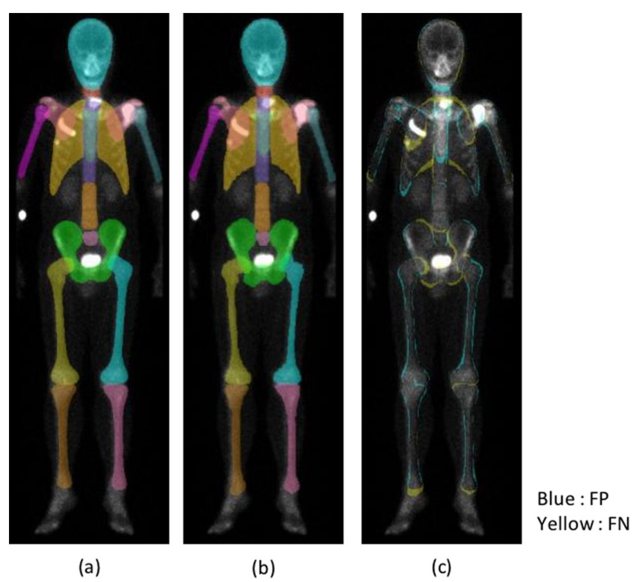

Fig. 1 **a** Segmentation result, **b** true labels, and **c** subtraction image between (**a**) and (**b**)

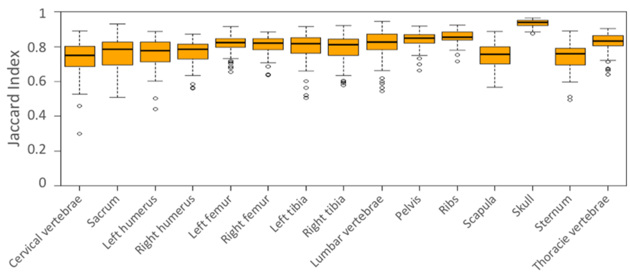

Fig. 2 JIs of segmentation results of 15 bones evaluated by the leave-one-out method

Conclusion

This paper proposed a skeleton segmentation algorithm of a bone scintigram. We applied the algorithm to scintigrams of 103 cases and demonstrated the effectiveness.

References

[1] Maffioli L, Florimonte L, Pagani L, Butti I, Roca I (2004) Current Role of Bone Scan with Phosphonates in the Follow-Up of Breast Cancer. European Journal of Nuclear Medicine and Molecular Imaging 31 Suppl 1: S143–S148

[2] Sadik M, Hamadeh I, Nordblom P, Suurkula M, Hoglund P, Ohlsson M, et al. (2008) Computer-assisted interpretation of planar whole-body bone scans. Journal of Nuclear Medicine 49(12): 1958–65

[3] Kikuchi A, Onoguchi M, Horikoshi H, Sjöstand K, Edenbrandt L (2012) Automated segmentation of the skeleton in whole-body bone scans: influence of difference in atlas. Nuclear Medicine Communications 31(9): 947–953

[4] Minami Y, Saito A, Nemoto M, Hanaoka S, Higashiyama S, Kawabe J, Shiomi S, Shimizu A (2017) Detection of Abnormal Accumulations on a Bone Scintigram Utilizing Anatomical Structure Information. IFMIA P2-19

[5] Iglesias JE, Sabuncu MR (2015) Multi-atlas segmentation of biomedical images: A survey. Medical Image Analysis 24(1): 205–219

Detection of bone metastasis in a scintigram using U-Net

H. Wakabayashi[1], A. Saito[1], S. Higashiyama[2], J. Kawabe[2], S. Shiomi[2], A. Shimizu[1]
[1]Tokyo University of Agriculture and Technology, Institute of Engineering, Koganei, Japan
[2]Osaka City University, Department of Nuclear Medicine, Graduate School of Medicine, Osaka, Japan

Keywords Detection support · U-net · Bone metastasis · Bone scintigram

Purpose

Prostate cancer is the third most frequently diagnosed type of cancer in males and is becoming a health priority in Japan. Bone scintigraphy is an effective nuclear medicine imaging technique to find bone metastasis occurring in prostate cancer patients. Quantification of the bone metastasis and differentiation of multiple benign osteolytic lesions from bone metastases are important considerations. To assist the detection and quantification of bone metastases, several papers have proposed a computer-aided diagnosis (CAD) system of bone metastasis in a scintigram [1, 2]. BONENAVI is a commercially available CAD system whose sensitivity was reported to be 83% [1], and a bone metastasis detection algorithm with a sensitivity of 95% has also been presented [2]. However, these methods result in many false positives (FPs), including benign lesions, leading to lower accuracy of quantification techniques such as bone scan index (BSI) [3].

This paper presents an algorithm to detect bone metastases in a bone scintigram using U-Net [4]. Subsequently, we report the results of applying the algorithm to bone scintigrams and discuss its effectiveness.

Methods

The proposed algorithm consists of two steps, namely, bone segmentation and bone metastases detection. Multi-atlas segmentation [5] was employed to extract bone regions from a scintigram. The extracted bone regions were used as a region of interest (ROI) in the second stage, in which U-net detected bone metastases from the ROI. U-net classified each pixel into two classes, namely, malignant hot spot (indicating bone metastasis) and other accumulations including benign hot spot (e.g. fracture and background).

Network Architecture

The network architecture of U-Net is shown in Fig. 1. The input and output were patch images of size 64 × 64 [pixels] because of the limitation of memory size in a GPU for training. Note that an original bone scintigram of size 512 × 1024 [pixels] was divided into patch images, and output patch images were tiled to reconstruct the detection result of a whole scintigram. After density normalization and convolution by 3 × 3 [pixels], a combination of bottleneck and max pooling was applied four times followed by bottleneck. Subsequently, a combination of deconvolution and bottleneck was performed four times followed by convolution of 1 × 1 [pixel]. The channel number and image size of each layer are presented in the figure.

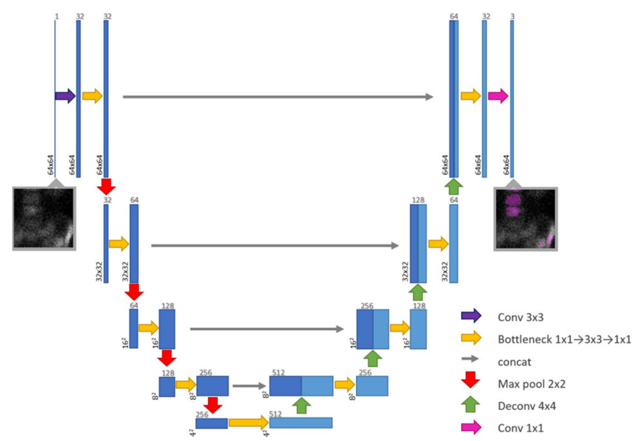

Fig. 1 U-Net architecture. Blue box denotes a multi-channel feature map. The number of channels and size of feature map are presented on the top and left of the box

Training

The following loss function was employed to optimize the network in the training process, in which softmax cross entropy was used:

$$Loss = -1/N \sum_{i=1}^{N} t_i log(p_i),$$

$$p_i = softmax(y_i) = e_i^y / \left(\sum_{i=1}^{N} e_i^y \right),$$

where N is the total number of classes, i denotes class index, t_i denotes true label, and p_i is the probability of output y_i.

Seventy images were used for training, and 8.1×10^6 patch images were generated in total, where 4.0×10^6 patch images corresponded to malignant hot spots. The Adam algorithm with parameters ($\alpha = 0.001$, $= 0.9$, $= 0.999$) was used for training, and size of the batch was 64.

Results

We applied the proposed algorithm to 23 test images. Parameters of the network as well as the number of iterations of training were experimentally decided using a validation dataset which includes 10 images consisting of 1.2×10^6 patch images and 5.0×10^5 patch images of malignant hot spots. Performance of the algorithm was evaluated in terms of sensitivity and number of FPs per image. Note that sensitivity is a percentage of malignant hot spots in which one or more pixels is detected, and FP is an 8-connected component that consists of pixels of other accumulation classes only.

Figure 2 presents detection results, where the left figure shows the result with a small number of FPs and the right figure presents the result with several FPs. On an average, sensitivity was 91% and the number of FPs was 9.17 per image, which is nearly one-sixth of that of CAD [2].

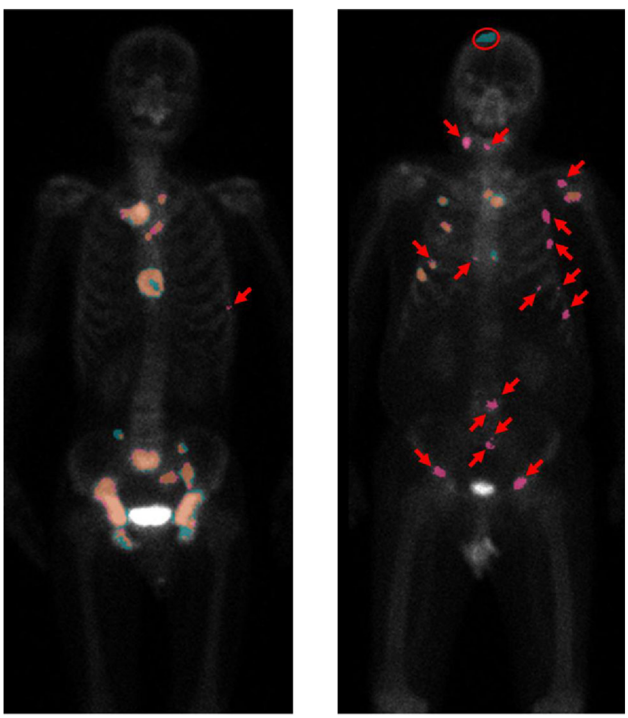

(a) Case 1 (Sensitivity = 1.0, #(FP)=1) (b) Case2 (Sensitivity = 0.88, #(FP)=16)

Fig. 2 Detection results with (**a**) small and (**b**) large number of FPs. Colors of each pixel mean as follows: brown for true positive, pink for FP and blue for false negative. A red circle corresponds to a false negative of malignant hot spot and red arrows indicate FPs

Conclusion

This paper presented a detection algorithm of bone metastasis from a scintigram, in which U-Net played an important role. The algorithm was trained using 70 images, and the performance was evaluated using 23 test images in terms of sensitivity and number of FPs. It was found from the results that the number of false positives was significantly smaller than that of CAD [2] while keeping the sensitivity at the same level. We concluded that the algorithm was effective in detecting malignant hot spots in a bone scintigram.

References

[1] Koizumi M, Miyaji N, Murata T, Motegi K, Miwa K, Koyama M, Terauchi T, Wagatsuma K, Kawakami K, Richter J (2015) Evaluation of a revised version of computer-assisted diagnosis system, BONENAVI version 2.1.7, for bone scintigraphy in cancer patients. Annals of Nuclear Medicine 29(8): 659–665

[2] Minami Y, Saito A, Nemoto M, Hanaoka S, Higashiyama S, Kawabe J, Shiomi S, Shimizu A (2017) Detection of Abnormal Accumulations on a Bone Scintigram Utilizing Anatomical Structure Information. International Forum on Medical Imagin in Asia P2-19

[3] Anand A, Morris MJ, Kaboteh R, Båth L, Sadik M, Gjertsson P, Lomsky M, Edenbrandt L, Minarik D, Bjartell A (2016) Analytic Validation of the Automated Bone Scan Index as an Imaging Biomarker to Standardize Quantitative Changes in Bone Scans of Patients with Metastatic Prostate Cancer. Journal of Nuclear Medicine 57(1): 41–45

[4] Ronneberger O, Fischer P, Brox T (2015) U-net: Convolutional networks for biomedical image segmentation. Medical Image Computing and Computer-Assisted Intervention MICCAI 2015, Springer 9351: 234–241

[5] Iglesias JE, Sabuncu MR (2015) Multi-atlas segmentation of biomedical images: A survey. Medical Image Analysis 24(1): 205–219

Artificial intelligence aided detection and diagnosis of ground-glass opacity nodules

D. Yuan[1], W. Du[2], J. Wang[1], X. Duan[1], Y. Ma[3], H. Zhang[3]
[1]Tianjin Polytechnic University, Tianjin, China
[2]Kyoto Institute of Technology, Kyoto, Japan
[3]Tianjin Chest Hospital, Tianjin, China

Keywords Artificial intelligence · Detection and diagnosis of ground · Interface · GGO nodules

Purpose

Morbidity and mortality of lung cancer are the top in all malignancies. Moreover, lung cancer is difficult to be treated and the cost of treatment is high [1]. But survival rate of lung cancer will increase if lung cancer is found during the early stages. Therefore, it is important to find the benign or malignant of lung nodules in the early stages. Especially, the benign or malignant of ground–glass opacity (GGO) nodules, which are a type of lung nodules, are difficult to be judged. Additionally, Computed Tomography (CT) as the main ways of detection and diagnosis of lung nodules can generate many slices with different parameters to one person. Radiologists will take a lot of workload. To reduce radiologists' burden, this study proposes an interface that can obtain features of lung nodules to detect or diagnose the benign or malignant of lung nodules by assistance of Artificial Intelligence (AI) [2].

Methods

The flowchart of the proposed interface is showed (Fig. 1) as below. 1. The similar nodules are obtained by assistance of AI. 2. A radiologist gives a label to a lung nodule [3] based on 1 and the number of slices including lung nodules are obtained. 3. Lung nodules are segmented after confirmation of the number of slices including lung nodules by a radiologist. (4) The features of lung nodules such as GGO nodules are computed by statistics method.

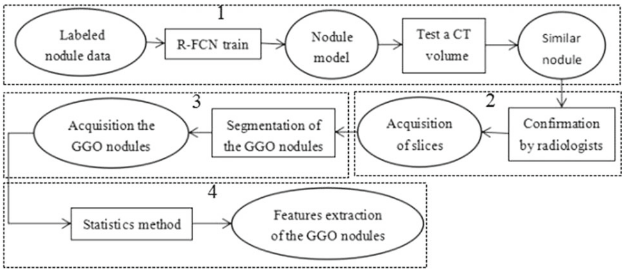

Fig. 1 A flowchart of the GGO nodules detection and diagnosis

R-FCN [4] is one of AI to detect the similar nodules. R-FCN includes the steps of train and test. In the step of train, 1244 lung nodules distributed 800 cases from LIDC-IDRI were as the training data. The diameters of the lung nodules are from 5 to 30 mm which can be distributed from 4 pixels to 56 pixels. The lung nodules had been labeled by 4 experience radiologists. In the step of test, 21 lung nodules distributed 21 cases from Tianjin Chest Hospital. Some lung nodules are GGO nodules. Features were extracted by using ResNet50 in the step of train. The time of iteration is 40,000. 12 h were used for training. Specification of workstation is NVIDIA Tesla K40 GPU Memory 12G.

Results

The proposed interface was showed in Fig. 2.

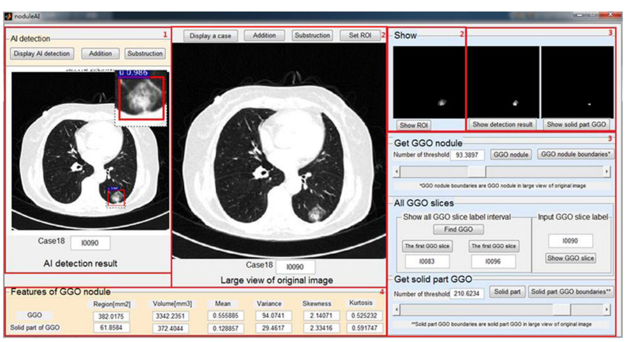

Fig. 2 The proposed interface that can obtain features of lung nodules to detect or diagnosis the benign or malignant of lung nodules by assistance of AI

Section1: The slice of one person with the similar nodule was obtained by assistance of AI. "Display AI detection" was to load all slices and showed them. "Addtion" and "Substruction" were to the previous and next page of the current slice with the similar nodule.

Section 2: One volume data was loaded by "Display a case" to one person. "Addtion" and "Substruction" were to the previous and next page of the current slice with the similar nodule. A radiologist gave a boundary named label by "Set ROI". The part of the label was showed by "Show ROI".

Section 3: The boundary of the whole GGO nodule can be adjusted by the threshold which can be changed by the slider. The boundary of the whole GGO nodule can be obtained as the habit of the radiologist and showed by "GGO nodule boundaries". Range of the slices including the GGO slices can be obtained by "Find GGO". The boundaries of the solid part of GGO nodule can be adjusted by the slider.

Section 4: The features of the whole GGO nodule and solid part of GGO nodule can be obtained. The features included region, volume, mean, variance, skewness and kurtosis of the whole GGO nodule and solid part of GGO nodule. The features can give a reference and help radiologists to judge the benign or malignant of lung nodule.

Conclusion

An interface has been proposed and obtained obtain features of lung nodules to detect or diagnose the benign or malignant of lung nodules by assistance of AI. The merits of the proposed interface:

1. The boundaries of the whole GGO nodule and solid part of GGO nodule can be obtained as the habit of the radiologist.
2. Give the radiologist a reference to find the slices including the whole GGO nodule. Thus, the proposed interface can reduce the burden of doctors.
3. The proposed interface is easy to be operated.

References

[1] Sheehan J, Kondziolka D, Flickinger J, Lunsford LD (2005) Radiosurgery for patients with recurrent small cell lung carcinoma metastatic to the brain: outcomes and prognostic factors [J]. Journal of Neurosurgery, 102 Suppl: 247
[2] Ding J, Li A, Hu Z, Wang L (2017) Accurate Pulmonary Nodule Detection in Computed Tomography Images Using Deep Convolutional Neural Networks [J]: 559–567
[3] Du W, Yuan D, Duan X, Wang J, Ma Y, Zhang H (2017) Development of an interface for volumetric measurement on a ground-glass opacity nodule, Computer and Information Science Volume 719 of the series Studies in Computational Intelligence pp 207–217
[4] Dai J, Li Y, He K, Sun J (2016) R-FCN: Object Detection via Region-based Fully Convolutional Networks

Poster Session

24th Computed Maxillofacial Imaging Congress

Collision detection from force/torque information using a neural network

S. Y. Woo[1], S. J. Lee[1], J. Y. Yoo[1], W. J. Yi[2]
[1]Seoul National University, Department of Biomedical Radiation Sciences, Graduate School of Convergence Science and Technology, Seoul, South Korea
[2]Seoul National University, Department of Oral and Maxillofacial Radiology and Dental Research Institute, Seoul, South Korea

Keywords Collision detection · bone reposition · Force/torque sensor · Neural network

Purpose

Bone reposition or reduction is surgical procedure for correcting and treating the bone segment. This surgical operation involves positioning of the bone segment in oral and maxillofacial surgery [1] or orthopedic surgery [2]. Conventional procedure depends on manual reposition and fixation by surgeons. Recently, state-of-art methods and techniques have been applied to avoid clinical complications and error. Several robot-assisted systems have been reported for reposition procedures such as joint fracture surgery [2] and orthognathic surgery [3] for improving surgical outcomes. These systems, however, consisted of mechanical components, they lacked of tactile information during manipulation tasks. While surgeon repeatedly correct the position of the bone segment, it is necessary to aware of the collision area. In this research, we developed a collision area detection algorithm from force/torque information to support surgeons decision and enhance safety issue during bone reposition procedure.

Methods

In this study, we focused on reposition procedure during orthognathic surgery. For simulating the procedure, a test bed of the lab environment has been configured in Fig. 1. A plastic phantom (Sawbone skull phantom, Pacific Research Laboratories Inc., Vashon, WA, USA) with the maxilla and skull composed of separable bone segments to simulate the bone reposition procedure. We developed a robot system consisting of a robot arm with seven degrees of freedom (CyborgLab, Suwon, Korea), a robot motion controller (Precise Automation, Fremont, CA, USA), and a workstation. The movement of the robot arm was controlled by the PC via the robot motion controller. Maxillary bone was connected with the end-effector of robot arm. A six-dimensional force/moment sensor (RFT60-HA01, Robotous, Seongnam, Korea) was placed between the robot and the end-effector, so that the force applied from the maxillary was measured by the sensor.

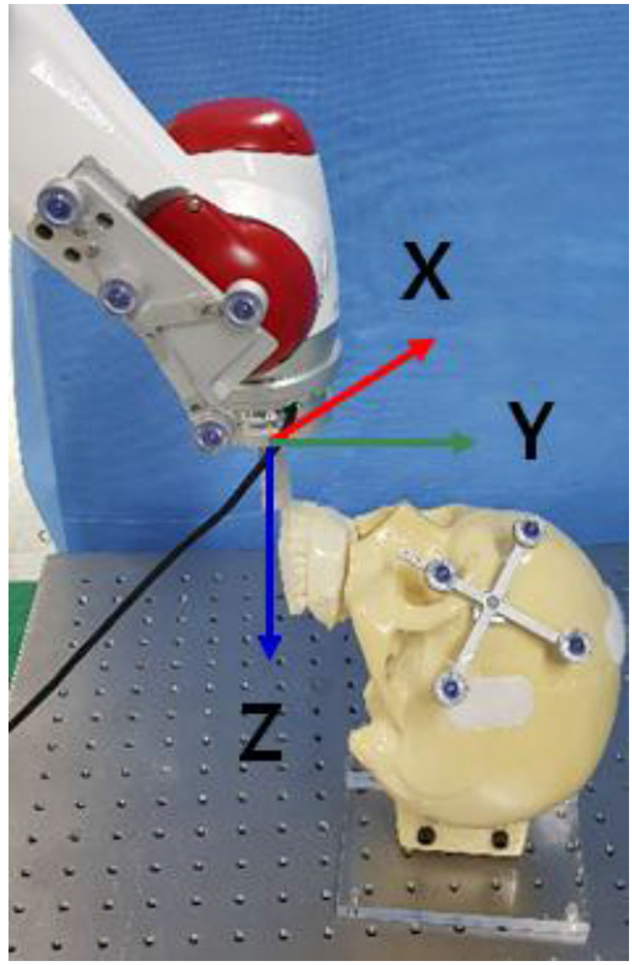

Fig. 1 Robot-assisted bone system with a force/moment sensor for a simulated bone repositoin procedure. The red, green and blue arrows represent the force/moment sensor coordinate system

To estimate the collision position, we constructed a neural network. It has one input layer of six inputs, two hidden layers and one output layer with four outputs. The input consisted of a three-dimensional force vector and a moment vector, respectively, and the output consisted of four quadrants of the contact surface. This contact surface was the cutting plane of the maxilla and received the force and moment during the reposition. The quadrant was set with the center of the contact surface as the origin. In our application, a hyperbolic tangent was used as a smooth non-linearity transfer function and the initial weights were randomly generated for all layers. The momentum and learning rates were chosen by trial and error. Then, we applied force to the quadrant and the force and moment data was measured at the force/moment sensor. The overall net learning rate in the neural network was set to 0.15 and the momentum to 0.5. After the learning of the neural network, validation test of validation test of collision area detection was performed with ten landmarks on cutting surface of the maxilla. We controlled the robot arm to move the maxilla toward the skull. When a collision occurred during the movement, the contact point was calculated using the measured sensor data.

Results

Signals of force and moment were stored and plotted as a graph when a collision was applied to the maxillary bone. When a collision occurs, the data on the x, y and z axes of the force and moment measured from the sensor was shown in the Fig. 2. In the designed neural network, the weighting factor was calculated by using the input data measured by the sensor and the contact points information. After the learning of the neural network, the collided position was determined as one of the quadrants. When forces were applied in all ten landmarks, the estimated collision points were classified in the corresponding quadrant.

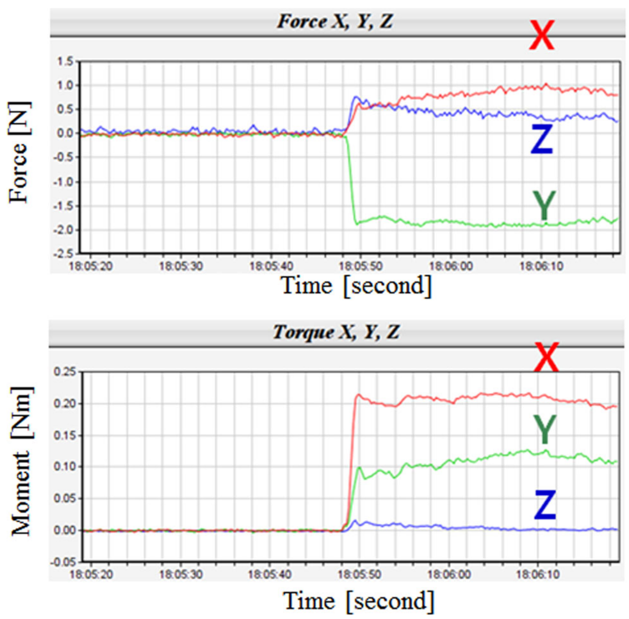

Fig. 2 Force and moment data measured from force/moment sensor

Conclusion

A neural network algorithm of collision area detection was established for enhancing bone reposition procedure by robotic system. Learned network classified direction of collision area after calculating force/moment signals. Using this information, the surgeon can determine the operation, such as cutting the collisional bone part. This technique can be applied in robot-assisted interventions such as bone reposition/reduction and reconstructive surgery. In the future study, we will improve accuracy and precision of this algorithm through optimizing neural network. A phantom and clinical study also will be performed to validate robot-assisted intervention.

Acknowledgments

This work was supported by the Technology Innovation Program (10063389) funded By the Ministry of Trade, Industry & Energy (MOTIE, Korea)

References

[1] Stokbro K, Aagaard E, Torkov P, Bell RB, Thygesen T (2014) Virtual planning in orthognathic surgery. International Association of Oral and Maxillofacial Surgeons, 43: 957–965

[2] Dagnino G, Georgilas I, Tarassoli P, Atkins R, Dogramadzi S (2016) Vision-based real-time position control of a semi-automated system for robot-assisted joint fracture surgery. Int J CARS 11: 437–455

[3] Woo SY, Lee SJ, Yoo JY, Han JJ, Hwang SJ, Huh KH, Lee SS, Heo MS, Choi SC, Yi WJ (2017) Autonomous bone reposition around anatomical landmark for robot-assisted orthognathic surgery. J Craniomaxillofac Surg 45: 1980–1988

Evaluation of atlantodental interval using 3D CBCT images reconstructed from a volumetric rendering program

B. Bilecenoglu[1], K. Orhan[2], B. U. Sakul[3]

[1]Ankara University, Faculty of Dentistry, Department of Anatomy, Ankara, Turkey

[2]Ankara University, Faculty of Dentistry, Department of Oral and Maxillofacial Radiology, Ankara, Turkey

[3]Medipol University, Faculty of Medicine, Department of Anatomy, Istanbul, Turkey

Keywords Atlantodental interval · Cone-beam computed tomography · Atlantoaxial instability · Atlantodental asymmetry

Purpose

The atlantodental interval, including the lateral atlantodental interval (LADI) and anterior atlantodental interval (AADI), has been widely used for the evaluation of atlantoaxial instability [1–3]. However, the sensitivity and specificity of the atlantodental interval, especially the LADI, in evaluating the instability of the atlantoaxial region is still controversial because LADI asymmetry is occasionally found in patients with a few or no symptoms following trauma, and in healthy patients as well. Some authors [2–4] believe that this asymmetry may be a normal variant and is unreliable for detecting atlantoaxial instability, while others [5] consider that LADI asymmetry in patients, following trauma, may represent atlantoaxial rotatory subluxation or fixation. The recent popularity of the use of interbody fusion cages fused to the spine suggests that atlantoaxial lateral mass fusion with the use of a cage could be an alternative treatment for atlantoaxial stabilization when previous surgeries have failed or when regional anatomic variation makes posterior atlantoaxial fusion impossible. However, the exact anatomy of this region together with population difference must be known for developing such techniques. Visualization of the craniocervical region can be obscure and often are hard to diagnose on conventional radiography of the cervical spine. With the growing use of advanced technologies in healthcare and the advent of CT scanners, those anatomical regions can be evaluated easily with 3D imaging. New technological advances in craniofacial imaging have been able to solve these problems and are becoming increasingly popular for use in diagnosis and treatment assessment. Cone-beam computed tomography (CBCT) is a technique that has been proposed for maxillofacial imaging during the last decade and was first reported on in the literature. No studies were found on CBCT imaging with generated 3D skull representations using a surface rendering program to identify and investigate atlantodental intervals. Thus, this study consists of anatomic research of atlantodental interval using 3D CBCT images reconstructed from a volumetric rendering program.

Methods

116 sides of 58 subjects (35 men and 23 women) ranging in age from 22 to 64 years (mean: 37.82) who had craniofacial CBCT scans were retrospectively investigated. CBCT images were taken for various purposes such as pre-implant imaging, paranasal sinus examinations, or orthodontic purposes. CBCT scans were made with Newtom 3G (Quantitative Radiology s.r.l., Verona, Italy). The imaging protocol used a 12-inch field of view to include the entire head anatomy. The axial slice thickness was 0.3 mm, and the voxels were isotropic. The axial images were exported as 512 × 512 matrix in DICOM file format and then were imported in Maxilim® software version 2.3.0. (Medicim, Mechelen, Belgium). A consultant who is experienced on 3D imaging made high-quality 3D hard tissue surface representations are computed from the patients CBCT data set. Measurements of 3D

images were located and marked on the 3D surface rendered volumetric image using rotation and translation of the rendered images. Landmarks were identified by using a cursor driven pointer. The mid-sagittal and mid-coronal image of the dens were chosen for measuring parameters as follows AADI, anterior atlantodental interval; LADI, lateral atlantodental interval; LADI asymmetry: the absolute value of the variance of left LADI and right LADI. All measurements were done 3 times by the same observer and the mean of these measurements was noted for analysis. The observer also performed the study two times with an interval of 2 weeks in order to detect intra-observer variability. To assess intra-observer reliability, Wilcoxon matched-pairs signed-ranks test was used for repeat measurements of the observer. Pearson Chi square and Student t-test were performed for statistical analysis of age, gender, localization and measurements ($p < 0.05$).

Results

Repeated measurement of CBCTs indicated no significant intra-observer difference ($p > 0.05$). Intra-observer consistency was rated at 94.6 percent between two measurements. The AADI was found to be 2.01 ± 0.36 mm in males and 1.82 ± 0.42 mm in females. The AADI was significantly greater in males than in females ($p < 0.05$). Most of the patients have an AADI ranging between 1.0 and 3.0 mm. The left LADI was found to be 3.76 ± 0.62 mm, and the right LADI was 3.48 ± 0.72 mm in males, while the left LADI was 3.54 ± 0.63 mm and the right LADI was 3.57 ± 0.82 mm in females.

Conclusion

The current study shows that LADI asymmetry is common in patients without any cervical spine abnormalities. LADI asymmetry may be a normal anatomic variant in this population and there is no evidence to confirm that LADI asymmetry is a sensitive or specific indicator of traumatic atlantoaxial instability. CBCT can be a powerful tool for examination of this zone with capable of making measurements and 3D representations of the region with less ionizing radiation.

References

[1] Lee S, Joyce S, Seeger J (1986) Asymmetry of the odontoid-lateralmass interspaces: a radiographic finding of questionableclinical significance. Ann Emerg Med 15: 1173–1176.

[2] Mirvis SE (1998) How much lateral atlantodental interval asymmetry and atlantoaxial lateral mass asymmetry is acceptable on an open-mouth odontoid radiograph, and when is additional investigation necessary? AJR Am J Roentgenol 170: 1106–1107.

[3] Monu J, Bohrer SP, Howard G (1987) Some upper cervical spine norms. Spine 12: 515–519.

[4] Sutherland JP Jr, Yaszemski MJ, White AA 3rd (1995) Radiographic appearance of the odontoid lateral mass interspace in the occipitoatlantoaxial complex. Spine 20: 2221–2225.

[5] Ajmal M, O'Rourke SK (2005) Odontoid Lateral Mass Interval (OLMI) asymmetry and rotary subluxation: a retrospective study in cervical spine injury. J Surg Orthop Adv 14: 23–26

Orbital floor reconstruction workflow based on 3D printing and surgical navigation

D. García-Mato[1,2], S. Ochandiano[3,4], M. Tousidonis[3,4], R. Moreta-Martinez[1,2], M. García-Sevilla[1,5], M. Desco[1,5,6,7], J. Pascau[1,5]

[1]Universidad Carlos III de Madrid, Departamento de Bioingeniería e Ingeniería Aeroespacial, Madrid, Spain

[2]Instituto de Investigación Sanitaria Gregorio Marañón, Madrid, Spain

[3]Hospital General Universitario Gregorio Marañón, Servicio de Cirugía Maxilofacial, Madrid, Spain

[4]Universidad Complutense de Madrid, Departamento de Cirugía, Madrid, Spain

[5]Instituto investigación Sanitaria Gregorio Marañón, Madrid, Spain

[6]Centro de Investigación Biomédica en Red de Salud Mental (CIBERSAM), Madrid, Spain

[7]Centro Nacional de Investigaciones Cardiovasculares Carlos III (CNIC), Madrid, Spain

Keywords Orbital fracture · Computer-assisted surgery · 3D printing · Implant

Purpose

Orbital structures are frequently affected in craniofacial trauma. Fractures of the orbital cavity produce modifications of the orbital dimensions, causing changes in the position and function of intraorbital structures. The inadequate treatment can lead to serious complications such as diplopia, enophthalmos, restriction in ocular motility, ocular or orbital dystopia or aesthetic deformities [1].

Multiple surgical techniques have been described in the literature for the treatment of these fractures, proposing different materials for the reconstruction. One of these solutions uses titanium implants. Due to the extremely narrow operating field, the process of positioning the implant in the optimal location within the orbit is operator-dependent and time consuming [2].

In this context, 3D printing and computer-assisted navigation technologies may improve preoperative planning and provide surgical guidance. In the planning phase, 3D printing technology enables the rapid prototyping of precise anatomical templates which can be used to shape and design the implant prior to the surgical procedure [3]. In addition, computer-assisted navigation has been used in orbital reconstruction surgeries in order to improve accuracy and predictability in the results [4]. Although some clinical applications of these technologies have been reported, they are not included in the standard of care for orbital reconstruction mainly due to the lack of flexibility of commercially available software.

In this work, a workflow combining surgical navigation and 3D printed anatomical models and templates for orbital floor fracture reconstruction is presented. Desktop 3D printing and open-source navigation software enable a customized preoperative planning and surgical guidance for each patient. The proposal has been evaluated in a patient presenting an orbital floor fracture.

Methods

A preoperative high-resolution computed tomography (CT) scan of a patient presenting a left orbital floor fracture was acquired. This CT scan was segmented, and virtual models of the affected and unaffected orbits were generated. By mirroring the unaffected orbit's model onto the contralateral side (injured orbit) it was possible to create a new model which will serve as a reference for the orbital reconstruction. These models were 3D printed in polylactic acid (PLA) with a desktop fused deposition modelling device (Witbox-2, BQ, Spain). The resulting models were then used to shape and position the orbit titanium implant. Finally, a CT scan of the 3D model with the implant in-place was then acquired and virtually imported to the surgical navigation software.

Surgical navigation to assist implant positioning was performed using the Polaris Spectra (NDI, Waterloo, Canada) optical tracking system (OTS) and a tracked pointer tool composed of 4 reflective markers. An application was developed in 3D Slicer, a free open-source platform for the analysis and visualization of medical images (Fig. 1). The tracked pointer tool was used by the surgeon to visualize the real-time location of the implant with respect to the preoperative CT image and the virtual anatomical models of the patient.

Fig. 1 Surgical navigation setup (top) and software developed on 3D Slicer platform showing pointer location on CT slice and 3D models (bottom)

Registration of the image dataset to the patient was performed using 4 anatomical landmarks on the face of the patient: lateral and medial canthus of the right eye, glabella, and nasal tip. The skull of the patient was not fixed during surgery and no tracking references were attached to the bone, so the registration process was frequently repeated during surgery to minimize navigation error.

Navigation accuracy was evaluated collecting points along the skin surface of the patient's forehead and on the implant after it was fixated to the orbit. The reference position of the implant was obtained from the postoperative CT scan of the patient, acquired 2 days after surgery. The surgical navigation error was computed as the distance between each collected point to the virtual models of the skin and the implant, respectively.

Results

A total of 548 points were collected on the forehead of the patient during surgery using the tracked pointer tool. An error of 0.31 ± 0.22 mm was obtained for the right side (unaffected) and 0.54 ± 0.39 mm for the left side (injured) (Fig. 2). Moreover, 23 points were recorded on the left orbit implant when it was fixed in the final position obtaining an average error of 2.90 ± 0.96 mm.

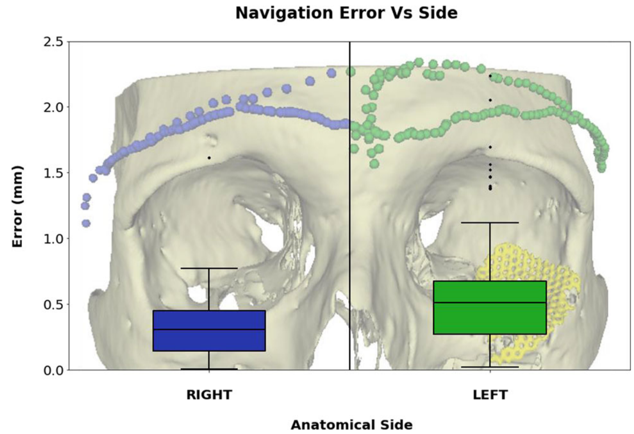

Fig. 2 Navigation error measured in the forehead. Comparison between right and left sides

Conclusion

A workflow based on 3D printing and surgical navigation for orbital floor reconstruction was proposed and evaluated. The use of desktop 3D printing allows for rapid and low-cost production of personalized orbital models which facilitate surgical planning and implant shape definition. The navigation system proved to be a useful addition in orbital floor reconstruction procedures as long as the surgeons were aware of the limitations of the navigation and performed the registration process regularly. Intraoperative navigation was helpful for the surgeons in order to establish orbital symmetry, determine the exact position of the implant and visualize the distance to important anatomical structures, such as the optic nerve.

The main source of error during navigation was the registration procedure, since anatomical landmarks cannot be detected with high accuracy. Moreover, landmarks were located on the contralateral side of the lesion, due to inflammation of the injured orbit, leading to an increased target registration error on the injured orbit. From our initial experience, we think that navigation accuracy could be improved by performing marker-based registration using alternative references or 3D printed models.

References

[1] Manolidis S, Weeks BH, Kirby M, Scarlett M, Hollier L (2002) Classification and surgical management of orbital fractures: experience with 111 orbital reconstructions. The Journal of Craniofacial Surgery 13(6): 726–737

[2] Kozakiewicz M, Elgalal M, Loba P, Komuński P, Arkuszewski P, Broniarczyk-Loba A, Stefańczyk L (2009) Clinical application of 3D pre-bent titanium implants for orbital floor fractures. Journal of Cranio-Maxillofacial Surgery 37(4): 229–234

[3] Metzger MC, Schön R, Schulze D, Carvalho C, Gutwald R, Schmelzeisen R (2006) Individual preformed titanium meshes for orbital fractures. Oral Surgery, Oral Medicine, Oral Pathology, Oral Radiology and Endodontology 102(4): 442–447

[4] Schmelzeisen R, Gellrich NC, Schoen R, Gutwald R, Zizelmann C, Schramm A (2004) Navigation-aided reconstruction of medial orbital wall and floor contour in cranio-maxillofacial reconstruction. Injury 35(10): 955–962

The addition of 3D segmented virtual models in the diagnosis of temporomandibular joint disorders

H. Kohltfarber[1,2], A. Al-Hadidi[3], F. Festy[4], D. Tyndall[2]
[1]Loma Linda University School of Dentistry, Radiology and Imaging Sciences, Loma Linda, United States
[2]UNC-Chapel Hill, Diagnostic Sciences, Chapel Hill, United States
[3]University of Jordan, Amman, Jordan
[4]King's College London, London, United Kingdom

Keywords Temporomandibular joints · 3D virtual models · Cone beam CT · Radiology

Purpose

Temporomandibular joint disorders (TMD) affect many patients worldwide [1]. TMD is a complicated disorder difficult to diagnose and treat. It follows that clinicians need better diagnostic imaging modalities to help not only in the diagnosis and staging of disease but to better monitor treatment. Three-dimensional virtual models can be segmented using cone beam CT data, which may enhance diagnostic decisions within the region of the temporomandibular joints. However, no published efficacy studies were found that evaluated whether diagnostic decisions made with the addition of 3D surface models resulted in a more accurate diagnosis when compared to the actual ground truth. The purpose of this study was to evaluate and compare osteoarthritic changes in a known sample of dry mandibles using multiplanar viewing (MPV) of cone beam CT alone, segmented 3D virtual surface models alone as well as a combination of both imaging modalities together to comparatively analyse the diagnostic efficacy of these technologies.

Methods

An IRB-approved ex vivo study was conducted with a ground truth sample of 38 digitized dry mandibles, with the addition of soft tissue equivalent material, scanned by three different cone beam CT units and subsequently segmented into virtual 3D surface models using both fixed and threshold based segmentation software (n = 114 condyles). Diagnostic efficacy studies with the actual condyles were performed. The modalities compared were MPV cone beam CT, 3D virtual models and a combination of both MPV cone beam CT and 3D virtual models. Five oral and maxillofacial radiologists using the Research Diagnostic Criteria for Temporomandibular Joint Disorders (RDC/TMD) served as observers. Descriptive statistics with sensitivity, specificity and overall accuracy of the modalities was conducted in addition to Chi square analysis to observe differences between imaging modalities and kappa statistics to observe agreement between the ground truth data and the different imaging modalities [2–4].

Results

The 3D virtual modelsused alone or in conjunction with MPV cone beam CT demonstrated a higher sensitivity (70.4 and 61.1% respectively) to the diagnoses of osteoarthritic changes than did the MPV cone beam CT alone (42.6%). However, the MPV cone beam CT used alone or in conjunction with the 3D virtual models demonstrated a higher specificity (81.7 and 80% respectively) for a diagnoses of a healthy temporomandibular joint than did the 3D models alone (73.3%). Accuracy was higher for the 3D models used alone (72%) or in conjunction with MPV cone beam CT (71%) than with the MPV cone beam CT data used alone (63%) when compared to the ground truth (Fig. 1).

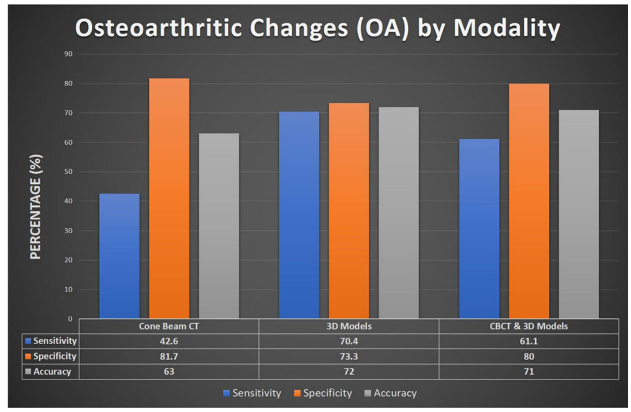

Fig. 1 Bar chart of osteoarthritic changes by imaging modalities

Chi square analysis demonstrated a statistically significant difference between imaging modalities ($p < 0.0001$) and Kappa agreement was stronger for the imaging modalities employing the use of the 3D virtual models than for the use of MPV cone beam CT information alone. In addition, the agreement between the 3D virtual models used alone and those in conjunction with MPV cone beam CT exhibited a substantial kappa agreement (0.698) while the agreement between the MPV cone beam CT alone exhibited only a moderate agreement (0.482) with the other imaging modalities.

Conclusion

The imaging modality using a combination of both MPV cone beam CT and the 3D virtual models exhibited the best combination of sensitivity, specificity and accuracy than using either imaging modality alone when compared to the ground truth data. The kappa statistics revealed that the 3D models better influenced the decision making process leading to a more accurate diagnosis of OA changes than using just MPV cone beam CT alone when compared to the ground truth data.

References

[1] White S, Pharoah M (2008), Oral radiology: principles and interpretation. Elsevier Health Sciences.
[2] Cevidanes LH, Hajati AK, Paniagua B, Lim PF, Walker DG, Palconet G, Nackley AG, Styner M, Ludlow JB, Zhu H, Phillips C (2010), Quantification of condylar resorption in temporomandibular joint osteoarthritis. Oral Surgery, Oral Medicine, Oral Pathology, Oral Radiology, and Endodontology 110: 110–117.
[3] Gomes LR, Gomes MR, Gonçalves JR, Ruellas AC, Wolford LM, Paniagua B, Benavides E, Cevidanes LH (2016), Cone beam computed tomography-based models versus multislice spiral computed tomography-based models for assessing condylar morphology. Oral Surgery, Oral Medicine, Oral Pathology and Oral Radiology; 121: 96–105.
[4] Ahmad M, Hollender L, Anderson Q, Kartha K, Ohrbach R, Truelove EL, John MT, Schiffman EL (2009), Research diagnostic criteria for temporomandibular disorders (RDC/TMD): development of image analysis criteria and examiner reliability for image analysis. Oral Surgery, Oral Medicine, Oral Pathology, Oral Radiology, and Endodontology; 107: 844–860.

Registration of histopathology and micro-CT slices for quantifying periapical lesions in a rat model

K. Orhan[1], U. Aksoy[2], A BuyukSungur[3], G. Savtekin[4], AO Ozsehirli[5], H. Ozkayalar[6]
[1]Ankara University, Dentomaxillofacial Radiology, Ankara, Turkey
[2]Near East University, Endodontics, Mersin 10, Turkey
[3]BIOMATEN and Department of Biotechnology, Middle East Technical University, Ankara, Turkey
[4]Near East University, Oral and Maxillofacial Surgery, Mersin 10, Turkey
[5]Near East University, Basic Health Sciences, Mersin 10, Turkey
[6]Near East University, Pathology, Mersin 10, Turkey

Keywords Micro-CT · Periapical pathology · Fusion · Histopathology

Purpose

There is clinical evidence that as the periapical lesions increase in size, the proportion of the radicular cysts increases [1]. Moreover, the diagnosis of a cyst can be made only by a histological examination. However, a preliminary clinical diagnosis of a periapical cyst can be made if the lesion is greater than 200 mm2 in size, and the lesion is seen radiographically as a circumscribed [2]. It is crucial that the clinician establishes the correct diagnosis to avoid unnecessary treatment of vital healthy teeth. In the meantime, the proximity of the periapical lesion to adjacent vital teeth is also important since, when the periapical lesion is near the apices of vital teeth, adopting a surgical approach may result in injury to the blood vessels and nerves of the adjacent teeth, thereby compromising the vitality. Recently, the development of novel technologies plays an important role in endodontic studies. Micro-CT analyses, as one of the novel three-dimensional (3D) methods, have substantially improved perspectives of endodontic researches about quality of root canal fillings [3]. It is crucial to understand whether the section where the measurement was performed is suitable with respect to bone or even the teeth. The aim of this study is to present a workflow and technique that allow us to integrate 2D information into a 3D micro-CT volume to evaluate and quantify periapical lesions in a Rat Model [4].

Methods

In this study, 3 male Wistar rats (weighting 250–390 g at the beginning of the experiments) were used. The pulps of the mandibular first molars were surgically exposed with a ¼-size round steel bur in high-speed rotation under constant irrigation. Pulps were left open to the oral cavity for 21 days to allow establishment of periapical lesion. After 21 days of periapical lesion induction, the animals were sacrificed by decapitation. The mandibles were then surgically removed, dissected, and fixed in 10% neutral-buffered formalin solution. The samples were demineralized with 5% nitric acid (pH 7.4), which was renewed every 2 days. Paraffin blocks containing the mandibles were serially sectioned with average thickness of 10 10 µm in a mesio-distal plane. Sections were stained with hematoxylin–eosin and examined under light microscopy (200 × magnification). Two histologic slides (4 fields in each) were evaluated for every tooth, which included the root dentin, the apical foramen, and the periapical tissues.

Micro-CT Acquisition

All rat mandibles were scanned with a high-resolution micro CT system (Bruker Skyscan 1275, Kontich, Belgium). The scanning parameters were set at 100 kVp, 100µA, 0.5 mm of Cu filter, 10 µm of pixel size and 0.5 degree of rotation step. To minimize the ring artifacts, air calibration of the detector was carried out prior to each scanning. Each sample was rotated 360° within an integration time of 5 min. The mean time of scanning was around 4 h. Other settings included beam-hardening correction and optimal contrast limits adjustments were done, during the reconstruction step, according to the manufacturers instructions, using the NRecon software (version 1.6.7.2, SkyScan, Kontich, Belgium). In the reconstruction step, the ring artifact correction and smoothing were fixed at zero and the beam artifact correction was set at 40%.

Micro-CT Imaging Analysis

For the 3D volumes, the original grayscale images were processed with a Gaussian low-pass filter for noise reduction and an automatic segmentation threshold was applied using CTAn (ver. 1.16.1.0, SkyScan). A thresholding (binarization) process was used, which entails processing the range of grey levels to obtain an imposed image of black/white pixels only. Then, separately for each slice, a region of interest was chosen to contain a single object entirely to allow the registration on histopathology using a 3D software (3D Synapse, Fuji Film, Japan). Each slice was detected perpendicular to rotation axis and then register match the 3D volume and 2D slice. After registration the loss of bone and density measurements was made from histopathology, Micro-CT Images and fused image. Differences among measurements evaluated using the Kruskal–Wallis test and the Mann–Whitney U-test at a significance level of 5%.

Results

To register a 2D Histopathology image into a 3D micro-CT dataset, a semi-automatic approach was used. A gray scale based approach was used to transform the 2D image. The fine structures both in bone as well also the teeth such as cement/dentin-cement junction was used for fixed standardized points to use the registration method. The initial registrations obtained by applying the thresholds were then improved using a standard image registration method. The whole registration was performed using CTAn, (ver. 1.16.1.0, SkyScan) and 3D software (3D Synapse, Fuji Film, Japan). The whole registration process was visually guided. Once the datasets loaded, the registration was made semi-automatically or manually. If the orientation of the bone was already roughly the same images. A semiautomatic registration tool allowing quantification and comparison of registration quality for periapical lesions in a rat model was defined. The results showed significant differences among measurements from histopathology and fused images with Micro-CT ($p < 0.05$).

Conclusion

In generally, combining different measurement methods and integrating their results into a 3D frame is nowadays a common task to answer specific research questions. Since bone is a mineralized biological tissue, the semi-automatic registration of 2D slices into a 3D volume is crucial especially for evaluating the bone diseases. As a consequence, a semiautomatic registration tool allowing quantification and comparison of registration quality for periapical lesions in a rat model was defined. The periapical lesions can be evaluated the registration result and compare the quality among the different samples.

References

[1] Natkin E, Oswald RJ, Carnes LI (1984) The relationship of lesion size to diagnosis, incidence, and treatment of periapical cysts and granulomas. Oral Surg Oral Med Oral Pathol. 57: 82–94.
[2] Eversole LR (1984) Clinical outline of oral pathology: Diagnosis and treatment. 2nd ed. Philadelphia: Lea and Febiger; p. 203–59.
[3] Guerrero ME, Jacobs R, Loubele M, Schutyser F, Suetens P, van Steenberghe D (2006) State-of-the-art on cone beam CT imaging for preoperative planning of implant placement. Clin Oral Investig 10: 1–7.
[4] Feldkamp LA, Goldstein SA, Parfitt AM, Jesion G, Kleerekoper M. 1989. The direct examination of three-dimensional bone architecture in vitro by computed tomography. J Bone Miner Res 4: 3–11.

Landmark based midsagittal plane analyzing in patients with facial symmetry and asymmetry

A. Dobai[1], T. Vízkelety[1], Z. Markella[2], A. Rosta[3], C. Fouquet[3], J. Barabás[1]
[1]Semmelweis University, Budapest, Hungary
[2]Óbudai University, Budapest, Hungary
[3]Dento-Cura Kft, Budapest, Hungary

Keywords Midsagittal plane · Landmark based cephalometry · Facial symmetry · Facial asymmetry

Purpose
The facial midsagittal plane (MSP) can be generated in different ways. The morphometric calculation is able to determine the real MSP, but it is hard to use in clinical practice. Shin et al. reported that the regression plane based on nasion, anterior nasal spine and posterior nasal spine (N-ANS-PNS) landmarks is nearly same as the morphometric MSP [1]. As these points are vulnerable, the aim of this study was to examine which combinations of landmarks can substitute these points in groups with facial symmetry and asymmetry.
Methods
In this study 60 patients were examined in two groups: I. 30 patients (19 female, 11 male, aged 18–30 years) with facial symmetry, II. 30 patients (18 female, 12 male, aged 20–28 years) with severe facial asymmetry. On CBCT scans 22 cephalometric landmarks (8 unpaired, 7 paired) were detected with CranioViewer software. 35–35 regression planes were generated by the means of unpaired or paired landmarks. By the paired landmarks the midpoints were used to calculate regression planes.

For the reliability the intraclass-correlation coefficient was calculated. In the further investigation the N-ANS-PNS regression plane was used as reference plane, and the angle between the generated regression plane and the reference plane was calculated in group I and II. We described the difference from the reference plane with the mean and standard deviation and contrasted the same angle between the two groups with unpaired t-test. Finally, we selected the regression planes which were the closest to the reference plane in both groups.
Results
The ICC was higher than 0.9. Figures 1 and 2 show the mean angels of the deviation from the reference plane. We classified three groups based on the degree of the angles: 1. lower than 5°, 2. 5–10° 3. > 10°. In the symmetric group by the unpaired points 88% of angles were lower than 5°, comparing to the paired points where 74% were < 5°, 14% of angles were between 5° and 10° and 11% of angles were higher than 10°. All angles except for 3 cases were higher in the asymmetric group than in the symmetric group (Figs. 1, 2).

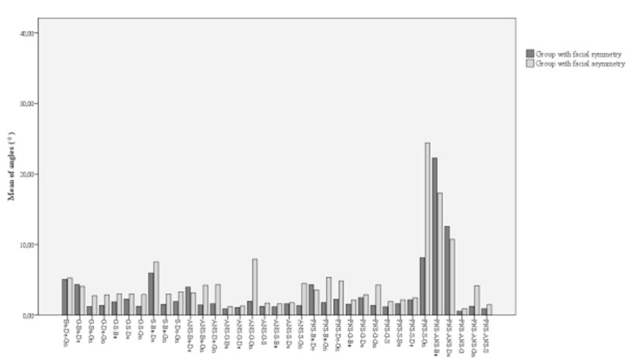

Fig. 1 Means of angles closed by N-ANS-PNS plane and the different regression plane created by cephalometric unpaired points

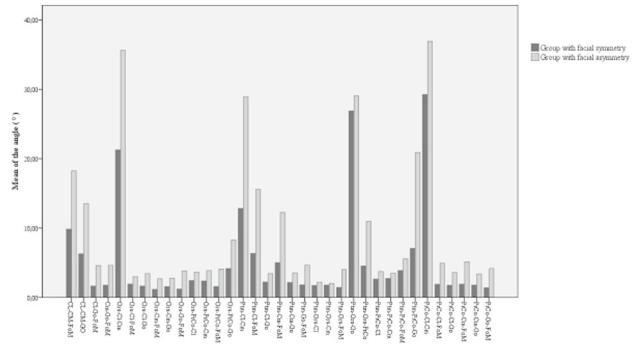

Fig. 2 Means of angles closed by N-ANS-PNS plane and the different regression plane created by cephalometric paired points

The unpaired t-test showed significant differences between the group I and II by 8 from 35 angles generated from midline cephalometric points and by 17 from 35 angles generated from paired points. In all cases the angles were increased in the asymmetric group.

The selection of the ideal planes, which could substitute the N-ANS-ANP plane was made in two steps. We selected the planes, 1. which had low difference (< 2°) from the reference plane, 2. which showed no significant deviation between the symmetric and asymmetric groups. By the regression planes based on unpaired landmarks the following combinations were proper for the criteria: ANS-G-Ba, ANS-G-S, ANS-S-De, PNS-G-Ba, PNS-S-Ba, PNS-ANS-G. By the regression planes based on paired landmarks no angles were lower than 2° in the asymmetric group and those planes showed the highest difference (> 20°) from the N-ANS-PNS plane, which contained lateral or medial condyle or orbitale superior.
Conclusion
The present study provides that the regression plane generated from unpaired cephalometric points are more accurate than the planes from unpaired landmarks. The N-ANS-PNS reference plane, which symbolized the ideal morphometric midplane can be substitute with the following landmarks combination: ANS-G-Ba, ANS-G-S, ANS-S-De, PNS-G-Ba, PNS-S-Ba, PNS-ANS-G.

References
[1] Shin SM, Kim YM, Kim NR, Choi YS, Park SB, Kim YI (2016) Statistical shape analysis-based determination of optimal midsagittal reference plane for evaluation of facial asymmetry. American journal of orthodontics and dentofacial orthopedics 150(2): 252–260.

A pilot study of mandibular reconstruction surgery based on augmented reality using Microsoft HoloLens

P. Sun[1], X. Chen[1], R. Yang[1], T. Ji[1]
[1]Shanghai Jiao Tong University, Shanghai, China

Keywords Mandibular reconstruction · Augmented reality · Microsoft HoloLens · Reconstruction

Purpose
Mandibular defects are common disease in oral and maxillofacial surgery. Most of them are caused by excision of various benign and malignant tumors. Currently, the fibula musculocutaneous flap transplantation is widely used to repair the mandible defect. In the traditional surgery, mandibular reconstruction templates are usually applied to determine the boundaries of resection. However, sometimes the fibula cannot be embedded in the cutting guide for the reason that resection and cutting guides are designed on the basis of

original CT data without considering the soft tissue. This definitely results in deviation which, even worse, may lead to the failure of surgery. Aiming at solving this problem, we attempt to reduce the risk in mandibular reconstruction surgery using augmented reality–an emerging technology which combines the virtual object generated by computer with the real environment and interacts in real time [1].

In this study, we proposed a novel method based on AR in mandibular reconstruction surgery and developed a software using Microsoft HoloLens to guide surgeons to remove the tumor, cut the fibula, and reconstruct the mandible precisely, and a pilot clinical trial was conducted.

Methods

On the basis of Microsoft Visual Studio 2017 and Unity3D 2017, a cross-platform game engine, we developed an AR-based mandibular reconstruction surgery system using Microsoft HoloLens. The key technology involved in it is to accurately map the virtual 3D-reconstructed anatomical models to real one simultaneously even with the user's movement, which is described as follows:

In the beginning, the surface information of the surrounding scenes in the operating room is constructed and the complete perception of the environment is established so that the software can automatically calculate the size and rotation of the virtual model according to the stored environment information with the user's movement [2]. Therefore, the virtual bone models can be anchored steadily in the real environment.

The main procedures of 3D scene reconstruction are as follow:

1. The depth image loaded from the camera is converted into 3D point cloud and the normal vector of each point is calculated.
2. Camera tracking, which is the most important step. Kinect Fusion is a calculated point cloud with a normal vector, and a point cloud projected from the model using the light projection algorithm according to the position of a previous frame. The ICP algorithm is used to calculate the position. The location of the camera is calculated using an environment-aware camera.
3. Based on the location of the camera, the point cloud of the current frame is fused into the grid model.
4. According to the current frame camera location, the ray casting algorithm is used to obtain the point cloud from the perspective of the model, and to calculate its normal vector to match the input image of the next frame.

After constructing the surface of the real-world environment, the distance of the target bones and the HoloLens can be obtained. The monocular SLAM algorithm is used to calculate the position of the camera relative to the scene according to some key feature points during the registration.

Results

A pilot clinical trial was conducted using our system. First of all, a high-solution CT scan of the patient's cranio-maxillofacial anatomy and lower extremities was conducted, and then the DICOM files with an axial slice thickness of 0.6 mm were loaded into the software of Geomagics for 3D-reconstruction and pre-operative planning. The tumor boundaries of the resection can be marked on the surface of the STL model. During the operation, the surgeon wearing the HoloLens (Fig. 1) conducted the registration procedure, and then, the tumor was removed and the fibula was segmented under the guidance of the matching between the virtual models and real ones (Fig. 2).

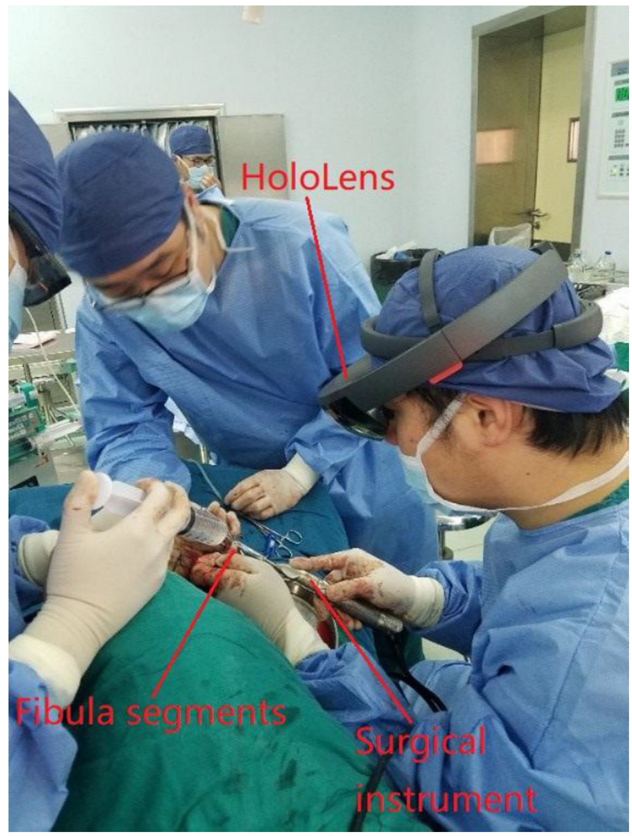

Fig. 1 The surgeon wearing HoloLens was cutting the fibula

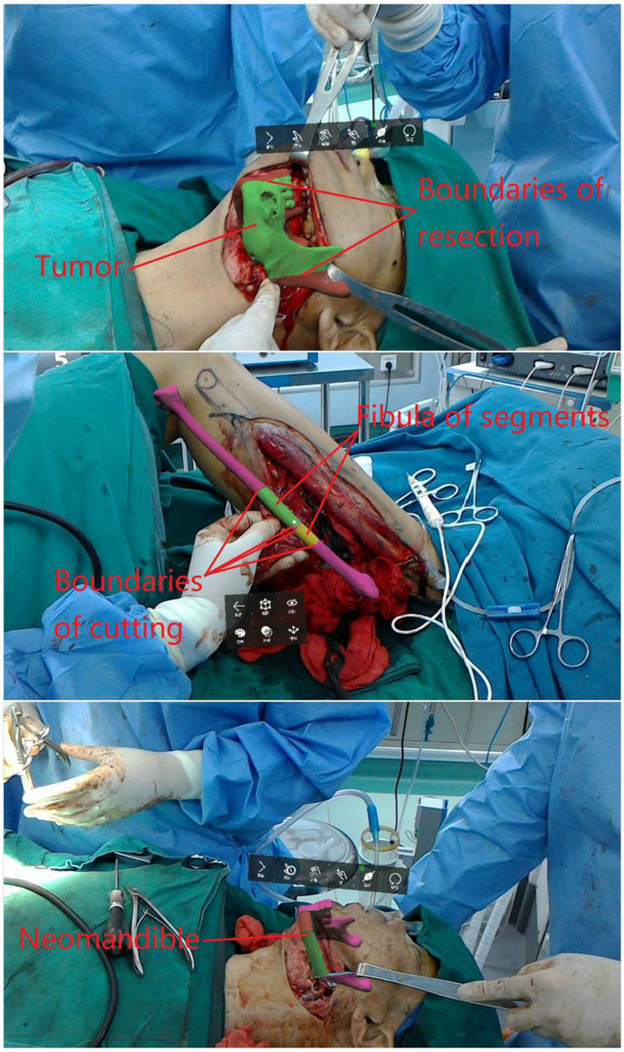

Fig. 2 Three scenes of AR-assisted mandibular reconstruction from the perspective of the surgeon wearing HoloLens

Conclusion

In this study, we proposed a novel AR-based mandibular reconstruction using Kinect Fusion and monocular SLAM algorithm which effectively allows the virtual bone being anchored steadily in the real environment despite of the movement of the surgeon in the operation. A pilot clinical trial was conducted demonstrating it may provide a new effective method for the reconstruction of mandible surgery and reduce the risk.

Acknowledgements

This study was supported by the National Key Research and Development Program of China (2017YFB1302903, 2017YFB1104100), Foundation of Science and Technology Commission of Shanghai Municipality (15510722200, 16441908400), Shanghai Jiao Tong University Foundation on Medical and Technological Joint Science Research (YG2016ZD01, YG2015MS26), and the Interdisciplinary Program of Shanghai Jiao Tong University (project number YG2017QN01).

References

[1] Chen X, Xu L, Wang Y, Wang H, Wang F, Zeng X, Wang Q, Egger J (2015) Development of a surgical navigation system based on augmented reality using an optical see-through head-mounted display. Journal of Biomedical Informatics, 2015, 55(C): 124–131.

[2] Izadi S, Kim D, Hilliges O, Molyneaux D, Newcombe R, Kohli P, Shotton J, Hodges S, Freeman D, Davison A, Fitzgibbon A (2011) KinectFusion: real-time 3D reconstruction and interaction using a moving depth camera [C]//ACM Symposium on User Interface Software and Technology, Santa Barbara, Ca, Usa, October. 2011: 559–568.

An image-guided surgery system for mandibular proximal segment repositioning using electromagnetic tracking technology

S. J. Lee[1], S. Y. Woo[1], J. Y. Yoo[1], M. H. Choi[1], S. R. Kang[1], W. J. Yi[2]

[1]Seoul National University, Department of Biomedical Radiation Sciences, GSCST, Seoul, South Korea

[2]Seoul National University, Department of Oral and Maxillofacial Radiology, School of Dentistry, Seoul, South Korea

Keywords Image-guided surgery · Mandibular proximal segment · Registration · Electromagnetic tracking

Purpose

Orthognathic surgery is a procedure to correct facial structure and dental problems. After mandibular osteotomy, the mandibular proximal segments (MPS) repositioning process was performed. Electromagnetic (EM) tracking system had the advantage of using relatively small tools and being easy to use for tracking internal organs because there was no line-of-sight requirement. In this study, we developed an image-guided surgery system for MPS reposition using EM tracking system. The developed system was also applied to actual surgery patient to perform image guided reposition of MPS (Fig. 1).

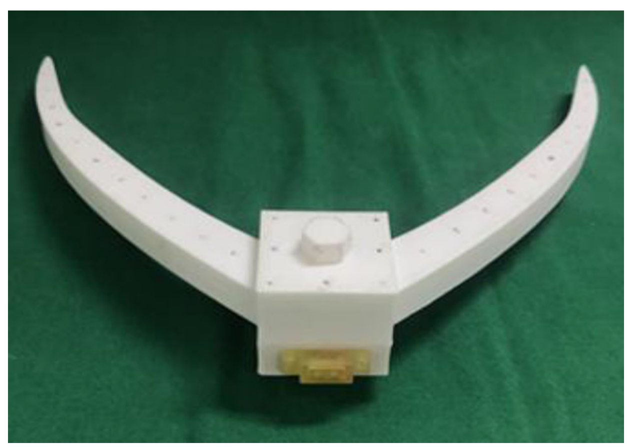

Fig. 1 The reusable registration

Methods

Design of a reusable registration body

The reusable registration body consisted of an upper part with thirty 1-mm diameter ceramic beads with five different depths to be used as fiducial points for registration, a lower part to which the electromagnetic tracking tool was to be fixed, and a screw to fix the upper and lower parts. LEGO block was attached to the bottom of the lower part so that it could be combined with the splints.

Acquisition of CT image

CT images were acquired using MDCT (SOMATOM Sensation 10, Siemens, Munich, Germany) under 120 kVp and 80 mAs conditions with a slice thickness of 0.75 mm.

Virtual model generation and virtual surgery planning

The maxillary, mandibular, MPSs, and the remaining skull models were separated according to the cutting plane used in the actual surgery from the generated virtual skull model using the marching cube algorithm. To obtain MPS models that were transferred to the postoperative position, a virtual surgery planning was performed which followed the actual surgery plan [1, 2].

Preoperative registration

Preoperative registration was performed to match the patient's physical and CT image space using six fiducial points on the registration body. The position of the fiducials on the physical space were measured using the indicator of the EM tracking system (Aurora, Northern Digital Inc., Ontario, Canada) with respect to the tracking tool on the splint. The measured positions were then matched to the corresponding positions on the image space by point-to-point registration. The transformation between the patient's physical and the image space was derived as a result of the matching (M_{reg} in Eq. 1).

Reposition of mandibular proximal segments

(1) Before surgery, a reference tracking tool was fixed to the patient's skull to exclude head movement during surgery [2]. The tracking tool was fixed to the splint as the same geometrical position as in the preoperative registration procedure. (2) The relative position of the reference tracking tool with respect to the tracking tool attached to the splint was recorded and used as a new reference point of preoperative registration. Intraoperative registration process was finished immediately [2]. (3) After removing the registration splint from the patient's maxillary dentition, the tracking tool was separated from the splint and attached to the MPS using a fixation frame. Then, the initial position of the MPS was recorded to use in tracking during repositioning. After detaching the tracking tool from the MPS, bi-maxillary osteotomy and repositioning were performed sequentially. (4) After repositioning of the maxillary and mandibular bone segments, the patient's MPS was recombined with the EM tracking tool. (5) The movement of the patient's MPS was simulated using the (Eq. 1) and the virtual models and pre-defined anatomical landmarks were visualized on the monitoring screen continuously while the MPS was handled freely by a surgeon for repositioning (Fig. 2) [2].

$$T_{PS\_Image} = M_{reg}\left(T^{-1}_{ref\_init} T_{PS\_init}\right)^{-1} T^{-1}_{ref\_physical} T_{PS\_physical} \qquad (1)$$

where $T_{PS\_physical}$ is current position of the MPS tracking tool, $T_{ref\_physical}$ is the current position of the reference tracking tool, T_{PS_init} is the initial position of the MPS tracking tool, and T_{ref_init} is the initial position of the reference tracking tool.

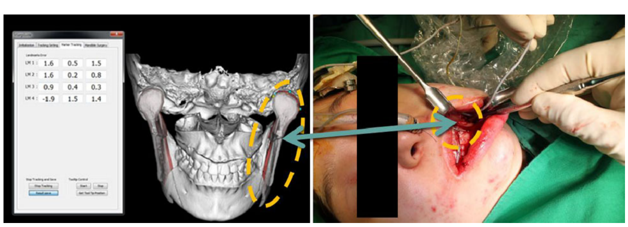

Fig. 2 The patient's left MPS handled freely by a surgeon to reach the planned goal position and the movement of the left MPS was simulated and visualized on the screen continuously during repositioning

Results

A 23-year-old female patient presented with dentofacial deformity. The resulting rotational movements of the maxillary model were 4.5, 2.0 mm at anterior pitch, posterior pitch, respectively. Translational movements were 1.0, 1.0 mm on the x-, y-axes, respectively. The planning was transferred to the patient for left MPS repositioning through image-guided surgery. The intraoperative position of the MPS was continuously tracked and simultaneously visualized on the screen (Fig. 2). Immediately after the repositioning, the mean absolute differences between the planned and by the guidance positions were 1.51 ± 0.44, 0.64 ± 0.58 and 1.03 ± 0.56 mm on the x-, y-, and z-axes, respectively, and the mean RMS difference was 1.94 ± 0.76 mm (Table 1).

Conclusion

In this paper, we have confirmed that our developed system had sufficient accuracy for clinical use and has high potential for various clinical application.

Table 1 Absolute difference in x-, y-, and z-axes, and root mean square (RMS) difference between positions in planning and intraoperative guidance for four left MPS landmarks

Landmarks	Left MPS (mm)		
	x	y	z
1	1.57	0.50	1.51
2	1.66	0.21	0.83
3	0.89	0.36	0.33
4	1.92	1.50	1.45
Mean	1.51 ± 0.44	0.64 ± 0.58	1.03 ± 0.56
RMS	1.94 ± 0.76		

Acknowledgments

This work was supported by the Technology Innovation Program (10063389) funded by the Ministry of Trade, Industry & Energy (MOTIE, Korea)

References

[1] Kim DS, Woo SY, Yang HJ, Huh KH, Lee SS, Heo MS, Choi SC, Hwang SJ, Yi WJ (2014), An integrated orthognathic surgery system for virtual planning and image-guided transfer without intermediate splint, *Journal of Cranio-Maxillo-Facial Surgery*, 42(8): 2010–2017

[2] Lee SJ, Woo SY, Huh KH, Lee SS, Heo MS, Choi SC, Han JJ, Yang HJ, Hwang SJ, Yi WJ (2016), Virtual skeletal complex model- and landmark-guided orthognathic surgery system, *Journal of Cranio-Maxillo-Facial Surgery*, 44(5): 557–568